

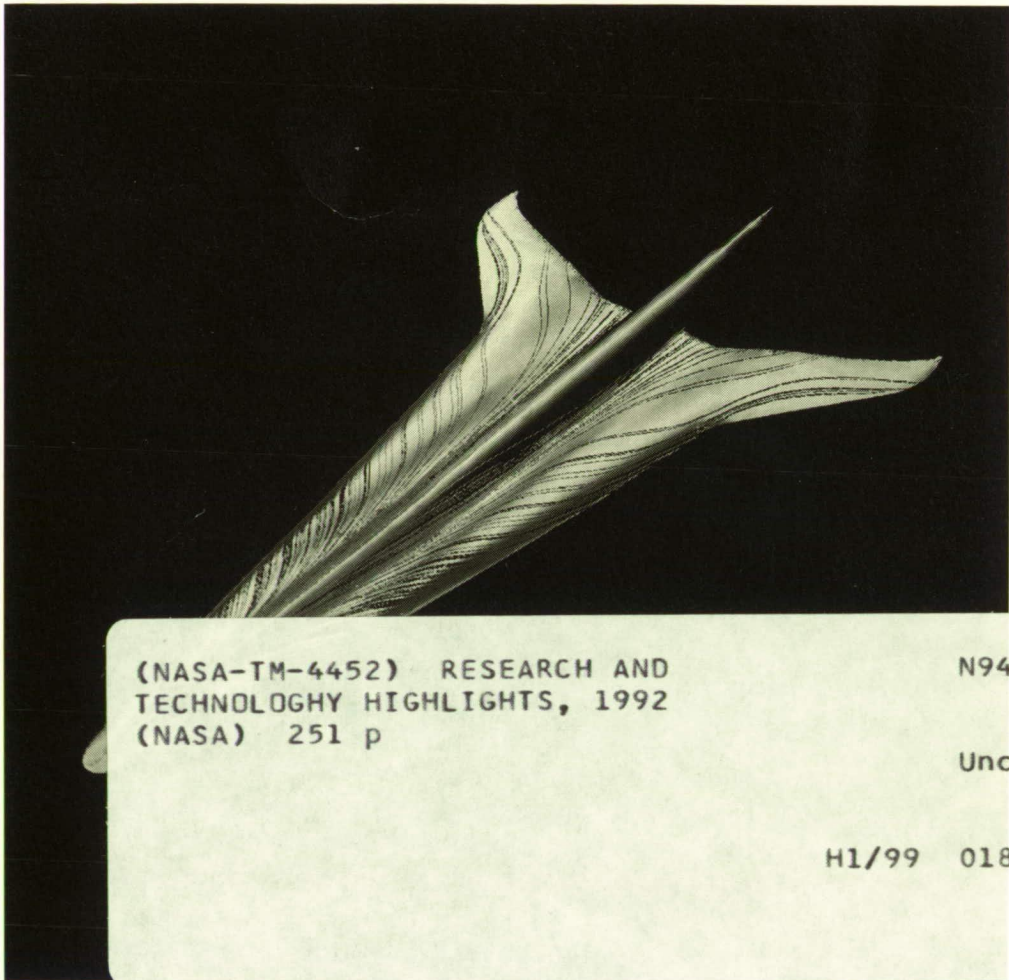
1N-99
187792

NASA-TM-4452

p. 251

44752

RESEARCH AND TECHNOLOGY



(NASA-TM-4452) RESEARCH AND
TECHNOLOGY HIGHLIGHTS, 1992
(NASA) 251 p

N94-13962

Unclass

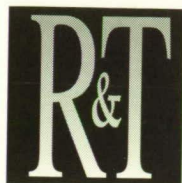
H1/99 0187792

HIGHLIGHTS 1992



Langley Research Center
NASA Technical Memorandum 4452

RESEARCH AND TECHNOLOGY



HIGHLIGHTS 1992

National Aeronautics and
Space Administration

Langley Research Center
Hampton, Virginia 23681-0001

Langley Research Center
NASA Technical Memorandum 4452

ORIGINAL CONTAINS
SPACE ILLUSTRATIONS

FOREWORD

The mission of the NASA Langley Research Center is to increase the knowledge and capability of the United States in a full range of aeronautics disciplines and in selected space disciplines. This mission will be accomplished by performing innovative research relevant to national needs and Agency goals, transferring technology to users in a timely manner, and providing development support to other United States Government agencies, industry, and other NASA centers. This report contains highlights of the major accomplishments and applications that have been made by Langley researchers and by our university and industry colleagues during the past year. The highlights illustrate both the broad range of research and technology (R&T) activities supported by NASA Langley Research Center and the contributions of this work toward maintaining United States leadership in aeronautics and space research. The report also describes some of the Center's most important research and testing facilities. For further information concerning the report, contact Dr. Michael F. Card, Chief Scientist, Mail Stop 105-A, NASA Langley Research Center, Hampton, Virginia 23681, (804) 864-6062.

Paul F. Holloway
Director

PRECEDING PAGE BLANK NOT FILMED

AVAILABILITY INFORMATION

The NASA program office and the corresponding Agency-wide Research and Technology Objectives and Plans (RTOP's) work breakdown structures are listed in the Contents for each research and technology accomplishment. OAST designates the Office of Aeronautics and Space Technology; OSSA designates the Office of Space Science and Applications; AA designates the Associate Administrator; OCE designates the Office of the Chief Engineer; OCP designates the Office of Commercial Programs; OSF designates the Office of Space Flight; and OSMQ designates the Office of Safety and Mission Quality.

The accomplishments are grouped in 12 strategic thrusts including contributions in Discipline Research, Subsonic Aircraft, High-Speed Civil Transport, High-Performance Military Aircraft, Hypersonic and Transatmospheric Vehicles, Space Transportation, Space Platforms, Space Science, Planetary Surface Technology, Operations Technology, Facilities, and Technology Transfer and Utilization. In addition, descriptions are included of some of the most important Aerospace Test Facilities at the NASA Langley Research Center. The use of these facilities in the research described herein is noted in the Contents.

For additional information on any summary, contact the individual identified with the highlight. This individual is generally either a member or a leader of the research group submitting the highlight. Commercial telephone users may dial the listed extension preceded by (804) 86.

CONTENTS

Foreword	iii
Availability Information	iv

Discipline Research

Method for High-Speed Boundary-Layer Flow	1
(OAST 505-59-40): C. Dave Pruett and Chau-Lyan Chang	
Effect of Mach Number on Boundary-Layer Instability Waves	2
(OAST 505-59-50): P. Balakumar and M. R. Malik	
Simulation of Transition on Swept Wings	3
(OAST 505-59-50): Ronald D. Joslin and Craig L. Streett	
Passive Control of Shock-Induced Separation	3
(OAST 505-59-50; Hypersonic Facilities Complex): R. Rallo	
Separation Control With Miniature Vortex Generators	4
(OAST 505-59-50; Low-Turbulence Pressure Tunnel): John C. Lin	
Automatic Computation of Wing-Fuselage Intersection Lines and Fillets	5
(OAST 505-59-53): Raymond L. Barger and Mary S. Adams	
Multigrid-Based Navier-Stokes Solver for Aerothermodynamic Problems	5
(OAST 505-59-53): Veer N. Vatsa	
Numerical Simulation of Shadowgraph and Schlieren Flow Visualization Methods	6
(OAST 505-59-53): Beyung S. Kim	
Consistent Aerodynamic Sensitivity Derivatives for Advanced CFD Codes	7
(OAST 505-59-53): P. A. Newman, H. E. Jones, A. C. Taylor III, V. M. Korivi, and G. W. Hou	
Structured Background Grids for Unstructured Grid Generation	8
(OAST 505-59-53): S. Pirzadeh and N. T. Frink	
An Adaptive Remeshing Procedure for Three-Dimensional Unstructured Grids	8
(OAST 505-59-53): P. Parikh and N. T. Frink	
Hydrogen Combustion Velocity Measurements Using Particle Image Velocimetry	9
(OAST 505-59-53): William M. Humphreys, Jr.	
Doppler Global Velocimetry—A New Nonintrusive Flow Diagnostic Tool	10
(OAST 505-59-54; Basic Aerodynamics Research Tunnel): James F. Meyers	
Prediction of Exhaust Systems Performance	11
(OAST 505-62-30): John R. Carlson	
Ignitability Test Method	11
(OAST 505-63-01; Pyrotechnic Test Facility): Laurence J. Bement	
Analytic Sensitivity Derivatives Developed for Key Tire Response Parameters	12
(OAST 505-63-10): Ahmed K. Noor, John A. Tanner, Jeanne M. Peters, and Martha P. Robinson	

Fully Integrated Aerodynamic-Dynamic Optimization Procedure for Helicopter Rotor Blades	13
(OAST 505-63-36): Joanne L. Walsh, William J. LaMarsh II, and Howard M. Adelman	
Method for Reducing Helicopter Rotor Blade Vibration	14
(OAST 505-63-36; Transonic Dynamics Tunnel): Jocelyn I. Pritchard, Howard M. Adelman, Joanne L. Walsh, and Matthew L. Wilbur	
Open-Loop Flutter Condition Determined From Closed-Loop Measurements	14
(OAST 505-63-50; Transonic Dynamics Tunnel): Anthony S. Pototzky, Carol D. Wieseman, Sherwood T. Hoadley, and Vivek Mukhopadhyay	
Digital Controller Developed To Provide Multifunction Control of Aeroelastic Response	15
(OAST 505-63-50): Sherwood T. Hoadley and Sandra M. McGraw	
Wing Loads Actively Controlled During Rolling Maneuvers	16
(OAST 505-63-50): Jessica A. Woods-Vedeler and Anthony S. Pototzky	
Buffet Load Alleviation Accomplished Via Piezoelectric Actuation	17
(OAST 505-63-50): Jennifer Heeg, Robert Doggett, and Jonathan Miller	
Automatic Differentiation Adapted and Evaluated as a Tool for Engineering Design	18
(OAST 505-63-50): Jean-Francois M. Barthelemy and Laura E. Hall	
Implicit Upwind Algorithm Developed for Unstructured Meshes	19
(OAST 505-63-50): John T. Batina	
Symmetric and Antisymmetric Flutter Boundaries Computed With the CAP-TSD Code	19
(OAST 505-63-50): Walter A. Silva and Robert M. Bennett	
Transonic Shock Oscillations Calculated With a New Boundary-Layer Coupling Method	20
(OAST 505-63-50): John W. Edwards	
Subsonic-Transonic Flutter Boundary Computed With Unsteady Euler Aerodynamic Method	21
(OAST 505-63-50; Transonic Dynamics Tunnel): Elizabeth M. Lee and John T. Batina	
Euler Flutter Analysis of a Complex Aircraft Configuration Demonstrated With Unstructured Deforming Meshes	22
(OAST 505-63-50; Transonic Dynamics Tunnel): Russ D. Rausch and John T. Batina	
Scale Effects on the Transverse Tensile Strength of Graphite/Epoxy Laminates	23
(OAST 505-63-50; Materials Research Laboratory): T. K. O'Brien	
Damage Resistance of Carbon/Epoxy Composites	24
(OAST 505-63-50; Materials Research Laboratory): C. C. Poe, Jr., and Wade C. Jackson	
A Failure Criterion for Mixed-Mode Delamination	24
(OAST 505-63-50; Materials Research Laboratory): James R. Reeder	
Use of Scanning Laser Vibrometer Data for Nondestructive Evaluation	25
(OAST 505-63-50; Acoustics Research Laboratory): Stephen A. Rizzi	
Pressure Measurements During Flutter of NACA 0012 Model	26
(OAST 505-63-50; Transonic Dynamics Tunnel): José A. Rivera, Jr.	
Neural Networks Offer Significant Payoffs in Optimization	27
(OAST 505-63-50): James L. Rogers and William J. LaMarsh II	
Functional Interface Method Accurately Joins Independently Modeled Structural Regions	27
(OAST 505-63-53): Jonathan B. Ransom, Susan L. McCleary, and Mohammad A. Aminpour	
Potential Improvement of Composite Joint Strength Through Use of Elliptic-Shaped Bolt	28
(OAST 505-63-53): John T. Wang	
Fast Algorithm Developed To Generate and Assemble Global Stiffness and Mass Matrices in Parallel	29
(OAST 505-63-53): Olaf O. Storaasli	

Microstructural Characterization of Thin Polyimide Films by Positron Lifetime Spectroscopy	30
(OAST 505-63-70): Jag J. Singh and Abe Eftekhari	
Automatic Specification of Reliability Models for Fault-Tolerant Computers	31
(OAST 505-64-10): Carlos A. Liceaga and Daniel P. Siewiorek	
The Helicopter Antenna Radiation Prediction (HARP) Code.....	32
(OAST 505-64-52): George C. Barber	
Detrimental Effects of Automation-Induced Complacency Demonstrated	33
(OAST 505-64-53): Alan T. Pope and Raja Parasuraman	
Finite-Difference Time-Domain Technique for Compact Range Applications.....	34
(OAST 505-64-70; Compact Range Pilot Facility): Fred B. Beck and Truong X. Nguyen	
High-Speed Airframe Integration Research (HiSAIR)	35
(OAST 505-69-50): Peter G. Coen	
Adaptive Grid Method for Computing High-Speed Flow	35
(OAST 505-90-53): Robert E. Smith	
LARC TM RP46 for High-Performance Aircraft and High-Speed Civil Transport Applications	36
(OAST 506-43-11; Polymeric Materials Laboratory): Ruth H. Pater	
Modeling Surface Cloth Impressions on Composites as an Ultrasonic Reflection Grating.....	37
(OAST 506-43-11; NDE Research Laboratory): Eric I. Madaras	
Multiresponse Imaging for Improved Resolution	38
(OAST 506-59-21): Carl L. Fales and Friedrich O. Huck	
Characterization of Silvered FEP Teflon Coating Exposed on LDEF.....	38
(OAST 506-43-21): W. S. Slemple and P. R. Young	
Adaptive Unstructured Meshing Demonstrated for Thermal Stress Analysis of Built-Up Structures.....	39
(OAST 506-43-31): Pramote Dechaumphai	
High-Strength Carbon-Carbon Composites With Three-Directional Reinforcement and Chemical Vapor Infiltration Densification.....	40
(OAST 506-43-71; Structures and Materials Research Laboratory): Philip O. Ransone	
Fiber Surface Conditions Control Carbon-Carbon Composite Mechanical Properties.....	41
(OAST 506-43-71; Structures and Materials Research Laboratory): H. G. Maahs and Y. R. Yamaki	
Stiffness Tailoring for Improved Compression Buckling and Postbuckling Response for Composite Plates.....	42
(OAST 510-02-12): S. B. Biggers and M. J. Stuart	
Euler Code for Turbofan Transports.....	43
(OAST 535-03-10): D. A. Naik	
Improved Accuracy in Finite-Difference Analysis of Long-Distance Elastic Wave Propagation.....	44
(OAST 538-02-11; NDE Research Laboratory): Doron Kishoni and Shlomo Ta'asan	
The Large-Angle Magnetic Suspension Test Fixture (LAMSTF).....	44
(OAST 590-14-11): Nelson J. Groom	
Techniques for Optimizing Wide-Scanning Reflector Configurations	45
(OAST 590-14-41): M. C. Bailey and L. C. Schroeder	
Effect of Braze Processing on β 21S Titanium Matrix Composite.....	46
(OAST 763-23-41; Structures and Materials Research Laboratory): R. Keith Bird and Eric K. Hoffman	

Subsonic Aircraft

Optical Disk Recorder-Playback System	49
(OAST 505-59-10): Jennifer J. Reilly	
General Aviation E-Z Fly Studies	49
(OAST 505-59-10; General Aviation Simulator): Eric C. Stewart	
Subsonic Transport High-Lift Flight Research—Phase IIA	50
(OAST 505-59-10; Transport Systems Research Vehicle): Long P. Yip	
Automated Transonic Wing Design Using an Unstructured Euler Method	51
(OAST 505-59-10): L. A. Smith and S. Pirzadeh	
Digital Resolver System for Helicopter Model Blade Motion Analysis.....	51
(OAST 505-59-36; 14- by 22-Foot Subsonic Tunnel): Taumi S. Daniels and John D. Berry	
Predicted Rotor Impulsive Noise Directivity and Measured Wake Interaction Locations.....	52
(OAST 505-63-36): M. A. Marcolini and R. M. Martin	
Wavelength Division Multiplexing Digital Controller (WDM-DC).....	53
(OAST 505-64-10): James D. Patterson and Daniel L. Palumbo	
Assessment of High-Intensity Radiated Field Effects	54
(OAST 505-64-10): Felix L. Pitts	
Model-Based Techniques Developed for Estimation of Microburst Downdraft.....	55
(OAST 505-64-12): Dan D. Vicroy	
Airborne Wind Shear Detector.....	56
(OAST 505-64-12; Transport Systems Research Vehicle): Philip Brockman and Raymond S. Calloway	
<i>In Situ</i> Wind Shear Detection Algorithm Developed for Modern Transport Aircraft.....	56
(OAST 505-64-12; Transport Systems Research Vehicle and Simulator): Rosa M. Oseguera	
Wind Shear Hazard From Terminal Doppler Weather Radar Information.....	57
(OAST 505-64-12): David A. Hinton	
Accident Data Used To Validate Faultfinder Concept	58
(OAST 505-64-13): Paul C. Schutte	
Types of Information Desired From Intelligent Decision Aiding.....	59
(OAST 505-64-13): Kathy Abbott and Mindy Howard	
Air-Ground Descent Profile Negotiation for Improved Airspace Efficiency.....	60
(OAST 505-64-13; Transport Systems Research Vehicle Simulator): David H. Williams	
Study of Large Subsonic Transport.....	61
(OAST 505-69-10): Dennis W. Bartlett, Philip C. Arcara, Jr., and Marvin E. McGraw	
Langley Dry Powder Prepreg Tow Process	61
(OAST 510-02-11; Polymeric Materials Laboratory): Norman J. Johnston, Robert M. Baucom, Joseph M. Marchello, and Maylene K. Hugh	
Damage-Tolerant Concept for Transport Aircraft Wing Structures	62
(OAST 510-02-11; Structures and Materials Research Laboratory): Jerry W. Deaton	
Composite Fuselage Concept for Civil Tilt-Rotor.....	63
(OAST 532-06-37): Donald J. Baker	
Effect of Pylon Geometry Transport Drag	63
(OAST 535-03-10; 16-Foot Transonic Tunnel): Anthony M. Ingraldi, Dinesh A. Naik, and Odis C. Pendergraft, Jr.	

The Optimization of Force Inputs for Active Structural-Acoustic Control Using Neural Networks	64
(OAST 535-03-11): Harold C. Lester, Ran H. Cabell, and Richard J. Silcox	
Analysis of Fatigue Crack Growth From Countersunk Rivet Lap Joints	65
(OAST 538-02-10; Materials Research Laboratory): E. P. Phillips and D. S. Dawicke	
Verification of the Crack Tip Opening Angle Fracture Criterion	66
(OAST 538-02-10; Materials Research Laboratory): J. C. Newman, Jr., D. S. Dawicke, and C. A. Bigelow	
Quantitative Study of Corrosion Detection in Aircraft Lap Joints	67
(OAST 538-02-11; NDE Research Laboratory): Hazari I. Syed	
Optical Nondestructive Evaluation of Composite Structures for Commercial Aircraft Applications.....	67
(OAST 538-02-11; NDE Research Laboratory): J. B. Deaton, L. D. Melvin, and R. S. Rogowski	
Magneto-Optic Imaging of Airframe Fatigue Cracks.....	68
(OAST 538-02-11; NDE Research Laboratory): Buzz Wincheski, Min Namkung, Jim Fulton, and Ron Todhunter	
Injection-Seeded Ti:Al ₂ O ₃ Laser Transmitter for Lidar Atmospheric Sensing Experiment.....	69
(OAST 590-31-31): James C. Barnes	

High-Speed Civil Transport

Conceptual Studies for HSR Wing Structures	71
(OAST 510-02-12): Stephen J. Scotti	
Noise Associated With a High-Temperature Supersonic Jet.....	71
(OAST 537-02-22; Jet Noise Laboratory): John M. Seiner, Bernard J. Jansen, and Michael K. Ponton	
Comparison of Noise Prediction for HSCT Climb to Cruise.....	72
(OAST 537-03-20): R. A. Golub	
Climb-to-Cruise Experiment	73
(OAST 537-03-21): William L. Willshire, Jr., and Robert A. Golub	
Sonic Boom Propagation Experiment	74
(OAST 537-03-21): William L. Willshire, Jr.	
Sonic-Boom Predictions With Computational Methods	74
(OAST 537-03-21): Christine M. Darden and Kamran Fouladi	
Computational Predictions of an HSCT-Type Configuration.....	75
(OAST 537-03-22; 14- by 22-Foot Subsonic Tunnel): Victor R. Lessard and Bryan A. Campbell	
Leading-Edge Suction for Vortex Suppression on an HSCT Configuration	76
(OAST 537-03-22; 14- by 22-Foot Subsonic Tunnel): Guy T. Kemmerly, Zachary T. Applin, and Bryan A. Campbell	
Prediction of Boundary-Layer Receptivity Due to Surface Disturbances	77
(OAST 537-03-23): Meelan Choudhari and Craig Streett	
Thermographic Diffusivity Imaging of Ceramic Composite Materials.....	77
(OAST 763-23-45; NDE Research Laboratory): K. E. Cramer	

High-Performance Military Aircraft

Cavity Surface Flow Fields at Supersonic Speeds.....	81
(OAST 505-59-30; Unitary Plan Wind Tunnel): Floyd J. Wilcox, Jr.	

Use of Passive Porosity to Alleviate Asymmetric Loads on Forebodies	82
(OAST 505-59-30; 7- by 10-Foot High-Speed Tunnel): Steven X. S. Bauer and Michael J. Hemsch	
F-15E Stability and Control Studies.....	82
(OAST 505-59-30; 30- by 60-Foot Tunnel): Sue Grafton, Scott Fears, and Dan Murri	
F-16 Free-Spin Tests	83
(OAST 505-59-30; 20-Foot Vertical Spin Tunnel): C. Michael Fremaux	
Flight Tests of a 0.27-Scale X-31 Drop Model at High Angles of Attack	84
(OAST 505-59-30; Flight Research Facility): Mark A. Croom and David J. Fratello	
Research on Advanced Multiaxis Vectoring Plug Nozzle.....	85
(OAST 505-62-30; 16-Foot Transonic Tunnel): Daniel L. Cler and Mary L. Mason	
Thrust Vectoring Characteristics of the F/A-18 HARV	86
(OAST 505-62-30; 16-Foot Transonic Tunnel): Scott C. Asbury	
Tactical Maneuvering Simulator.....	86
(OAST 505-64-30): K. H. Goodrich	
Wide-Field-of-View, Binocular Helmet-Mounted Display.....	87
(OAST 505-68-30): James R. Burley II	
Longitudinal Control Design of High Alpha Research Vehicle (HARV)	88
(OAST 505-68-30): Aaron J. Ostroff and Melissa Proffitt	
Surface Porosity Effects on Vortex Interactions	89
(OAST 505-68-30; 7- by 10-Foot High-Speed Tunnel): G. E. Erickson	
High-Alpha Gritting To Simulate Flight Reynolds Number Data	90
(OAST 505-68-30; 7- by 10-Foot High-Speed Tunnel): R. M. Hall, D. W. Banks, and W. G. Sewall	
Transonic Investigation of Shallow-Cavity Passive-Venting Configurations.....	90
(OAST 505-68-70): R. L. Stallings, E. B. Plentovich, M. B. Tracy, and M. J. Hemsch	
Loudness of Asymmetrical Sonic Booms	91
(OAST 537-03-21; Acoustics Research Laboratory): Jack D. Leatherwood and Kevin P. Shepherd	

Hypersonic and Transatmospheric Vehicles

CFD Prediction of Boundary-Layer Transition on a Blunt Cone.....	95
(OAST 505-59-40): Sharon H. Stack, Arthur D. Dilley, and Richard W. Hawkins	
Effect of Inlet Representation on Hypersonic Model Afterbody Flows.....	95
(OAST 505-59-40): Lawrence D. Huebner and Kenneth E. Tatum	
Subsonic Aerodynamic Characteristics of a NASP Test Technique Demonstrator Configuration	96
(OAST 505-59-40; 7- by 10-Foot High-Speed Tunnel): Richmond P. Boyden and David A. Dress	
Supersonic Velocity Measurements Over a Wedge Model Obtained With Particle Image Velocimetry	97
(OAST 505-59-53; Hypersonic Facilities Complex): William M. Humphreys, Jr.	
Effects of Expansion on Supersonic Combustor Flow Fields	98
(OAST 505-62-40): Dean R. Eklund and G. Burton Northam	
Ignition and Structure of a Diffusion Flame With Vortex Interaction	98
(OAST 505-62-40): M. G. Macaraeg, T. L. Jackson, and M. Y. Hussaini	
Interaction of Compressible Turbulence and Chemistry	99
(OAST 505-62-40): R. L. Gaffney, J. A. White, S. S. Girimaji, and J. P. Drummond	

Shock-Induced Combustion in a Hydrogen-Air System	100
(OAST 505-62-40): J. K. Ahuja, S. N. Tiwari, and D. J. Singh	
Stochastic and Nonlinear Response and Acoustic Radiation From a Panel-Stringer Structure Near a Supersonic Jet.....	101
(OAST 505-63-40; Acoustics Research Laboratory): Lucio Maestrello	
Langley Heat-Pipe Concept for NASP Wing Leading Edge	102
(OAST 505-63-50): David E. Glass and Charles J. Camarda	
Hypersonic Vehicle Control Law Development With H_∞ and μ -Synthesis.....	102
(OAST 505-64-40): Irene M. Gregory	
New Shock-Shock Interference Pattern Identified for Concomitant Supersonic Jets	103
(OAST 506-40-21): Allan R. Wieting	
Experimental Parametric Study of a Three-Dimensional Sidewall Compression Scramjet Inlet	104
(OAST 506-40-41; Hypersonic Facilities Complex): Kelly Murphy and Scott Holland	
An Engineering Aerodynamic Heating Method for Hypersonic Flow	105
(OAST 506-41-71): Christopher J. Riley	
Direct Simulation of a Hypersonic Shock Interference Problem	106
(OAST 506-40-91): Ann B. Carlson and Richard G. Wilmoth	
Instrumentation Platelet Sections for 8-Foot High-Temperature Structures Wind Tunnel Nozzle	106
(OAST 506-43-31; Aerothermal Loads Complex): Danny A. Barrows	
Ti-1100 Matrix Composites Show Good Potential for Lightweight High-Temperature Applications	107
(OAST 506-43-71; Structures and Materials Research Laboratory): R. Keith Bird	
Nose-to-Tail CFD Analysis of NASP 201/21	108
(OAST 763-01-61): Charles R. McClinton and Thomas N. Jentink	
NASP High-Speed Injector Design.....	108
(OAST 763-01-61): Charles R. McClinton, Pradeep Kamath, Marlon Mao, and Paul G. Ferlemann	
A Theory To Analyze Composite-Stiffened Panels for NASP	109
(OAST 763-01-61): Craig S. Collier and James L. Hunt	
The Effect of Film Cooling on Wall Heating in a 2-D Scramjet Nozzle	110
(OAST 763-23-21): Nathaniel R. Baker, G. Burton Northam, and Diego Capriotti	
High Mach Number Mixing in a Shock Tunnel Environment.....	110
(OAST 763-23-25): Charles R. McClinton and Robert D. Bittner	
Simulated Powered Tests of the Test Technique Demonstrator at Mach 6.....	111
(OAST 763-23-31; Hypersonic Facilities Complex): David W. Witte, Lawrence D. Huebner, and William J. Monta	
Aerodynamic and Aerothermodynamic Assessment of the NASP 201 Configuration	112
(OAST 763-23-31; Hypersonic Facilities Complex): Tom Horvath	
Interaction of Reaction Control System Plume and Flow Field on Langley Test Technique Demonstrator.....	113
(OAST 763-23-31; Unitary Plan Wind Tunnel): Gregory J. Brauckmann	
Interactions of Swept Shock Wave and Laminar Boundary Layer in Hypervelocity Flows	114
(OAST 763-23-31): Charles M. Hackett	
Titanium Matrix Composites: Hypersonic Flight Profile Testing and Analysis	115
(OAST 763-23-41; Materials Research Laboratory): M. Mirdamadi and W. S. Johnson	
Response of NASP-Type Panels to Acoustic Loads.....	116
(OAST 763-23-41; Acoustics Research Laboratory): Stephen A. Rizzi and Jay H. Robinson	

Thermal Measurement Device for Thin-Skin Aerospace Structures.....	117
(OAST 763-23-45): Danny A. Barrows	

Space Transportation

Near-Net-Shape Aluminum-Lithium Extrusions.....	119
(OAST 505-63-50; Structures and Materials Research Laboratory): J. Wagner, W. Pollock, M. Birt, and R. Hafley	
Development of Optimum Configuration for Lifting Body Personnel Launch System.....	119
(OAST 506-40-41; Hypersonic Facilities Complex, Unitary Plan Wind Tunnel, 7- by 10-Foot High-Speed Tunnel, Low-Turbulence Pressure Tunnel): Bernard Spencer and George Ware	
Flow Visualization Results on Pegasus Air-Launched Booster at Mach 6.....	120
(OAST 506-40-71; Hypersonic Facilities Complex): Matthew N. Rhode	
Solution Strategies for Three-Dimensional Configurations at Hypersonic Speeds	121
(OAST 506-40-91): K. James Weilmuenster and Peter A. Gnoffo	
Computed Viscous Equilibrium-Air Flow Over the HL-20 Space Vehicle	122
(OAST 506-40-91): Francis A. Greene	
Space Shuttle Orbiter Analysis.....	122
(OAST 506-40-91): William L. Kleb	
Solid Modeling Aerospace Research Tools (SMART) Surface Smoothing Enhancements.....	123
(OAST 506-49-11): Mark L. McMillin	
Joint NASA/USAF Airborne Field Mill Program.....	124
(OSF 560-01-00; Flight Research Facility): Bruce D. Fisher and Richard T. Bright II	
Dual-Mixture-Ratio Propulsion-System Optimization for SSTO Vehicles.....	125
(OAST 590-21-11): Douglas O. Stanley	
Advanced Manned Launch System Two-Stage-to-Orbit Concept	126
(OSF 906-11-01): Howard Stone	
Structural Analysis of Proposed HL-20 PLS Concept	127
(OSF 906-11-01): Lance B. Bush, Deborah M. Wahls, and James C. Robinson	
CLAWS: A Real-Time Launch Vehicle Wind Sensor.....	128
(OSF 946-01-00): Kevin E. Dutton	

Space Platforms

Imaging of Flaws in Thin Metallic Plates	131
(OSMQ 323-51-66): William T. Yost, C. G. Clendenin, and M. Namkung	
Ambient-Temperature Catalyst for Space-Based CO ₂ Lasers	131
(OSSA 460-28-44): Billy T. Upchurch and David R. Schryer	
Conceptual Design of a Large-Aperture Microwave Radiometer Geostationary Platform	132
(OSSA 476-14-15): Richard A. Russell and Paul A. Garn	
Continuous Orbiter Utilization at Space Station <i>Freedom</i>	133
(OSSA 476-14-15): Patrick A. Troutman	
Restructured Space Station <i>Freedom</i> Flight Control Characteristics	133
(OSSA 476-14-15): Patrick A. Troutman and Michael Heck	

Reaction Wheel and Magnetic Torque Attitude Control	134
(OSSA 476-14-15): Richard A. Russell	
Minimum-Time Space Station Reboost	134
(OSSA 476-14-15): Richard A. Russell, Renjith R. Kumar, and Hans Seywald	
Aerodynamic Characteristics of <i>Magellan</i> in the Upper Atmosphere of Venus	135
(OAST 506-40-91): Didier F. G. Rault	
Large-Meteoroid Impact Craters on the Long Duration Exposure Facility	136
(OAST 506-43-21; Advanced Technology Research Laboratory): D. H. Humes	
Erectable Truss Hardware for Space Construction and INTELSAT Retrieval Support	136
(OAST 506-43-41): Harold G. Bush, Richard E. Wallsom, and James E. Phelps	
EVA Assembly Procedure for 14-m-Diameter Precision Reflector Verified in Neutral Buoyancy Tests	137
(OAST 506-43-41): Mark S. Lake and Walter L. Heard, Jr.	
Middeck 0-Gravity Dynamics Experiment (MODE)	138
(OAST 589-01-21): Sherwin M. Beck	
A Validation of Integrated Controls-Structures Design Methodology	139
(OAST 590-14-15; Spacecraft Dynamics Laboratory): Peiman G. Maghami	
Commercial Piezoelectric Devices Adapted for Smart Structure Application	140
(OAST 590-14-21): Chin Chung Won, Dean Sparks, Jr., Jeff Sulla, and W. Keith Belvin	
DSMT Analysis Model Updated Using Test-Verified Component Models	140
(OAST 590-14-21): Mehzad Javeed, Harold H. Edighoffer, and Paul E. McGowan	
Adaptive Control Using On-Line Identification	141
(OAST 590-14-21): Lucas G. Horta and Chris A. Sandridge	
Phase 0 CSI Evolutionary Model Tests Complete	142
(OAST 590-14-21): W. Keith Belvin, Lucas G. Horta, and Kenny B. Elliott	
Damage Detection in Large Space Structures From Best Achievable Eigenvectors	142
(OAST 590-14-31): Thomas A. L. Kashangaki and Tae W. Lim	
Second-Order State Estimators for Structural Systems	143
(OAST 590-14-61): W. Keith Belvin	
Phase 1 CSI Evolutionary Model Test-Bed	144
(OAST 590-14-61): K. B. Elliott, L. G. Horta, and M. J. Gronet	

Space Science

Satellite Monitoring of Biomass Burning in the Savanna Grasslands of Africa	147
(OSSA 199-30-76): Donald R. Cahoon, Jr., Joel S. Levine, and Wesley R. Cofer III	
Ground-Based Lidar Observations of the Mount Pinatubo Volcanic Cloud	147
(OSSA 460-41-41): D. C. Woods	
Ozone and Aerosol Distributions Measured in Arctic Stratosphere With Airborne Lidar	148
(OSSA 464-14-34): Edward V. Browell	
Accuracy Requirements for Parameters Used in Radiative Transfer Models of Ozone	149
(OSSA 464-23-22): Martin G. Mlynczak	
Airborne Lidar Measurements of Ozone and Aerosols Over the Western Pacific	150
(OSSA 464-54-16): Edward V. Browell	

Airborne Lidar Observations of Recently Injected Mount Pinatubo Volcanic Aerosols.....	151
(OSSA 465-44-05): D. M. Winker	
Ozone Depletion in the Lower, Middle, and Upper Stratosphere.....	152
(OSSA 579-22-42): Gerald M. Keating, Linda S. Chiou, and N. Christina Hsu	
Laser Heterodyne Frequency Line Width at the Hertz Level	153
(OAST 589-01-11): Stephen P. Sandford	
New Spaceflight Computer for Instrument Control and Data Acquisition.....	153
(OAST 589-01-11): Stephen P. Sandford	
Design and Fabrication of an Electro-Optic Modulator	154
(OAST 589-01-11): Cheryl C. Jackson	
SUNLITE Vibration and Thermal Cycle Test on Optical Bond.....	154
(OAST 589-01-11; Space Simulation and Environmental Test Complex): Richard W. Faison	
SUNLITE Passive Cavity Mount	155
(OAST 589-01-11): Stephen J. Hughes	
Modeled Environment and Exposures for the SAGE III Instrument Configuration	156
(OAST 593-42-31): John E. Nealy, Garry D. Qualls, and Lisa C. Simonsen	
The 1985 Chlorine and Fluorine Budgets in the Stratosphere.....	157
(OSSA 618-21-00): Curtis P. Rinsland	
Classification of Satellite-Observed Cloud Fields Over the Amazon Basin.....	157
(OSSA 618-22-31): Vickie S. Connors	
Laser Energy and Beam Quality Monitors for Lidar Applications	158
(OSSA 618-32-33): C. D. Armstrong	
SAGE II Observation of Mount Pinatubo Volcanic Aerosols	159
(OSSA 665-45-30): M. P. McCormick	
SAGE II Observations of Decreased Nitrogen Dioxide Following the Mount Pinatubo Eruption	160
(OSSA 665-45-30): J. M. Zawodny	
Frequency-Stabilized Laser Diode for Fourier Transform Spectrometer Control.....	161
(OSSA 665-70-01): Ira G. Nolt and Don Jennings	
Validation of UARS-HALOE Measurements by Far Infrared Balloon Emission Spectroscopy.....	161
(OSSA 665-70-01): Ira G. Nolt and B. Carli	
Onboard Optical Disk Telemetry Recording System for Balloon Experiments.....	162
(OSSA 665-70-01): Michael D. Vanek	

Planetary Surface Technology

Separation of O ₂ From the Martian Atmosphere	165
(AA 307-51-12; Advanced Technology Research Laboratory): R. A. Outlaw	
Determination of Mars Parking Orbits	165
(OAST 506-40-61): Prasun N. Desai and James J. Buglia	
Plasmadynamic Effects in Thermochemical Nonequilibrium Aerobrake Flows	166
(OAST 506-40-91): R. A. Mitcheltree and J. V. Shebalin	
Radiation Exposure Predictions for Short-Duration-Stay Mars Missions.....	167
(OAST 506-49-11): Scott A. Striepe, John E. Nealy, and Lisa C. Simonsen	

Galactic Cosmic Ray Fragmentation Cross-Section Uncertainty Analyses.....	168
(OAST 593-42-21; Advanced Technology Research Laboratory): L. W. Townsend	
In-Space Assembly, Servicing, and Operations.....	169
(OAST 594-81-21): Charles E. Cockrell	
SEI Early Lunar Rover Mission Studies.....	169
(OAST 594-81-21): Vernon P. Gillespie	
A Space-Based Aerobrake Reference Configuration	169
(OAST 594-81-21): Stephen J. Katzberg	

Operations Technology

Elimination of Relative Intensity Noise From Linear Diode Laser Array of Space Optical Disk Recorder	173
(OAST 590-32-11): Anthony L. Cook and Herbert D. Hendricks	
High-Speed Fiber Optic Transceiver.....	174
(OAST 590-32-11): Herbert D. Hendricks	
Study of Force Reflection With Telerobotic Hand Controller in Position Control Mode	174
(OAST 595-11-22): Kelli F. Willshire	
Quantitative Determination of Ice Thickness With the Thermal Remote Ice Measurement (TRIM) System.....	175
(OSF 906-20-03; NDE Research Laboratory): D. M. Heath	

Facilities

Three-Component Laser Velocimeter for the 14- by 22-Foot Subsonic Tunnel.....	177
(OAST 505-59-36; 14- by 22-Foot Subsonic Tunnel): Joe W. Elliott, W. Derry Mace, Jr., Susan A. Gorton, Terence A. Ghee, Judith K. Jumper, Fred H. Miandoab, and Timothy E. Hepner	
Aerodynamic Stability Test Instrumentation That Uses Digital Signal Processing Techniques.....	177
(OAST 505-59-40): John S. Tripp and Taumi S. Daniels	
Laser Fluorescence Anemometer for the 16- by 24-Inch Water Tunnel.....	178
(OAST 505-62-30; 16- by 24-Inch Water Tunnel): Dan H. Neuhart and David J. Wing	
New Rotary Balance System for the 20-Foot Vertical Spin Tunnel	179
(OAST 505-68-30; 20-Foot Vertical Spin Tunnel): Johnny W. Allred	
Nondestructive Evaluation Sciences	179
(OAST 506-43-11): Joseph S. Heyman	
Transient-Structural Analysis of the 8-Foot High-Temperature Tunnel Combustor Under Detonation Loads	180
(OAST 506-43-31; Aerothermal Loads Complex): Peyton B. Gregory and Anne D. Holland	
Thermal-Structural Analysis of a Methane Spraybar Burner for the 8-Foot High-Temperature Tunnel.....	181
(OAST 506-43-31; Aerothermal Loads Complex): Chris A. Mouring and Jon E. Thompson	
Development of an Optical Flameout Detector	182
(OAST 506-43-31; Aerothermal Loads Complex): Stephen E. Borg	

Technology Transfer and Utilization

Characterization of Thin Protective Coatings on Solid Substrates	185
(OCP 141-20-06): Jag J. Singh, Abe Eftekhari, and Danny R. Sprinkle	
Improved Magnet Design for Residual Stress Characterization in Ferrous Components.....	185
(OCP 141-20-10): Jim Fulton, Buzz Wincheski, and Min Namkung	
PC/AT-Based Telerobotic Control System	186
(OCP 141-20-10): Randy Mixon and Bill Barr	
Portable Fetal Heart Rate Monitor.....	187
(OCP 141-20-40): Allan J. Zuckerwar	
Shear Stress Calibration Device	189
(OCP 141-30-10): Bruce D. Little	
Noninvasive Method and Apparatus To Determine Fiber Direction in Composite Materials	189
(OCP 141-30-10): Robert L. Fox and John D. Buckley	
Blind-Fastener Apparatus.....	190
(OAST 506-48-71; Space Simulation and Environmental Test Complex): Norman F. Willey, Jr.	
Slip Casting of Ceramic Heaters, Mounts, and Lens Holders for Optical Benches	191
(OAST 590-31-31): Peter Vasquez, Melissa A. Long, Robert L. Fox, and Stephen P. Sandford	
Optical Alignment and Reference Cube for Laser Calibration	192
(OAST 590-31-31): Melissa A. Long	
Liquid-Nitrogen-Temperature Cryoseals.....	192
(OAST 590-31-31): Robert L. Fox and Melissa A. Long	
Calibration Without a Standard.....	193
(OAST 992-35-12): Tom Finley	

Aerospace Test Facilities

30- by 60-Foot Tunnel.....	195
(Contact: Frank Jordan, 41136)	
Low-Turbulence Pressure Tunnel	195
(Contact: Robert J. McGhee, 41005)	
20-Foot Vertical Spin Tunnel.....	196
(Contact: Ray Whipple, 41194)	
7- by 10-Foot High-Speed Tunnel.....	197
(Contact: J. M. Luckring, 42869)	
14- by 22-Foot Subsonic Tunnel	197
(Contact: Harry L. Morgan, Jr., 41069)	
8-Foot Transonic Pressure Tunnel.....	198
(Contact: J. M. Luckring, 42869)	
Transonic Dynamics Tunnel.....	199
(Contact: Bryce M. Kepley, 41244)	
16-Foot Transonic Tunnel	199
(Contact: Bobby L. Berrier, 43001)	

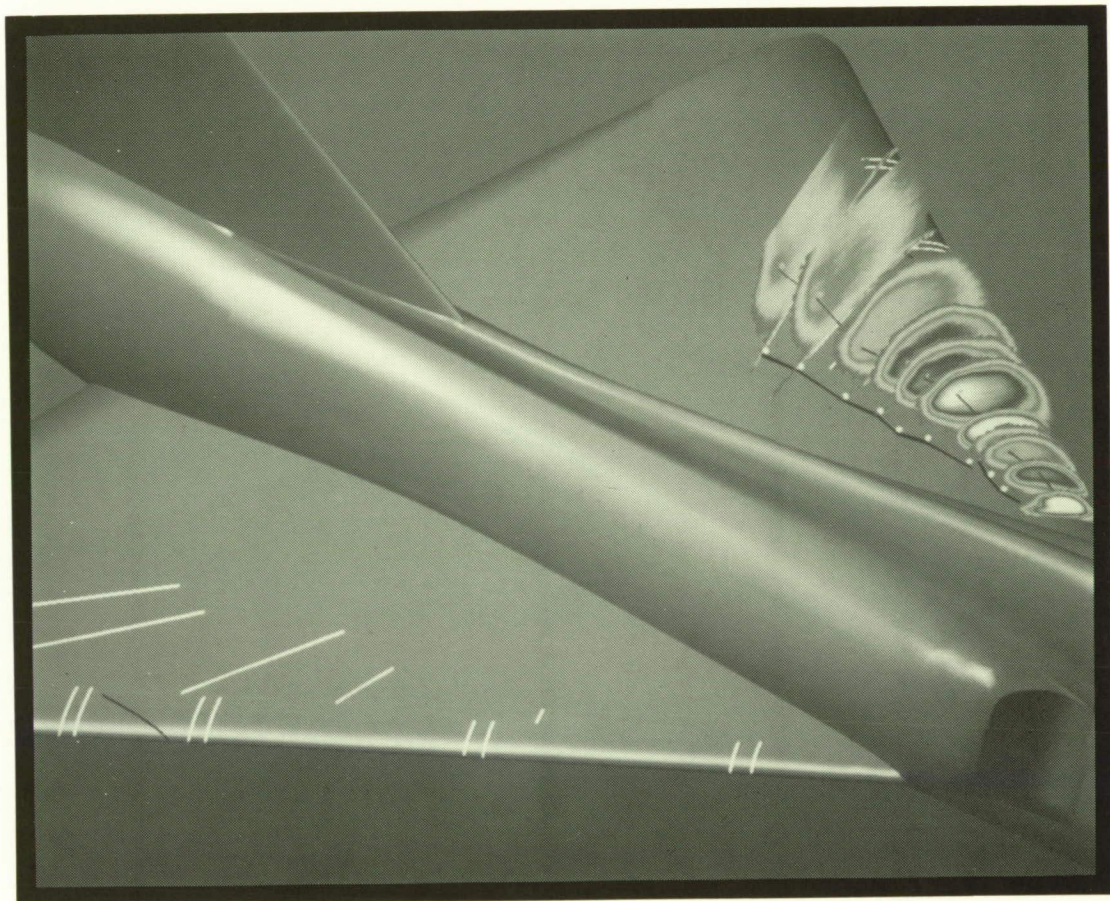
National Transonic Facility.....	200
(Contact: Dennis E. Fuller, 45129)	
0.3-Meter Transonic Cryogenic Tunnel	201
(Contact: Stuart G. Flechner, 46360)	
Unitary Plan Wind Tunnel	201
(Contact: William A. Corlett, 45911)	
Hypersonic Facilities Complex	202
(Contact: C. G. Miller, 45221)	
Scramjet Test Complex.....	203
(Contact: Wayne Guy, 46272)	
Aerothermal Loads Complex	204
(Contact: Allan R. Wieting, 41359)	
Acoustics Research Laboratory.....	205
(Contact: Lorenzo R. Clark, 43637)	
Avionics Integration Research Laboratory (AIRLAB).....	205
(Contact: Charles W. Meissner, Jr., 46218)	
Aerospace Controls Research Laboratory	206
(Contact: Douglas Price, 46605)	
Transport Systems Research Vehicle (TSRV) and TSRV Simulator	207
(Contact: George Steinmetz, 43842, Billy Ashworth, and Jacob A. Houck)	
Enhanced/Synthetic Vision & Spatial Displays Laboratory	208
(Contact: Jack Hatfield, 42012)	
Human Engineering Methods Laboratory	208
(Contact: Alan Pope, 46642)	
General Aviation Simulator.....	209
(Contact: Lemuel E. Meetze, 46452)	
Differential Maneuvering Simulator	210
(Contact: Lemuel E. Meetze, 46452)	
Visual Motion Simulator	210
(Contact: John D. Rollins, 46448)	
Space Simulation and Environmental Test Complex	211
(Contact: Thomas J. Lash, 45644)	
Advanced Technology Research Laboratory.....	212
(Contact: E. J. Conway, 41435)	
Spacecraft Dynamics Laboratory.....	212
(Contact: Robert Miserentino, 44318)	
Materials Research Laboratory	213
(Contact: Charles E. Harris, 43449)	
Structures and Materials Research Laboratory	214
(Contact: James H. Starnes, 43168)	
Polymeric Materials Laboratory	215
(Contact: H. D. Burks, 44272)	
NDE Research Laboratory	215
(Contact: Eric I. Madaras, 44970)	

Low-Frequency Antenna Test Facility	216
(Contact: Tom Campbell, 41772)	
Compact Range Pilot Facility	217
(Contact: Tom Campbell, 41772)	
Experimental Test Range	217
(Contact: Tom Campbell, 41772)	
Impact Dynamics Research Facility	218
(Contact: Granville Webb, 41303)	
Aircraft Landing Dynamics Facility	218
(Contact: Granville Webb, 41303)	
Basic Aerodynamics Research Tunnel	219
(Contact: Luther N. Jenkins, 48026)	
Flight Research Facility	220
(Contact: Haug Verstynen, 43875)	
16- by 24-Inch Water Tunnel	220
(Contact: Bobby L. Berrier, 43001)	
Scientific Visualization System	221
(Contact: Bill von Ofenheim, 46712)	
Supersonic Low-Disturbance Pilot Tunnel	222
(Contact: Mike Walsh, 45542)	
Pyrotechnic Test Facility	222
(Contact: Laurence J. Bement, 47084)	

Contributing Organizations

Aeronautics Directorate	225
Electronics Directorate	225
Flight Systems Directorate	226
National Aero-Space Plane Office	227
Space Directorate	227
Structures Directorate	228
Systems Engineering and Operations Directorate	229
Technology Utilization and Applications Office	230

■ DISCIPLINE RESEARCH



*Provide understanding of
physical phenomena and
verified computational
techniques important to
the design and operation of
advanced aerospace systems*

Method for High-Speed Boundary-Layer Flow

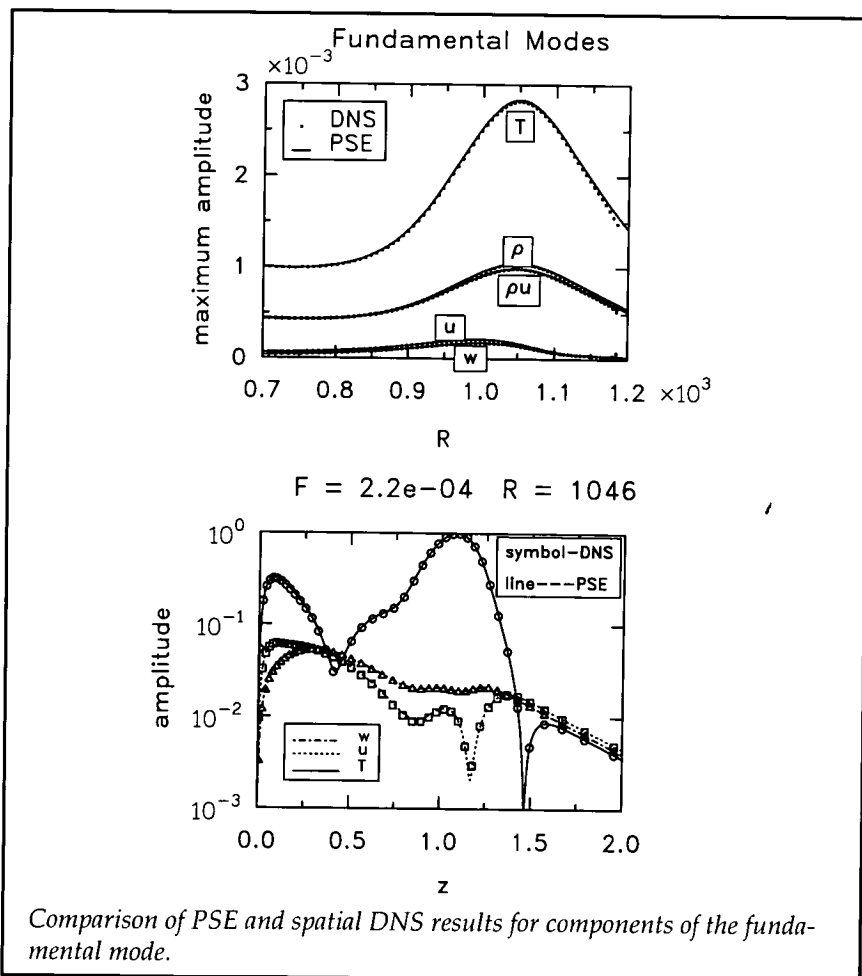
Boundary-layer instability and transition prediction in high-speed boundary layers have been major concerns for the design of high Mach number aerodynamic vehicles. Traditionally, prediction of the onset of laminar-turbulent transition has relied on the N -factor method based on linear stability theory (LST). Recent progress in the parabolized stability equations (PSE) method has provided an alternative based on the absolute-amplitude concept. To verify the PSE method as a reliable transition prediction tool, the present investigation focuses on the cross validation of spatial direct numerical simulation (DNS) and the PSE method for simulating spatially evolving instability waves in high-speed boundary-layer flows.

Spatial DNS and PSE approaches were applied to the simulation of a two-dimensional instability wave of linear amplitude in a Mach 4.5 flat-plate boundary layer. Identical second-mode disturbances were excited in each computation by means of periodic forcing at the inflow boundary, and the spatial evolution of the wave was tracked as it propagated through the second-mode unstable region from a Reynolds number R of 700 to 1200. The resulting amplitudes and disturbance structures obtained by the two methods were

then compared. As shown in the figure, the results from the two independently derived methods agree extremely well, so that both approaches for small-amplitude disturbances are validated. The amplitude maxima of the various components of the disturbance agree well over the entire range of Reynolds numbers. Moreover, despite the complex nature of second-mode disturbances evolving in a nonparallel boundary-

layer flow, the disturbance structures obtained by the two methods at $R = 1046$, far from the inflow boundary, are also in near-perfect agreement.

Whereas the well-resolved spatial DNS results required some 20 hours of CPU time on a Cray Y-MP computer, the PSE results were obtained in a matter of minutes. Close agreement of the PSE results with results obtained



from solution of the complete Navier-Stokes equations gives confidence in the potential of the PSE method as an eventual replacement of the N -factor method for transition prediction. This work was done under contract with Analytical Services & Materials, Inc., and High Technology Corp. (C. Dave Pruett, 46788, and Chau-Lyan Chang)
Aeronautics Directorate

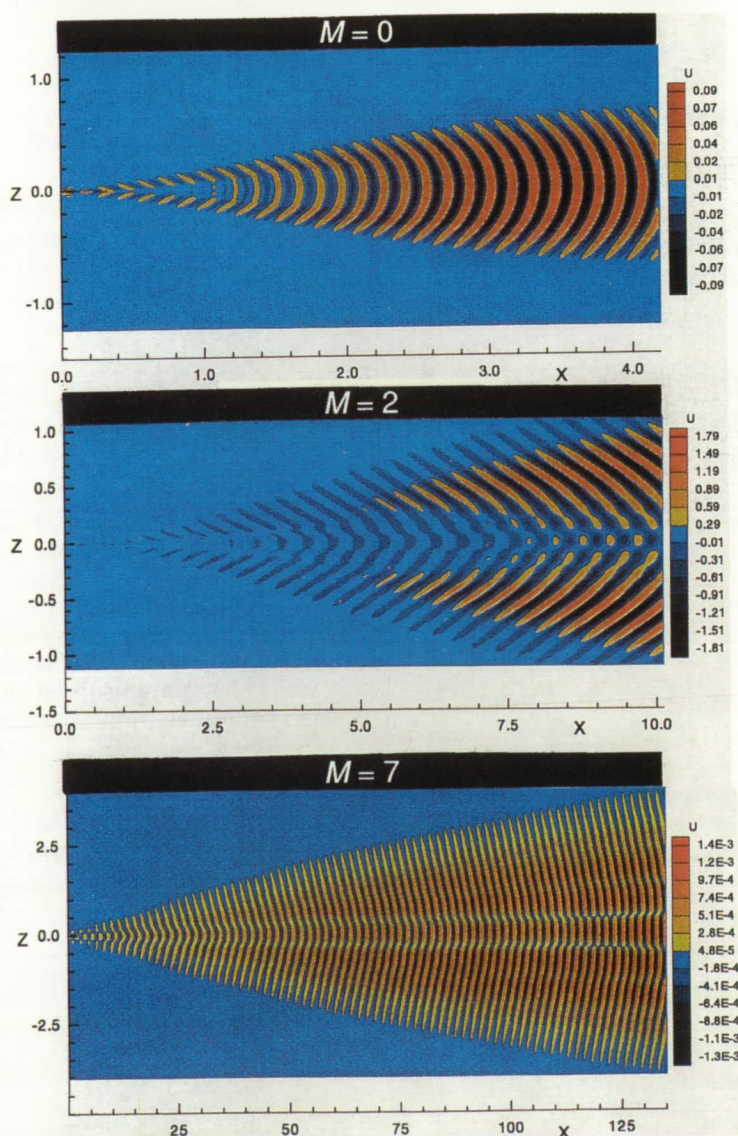
Effect of Mach Number on Boundary-Layer Instability Waves

Viscous drag reduction using laminar flow control (LFC) technology is an important issue in modern aerodynamic design. Because it offers the added advantage of lower skin temperatures for high-speed vehicles, LFC should be applied to the supersonic High-Speed Civil Transport (HSCT). To achieve successful control, reliable methods for prediction of boundary-layer transition are required. Transition is the result of amplification of instability waves in the boundary layer. Hence, understanding the evolution of disturbances in a boundary layer will help us improve transition prediction techniques.

A computer code was developed to solve linearized equations of motion for the instability waves produced from a harmonic point source in a two-dimensional flat-plate boundary layer. The figure shows the wave pattern produced downstream of the point source (located at $x = 0, z = 0$) in the boundary layer for three Mach numbers: $M = 0, 2$, and 7 . The results show that the maximum

amplitude occurs along the centerline in incompressible flows, and the three-dimensionality gradually fades away. For Mach 2, the maximum amplitude occurs along the oblique directions, and the amplitude remains very small along the centerline. This is because the nature of instability is different for supersonic flows. For hypersonic flows, a new type of instabil-

ity called "second mode" instability appears, and thus for Mach 7 the maximum amplitude occurs along both the centerline and the oblique directions. The wave pattern in the figure also indicates the lateral spread of disturbances in the boundary layer. The spreading angle decreases with increasing Mach number, a finding which is in agreement with experimental



Waves produced from a point source.

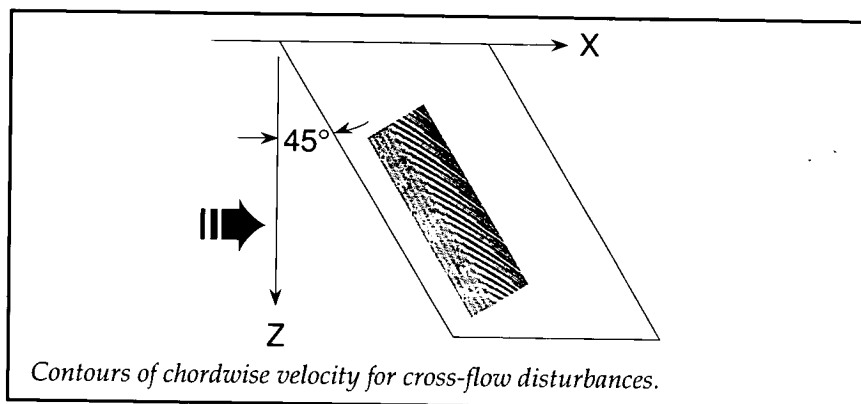
findings for lateral spread of turbulence in supersonic flow. It is planned to extend these calculations to study the evolution of disturbances in three-dimensional boundary layers. This work was done under contract with High Technology Corp.

(P. Balakumar, 45729, and
M. R. Malik)
Aeronautics Directorate

Simulation of Transition on Swept Wings

The use of laminar flow control (LFC) techniques to reduce skin-friction drag on aircraft wings is of significant importance to the aerospace industry. The thrust of the present research is to simulate the evolution and control of boundary-layer instabilities on swept wings.

The nonlinear evolution of disturbances leading to transition on a swept wing is computed by direct numerical simulation (DNS) techniques. A flat-plate boundary-layer simulation code, which solves the fully nonlinear Navier-Stokes equations, has been modified to compute the evolution of cross-flow vortices, traveling waves, and vortex-wave interactions in three-dimensional boundary-layer flows on swept wings with infinite span. For the computations, stationary disturbances are generated at the wall by a steady suction-blowing technique. The computed disturbances mimic transition in quiet tunnels, where low free-stream turbulence levels are present. By combining wall suction-blowing with random noise at the computational inflow, the simulations can also mimic transition in tunnels with higher



levels of free-stream turbulence, or noise.

In this first study, transition on a wing swept 45° with an imposed pressure field is computed. Steady suction-blowing through orifices at the wall near 20 percent of the chord is used to generate the cross-flow disturbances. Contours of the largest amplitude chordwise velocities are shown in the figure in a plan view of the wing. The cross-flow disturbances, which have amplified in the chordwise directions, are approaching the computational outflow boundary located near 52 percent of the chord.

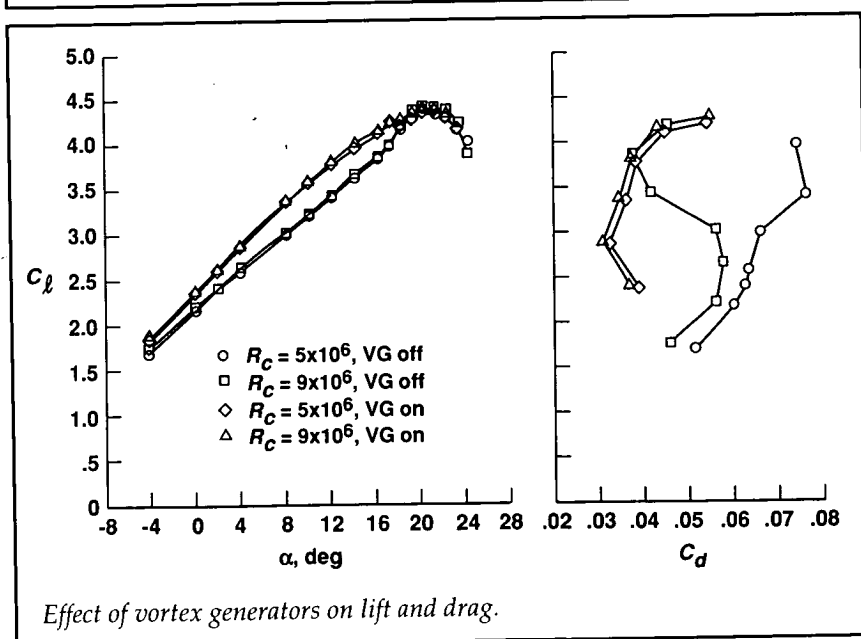
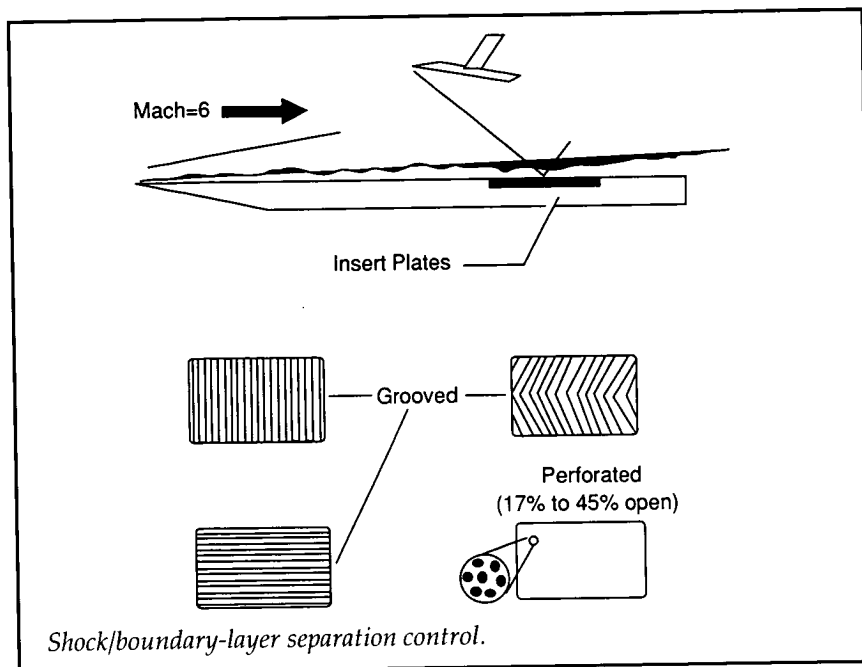
This initial investigation has produced results that are in good qualitative agreement with experimental observations for swept-wing flows. With the simulation code, the effectiveness of LFC methodologies will be investigated. (Ronald D. Joslin, 42234, and Craig L. Streett)
Aeronautics Directorate

Passive Control of Shock-Induced Separation

An investigation into the effectiveness of passive control techniques on shock-induced

boundary-layer separation at hypersonic speeds has been conducted. Two approaches to alleviating the losses from turbulent separation were examined: (1) porous-surface mass transfer and (2) surface grooving. A total of four perforated surfaces with varying porosities were evaluated. Three groove orientations with respect to the free-stream direction were also studied: transverse, swept, and longitudinal. Test results from these passive control techniques were compared with results from an "uncontrolled" shock impingement to determine the relative effectiveness of the devices. These comparisons indicated that the porous surface with the greatest porosity provided the largest reduction in the pressure rise across the oblique shock wave; however, the length of the interaction region was significantly extended. Each of the grooved configurations examined increased the peak pressure value. In general, the grooved surfaces tested were ineffective at suppressing the losses across the shock system at hypersonic (Mach 6) speeds.

In addition to the experimental efforts to examine the shock-induced boundary-layer separation, two-dimensional, thin-layer



Navier-Stokes computations were undertaken. Results from the Navier-Stokes code compared favorably with the experimental data for the solid wall (i.e., reference) configuration.

(R. Rallo, 47717)

Aeronautics Directorate

Separation Control With Miniature Vortex Generators

A cooperative test program between the Douglas Aircraft Company and Langley Research Center is underway in the Low-Turbulence Pressure Tunnel

(LTPT). One aspect of this effort includes the evaluation of vortex generators (VG's) for controlling boundary-layer separation on multielement high-lift airfoils. Low-profile vortex generators were mounted on the flap of a Douglas two-dimensional, three-element wing model set at landing configuration. The experimental investigation was conducted at near flight conditions, with a free-stream Mach number of 0.2 and chord Reynolds numbers R_C of 5 and 9 million. Measurements included lift, drag, surface pressure, wake profile, and fluctuating surface heat fluxes.

The low-profile vortex generators had a device height of only 0.04 in. (or 0.2 in. for full-scale aircraft). The vortex generators were oriented to produce either counter-rotating or corotating vortex pairs. The results indicate that both counter-rotating and corotating streamwise vortices were effective in reducing flow separation on the flap. Separation alleviation on the flap can significantly improve the aerodynamic performance of the entire high-lift system via increased lift and reduced drag, as shown in the figure. The figure shows that at a typical angle of attack α of 8° during approach, the generator-induced attached flow on the flap could increase the lift coefficient C_l on the order of 10 percent and reduce the drag coefficient C_d at least 40 percent. Additional tests in the LTPT are underway. The optimum chordwise location of the subscale vortex generators allows them to be hidden inside the flap well during aircraft cruise, so that no cruise drag penalty is incurred.

(John C. Lin, 45556)

Aeronautics Directorate

Automatic Computation of Wing-Fuselage Intersection Lines and Fillets

The preliminary "rough-cut" design and analysis of supersonic configurations is usually accomplished with linear computer codes. These codes utilize a surface definition that describes the configuration as a set of disjoint components. However, nonlinear codes, which are utilized for refined design and analysis, require a complete geometry, including the wing-fuselage intersection line or a smooth fillet connecting the wing and fuselage. A code for automatic calculation of these wing-fuselage intersection lines and fillets has been developed. An example is shown in the figure, which shows the disjoint wing and fuselage components as described by the original wave drag data and the automatically re lofted geometry with the intersection line.

Two types of filleting procedures were developed. One of

these uses circular arcs at specified streamwise locations. This procedure is useful when the extrapolated wing actually intersects the fuselage. The other procedure utilizes cubic arcs to connect fuselage and wing construction lines. This method allows one to model a configuration for which the extrapolated wing lower surface fails to intersect the fuselage, and it has better continuity characteristics than the first method. Since the supersonic wave drag depends sensitively on the longitudinal distribution of cross-sectional area, these procedures incorporate an optional algorithm for redesigning the fuselage to compensate for the added area due to the fillet.

A combination of analytical and numerical-iterative techniques are employed. The procedures all utilize automatic calculation and do not require the time-consuming "hands-on" interaction that is required in the traditional computer-aided-design (CAD) approach to problems of this type. These techniques facilitate the

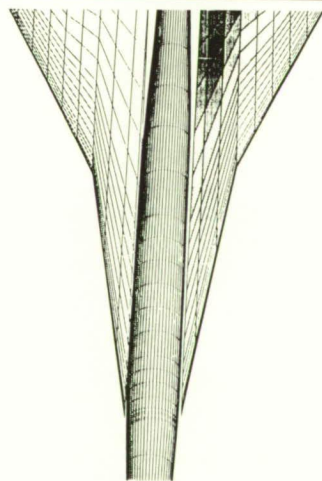
incorporation of nonlinear calculations into the design process and the redesign of fuselage cross sections to prevent increased wave drag due to the addition of fillets. (Raymond L. Barger, 42315, and Mary S. Adams)

Aeronautics Directorate

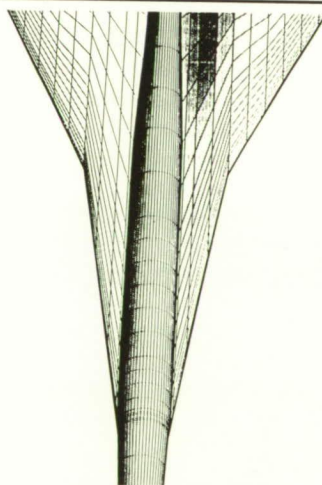
Multigrid-Based Navier-Stokes Solver for Aerothermodynamic Problems

During the last decade, computational fluid dynamics (CFD) has acquired the status of a legitimate and useful tool for solving aerothermodynamic problems for hypersonic speeds. However, most of the CFD codes in use require prohibitive amounts of computer time, even on the current supercomputers, to analyze a realistic configuration. Recently, a very efficient numerical scheme known as TLNS3D, which was originally developed for transonic flows over aircraft configurations, has been extended to supersonic and hypersonic flows. The basic numerical scheme is a finite-volume central-difference scheme and achieves its efficiency mainly through the use of a multigrid acceleration technique. Several computations have been made that indicate TLNS3D is an efficient and accurate scheme for solving practical aerothermodynamic problems.

The computations for flow at a Mach number of 6 over a modified Space Shuttle orbiter model, known as "HALIS," have been performed with the TLNS3D code. The computations were performed

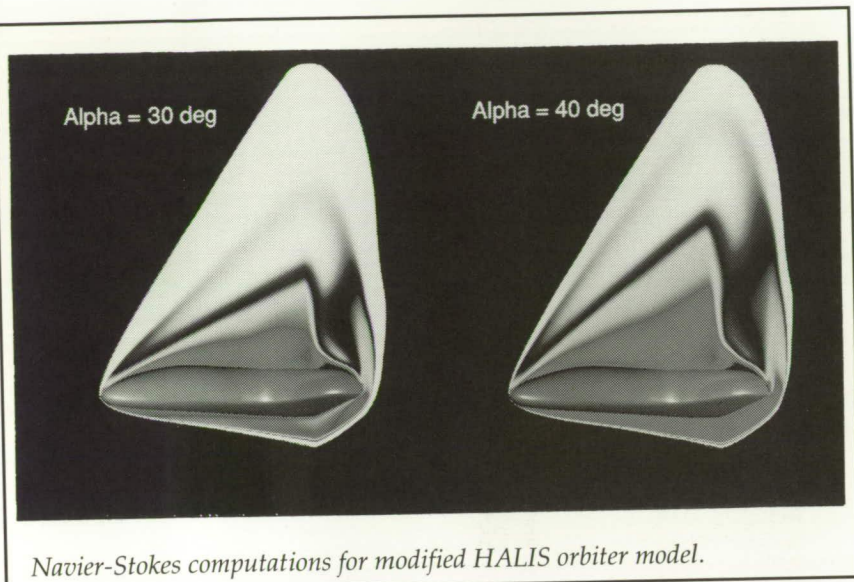


Original wave drag data



Automatically re lofted geometry

Example of wing-fuselage intersection.



at angles of attack of 30° and 40° to correspond to a previous in-house experimental and computational investigation. The Mach number contours for these two cases are shown in the figure to illustrate the effect of angle of attack on overall flow structure. The computed heat-transfer coefficients (not shown here) compared well with the experimental data and the previously computed results. Each test condition required approximately 3 hours of computer time on a Cray-2 computer to reach the steady state, a time which is approximately an order of magnitude faster than the computational effort required by most CFD codes currently in use for solving such problems. (Veer N. Vatsa, 42236)
Aeronautics Directorate

Numerical Simulation of Shadowgraph and Schlieren Flow Visualization Methods

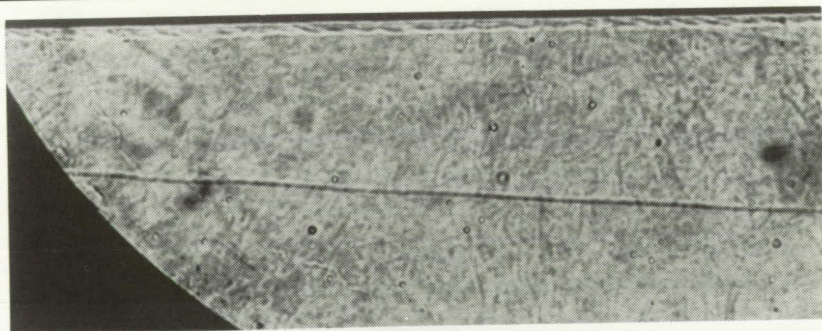
Software was developed to simulate schlieren and shadow-

graph image, the second derivative of the density gradient, rather than density gradient itself, dictates the intensity.

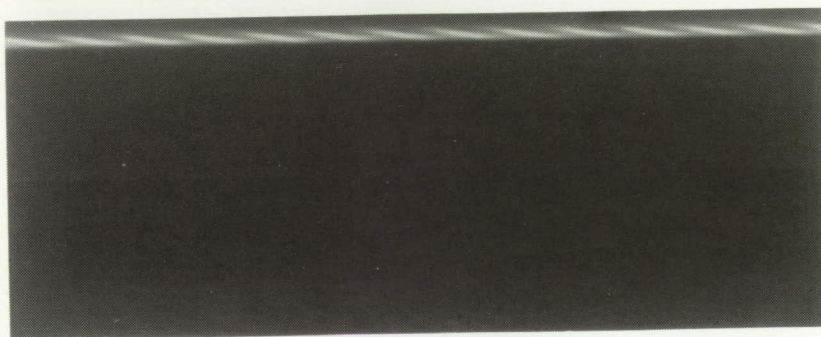
The numerical algorithm performs an analogous integration process on three-dimensional computational fluid dynamics (CFD) solutions. In order to accommodate structured grids, each quadrilateral cell is divided into five tetrahedrons. The computations for the intensity in each cell are thereafter identical for both types of grids.

The figure shows the comparison of a simulated schlieren image with an experimental schlieren photograph for laminar breakdown in a high-speed axisymmetric boundary-layer flow. In high-speed transition experiments, a "rope-like wave" effect is often observed near the edge of the

graph flow visualization methods for three-dimensional structured and unstructured grid solutions. The intensity of each point in a schlieren image is the integral of the density gradient along the direction of the ray. In a shadow-



Schlieren photograph of typical rope-like wave.



Simulated schlieren image (enlarged) from CFD result.

boundary layer. The simulation schlieren image confirms that the CFD solution replicates this phenomenon.

The software allows more meaningful comparisons between three-dimensional CFD computations and two-dimensional schlieren photographs for experiments. Numerical solutions on both structured and unstructured grids can be used to generate black-and-white or color schlieren and shadowgraph images. This work was done under contract with Analytical Services & Materials, Inc. (Beyung S. Kim, 42151) Aeronautics Directorate

Consistent Aerodynamic Sensitivity Derivatives for Advanced CFD Codes

Computational methodologies relevant to large-scale, multi-disciplinary, gradient-based optimization for aerospace vehicle design are being investigated. The present study addresses the situation where the aerodynamics discipline response must be obtained from the solution of a system of nonlinear partial differential equations; when discretized, these form a very large set of algebraic equations that must be solved iteratively, that is, with advanced computational fluid dynamics (CFD) codes. A technique to obtain consistent aerodynamic sensitivity derivatives (SD's) for such codes has been proposed and is being developed. This technique permits (1) some leeway in the CFD solution algorithms that can be used, (2) an extension to three-dimensional problems, and (3) straightforward

use of other computational methodologies.

Two significant issues for obtaining SD's are the differentiation and solution methods used. Four differentiation methods have been investigated: (1) divided differences, (2) quasi-analytical, (3) symbolic manipulation, and (4) automatic differentiation (AD). Three means for solving the resulting linear matrix system are (1) direction solution (DS), (2) matrix iteration (MI), and (3) incremental iterative. Use of a new AD method is being jointly investigated with Argonne National Laboratories; other techniques are being investigated jointly under NASA grants with Texas A&M and Old Dominion Universities.

The table shows that the combination of quasi-analytical differentiation and approximate-factorization (AF) solution of the incremental iterative form equations reduces computing time for six SD's from

Solution method	Number solutions	Time, sec*
Flow equation, Divided differences, AF method	6 Nonlinear	840
Standard form, quasi-analytical, hybrid DS/MI	3 Linear	191
Incremental form, quasi-analytical, AF method	3 Linear	50

*All calculations performed on a Cray-2 computer.

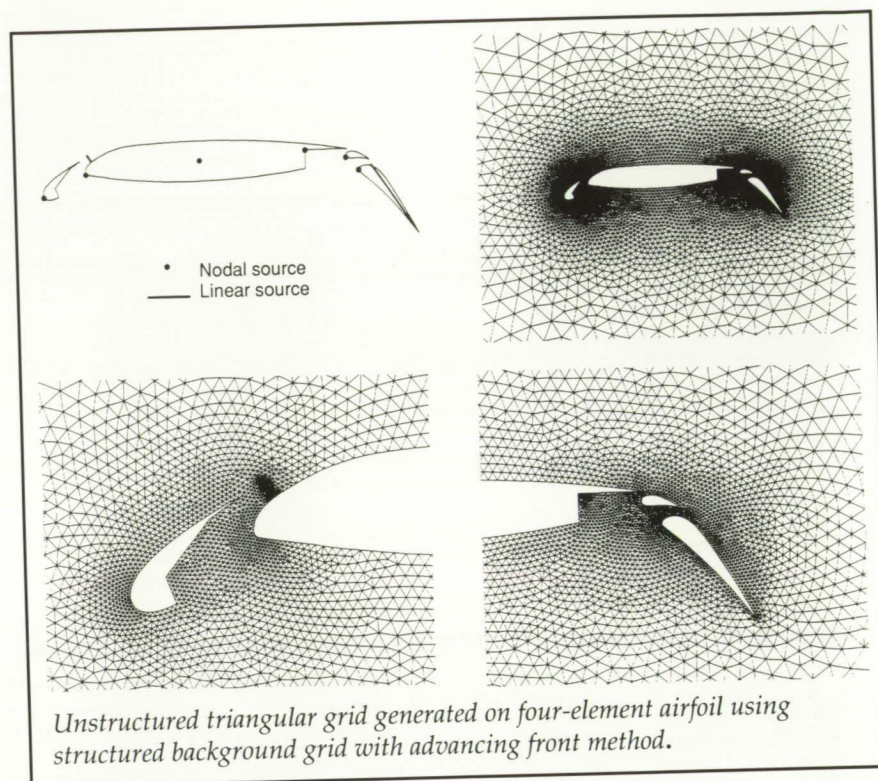
Computation time for six sensitivity derivatives (NACA 2412 airfoil; transonic viscous flow).

that for "brute force" central-divided differences. Additional studies indicate that a more efficient procedure may be to obtain elements in the SD equation via AD and solve in the incremental form. This form allows approximation of the iterative equation operator with one which can be adapted for efficiency, machine architecture, computational algorithm, etc.; all that is required of the approximation is convergence. In addition, significantly reduced storage requirements allow three-dimensional applications. For details, see NASA TM-104206 and NASA TM-104207, both dated February 1992. (P. A. Newman, 42247, H. E. Jones, A. C. Taylor III, V. M. Korivi, and G. W. Hou) Aeronautics Directorate

Structured Background Grids for Unstructured Grid Generation

The objective of this research is to formulate a new approach for generating unstructured triangular and tetrahedral grids that has a rigorous mathematical basis for controlling grid point distribution. In the Advancing Front Method, a grid is generated by forming cells starting at the boundaries and marching toward the interior of a domain. The distribution of grid points is controlled by information stored at the nodes of a secondary coarse mesh referred to as the "background grid."

Prior methodology utilizes *unstructured* background grids, which are usually constructed by a tedious manual process that often leads to less than desirable results. The present approach utilizes a *structured* uniform Cartesian background grid, which is generated automatically. Grid spacing is controlled by the solution to an elliptic partial differential equation. Associated with structured background grids is an arbitrary number of user-prescribed source elements at which grid spacings are stored. The distribution of spacing parameters to the nodes of the background grid is achieved by solving the Poisson equation. This process is similar to that of solving for the diffusion of heat from discrete heat sources in a conducting medium where the resulting distribution of grid spacing resembles "isotherms" varying smoothly from high- to low-potential regions. Several control features are built into the method to allow for control of the



direction and the extent of influence of the sources.

The capability of the new method is demonstrated by generating a grid around a four-element airfoil. A 21×21 Cartesian background grid (not shown) was generated automatically for this configuration. Six nodal and two linear source elements were positioned close to the airfoil section, as shown in the figure. Four nodal elements were placed at the corners of the outer boundary (not shown). The resulting grid had 13 363 cells, 7020 points, and 410 boundary points. The distribution of points was smooth and efficiently resolved all the details of the configuration, including an assumed shock wave on the front portion of the main airfoil. Producing a grid of this quality and degree of control using the prior approach would have been extremely difficult and time

consuming. The new structured background grid approach has been extended to three dimensions, where the greatest benefits are realized.

(S. Pirzadeh, 42245, and N. T. Frink)

Aeronautics Directorate

An Adaptive Remeshing Procedure for Three-Dimensional Unstructured Grids

The objective of this research is to develop and demonstrate a solution adaptive remeshing procedure for three-dimensional unstructured grids. In this procedure, an advancing front grid generator (VGRID3D) is coupled with an efficient inviscid flow solver (USM3D) in such a manner

that the information produced by one is successively used by the other to allow the grid to adapt to dominant features of the flow.

In the advancing front grid generator, the grid size is controlled by the spacing information stored at the nodes of a secondary coarse grid referred to as the "background grid." In the conventional technique, the background grid and the spacing parameter are user specified. In the present adaptive scheme, this process is automated by computing the required grid spacing on the current grid with the second gradient of density used as an error indicator. A new grid is then generated from this information in such a way that the grid is refined in the regions of high flow gradients and derefined elsewhere. Special care is taken to ascertain that adequate grid resolution is retained in flow regions ahead of the shock. A new flow solution is

next obtained on the new grid. This completes one adaptive cycle. Several cycles are usually required to obtain desired accuracy.

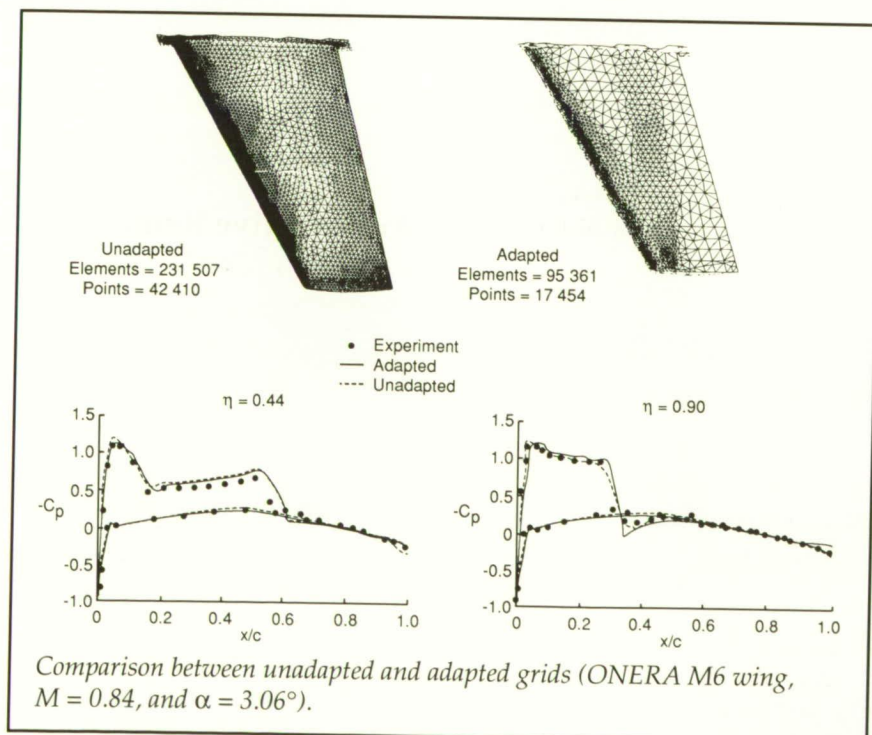
As demonstration of the technique, the flow over an ONERA M6 wing at a Mach number of 0.84 and an angle of attack of 3.06° was considered. The procedure was initiated with a coarse, almost uniform grid made up of 52 567 tetrahedral elements and 9646 points. Three remeshing cycles were performed, resulting in a grid with 95 361 elements and 17 454 points. The efficiency of the adaptive procedure is shown in the figure by comparing the results after three remeshing cycles with an unadapted flow solution. The unadapted grid has 231 507 tetrahedral elements and 42 410 points. The top portion of the figure shows the upper-surface triangulation for both the grids, while in the bottom portion the computed pressure distributions

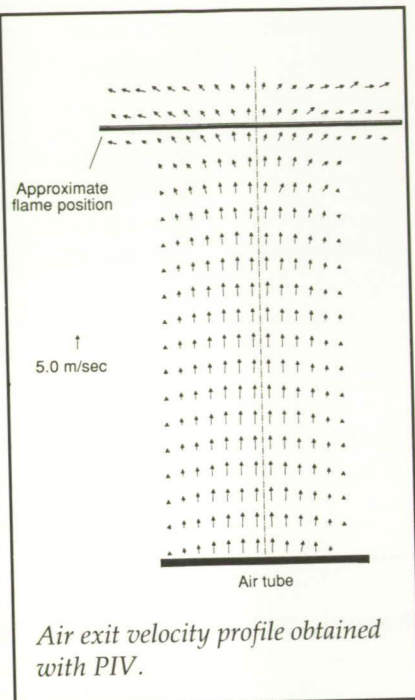
at two spanwise locations are compared with the experimental data. The adapted solution is in very good agreement with the unadapted one, which has about 2.5 times the number of elements. This work was done in part performed under contract with ViGYAN, Inc.

(P. Parikh, 42244, and N. T. Frink)
Aeronautics Directorate

Hydrogen Combustion Velocity Measurements Using Particle Image Velocimetry

Two-dimensional velocity measurements on the air side of the stagnation plane in a laminar, axisymmetric hydrogen-air counterflow diffusion flame have been successfully obtained using particle image velocimetry (PIV). This test demonstrates the capability of obtaining global velocity measurements in combustion flows. The PIV system consists of two frequency-doubled Nd:YAG lasers fired in sequence to generate a 1.0-mm-thick double-pulsed light that bisects the air jet flow along the jet centerline. A 70-mm camera system oriented normal to the plane of the light sheet images particles embedded in the airflow onto a photographic plate. Double-exposure photographs are interrogated to track the movement of individual seed particles and ascertain the local flow velocities. The counterflow flame burner consists of two uniform, centered, equal-diameter tubes or nozzles mounted vertically in a polycarbonate box purged with argon to produce a stable flame disk. The upper jet supplies hydrogen diluted with nitrogen to the flame





while the lower jet, two jet diameters below, supplies air seeded with 1.0- μ m aluminum oxide particles to the flame.

Two-dimensional velocity fields have been obtained using jet burner tube and nozzle diameters ranging from 2.5 mm to 7.0 mm and dilutions of hydrogen ranging from 25 to 100 percent. A typical two-dimensional velocity field is shown in the figure for a 5.0-mm-tube configuration that uses a 40-percent dilution of hydrogen. The peak centerline velocity is approximately 5.0 m/sec, as represented by the reference vector shown on the left side of the figure. This test represents the first use of PIV in a combustion flow at Langley, and the results agree well with previously obtained Doppler velocimetry measurements in similar flows. The PIV data are currently being used to validate compu-

tational fluid dynamics codes for these flows.

(William M. Humphreys, Jr., 44601)

Electronics Directorate

Doppler Global Velocimetry—A New Nonintrusive Flow Diagnostic Tool

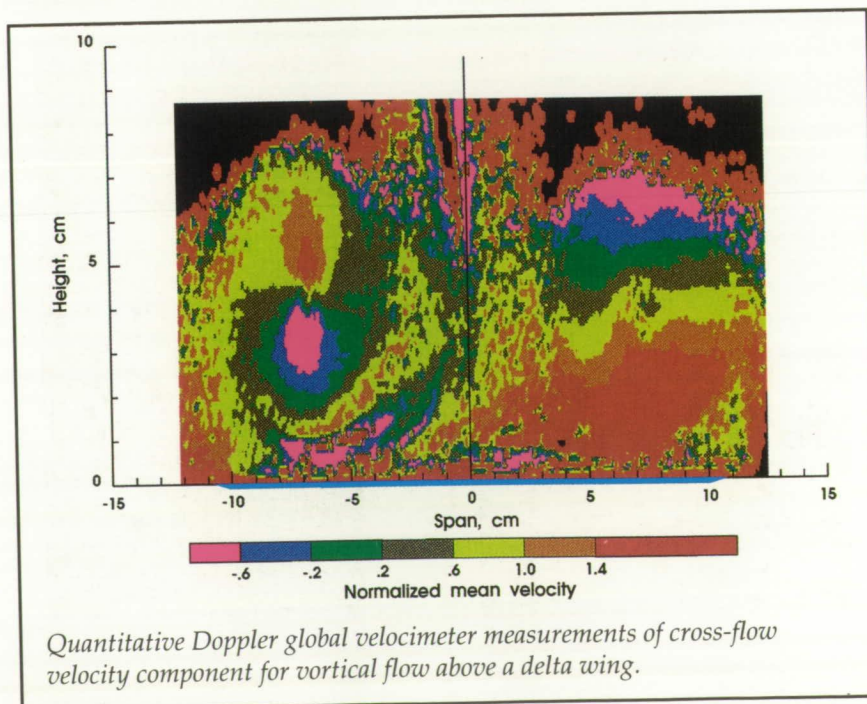
Doppler global velocimetry is a new laser-based technique that is capable of nonintrusively measuring three components of velocity within a selected measurement plane. The technique uses the edge of an iodine absorption line as an optical frequency-to-amplitude converter to determine the Doppler shifted frequency of scattered light from particles passing through a laser light sheet. Viewing the light sheet through an iodine vapor cell, a video camera produces images whose

intensity pattern is directly related to the velocity of the particle field. The additional two velocity components are obtained by placing camera systems at orthogonal viewing angles from the original camera.

Results from the proof-of-concept investigation of the vortical flow field above a 75° delta wing illustrate the capability of the technique. The cross-flow component of velocity is shown in the figure. The measurements of the left vortex exhibit the classic velocity map for a fully developed vortex flow. However, measurements of the right vortex indicate that the flow is acting as a solid body of revolution, possibly an indication of flow transition to a burst condition. Since the model had a 0.2° yaw from free stream that caused the right vortex to burst at a lower angle of attack than that at which the left burst, this speculation may be reasonable.

(James F. Meyers, 44598)

Electronics Directorate



Prediction of Exhaust Systems Performance

Improvements to supercomputer systems and Navier-Stokes computational methods have allowed for more timely and accurate analytical investigations of exhaust systems. The capability to predict propulsion system performance has benefits in possibly reducing test hardware requirements, test matrix dimensions, and facility occupancy time, as well as in determining some performance parameters for conditions that present testing facilities are unable to achieve. These analytical methods have to achieve similar levels of repeatability and accuracy as the related testing facilities to be used as reliable indicators of the relative merits of various propulsion systems.

Researchers in the Propulsion Aerodynamics Branch have been involved in the development and testing of a nozzle performance prediction package that has been implemented into an in-house 3-D Navier-Stokes method called PAB3D. Propulsion system configurations ranging from turbofan

transport nacelles to nonaxisymmetric thrust vectoring nozzles operating at on- and off-design conditions and exhausting into the freestream at conditions from static to supersonic air have been examined. A high degree of confidence has been developed in predicting various performance parameters as a result of these investigations.

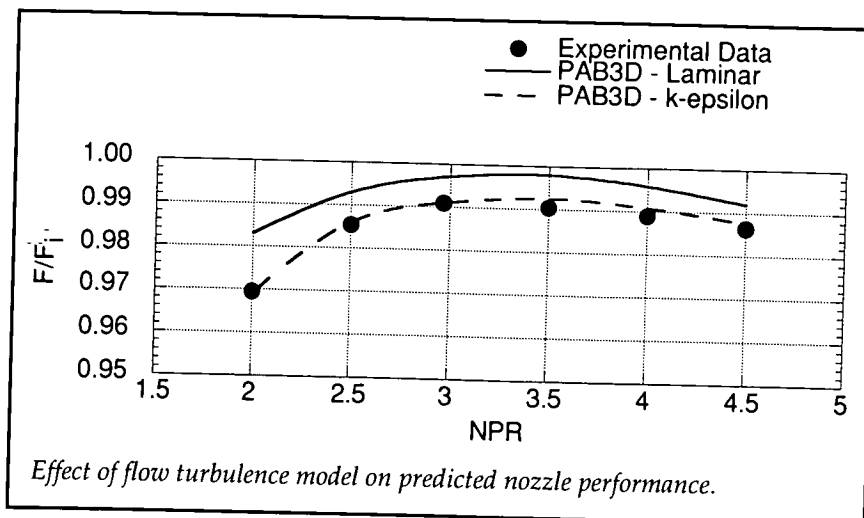
The recent implementation of a k -epsilon turbulence model has improved the accuracy of these performance predictions. The figure shows the calculation of thrust ratio F/F_i with nozzle pressure ratio (NPR) for a nonaxisymmetric convergent-divergent nozzle. The original laminar predictions were accurate in capturing the trend of thrust with nozzle pressure ratio but not the level. The advancement in turbulence modeling refined the predictions such that the level of the prediction was typically with 1/4 percent of the experimental data.

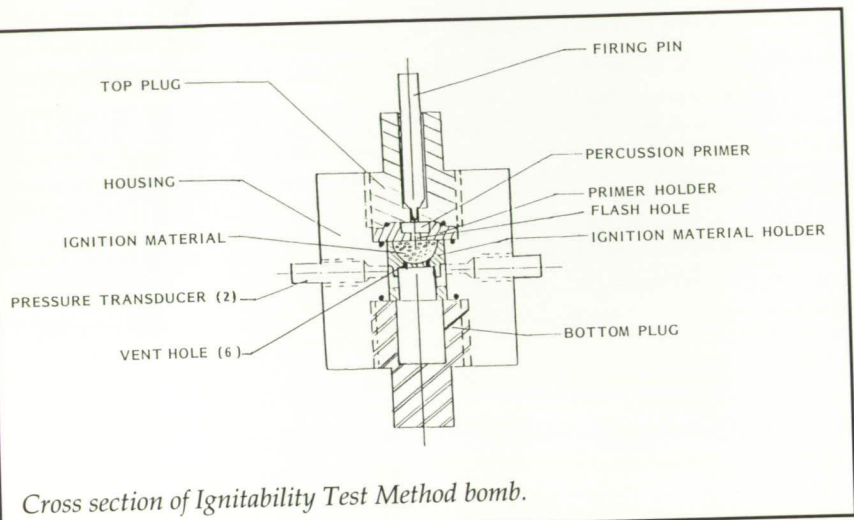
(John R. Carlson, 43047)
Aeronautics Directorate

Ignitability Test Method

A test method has been developed at Langley that measures pyrotechnic ignition. Since the invention of percussion primers in the early 1800's, no test method has gained general acceptance to be used as the basis for performance specification. Researchers have been unsuccessful in attempts to measure the extreme dynamics of primer output: heat, gas, light, and burning particles. The NASA Ignitability Test Method has overcome these technical difficulties and has provided an approach that can measure the output of initiators as well as measure the sensitivity of materials to be ignited.

The principle on which the NASA Ignitability Test Method is based is that materials to be ignited respond to the relative magnitude of initiation stimuli. That is, an initiator that has a relatively large output will ignite and burn materials more rapidly than would an initiator with a small output. To measure this relative influence, an ignition material is placed in a small-volume container (ignition material holder) within a closed chamber (bomb), as shown in a cross-sectional view in the sketch. As the ignition material ignites and burns, the gas produced is vented into the lower portion of the chamber, where pressure is measured. The rate of pressure increase is directly dependent on the total output of the initiator. The relative output performance of initiator types can be determined by firings into a single type of ignition material or standard. The relative sensitivity of materials to be ignited can be determined





by firings that use a standard initiator.

The NASA Ignitability Test Method, patented in 1991, has

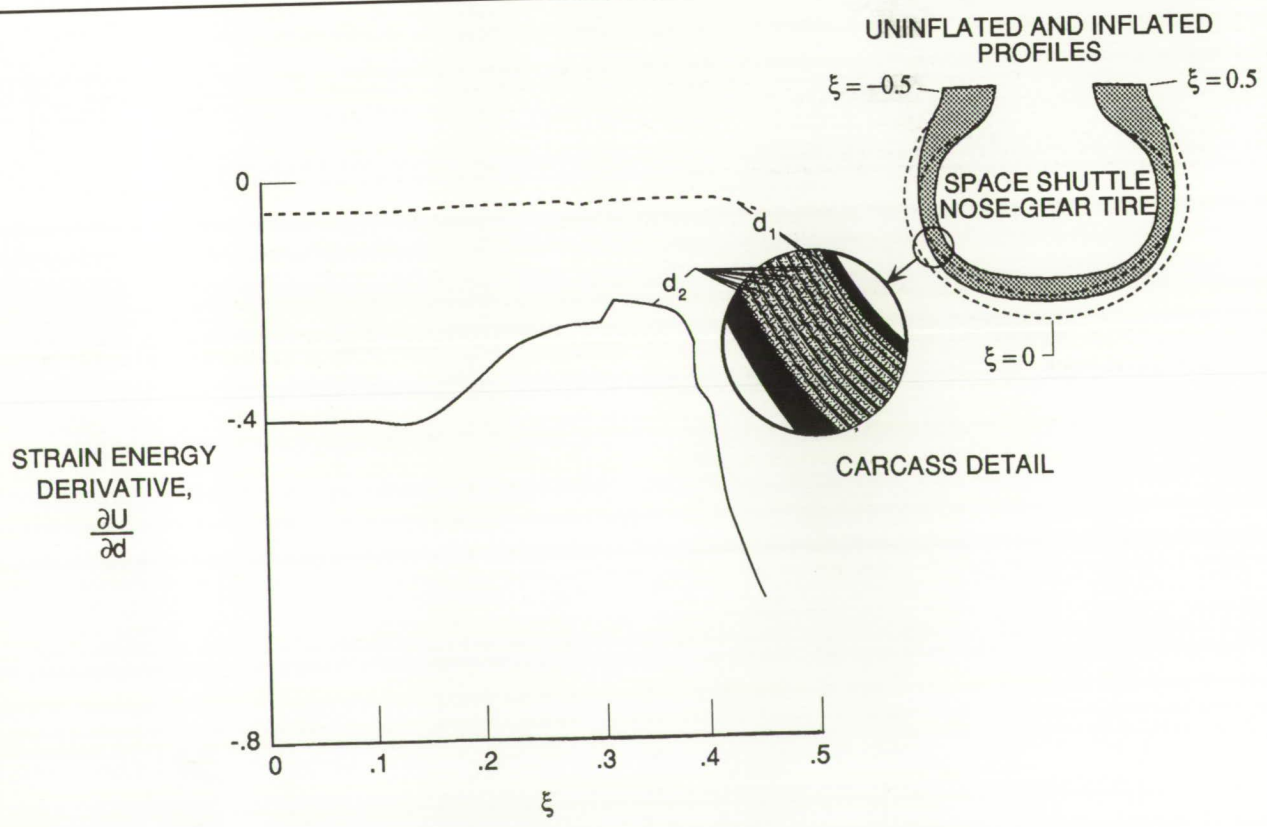
proved useful for several programs: service life evaluation of aircraft escape primers, redesign for U.S. Army and Navy percussion and electrical primers for muni-

tions, and evaluation of a material intended as a black powder replacement.

(Laurence J. Bement, 47084)
Systems Engineering and Operations Directorate

Analytic Sensitivity Derivatives Developed for Key Tire Response Parameters

A computational procedure has been developed for evaluating the analytic sensitivity derivatives of tire response with respect to material and geometric parameters of the tire. The computational



Space Shuttle nose-gear tire strain energy sensitivity derivatives.

procedure is applied to the 32×8.8 Space Shuttle orbiter nose-gear tire subjected to a uniform inflation pressure load.

The uninflated and inflated profiles of the Space Shuttle orbiter nose-gear tire are shown in the figure. The effect of the 300-psi inflation load is to force the tire profile to grow radially outward, as denoted by the dashed line in the figure. The tire carcass is composed of 10 plies of rubber and nylon cords and is covered with an inner liner and a natural rubber sidewall and tread outer layer. The carcass plies are constructed with nylon cords of two different diameters. The two inner plies contain the smaller diameter cords, denoted by d_1 , and the remaining plies contain the larger diameter cords, denoted by d_2 . The sensitivity derivatives indicate that increasing cord diameter decreases the strain energy density of the tire due to inflation. Additional analytic sensitivity derivatives have been developed for transverse shear strain energy density, stress resultants, and generalized displacements with respect to tire design parameters such as the elastic and shear moduli of the cord and the rubber.

The development of analytic sensitivity derivatives of tire response with respect to tire material and geometry parameters will provide the tire industry with powerful analytical tools for tire design and analyses.

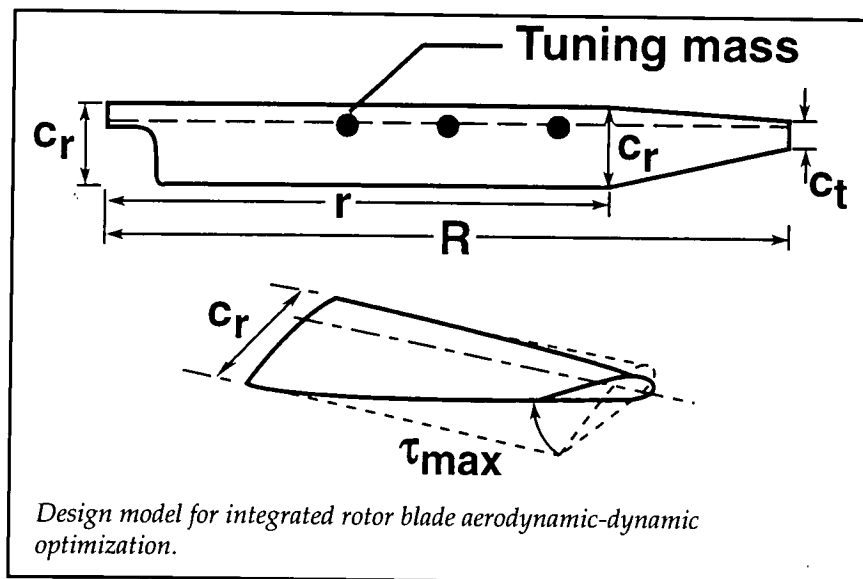
(Ahmed K. Noor, 41978, John A. Tanner, Jeanne M. Peters, and Martha P. Robinson)
Structures Directorate

Fully Integrated Aerodynamic-Dynamic Optimization Procedure for Helicopter Rotor Blades

A fully integrated aerodynamic-dynamic optimization procedure that accounts for aerodynamics (loads), performance, and dynamics simultaneously has been developed. The procedure can be used to optimize the aerodynamic and dynamic performance of rotor blades by determining the planform shape, pretwist, stiffness distributions, and mass distribution that minimize an objective function, which is a linear combination of horsepowers required for hover, forward flight, and maneuver and 4 per rev vertical hub shear for forward flight. The design variables (see figure) are blade root chord c_r , taper ratio c_r/c_t , point of taper initiation r/R , maximum pretwist τ_{\max} , blade bending and torsional stiffnesses, tuning masses, and tuning mass locations. The procedure uses a strip theory momentum analysis

to compute hover horsepower and the comprehensive helicopter analysis program CAMRAD/JA to determine forward flight and maneuver performance and dynamics. The optimization algorithm consists of the general purpose optimization program CONMIN and approximate analyses. Constraints include limits on required horsepowers, frequencies, airfoil stall, weight, autorotational inertia, and tip chord.

The procedure has been applied to show that it can reproduce the design of an existing wind tunnel model of a growth utility rotor blade designed through parametric studies. The final blade, determined by the optimization procedure, is similar in planform to the existing blade and has performance measures quite close to those of the existing blade. Specifically, the horsepowers required for hover, forward flight, and maneuver for the optimized blade are 14.41 hp, 12.54 hp, and 11.78 hp, respectively, and the 4 per rev vertical hub shear for forward flight is 1.17 lbf. For the



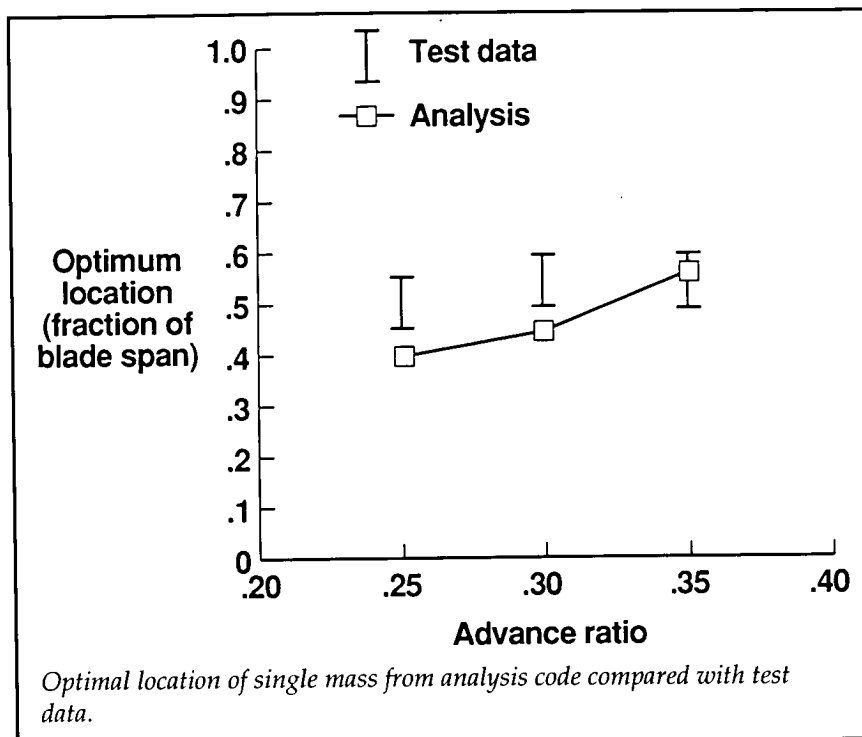
existing blade these values are 14.84 hp, 13.13 hp, 11.83 hp, and 1.52 lbf, respectively.

(Joanne L. Walsh, 42806, William J. LaMarsh II, and Howard M. Adelman)
Structures Directorate

Method for Reducing Helicopter Rotor Blade Vibration

The concept of tuning mass placement has been demonstrated to reduce vibration in helicopter rotor blades. Conventionally, the masses and locations are varied by trial and error. An optimization procedure has been developed that systematically determines the best locations and values for tuning masses to reduce vibratory vertical hub shear in helicopter rotor blades. Optimal placement of the mass tailors the mode shapes and air loads and thus reduces generalized force and response of the blade. The method entails formulating an optimization procedure that employs the tuning masses and their locations as design variables to minimize vertical hub shear without a large mass penalty. The optimizer is combined with a comprehensive helicopter analysis code (CAMRAD/JA) that calculates mode shapes, frequencies, air loads, and hub shears. The variation in the air loads due to changes in the design variables is taken into account by using CAMRAD/JA.

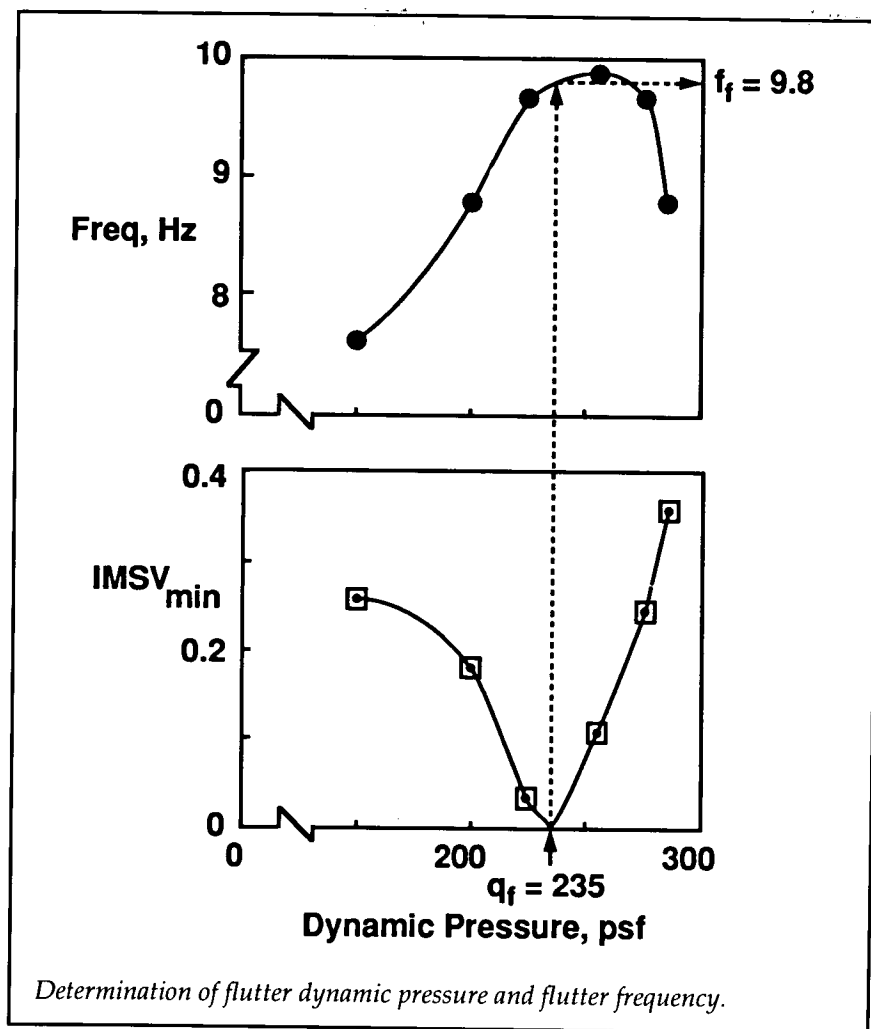
The procedure has been applied to a wind-tunnel model blade that has the capability for adding tuning masses along the blade span. The model, designed to



study passive means for minimizing fixed-system loads, was tested in the Langley Transonic Dynamics Tunnel and provided an opportunity to validate the optimization procedure. The test data included 4-per-rev hub shear as a function of the location of a tuning mass of 0.27 lbm for several flight conditions. The figure shows the comparison between the optimization results and the test data for three advance ratios. The test data are shown as a range because the data were only available at 10-percent increments along the blade. The optimization procedure was able to predict an optimization location that was within the range of the test data for the advance ratio of 0.35. The other two cases were within 12 percent of being in the range. (Jocelyn I. Pritchard, 42805, Howard M. Adelman, Joanne L. Walsh, and Matthew L. Wilbur)
Structures Directorate

Open-Loop Flutter Condition Determined From Closed-Loop Measurements

The objective of this work is to determine, under near real-time conditions, the open-loop flutter dynamic pressure and the open-loop flutter frequency from multi-input-multi-output closed-loop flutter suppression wind-tunnel test results. At various test conditions, a closed-loop system is excited systematically and the excitation and associated response time histories are measured. These time histories are then processed with fast Fourier transforms used to determine the closed-loop frequency response matrix, from which the open-loop frequency response matrix is extracted through the use of matrix analysis procedures. The inverse of the



maximum singular values (IMSV) of the open-loop frequency response matrix can now be calculated. The minimum of the IMSV ($IMSV_{min}$) is an indication of an impending open-loop instability (open-loop flutter), and the frequency at which the minimum occurs is the frequency of the instability. To obtain a flutter prediction, these calculations are performed with data acquired at a number of dynamic pressures. The values of $IMSV_{min}$ and their associated frequencies are then plotted as a function of dynamic pressure. Instability is defined to occur when $IMSV_{min} = 0$. This

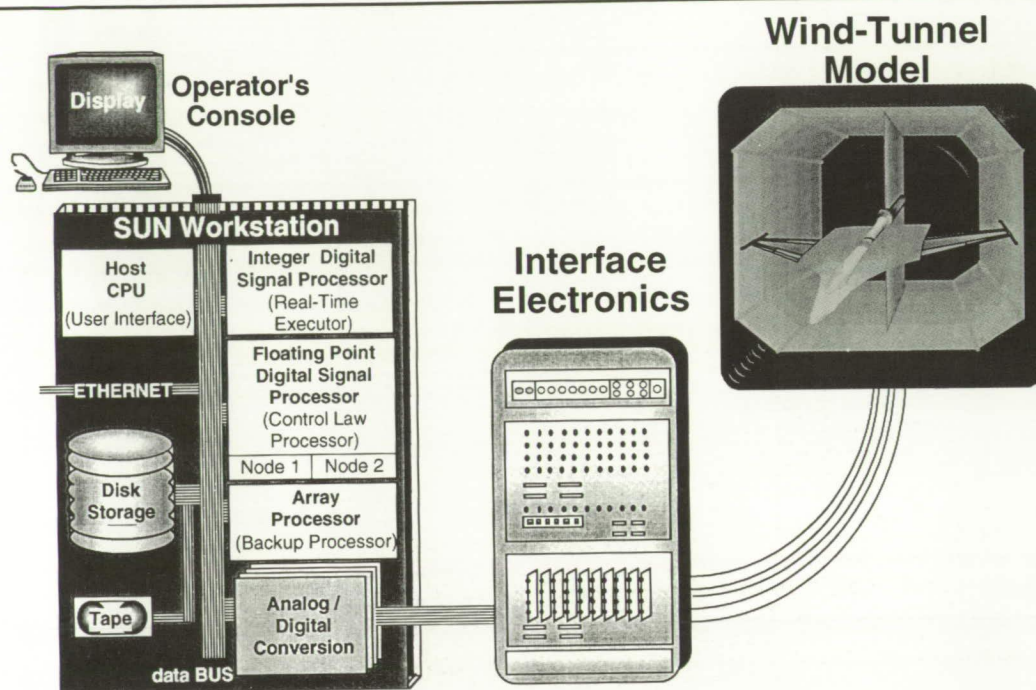
methodology was applied during recent wind-tunnel tests of a sophisticated aeroelastic model. The data presented in the figure show $IMSV_{min}$ and its associated frequency plotted as functions of dynamic pressure. From the figure, the predicted open-loop flutter dynamic pressure q_f is 235 psf; the predicted flutter frequency f_f is 9.8 Hz. These predictions are in very close agreement with flutter characteristics measured by a traditional technique employed during open-loop tests. This method provides a means of assessing the stability of an open-loop system under closed-loop

conditions. The procedures can be implemented easily on microcomputers and are readily adaptable to wind-tunnel and flight flutter investigations.

(Anthony S. Pototzky, 42827, Carol D. Wieseman, Sherwood T. Hoadley, and Vivek Mukhopadhyay)
Structures Directorate

Digital Controller Developed To Provide Multifunction Control of Aeroelastic Response

The Active Flexible Wing (AFW) Program was a cooperative effort between the NASA Langley Research Center and Rockwell International Corporation. The overall goal of the program was to demonstrate aeroelastic control, through the application of active controls technology, with a sophisticated aeroelastic wind-tunnel model. The control functions investigated were flutter suppression (FS), rolling maneuver load alleviation (RMLA), and multifunction control (simultaneous operation of FS and RMLA). The AFW wind-tunnel model was an aeroelastically scaled, full-span, free-to-roll model of an advanced fighter configuration. Among the program objectives was gaining practical experience in designing, fabricating, and implementing a real-time multifunction multi-input-multi-output digital controller system and its hardware-software interfaces. The figure depicts the digital controller system, the AFW wind-tunnel model, and the electronics interface between them. As shown in the figure, the digital controller system consisted



Digital Controller System

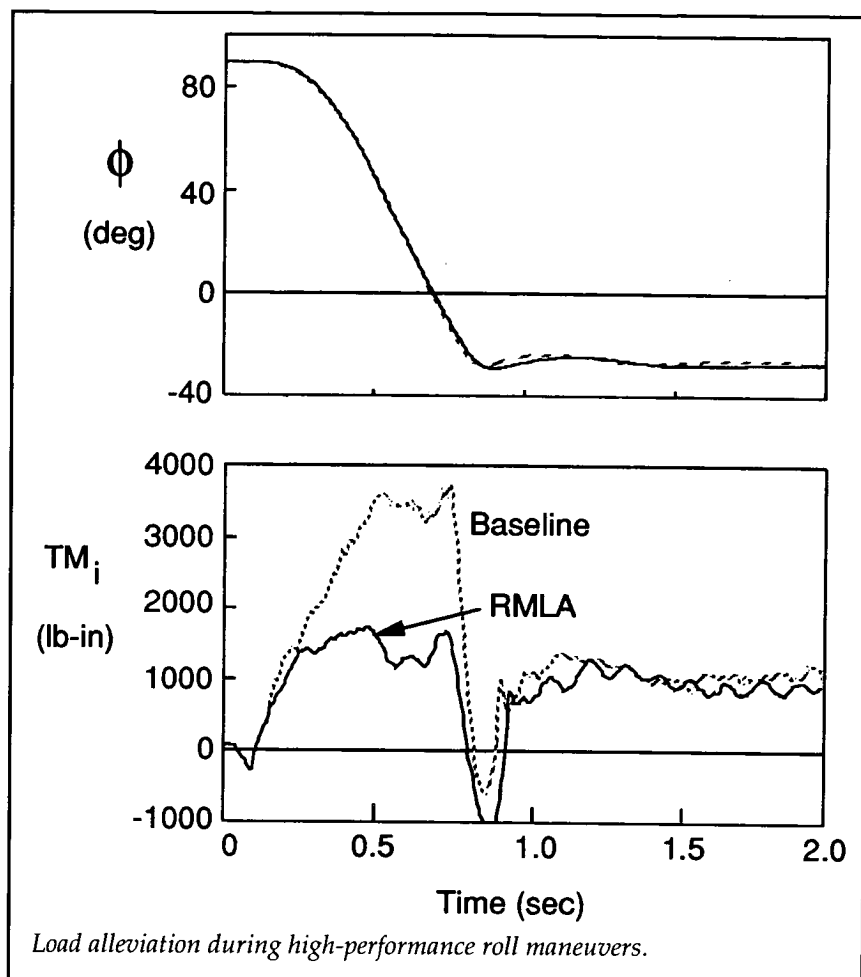
Multifunction digital controller.

of a host computer, a real-time executor, a control law processor, a backup processor, and analog-to-digital conversion boards. The real-time executor performed timing control of the entire digital controller system, operating at 200 Hz within the much slower (60 Hz) host time-share operating system environment. It synchronized the operation of four processing units, coordinated the acquisition, storage, and transfer of data, and allowed simultaneous execution of different control laws. The digital controller system was a key element in the AFW Program, allowing four combinations of control laws (FS and RMLA) to perform very aggressive roll maneuvers above the open-loop flutter boundary. (Sherwood T. Hoadley, 42832, and Sandra M. McGraw) Structures Directorate

Wing Loads Actively Controlled During Rolling Maneuvers

The objective of this research was to develop an active control law that would reduce incremental wing loads generated on the Active Flexible Wing (AFW) aeroelastic wind-tunnel model during rolling maneuvers while constant roll performance was maintained. To meet this objective a rolling maneuver load alleviation (RMLA) control law was designed with roll-rate feedback and two pairs of control surfaces on the wing, one trailing-edge pair and one leading-edge pair. This choice of control surfaces made load alleviation possible because of the ability of the outboard pair to deform the wing and thereby

oppose increases in incremental loads. In addition, the control law was designed to produce control surface deflections and rates that were moderate and analytically did not saturate. The closed-loop system gains were determined by using classical techniques and by employing optimization to achieve a specified roll performance. For purposes of comparison, a baseline control law was designed with no consideration made for reducing incremental wing loads. Peak torsion and bending moment incremental loads obtained during the RMLA-controlled roll maneuvers were compared with baseline incremental loads to determine the RMLA effectiveness. A comparison of the incremental inboard torsional moments TM_i , shown at the bottom of the figure, shows that the RMLA control law



reduced the incremental loads by up to 60 percent. The plot of model roll angle ϕ as a function of time with and without the RMLA control law activated (top of the figure) shows that the RMLA control law provided identical roll performance as that of the baseline control law.

(Jessica A. Woods-Vedeler, 42829, and Anthony S. Pototzky)
Structures Directorate

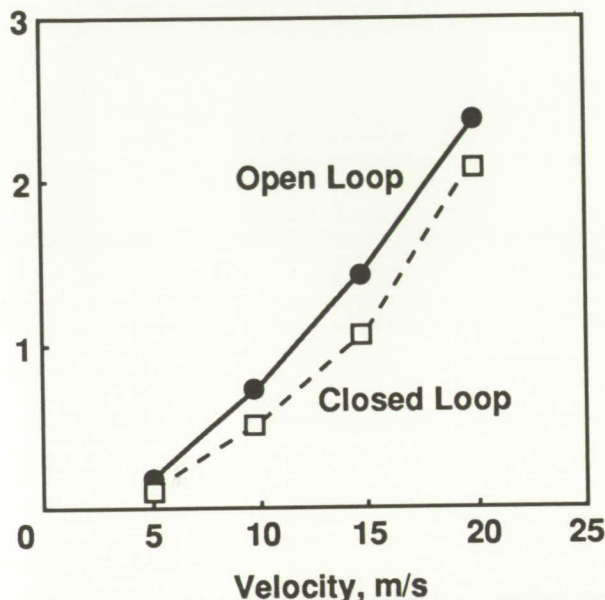
Buffet Load Alleviation Accomplished Via Piezoelectric Actuation

Fighter aircraft operating at high speed and at high angles of attack often experience severe buffeting of the empennage. The buffet phenomenon generally involves turbulent flows produced by flow over an upstream component such as the wing. The turbulent wake is transported downstream and may impinge directly on the empennage. The resulting buffet loads can cause severe structural damage. Traditional solutions to the buffet

are to add structural support so that the surface can withstand the buffeting air loads or to divert the turbulent flow away from the surface. These passive techniques degrade performance and are very costly. A new, promising solution is to apply active control principles that use piezoelectric actuators embedded in the structure. To investigate the feasibility of this alternate solution, an experiment was conducted in an open-circuit tabletop wind tunnel. In the test section, a rigid horizontal tail was attached to a flexible mount system that provided a single-degree-of-freedom plunging motion. A rigid wing was placed upstream of the test section to generate a wake flow representative of a wing-horizontal-tail configuration. The control system consisted of a strain-gage sensor, a gain feedback control law implemented on a digital controller, and a piezoelectric-ceramic (lead zirconate titanate) actuator. Open- and closed-loop values of a parameter proportional to strain were measured and plotted in the figure as functions of velocity. In the closed-loop condition, the parameter was reduced an average of 27 percent over the entire velocity range tested; at one velocity condition the strain parameter, and thus the buffet loads, were alleviated by 41 percent. This solution involving active controls with a unique actuation concept offers the promise of being a low-weight and low-cost approach for alleviating buffet loads.

(Jennifer Heeg, 42795, Robert Doggett, and Jonathan Miller)
Structures Directorate

**Buffet
Response
Parameter**



Buffet responses as functions of velocity.

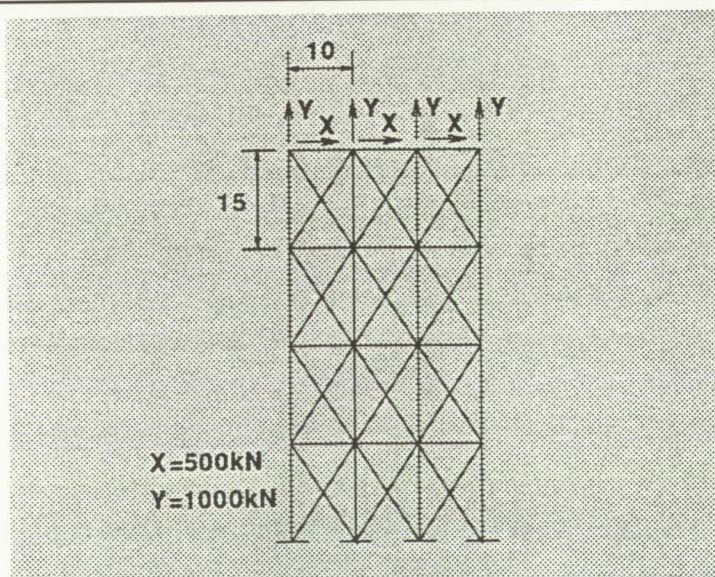
Automatic Differentiation Adapted and Evaluated as a Tool for Engineering Design

Engineering design and optimization require sensitivity information. For some engineering disciplines, analytical techniques exist to generate those sensitivities; for most disciplines, however, those derivatives have not yet been developed. Automatic differentiation (AD) is a viable alternative for generating those sensitivities. Automatic differentiation is a technique that automatically derives a computer program that performs exact sensitivity analysis of a problem solution, starting from a program implementing that solution. If the original program calculates a set of dependent variables from a set of independent variables, the modified program calculates the

derivatives of the dependent variables with respect to the independent variables. Automatic differentiation is a systematic implementation of the chain rule of differentiation, at a cost general-

ly lower than that of conventional finite differencing.

The purpose of this initial phase of the research was to demonstrate the use of an AD code in engineering applications. The code GRESS, development at Oak Ridge National Laboratory, was selected as a representative AD code. It was applied to the finite-element analysis program STAP, which performs static analysis of space trusses. An example solved was the planar truss shown in the figure. The truss was fixed at the lower end and loaded with X- and Y-forces at the free upper end. The independent variables were the 52 member cross-sectional areas, while the dependent variables were 113 quantities including structural weight, nodal displacements, and member stresses. The resulting derivatives were generated in 7 sec on a Sun SPARCstation 1+; generating the corresponding derivatives by finite differencing would have taken 36 sec. Therefore, AD offers a means for



Planar truss.

generating exact derivatives at a cost that can be lower than finite differencing.

(Jean-Francois M. Barthelemy, 42809, and Laura E. Hall)
Structures Directorate

Implicit Upwind Algorithm Developed for Unstructured Meshes

A new algorithm was developed for the numerical solution of the time-dependent Euler equations on unstructured meshes. The algorithm involves accurate and efficient spatial and temporal discretizations of the Euler equations, based on unstructured meshes of tetrahedral grid cells. The spatial discretization involves an upwind approach that accounts for the local wave-propagation characteristics of the flow and captures shock waves sharply with, at most, one grid point within the shock structure. The temporal discretization is an implicit time-integration scheme involving

a Gauss-Seidel relaxation procedure. The scheme allows the selection of the step size based on the temporal accuracy dictated by the physical problem being considered, rather than on the numerical stability of the algorithm. Consequently, very large time steps may be used for rapid convergence to steady state, and an appropriate step size may be selected for unsteady cases, independent of numerical stability issues.

To demonstrate the implicit upwind algorithm, calculations were performed for the Boeing 747 aircraft at a free-stream Mach number of 0.84 and an angle of attack of 2.73° . The resulting steady-pressure-coefficient contours on the surface of the 747 aircraft are shown in the figure. The contours indicate that there is a significant amount of flow compression on the nose of the aircraft, along the inboard leading edge of the wing, and inside the cowl of the engine nacelle. There is a flow expansion terminated by a shock wave on the forward fuselage, on the horizontal and

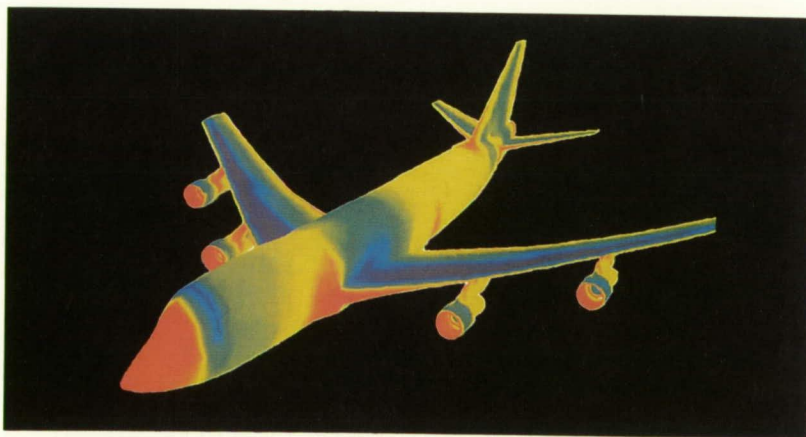
vertical tail surfaces, and on the upper surface of the wing. The solution required less than 1 hour of CPU time on a Cray-2 computer, which is an order of magnitude less time than that required for previous methods.

(John T. Batina, 42268)
Structures Directorate

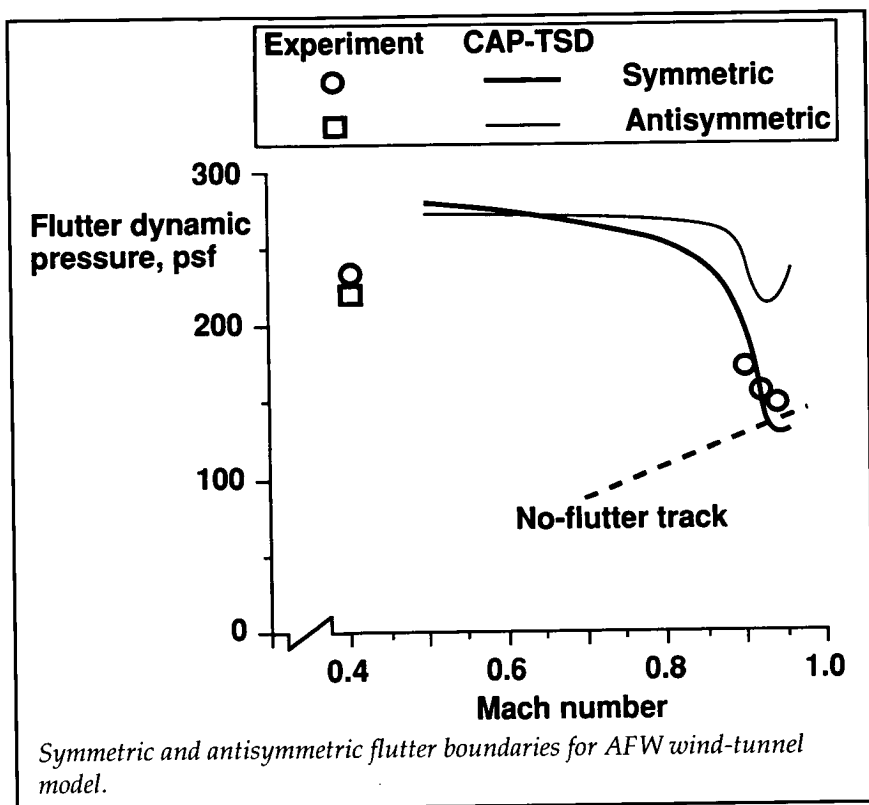
Symmetric and Antisymmetric Flutter Boundaries Computed With the CAP-TSD Code

The computational fluid dynamics (CFD) code known as CAP-TSD (Computational Aeroelasticity Program-Transonic Small Disturbance) was applied to the AFW (Active Flexible Wing) wind-tunnel model for the purpose of predicting the aeroelastic behavior of the model. The code solves the nonlinear transonic small-disturbance equation, which models some of the aerodynamic nonlinearities that can be encountered at transonic Mach numbers that are not modeled in linear aerodynamic codes.

The AFW wind-tunnel model is a full-span model, and its aeroelastic motion therefore consists of both symmetric and antisymmetric motions about its centerline. Analysis of the aeroelastic behavior of the model consisted of symmetric and antisymmetric computational models. The resultant computed symmetric and antisymmetric flutter boundaries are shown in the figure, along with the experimental flutter results. As shown, comparison of the CAP-TSD symmetric flutter boundary with the symmetric



Steady-pressure-coefficient contours on surface of Boeing 747 aircraft.



experimental flutter points indicates excellent agreement at the highly critical transonic Mach numbers.

The CAP-TSD symmetric flutter boundary was computed for a semispan model of the AFW, while the computation of the antisymmetric flutter boundary required a full-span model of the AFW that increased the complexity of the analysis. The CAP-TSD antisymmetric flutter boundary shown in the figure is thought to be the first antisymmetric flutter boundary computed with an aeroelastic CFD code. Comparison with the only antisymmetric experimental flutter point indicates a slight discrepancy. The computed results, however, indicate that the antisymmetric flutter dynamic pressure is lower than the symmetric flutter dynamic pressure at

subsonic Mach numbers but higher than the symmetric flutter dynamic pressure at transonic Mach numbers. This trend is consistent with the experimental flutter results.

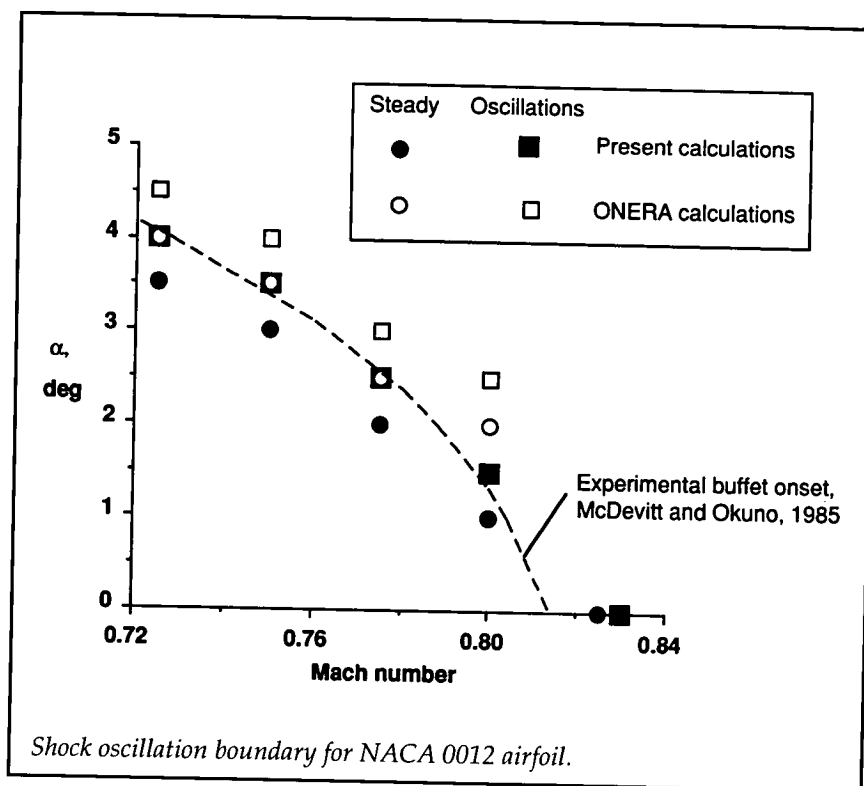
(Walter A. Silva, 42834, and Robert M. Bennett)
Structures Directorate

Transonic Shock Oscillations Calculated With a New Boundary-Layer Coupling Method

At transonic speeds, the interaction of a shock wave over an airfoil with the viscous boundary layer adjacent to the airfoil surface can lead to oscillations of the shock wave over large portions of the chord. This effect can mark the

onset of separated flow and is critical in determining minimum transonic flutter speeds and the onset of buffeting response. Direct calculation of such flows with higher order computational codes is possible but is very expensive and can suffer from the lack of grid resolution in tracking the dynamic "off the surface" free shear layers involved. The present approach uses the interacting boundary-layer method, wherein two separate numerical simulations calculate (1) the outer inviscid flow (including the shock wave) and (2) the inner viscous-boundary-layer flow. The inviscid solution is provided by the transonic small disturbance potential equation, while the lag-entrainment integral boundary-layer equations provide the viscous solution. A difficulty has been the procedure for coupling the inner and outer solutions (the two solutions should match at the edge of the boundary layer) for cases involving self-induced shock oscillations.

The new coupling method uses active control elements to minimize the coupling error for cases involving unsteady flow separations; a variable-gain integral control element provides the boundary-layer displacement thickness needed for the two simulations. The new method is robust and efficient and allows the calculations of the following types of transonic flows: steady attached flow, shock-induced separation bubbles, trailing-edge flow separation, and unsteady shock-induced separating and reattaching flows. The figure shows the boundary for shock oscillations ("buffet" onset) for the NACA 0012 airfoil calculated with the present method to be in excellent agreement with



experimental data (from McDevitt and Okuno, NASA TP-2485, 1985) and an improvement over calculations made by ONERA researchers. The shock oscillates over 25 percent of the airfoil chord, and this shock oscillation causes large variations in the air loads. (John W. Edwards, 42273) Structures Directorate

Subsonic-Transonic Flutter Boundary Computed With Unsteady Euler Aerodynamic Method

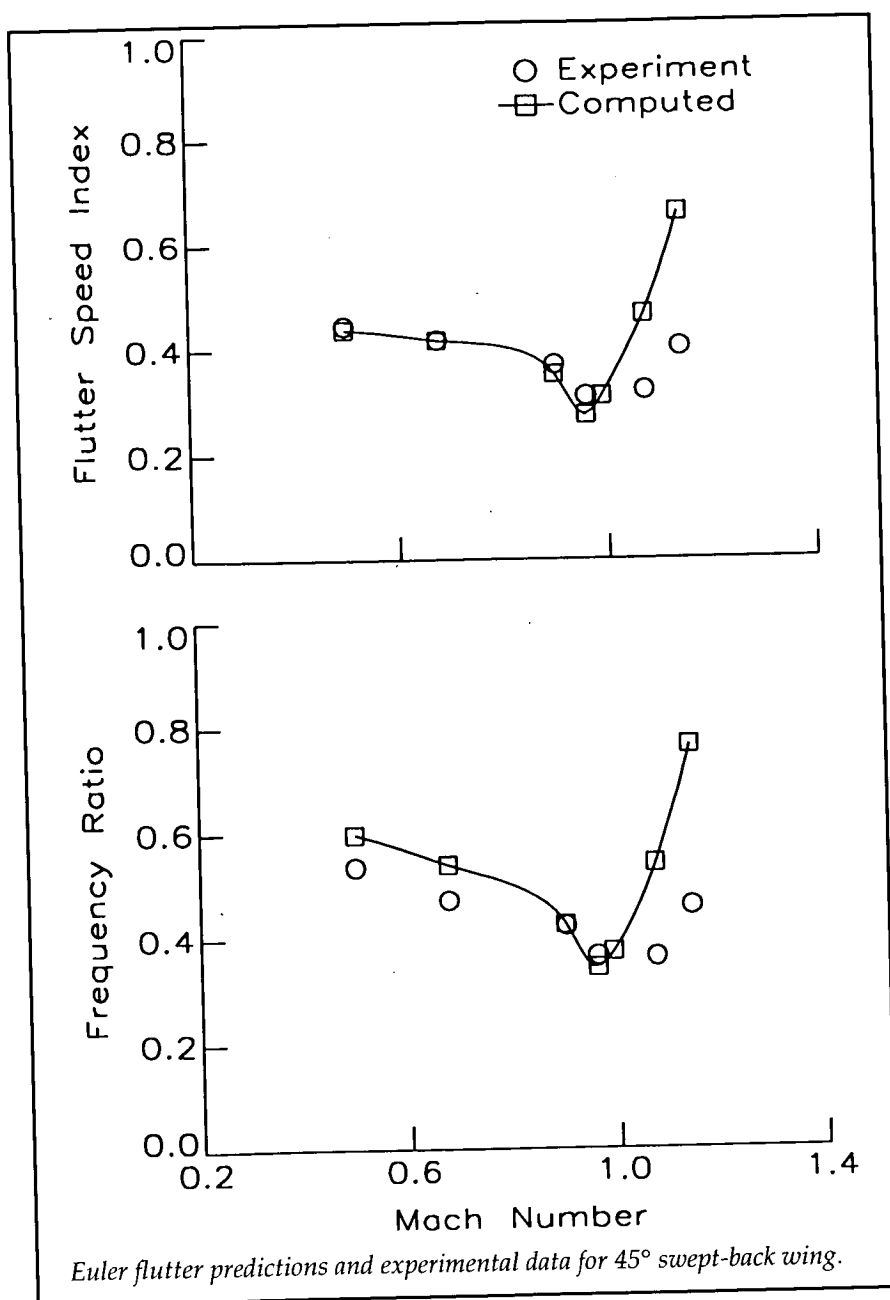
The research during the last decade on the application of computational fluid dynamics methods to unsteady flows and aeroelastic analysis has been

rapidly progressing. The transonic speed range has been a main focus of activity because flutter dynamic pressures are typically critical (i.e., lower) in this speed range. Much of this research, especially for three-dimensional configurations, has focused on the development of finite-difference methods for the solution of the transonic small-disturbance and full-potential equations. However, many critical challenges facing computational aeroelasticity will require the modeling of more complex flow physics. To meet these challenges, a higher order method that uses the Euler equations is being developed and validated for unsteady aerodynamic and aeroelastic analysis.

In order to allow for aeroelastic analysis, the structural dynamics equations of motion and a dynamic mesh capability were added to

the CFL3D Euler/Navier-Stokes computational aerodynamics program (originally developed in the NASA Langley Computational Aerodynamics Branch, Fluid Mechanics Division). The flow equations and structural dynamics equation were integrated simultaneously with the fluid flow equations, and a dynamic mesh was used to model wing motion. The resulting method was applied to an AGARD standard aeroelastic wing that was tested for dynamic response in the Langley Transonic Dynamics Tunnel (TDT). This wing has a quarter-chord sweep angle of 45°, a panel aspect ratio of 1.65, a taper ratio of 0.66, and NACA 65A004 airfoil sections. Flutter analyses were performed at free-stream Mach numbers of 0.388, 0.678, 0.90, 0.96, 1.07, and 1.14.

The results of these analyses are compared with the experimentally determined flutter speed index and flutter frequency ratio in the upper and lower parts of the figure. These results show that at subsonic free-stream Mach numbers, the computed flutter speed index agrees well with the experimental values, while the computed frequency ratio is slightly below the experimental value. As the free-stream Mach number approaches 1.0, the computed flutter speed index is slightly below the experimental value, and the computed frequency ratio agrees well with the experimental value. At speeds above Mach 1.0, where the flutter boundary is particularly sensitive to Mach number, the computed boundary indicates a sharper rise than was measured. These results are believed to be some of the first wing flutter boundary calculations



obtained with Euler equation aerodynamics.
(Elizabeth M. Lee, 42269, and John T. Batina)
Structures Directorate

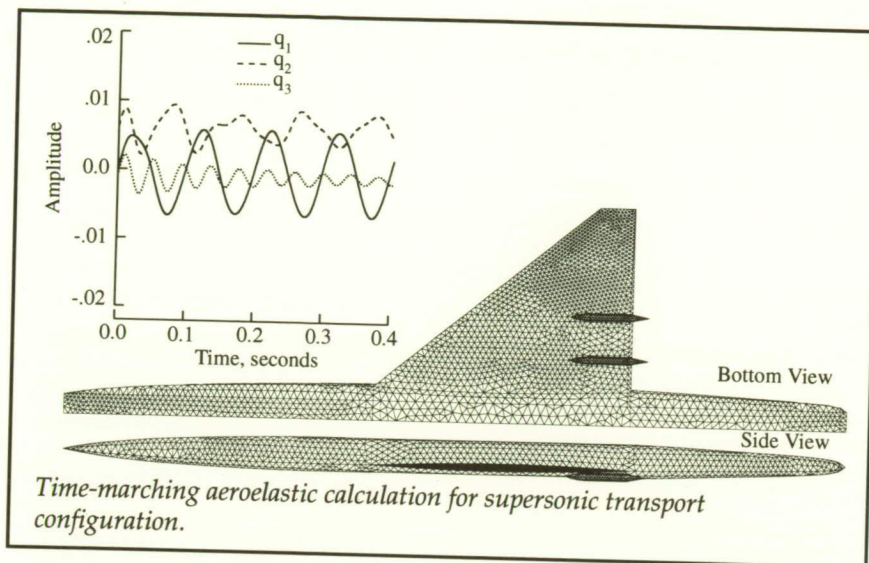
Euler Flutter Analysis of a Complex Aircraft Configuration Demonstrated With Unstructured Deforming Meshes

Unstructured-grid methods have advantages over structured-

grid methods for steady flow analysis, such as the ability to treat very complicated geometries and the ability to adaptively refine the grid for maximum accuracy and computational efficiency. This advantage suggests that the methodology also may have greater capabilities for unsteady aerodynamic and aeroelastic analysis. Consequently, a study was undertaken to assess the accuracy of the unstructured-grid methodology for flutter analysis of a complex aircraft as the first step toward aeroelastic analysis of complete aircraft configurations.

Modifications were made to a three-dimensional, upwind-type Euler code that uses unstructured grids of tetrahedrons to include the structural equations of motion for their simultaneous time integration with the governing fluid flow equations. A novel aspect of the capability is that the solution is obtained through the use of an unstructured grid made up of tetrahedrons. The code also includes a deforming mesh algorithm that is capable of treating aeroelastic motions of complete aircraft configurations.

A calculation was performed for a supersonic transport configuration at a free-stream Mach number of 0.907 and at an angle of attack of 0°. The configuration, which was tested in the Langley Transonic Dynamics Tunnel, consists of a rigid fuselage and a flexible clipped delta wing with two identical slender underwing bodies to simulate engine nacelles. The bottom and side views of the surface mesh are shown in the figure. These views show that cells have been clustered near the wing tip and around the simulated nacelles. The complete mesh for



the configuration contains 323 818 tetrahedrons and 59 429 nodes. An aeroelastic time-marching calculation was performed at a value of dynamic pressure that was found experimentally to correspond to flutter. The generalized displacements for the first three structural modes are shown in the figure. The near neutrally stable transient of the first generalized displacement q_1 indicates that the computed aeroelastic transient is near the flutter point. Therefore, the computed value of dynamic pressure is in good agreement with the experimental value. (Russ D. Rausch, 42261, and John T. Batina) Structures Directorate

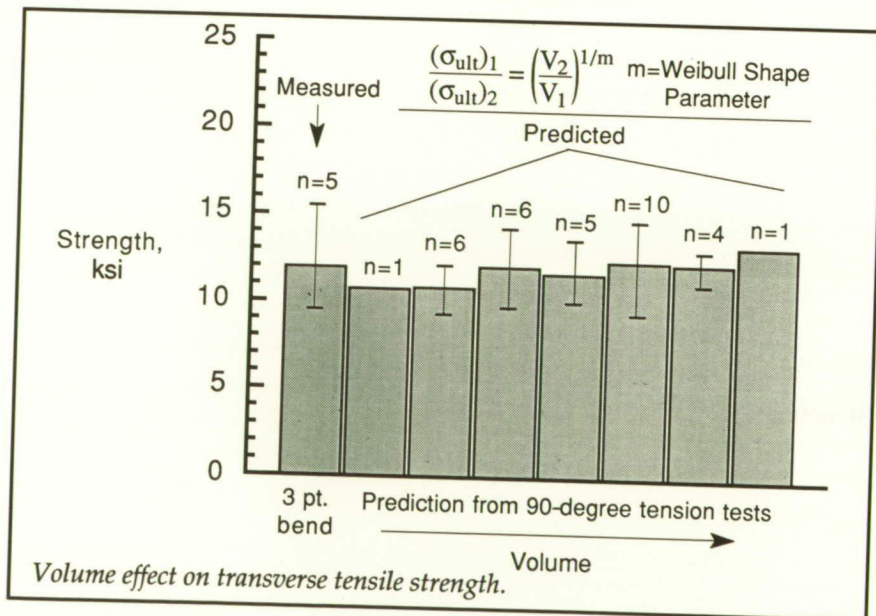
Scale Effects on the Transverse Tensile Strength of Graphite/Epoxy Laminates

Ninety-degree tension tests are routinely performed to evaluate alternate suppliers for the same

material and to compare the transverse tensile strength of new materials. Also, these data are used in progressive damage models to predict matrix cracking, or "first ply failure." Furthermore, these data are often used to estimate the out-of-plane strength, or interlaminar tension strength. The present study was conducted to determine if there is a volumetric dependence on the transverse tensile strength measured in a 90° tension test.

Ninety-degree tension tests were conducted on AS4/3501-6 graphite/epoxy laminates with five different thicknesses and three different widths. A volumetric scale law based on Weibull statistics was used to predict the strength of 90° laminates in bending and the interlaminar tensile strength measured on a 0° curved beam specimen.

The Weibull scale law with data from any single 90° tension test configuration could be used to predict the transverse tensile strength measured in the 90° bend test (see figure) and the interlaminar tensile strength measured in the 0° curved beam test. Hence, any one of these three test configurations may be used to generate the strength and may be scaled through use of Weibull statistics to determine the strength in any other configuration. This scaling capability will greatly reduce the amount of testing required to qualify new materials and to generate failure criteria. (T. K. O'Brien, 43465) Structures Directorate



Damage Resistance of Carbon/Epoxy Composites

Carbon/epoxy composite laminates are damaged more easily than metals are by transverse impacts from dropped tools, runway debris, collisions, hail, etc. "Tougher" composites suffer less damage for a given kinetic energy, but tend to have the same strength for the same level of damage. Thus, material comparisons are best made using damage size rather than residual strength. For a large impactor mass, a small plate behaves as though the impact force were applied quasi-statically and the nominal plate stresses depend only on the impact force. (Larger plates will respond quasi-statically if impactor mass is increased accordingly.) Thus, the size of damage will depend largely on the impact force.

Impact damage in laminated composites initiates near the contact site as matrix ply cracks and broken fibers. Delaminations initiate from the cracks at interfaces

between lamina of different orientations and propagate outward. The overall damage size, which circumscribes delaminations, can be readily determined through the use of C-scan ultrasonic images. Damage diameters are plotted against impact force in the figure for static indentation tests of circular specimens and for pendulum impact tests. The data coalesce, which verifies that damage size depends only on impact force for a given laminate when the response is quasi-static. The damage diameters are approximately proportional to impact force. The constant of proportionality of 41.5 kN/m corresponds to a constant value of transverse shear force per unit circumference for a quasi-isotropic laminate. Tests of the same laminate made with a toughened matrix gave a value of 158 kN/m; thus, nearly four times the impact force (about two times the kinetic energy) was required to propagate a delamination in the toughened material. Based on interlaminar fracture mechanics, it is expected that the constant of proportionality of 41.5 kN/m is

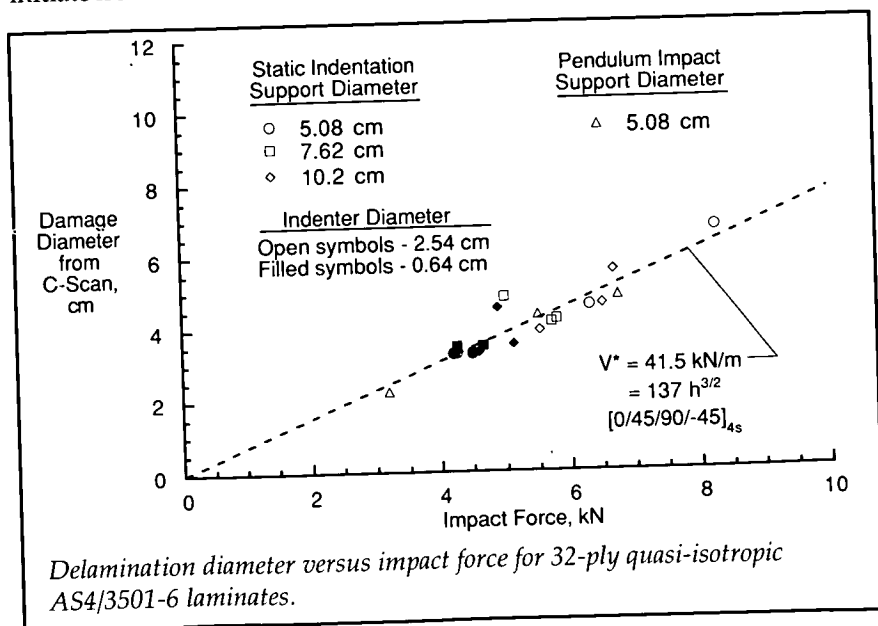
proportional to $t^{3/2}$, where t is the thickness of the laminate. Thus, larger impact forces are required to propagate delaminations in thicker laminates.

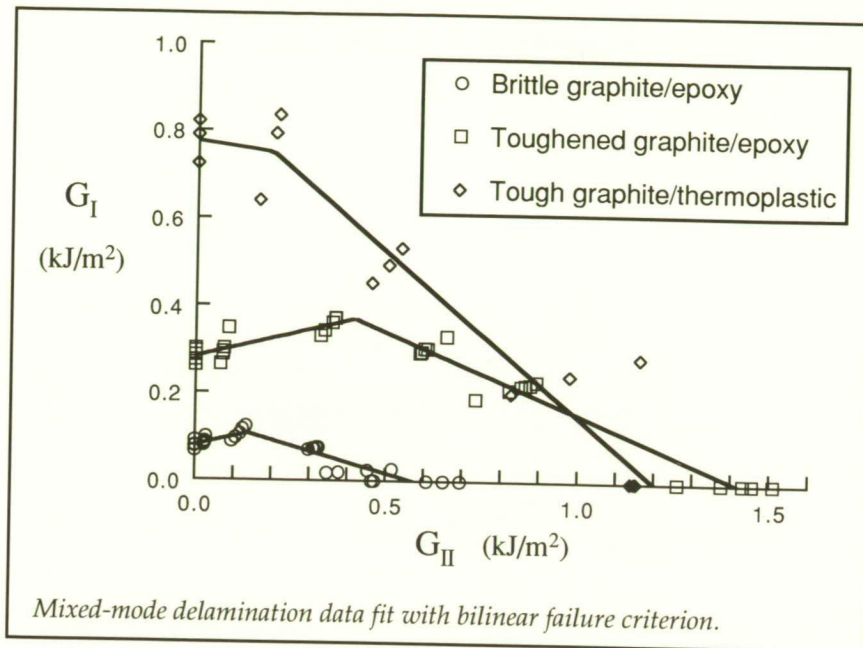
(C. C. Poe, Jr., 43467, and Wade C. Jackson)
Structures Directorate

A Failure Criterion for Mixed-Mode Delamination

The increased use of composite materials in aircraft structures has made the understanding and prediction of composite failures very important. In laminated composites, the primary failure mode is delamination, a crack between the layers of the composite. These cracks extend because of stresses that pull the layers apart (mode I) or because of stresses that slide the layers relative to one another (mode II). Typical structural delaminations would be subjected to a combination of mode I and mode II loading. Therefore, characterizing a material's resistance to this type of mixed-mode loading is important. To characterize this material response, the delamination resistance must first be measured and then modeled as a failure criterion.

The fracture toughness of three classes of materials was measured with the mixed-mode bending test, which was recently developed at Langley. This test allowed delaminations to be extended with prescribed ratios of mode I to mode II loading. Fracture toughness G was used as the measure of a material's resistance to delamination, and the test results are shown in the figure as the mode I component of fracture





toughness G_I plotted versus the mode II component G_{II} . The mixed-mode fracture toughness response was found to be quite different for the three materials.

Various delamination failure criteria have been suggested in the past by fitting different mathematical expressions to mixed-mode toughness data. Unfortunately, most of such failure criteria have been found to do a poor job of modeling the different material responses. The ones that can model the different material responses are complex and difficult to use. A bilinear failure criterion has been developed which is quite simple. As indicated by the solid lines in the figure, this new criterion does a good job modeling each of the material responses and, therefore, provides a basis for predicting when a delamination in a structure will extend.

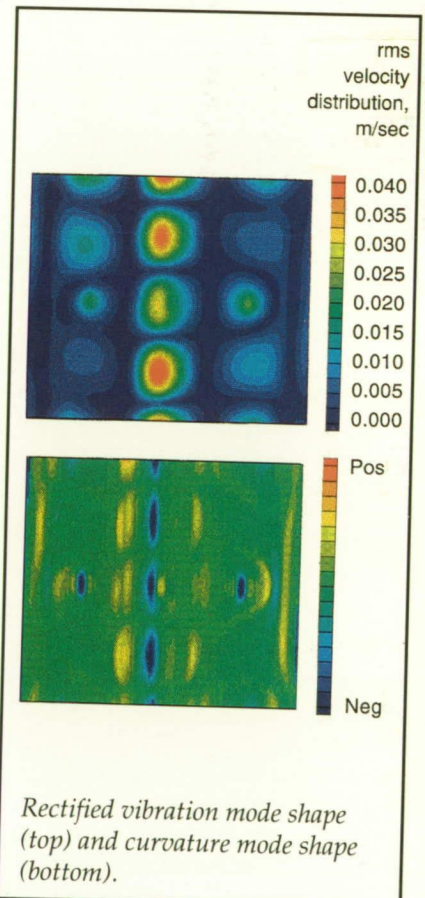
(James R. Reeder, 43456)
Structures Directorate

Use of Scanning Laser Vibrometer Data for Nondestructive Evaluation

The vibration characteristics of a structure are known to undergo change when the structure becomes damaged. For example, when a structure loses stiffness, as would be the case for a delaminated composite, the natural frequency decreases. In addition, an increase in damping is often observed when damage is present. Much effort has been spent on quantifying the damage through correlation of a detectable damaged area with observed shifts in natural frequency and/or damping. An alternative measure of the damage can be obtained through observation of changes in the vibration mode shape with increasing damage. Unfortunately, the latter method often lacks sensitivity for all but severely damaged structures. This work focuses on the use of mode shape data

obtained from a scanning laser vibrometer for the detection and measurement of damage using a recently developed parameter called the curvature mode shape.

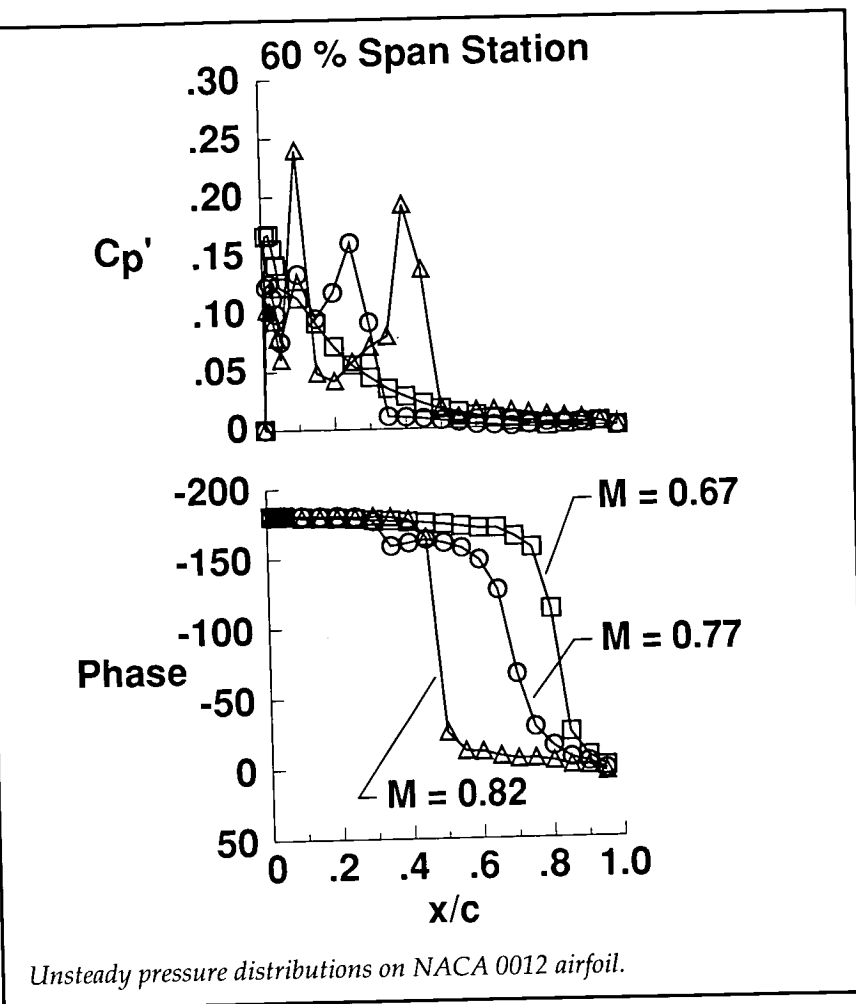
An acoustic fatigue test was performed in the Thermal Acoustic Fatigue Apparatus (TAFE) facility. A stiffened carbon-carbon panel structure was subjected to high-intensity noise that was suspended periodically so that smaller amplitude vibration inspections could be performed. Rectified mode shape scans were taken of the structure vibrating at a single frequency in the vicinity of a vibration mode. The curvature mode shapes were then computed by taking the second derivative of the data (with respect to a spatial



coordinate) through use of a finite-difference approach. The figure shows the rectified mode shape data and its second derivative with respect to the horizontal coordinate. An independent visual and thermographic inspection revealed that the dark vertical bands down the middle of the panel indicate the location of surface and near-surface damage. High curvatures were also noted in the vicinity of the excitation (left and right of the vertical band). A possible future application of the technique for direct measurement of bending strain, which is proportional to the curvature, could aid in determining where damage might be likely to occur. (Stephen A. Rizzi, 43599)
Structures Directorate

Pressure Measurements During Flutter of NACA 0012 Model

A Benchmark Models Program (BMP) was initiated at Langley with the primary objectives of defining the conventional flutter boundary of an NACA 0012 airfoil and measuring unsteady surface pressures during flutter. A rigid rectangular wing with a panel aspect ratio of 2.0 and an NACA 0012 airfoil cross section was tested in the Transonic Dynamics Tunnel (TDT) on the flexible Pitch and Plunge Apparatus. The model was equipped with 80 in situ pressure transducers located on the wing upper and lower surfaces at the 60- and 95-percent-span stations to measure steady and unsteady pressures. A ground vibration test defined the structural dynamic characteristics of the



model system. The model was tested at an angle of attack of 0° at Mach numbers M from 0.3 to 0.97. Discrete Fourier analysis at the flutter frequency determined the magnitude and phase of the oscillating pressures during flutter. The magnitudes of the pressures C_p' were normalized by the magnitude of the oscillating pitch angle, and the phase angles were calculated relative to the pitch motion. (A phase angle is positive when a pressure leads the wing pitch motion.) The C_p' and phase plots are shown in the figure for $M = 0.67, 0.77$, and 0.82 . Only the upper surface C_p' and phase values are presented for the

60-percent-span station. The effect of the shock on the unsteady pressure distribution as Mach number increases from 0.67 to 0.82 is shown in the figure. This comprehensive data set defining the model structural dynamic characteristics, the measured flutter boundaries, and the associated steady and unsteady pressure measurements will be a useful tool for the development, evaluation, and validation of CFD methods.

(José A. Rivera, Jr., 41270)
Structures Directorate

Neural Networks Offer Significant Payoffs in Optimization

Many types of analysis, such as finite-element analysis, are costly and time consuming to execute. In an optimization process where analyses may have to be repeated many times, the time and cost problems are compounded. On the other hand, once "trained," neural networks execute rapidly with little cost. Therefore, if a neural network can be trained through use of a relatively small number of design variable combinations and still result in a close approximation of an analysis program, then neural networks can replace the analysis programs and significantly reduce the time and cost in an optimization process. In this research, an optimization procedure was developed wherein a neural network developed at NASA Johnson Space Center was trained to approximate the finite-element analysis and coupled to an optimizer. The neural network was trained by collecting data obtained by exercising

a few cycles of a conventional optimization procedure with a traditional finite-element analysis.

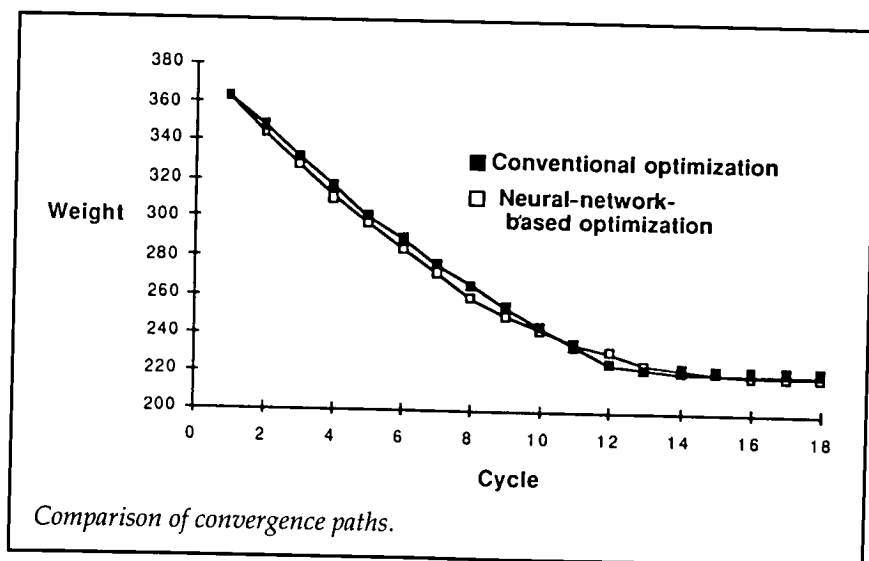
For purposes of illustration the new neural-network-based method was applied to determine the minimum weight of a 3000-degree-of-freedom cantilever beam loaded at the tip. Forty internal stresses in the beam were used as constraints. Thicknesses of the beam at five locations along its length were used as design variables. The accuracy and the efficiency of the neural network analysis were evaluated through comparison of the results with the optimization results obtained with the conventional finite-element analysis. As shown in the figure, the variation of beam weight with optimization cycle indicates that the neural-network-based optimization procedure followed the same path as the conventional optimization procedure. The total computer time required to obtain the neural-network-based solution, however, was only about one-third of that required by the conventional method. Therefore, an investment of time in training neural networks may lead to significant

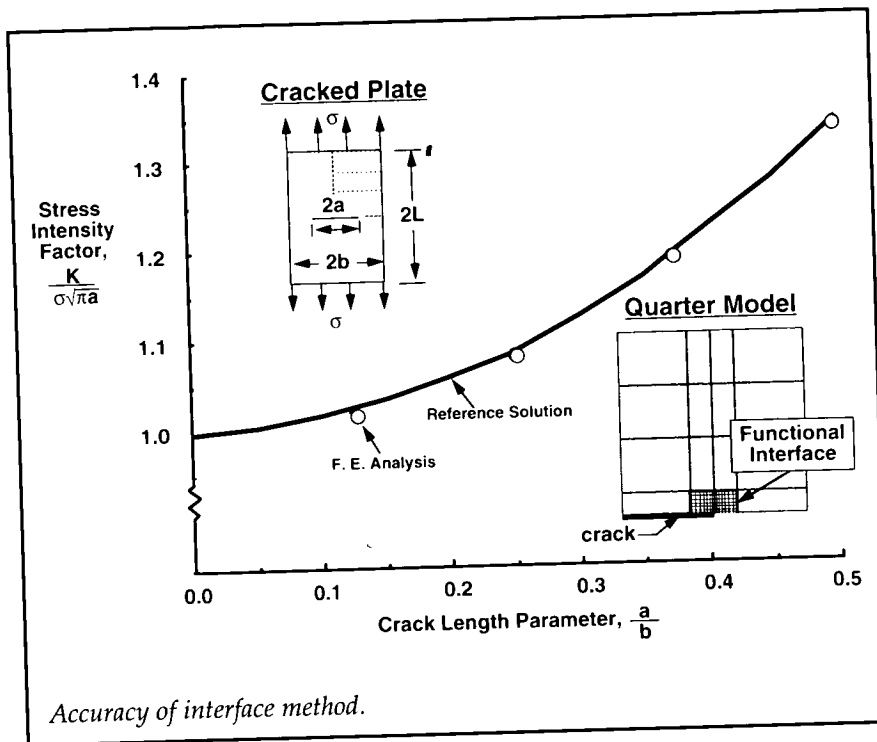
time and cost savings in structural optimization analysis.

(James L. Rogers, 42810, and William J. LaMarsh II)
Structures Directorate

Functional Interface Method Accurately Joins Independently Modeled Structural Regions

Aircraft structural components typically involve cutouts, abrupt stiffener terminations, composite ply drop-offs, and other discontinuous changes in geometry and material properties. Such discontinuities lead to stress concentrations, and it is in these local regions where structural failures usually initiate. Modeling such discontinuities can be quite tedious and time consuming for the engineer. One facet of this complexity has been the transitional modeling required to join the coarser global region finite-element model with the finer local region model required near the stress concentration. To remove this complexity and hence allow engineers to more rapidly assess design details early in the design process, a new modeling approach has been developed. This method permits global and local regions (or substructures) to be developed independently of one another and tied together in a single model. The method uses a functional interfacing technique that is solidly based on hybrid variational principles of mechanics. The functional form has its own free parameters to represent the structural response at the interface, and experience has shown that piecewise cubic splines generally work best as the functional form.





The variational principle used results in accurate solutions even at the interface and does not have the oscillatory behavior usually associated with collocation-type constraints such as multipoint constraints.

Since the method does not require the finite-element node points of the global and local regions to coincide, it eliminates transitional modeling between regions and thus provides simplicity and enhanced modeling flexibility. This is illustrated by comparing the modeling of cutouts done with transitioning between local and global regions with that possible with the new functional interface approach.

To demonstrate the method, a global-local analysis of an isotropic plate with a center crack loaded in axial tension has been performed. This example was characterized

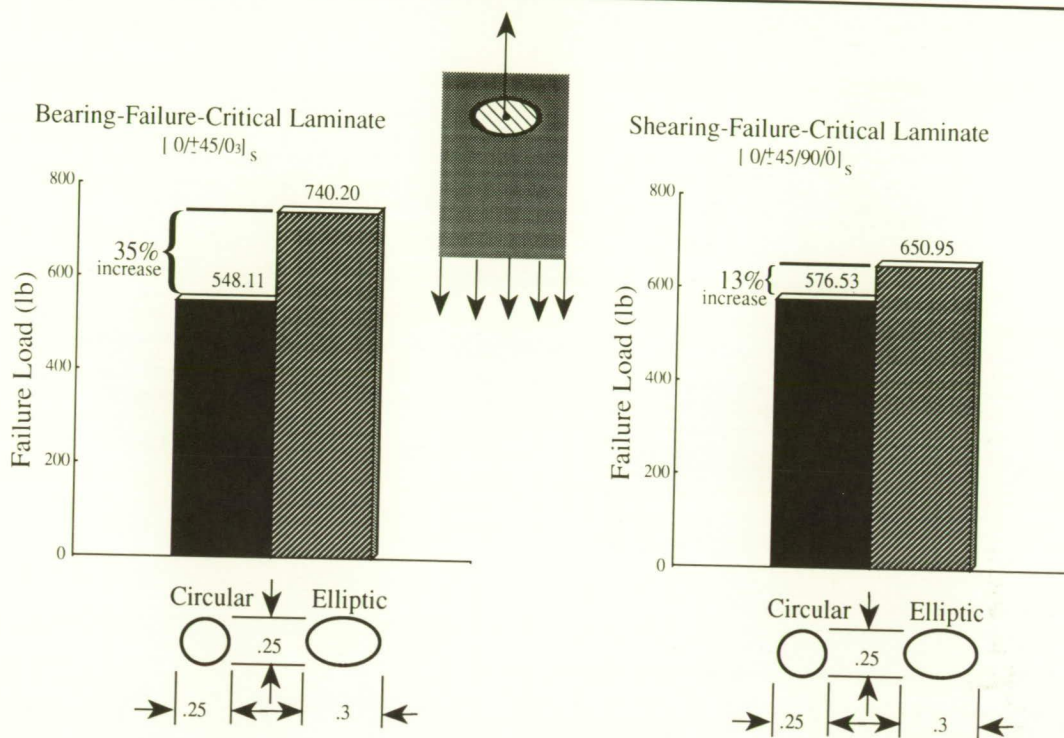
by a stress singularity at the crack tip. A refined finite-element model was used near the crack tip, and a much-less-refined model was used for the remainder of the plate. The models were highly incompatible across the interface, that is, the grid points of the models did not coincide at the interface. The normalized stress intensity factor as a function of the ratio of crack length to width is shown in the figure. The solid curve represents the reference solution found in the literature. The open circles represent the stress intensity factors obtained with the new procedure and are in excellent agreement with the reference solution. The crack could be placed anywhere at any orientation in the component using nearly the same global and local models without regard to grid point compatibility. Moreover, the methodology has been tested successfully on shell compo-

nents, where coupled membranes and bending action occur.
(Jonathan B. Ransom, 42924,
Susan L. McCleary, and
Mohammad A. Aminpour)
Structures Directorate

Potential Improvement of Composite Joint Strength Through Use of Elliptic-Shaped Bolt

Composite aircraft structural components are often joined with circular bolts. These joints often fail in the composite laminate as a result of excessive bearing or shearing stresses. Increasing the bolt diameter reduces these stresses, but because it also reduces the distance from the edge of the bolt hole to the edge of the joint, it may not be practical. An alternative to reducing these stresses is to use an elliptic-shaped bolt. Such a bolt may be fastened with an attached circular threaded shaft and the elliptic hole may be cut with water jet technology.

The potential advantage of elliptic-shaped bolts has been demonstrated analytically. A closed-form approximate solution for bolt-loaded elliptical holes was formulated based on laminate theory and anisotropic elasticity. The normal load distribution on the edge of the elliptical hole was represented by a cosine series. Unknown coefficients of the cosine series were determined by a boundary collocation procedure in which the bolt was assumed to be rigid. A modified Tsai-Wu failure criterion was used to predict joint failure.



Increased failure loads for elliptical bolt joints.

As demonstrated in the figure, two composite laminate constructions were studied. One was chosen because it is bearing-failure critical, while the other is shearing-failure critical. Also, a circular-bolt diameter of 1/4 in., typical of aircraft joints, was used. The elliptic bolt was chosen to retain the 0.25-in. dimension along the minor ellipse axis with a 0.30-in. dimension along the major axis. The chart shows a 35-percent strength improvement for the bearing-failure-critical laminate design and a 13-percent strength improvement for the shearing-failure-critical design. These results were predicted by the closed-form approximate solution and confirmed by a detailed finite-element solution.

Elliptic-shaped bolts can be employed in design and redesign field modifications of composite

laminates. If a joint design with circular bolts was found to fail on some aircraft in service, the circular bolt holes on unfailed joints could be reshaped to accommodate elliptic bolts. This would constitute a relatively inexpensive fix.

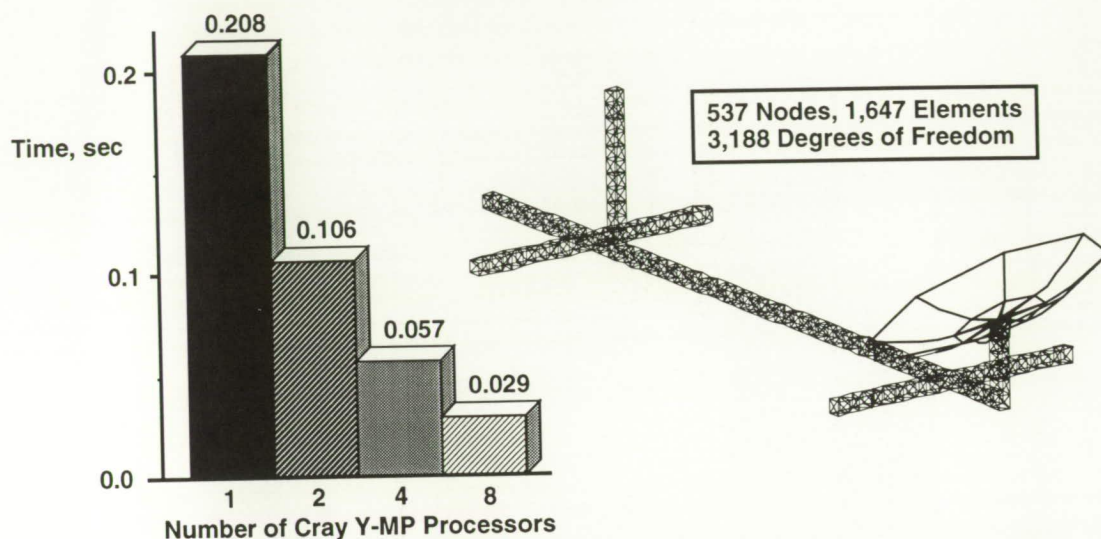
(John T. Wang, 48185)
Structures Directorate

Fast Algorithm Developed To Generate and Assemble Global Stiffness and Mass Matrices in Parallel

Over the last several years Langley Research Center has been developing algorithms for rapid solution of structural analysis equations on supercomputers. In

1989 the Cray Gigaflop Performance Award was presented for the development of a highly efficient linear equation solver, PVSOLVE. Recently a new parallel algorithm has been developed to reduce the time needed to generate and assemble stiffness and mass matrices on supercomputers.

Conventional finite-element codes generate and assemble stiffness and mass matrices element by element. Each element makes stiffness and mass contributions to degrees of freedom associated with many nodes of the finite-element model. When this conventional procedure is performed in parallel, with element calculations distributed to various processors, many processors attempt to simultaneously write stiffness and mass contributions to the same nodal



Performance of new method for 3-D geostationary platform.

degrees of freedom. This creates a hardware bottleneck and synchronization problem that seriously degrades performance. To circumvent this problem, an alternative node-by-node generation and assembly algorithm was developed that distributes nodal calculations rather than element calculations to processors.

The algorithm was tested on several structural applications, including the geostationary platform shown. The figure shows that on multiple Cray Y-MP processors, the computation speedup of the new algorithm is near optimum, that is, nearly proportional to the number of processors used.

The accuracy of the algorithm has been verified by comparison with other codes and known solutions. In addition, the code runs rapidly, is robust, and is of general purpose use. It is well suited for applications wherein the global stiffness and mass matrices are calculated repeatedly,

such as structural optimization, nonlinear static and dynamic analysis, panel flutter analysis, and control of large flexible space structures.

The algorithm is operational on both share-memory parallel computers, such as the Cray, and local-memory parallel computers, such as the Intel 860 Gamma and Delta with 128 and 512 processors, respectively. It has provided outstanding performance on applications such as the high-speed civil transport, for which the structural model contained 88 422 degrees of freedom (or equations). The algorithm has been combined with PVSOLVE to form the nucleus of future advanced finite-element structural analysis software running efficiently on both shared- and local-memory supercomputers. (Olaf O. Storaasli, 42927) Structures Directorate

Microstructural Characterization of Thin Polyimide Films by Positron Lifetime Spectroscopy

Thin polyimide films are ideal candidates for protective coatings on antenna reflectors and other electronic applications. Their properties, both physical and electrical, are strongly influenced by their morphology. We have developed a novel technique for monitoring the microstructural characteristics of thin polymer films. It is based on the sensitivity of positron lifetimes to the molecular architecture of the test films. Positron lifetimes are higher in films that have a looser architecture, that is, higher free volume fractions f . Thus, free volume fractions in the test films can be measured rather accurately by positron lifetime spectroscopy. A free volume model has been developed to calculate the dielectric

Sample	Free volume fraction, f , percent	Dielectric constant (at 10 GHz)		Experimental saturation moisture content,* volume percent
		Experimental	Calculated	
Kapton (ref.)	2.02 ± 0.27	3.20 ± 0.03	3.31 ± 0.03	2.02
BFDA + ODA	12.43 ± 1.09	2.63 ± 0.03	2.69 ± 0.05	.74
BFDA + 4-BDAF	19.56 ± 0.91	2.44 ± 0.03	2.37 ± 0.04	1.38
6FDA + DDSO ₂	8.26 ± 0.79	2.86 ± 0.03	2.93 ± 0.05	.74
BFDA + DABTF	11.41 ± 1.14	2.55 ± 0.03	2.74 ± 0.06	.49
6FDA + APB	12.50 ± 1.48	2.71 ± 0.03	2.70 ± 0.07	.53
BTDA + ODA	5.48 ± 0.37	3.15 ± 0.03	3.12 ± 0.03	1.21

*If there were no inhibition, the saturation moisture uptake should have equalled the free volume fraction in the sample.

Comparison between experimental and calculated values of physical properties of the test films.

constant ϵ as well as the moisture susceptibility of the test films.

The free volume model has been tested on a series of special purpose aromatic polyimide films developed for aerospace communication networks. Some of the test films had CF₃ groups and meta linkages in their structure and were, therefore, expected to have large free volume fractions in them. The results are summarized in the table. It is apparent that the presence of fluorine atoms in the polymer structure reduces their moisture uptake. Also, the presence of bulky CF₃ groups and meta linkages in their structure reduces the dielectric constants of the test films, as expected.

(Jag J. Singh, 44760, and Abe Eftekhari)

Electronics Directorate

Automatic Specification of Reliability Models for Fault-Tolerant Computers

The calculation of reliability measures using Markov models is required for life-critical processor-memory-switch structures that have standby redundancy or are subject to transient or intermittent faults (or repair). The task of specifying these models is tedious and prone to human error due to the large number of states and transitions required in any reasonable system. Therefore, model specification is a major analysis bottleneck, and model verification is a major validation problem. The general unfamiliarity of computer architects with Markov modeling techniques further increases the necessity of automating the model specification.

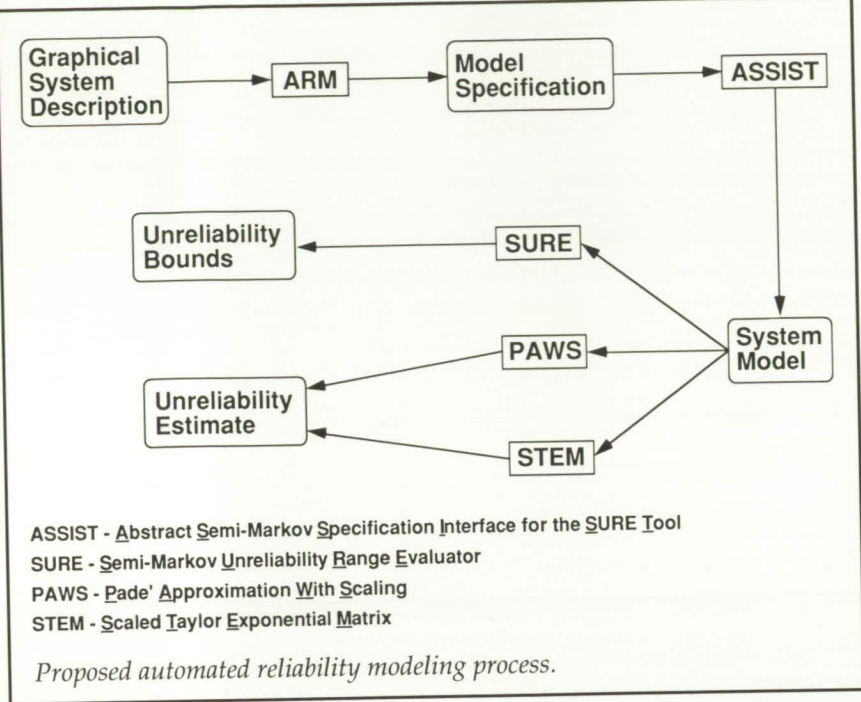
Automation requires a general system description language (SDL) that can accommodate new fault-tolerant techniques and system designs. For practicality, this SDL

should also (1) provide a high level of abstraction and (2) be easy to learn and use.

A program named ARM (Automated Reliability Modeling) was constructed as a first attempt to define and implement an SDL with those characteristics. ARM uses a graphical user interface (GUI) as its SDL. This GUI is based on a hierarchy of windows. Some windows have graphical editing capabilities for specifying the system's communication structure, hierarchy, reconfiguration capabilities, and requirements. Other windows have text fields, pull-down menus, and buttons for specifying parameters and selecting actions.

ARM outputs a Markov reliability model specification formulated for direct use by programs that generate and evaluate the model. A 1-hour session with ARM specified a 46 338-state Markov model.

(Carlos A. Liceaga, 46191, and Daniel P. Siewiorek)
Flight Systems Directorate



mentary computational techniques, known as the Moment Method and the Uniform Geometrical Theory of Diffraction, are used to compute the radiated near and far fields of user-specified antennas. Once the basic structure is modeled geometrically and displayed, appropriate parameters are automatically generated and stored for subsequent use by the EM analysis method best suited to the specific application.

New EM modeling methods are being developed to analyze antennas radiating from nonmetallic aircraft structures. Use of composite skin materials for advanced airframes requires extension of existing computational codes and analysis methods in order to predict the antenna performance of these vehicles.

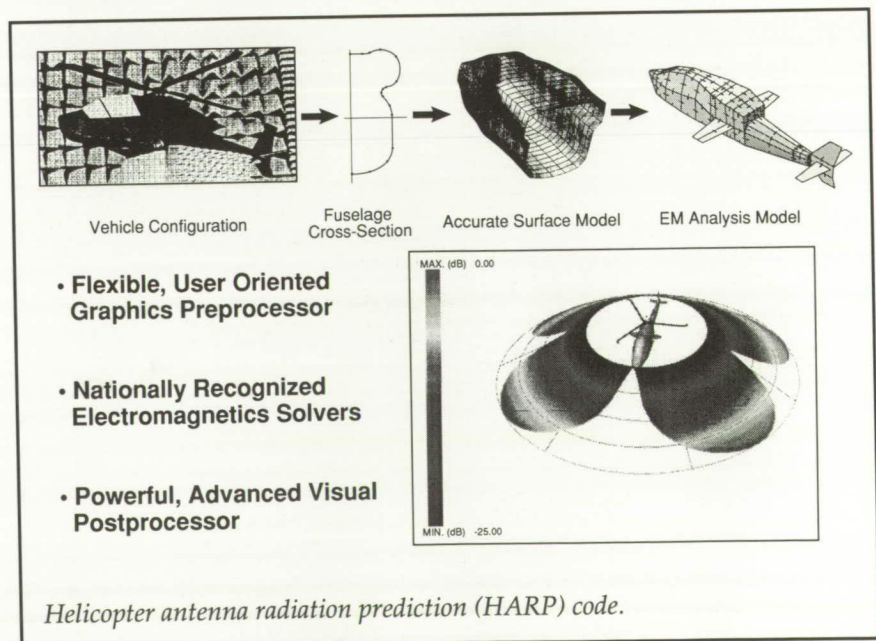
The Helicopter Antenna Radiation Prediction (HARP) Code

In order to accurately predict the performance of communication system antennas located on complex aircraft structures, such as helicopters, over a wide range of frequencies and configurations, new analysis tools that electromagnetically model airframe materials and structural geometry are required. Current analysis methods are computationally inefficient and offer impractical limitations on vehicle size, shape, materials, and antenna configurations.

A new method to model complex vehicles with arbitrarily placed antennas has been developed to improve both the accuracy and the efficiency of the electromagnetic (EM) simulation process by combining modern computer

graphics and advanced computational techniques into an integrated package. This software package, called the Helicopter Antenna Radiation Prediction (HARP) code, is designed to run on a conventional graphics workstation. Comple-

Although specifically designed for helicopters, HARP is applicable to nearly any geometry consisting of an arbitrarily shaped main body, or fuselage, with attached wings or fins. Thus, HARP may



be applied to a wide variety of vehicles, including aircraft, missiles, and spacecraft. Using interactive, computer-aided techniques, users can easily determine the effects of structural modifications, antenna placement, and operating frequency on antenna system performance. HARP provides the benefits of improved accuracy, reduced cost, greater flexibility, and reduced simulation time and can ultimately serve as a valuable system integration and evaluation tool for both current and future aircraft.

(George C. Barber, 41818)
Flight Systems Directorate

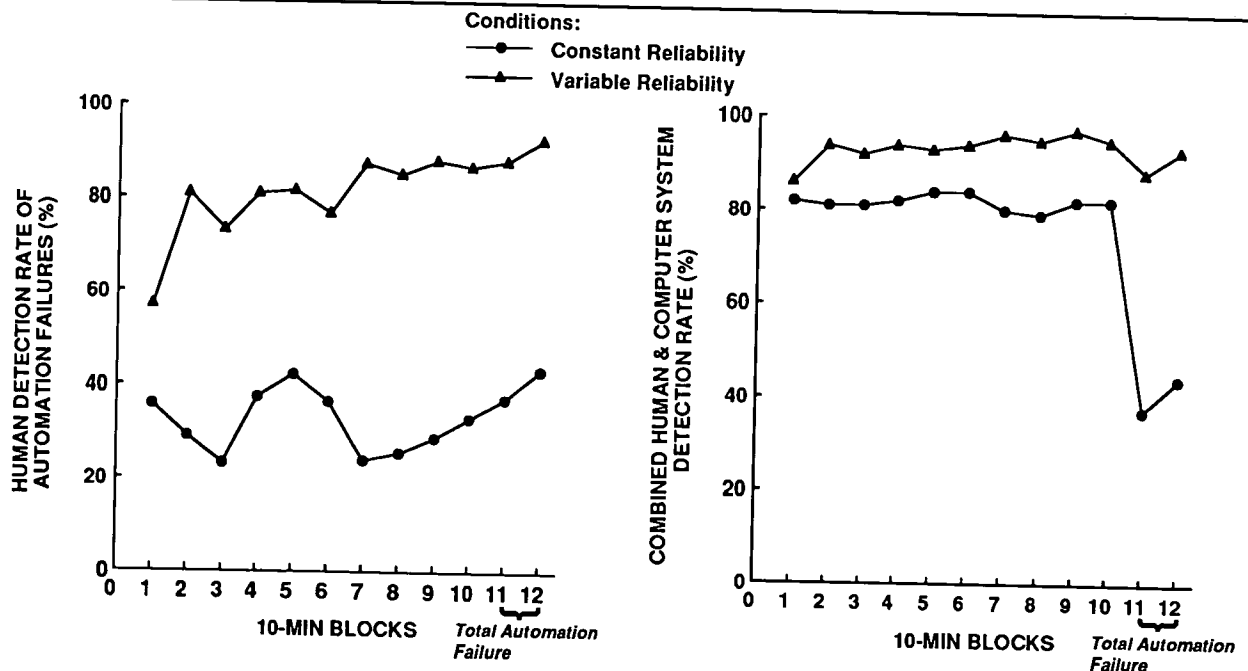
Detrimental Effects of Automation-Induced Complacency Demonstrated

Pilot "complacency" resulting from overconfidence or trust in

automation capabilities is often mentioned as a possible negative consequence of automation. However, the evidence for effects of complacency on pilot performance was largely anecdotal and post hoc. The goal of this study was to obtain empirical evidence of the effects of automation, in particular automation reliability, on operator complacency, defined for this study as reduced effectiveness in manual monitoring of automation failure.

"Automation-induced complacency" was examined by investigating the effects of automation reliability on operator monitoring of system failures during multi-task, simulated flight performance. It was hypothesized that automation that was unchanging in reliability (but less than 100 percent reliable) would be more likely to induce a condition of complacency than would automation that varied in reliability.

Twenty-four subjects performed a multi-task set consisting of manual tracking, manual fuel management, and manual management of automated monitoring systems. The monitoring task consisted of four gages on which occasional "system malfunctions" were presented as out-of-range meter deviations. These malfunctions were automatically detected and reset except when the automation failed, in which case the subject was required to respond. Automation reliability (the percentage of malfunctions correctly detected by the automation) differed between group conditions. For the constant-reliability condition, automation reliability was fixed, whereas for the variable-reliability condition, reliability alternated every 10 minutes. In both conditions, the automation routine was disabled for the last 20 minutes in order to simulate catastrophic automation failure.

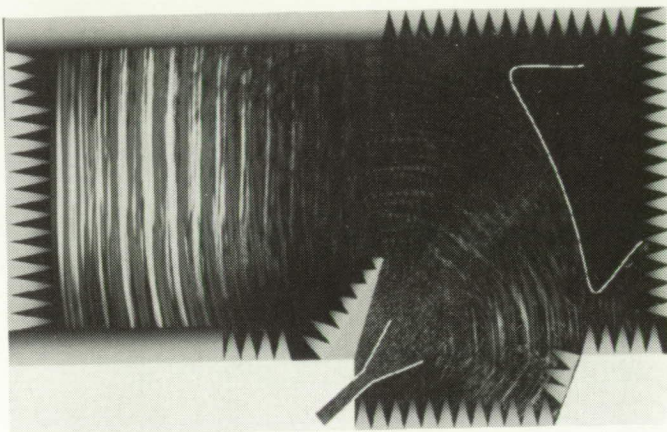


Effects of automation-induced complacency on monitoring performance (average for 12 subjects per condition).

Strong behavioral evidence for complacency effects due to automation was obtained. Initially, the accuracy of manual intervention in the automated monitoring task was roughly the same for the two reliability conditions, but later performance for the variable-reliability condition was superior to that for the constant-reliability condition (left side of figure). Following the total automation failure, performance of the constant-reliability group improved but still did not recover to the level of the variable-reliability group. Combined system (i.e., human plus computer) monitoring performance was relatively good for either condition but dropped dramatically and recovered slowly following total automation failure for the constant-reliability condition (right side of figure). Thus, the evidence shows that performance consequences of complacency in monitoring are related to characteristics of the automation, namely, automation reliability and consistency. While combined human and machine monitoring is better than unaided human performance, complacency effects limit "backup" monitoring of automated systems even if automation reliability is very high. (Alan T. Pope, 46642, and Raja Parasuraman) Flight Systems Directorate

Finite-Difference Time-Domain Technique for Compact Range Applications

It is difficult to predict the total overall performance of a compact range (an electromagnetic meas-



Simulation of wave propagations and interactions in compact range. (Photograph courtesy of Pennsylvania State University.)

urement system used to simulate a plane wave illuminating an antenna or scattering body). The performance is normally estimated through the analysis of each individual system inside the compact range system. The finite-difference time-domain (FDTD) technique, a direct solution to Maxwell equations, is suitable to address this type of problem because of its ability to model materials. In addition, the bounded volume in a radio-frequency-shielded chamber makes an artificial absorbing boundary unnecessary. A three-dimensional FDTD solution for compact range applications is possible with current computers, but only up to frequencies much lower than the chamber design frequencies. However, two-dimensional FDTD modeling allows much greater detail at higher frequencies with reasonable accuracy.

A two-dimensional FDTD program written specifically for compact range analysis was developed through collaboration with

researchers at Pennsylvania State University. It provides easy ways to model various components in a compact range, such as wall absorbers, blended rolled-edge reflector systems, antennas, and feed covers. Only the centerline cut of the compact range is modeled. Three-dimensional components such as pyramidal absorbers are modeled in two dimensions by varying the constitutive parameters of the materials from bases to tips.

The solution offers significant insights into potential designs or design changes in providing data about the quiet zone, antenna spillover, feed blockage, and edge diffractions. It also provides guidance in wall absorber placements and diffraction treatments to improve performance and reduce costs.

(Fred B. Beck, 41829, and Truong X. Nguyen) Flight Systems Directorate

High-Speed Airframe Integration Research (HiSAIR)

The NASA Langley Research Center is currently involved in an effort to strengthen multidisciplinary interaction among the traditional research areas at the Center. An important part of this effort is the High-Speed Airframe Integration Research (HiSAIR) project. The HiSAIR project is using the study of a High-Speed Civil Transport (HSCT) aircraft as a focus for developing more rigorous interaction methodology. Significant progress has been made toward the accomplishment of the HiSAIR project near-term objectives. An analysis process that includes geometry generation coupled with aerodynamic, structural, weight and inertia, aeroservoelastic, dynamics, control systems, and

vehicle performance has been developed. This process has been used to perform an analysis of a Mach 3.0 HSCT configuration. A data management system that incorporates interactive data tracking and application program execution functions is being assembled. Multidisciplinary optimization methods are being explored through utilization of a subset of the overall analysis process. Thus far, the disciplines of aerodynamics and structures have been coupled to design a minimum-weight wing subject to flexible loads. The results of this optimization show that the Tsai-Hill stress constraint values in the wing covers become much more critical (less negative in value). This indicates a more efficient distribution of material and a reduced wing weight. Several new areas of research have been initiated as a result of the inter-

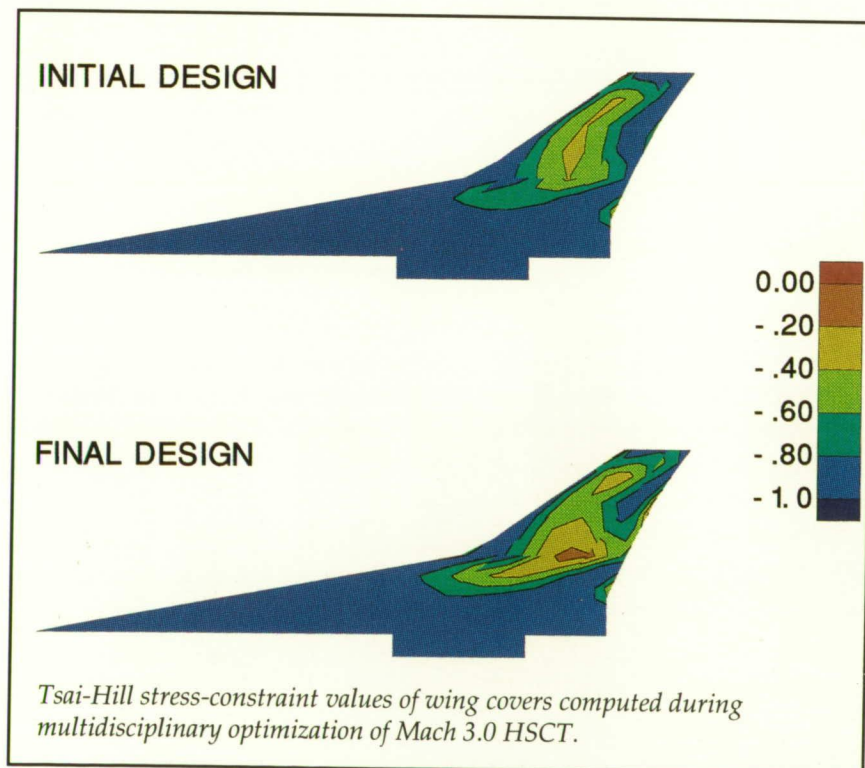
actions among the participating disciplines. These include parameterization of grid geometry in terms of design variables and development of sensitivity derivatives from nonlinear aerodynamic solutions.

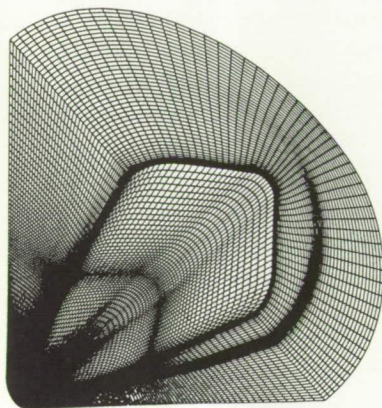
(Peter G. Coen, 45991)
Aeronautics Directorate

Adaptive Grid Method for Computing High-Speed Flow

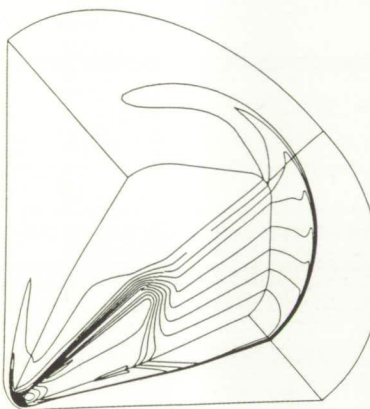
An algebraic solution and adaptive-grid-generation method that allows adaptation of the grid in all three coordinate directions has been developed. The technique maintains the integrity of the original vehicle definition for grid point movement on the vehicle surface and avoids grid crossover in the boundary-layer portion of the grid lying next to the surface. The grid movement operates directly on the grid in the physical domain and redistributes the grid points along the coordinate curves on a curve by curve basis. Hence, the redistribution of the three-dimensional grid reduces to a series of unidirectional adaptations.

The adaptive grid method is applied to Mach 6 hypersonic three-dimensional viscous flow about a proposed Mars entry vehicle. The flow solver that works in conjunction with the adaptive procedure is the TLNS3D code. The TLNS3D code applies a finite-volume, shock-capturing formulation to solve the thin-layer Navier-Stokes equations for viscous compressible flow. Computing flow solutions on the adaptive grid results in more accurate





Adaptive grid about Mars entry vehicle at 12° flow incidence.



Contours of pressure coefficient (50 contours).

predictions of the stagnation values and better overall resolution in the nose region. The top part of the figure shows an adaptive grid on the vehicle surface, in the symmetry plane and on the end surface. The bottom part of the figure shows contours of the pressure coefficient on the same grid surfaces. The flow incidence is 12°.

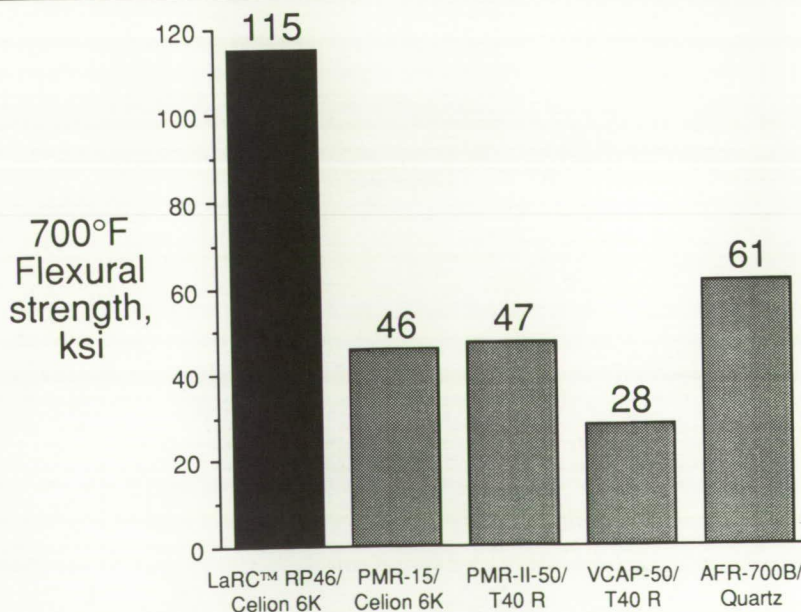
(Robert E. Smith, 45774)
Electronics Directorate

LARC™ RP46 for High-Performance Aircraft and High-Speed Civil Transport Applications

Langley Research Center is a recipient of a 1992 R&D 100 Award for LARC™ RP46 polyimide. The primary use for LARC™ RP46 is as a matrix resin for structurally efficient, advanced composite materials for high-temperature applications. This new matrix resin is prepared for the *in situ* polymerization of three monomer reactants: monomethyl ester of 5-norbornene-2,3-dicarboxylic acid (NE), 3,4'-oxydianiline 3,4'-ODA), and dimethyl ester of 3,3',4,4'-benzophenonetetracarboxylic acid (BTDE). Composites made with LARC™ RP46 can be processed easily by numerous conventional processing techniques, including autoclave processing, compression molding, powder

tow pregging, solution frame winding and filament winding, stamping, and resin flow molding. In addition to the LARC™ RP46 baseline material, a toughened version of LARC™ RP46 has also been developed for applications where damage tolerance and microcracking resistance are essential requirements.

LARC™ RP46 is easier to process, is tougher, and has substantially higher mechanical properties at 700°F than the standard high-temperature matrix resin PMR-15. (See figure.) Its raw material cost is comparable to that of PMR-15 and much lower than the other new matrix resins. This new material has the potential to meet all OSHA standards in the workplace because of the use of a novel chemical building block. Outstanding overall mechanical properties and low raw material and processing costs make this new material very attractive for aerospace applications. LARC™



Mechanical performance of matrix resins at 700°F.

RP46 prepegs are now commercially available. Several major aerospace companies are currently evaluating LARC™ RP46 for high-performance military and commercial aircraft engine and High-Speed Civil Transport applications. (Ruth H. Pater, 44277) Structures Directorate

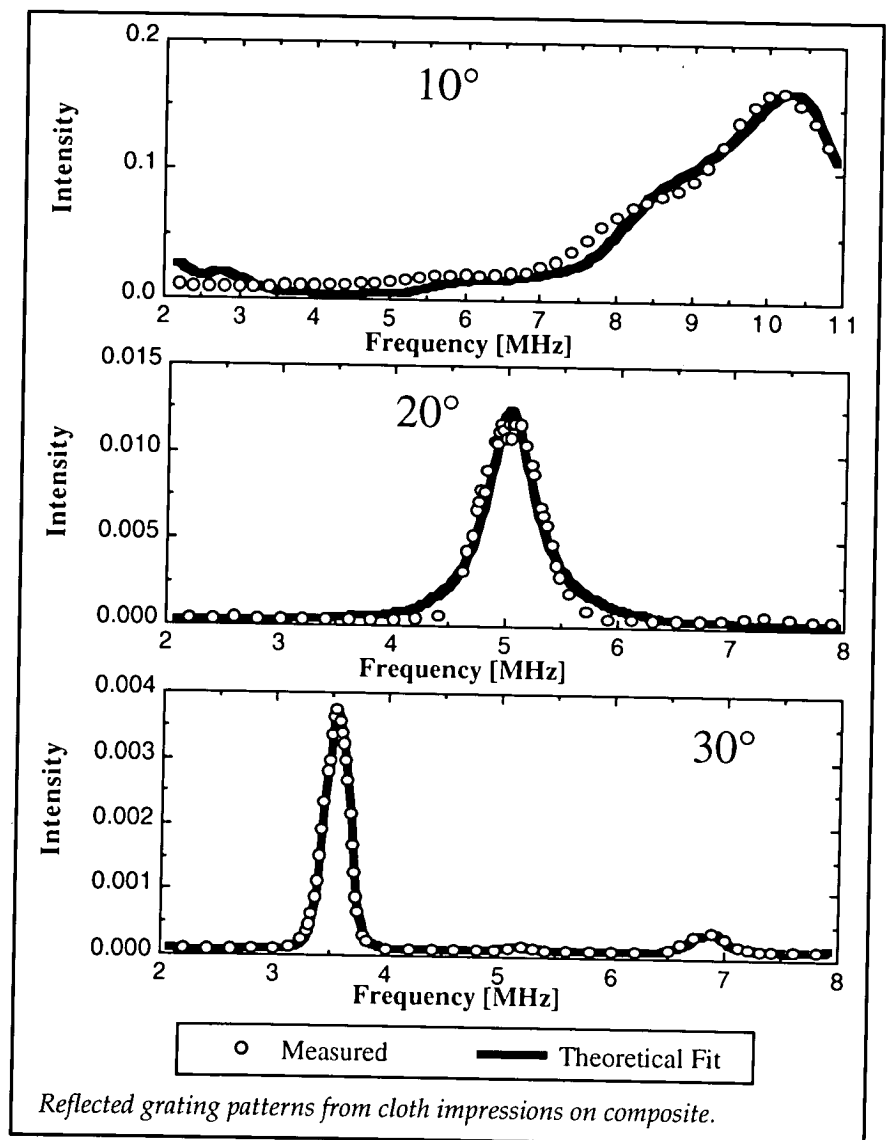
Modeling Surface Cloth Impressions on Composites as an Ultrasonic Reflection Grating

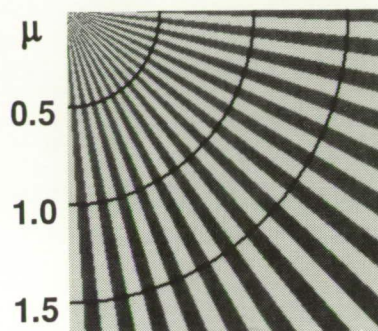
A new theory recently developed at NASA Langley Research Center accounts for the ultrasonic effects of surface cloth impressions on composites and has allowed for the suggestion of a better ultrasonic nondestructive evaluation (NDE) method. Successful implementation of quantitative ultrasonic characterization methods based on polar backscatter techniques has been hampered by surface effects in composites. Our previous measurements have shown that integrated (i.e., frequency averaged) polar backscatter levels due to bleeder-release cloth impressions are sufficient to prohibit the detection of porosity in graphite/epoxy composites. As a test of our theory, an epoxy panel (3501-6), 15 cm by 15 cm by 0.3 cm, was fabricated with release cloth impressions on both faces.

Measurements were made using a 10-cm-focal-length, 5-MHz broadband ultrasonic transducer for polar angles of 10°, 20°, and 30° and an azimuthal angle perpendicular to the warp thread direction. The backscattered

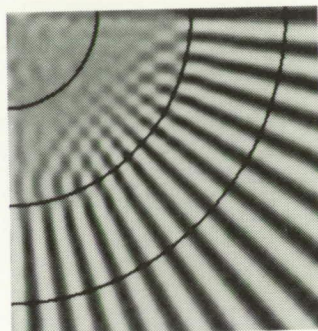
signals were analyzed, and results exhibited localized (in frequency) peaks with values comparable to integrated backscatter values obtained from graphite/epoxy composites with known porosity. By modeling the surface impressions as an interference reflection grating and treating the grating spacing as a spatial distribution using Gaussian statistics, good agreement with experiment was obtained. (See figure.) This model has suggested several useful, rapid yet quantitative approaches for

compensating for the effects of surface impressions and hence increase the detectability of flaws such as matrix cracks, fiber breaks, porosity, inclusions, delaminations, and fiber waviness. (Eric I. Madaras, 44970) Electronics Directorate

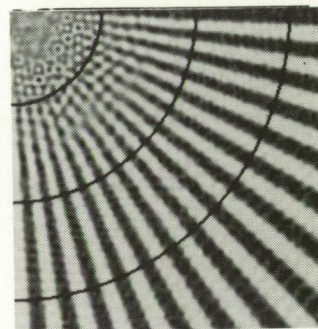




Target, where μ is the bar width per sampling interval



Conventional imaging with Wiener restoration



Multiresponse imaging with Wiener-matrix restoration for $A = 9$

Improvement in resolution through multiresponse imaging.

Multiresponse Imaging for Improved Resolution

Image systems, including television cameras, charge-coupled device imagers, forward-looking infrared sensors, and infrared detectors, produce a video image that has a resolution limited to the sampling interval (i.e., the space between photodetectors) of the imager. Hitherto, it has not been possible to produce images of random scenes with a resolution that is finer than the sampling interval or, stated differently, with a spatial frequency that is higher than the sampling pass-band, or Nyquist frequency, of the imager.

A recent study of image gathering and digital restoration has revealed an imaging process that overcomes the sampling-interval constraint and is critically constrained only by the optical response and the sensitivity. This imaging process consists of multi-

response image gathering and Wiener-matrix restoration. The image-gathering process acquires a sequence of images, each with a different optical response (e.g., aperture opening) so that the sufficiently and insufficiently sampled signal components are weighted differently. The Wiener-matrix filter, in turn, unscrambles these signal components and reassembles from A multiresponse images a single image with a resolution that is \sqrt{A} times finer than the sampling interval.

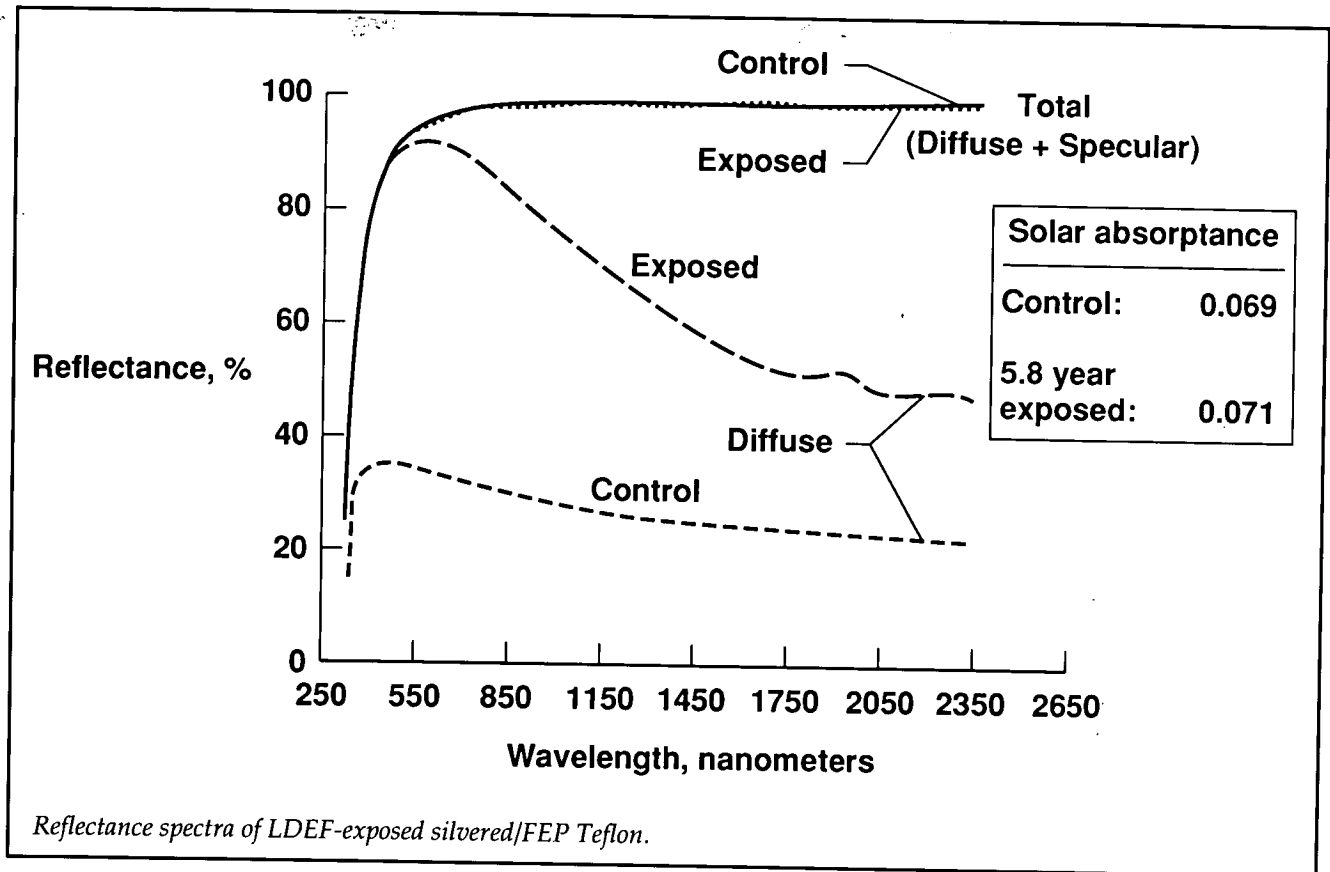
(Carl L. Fales, 41529, and Friedrich O. Huck)

Flight Systems Directorate

Characterization of Silvered FEP Teflon Coating Exposed on LDEF

Silvered Dupont FEP Teflon is used in many space vehicles. It was used in the form of thermal blankets to control the temperature of many LDEF experiments. In

areas where it experienced a high fluence of atomic oxygen and solar ultraviolet radiation over the 5.8 years of space exposure, the FEP Teflon appeared to have become nontransparent and diffusely reflecting. This change in appearance was studied utilizing a special reflectance measurement system that allows the specular and diffuse reflectance components to be measured separately. The figure shows that at a wavelength of about 500 nm, the diffuse reflectance of the exposed specimen was close to 90 percent, whereas that of the control specimen was approximately 35 percent. However, the total reflectance, which is the sum of the diffuse and specular components, was virtually identical for the exposed and ground control specimens. This indicates that surface roughening due to atomic oxygen exposure increased the diffuse reflectance substantially in the visible wavelength region while, at the same time, the total reflectance remained virtually unchanged. The measured change

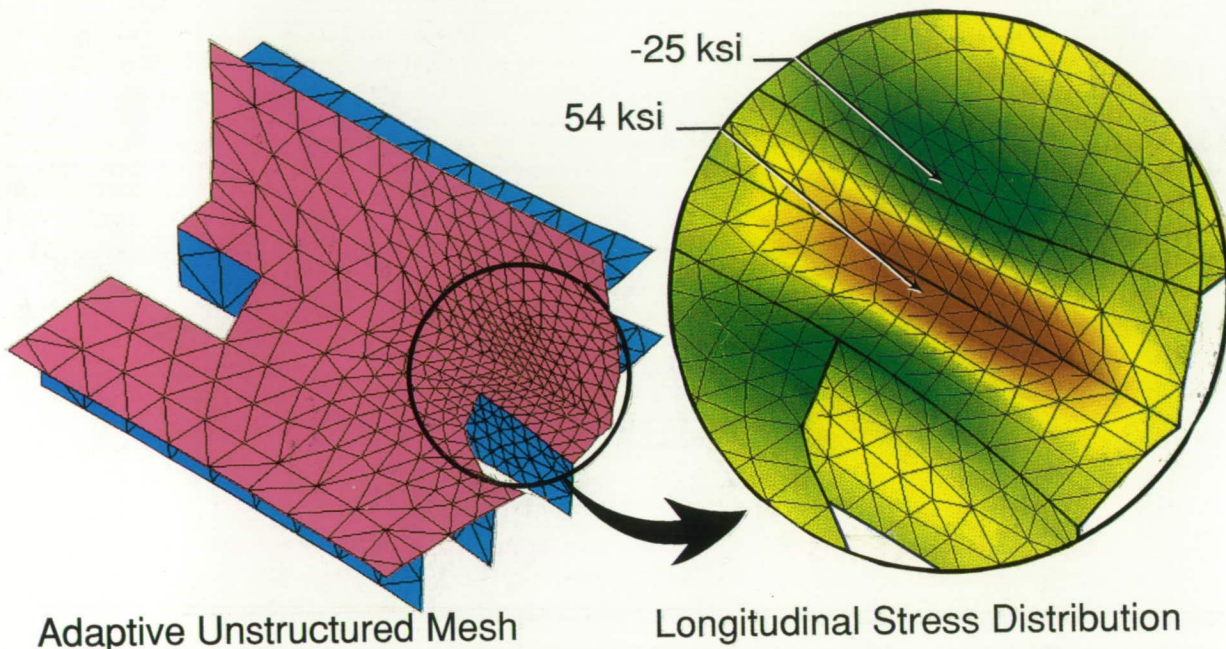


of 0.002 in solar absorption due to exposure (see figure) was within experimental error of the measurement. These results demonstrate that although FEP Teflon will exhibit some surface erosion when exposed to a high fluence of atomic oxygen and solar ultraviolet radiation in space, the effect of the erosion on the solar absorptance of this coating is minimal. Since thermal emittance of this material is also unaffected by erosion, the thermal control properties of silvered FEP Teflon were not affected by the 5.8-year exposure. (W. S. Slemp, 41334, and P. R. Young)
Structures Directorate

Adaptive Unstructured Meshing Demonstrated for Thermal Stress Analysis of Built-Up Structures

Traditionally, in finite-element analysis of complex structural shapes, if high stress gradient regions are not anticipated prior to analysis of a problem, conventional meshing procedures are inaccurate or too computationally intensive. An adaptive unstructured meshing technique for thermal stress analysis of built-up structures has been developed to improve the solution accuracy and analysis efficiency without *a priori* knowledge of the solution.

The adaptive unstructured remeshing technique is combined with a finite-element thermal stress analysis algorithm. The temperature and the Von Mises stress are selected as the key parameters ϕ for constructing an adaptive mesh. At a typical node in a previous mesh, the second derivatives ϕ'' of the two key parameters are computed. The higher quantity is selected to determine a new nodal spacing h for an adaptive mesh based on the equidistribution principle of error, $|\phi''| h^2 = |\phi''|_{\max} h_{\min}^2$, where $|\phi''|_{\max}$ is the maximum absolute second derivative for the entire computational domain and h_{\min} is the specified minimum nodal spacing. Triangular membrane elements and triangular discrete Kirchhoff bending elements are



Adaptive mesh for scramjet engine inlet panel.

used in the adaptive unstructured mesh for predicting deformations and thermal stresses.

The method is demonstrated by the thermal stress analysis of a representative scramjet engine inlet panel section. The structure experiences nonuniform heat transfer rates due to the interaction of planar shocks generated from the strut and cowl leading edges. A portion of the structure consisting of intersecting panels and stiffeners is first discretized by a uniform finite-element mesh, and temperatures are prescribed that vary quadratically from 700°R at the centers of the two "hot spots" to 50°R in the regions away from the two hot spots. With this initial mesh and temperature distribution, a thermal stress analysis is performed to provide a thermal stress solution. Using the adaptive remeshing procedure, a new adap-

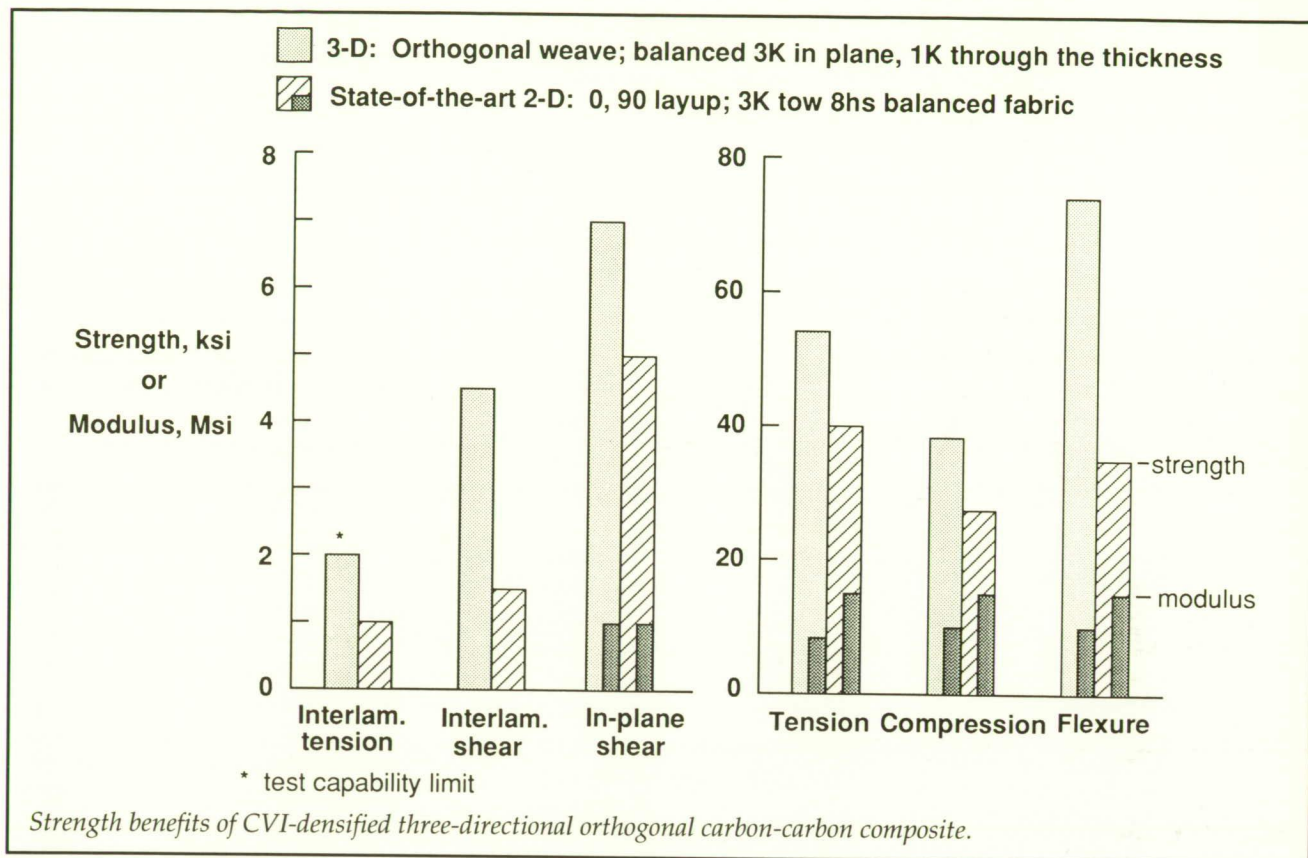
tive mesh is constructed as shown in the figure, with an enlargement to highlight the finite-element discretization of the stiffeners. The figure also shows that triangles provide smooth mesh transition from fine to coarse mesh regions, and this smooth transition will further provide a more accurate stress distribution. As expected, the high localized temperatures result in compressive stress (-25 ksi) at the two hot spots (green areas) which cause the panels to expand and bend out of plane. In addition, a much higher tensile stress (54 ksi) appears at the panel intersection to maintain equilibrium.

To summarize, the adaptive unstructured meshing technique results in small elements in the regions of high thermal stress to increase accuracy and larger elements in other regions to reduce

the problem size and thus the computational effort.
(Pramote Dechaumphai, 41357)
Structures Directorate

High-Strength Carbon-Carbon Composites With Three-Directional Reinforcement and Chemical Vapor Infiltration Densification

Although state-of-the-art (SOA) two-directional (2-D) reinforced thin carbon-carbon (C-C) composites have attractive in-plane mechanical properties, their interlaminar strengths are lower than desired for some applications. Hence, research is in progress to improve C-C interlaminar strengths without degrading their in-plane mechanical properties.



In this study, three-directional (3-D) reinforcement geometries in conjunction with several different densification matrices were evaluated.

The figure compares the mechanical properties of the best performing 3-D C-C composite with the SOA 2-D material. The 3-D composite consisted of 3K carbon fiber tows in plane, balanced in the 0° and 90° directions and woven through the thickness with 1K tows; densification was effected by chemical vapor infiltration (CVI). The SOA 2-D composite consisted of planar layers of 8-harness (8-hs) satin weave fabric, densified with phenolic resin as the matrix precursor. For the 3-D composite, interlaminar strengths are significantly higher (by up to 200 percent) and in-plane strengths

are also significantly higher. These in-plane strengths are high because the in-plane tows in the 3-D composite were straight instead of being crimped as they were in the fabric reinforcing the two-directional composite. Hence, better fiber strength efficiency is obtained. However, the tensile and compressive stiffnesses of the 3-D composite are lower than those for the 2-D composite because of the lower in-plane fiber volume fraction (0.45 compared with 0.62), which is an artifact of the orthogonal weave construction.

These results show that, for applications that are not stiffness critical, the 3-D orthogonal construction densified by CVI can be employed to achieve significant increases in interlaminar strength over that of SOA 2-D composites.

At the same time, notable increases in in-plane strengths are achieved. Material densification and testing were conducted by Rohr Industries and Langley under a cooperative agreement.

(Philip O. Ransone, 43503)
Structures Directorate

Fiber Surface Conditions Control Carbon-Carbon Composite Mechanical Properties

It is well established for conventional carbon-fiber-reinforced polymeric matrix composites that the chemical nature of the fiber surface influences the degree of interaction between the fiber and the matrix and, hence, the

mechanical properties of the composite. It was uncertain, however, whether this situation is similarly true for carbon-carbon composites because these composites are processed at extremely high temperatures (as high as 2500°C), and such high temperatures may destroy any effects of fiber surface chemistry.

Accordingly, a study was conducted in which four variants of one fiber type were used as the reinforcement to fabricate unidirectional carbon-carbon composites. Hercules HM fibers were obtained both with and without their commercial standard surface treatment (which is proprietary, but basically consists of a very slight surface oxidation). These two fiber variations were obtained with two different types of sizings: the commercial standard epoxy-compatible "G" (proprietary) sizing and a special phenolic sizing.

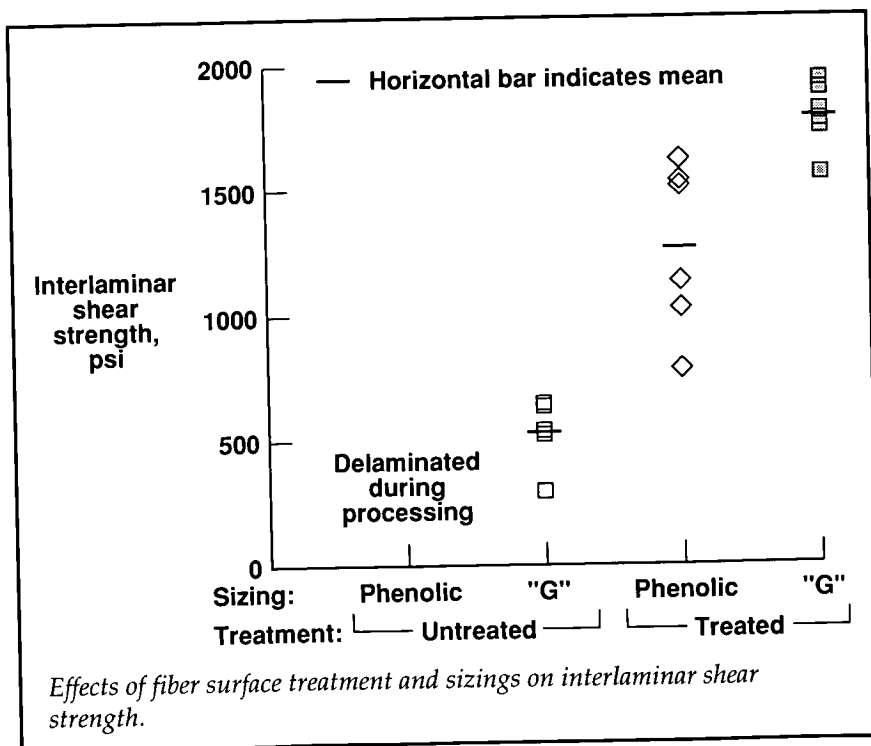
Mechanical properties of the composites were measured and effects on interlaminar shear strength are shown in the figure. The surface-treated fibers provide significantly greater interaction with the matrix than do untreated fibers, and there is also a significant, but somewhat smaller, influence on sizing. These results demonstrate that it is possible to exercise considerable control over fiber/matrix bonding in carbon-carbon composites by adjusting the fiber surface treatment and the chemistry of the sizing. Hence, considerable latitude exists for exploiting these two parameters to improve interlaminar strengths and to optimize mechanical properties in carbon-carbon composites.

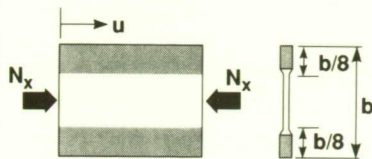
(H. G. Maahs, 43498, and Y. R. Yamaki)
Structures Directorate

Stiffness Tailoring for Improved Compression Buckling and Postbuckling Response for Composite Plates

The objective of this study was to evaluate a simple stiffness tailoring concept for potential structural performance benefits through increased compression buckling load and improved postbuckling stiffness and strength. Design concepts that lead to increased buckling loads can directly lower the structural weight and/or cost. Concepts that also increase postbuckling membrane stiffness and reduce out-of-plane deformations and bending stresses can further reduce weight and/or cost when postbuckling loading is allowed. The approach is to position the 0° plies through the thickness and over the planform of the plate so that the buckling load is increased with no loss in in-plane stiffness or increase in weight. Finite-element analyses have been used to determine the effects of tailoring on the buckling load of plates with various boundary conditions, aspect ratios, thicknesses, and membrane stiffnesses.

Stiffness tailoring has been especially advantageous when the plate is relatively thin, when the unloaded edges are simply supported, and when the average in-plane stiffness of the laminate is relatively high. The results shown in the figure are for a thin, square, quasi-isotropic plate with 0° plies relocated from the center to the unloaded edges of the plate. When the tailored plate is optimized for maximum buckling load, an improvement of 138 percent in





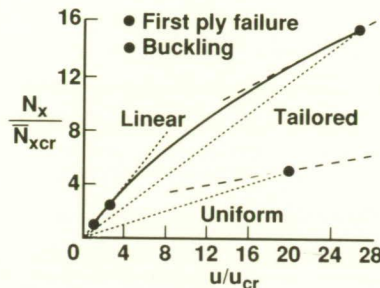
Results for a square, thin, quasi-isotropic plate:

Maximum improvements:

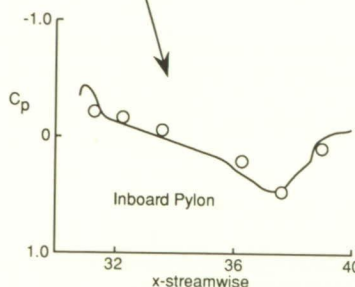
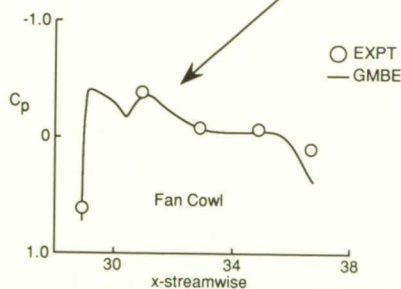
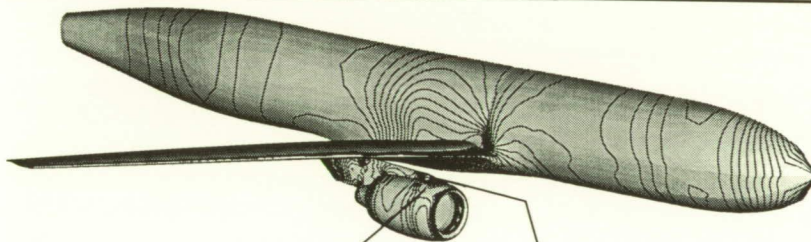
- Buckling:
 - Buckling load + 138%
- Postbuckling:
 - Secant stiffness + 135%
 - Tangent stiffness + 142%
 - Failure load + 215%
 - Edge failure strain + 38%

\bar{u}_{cr} : buckling displacement for a uniform thickness plate

\bar{N}_{xcr} : buckling stress resultant for a uniform thickness plate



Improvements observed for simple stiffness tailoring concept.



Airplane surface pressure contours computed with the general multiblock Euler code ($M_\infty = 0.77$ and $C_L \approx 0.55$).

the buckling load is achieved, as noted by the open circle on the figure. When this plate is located past buckling, both the secant stiffness (a measure of the plate's ability to carry increased load) and the tangent stiffness (a measure of the plate's contribution

to the stability of a stiffened panel) are increased by similar percentages. This study was conducted under grant with Clemson University.

(S. B. Biggers, 43170, and M. J. Stuart)
Structures Directorate

Euler Code for Turbofan Transports

A general, multiblock, multigrid Euler (GMBE) code has been developed for the analysis of complete airplanes with underwing turbofans. The GMBE code is a generalized version of a code that was successfully used to address the problem of engine-airframe integration for wing-mounted and aft-mounted turboprop engines. Powered nacelles may be simulated by prescribing inflow and outflow conditions at the fan inlet face and at the fan-core exit faces, respectively. Flow-through nacelles are analyzed by prescribing solid-surface boundary conditions along the inner walls of the nacelles.

The volume grid for a fuselage-wing-pylon-nacelle configuration is typically composed of 1 to 2 million grid points distributed among 20 to 30 blocks. A solution takes 16 megawords of memory and 4 to 6 hours of computing time on a Cray Y-MP supercomputer. The computations are used to identify undesirable flow regions in the vicinity of the pylon and nacelle.

Pressure coefficients computed with GMBE are in reasonable agreement with experimental data (see figure). The GMBE solution indicates that a change in toe angle and pylon trailing-edge closure geometry will improve the propulsion integration.

The GMBE code is an effective tool for the analysis of turbofan-superfan engine-airframe integration. It is being coupled with a NASA Langley direct iteration surface curvature (DISC) algorithm

for the inverse design of installed nacelles. This work was done under contract with ViGYAN, Inc. (D. A. Naik, 43041) Aeronautics Directorate

Improved Accuracy in Finite-Difference Analysis of Long-Distance Elastic Wave Propagation

Ultrasonic evaluation of large plates, as occurs in evaluation of aging aircraft, requires understanding of the propagating waveforms. Exact theoretical solution is often impossible to obtain because of the complexity of the structure, thus necessitating the development of numerical models. High-order finite-difference methods are required to describe long-time behavior of wave propagation. Standard methods produce artificial high-frequency waves due to numerical dispersion when long-time calculations necessary for long-distance propagation are performed. This limitation forces

the use of fine grids, which make the calculation expensive and limit the size of the physical problem that can practically be solved.

An improved spatial operator was developed that features higher accuracy and thus enables the treatment of larger problems and longer propagation times. The figure demonstrates the distortion of the wave while propagating. While the standard staggered method causes significant dispersion after propagating 500 wavelengths at a particular configuration, the improved method displays much better response under the same settings.

(Doron Kishoni, 44787, and Shlomo Ta'asan) Electronics Directorate

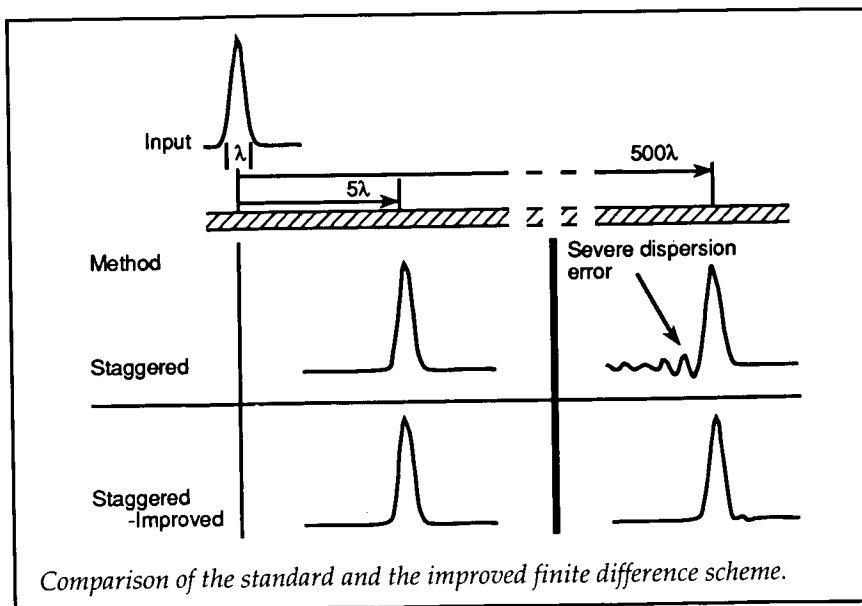
The Large-Angle Magnetic Suspension Test Fixture (LAMSTF)

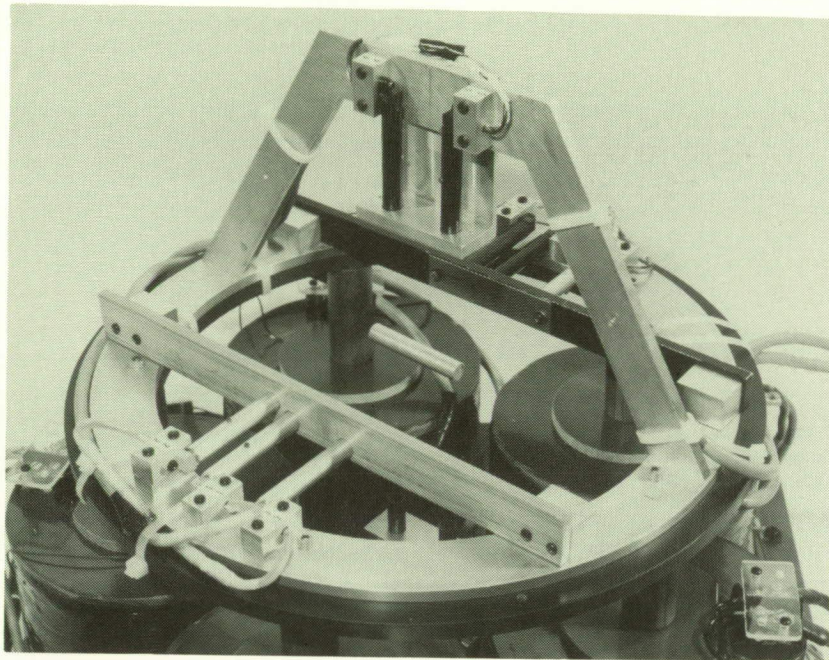
The objective of this research is to develop the technology for

large-gap magnetic suspension systems to meet the requirements of microgravity and low-frequency-vibration isolation systems, magnetically suspended ultra-accuracy payload pointing mounts, large-motion suspension systems for advanced actuators, and wind-tunnel systems. The emphasis of this particular effort was to develop a laboratory test fixture that incorporates large-gap magnetic suspension element concepts and to evaluate the viability of control and suspension techniques.

The needs of potential applications for this technology were examined and converted into system requirements, and a candidate test fixture was defined. Analysis and simulation resulted in a fixture consisting of a planar array of five room-temperature electromagnets arranged in a circular configuration with associated sensors, control electronics, and power amplifiers. As shown in the figure, LAMSTF levitates and controls a cylindrical suspended element that contains a core composed of neodymium-iron-boron permanent magnet material that is magnetized along the long axis of the cylinder. The core is controlled in five degrees of freedom, with roll being the uncontrolled axis.

Components of the LAMSTF have been designed, fabricated, tested, and assembled. Successful levitation and control of the suspended element has been demonstrated. This is believed to be the first demonstration of levitation and control, in five degrees of freedom, of a suspended element with a permanent magnet core by a planar array of five electromagnets.





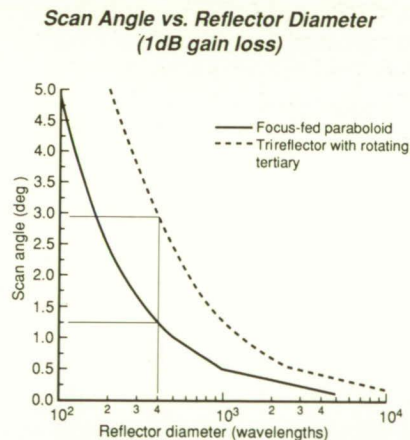
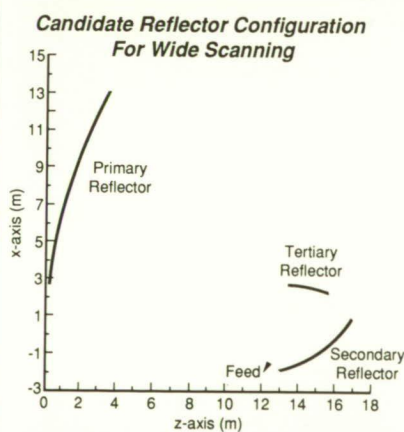
Large-angle magnetic suspension test fixture.

Techniques for Optimizing Wide-Scanning Reflector Configurations

Recent research at Langley has demonstrated the ability of innovative methods to scan large-aperture reflector systems. Large-aperture antennas are required for high-resolution microwave remote sensing missions from low Earth and geostationary orbits. Mechanical scanning required for meaningful satellite sampling swaths of these large-aperture systems is very costly.

Reflector configurations using one or more subreflectors are being studied to determine the potential for scanning high-resolution radiometer reflector antennas over hundreds of beam widths while maintaining good beam efficiency. The objective of these optimized designs is to utilize subreflector motion and electronic beam shaping with array feeds to minimize the amount of mechanical movement necessary to scan and maintain good beam efficiency. Configurations are being studied with a three-dimensional analytical reflector code used to determine optimum reflector configurations.

Results have been encouraging. For example, it has been shown that a simple rotation of a tertiary reflector in a Gregorian trireflector configuration can improve beam scan performance a factor of 2 compared with that of a similar prime-focus single reflector with large three-axis movements of the feed. (See figure.) Further optimization of the trireflector configuration is planned through combinations of tertiary reflector



Optimization of wide-scanning reflector configurations.

The LAMSTF will be instrumental in the development of the technology for future large-gap magnetic suspension systems by providing the experimental validation of design concepts in the areas of electromagnetics, control, sensing, and electronics. It will

also provide insight into the requirements and challenges introduced by larger scale systems. (Nelson J. Groom, 46613) Flight Systems Directorate

translation, variable tertiary reflector shape, and array feed compensation.

(M. C. Bailey, 41802, and L. C. Schroeder)
Flight Systems Directorate

Effect of Braze Processing on β 21S Titanium Matrix Composite

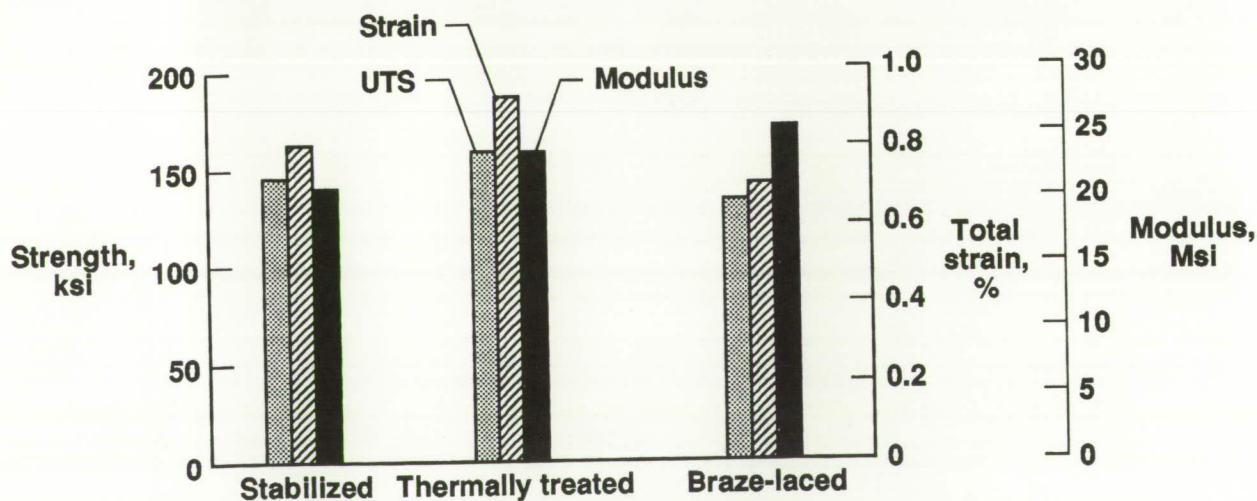
The National Aero-Space Plane (NASP) will require the development of lightweight, high-temperature materials as well as joining processes capable of incorporating these materials into efficient structural components. Titanium matrix composites (TMC) are one class of materials that have demonstrated the potential for meeting NASP objectives for airframe applications. Brazing is a candidate joining process for fabricating TMC into airframe structural components. Research is being conducted to determine the ability of brazing to provide adequate

joint strength at NASP service temperatures without degrading the properties of the TMC.

The figure shows results of tests conducted at room temperature on three sets of $[0/90]_s$ SCS-6/ β 21S TMC specimens to determine the effect of braze processing on the tensile properties of the composite. A control set (stabilized) was given a stabilization aging heat treatment. A second set (thermally treated) was subjected to the braze process thermal cycle and stabilized. A third set (braze-laced) had braze alloy applied to one side of each specimen and was thermally treated and stabilized. These last two sets of specimens were used to differentiate between the braze processing effects caused solely by the thermal cycle and those effects involving interaction between the braze alloy and the TMC. When compared with the stabilized specimens, the thermal treatment resulted in a small increase in strength and total strain. The braze-laced specimens,

however, exhibited a small decrease in these properties. The modulus of the braze-laced specimens was slightly higher than those of the thermally treated or the stabilized specimen. Thus, braze processing had only small deleterious effects on the tensile properties of the TMC at room temperature. However, other tests showed that the β 21S matrix is severely embrittled by braze processing. This suggests that fatigue behavior of TMC may be more seriously affected by braze processing.

(R. Keith Bird, 43512, and Eric K. Hoffman)
Structures Directorate



Effect of braze processing on tensile properties of $[0/90]_s$ SCS-6/ β 21S TMC at room temperature.

■ SUBSONIC AIRCRAFT



*Develop technologies to ensure
the competitiveness of U.S.
subsonic aircraft and to enhance
the safety and capacity of our
national airspace system*

Preceding Page Blank

Optical Disk Recorder-Playback System

An advanced optical disk recorder-playback system is required to enable flight-test engineers and aeronautics researchers to do postflight engineering unit and "quick look" processing of flight data recorded on optical disk with existing pulse code modulation (PCM) data processing equipment. Through software running on a personal computer (PC), data can be read off the optical disk and written to a board in an Inter-Range-Instrumentation Group (IRIG) compatible format. The board then converts the data to a serial PCM stream, which can be easily handled by standard

IRIG PCM decommutators already in wide use.

The hardware is based on first-in-first-out (FIFO) memory, which allows the software to write the data to one address in the desired output order. The FIFO is written to on a "half empty" condition. This servicing may be done through jumper-selectable interrupts or by polling a half empty status flag.

The control commands allow the PCM output to be tailored for different applications. The output bit rate is based on a socketed, on-board oscillator and is programmed using the "Bit rate write" command to write a 16-bit divisor. Consequently, the bit rate can be varied by changing the oscillator and/or using a different bit rate

divisor. The output word length is programmable from 8 to 16 bits, and two serial encoding schemes including a bit clock are provided at the output.

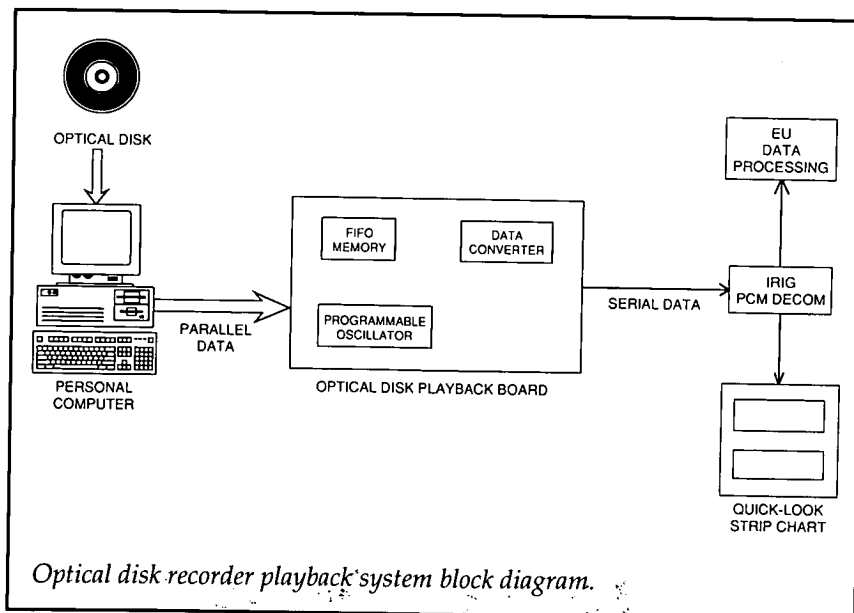
This playback system has been implemented in Langley's Research Aircraft Ground Station and in remote-site playback equipment in support of ATOPS flight research projects.

(Jennifer J. Reilly, 41662)
Electronics Directorate

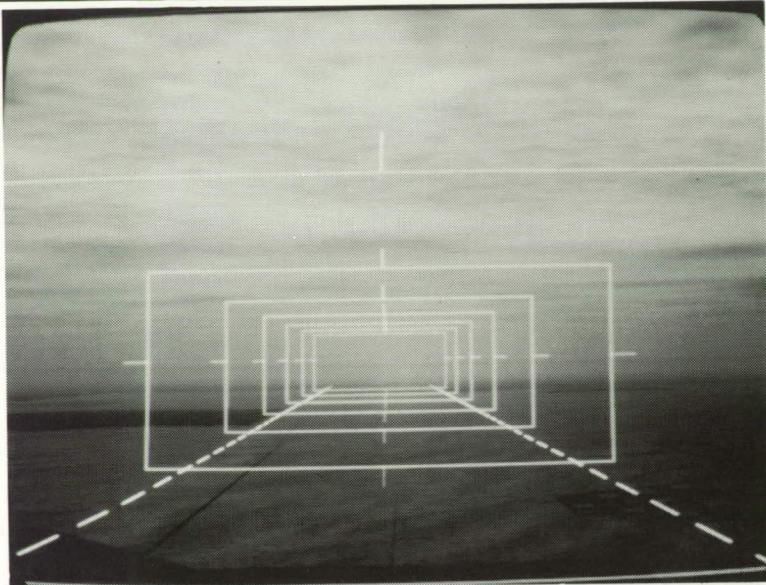
General Aviation E-Z Fly Studies

A piloted simulation study on the Langley General Aviation Simulator has demonstrated the revolutionary potential of the combination of two advanced systems for safely reducing the training and proficiency requirements for private pilots. Approximately 90 percent of the nonpilot test subjects successfully completed a flight in reduced visibility conditions without any prior practice or training. In a conventional airplane in similar conditions the chance of success is virtually zero.

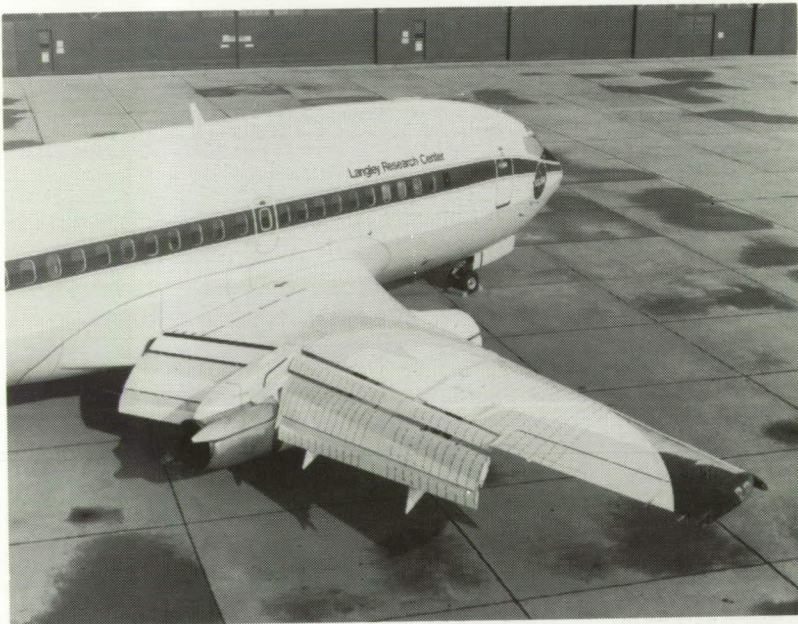
The two advanced systems were a (fly-by-wire) decoupled control system and a head-up pictorial display. The decoupled control system eliminated the natural coupling of airplane responses such as airspeed and



ORIGINAL PAGE
BLACK AND WHITE PHOTOGRAPH



"Highway in the Sky" head-up pictorial display used in piloted simulation studies.



NASA Transport Systems Research Vehicle (B737-100 aircraft) instrumented for pressure measurements on high-lift wing section.

vertical speed when the pilot moved one control at a time. This decoupling produced a much more intuitive control, which was similar to that on an automobile. The head-up pictorial display (see

figure) drew a road or tunnel that remained fixed with respect to the Earth. The pilot was able to extract all the necessary navigation and control information from this one display without training. A con-

ventional instrument panel uses several different indicators to provide the same information, but the pilot must be highly trained to perform the mental calculations to integrate all the individual pieces of information into a picture of what the airplane is doing. The combination of the decoupled control system and the head-up pictorial display made the flying task many times easier and safer than flying a conventional airplane.

(Eric C. Stewart, 43939)
Aeronautics Directorate

Subsonic Transport High-Lift Flight Research—Phase IIA

As part of a research program to improve the design methodology of high-lift systems on subsonic transports, flight experiments are being conducted on the NASA Transport Systems Research Vehicle Boeing 737 aircraft to obtain detailed flow measurements of a transport high-lift system. The objective of this research is to improve the understanding of high-lift flows at flight Reynolds numbers and in three dimensions for correlation, validation, and improvement of ground-based predictive tools (wind tunnel or computational) for high-lift systems.

In recent Phase IIA flight experiments, pressure distributions were measured for a full-chord wing section including the slat, main-wing, and flap elements. Highly favorable pressure gradients, conducive for relaminarization of turbulent flows, were measured

on the slat, main-wing, and fore-flap leading edges. Skin-friction measurements on the slat upper surface provided evidence of relaminarization of turbulent flows. Since the attachment-line boundary-layer state and the potential for relaminarization can have significant impacts on maximum lift, these test results are of particular interest to aircraft designers.

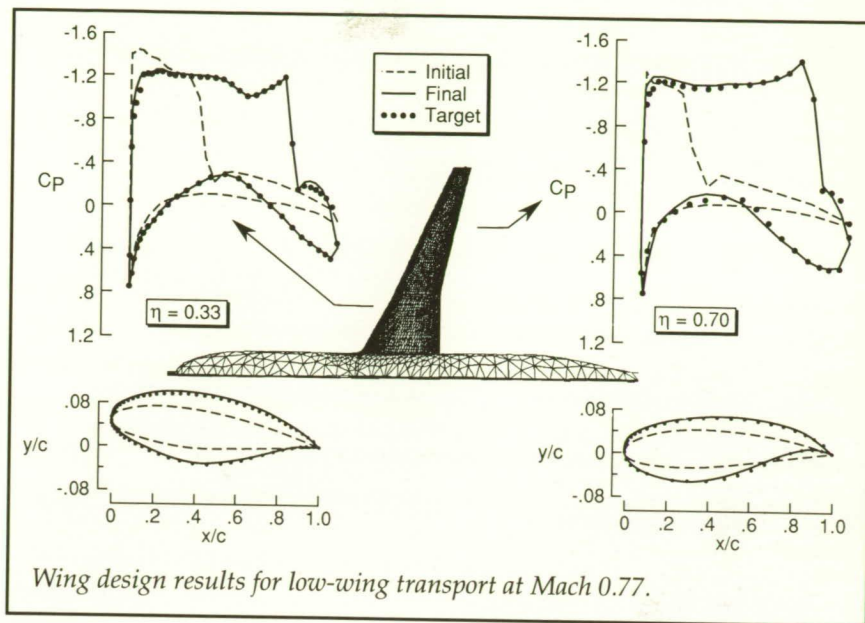
These high-lift flow measurements provide previously unavailable flow details at full-scale flight Reynolds numbers for correlation of ground-based wind-tunnel results. The measurements also provide a challenging validation test case for CFD analysis, particularly in the modeling of three-dimensional viscous effects.

(Long P. Yip, 43866)

Aeronautics Directorate

Automated Transonic Wing Design Using an Unstructured Euler Method

A design approach for geometrically complex configurations has been created by combining the direct iterative surface curvature (DISC) design method with the Unstructured Method 3-D (USM3D) Euler code. The DISC design method is a technique that modifies the surface curvatures and slopes of an initial geometry so that a target pressure distribution is matched. This method has been successfully coupled with a number of codes and has been applied to the design of a variety of aircraft components, such as airfoils, wings, winglets, and nacelles. The choice of



USM3D and the unstructured grid generation code VGRID3D allow for the study of full configurations and thus the potential to design any component in the presence of other components.

Critical to this technology was the development of a routine for grid perturbation based on the spring analogy technique. This technique allows the modifications to the surface definition computed by the design method to be easily assimilated into the surrounding grid. For the verification exercise, an existing generic transport configuration was analyzed in USM3D. The resulting wing pressure distributions were used as target pressure distributions for the design. An initial configuration was created by replacing the transport's supercritical airfoils with NACA 0006 airfoil sections. The figure shows the results of this design effort for two span stations. Pressure distributions and airfoils are shown for the original wing (target), the starting configuration (initial), and the resulting design (final). These plots show that the

design method was successful in reproducing the target pressures and airfoils. This work was done in part under contract with ViGYAN, Inc.

(L. A. Smith, 42878, and S. Pirzadeh)

Aeronautics Directorate

Digital Resolver System for Helicopter Model Blade Motion Analysis

Powered helicopter model tests performed in the Langley 14- by 22-Foot Subsonic Tunnel require resolver instrumentation for harmonic analysis of blade motion. Existing analog instrumentation provides information only at the fundamental rotation frequency. Second-harmonic information is required to characterize blade bending. A new digital signal processor (DSP) based resolver system has been developed and tested to perform fast Fourier transform (FFT) analysis of blade

flapping angles in real time. The additional harmonic information now available allows complete characterization of blade bending. Real-time displays enable a test pilot to adjust the helicopter model controls to achieve desired aerodynamic test conditions.

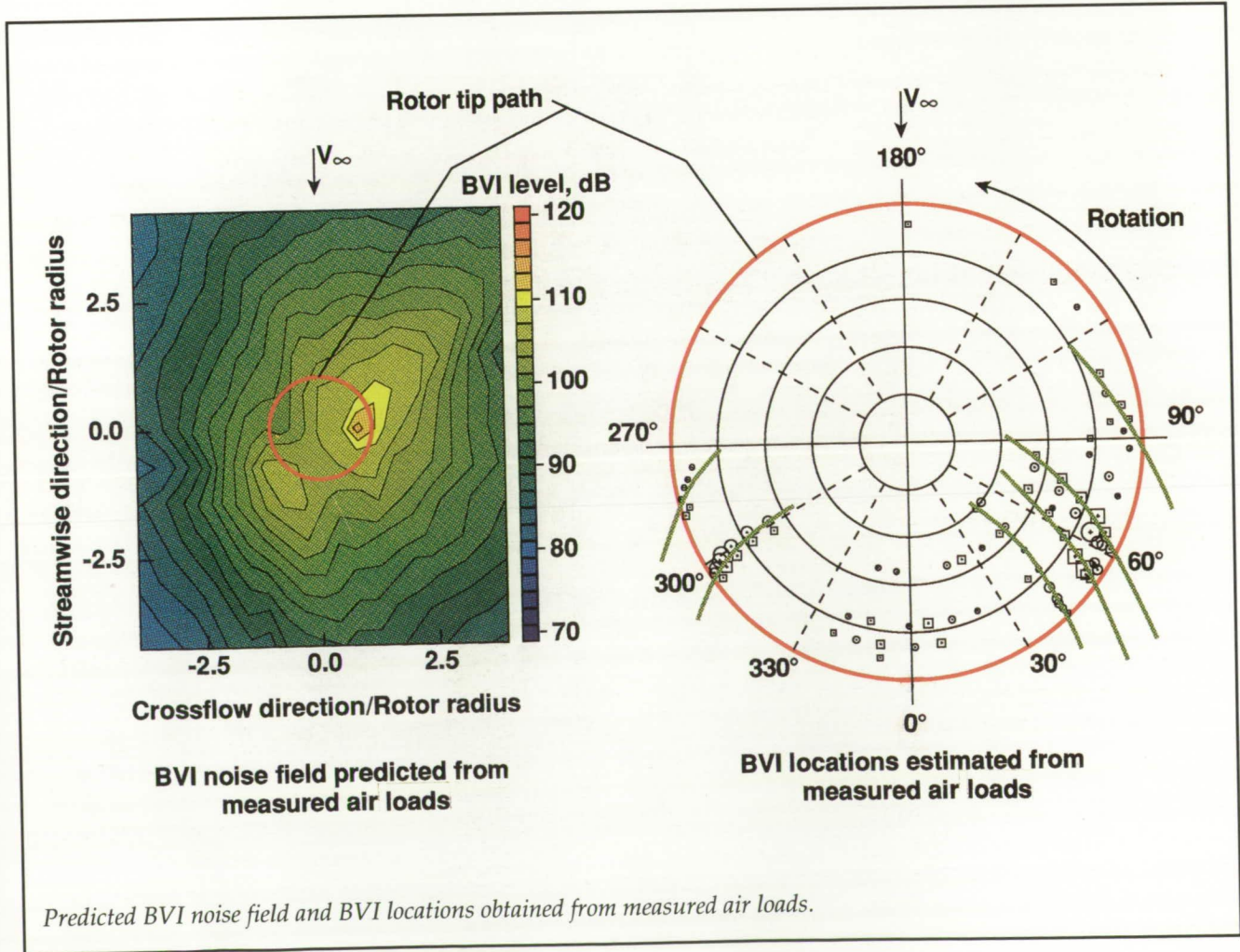
The new instrument incorporates a DSP microcomputer within a host personal computer. The DSP processed data are uploaded to a minicomputer for real-time graphic display. Potentiometers mounted on one of four articulated blades measure flapping angle. A shaft encoder geared to the rotor

provides a synchronized sampling clock and an azimuth synchronizing pulse to initiate data acquisition. A unique data acquisition technique minimizes error normally encountered with FFT analysis. Data are acquired in four blocks, each periodic with one blade rotation regardless of rotation speed. This scheme eliminates the need to search for peaks and prevents spectral leakage errors in the FFT result. Although inherent rectangular windowing is performed prior to the FFT computation, no line-splitting error occurs since the sampling rate is fixed at an integer multiple of the

rotor rotational rate. Calibration testing has shown a high degree of accuracy for this system.
(Taumi S. Daniels, 44659, and John D. Berry)
 Electronics Directorate

Predicted Rotor Impulsive Noise Directivity and Measured Wake Interaction Locations

Rotor blade-vortex interaction (BVI) noise is an intense, impulsive, mid-frequency noise source caused



by close encounters between rotor blades and previously shed tip vortices. As BVI is one of the most objectionable rotorcraft noise sources, detailed understanding of the interaction process is necessary in order to develop an accurate prediction method both to design low-noise rotor systems and to identify low-noise flight procedures.

The measured surface pressure loading of a model rotor is used both to predict the BVI far-field noise directivity and to estimate the location and intensity of the interactions on the rotor disk. The model rotor is a pressure-instrumented four-bladed system (owned by United Technologies Research Center). This rotor was tested in the German-Dutch Wind Tunnel (DNW) by a team of Army, UTRC, and NASA researchers. The measured dynamic surface pressures on the rotor are used as input to the noise prediction program WOPWOP to predict the BVI noise field on a large plane under the rotor. Local maxima and minima in the high-frequency component of the dynamic section thrust coefficient are used to identify the locations and strengths of the interactions.

The BVI noise field predicted from the measured rotor loading is shown at the left in the figure. Two regions of intense BVI noise radiation can be seen, one (114 dB) under the rotor's advancing (right) side and one (106 dB) under the retreating (left) side. The character of this predicted field compares very well with that of previously measured BVI noise fields. The location and the intensity of the interactions are shown at the right in the figure. The sizes of the symbols are scaled by strength;

the circles represent positive peaks, and the boxes represent negative peaks. The symbols clustered near 60° azimuth represent the strongest fluctuations and produce the advancing-side BVI noise. Similarly, those near 300° azimuth are the source of the retreating-side noise. Current theoretical understanding of BVI directivity as a function of interaction location agrees with these results.

Given accurate data or prediction of a rotor's aerodynamic loads, BVI noise predictions can be made over a large area with only the dynamic surface pressures used as input. The general characteristics of BVI directivity can be estimated from only the BVI locations and strengths, providing an empirical approach to identifying low-noise rotor designs and flight conditions.

(M. A. Marcolini, 43629, and R. M. Martin)

Structures Directorate

Wavelength Division Multiplexing Digital Controller (WDM-DC)

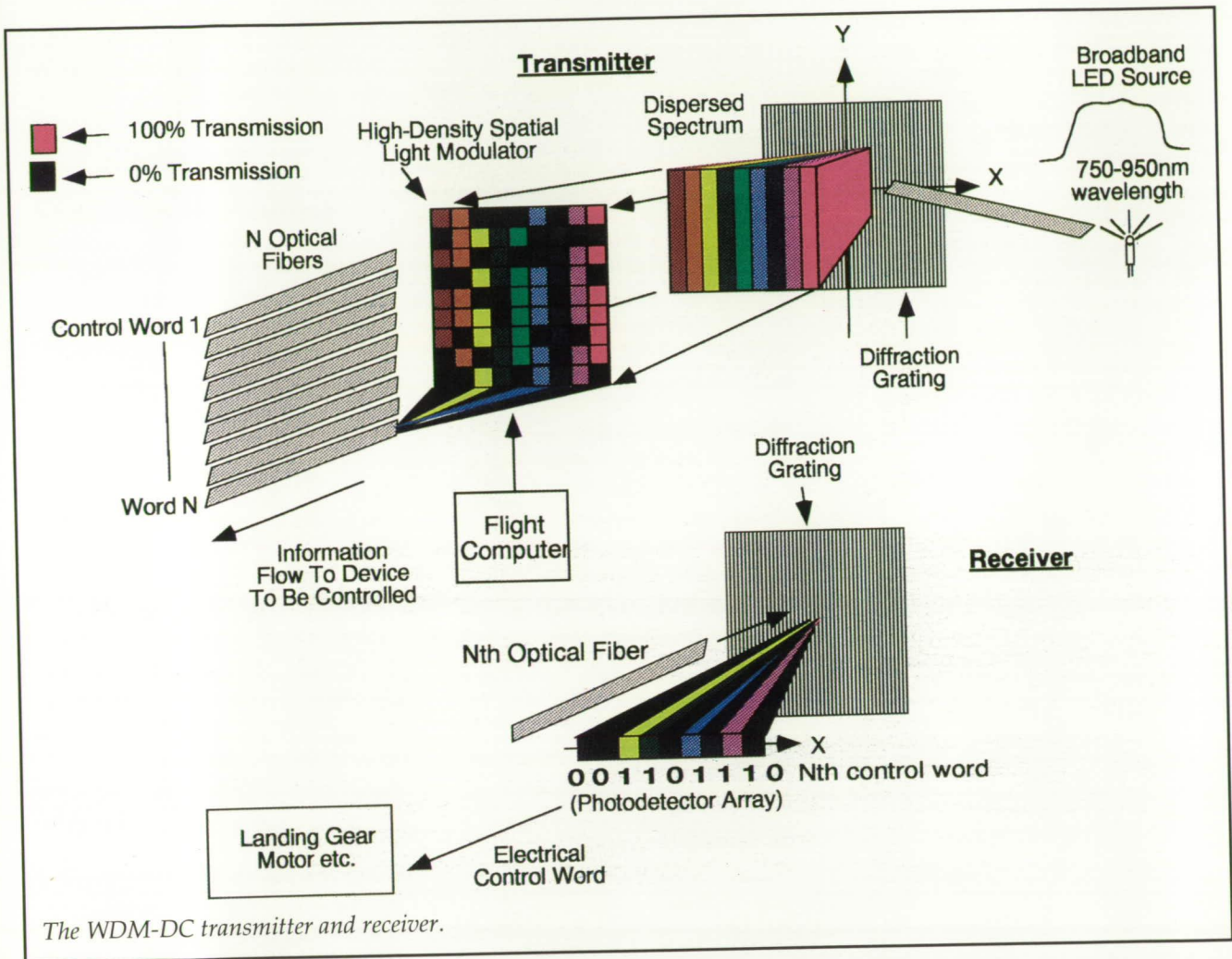
The threat of electromagnetic interference (EMI) on the safety of air transportation has continued to increase because of the proliferation of high-intensity electromagnetic wave transmitters. Subsequently, there has been a flurry of interest in the use of fiber-optic communication and sensing on military and commercial aircraft. This interest has been fueled by the inherent immunity of fiber-optic communication links to EMI. A highly beneficial application of

fiber-optic communication and sensing to avionics is the control of fly-by-wire (FBW) aircraft actuators. Because the FBW actuators generally require digital electronic circuitry (i.e., smart actuators), they are susceptible to electromagnetic upset. Decreased digital circuitry at the actuator and a fiber-optic communication link would lead to increased reliability. This could be achieved by a highly parallel optical communication link.

We have designed and are presently fabricating a WDM transmitter and receiver pair that renders highly parallel optical control of actuators. The figure demonstrates the concept behind the WDM-DC. At the transmitter, infrared light from a broad-spectrum light emitting diode (LED) is dispersed spectrally by a diffraction grating and focused onto a spatial light modulator (SLM). The SLM receives electronic signals from a flight computer which control the transmission state of each pixel or light valve (on or off for binary operation). Each row of the SLM modulates a unique control word meant for a specific actuator. At the output side of the SLM, the modulated light from each row is gathered and coupled to optical fibers and routed to optical receivers that are located at the actuators. At the receivers, the light is again dispersed by a diffraction grating and shone onto a photodetector array, where the optical control word is converted into an electronic control word and applied to the actuator electronics.

(James D. Patterson, 46202, and Daniel L. Palumbo)

Flight Systems Directorate



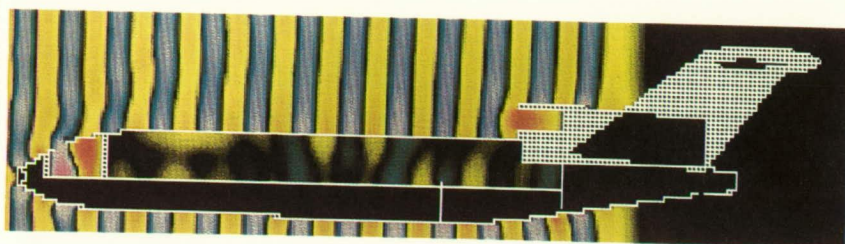
Assessment of High-Intensity Radiated Field Effects

The purpose of this effort is to develop a quantitative assessment of high-intensity radiated fields (HIRF) effects on current and future transport aircraft. The HIRF effects involve the *man-made* electromagnetic radiation that can cause a threat to aircraft. HIRF emitters include radars, radio broadcast transmitters, and any other man-made emitters of electromagnetic energy. Digital computers employed in future

transport aircraft will be critical to flight and must operate reliably in harsh electromagnetic environments (EME) such as HIRF's. HIRF's are of interest since the digital computer-based systems in aircraft can be upset by HIRF-generated electrical transients. The term *upset* refers to the propensity for digital electronic systems to malfunction as a result of electrical transients and is one of the most illusive and insidious problems caused by the electromagnetic environment affecting digital computers. Upset refers to function error modes, wherein the digital computer, although not

permanently damaged, no longer performs its intended function until it is either reset or the memory is reloaded. As part of the Fly-By-Light/Power-By-Wire program, Langley Research Center has supported the Lawrence Livermore National Laboratory (LLNL) in adapting and applying modeling tools LLNL developed for Nuclear Electromagnetic Pulse and High-Power Microwave Programs to civil transport aircraft. Such modeling tools are the key to low-cost system EME upset assessment.

LLNL has applied their Temporal Scattering and Response (TSAR) code to the prediction of



Boeing 727 model internal fields at 140 MHz.

the electromagnetic interaction of plane continuous wave excitation with a Boeing 727 aircraft. The figure shows the response of the impingement of 13 cycles of a vertically polarized 140 MHz electric field on the aircraft as computed by the TSAR code. The colors yellow, orange, and red represent positive values, black represents zero, and green, blue, and violet represent negative values. The data have been normalized so that the strongest field values in the run are red; the peak incident field strength is a factor of 3 less than this. Resonance effects in the cockpit and engine inlets are thus seen to create fields about 3 times higher than the incident field. The diffuse yellow-green shows the fields coupled into the cabin through the windows.

(Felix L. Pitts, 46186)
Flight Systems Directorate

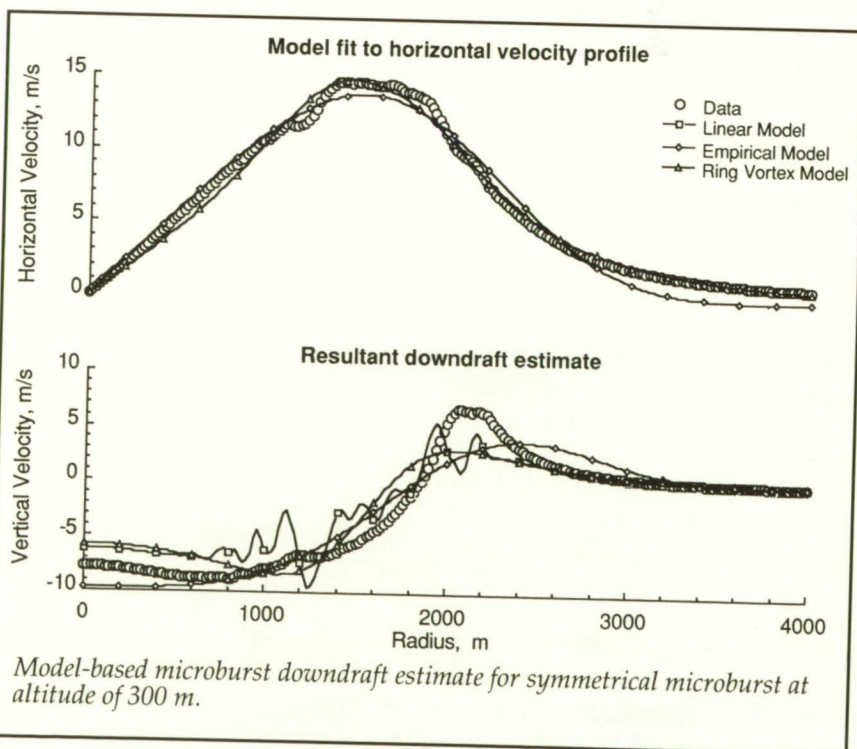
Model-Based Techniques Developed for Estimation of Microburst Downdraft

Doppler radar and lidar are two candidate forward-looking sensor technologies being tested to detect hazardous wind shear.

An inherent limitation of these technologies is their inability to measure velocities perpendicular to the line of sight. Although these systems can detect the presence of a wind shear by measuring the divergence of the horizontal wind profile, their inability to measure the downdraft can result in a significant underestimate of the magnitude of the hazard. One method of overcoming this limitation is to estimate the vertical wind com-

ponent from the horizontal wind profile through theoretical or empirical microburst models. The objective of this research was to develop and test candidate microburst models for this purpose.

Three different approaches were used to develop candidate models. One was a very simplistic approach that assumed a linear variation of the vertical wind with altitude and conservation of mass. This model directly computed the downdraft from the measured winds. The second approach was an empirical method that used data from measured microburst events to develop characteristic shaping functions. The shaping function variables were defined by the size and magnitude of the microburst. The third approach was a theoretical one that assumed a microburst to be similar to a ring vortex approaching a flat plate. Multiple ring vortex models



have been used in the past to simulate microbursts. The second and third models used a multi-dimensional search technique to determine the model variable values that yield the best fit to the horizontal wind measurements. These values were then used to compute the associated downdraft. Examples of the results of the model fit to the horizontal wind profile and the resultant downdraft estimate are shown in the figure.

Following validation, the results of this research can be applied to airborne forward-looking systems and to the ground-based Terminal Doppler Weather Radar systems to enhance their estimation of the microburst hazard potential. (Dan D. Vicroy, 42022)
Flight Systems Directorate

Airborne Wind Shear Detector

The Coherent Lidar Airborne Shear Sensor (CLASS) has been developed under contract with Lockheed, United Technology Optical Systems, and Lassen Research to remotely measure wind velocity in the flight path of transport aircraft to enable the aircraft pilot to detect and avoid hazardous wind shear conditions. A 10.6- μm laser was selected for the lidar because of the technology readiness of carbon dioxide (CO_2) lasers. A radio frequency (RF) pumped-injection-seeded CO_2 master oscillator power amplifier was chosen for the laser, with the master oscillator continuously pumped to reduce chirp and the amplifier pulse pumped for efficiency. The laser output is

8 mJ at 100 pulses per second. The pulse duration is 2 μsec , with chirp less than 200 000 Hz. The data system utilizes a poly-pulse pair processor and the beam is propagated through a 15-cm scanner mounted below the aircraft. The system measures velocity with a range resolution of 300 m and a velocity resolution of 1 m/sec.

The CLASS has been installed on the NASA Transport Systems Research Vehicle (TSRV) Boeing 737 aircraft as part of the NASA/FAA Airborne Wind Shear Detection and Avoidance program. Flight tests have demonstrated a sensor operation range of 4 to 10 km, depending on humidity. Wind shear experiments

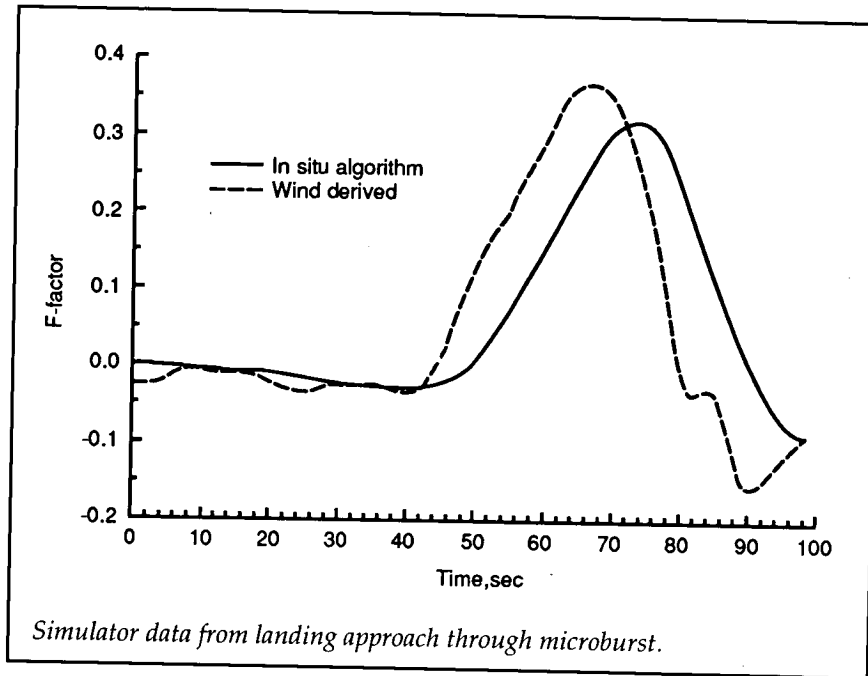
are being conducted at Denver, Colorado, and Orlando, Florida. (Philip Brockman, 41679, and Raymond S. Calloway)
Electronics Directorate

In Situ Wind Shear Detection Algorithm Developed for Modern Transport Aircraft

The threat of microburst wind shear to transport aircraft has prompted the development of forward-looking wind shear sensors, which detect wind conditions far enough ahead of an aircraft to give advanced warning of hazardous conditions. In order



CLASS installed on NASA TSRV-Boeing 737 aircraft.



to validate these sensors in flight, a reliable measure of the wind shear hazard index (F -factor) is needed to ascertain the accuracy of the forward-looking sensor measurement. The objective of this research was to evaluate an algorithm for *in situ* computation of the F -factor, based on standard air data and inertial reference system data. This computation should be insensitive to aircraft maneuvering and should exhibit decreased latency over existing *in situ* systems to meet flight-test operational requirements.

Mathematical analysis of the airplane equations of motion indicated that F -factor can be computed by differencing the rate of change of energy computed in air-mass relative and inertial frames of reference. This algorithm was implemented in a Boeing 737-100 airplane simulation with an analytic microburst wind field. Data were collected with various airplane flap settings and wind

conditions, including microburst wind shear, to evaluate the algorithm's ability to correctly detect wind shear conditions. Maneuvers that caused extremely high levels of acceleration were performed to evaluate the algorithm's ability to reject "false alarms" from aircraft maneuvering. Following this simulation, the algorithm was tested in flight on the NASA Transport Systems Research Vehicle (TSRV) in normal terminal-area type operations as well as in maneuvering conditions.

Results from the simulation study indicated that, for significant changes in longitudinal and normal accelerations as well as for changes more typical of transport aircraft operations, aircraft maneuvering produced little error in the computed F -factor. Additionally, for operations in a wind shear environment, the *in situ* F -factor tracked the actual F -factor, with appropriate filter lags (see figure). Flight tests consisted of similar

maneuvers as those in the simulator, and results showed good agreement with simulator results. Deployment flight tests in Orlando, Florida, during the summer of 1991 verified (based on ground radar) the algorithm's accurate performance in detecting actual wind shear conditions. (Rosa M. Oseguera, 42039) Flight Systems Directorate

Wind Shear Hazard From Terminal Doppler Weather Radar Information

The Terminal Doppler Weather Radar (TDWR), previously developed by the FAA, has shown its ability to detect microbursts during operational demonstrations, but the format and timeliness of the information reaching crews has deficiencies. The scope of the NASA/FAA Airborne Wind Shear Detection and Avoidance program includes the integration of TDWR wind shear information on the flight deck. The objective of this effort was to develop and evaluate an algorithm for estimating the microburst F -factor (wind shear hazard index) from TDWR data. A secondary objective was to gain experience with research aircraft microburst penetrations in preparation for planned NASA aircraft experiments.

An algorithm was developed at Langley Research Center to estimate a character F -factor for a microburst event given TDWR-measured parameters and aircraft airspeed. During a flight-test experiment conducted at Orlando, Florida, during the summer of 1990 by the MIT Lincoln Laboratory

and the University of North Dakota (UND), the NASA algorithm was used to calculate the *F*-factor of each microburst event that was penetrated by the UND Cessna Citation research aircraft. The TDWR *F*-factor was then compared with *in situ* data collected by the aircraft as it passed through a microburst.

Numerous microburst penetrations were made by the UND aircraft while in TDWR coverage. *In situ* *F*-factor threshold crossings ($F > 0.1$) were compared with TDWR *F*-factor crossings and with the present baseline TDWR microburst warning criteria of a 30-knot wind divergence. Although data were analyzed with a TDWR wind threshold calculation that was improved over the operational algorithm, the wind threshold crossings agreed with the aircraft *in situ* threshold crossing in only 58 percent of the events, while the NASA TDWR *F*-factor threshold crossing agreed in 68 percent of the events. A strong microburst penetration taken from this sample has been analyzed in detail and showed excellent agreement between the TDWR *F*-factor prediction and the *in situ* measurement.

The experiment validates the concept of calculating a microburst *F*-factor value from ground-based radar measurements. The correlation between TDWR-derived *F*-factors and airplane measured *F*-factors is essential for fusion of TDWR data with onboard wind shear information and for deriving wind shear alerts from ground data.

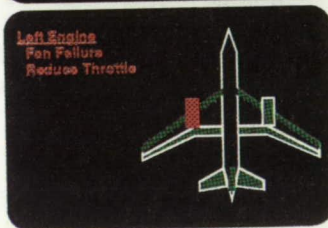
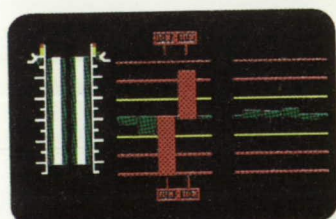
(David A. Hinton, 42040)
Flight Systems Directorate

Accident Data Used To Validate Faultfinder Concept

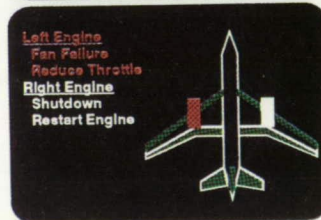
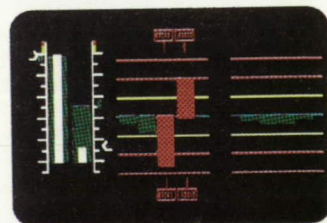
Propulsion-system-related accidents comprise 12 percent of all aircraft accidents. Of those 12 percent, approximately one-third have crew error as a major cause. Therefore, a concept named Faultfinder was designed and implemented for the propulsion subsystem of a twin-jet aircraft to investigate aid to flight crews in managing in-flight subsystem failures. Faultfinder provides fault monitoring, diagnosis, and response recommendations for aircraft subsystems. The fault monitor uses a numerical simulation of a normally functioning aircraft engine to detect abnormalities in sensor data. These abnormalities (symptoms) are passed to the diagnostic process, which uses those symptoms to isolate and diagnose the fault and to identify the system status. The diagnostic

process is performed in two stages. The first stage uses rules to diagnose common or anticipated faults (e.g., compressor stall or fuel leak). The second stage uses model-based reasoning to diagnose faults that are not included in the rules. The second stage also describes the system status after the fault. Finally, Faultfinder recommends actions to be taken in response to the fault.

Flight recorder data from the British Midland Airways Boeing 737-400 aircraft that crashed outside East Midlands Airport in England in January of 1989 was used to test Faultfinder. In this accident, the left engine suffered a fan failure that caused heavy vibration and smoke in the cockpit. The pilots incorrectly diagnosed that the right engine had failed and shut that engine down. After the right engine was shut down, the left engine was operating in a degraded mode but was still producing thrust. None of the



Faultfinder Output
Prior to Right Engine
Shut Down



Faultfinder Output
After Right Engine
Shut Down

Results of running Faultfinder on flight recorder data of British Midland Airways Boeing 737-400, January 8, 1989.

left-engine instrument indications showed values in the caution or warning ranges. Vibration was excessively high on the left engine, but there was no designated normal range on that indicator and the pilots evidently did not use that data. After shutting down the right engine, the vibration coincidentally decreased. Thus, the pilots felt that they had correctly responded to the situation. Sixteen minutes after the right engine was shut down, the left engine failed completely. The aircraft crashed within sight of the airport. The data from the flight data recorder were run through Faultfinder. The results of the study were compared with the actual findings of the British Air Accidents Investigation Branch of the Civil Aviation Authority.

The results of this evaluation showed that the fault monitoring stage of Faultfinder was able to correctly detect all abnormalities in the left-engine sensor indications. This was true both before and after the right engine was shut down. The fault diagnostic function of Faultfinder was able to correctly identify the responsible component as the fan. It also correctly identified the fault propagation from the fan to the other engine systems. The figure shows the information that was produced by Faultfinder 2 sec prior to and 8 sec after shutting down the right engine. The successful results of this evaluation demonstrate that the Faultfinder concept can detect and diagnose failures to provide fault management information that current onboard systems cannot provide. Moreover, the information generated by the Faultfinder concept provides a comprehensive,

integrated view of the failure situations that has the potential to aid flight crews in preventing accidents or reducing their consequences.

(Paul C. Schutte, 42019)
Flight Systems Directorate

Types of Information Desired From Intelligent Decision Aiding

Analyses of accidents and incidents reveal that pilot error is a major causal factor in approximately 75 percent of the cases. The objective of this research effort was to understand why pilot misunderstandings arise in failure situations through analysis of

pilot behavior in diagnosing subsystem failures. In particular, the purpose was to identify pilot mental models of the aircraft subsystems, to determine if the accuracy of those mental models correlates with the accuracy of diagnosis of subsystems behavior, and to analyze the types of errors made.

Fourteen Boeing 737-qualified pilots served as test subjects. Their mental models of the aircraft systems were probed, and their diagnostic behavior of 17 fault cases were analyzed. In a workstation environment, the pilots were shown the gages as they would appear in the cockpit in the fault situation and told the current flight situation and any aural and olfactory cues. They were not

Error type	Frequency, percent
Inadvertently ignoring symptoms	6
Consciously ignoring symptoms in order to support an incorrect hypothesis	29
On the wrong track entirely	15
General knowledge of system okay, but couldn't quite pinpoint the actual component that failed	16
Meant to say the right answer but didn't	3
Did not weigh all the cues correctly	17
Too general a diagnosis	5
Perception problem with the symptoms	2
No answer	7

Pilot errors in diagnostic reasoning when their mental models are correct.

given any time constraints, but rather were asked to examine the information presented until they were comfortable that they had diagnosed the problem. The resulting answers, as well as the mental models, were analyzed for correctness by an expert instructor from an airline training center.

The results of the analysis were grouped according to the correctness of the pilot's mental model and the correctness of the diagnosis. The results show that 87 percent of the time pilots had an accurate mental model of the aircraft and its subsystems. When they had an accurate mental model, they were able to correctly diagnose the failure of 62 percent of the cases. This implies that knowledge of the pilot's mental model is a predictor of their diagnostic behavior, albeit a somewhat weak one. The situations where they had a current model but an incorrect diagnosis were analyzed for nine types of errors, with the results shown in the figure. Approximately half the errors were of two types: consciously ignoring symptoms in order to support an incorrect hypothesis, and not weighing all cues correctly. These two error types represent cognitive biases to which humans are generally subject.

The results of this effort have important implications for identifying the appropriate type of information that a decision aid for fault management should provide. Most pilots are shown to have a good understanding of the aircraft systems but may not always use the information correctly. One reason might be that pilots are trained to respond to faults (i.e., carry out preplanned

procedures), not diagnose them. This test did not evaluate the responses to failures. By highlighting symptoms that might be ignored or improperly weighted, or by providing a diagnosis directly, pilot performance may be improved.

(Kathy Abbott, 48262, and Mindy Howard)
Flight Systems Directorate

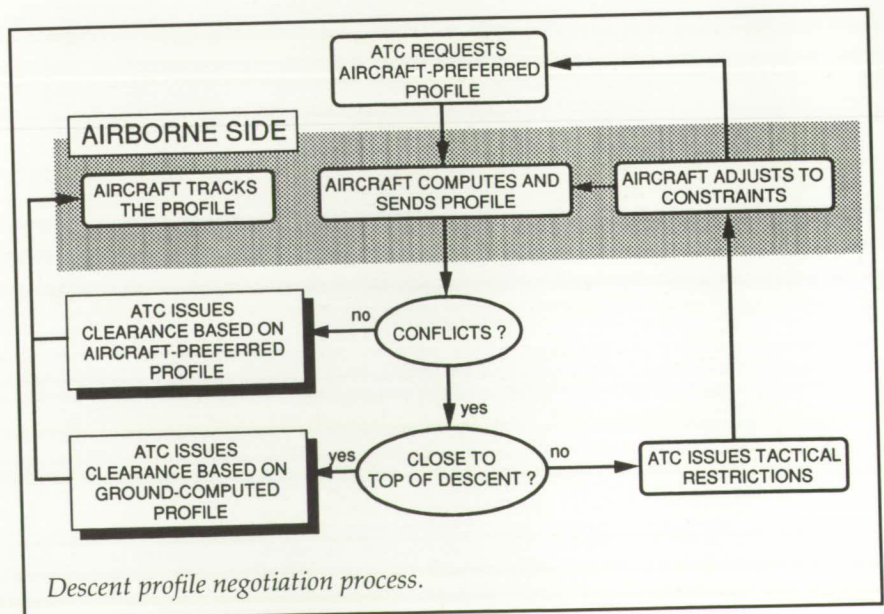
Air-Ground Descent Profile Negotiation for Improved Airspace Efficiency

The objective of this experiment was to develop and evaluate a descent profile negotiation process between time-based air traffic control (ATC) system and an aircraft equipped with a four-dimensional flight management system (4-D FMS). The negotiation enables the aircraft to propose an efficient trajectory that satisfies ATC-imposed routing and arrival

time constraints. The ATC automation assists the controller in clearing the aircraft for a trajectory that satisfies the constraints, is close to the aircraft-preferred trajectory, and is free of conflicts with other traffic.

The Langley Transport System Research Vehicle (TSRV) Simulator was linked to the Ames Center/Tracon Automation System (CTAS) ATC simulation for the experiment. A 4-D trajectory generation algorithm and time guidance were integrated with a digital data-link system and baseline TSRV displays. Data-link capability and conflict probing of aircraft-preferred descent trajectories were added to the Ames CTAS simulation.

The descent profile negotiation process developed in this study is illustrated in the figure. The process is initiated by ATC with a request for the aircraft-preferred trajectory along a specified route with a specified arrival time. Clearances are only issued by ATC when the preferred profile is



Descent profile negotiation process.

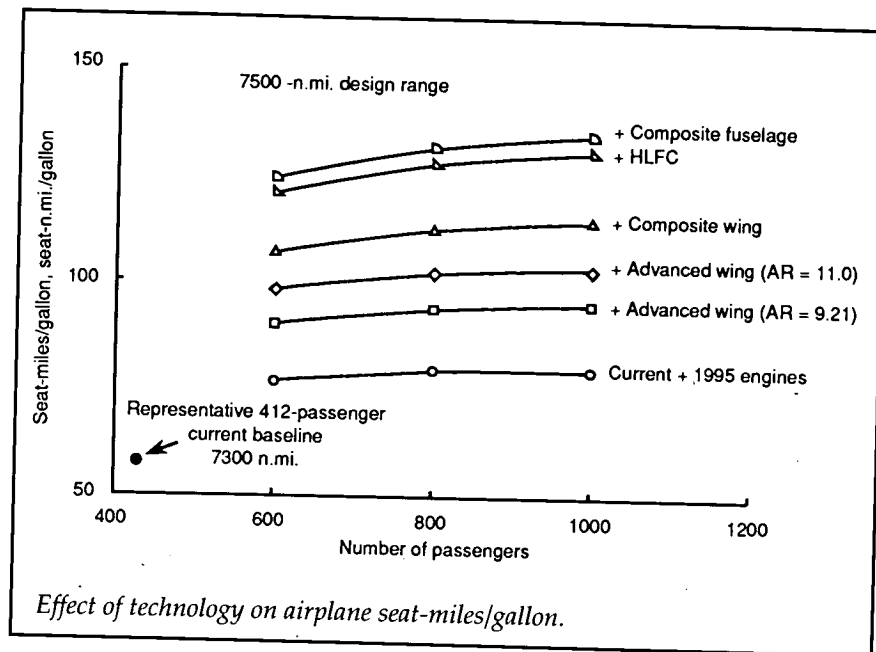
conflict free or when the aircraft has reached the ground-computed top of descent (TOD).

The data-link exchange of trajectory information worked well in simulation and potential traffic conflicts were avoided. The message presentation for this exchange was generally unacceptable to pilots. The pilots suggested simplifying the messages, crew control of the minimum speed used by the 4-D FMS for the preferred profile, and uplinking ground-computed speed schedules directly to the aircraft FMS. Although controller reaction at Ames was very favorable to the data-link operation, a need to simplify the negotiation process was also indicated.

Aircraft with a 4-D FMS have routinely demonstrated the ability to achieve precise arrival times. This capability should enable achievement of the full-capacity benefits of ATC systems such as CTAS. Further, the ability of aircraft to fly preferred trajectories rather than ATC-computed nominal profiles may result in significant fuel savings.
(David H. Williams, 42023)
Flight Systems Directorate

Study of Large Subsonic Transport

A system study has been conducted at the Langley Research Center that examined the effect of advanced technologies on very large, long-range subsonic transports. The study was conducted using the Langley Flight Optimization System (FLOPS), a multidisciplinary system of computer programs that has been coupled



for conceptual and preliminary design and evaluation of advanced aircraft concepts.

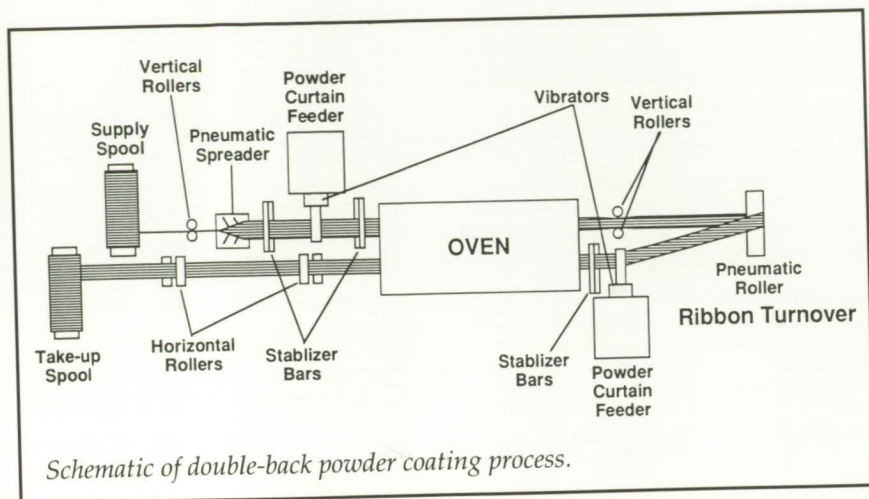
A representative, current, four-engine baseline configuration was defined as having a payload of 412 passengers for a design range of 7300 n.mi. Then, new 600-, 800-, and 1000-passenger transport concepts were developed with different technology projections and compared with the baseline configuration. The technologies examined included high-aspect-ratio supercritical wings, composite materials for the wing and fuselage, and hybrid laminar-flow control (HLFC). An engine technology level representative of entry into service in about 1995 was used for all the new transport concepts.

The results of the study indicate that a 600-passenger transport configuration, incorporating all the technologies, would have an available seat-miles/gallon capability about twice as large as that of the 412-passenger current baseline configuration (see figure).

In addition, the maximum takeoff gross weight of the advanced 600-passenger concept would be about 140 000 lb less than that of the baseline configuration. For payloads between 600 and 1000 passengers, the trend in seat-miles/gallon is relatively flat for current technology. At the higher levels of technology, increases in seat-miles/gallon are still indicated. This work was done in part under contract with Lockheed Engineering and Sciences Co.
(Dennis W. Bartlett, 41916, Philip C. Arcara, Jr., and Marvin E. McGraw)
Aeronautics Directorate

Langley Dry Powder Prepreg Tow Process

As part of the Advanced Composites Technology (ACT) Program, a novel technique has been developed for producing prepreg tow from dry polymer powder and carbon fiber. Tow



bundles of 3K, 6K, and 12K carbon filaments are spread under tension to approximately 4 in. A curtain of dry polymer powder is created by a material feeder and is deposited directly onto the spread carbon fiber tow. The powder-coated tow passes through a three-stage, 4-ft-long radiant oven to melt and fuse the polymer to the fibers. To ensure full impregnation of the spread tow with polymer, the tow is turned over after the first pass through the oven, coated again with a polymer powder curtain and passed back through the oven. The tow is handled with proper care through the use of ceramic-coated, air bearing rollers and a carbon fiber textile winder and speed controller. Consistent resin content levels are obtained at speeds of 60 to 80 ft/min. Both thermoplastic and thermosetting resins have been successfully prepregged with this process. Unidirectional composite panels made from frame wrapping the flexible powder-coated prepreg tow exhibit excellent interlaminar shear and flexure properties. A patent application has been submitted.

This Langley-developed method has significant advantages

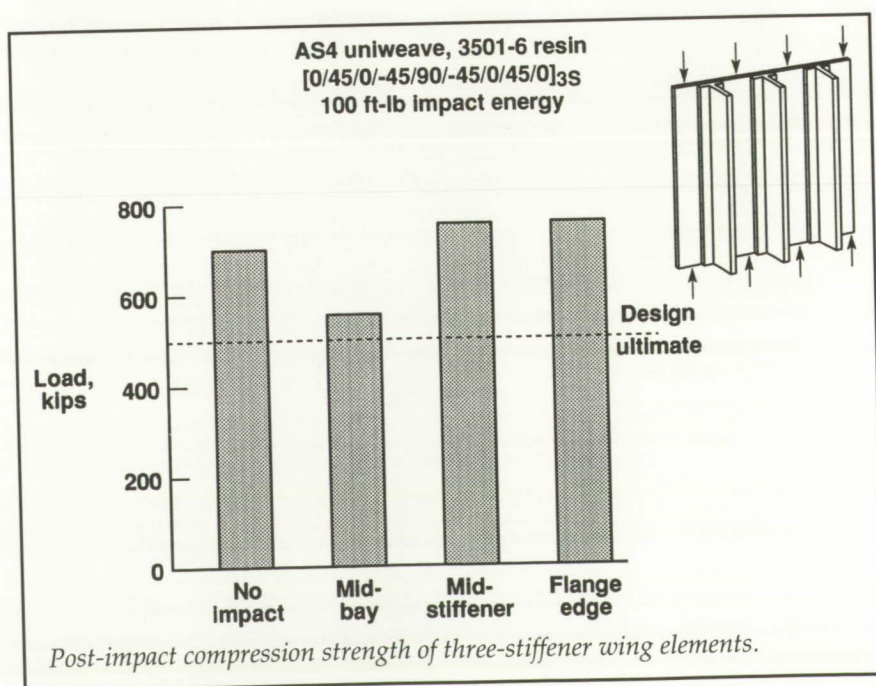
over state-of-the-art hot-melt and solution prepregging methods, including improved safety. Since costs for the fabrication of primary composite structures in subsonic aircraft can be reduced through automation, the product is being developed for use in the highly automated textile industry and the robotic tow and tape placement industry. Drapable fabrics have been successfully woven and braided from flexible powder-

coated yarns with LARC™ thermoplastic polyimide and several epoxies without loss of polymer powder.

(Norman J. Johnston, 44260, Robert M. Baucom, Joseph M. Marchello, and Maylene K. Hugh) Structures Directorate

Damage-Tolerant Concept for Transport Aircraft Wing Structures

Graphite-fiber-reinforced composite materials offer significant potential for weight savings (because of low weight-to-strength or stiffness ratios) for primary aircraft structures compared with conventional structural materials. However, low tolerance to projectile impact and fabrication costs sometimes negate the weight advantages. A new fabrication concept for graphite composite materials may produce both



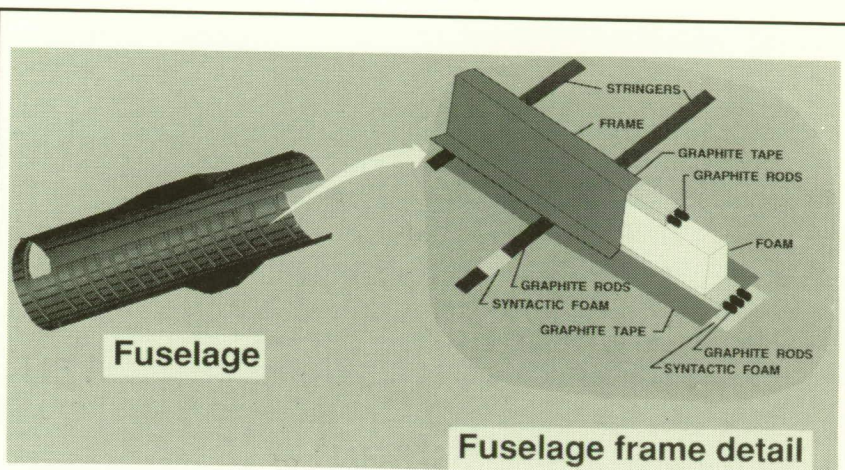
cost-effective and impact-damage-tolerant aircraft wing structures.

Blade-stiffened wing panels were fabricated by Douglas Aircraft Co. from dry-stitched skin and stiffeners followed by a resin transfer molding (RTM) process. Wing panels were impacted on the skin side midway between stiffeners, directly beneath a stiffener, or at the flange edge of a stiffener. Impact energies were selected to produce the onset of visual damage. Single stiffener crippling, stiffener pull off, and three-stiffener compression specimens were machined from the impacted panels and mechanically tested to evaluate the effects of impact on performance.

The figure shows the effect of impact (100 ft-lb) on the compression strength of specimens cut from impacted three-stiffener wing elements. Specimens were 21 in. wide and designed to carry 23.6 kip/in. ultimate load (approximately 500 kips), indicated on the figure by the dashed line. All impacted panels exceeded design ultimate load and failed without any skin-stiffener separation. The data indicate that the mid-bay impact is the most critical location for stitched panels subjected to compression loading. Data obtained for the impacted single stiffener crippling and pull-off specimens also exceeded design requirements.

The tests, conducted by both Douglas and Langley, demonstrate that stitched composite wing structures meeting damage tolerance goals can be designed and fabricated using a cost-effective RTM process.

(Jerry W. Deaton, 43087)
Structures Directorate



Cost-effective composite fuselage concept.

Composite Fuselage Concept for Civil Tilt-Rotor

The objective of this study was to develop cost-effective, advanced concepts for a civil tilt-rotor center fuselage with innovative structural and material technologies used to achieve structurally efficient designs. Such a concept is shown in the figure for a 40-passenger civil tilt-rotor aircraft. The fuselage is a frame- and stringer-stiffened pressurized cylindrical shell. To minimize structural complexity and part count, structural members pass by each other on different planes rather than intersecting each other in the manner typical of the conventional frame- and stringer-stiffened arrangement. The fuselage skins are fabricated using $\pm 45^\circ$ graphite-epoxy tape with a layer of syntactic foam at the laminate mid-plane. The stringers are made from a single layer of graphite-epoxy pultruded rods on each side of a layer of syntactic foam. A pad-up of foam is added to the skin between the stringers at the frame locations to

allow the frame outside diameter to be constant. The frame is a narrow hat stiffener that uses multiple layers of pultruded rods in the cap of the hat. Angle-ply tapes entrap each layer of rods and form the hat webs and skin attachment flanges. This concept was designed for tooled surfaces to be at assembly interfaces in order to minimize the requirement for shimming during assembly. Increased design allowables may be achieved by using the relatively soft, $\pm 45^\circ$ cover skins to reduce the effects of impact damage and by putting the fasteners in the angle plies to reduce the effects of the stress concentrations. This study was conducted under contract with Textron, Inc., and was jointly funded by Langley and the Army.

(Donald J. Baker, 43171)
Structures Directorate

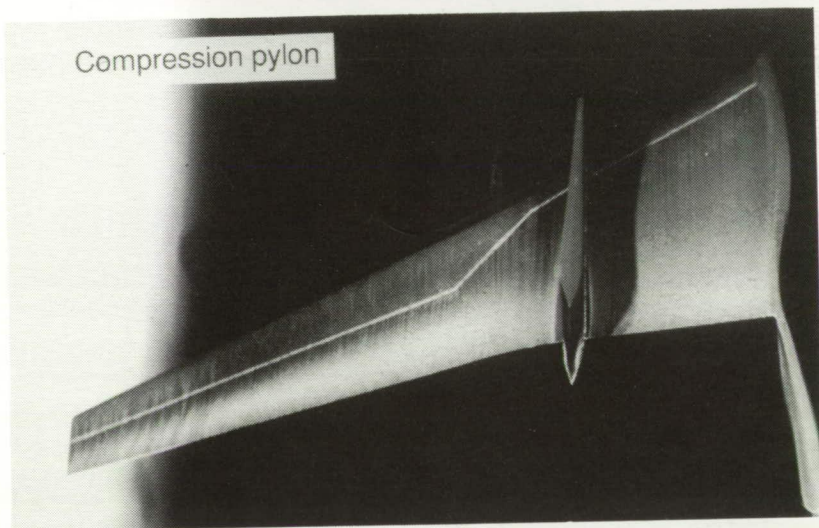
Effect of Pylon Geometry Transport Drag

Many subsonic transport aircraft have wing-mounted engines that are supported by

NASA SC(2)-0012 pylon



Compression pylon



Fluorescent oil flow visualization on wing lower surface.

pylons. The presence of the pylon on the lower surface of the wing can introduce adverse interference effects. Increased velocities in the vicinity of the wing-pylon junction may cause a loss of lift relative to the clean wing. Aircraft drag can also be significantly affected if these local flow accelerations induce adverse pressure gradients on the wing or produce shocks. The objective of the subject test program was to determine the

effect of pylon cross section on the drag of a low-wing transport.

Several pylons of differing cross section were installed on a low-wing transport model and investigated in the 16-Foot Transonic Tunnel. The model incorporated a supercritical wing designed for cruise at a Mach number of 0.77 and a lift coefficient of 0.55. The effects of installing the various pylons were determined from the total aircraft lift and drag data,

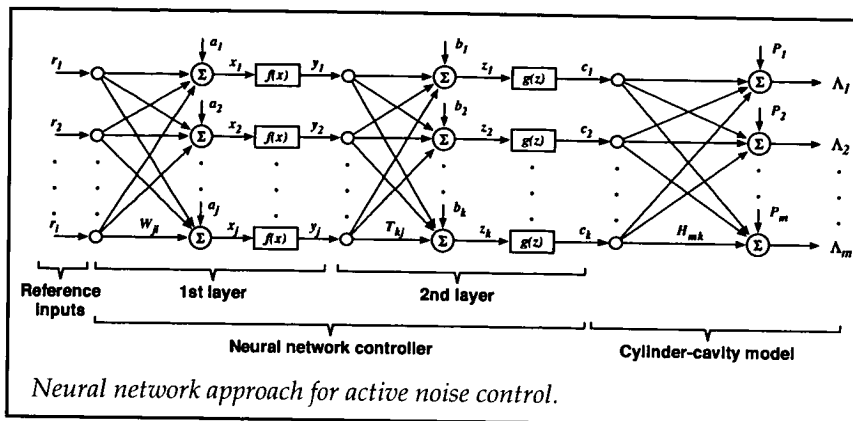
wing surface pressure measurements, and flow visualization data.

Results indicate that a NASA SC(2)-0012 pylon installation caused a larger disturbance in the wing lower-surface flow field than did a "compression" pylon installation. A compression pylon design places the pylon maximum thickness at the trailing edge of the wing, thereby moving the pylon trailing-edge closure aft of the wing trailing edge. This tends to minimize the local flow acceleration near the wing-pylon junction. This work was done in part under contract with ViGYAN, Inc. (Anthony M. Ingraldi, 43039, Dinesh A. Naik, and Odis C. Pendergraft, Jr.)
Aeronautics Directorate

The Optimization of Force Inputs for Active Structural-Acoustic Control Using Neural Networks

The focus of this research is to study the feasibility of using neural networks to control force actuators for reducing interior noise in vibrating structures. The potential payoff of this technology includes (1) reduced controller complexity (fewer degrees of freedom), (2) enhanced control effectiveness over a range of frequencies and operating conditions, and (3) reduced structural fatigue impact as a result of less energy spillover into undesired structural vibration modes.

The figure shows a two-layer network generating the control



actuator forces c_k on an elastic cylinder-cavity model. The defining feature of each network layer is that every input (y_j , for example) is connected to every output (c_k) through a matrix of weighting coefficients (T_{kj}). The control objective is to minimize the interior noise Λ_m at a number of error microphones located inside the cylindrical cavity. In the figure, P_m represents the error microphone outputs of the primary noise field, which exists with the neural network turned off. The total noise Λ_m is the sum of the primary noise component P_m and the component produced by each actuator output c_k via the predetermined transfer matrix H_{mk} , which represents the structural-acoustic coupling.

The network weighting coefficients W_{ji} and T_{kj} , as well as the biases a_j and b_k , are randomly initialized and iteratively updated through use of a gradient optimization procedure until convergence is achieved. This iterative process is referred to as a "learning exercise" for the neural network. Nonlinear sigmoid functions, $f(x)$ and $g(z)$, are sometimes employed in the learning process. Numerical simulations of analytical models indicate that the learning process

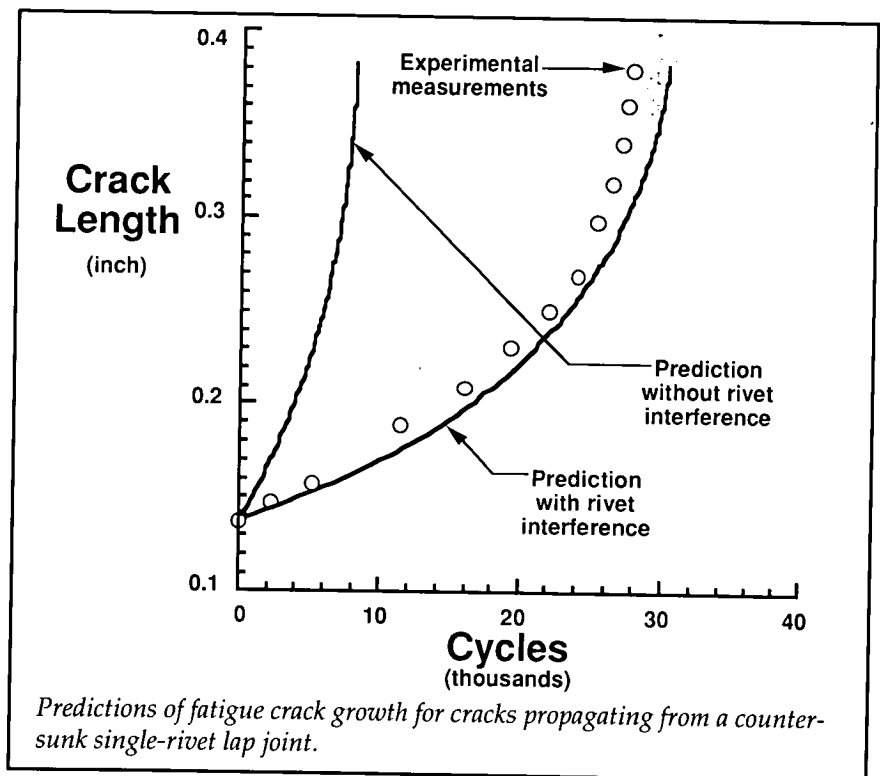
can be rapidly and accurately converged and that neural network controllers are capable of producing significant interior noise reductions. Excellent comparisons with the results of exact least-mean-square test cases have been demonstrated. Thus, neural network concepts may be a promising technology for accurately and efficiently controlling actuator inputs for reducing structural vibration and

interior noise levels in aerospace structures.

(Harold C. Lester, 43592, Ran H. Cabell, and Richard J. Silcox)
Structures Directorate

Analysis of Fatigue Crack Growth From Countersunk Rivet Lap Joints

The continued structural integrity of the aging commercial transport aircraft fleet is of great concern to the aerospace community. The long service life of these aircraft increases the possibility of a reduction or loss of structural integrity due to fatigue cracking. Fatigue cracks generally initiate in regions of elevated stress called stress concentration sites. In an aircraft structure a common stress concentration site is the edge of a



countersunk rivet hole, where the local stresses can be elevated by a factor of 3 or more.

An objective of the NASA Aircraft Structural Integrity Program is to develop the methodology to predict crack growth from loaded rivet holes. The approach is to use a two-dimensional finite-element analysis to model the behavior of cracks that have grown past the countersink region of a loaded rivet hole. Parameters governing crack growth from a loaded rivet include rivet interference, crack path trajectory, unequal crack lengths, load transfer due to friction and clamp up, shape of the countersink, and rivet stiffness.

Experiments conducted on 2024-T3 clad aluminum alloy single-rivet lap-joint specimens indicate that rivet interference has a strong influence on fatigue crack growth behavior. A layered two-dimensional finite-element model was used to model rivet interference. The model separated the lap joint into three layers (one each for the top and bottom sheets of the lap and one for the rivet) connected by spring elements, which transmit force only through compression. The rivet layer was expanded (to simulate interference) and the stress-intensity factor range was calculated as a function of crack length. The stress-intensity factor results were used to predict fatigue crack growth, as shown in the figure. The predictions and experimental results indicate that rivet interference can increase the fatigue crack growth life by a factor of 2 or more.

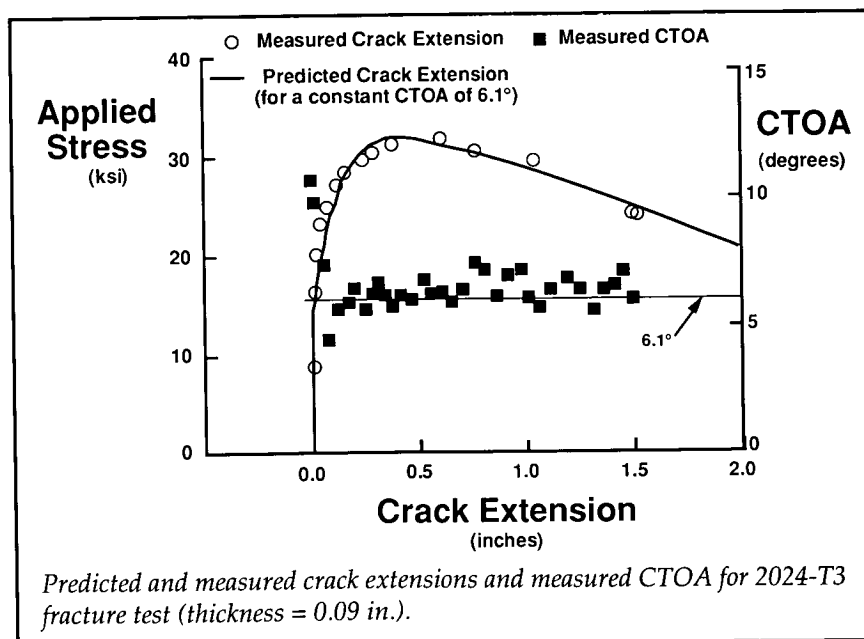
(E. P. Phillips, 43488, and D. S. Dawicke)
Structures Directorate

Verification of the Crack Tip Opening Angle Fracture Criterion

The advancing age of the commercial transport aircraft fleet has increased concerns for fatigue-related problems. One fatigue scenario involves a long, stably tearing crack in the aircraft fuselage. The fuselage is designed for the crack to turn and "flap." Flapping is the process by which a small region of the cracked fuselage structure peels open and leads to safe decompression. The presence of multisite or multi-element damage (MSD or MED) may retard flapping. One of the objectives of the NASA Aircraft Structural Integrity Program is to develop the methodology to predict flapping in an aircraft fuselage structure. The approach is to use a finite-element shell code with adaptive mesh capabilities and the crack tip opening angle (CTOA) fracture criterion to

predict residual strength and crack trajectory.

The CTOA criterion predicts that the crack will stably tear if the angle at which the crack opens, as measured a small distance from the crack tip (≈ 0.02 in.), reaches a critical angle. This criterion was investigated by conducting flat-panel fracture tests and predicting crack extension using an elastic-plastic finite-element analysis. The flat-panel tests were conducted on 2024-T3 aluminum alloy, with optical measurements made of the crack extension as a function of load and the crack opening angle as a function of crack length. The finite-element analysis used a constant CTOA of 6.1° to predict the crack extension, as shown in the figure. The measured CTOA decreased rapidly as the crack plane transitioned from flat to slant (45° shear lips) crack growth behavior in <0.1 in. (an extension roughly equal to the sheet thickness). After this initial transition the measured CTOA was roughly



constant at about 6° for over 2 in. of stable tearing to the point of crack instability.

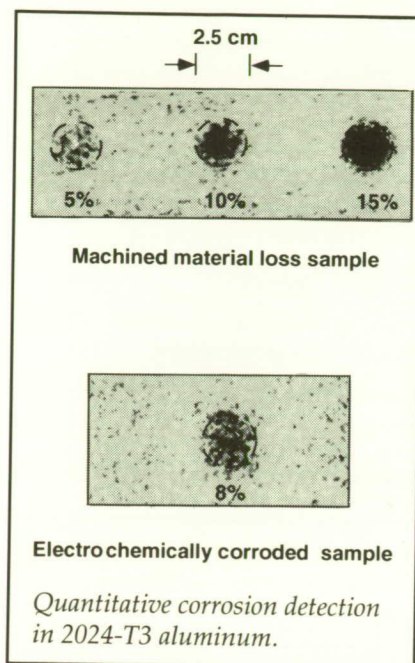
The results indicate that the CTOA criterion was successful in predicting crack extension. The angle used in the finite-element prediction agreed with the measured surface CTOA after slant crack growth was achieved. The CTOA criterion will be extended to mixed-mode loadings and will be experimentally verified in future research.

(J. C. Newman, Jr., 43487,
D. S. Dawicke, and C. A. Bigelow)
Structures Directorate

Quantitative Study of Corrosion Detection in Aircraft Lap Joints

The aging of aircraft and the integrity of lap joints and doublers are growing concerns both in the aircraft industry and to the commercial airline operators. Corrosion in aircraft lap joints and doublers is one of the problems encountered in the aging fleet. Researchers in nondestructive testing have applied various methods to characterize corrosion in lap joints. Thermal imaging is one such nondestructive evaluation (NDE) technique for characterizing corrosion in materials.

Aircraft skin samples were fabricated from a 1-mm-thick 2024-T3 aluminum panel. The samples had machined material loss spots and electrochemically corroded spots. The corroded spots had 5 to 15 percent material loss around a 2.5-cm-diameter circular region. The thermo-



graphic system used consisted of an infrared thermal camera digitizing at 30 frames per second and a computer system connected to an image processor to digitize the incoming thermal images. Photographic flash tubes were used to introduce thermal flux of 1.2 J/cm^2 into the sample.

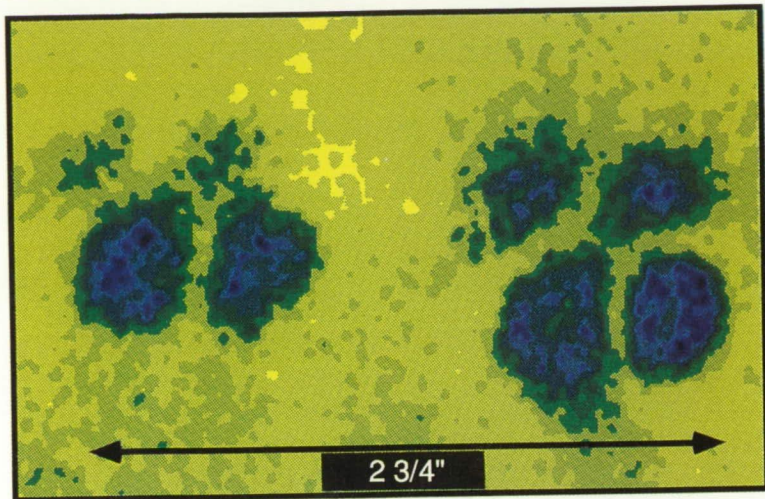
Temperature images were processed by doing a quadratic fit across the average surface image. The reduced image gives the quantitative contrast image showing the corrosion depth. Comparison of the electrochemically corroded sample results with the machined material loss sample results show the ability of this technique to detect hidden corrosion in aircraft structures. Thus, field application of this technique is warranted.

(Hazari I. Syed, 44811)
Electronics Directorate

Optical Nondestructive Evaluation of Composite Structures for Commercial Aircraft Applications

Laser-based electronic shearography has great potential for rapid nondestructive evaluation of aircraft fuselage and skin structures in the field. The basic inspection test procedure involves first recording a digital image of the test object, then applying a controlled load or excitation (which might be mechanical, thermal, or acoustic in nature) to the object to perturb the viewed surface. During the loading, additional digital images are acquired by the microcomputer at a rate of 30 frames each second to permit time display of the test data. Electronic subtraction of each image from the initial (reference) image of the object in its resting state displays an interference fringe pattern that represents a "contour map" of the displacement of the object surface induced by the applied load. With the proper choice of loading method, a structural defect in the object will induce a perturbation in the interference pattern, from which the size and location of the defect may be inferred.

The figure illustrates the capabilities of electronic shearography for locating defects in honeycomb composite structures, which are becoming increasingly common components in modern aircraft. The sample, constructed with a honeycomb core encased in a fiberglass/epoxy composition skin, was designed and fabricated at Boeing's Helicopter Division for evaluation as a component in the leading edge of wing structures



Shearographic laser image of two 1-in.-diameter disbands between the honeycomb core and the composite skin. The sample was driven at a frequency of 9.41 KHz to excite the disbands into resonance.

on the 757/777 class jetliners. Shearographic testing in concert with an acoustic excitation technique successfully revealed several 1-in.-diameter disbonded regions that had been manufactured between the composite skin and the honeycomb core. The frequencies of a piezoelectric driver were scanned to excite defects at specific resonant frequencies. At resonance the disbonded regions are clearly visible and are highlighted as anomalies (in blue) against the background of the well-bonded composite skin. Inspection time for an area of 8 in. by 6 in., including image processing, was about 1 minute.

(J. B. Deaton, 44789, L. D. Melvin, and R. S. Rogowski)
Electronics Directorate

Magneto-Optic Imaging of Airframe Fatigue Cracks

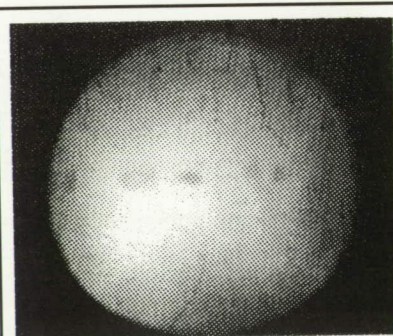
Recent developments have brought forward concerns over

the structural integrity of America's aging commercial aircraft fleet. The current nondestructive examination (NDE) methods used to ensure that aircraft are flightworthy have missed near-catastrophic flaws. Problems arise because a large amount of time is required to fully inspect an aircraft and high demands are placed on inspectors for the interpretation of complicated signals. In an effort to overcome these difficulties, magneto-optic imaging has been studied as a method for detection and characterization on fatigue cracks in airframe structures.

The magneto-optic imaging technique provides a direct visualization of airframe flaws such as fatigue cracks in real time; complicated flaw signatures are replaced by a simple video display highlighting rivets and fatigue cracks. These features allow for testing to be performed at a much faster rate than with conventional methods and simplify characterization of fatigue damage.

In order to improve the contrast between flawed and unflawed regions of a structure, a real-time digital image processing technique capable of removing all background variations and displaying flaws in a binary black on white format has been developed and demonstrated. The processed images provide clear flaw identification, which significantly improves the applicability of the technique as a practical NDE tool for airframe fatigue crack detection. Future plans are aimed at generating a computerized pattern recognition technique for operator-independent flaw characterization. (Buzz Wincheski, 44798, Min Namkung, Jim Fulton, and Ron Todhunter)

Electronics Directorate



Original (top) and digitally enhanced magneto-optic images of fatigue cracks in a fabricated lap-joint panel.

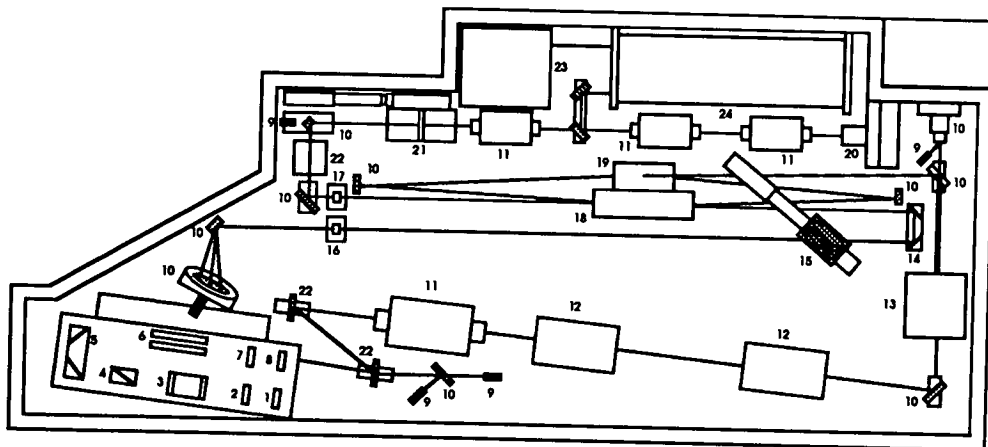
Injection-Seeded $\text{Ti}:\text{Al}_2\text{O}_3$ Laser Transmitter for Lidar Atmospheric Sensing Experiment

NASA's Lidar Atmospheric Sensing Experiment (LASE) utilizes the differential absorption lidar (DIAL) technique for measurement of atmospheric H_2O vapor from an ER-2 aircraft. The DIAL measurements require extremely narrow laser linewidths (less than 1.0 pm) and high laser spectral purity (i.e., >99 percent of the laser energy must reside within the 1-pm linewidth). The LASE design makes use of a continuous-wave, semiconductor laser diode injection seeding a

$\text{Ti}:\text{Al}_2\text{O}_3$ power oscillator to achieve narrow linewidth and wavelength control.

The figure is a schematic representation of the LASE tunable laser system (TLS). A single longitudinal mode laser diode (component 20) is used to injection seed the $\text{Ti}:\text{Al}_2\text{O}_3$ power oscillator shown in the middle of the schematic bounded by components 16 and 17. The diode seeded output of the power oscillator at the output coupler (component 16) is typically >150 mJ and has a measured linewidth of less than 0.5 pm, which corresponds to line narrowing of the power oscillator natural linewidth by a factor of 4×10^4 . Spectral purity of the TLS has been measured at >99.5 percent.

Development of the injection seeded $\text{Ti}:\text{Al}_2\text{O}_3$ laser transmitter for LASE has provided NASA DIAL applications with a technology capability that is unparalleled in the world. The wavelength accuracy and narrow linewidth of the TLS will enable atmospheric scientists to reduce measurement error from the current 20 percent to less than 4 percent. Integration of the TLS into the LASE instrument is scheduled for mid-1993, with engineering test flights to begin at the end of 1993. (James C. Barnes, 41637) Electronics Directorate



Nd:YAG oscillator

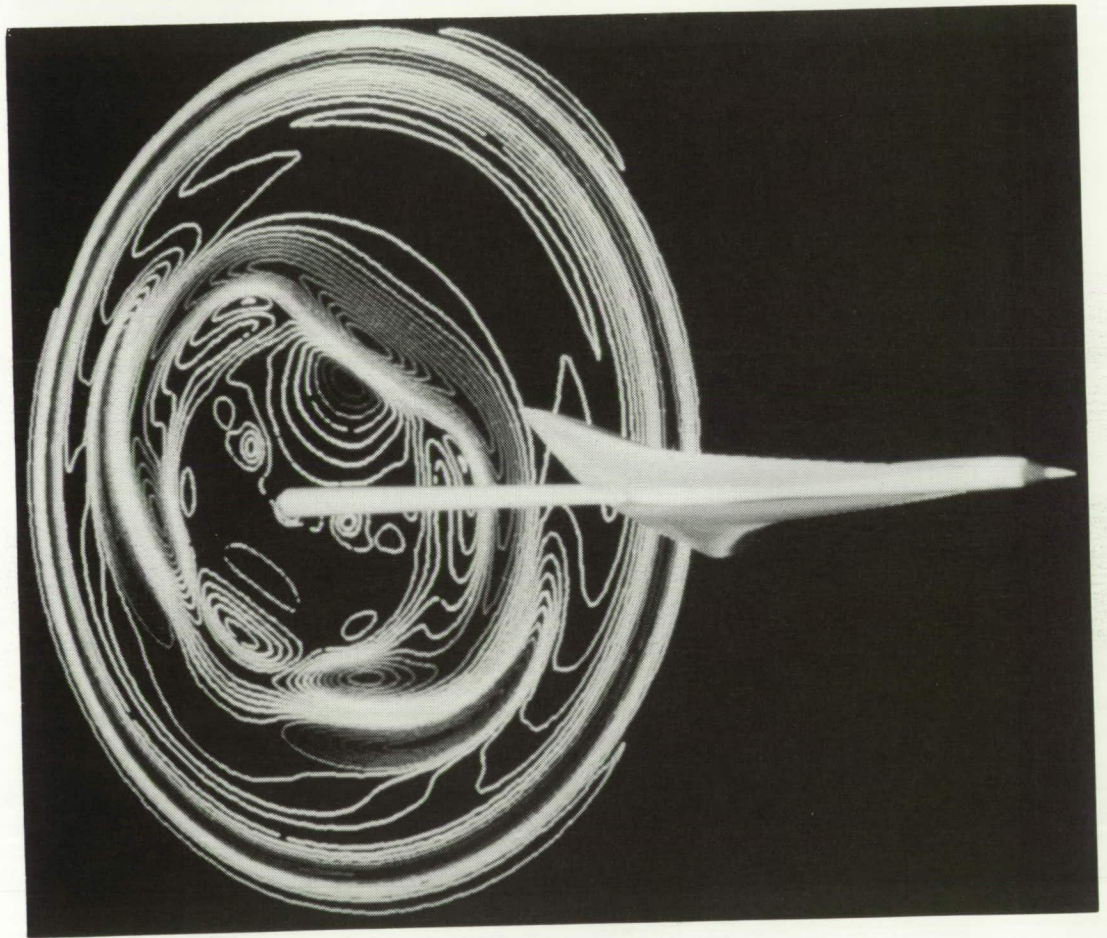
1. HR end mirror
2. 1/4 waveplate
3. Q-switch
4. Ward polarizer
5. Corner cube
6. Rod and flashlamp
7. 1/13 waveplate
8. Flat output coupler

9. Energy monitor fiber
10. Dichroic turning mirror
11. Faraday isolator
12. Amplifier
13. CD*A SHG w/oven
14. Hollow retroreflector
15. Birefringent filter
16. GRM output coupler

17. 97% R end mirror
18. Ti:Sapphire crystals
19. Beam splitter
20. Diode seed laser
21. Thin etalon
22. Telescope
23. Line locking detector/electronics
24. Reference White cell

Optical bench layout for LASE TLS.

■ HIGH-SPEED CIVIL TRANSPORT



*Resolve the critical
environmental issues and
provide the technology
base for future high-speed
air transportation*

Conceptual Studies for HSR Wing Structures

The objectives of this study were to determine the internal structure configuration and to calculate the structural response and weights for a preliminary High-Speed Research (HSR) wing. A finite-element model was developed for the wing structure, and five aerodynamic load cases for subsonic and supersonic flight conditions were applied to the model. Approximations to thermal loads at Mach 2.4 and to fuel, engine, and landing gear masses were also considered in the analysis. The wing panels were sized for two materials, titanium and a quasi-isotropic organic composite material.

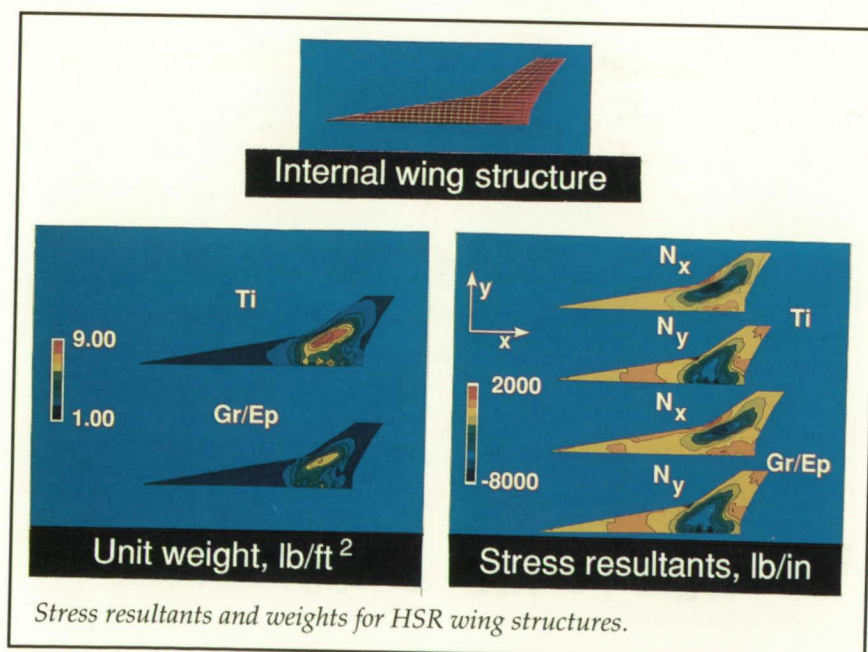
Honeycomb sandwich construction was assumed for the cover panels, and sine-wave webs were assumed for the ribs and spars.

The finite-element model that was generated for the internal wing structure is shown in the upper portion of the figure. The internal forces (stress resultants) for the upper-surface cover panels are shown in the lower right region of the figure for a maneuver load condition at Mach 2.4 and 2.5g. For both material systems, the longitudinal stress resultants N_x achieve their maximum compressive value near the leading-edge discontinuity (or crank) in the wing. This load concentration near the leading-edge spar is unfavorable and occurs because insufficient wing depth (i.e., bending

stiffness) exists at the rear spar. The spanwise internal forces achieve their maximum compressive value at locations where the main spars intersect the fuselage. The calculated weights of the upper-surface cover panels are shown in the lower left region of the figure. The crank region has the heaviest panel for both material systems, but the organic composite wing panels are significantly lighter than the baseline titanium panels. Wing tip deflections, though not shown, were also calculated and found to be high for this wing structure configuration. (Stephen J. Scotti, 45431) Structures Directorate

Noise Associated With a High-Temperature Supersonic Jet

The principal source of sound emission from high-temperature shock-free supersonic jets is a phenomenon known as eddy Mach wave emission. Sound is produced by this mechanism when turbulence is convected at speeds greater than the ambient sound speed. Shock tube measurements by Oertel ("Coherent Structures Producing Mach Waves Inside and Outside of the Supersonic Jet," *Structure of Complex Turbulent Shear Flow*, IUTAM Symposium, 1982, pp. 334-343) of ISL in France revealed the existence of two families of supersonically



convecting waves. Theoretical predictions by Tam of Florida State (Tam, Chen, and Seiner, "Relationship Between Instability Waves and Noise of High Speed Jets," *AIAA J.*, vol. 30, no. 7, July 1992, pp. 1747-1752) show the existence of these two families of waves for the high-temperature jet flow problem. These waves are known as the Kelvin-Helmholtz instability waves (KHIW) and the supersonic instability waves (SIW).

A recent study of a high-temperature supersonic jet in the

Langley Jet Noise Laboratory has linked, for the first time, measured noise emission to the predicted characteristics of both the KHIW and the SIW. This linking has been accomplished through comparison of solutions to the compressible Rayleigh equation and measured noise. The predicted frequency, amplitude, and emission direction of noise due to these waves were in reasonable agreement with data. The figure shows a spark schlieren of a supersonic nozzle operating overexpanded at a jet total temperature of 1363°K. Both the KHIW and the SIW can

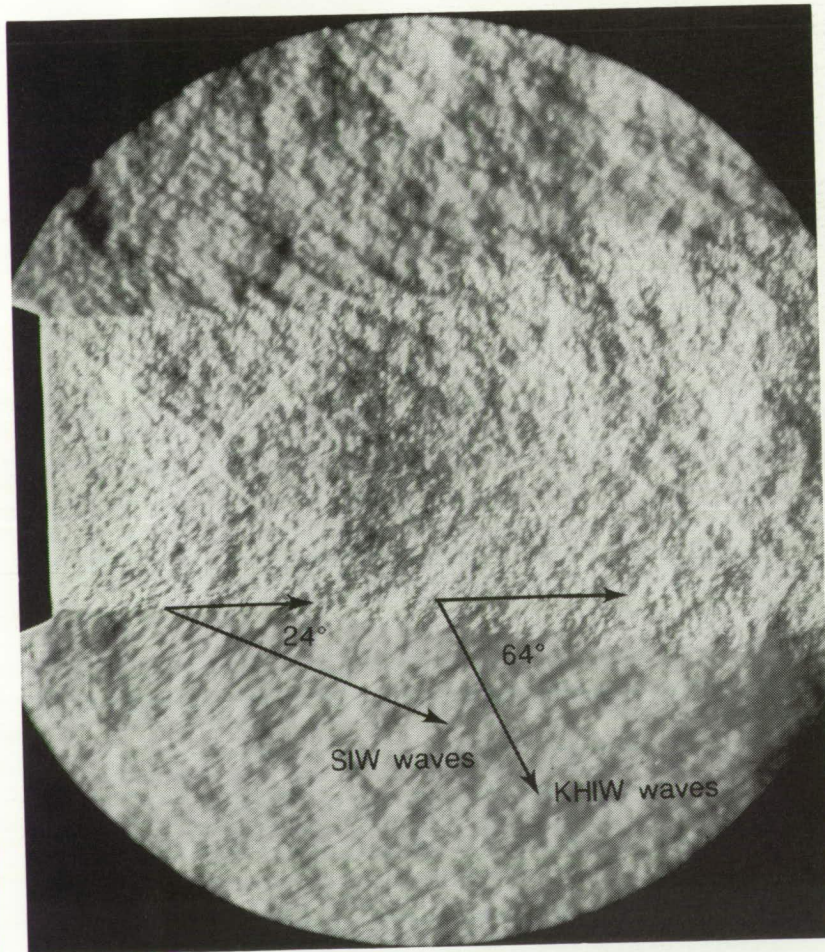
be observed in this photograph; the former radiates at 64° to the flow direction, and the latter radiates at 24°. The intensity of noise due to the KHIW was twice that due to the SIW at this temperature. Understanding the properties of KHIW and SIW through an appropriate model is important for formulation of an efficient jet noise reduction strategy.

(John M. Seiner, 46276, Bernard J. Jansen, and Michael K. Ponton)
Structures Directorate

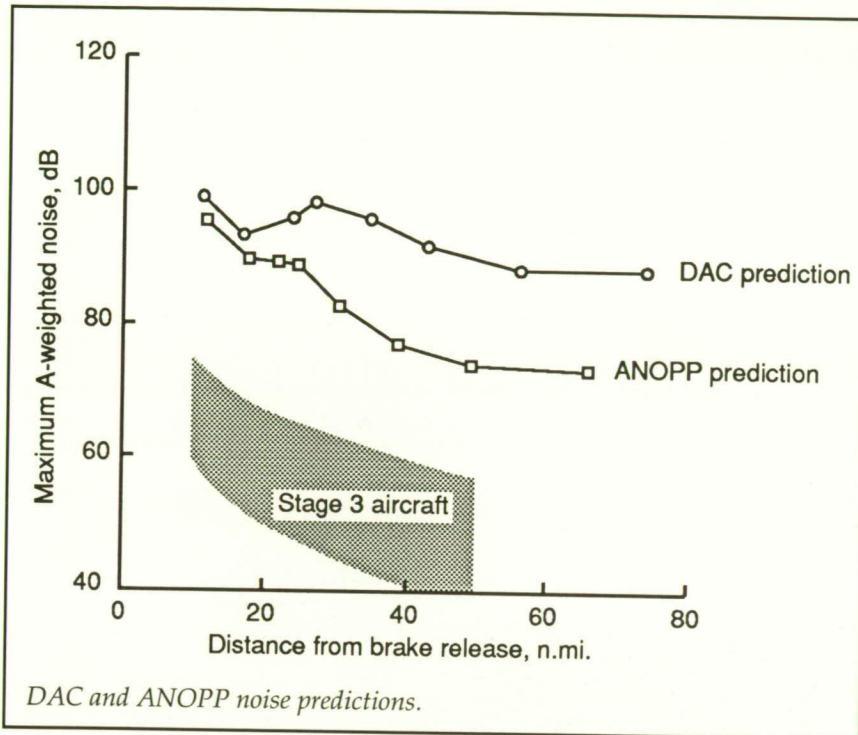
Comparison of Noise Prediction for HSCT Climb to Cruise

Noise predictions were made by researchers at Douglas Aircraft Company (DAC) and NASA Langley Research Center for a proposed Mach 3.2 High-Speed Civil Transport (HSCT) powered by four General Electric VCE-516 engines. The purpose of the noise study was to analyze a potential HSCT community noise problem that occurs during aircraft climb to cruise and extends noise concerns beyond the requirements of a FAR 36 noise certification rule.

Under a Langley Systems Study contract, DAC had determined a flight profile and flight Mach number schedule that was optimized for fuel economy. Ground noise predictions were made for several altitudes and flight Mach numbers with the assumptions of level flights at each point and jet noise dominance. A comparison of the predicted maximum A-weighted ground noise levels is shown. The DAC and Langley predictions differ because different prediction models were used. The DAC



Flow and sound field visualization of noise associated with KHIW and SIW.



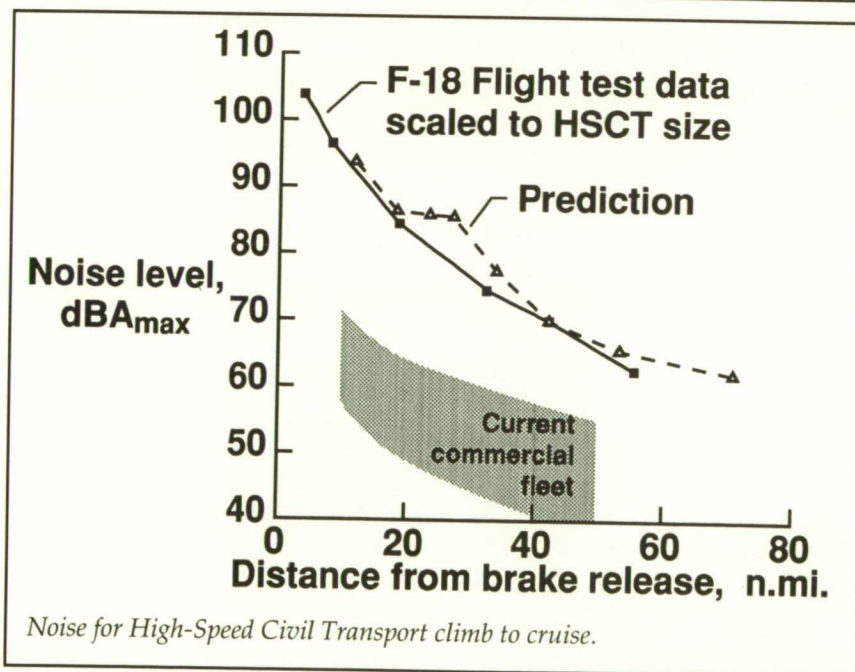
line from source to observer. It should be noted that these predictions were for unsuppressed engines.

The disagreement in amplitude level is not unreasonable, since both models are empirically based. The general noise history trends predicted by both models agree quite well. According to these predictions, this aircraft would propagate noise levels to the ground that are 20 to 30 dB greater than those of the current stage 3 subsonic aircraft. Any future HSCT aircraft will have suppression devices as part of the design to be able to meet the FAR 36 certification requirements. The present results suggest that the suppression devices may have to remain in use during the climb-to-cruise aircraft operations.

(R. A. Golub, 45281)
Structures Directorate

Climb-to-Cruise Experiment

The Climb-to-Cruise Experiment was designed to investigate community noise levels from a High-Speed Civil Transport (HSCT) during its climb from takeoff to cruise altitude. Preliminary noise predictions for the future HSCT, based on limited low-speed data bases, indicated that the new transport would have noise levels 30 to 40 dB higher than current subsonic transports. The Climb-to-Cruise Experiment was conducted during November 1991 at NASA Dryden Flight Research Center by a field measurement team from Langley Research Center. It consisted, in part, of an F-18A supersonic fighter aircraft performing simulated climb-to-cruise



used the Motsinger-Sieckman code developed by General Electric. Their noise propagation used empirical techniques developed in-house and included refraction effects. The Langley predic-

tions used the NASA Aircraft Noise Prediction Program (ANOPP), wherein jet noise was modeled with the SAE methods. Noise propagation was modeled with an SAE method and a straight

profiles over a ground-based microphone array. The test aircraft flew at altitudes from 1200 to 30 000 ft and speeds of Mach 0.3 to Mach 0.95.

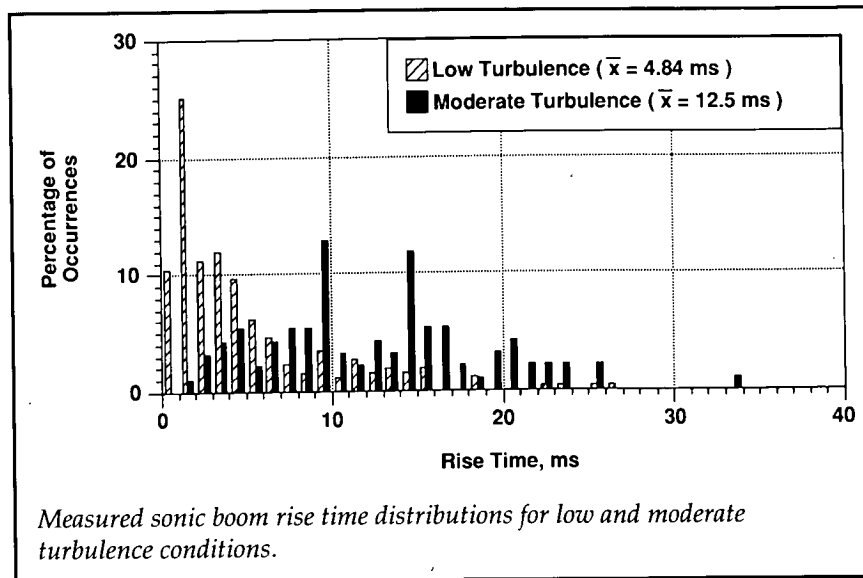
In the figure, measured F-18A climb-to-cruise maximum A-weighted noise levels scaled to an HSCT-size airplane are presented with predictions and some typical noise levels from the current commercial fleet. The results indicate that HSCT climb-to-cruise noise will be higher than that of the current commercial fleet, but only by 10 to 15 dB. Corrections to preliminary calculations produced the prediction shown, which agrees well with measured levels. The HSCT climb-to-cruise noise must be considered and minimized in the optimization-trade-off portion of HSCT system studies.

(William L. Willshire, Jr., 45270,
and Robert A. Golub)
Structures Directorate

Sonic Boom Propagation Experiment

The sonic boom propagation experiment investigated the influence of atmospheric turbulence on the propagation of sonic booms. An element of the High-Speed Research Program is to develop a High-Speed Civil Transport design that will generate a subjectively minimized (shaped) sonic boom. The technical question the experiment addressed is, Could atmospheric turbulence alter booms in such a way that the benefits of sonic boom shaping would be negated?

In August 1991, a T-38 supersonic aircraft flew at a Mach number



of 1.3 and an altitude of 30 000 feet over a Langley-developed microphone array at the White Sands Missile Range in New Mexico. Distributions of measured rise times of booms produced by the T-38 are presented in the figure for both low and moderate turbulence conditions. The difference in the two distributions is striking, with the mean rise time \bar{x} increasing by a factor of 3 for the moderate turbulence result. Differences between the distributions are attributed to and highly correlated with turbulence. These results and others will be used to validate propagation models that will in turn be used to predict the influence of turbulence on shaped sonic booms.

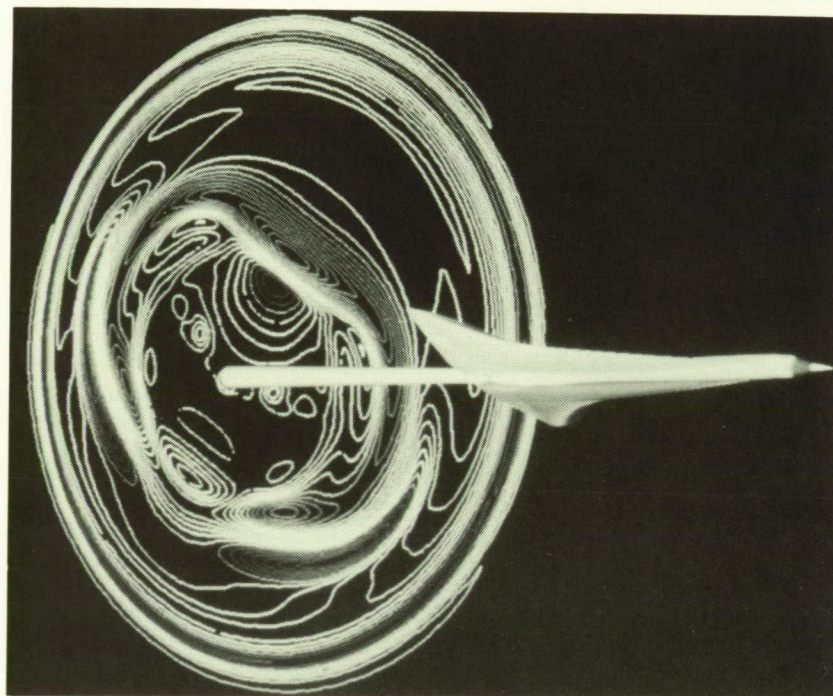
(William L. Willshire, Jr., 42570)
Structures Directorate

Sonic-Boom Predictions With Computational Methods

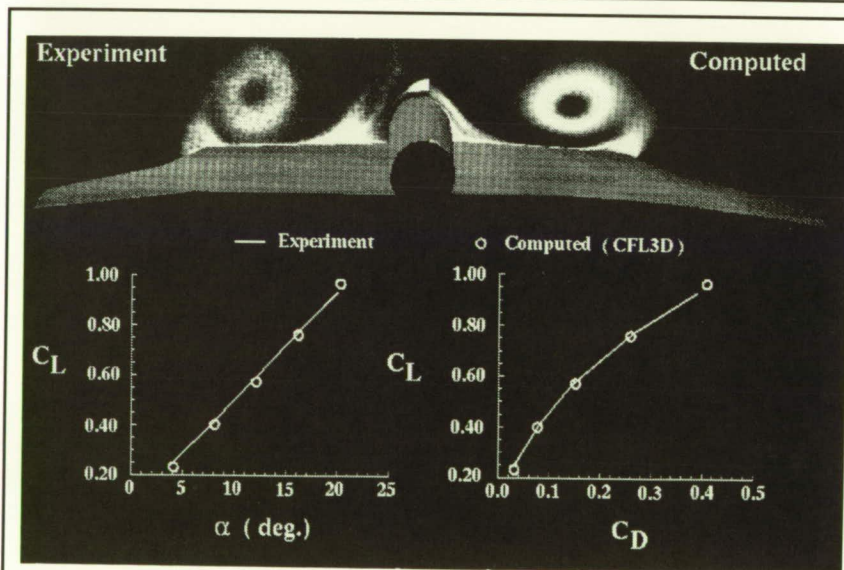
Low-sonic-boom supersonic configurations have traditionally

been designed and analyzed with linear theory and modified linear theory methods. However, these methods do not provide accurate predictions in the extreme near field, where the flow field is highly nonlinear, and sonic-boom predictions at nonzero azimuthal angles are questionable because of difficulty in obtaining accurate lift distributions at these off-flight-path angles.

Computational fluid dynamics (CFD) methods have been applied to the analysis of low-sonic-boom aircraft. Because pressures of interest are one to two body lengths away from the configuration rather than on the surface, some modifications to these methods have been necessary that included higher density grids in regions of high pressure gradients and calculations only in the pressure signature regions. Shown in the figure is a flow-field prediction of a Mach 3 low-boom concept in a plane approximately one body length behind the configuration. Note the low pressure gradients directly beneath the aircraft that are used to define the centerline



Predicted flow field for Mach 3 low-boom aircraft ($\alpha = 1.97^\circ$).



Computed and experimental lift and drag coefficients of AST-210.

boom signature—an objective of the low-boom design method. However, the traditional approach of minimizing the centerline boom may not produce a low-boom

concept because the lateral boom generated by the wing may be strengthened. With computational methods, the high-pressure area on either side of the plane just

beneath the aircraft can be monitored to ensure a low-boom concept.

With the use of CFD methods, flow fields of supersonic aircraft can be analyzed, and the designs of low-boom concepts can be modified to reduce and tailor pressure gradients prior to fabrication and testing. This work was done in part under contract with Lockheed Engineering and Sciences Co. (Christine M. Darden, 45258, and Kamran Fouladi) Aeronautics Directorate

Computational Predictions of an HSCT-Type Configuration

The intent of this study was to investigate the capability of a computational method to predict the subsonic, high-lift aerodynamic performance of an arrow-wing planform design for supersonic cruise. Experimental results obtained for this portion of the flight envelope provided a data base for the verification of the theoretical predictions.

Experimental investigations were conducted on the AST-210 model in the Langley 14- by 22-Foot Subsonic Tunnel. The data include force and moment measurements, surface flow visualization, and off-body flow visualization obtained with a laser light sheet. Theoretical results were obtained with the turbulent Navier-Stokes equations, computed on the Langley Cray-2S supercomputer. The code used to obtain the solution was CFL3D. A two-block-domain decomposition procedure was utilized to solve the entire flow domain of the

AST-210 cruise configuration. Surface forces and pressures were calculated along with off-body flow variables.

Computed lift and drag coefficients compare well with tunnel data over an angle-of-attack range of 4° to 20° at a dynamic pressure of 70 psf and a corresponding Reynolds number of $1.45 \times 10^6 \text{ ft}^{-1}$ (4.26×10^6 based on the mean aerodynamic chord). Additionally, the computed off-body total-pressure contours agree well with the resulting upper-surface vortices captured by the laser light sheet.

Although the comparisons thus far are for the baseline configuration, the good agreement between experimental and theoretical results demonstrate the potential of CFL3D to be an effective analysis tool for guiding engineers in the design and optimization of High-Speed Civil Transport (HSCT) configurations. Likely areas of application include parametric investigations conducted on such aspects as planform geometry and camber at subsonic speeds. This work was done in part under contract with ViGYAN, Inc.

(Victor R. Lessard, 45072, and Bryan A. Campbell)
Aeronautics Directorate

Leading-Edge Suction for Vortex Suppression on an HSCT Configuration

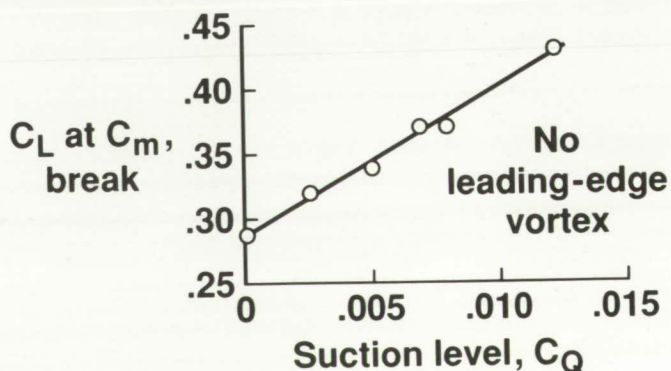
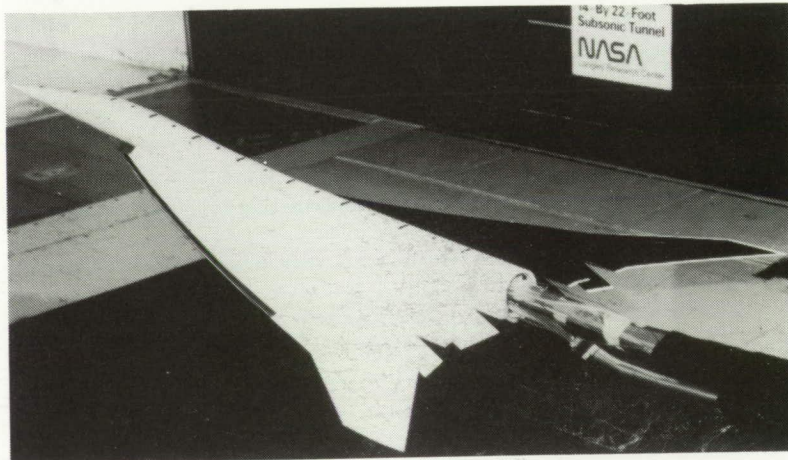
The objective of this investigation was to define the effectiveness of boundary-layer control as a means of suppressing the leading-edge vortex on a High-Speed Civil Transport (HSCT) configuration.

This suppression is sought to alleviate the nose-up pitching moment that these configurations develop at moderate angles of attack.

An HSCT-type model having a cranked-arrow-wing planform (74° inboard leading-edge sweep and a 50° outboard leading-edge sweep) as shown in the figure was modified to include a porous leading edge. Suction was applied to the surface to help maintain attached flow around the relatively

sharp leading edge of the wing. The model was tested at several angles of attack and suction levels and the effectiveness was assessed in terms of force and moment data, surface flow visualization, and off-body flow visualization.

Leading-edge suction was found to be effective at delaying severe nose-up pitching moment on this model, as shown in the figure. With no suction, pitching moment began to increase sharply at an angle of attack of about 5°



Leading-edge-vortex suppression for HSCT.

and $C_L = 0.29$. Moderate levels of suction delayed the pitch-up until an angle of attack of about 9° and $C_L = 0.43$.

Allowing the aircraft to fly with higher aerodynamic lift will reduce the noise generated by the aircraft near the airport. In addition, the levels of suction used in this study were reasonable for HSCT's equipped with laminar-flow control systems for drag reduction during noise.

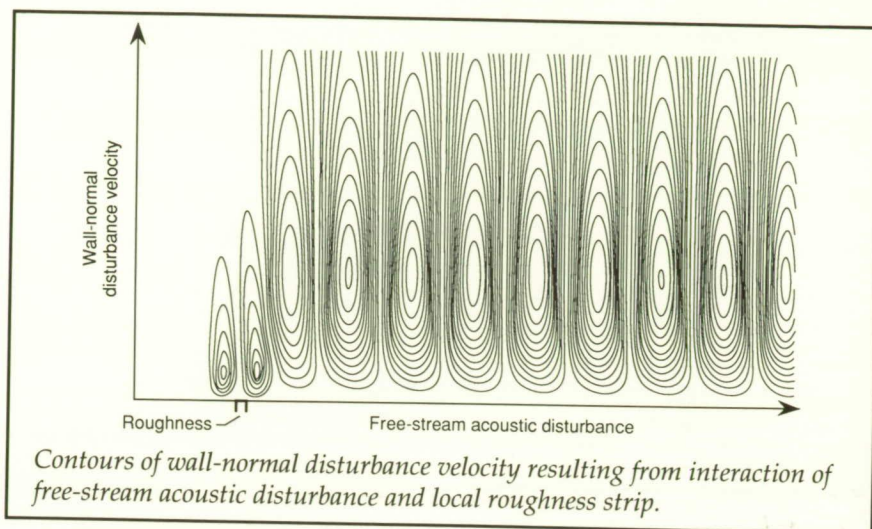
(Guy T. Kemmerly, 45070, Zachary T. Applin, and Bryan A. Campbell)

Aeronautics Directorate

Prediction of Boundary-Layer Receptivity Due to Surface Disturbances

The first stage in transition from laminar to turbulent flow within a boundary layer in a flight environment is usually the assimilation of free-stream unsteadiness into instability waves—a process known as receptivity. The physics of receptivity processes must be understood, and methods for quantitative prediction of recepted disturbances must be developed, if the reliability and accuracy of transition prediction schemes are to be improved. Also, identification of the "dangerous" receptivity path can suggest ways of delaying transition by controlling the generation of instabilities.

One important receptivity path is the interaction of free-stream acoustic waves or convected turbulence with short-scale surface inhomogeneities, such as roughness, localized suction, or wall-temperature variation. A



procedure has been developed that uses both asymptotic theory and numerical methods to predict the amplitude of instability waves, such as Tollmien-Schlichting waves, in a wide variety of situations. The method, known as the forced stability equation (FSE) method, is very general and additionally predicts the effects of Reynolds number, in contrast with previous purely asymptotic methods.

Computer codes incorporating the FSE method have been developed to quantify the receptivity in a variety of boundary-layer flows at low and high speeds, with and without pressure gradients, and in two-dimensional and three-dimensional configurations. The types of instabilities examined include Tollmien-Schlichting waves, inflectional instabilities, acoustic (Mack) modes, and cross-flow vortices. Results from these codes have been compared with previous theoretical predictions, and verification is in progress through comparisons with direct numerical simulations (DNS). Results from one such simulation are shown in the figure. A Tollmien-Schlichting wave, whose

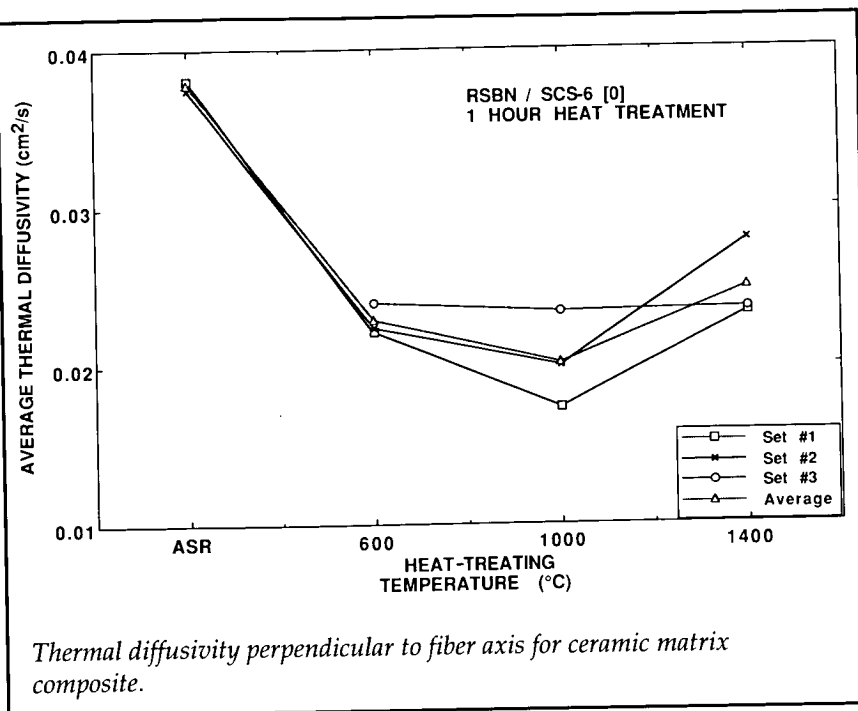
signature is displayed in terms of wall-normal disturbance velocity, was produced in an incompressible flat-plate boundary layer by the interaction of a free-stream acoustic disturbance with a roughness element.

Techniques to utilize FSE predictions of receptivity in engineering transition prediction methods are currently under study. The roles of entropy (temperature) and vorticity disturbances in the far field are also being investigated. This work was done in part under contract with High Technology Corp. (Meelan Choudhari, 42240, and Craig Streett)

Aeronautics Directorate

Thermographic Diffusivity Imaging of Ceramic Composite Materials

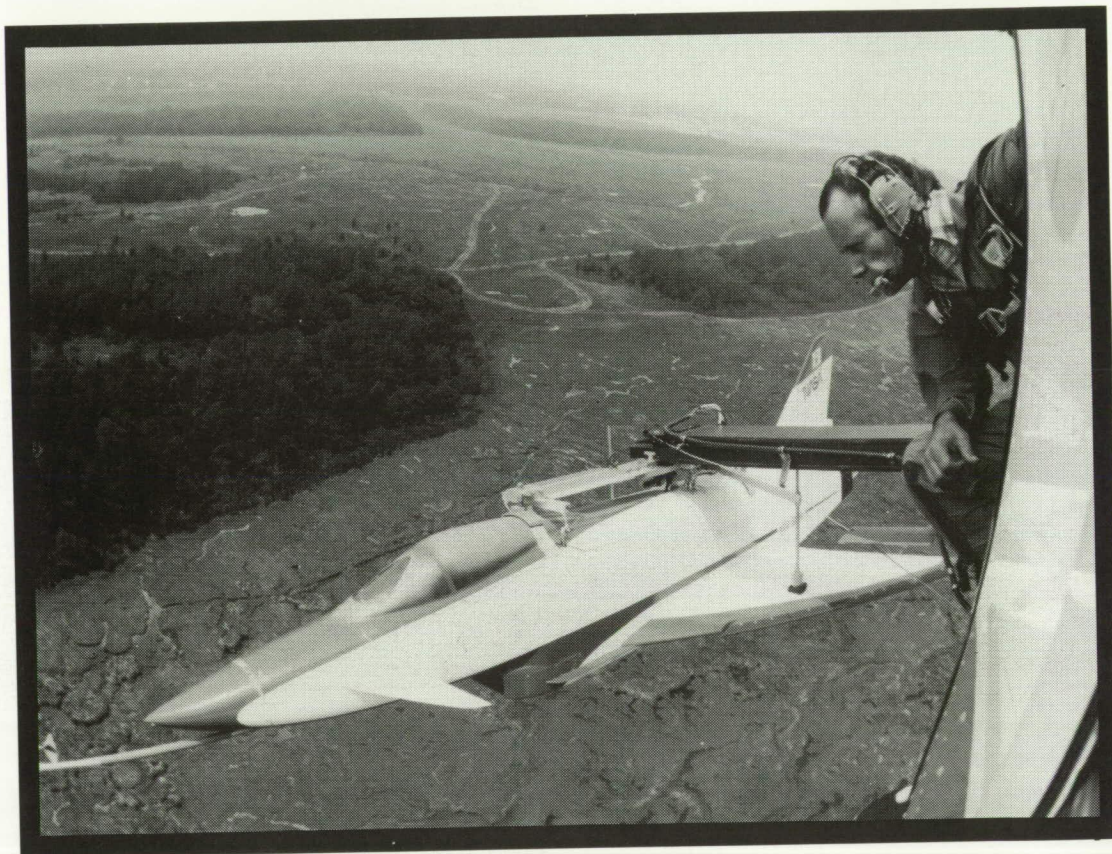
Strong, tough, high-temperature ceramic matrix composites are currently being developed at Lewis Research Center for application in advanced heat engines.



These new materials require new nondestructive inspection and material characterization techniques. One of the most promising of these new materials is SiC fiber-reinforced silicon nitride ceramic matrix composite ($\text{SiC}_f/\text{Si}_3\text{N}_4$). The high-temperature thermal and mechanical performance of ceramic matrix composites is strongly dependent on the thermal diffusivity and interfacial bond strength of the material. There is a concern regarding the interaction between the thermal diffusivity and the fracture toughness of $\text{SiC}_f/\text{Si}_3\text{N}_4$. A thermal imaging technique has been developed to provide rapid large-area measurements of the thermal diffusivity perpendicular to the fiber direction in these composites. Results are presented for a series of $\text{SiC}_f/\text{Si}_3\text{N}_4$ (reaction-bonded silicon nitride) composite samples heat-treated under various conditions. The figure shows the changes in thermal diffusivity, normal to the

fiber axis, that occur as a function of heat treating temperature. Three sets of three samples at each temperature were measured as well as two samples that were not heat-treated (ASR in figure). The trends in the diffusivity observed in these measurements agree with current understanding of changes in fiber-matrix bonding with heat treatment temperature. This technique will now allow a large-area, quantitative assessment of the heat treatment of ceramic matrix composite materials based on changes in the thermal diffusivity due to fiber matrix bonding.
(K. E. Cramer, 47945)
Electronics Directorate

■ HIGH-PERFORMANCE MILITARY AIRCRAFT



ORIGINAL PAGE
BLACK AND WHITE PHOTOGRAPH

*Provide technology options for
revolutionary new capabilities
in future high-performance
military aircraft*

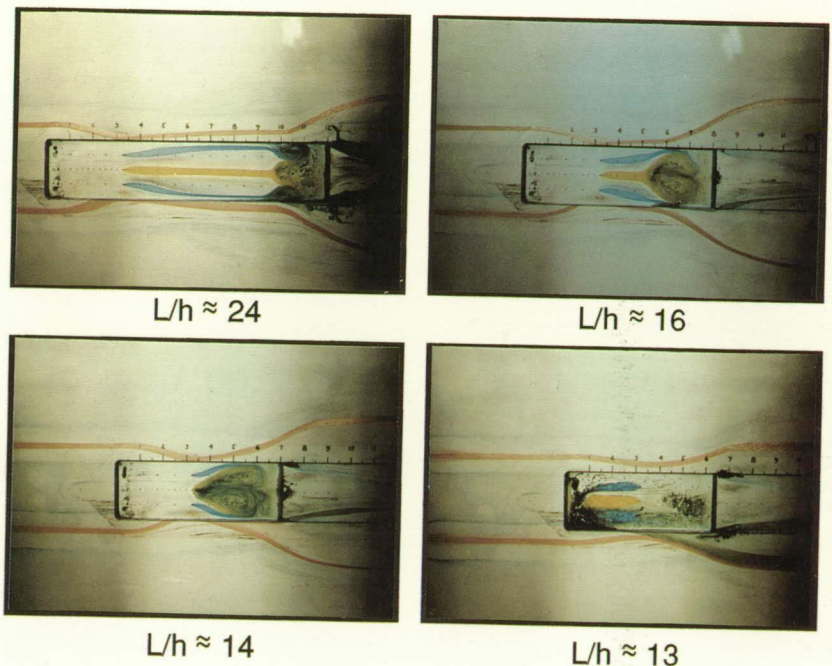
Preceding Page Blank

ORIGINAL PAGE
COLOR PHOTOGRAPH

Cavity Surface Flow Fields at Supersonic Speeds

To better understand the aerodynamics of weapons bays in supersonic military aircraft, a flow visualization study using a recently developed flow visualization technique was conducted on a rectangular box cavity. The technique consists of injecting water that has been tinted with food coloring through pressure orifices located on the surface of the wind-tunnel model. The colored water flows over the model surface and forms streaklines of the surface flows. Two main advantages of this technique are that the colored water allows easy interpretation of the flow visualization data and that the streaklines have a fast dynamic response to general flow unsteadiness and gross flow-field changes.

Wind-tunnel tests were conducted at free-stream Mach numbers M_∞ of 1.50 and 2.16 with a rectangular box cavity that was mounted in a flat plate. The longitudinal location of the rear face of the cavity was remotely controlled, to allow the length of the cavity to be varied while the tunnel was in operation. Colored water was injected at various locations inside the cavity and on the surface of the flat plate. Shown in the figure are a series of flow-field photographs that were acquired at



Cavity flow-field characterization that uses colored-water flow visualization technique ($M_\infty = 2.16$; flow is from left to right).

various cavity length-to-height ratios L/h .

As L/h decreased from 24 to approximately 16, the counterrotating vortices that formed ahead of the rear face dissipated and two new vortices formed that spanned the entire cavity width and rotated in directions opposite to those at $L/h = 24$. These new vortices continued to exist as L/h decreased to approximately 13, at which point the flow field rapidly changed and the flow along the cavity floor was opposite to the

free-stream flow. The location, size, and rotational direction of the cavity-floor vortices were previously unknown. The flow visualization technique has produced a unique set of data that has significantly improved the understanding of three-dimensional cavity flow fields.

(Floyd J. Wilcox, Jr., 45593)
Aeronautics Directorate

Use of Passive Porosity to Alleviate Asymmetric Loads on Forebodies

Side forces and yawing moments can exist on slender axisymmetric bodies at high angles of attack—even at 0° sideslip angle—as a result of asymmetric pressure loading caused by differences in the location of the separation-induced vortex on either side of the forebody. Previous studies have shown that passive porosity can be effective at reducing large pressure gradients on the surface of wings, inlets, nozzles, etc.

Therefore, an experimental investigation to determine the effectiveness of passive porosity for alleviating side forces on forebodies was conducted in the 7- by 10-Foot High-Speed Tunnel.

Force, moment, and surface-pressure data were obtained on solid and porous (22-percent porosity and hole diameter of 0.020 in.) tangent-ogive forebodies with fineness ratios of 2.5 and 5.0. The forebodies were tested with cylindrical afterbodies. The solid forebodies were tested with transition grit to simulate fully turbulent conditions and with transition grit to simulate free transition conditions. The porous region on the forebody was varied to determine the extent of porosity required to alleviate side forces. Static longitudinal and lateral-directional stability and surface pressure data were obtained at free-stream Mach numbers of 0.2, 0.5, and 0.8; angles of attack α from -5° to 45° ; and roll angles from -90° to 180° .

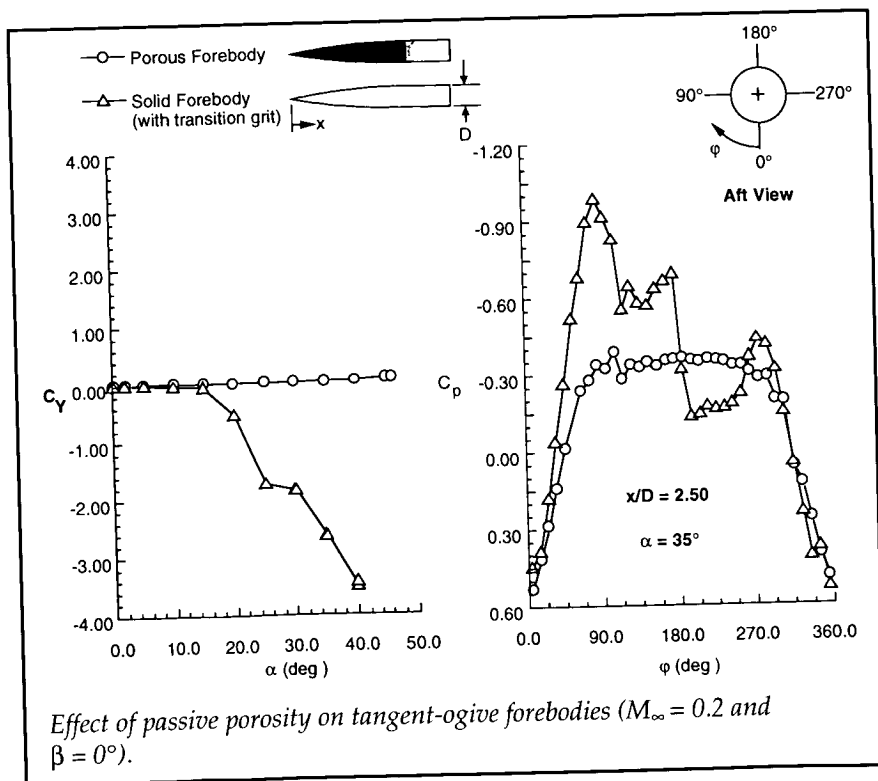
As shown in the figure, the solid forebodies exhibited large asymmetric pressure loads C_p at

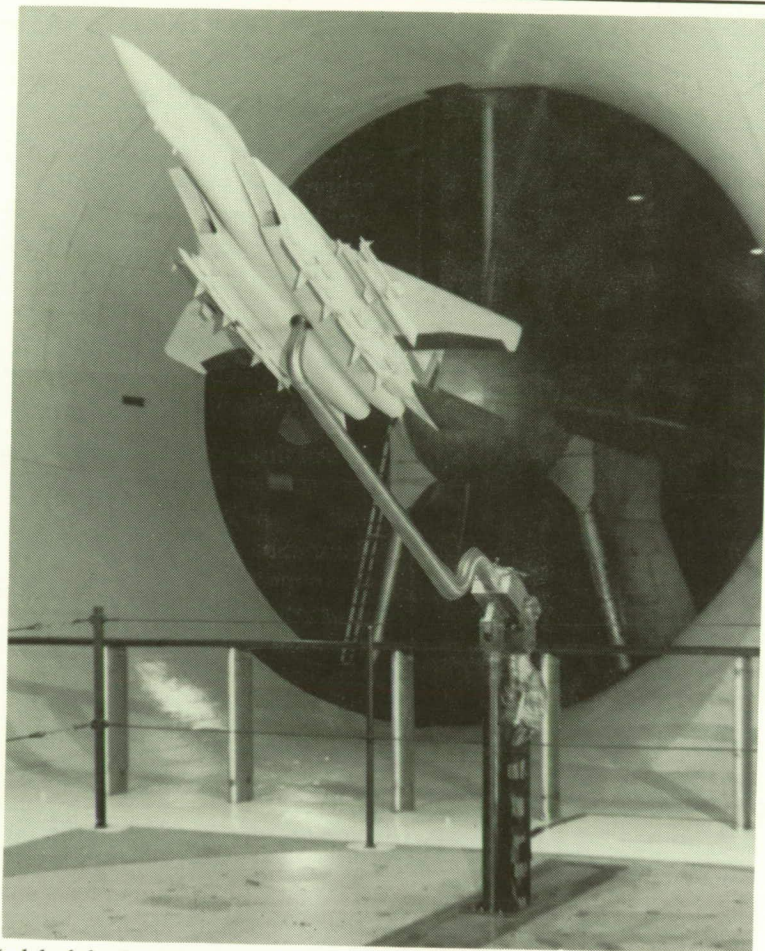
moderate to high angles of attack, and these loads caused large side forces C_Y . The transition grit had minimal effect on the asymmetric characteristics but had a large effect on the longitudinal characteristics. The porous forebodies exhibited no significant side forces or yawing moments at any test condition. The results of this study are encouraging because they indicate that a simple, low-cost, passive porous system can alleviate asymmetric loading conditions on axisymmetric bodies at high angles of attack. This work was done in part under contract with Lockheed Engineering and Sciences Co.

(Steven X. S. Bauer, 45946, and Michael J. Hemsch)
Aeronautics Directorate

F-15E Stability and Control Studies

Static wind-tunnel tests have been conducted in conjunction with the U.S. Air Force in the 30- by 60-Foot Tunnel to determine the effects of several modifications to the F-15E aircraft. The modifications included several antenna pods and new external store configurations that allow the aircraft to suppress hostile ground-based radar. The photograph shows several of these modifications applied to a 10-percent-scale model that is mounted for static-force tests in the tunnel. In addition to the antenna pods and external stores, two refueling probe modifications that would allow the aircraft to conduct aerial refueling from drogue-equipped tanker aircraft were also investigated. The objective of the tests was to determine the best method of





Model of the F-15E mounted for static-force tests in the 30- by 60-Foot Tunnel.

integrating these modifications on the aircraft without degrading the low-speed, high-angle-of-attack characteristics that are vital for good air-to-air combat effectiveness.

The results from the tests showed that the antenna pods and external stores did not significantly affect the static stability and control characteristics at low speeds and high angles of attack. On the other hand, the addition of either refueling probe degraded the static lateral stability (dihedral effect) in the angle-of-attack region near maximum lift. Even

with these reduced levels of static lateral stability, however, the data show that the airplane retains an adequate level of departure resistance with either refueling probe configuration. In summary, the modifications can provide significant new aircraft capabilities and should not degrade the aircraft's existing air-to-air combat effectiveness. This work was done in part under contract with Lockheed Engineering and Sciences Co.

(Sue Grafton, 41145, Scott Fears, and Dan Murri)
Aeronautics Directorate

F-16 Free-Spin Tests

Tests of dynamically scaled, free-spinning models of three current versions of the F-16 airplane have been conducted in the 20-Foot Vertical Spin Tunnel at the request of the U.S. Air Force. Current F-16C versions have increased weight, moments of inertia, and horizontal-tail area compared with the original F-16A and use the MCID (modular common inlet duct) engine inlet. This inlet is larger than the original NSI (normal shock inlet) engine inlet used on earlier airplanes. Flight tests have shown that the MCID inlet can cause the airplane to depart from controlled flight under certain conditions. This series of tests was made in part to determine whether the MCID also affected the developed spin and spin-recovery characteristics of the model.

Results of these tests indicate that the developed flat-spin mode of the models tested is similar to that of the original F-16A, but with a moderate increase in the spin rate. The MCID inlet was found to add only a small increment to the increased spin rate. The greatest contribution to the increased spin rate between the F-16A and the present configurations is due to the larger aerodynamic moments provided by the horizontal tails of increased area. In addition, the recovery characteristics are slightly degraded between the current and original models, mainly because of the increase in spin rate and larger moments of inertia. The degraded recoveries have necessitated an increase in the size of the parachute recommended for emergency spin recovery



F-16 model in 20-Foot Vertical Spin Tunnel.

during flight tests. This work was done under contract with Lockheed Engineering and Sciences Co. (C. Michael Fremaux, 41193) Aeronautics Directorate

Flight Tests of a 0.27-Scale X-31 Drop Model at High Angles of Attack

The X-31 drop model is designed to explore the tactical utility of enhanced high-angle-of-attack flight with particular emphasis on post-stall maneuvering. A two-vehicle test program is currently underway at Dryden Flight Research Center. A cooperative program between Langley

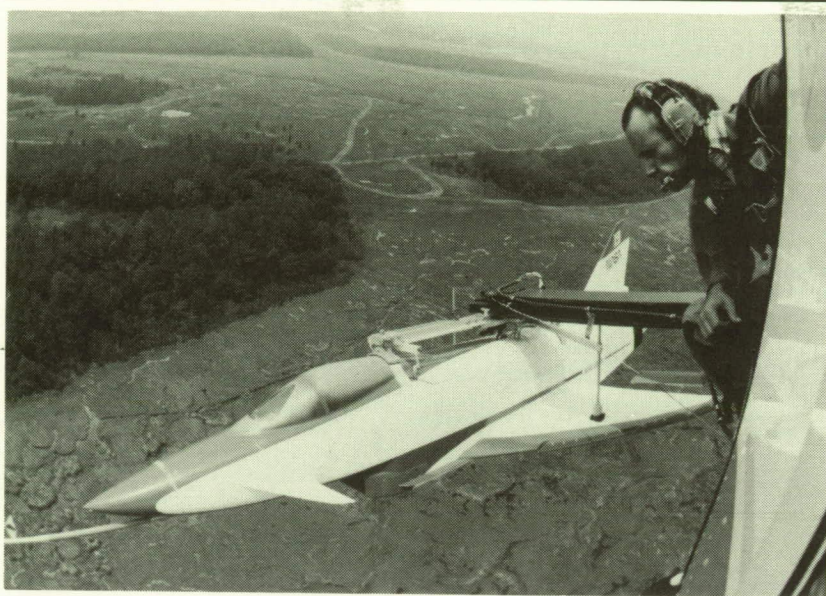
and the Defense Advanced Research Projects Agency is also being conducted. This program uses sub-scale models to study and predict the high-angle-of-attack flight dynamics of the X-31 configuration and to develop and evaluate control law concepts for application to the full-scale test airplane. As part of this program, free-flight tests of a 27-percent-scale drop model of the X-31 are being conducted at the Plum Tree Site. The 525-lb X-31 model represents the largest, heaviest, and most complex drop model ever tested at Langley.

The tests have focused on the wing-rock phenomenon that occurs in the stall regime as well as the departure-spin tendencies occurring in the extreme angle-of-

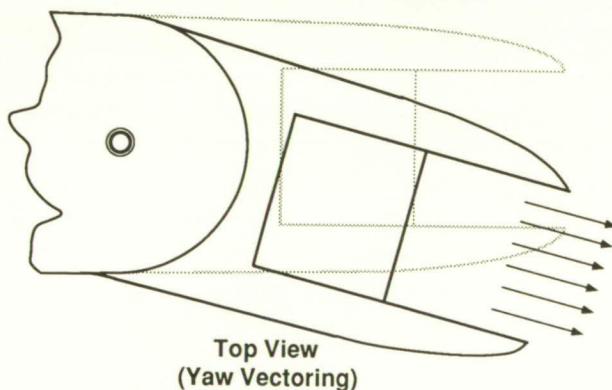
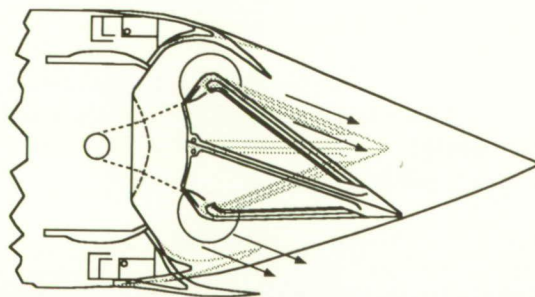
attack regime. Data have been obtained on the flight characteristics of the model over an angle-of-attack range from 25° to 75°. Earlier wind-tunnel and simulation studies predicted that the configuration would exhibit large-amplitude, undamped-roll oscillations. The drop tests have confirmed the existence of this wing rock and have verified that a simple flight-control-law scheme can effectively suppress the undesired oscillations.

All three spin modes that were previously determined during tests in the 20-Foot Vertical Spin Tunnel have been exhibited by the drop model. Moreover, results from the drop-model flights indicate that the configuration is susceptible to a very dynamic roll departure arising from sustained lateral control inputs in the spin regime. This disorienting, high-incidence, auto-rotative roll departure produces roll rates in excess of 275 deg/sec, with angles of attack and sideslip cyclically varying through a range of more than $\pm 60^\circ$. Recovery from the departure often leads to an unrecoverable inverted hung-stall flight condition. An anti-spin flight-control-law scheme has been identified that successfully inhibits the onset of the roll departure, thereby avoiding the potentially debilitating motion and subsequent dangerous hung-stall condition. Results from the drop-model tests are directly supporting the ongoing full-scale program in the areas of predictions of high-angle-of-attack flight dynamics and the development and validation of control-law concepts.

(Mark A. Croom, 41174, and David J. Fratello) Aeronautics Directorate

ORIGINAL PAGE
BLACK AND WHITE PHOTOGRAPH

0.27-scale X-31 drop model.

Top View
(Yaw Vectoring)Side View
(Pitch Vectoring)

Concept for a spherical convergent flap plug nozzle.

**Research on Advanced
Multiaxis Vectoring Plug
Nozzle**

Advanced fighter aircraft are being designed that use multiaxis (pitch and yaw) thrust vectoring. Multiaxis thrust vectoring allows control of an aircraft in flight regimes where aerodynamic controls become ineffective, in particular at pre-stall and post-stall conditions. An experimental investigation was conducted at static conditions (no external flow) to determine internal performance of a unique concept for a multiaxis thrust vectoring nozzle.

The nozzle concept features an axisymmetric, spherical convergence flap section, two-dimensional downstream (secondary) flaps, and a two-dimensional centerbody plug. Yaw vectoring is accomplished by gimbaling the nozzle left or right about its spherically shaped convergence flap section, much like a ball-and-socket joint. Pitch vectoring is accomplished by simultaneously deflecting the secondary flaps and plug in the same direction (up or down). Tests were conducted over a range of nozzle pressure ratios from 1.0 (jet off) to approximately 12.

Results of this investigation indicate that the nozzle tested had poor discharge coefficient performance ($w_p/w_i = 0.8$), compared with that of an axisymmetric nozzle. The nozzle also exhibited slightly lower axial and resultant thrust ratios than other nozzle concepts. However, this nozzle concept proved to be an effective mechanism for yaw thrust vectoring; resultant yaw vector angles near the geometric (metal)

vector angle values were obtained over the range of test nozzle pressure ratios.

(Daniel L. Cler, 43019, and Mary L. Mason)
Aeronautics Directorate

Thrust Vectoring Characteristics of the F/A-18 HARV

The F-18 High Alpha Research Vehicle (HARV) is an F/A-18 aircraft modified specifically for flight research at angles of attack up to 70° . One of the HARV modifications to the baseline F/A-18 aircraft was the addition of a multiaxis thrust vectoring system to the conventional exhaust nozzle propulsion system. The divergent section of the exhaust nozzle was removed from the flight test vehicle to simplify installation of the vane actuation system and minimize the weight increase that resulted from adding the thrust vectoring system to the F/A-18. The thrust vectoring system consists of three vanes mounted externally to each of the exhaust nozzles. Multiaxis thrust vectoring is achieved by deflection of the vanes into the flow of the nozzle exhaust.

An investigation was conducted in the 16-Foot Transonic Tunnel to determine the multiaxis thrust vectoring characteristics of the F/A-18 HARV. A 0.10-scale propulsion model of the F/A-18 airplane was modified with hardware to simulate the thrust vectoring system of the F/A-18 HARV. This investigation was conducted at Mach numbers ranging from 0.30 to 0.70, at angles of attack

from 0° to 70° , and at nozzle pressure ratios from 2.0 to approximately 5.0. A large combination of vane deflections were tested at military and afterburning power settings.

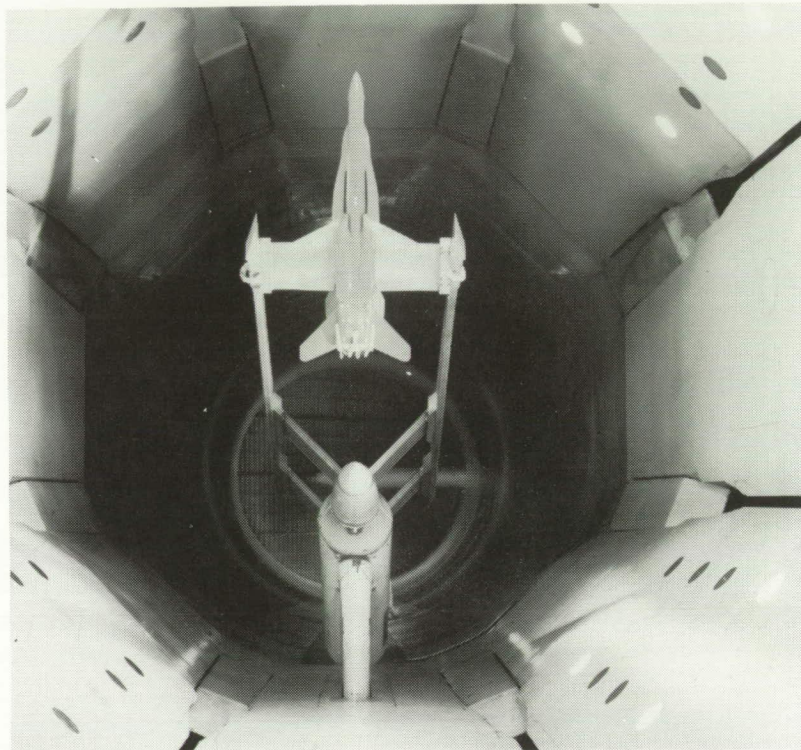
Results indicate that the thrust vectoring system of the F/A-18 HARV can generate useful levels of multiaxis thrust vectoring. During vectoring, resultant thrust vector angles were always less than the corresponding angle of geometric vane deflection and were accompanied by large thrust losses. At forward speeds, jet-induced external flow effects resulted in favorable increases in lift due to vectoring. At Mach 0.30 and 0.50, interference effects reduced the amount of side force generated at low angles of attack.

However, at higher angles of attack and higher Mach numbers, interference effects increased the amount of side force generated by vectoring. Finally, longitudinal control power from thrust vectoring was greater than that of the horizontal tail at angles of attack greater than 25° at Mach 0.30.

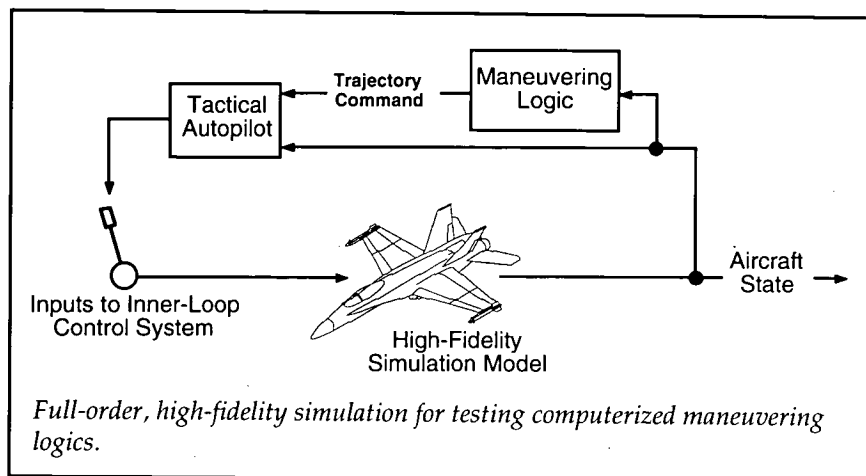
(Scott C. Asbury, 43040)
Aeronautics Directorate

Tactical Maneuvering Simulator

Batch air combat simulation provides a controlled and inexpensive means of analyzing air combat tactics and the tactical capabilities of new aircraft designs. In these



F/A-18 HARV model installed in 16-Foot Transonic Tunnel at angle of attack of 70° .



simulations, computerized maneuvering logics, implementing varying maneuvering strategies, guide participants in simulated engagements. The results of these engagements are used to develop effective maneuvering strategies and to assess the merit of new technologies or design variations. Because batch simulation does not include the human elements of air combat (e.g., unpredictability and adaptability), it is important for batch results to be validated in piloted simulation. The Tactical Maneuvering Simulator (TMS) has been developed to provide a batch simulation environment with fidelity equal to piloted simulations, allowing concepts developed in batch to be easily evaluated in piloted simulation.

Unlike previous batch simulations that use simplified aircraft models, the TMS uses equations of motion, control laws, aerodynamics, and propulsive characteristics identical to those in high-fidelity piloted simulation. The use of a high-fidelity model in the TMS is enabled by an outer-loop control system known as the tactical autopilot (TA). As shown in the figure, the function of the

TA is to convert guidance commands issued by a maneuvering logic into inputs to the inner-loop control augmentation system of the simulated aircraft, causing the aircraft to capture and track the desired trajectory. The ability of the TA to track representative guidance commands has been demonstrated to be equal or superior to the performance of human pilots.

The use of equivalent models in the TMS and piloted simulation allows maneuvering logics developed in the batch simulation environment of the TMS to be directly substituted for a human pilot in a multipilot, differential maneuvering simulator. This capability allows results from extensive batch simulation studies to be validated or refined with a minimum of piloted simulation. Differences in maneuvers and tactical effectiveness between the two environments can be directly attributed to the human pilots' ability to respond and adapt to the tactics of the computerized maneuvering logic.

The TMS is currently being used to study aircraft with enhanced agility and high-angle-of-

attack capability in one-versus-two engagements.

(K. H. Goodrich, 44009)

Flight Systems Directorate

Wide-Field-of-View, Binocular Helmet-Mounted Display

Binocular helmet-mounted displays (HMD's) have been under development for many years. Because of the narrow field of view (FOV) and the low image resolution of these designs, they have been employed principally as aiming devices or head-up-display (HUD) replacements. These early designs were driven with a monochromatic stroke symbol generator that severely restricted the display format designer. With access to today's full-color high-resolution raster-graphic workstations, display designers are free to explore their imagination and create naturally interpreted, shaded pictorial displays. The goal of this effort was to design and develop a binocular HMD that provided significant improvements in FOV, resolution, brightness, and research flexibility for real-time piloted simulation research.

Traditional off-axis catadioptric designs were poor light transmitters, so that the final image brightness at the viewer's eye was less than 2 foot/amberts. Hence, the image was usable only in very low ambient lighting situations. By applying holographics to the optical design, very high brightness and transmissivity were achieved so that the HMD is usable in normal daylight activities.

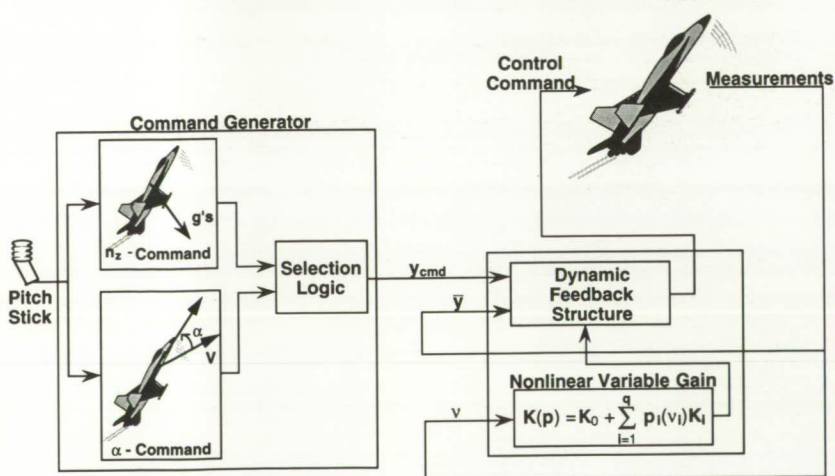


Wide-field-of-view, binocular helmet-mounted display.

for stereo capability. (See figure.) The image brightness at the eye has been measured at 300 foot/amberts, and the trichromatic holographic approach naturally enhances contrast by rejecting the ambient light at the design wavelengths.

This HMD development is revolutionary in that it combines wide FOV, high brightness, high resolution, and a color upgrade path in a compact, lightweight design. Further, the flexible interface to state-of-the-art graphics workstations provided by this HMD will allow many new three-dimensional display concepts to be evaluated in a real-time piloted simulation environment that could only be imagined before.

(James R. Burley II, 42008)
Flight Systems Directorate



Longitudinal control design approach for HARV.

Longitudinal Control Design of High Alpha Research Vehicle (HARV)

A trend of future high-performance aircraft is toward expanding the flight envelope in terms of speed, altitude, angle of attack α , and enhanced maneuverability. In particular, these aircraft must be able to operate in the post-stall regime at very high angles of attack, quickly and accurately point the aircraft nose, and execute fast turns with minimum turning radius.

To satisfy these requirements, a longitudinal control design based on a variable-gain, direct-digital, optimal, output-feedback control synthesis has been developed for the NASA F/A-18 High Alpha Research Vehicle (HARV).

Further, three holograms were superimposed, each tuned to a different wavelength of light (red, green, or blue) so that a full-color image will be seen by the wearer, once a full-color image source is developed (the present image

source is monochromatic). This holographic approach to design has resulted in a prototype binocular HMD with a variable FOV that can be set to a maximum horizontal FOV of 100° and to overlapped left-eye-right-eye fields of view

Variable-gain output and feedback is an efficient, integrated design approach in which all design operating conditions are handled simultaneously in contrast to single-point design approaches that are typically used. As shown in the figure, the developed controller is nonlinear; the feedback gains are a function of gain-scheduled parameters p , which in turn are functions of measured variables v . The feedback gains change continuously during flight and are then integrated with a dynamic feedback structure. An approximate design procedure based upon relationships between the penalty weights, feedback gains, and design performance has been established for the multi-input, single-output controller.

A second feature of the longitudinal controller is the command

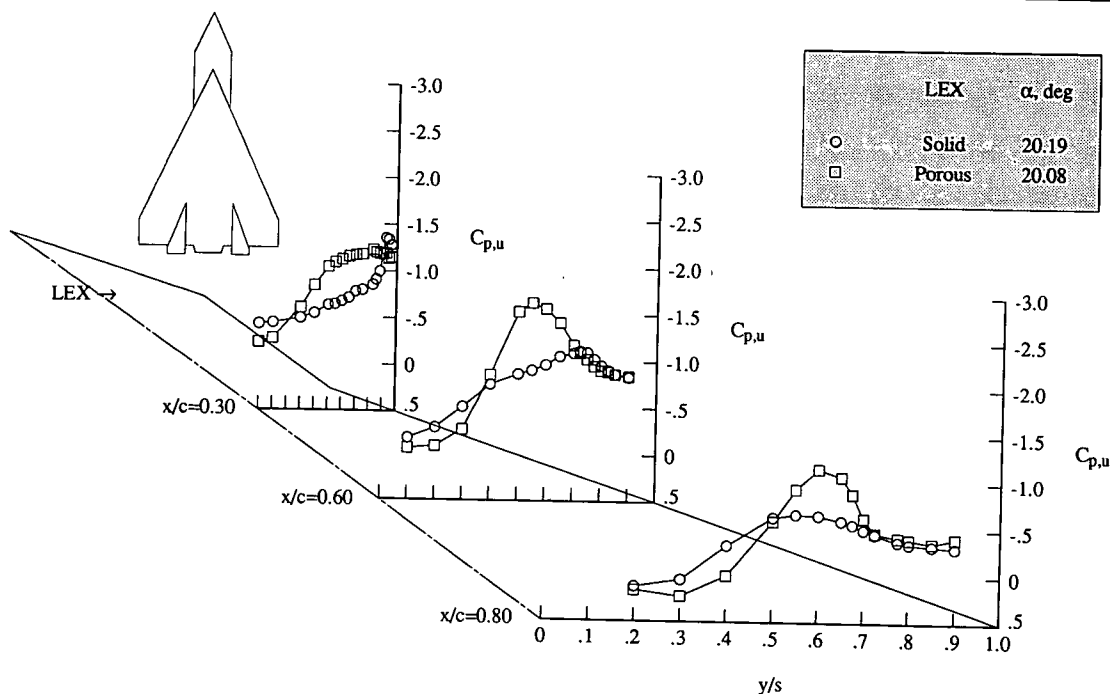
generator, which transforms the pilot-stick command into an equivalent command y_{cmd} that can be interpreted by the feedback controller. Selection logic determines load-factor n_z or α -command modes and ensures smooth transition between the two modes without additional work required from the pilot.

Results of linear analysis for single-loop gain and phase margins, multiloop sensitivity, and servo-elastic frequency response indicate a highly robust control system with good structural attenuation properties. Non-linear simulation results illustrate good pitch-up and pitch-down agility, smooth mode transition, and good α -regulation and capture characteristics.

(Aaron J. Ostroff, 44025, and
Melissa Proffitt)
Flight Systems Directorate

Surface Porosity Effects on Vortex Interactions

An experimental investigation was conducted in the 7- by 10-Foot High-Speed Tunnel on the effects of leading-edge extension (LEX) surface porosity on vortex-vortex and vortex-vertical tail interactions on a 65° cropped delta wing model. The planform of the model is sketched in the figure. Laser vapor-screen flow visualizations, distributions of wing upper-surface static pressures, and six-component forces and moments were obtained at Mach numbers of 0.2 to 0.5 (corresponding to Reynolds numbers based on wing mean aerodynamic chord of 2.8 to 5.9×10^6), angles of attack from 0° to 45° , and angles of sideslip of -5° , 0° , and 5° . The porous LEX was a flat plate with beveled leading

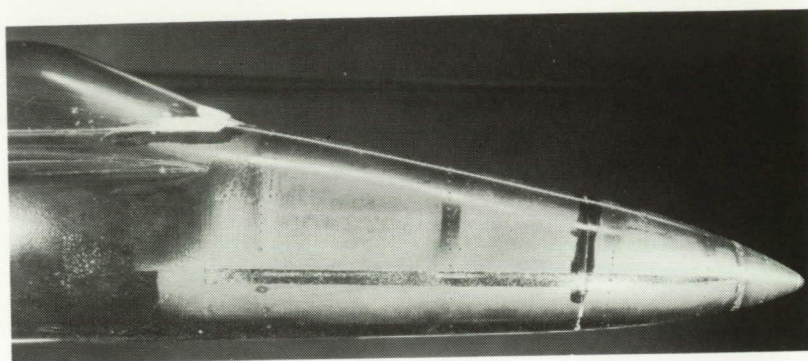


Effect of LEX porosity on wing surface pressures ($M_\infty = 0.50$ and $\delta_v = 30^\circ$).

edges and had a uniform distribution of through holes 0.05 in. in diameter, which provided a maximum porosity of 12 percent by area. The level of porosity was manually varied from 0 to 12 percent during the testing by covering selected regions of the LEX. Wing-mounted tail cant angles of -30° (inboard cant), 0° (vertical), and 30° (outboard cant) were tested with the porous LEX, with the nonporous LEX, and with the LEX off.

The test data showed that the porosity of the LEX surface had a significant effect on the global flow field. The surface pressure distributions on the right half of the model, shown in the figure, indicate that the location and magnitude of the wing-leading-edge vortex pressure signature are highly sensitive to the LEX surface porosity. The flow visualization results revealed reduced interaction between the LEX and wing vortex flows and diminished vortex-tail interactions in the presence of the porous LEX. The six-component force and moment data indicated that the principal effects of the porous LEX were to reduce the longitudinal instability and increase the lateral instability at the high angles of attack.

Follow-on experiments are planned in the 7- by 10-Foot High-Speed Tunnel to extend the existing data base to include porous leading-edge flaps, alternate tail locations and cant angles, and centerline tail arrangements. (G. E. Erickson, 42886)
Aeronautics Directorate



Narrow strip of no. 180 grit along side of forebody.

High-Alpha Gritting To Simulate Flight Reynolds Number Data

The majority of wind-tunnel testing is conducted at subscale values of flight Reynolds numbers. Ground testing programs involving fighter aircraft have not, at times, correctly predicted pitching moment or stability and control. Some of these differences have been attributed to effects of subscale Reynolds numbers on forebody flow separation at high angles of attack (high alpha). Consequently, a number of Langley experiments have been conducted over the past several years to determine if high-alpha gritting techniques can appropriately transition the boundary layer on smooth-sided forebodies to better simulate flight Reynolds numbers.

The availability of significant numbers of pressure ports on a 6-percent-scale model of the F/A-18 and on the F/A-18 High-Alpha Research Vehicle (HARV) permit a close comparison of forebody vortical flow fields at wind tunnel and flight conditions. The 6-percent-scale model was tested in the 7- by 10-Foot High-

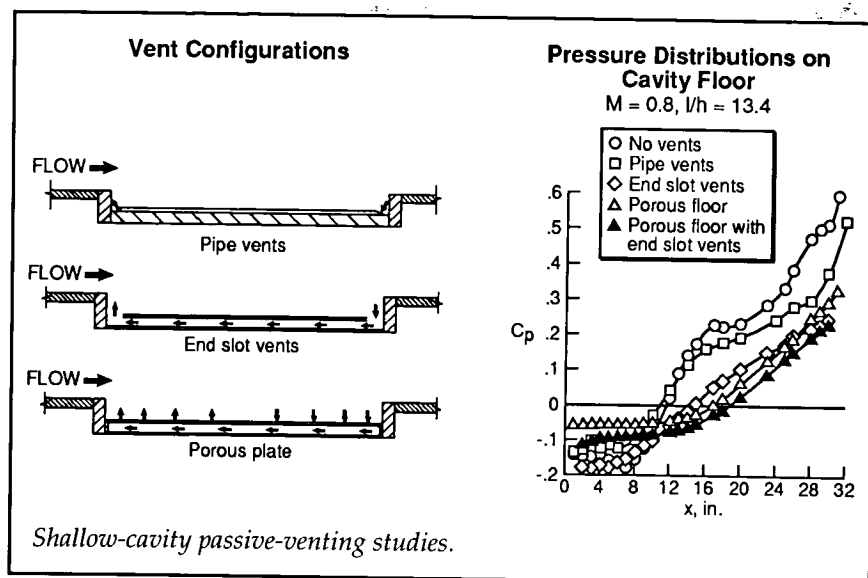
Speed Tunnel at conditions matching flight data except for the Reynolds number. The investigation explored both the classical low-alpha grit ring approach and several new high-alpha grit patterns designed to transition the forebody flow. One example of the high-alpha gritting was narrow strips situated along each side of the aircraft forebody as shown in the figure.

Pressure agreement with the flight data was significantly improved by using the high-alpha gritting patterns. For the F/A-18, this improved gritting on the forebody eliminated some of the nonlinearities in the lateral stability of the vehicle.

(R. M. Hall, 42883, D. W. Banks, and W. G. Sewall)
Aeronautics Directorate

Transonic Investigation of Shallow-Cavity Passive-Venting Configurations

Published experimental data have shown that at supersonic speeds, high drag levels and



adverse store separation characteristics are generally associated with shallow cavities. Missile bays on current and future fighter aircraft that contain a single level of missile carriage (i.e., only one missile deep) would likely fall into the shallow cavity category. At supersonic speeds, tests have also shown that passive venting concepts for cavities result in a reduction in longitudinal pressure gradients and flow turning angles in the cavity flow field. These reductions result in improved store separation characteristics and a reduction in cavity drag.

Because of interest in releasing weapons from internal carriage configurations at subsonic and transonic speeds, tests were conducted to determine if similar passive venting concepts would also be effective in this speed range. An additional passive venting configuration consisting of a rectangular slot at each end of the cavity was also tested. A sketch of the side view of the configurations is shown in the figure.

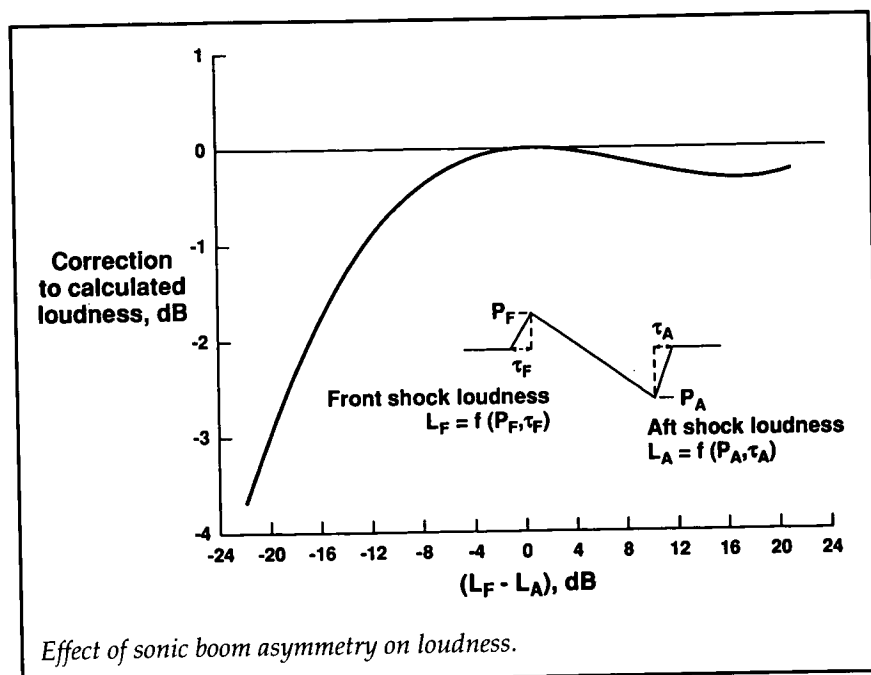
Measured pressure coefficient distributions on the cavity floor for the different passive venting configurations are shown in the figure for a Mach number of 0.8 and a cavity with a length-to-height ratio of 13.4. Also shown for reference is the cavity floor distribution for the case of no vents. The data show that for the no-vent configuration large pressure gradients occur on the cavity floor, and these gradients are indicative of large flow turning angles. The results for the pipe-vent configuration also are indicative of large flow turning angles, a fact that is contrary to the results obtained at supersonic speeds. For the porous plate, slot vents, and combined porous-plate slot-vent configurations, the pressure gradients on the cavity floor are much less than measured for the no-vent configuration. The flow field associated with these reduced pressure gradients should result in reduced cavity drag and improved store separation characteristics for this shallow cavity. The combination of porous floor and end slot vents will be studied further as this

combination showed reduced levels of fluctuating pressures as compared with the levels for either the porous floor or the end slot vents. This work was done in part under contract with Lockheed Engineering and Sciences Co. (R. L. Stallings, 42877, E. B. Plentovich, M. B. Tracy, and M. J. Hemsch) Aeronautics Directorate

Loudness of Asymmetrical Sonic Booms

Current designs for a low-boom supersonic aircraft are expected to produce a sonic boom on the ground which has front and rear shocks that differ from one another. These designs are in contrast to all existing supersonic aircraft, which generate symmetrical sonic boom signatures. To determine the effects of signature asymmetry on the acceptability of sonic booms, a study was conducted using the sonic boom simulator located at the Acoustics Research Laboratory.

Loudness judgments of selected asymmetrical sonic booms were obtained from 40 test subjects. Loudness asymmetry was achieved by independently varying the rise times t and peak pressure magnitudes P of the front and rear shocks (see figure). Asymmetry was defined as the difference, in decibels, between the perceived levels (PL's) calculated for the front and rear parts of a signature. Positive values of asymmetry indicate that the front part of a signature was loudest and negative values indicate that the rear part was loudest. Results indicated that the asymmetrical



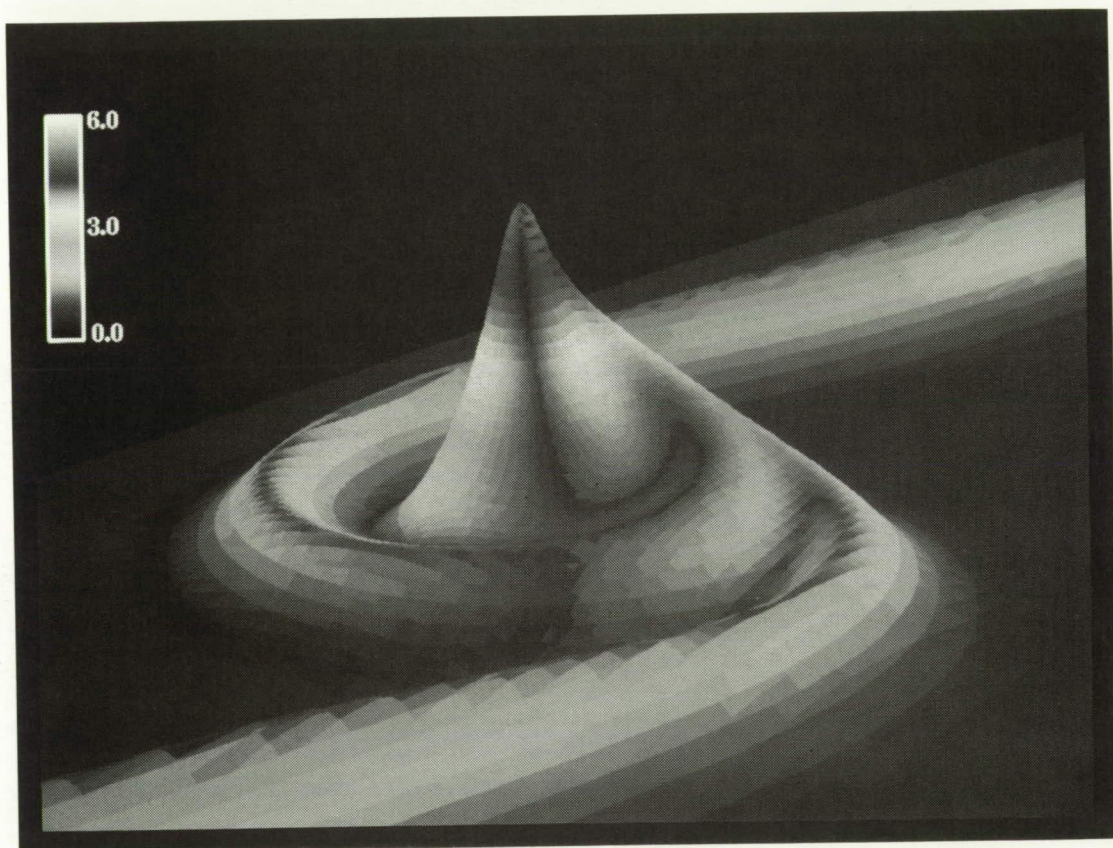
signatures were generally rated to be quieter than symmetrical signatures of equivalent total PL. These results are summarized in the figure in terms of corrections to PL. When the rear shock was loudest (negative values of asymmetry), corrections to PL of as much as -3 dB were observed. Positive values of asymmetry resulted in minor corrections to PL. Because efforts at sonic boom minimization are centered on reducing the loudness of the front part of the signature, the rear part of the signature will probably be loudest. The results of the present work indicate that such booms will be more acceptable than symmetrical signatures of the same calculated loudness.

(Jack D. Leatherwood, 43591,
and Kevin P. Shepherd)
Structures Directorate



HIGH-PERFORMANCE MILITARY AIRCRAFT

■ HYPERSONIC AND TRANSATMOSPHERIC VEHICLES



*Develop the critical technologies
for future hypersonic and
transatmospheric vehicles*

Preceding Page Blank

CFD Prediction of Boundary-Layer Transition on a Blunt Cone

Langley and Ames Research Centers and Sandia National Laboratories have compared computational fluid dynamics (CFD) predictions of boundary-layer transition on a blunt cone at Mach 15 and an angle of attack of 0° . The objective of this exercise was to perform independent CFD analyses for a common flight condition on a sphere or cone and basic wing-body to sort out numerical issues and to identify and correct physical modeling issues. Each organization used its own CFD methodology on the given geometry and flow conditions. The boundary-layer transition criterion for all participants was

stipulated. The boundary-layer edge was computed with a fixed value of total enthalpy, and for transition onset a Reynolds number based on momentum thickness divided by Mach number at the boundary-layer edge of 150 was used.

The CFD flow field solutions of the various codes were in good agreement as far as computed surface pressures and heat transfer were concerned. However, computed transition locations varied by 10 percent on a 22-ft vehicle, as shown in the figure. The source of the differences was found to be the method used for determining the boundary-layer edge. Further analysis indicated the boundary-layer edge prediction was highly sensitive to small oscillations in total enthalpy. Alternative techniques for defining boundary-layer edge based on derivatives of

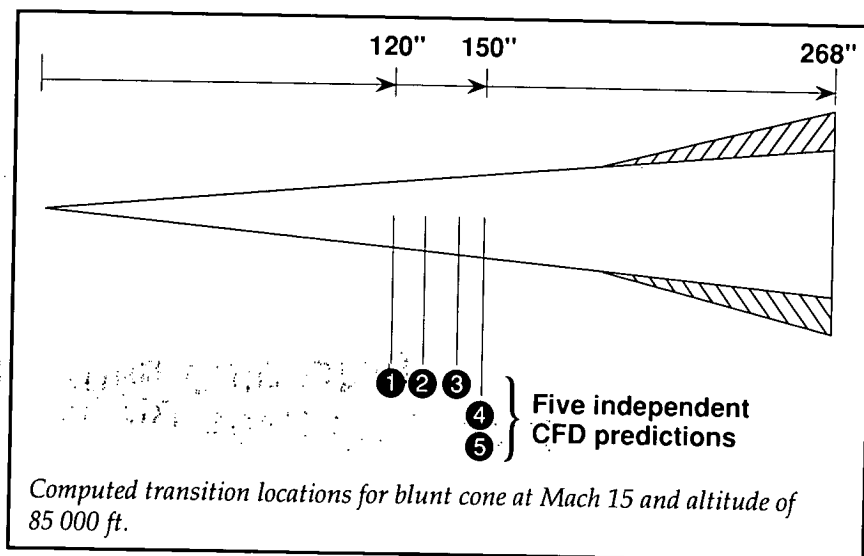
total enthalpy should be investigated for more consistent predictions of transition location. This work was done in part under contract with Analytical Services & Materials, Inc.

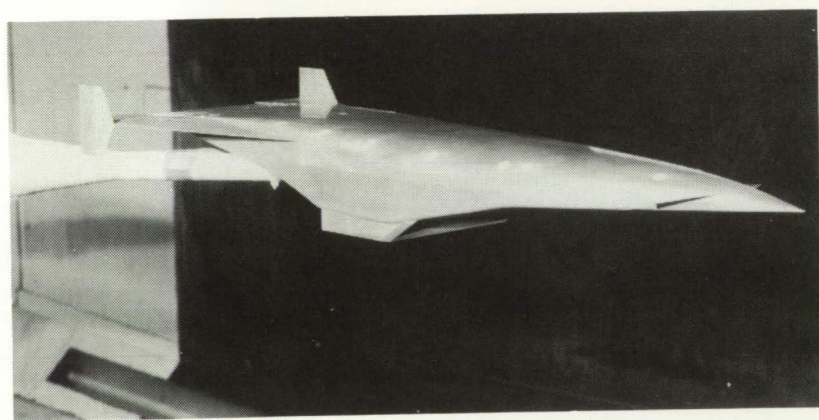
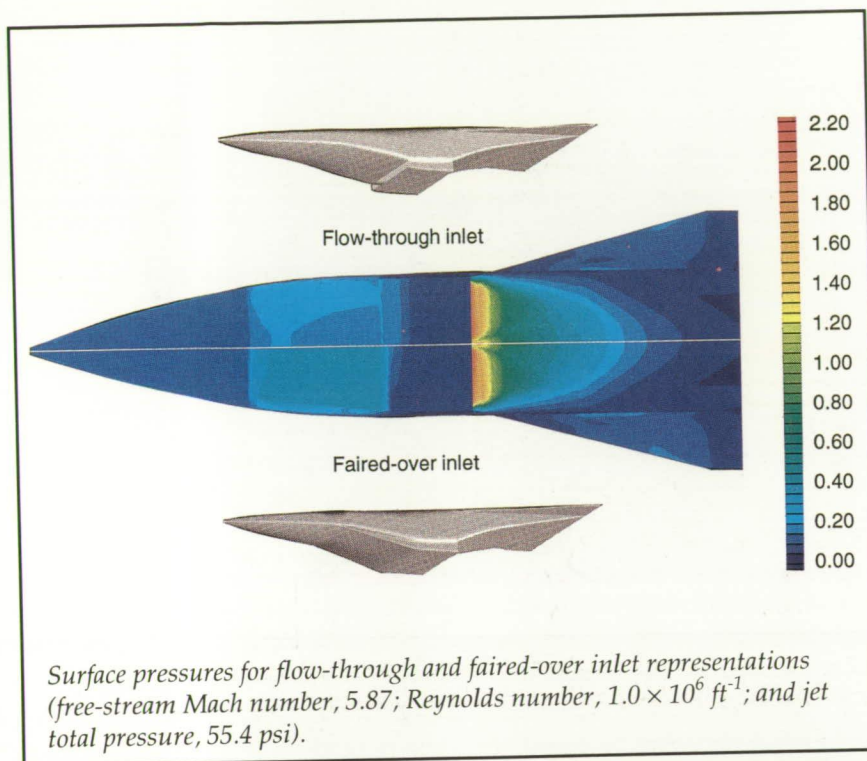
(Sharon H. Stack, 43742, Arthur D. Dilley, and Richard W. Hawkins)
National Aero-Space Plane Office

Effect of Inlet Representation on Hypersonic Model Afterbody Flows

It is impractical to perform combustion tests on hypersonic, air-breathing configurations because the models are limited in size by typically small hypersonic wind tunnels. One method of obtaining the effects of a "powered" test is to fair over the scramjet inlet and use a simulant gas that has been routed out the combustor nozzle. Various mixtures of simulant gases have produced acceptable pressure distributions on the afterbody as long as the proper ratio of specific heats is maintained. However, the flow diverted around a faired inlet creates a different flow field than the flow past a realistic inlet employing a sharp cowl leading edge, and this different flow field could affect pressures on the afterbody surface.

A three-dimensional (3-D) computational effort was undertaken using the parabolized





Static test on TTD model.

Navier-Stokes (PNS) equations to investigate the effect of inlet representation on powered model afterbody flows. Two configurations were studied: the flow-through inlet model provided the necessary inlet geometry to simulate the flow associated with the cowl leading edge (see figure),

while the faired-over inlet model eliminated all cowl leading-edge effects. A comparison of Mach number contours showed a vastly different flow field beneath the cowl, but the flow inside the shear layer was quite similar. A comparison of pressures on the lower surface (see figure) showed very

minor differences on the afterbody, with less than 1 percent difference present in afterbody integrated pressures. Therefore, this work shows that fairing over the inlet is a valid method for conducting powered hypersonic tests to determine afterbody performance effects.

(Lawrence D. Huebner, 45583, and Kenneth E. Tatum)
Aeronautics Directorate

Subsonic Aerodynamic Characteristics of a NASP Test Technique Demonstrator Configuration

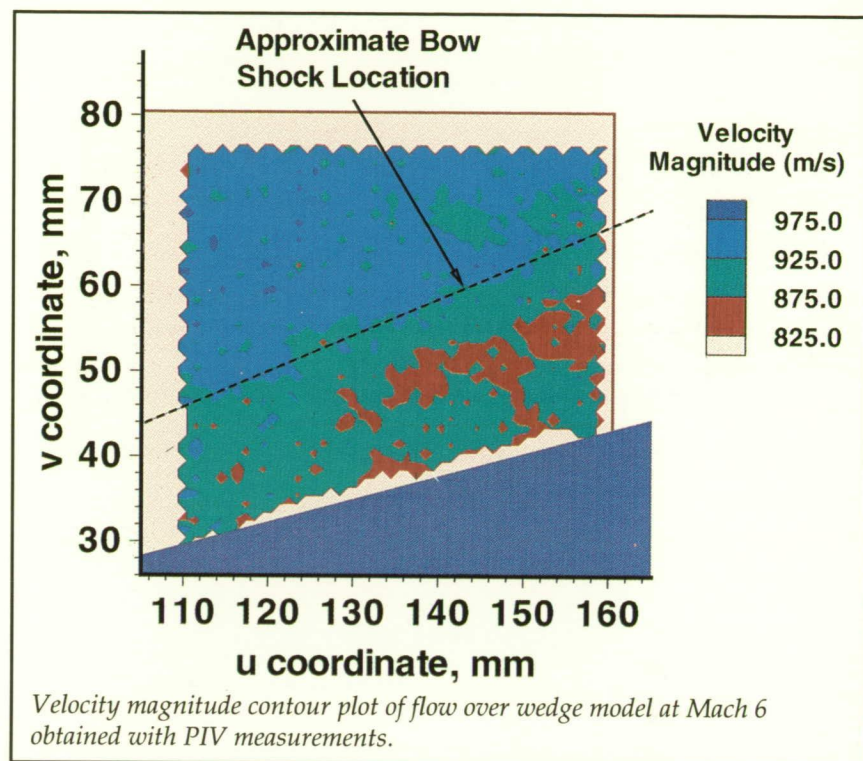
An experimental investigation was conducted in the Langley 7-by 10-Foot High-Speed Tunnel to determine the static longitudinal and lateral-directional characteristics of the National Aero-Space Plane (NASP) Test Technique Demonstrator (TTD) configuration. The effects of canards, canard deflection, body flap, body flap deflection, and vertical-tail spanwise location were also studied. Limited data were also obtained on the effects of rudder deflection and elevon deflection. The test data included six-component force and moment data as well as off-body flow visualization data obtained with a laser-light-sheet vapor screen technique. The tests were conducted at Mach numbers of 0.3, 0.6, and 0.8 over an angle-of-attack range of -4° to 16° at sideslip angles of 0° , -3° , and 3° . The basic configuration had positive static stability except at the highest angles of attack of 14° and 16° at Mach 0.8. The directional stability

was low or negative between angles of attack of 2° and 14° .

In addition, the aerodynamic damping in pitch, yaw, and roll was measured with the small-amplitude, forced-oscillation technique used for the same 2-percent-scale TTD model. Configuration breakdown tests were made to determine the influence of the wings, the canards, the body flap, the vertical tails, and the engine nacelle on the damping characteristics. The basic configuration had positive damping in pitch, yaw, and roll through the range of angle of attack and Mach number. (Richmond P. Boyden, 45160, and David A. Dress)
Aeronautics Directorate

Supersonic Velocity Measurements Over a Wedge Model Obtained With Particle Image Velocimetry

Two-dimensional velocity measurements have been taken of the flow over a wedge model in the Langley Mach 6 High Reynolds Number Tunnel facility using particle image velocimetry (PIV). These measurements represent the first known use of PIV in a Mach 6 flow. The model for these tests consists of a blade-mounted wedge with a length of 203 mm and a width of 127 mm and oriented at an angle of attack of -15° to produce a 22.67° oblique bow shock. The measurement region of interest consists of a two-dimensional plane normal to the surface of the model and positioned on the centerline approximately two-thirds back along the

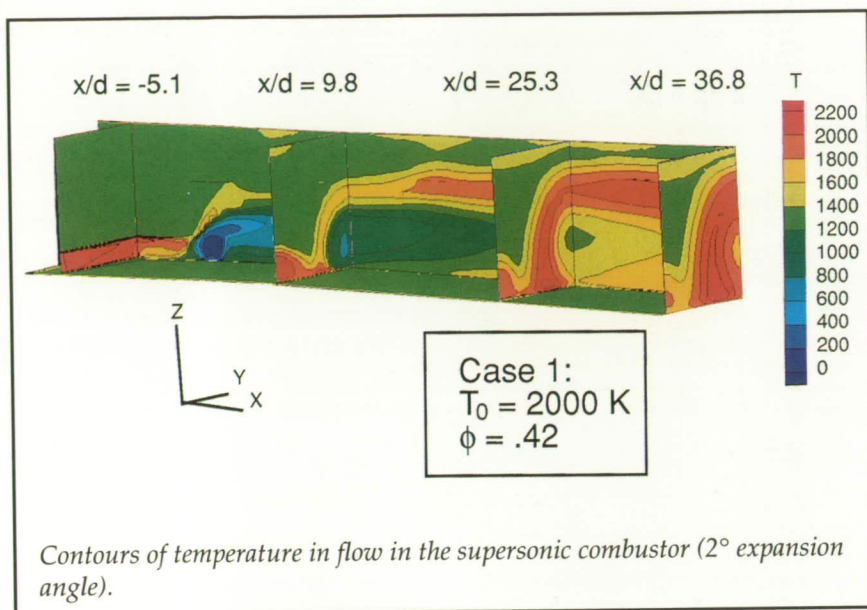


model chord. The tunnel is operated at a total pressure of 6.9 MPa and a temperature of 519 K to generate a free-stream velocity of approximately 930 m/sec. The flow is seeded with aluminum oxide powder with a nominal particle size of $1.0\ \mu\text{m}$ and delivered to the tunnel settling chamber via a fluidized-bed seeder. The PIV system consists of two frequency-doubled Nd:YAG lasers fired in sequence to generate a 1.0-mm-thick double-pulsed light sheet. A 70-mm camera system oriented normal to the plane of the light sheet images particles embedded in the flow onto a photographic plate. Double-exposure photographs are examined to track the movement of individual seed particles and ascertain the local flow velocities.

The figure shows a velocity magnitude field obtained by

analyzing and averaging together five separate photographs of the flow. The averaging provides a continuous vector field, which eliminates gaps present in individual negatives. The bow shock is discernible by the change in velocity magnitude approximately midway in the flow field. Measurements of the normal and tangential components of velocity as defined by the shock angle indicate a particle relaxation distance of approximately 10 mm before the particles reach 99 percent of the gas velocity. This indicates that the mean aerodynamic size of the particles is approximately $1.0\ \mu\text{m}$, as expected. (William M. Humphreys, Jr., 44601)

Electronics Directorate



Effects of Expansion on Supersonic Combustor Flow Fields

The SPARK three-dimensional Navier-Stokes code was used to make a series of calculations of the reacting flow from the transverse injection of hydrogen fuel behind a rearward-facing step into a vitiated-heated Mach 2 air-stream. The effect of the angle of the expanding portion of the duct and the length of the constant-area section on the extent of combustion within the combustor was examined. This combustor will be the focus of an experimental study to be performed at the NASA Langley Research Center in later 1992. The calculations will be compared with nitrogen temperature and density measurements obtained with a CARS (Coherent Anti-Raman Spectroscopy) system during the series of experiments.

The calculations revealed that even at the relatively low flight

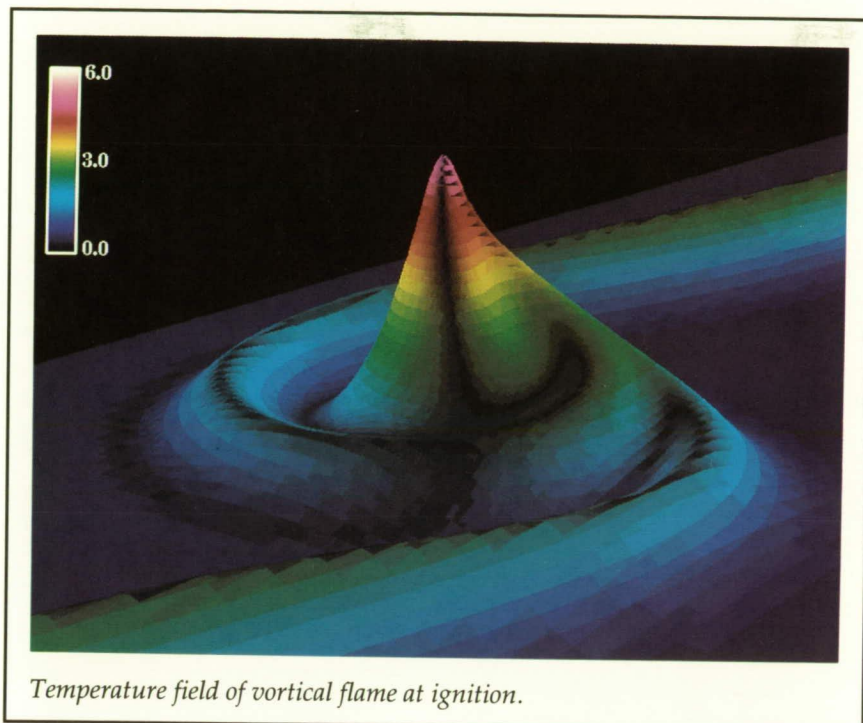
Mach numbers (5 to 7) associated with the conditions investigated, the chemical constituents are far from equilibrium, and hence kinetics effects are important. The figure shows the calculated temperature contours along the centerline plane of the injector, the bottom wall of the combustor, and four cross-flow planes. Reaction is observed (indicated by the high temperatures, or red contours) in the recirculating region upstream of the jet and in the mixing region between the injectant and the free stream downstream of the injector. The peak OH concentrations align closely with the peak temperatures and attain super-equilibrium values. This work was done in part under a grant with the National Research Council. (Dean R. Eklund, 47772, and G. Burton Northam) Aeronautics Directorate

Ignition and Structure of a Diffusion Flame With Vortex Interaction

The fundamental physics of turbulent combustion and combustion in vortical flows relevant to high-speed propulsion devices must be understood for key processes such as mixing enhancement to be controlled. Some turbulent combustion processes can be described as a collection of laminar flame structures, which retain their identity but are distorted by the turbulence. The present study shows that the onset of ignition and its location in a laminar flame are strongly dependent on the initial temperature differential and the vortex strength.

A detailed asymptotic analysis and a numerical simulation of the continuous evolution of the mixing between a fuel and oxidant that are allowed to mix and react in the presence of a viscous vortex are performed. Chemical reaction occurs in regions where reactants are intimately mixed on a molecular level; thus, reaction in a laminar diffusion flame depends on simultaneous processes of interdiffusion and chemical reaction. Emphasis is placed on the ignition time and location as a function of vortex Reynolds number R and the initial temperature differences β_T between the reacting species.

The focus is on understanding the controlling parameters necessary for ignition in a vortical flame. Ignition is seen as a hot spot in the temperature field T_1 displayed in the figure. The vortical structure is slightly asymmetric because of an imposed



perturbation temperature differential between the fuel and oxidant and the relatively weak vortex ($R = 28$). As the vortex strength is increased, the location of ignition moves to the center of an axisymmetric structure. Increasing the vortex strength also reduces ignition time, which approaches a constant that depends on the initial temperature differential β_T . In numerical simulations, the flame evolves from a single hot spot in the viscous core (ignition), which rapidly grows as time increases. At a later time, two diffusion flames begin to merge with the expanding, almost circular flame. The time progression of the reaction product shows the evolution of the flame from ignition (a small reacted region in the vortex center) to a burned-out core region, which develops at a later time. Analysis and parametric studies will continue, with the addition of acoustic effects and compressibility in more complex

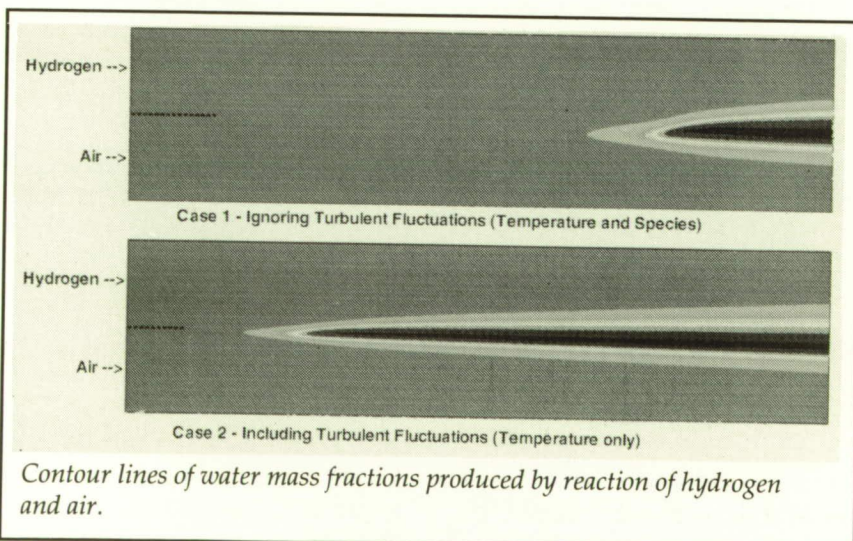
flow fields. From a systematic understanding of the relevant physics will follow a model that incorporates detailed chemical kinetics in a full numerical simulation.

(M. G. Macaraeg, 42295,
T. L. Jackson, and M. Y. Hussaini,
ICASE)
Aeronautics Directorate

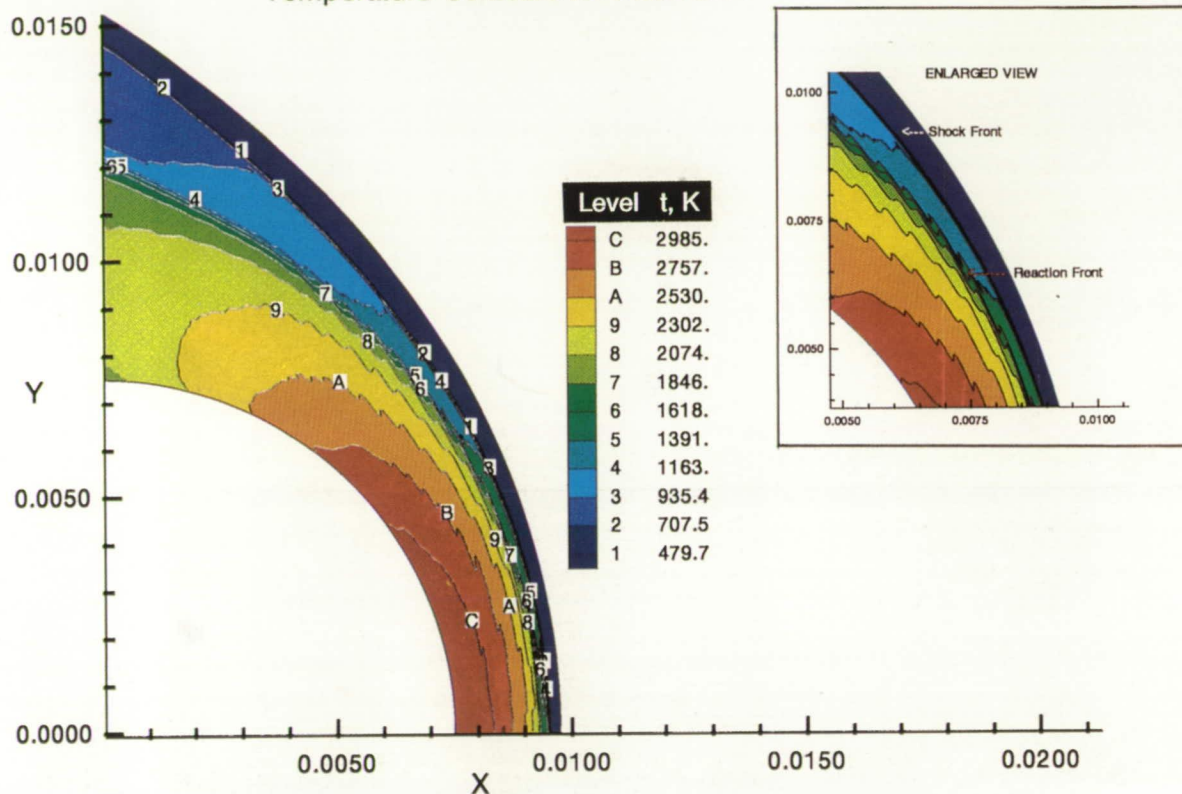
Interaction of Compressible Turbulence and Chemistry

In a high-speed turbulent reacting flow, turbulent temperature and species fluctuations affect the reaction process. Unfortunately, nonlinearities in the equations that describe such flows make it difficult to predict the effects of the fluctuations on the reaction process. In addition, at high speeds the effects of compressibility on the turbulence need to be included in a numerical simulation.

A compressible κ - ϵ turbulence model has been incorporated into a computer program that numerically solves the equations governing the mixing and reacting of a multiple-species flow. The compressible κ - ϵ model includes two compressible terms, the compressible dissipation term and the pressure dilatation term, which introduce the effects of compressibility on the turbulence. In addition, an assumed probability density function (pdf) has been incorporated into the program to account for temperature



Temperature Contours for Mach 5.11



Temperature contours for flow at Mach 5.11.

fluctuations in the reaction rate coefficient. The pdf requires information about the temperature variance, which is provided by the solution of one additional partial differential equation. Two assumed pdf's have been investigated for the inclusion of the effects of temperature fluctuations: a Gaussian pdf and a β pdf. These models have been tested on a two-dimensional turbulent combustor hydrogen-air mixing layer. The figure shows contour lines of water mass fractions produced by the reaction of the hydrogen and air in two cases, the first with temperature fluctuations ignored

and the second with their effects included using the Gaussian pdf. (The β pdf solution was similar to the Gaussian solution.) These contours clearly indicate that the temperature fluctuations have reduced the ignition delay time.

Work is currently under way to include the effects of species fluctuation on the species production rate using a recently developed multivariate β pdf. This work was done in part under contract with Analytical Services & Materials, Inc.

(R. L. Gaffney, 47872, J. A. White, S. S. Girimaji, and J. P. Drummond)
Aeronautics Directorate

Shock-Induced Combustion in a Hydrogen-Air System

For a propulsion system to be efficient at hypersonic speeds, the combustion must take place at supersonic speeds. One proposed mode of propulsion is called a shramjet (shock-induced combustion ramjet), for which a shock is employed to increase the temperature of premixed fuel and air to a point where chemical reaction will start.

The present study investigates the shock-induced combustion phenomena for a premixed hydrogen-air mixture flow past a 15-mm spherical projectile. The analysis is carried out using the SPARK code, a compressible Navier-Stokes reacting flow solver developed at Langley Research Center.

Solutions have been obtained at Mach 5.11 and Mach 6.46. At Mach 5.11, experimental results show an unsteady reaction front. These reaction instabilities are triggered and sustained through a close coupling between the gas dynamics and the chemical kinetics and are characterized by a periodic density variation behind the shock. In the figure, the main feature of the flow can be seen from the temperature contours, which show two distinct fronts. The outer front is the bow shock, and the inner, corrugated front is the reaction front. Note that the bow shock and the reaction front are separated from each other. The separation distance (known as the induction distance) increases away from the stagnation line. The instabilities in the reaction front, which arise near the stagnation line and then spread downstream, are clearly visible in the enlarged inset view. The calculated dominant frequency of the instability of the reaction front is about 2.0 MHz and the amplitude is about 0.004, which are in close agreement with the experimental results.

The results from the present study show that when the projectile velocity is close to a critical velocity (called the Chapman-Jouget velocity), the shock-induced reaction front is unstable, but with sufficient additional velocity it can be stabilized. This work was

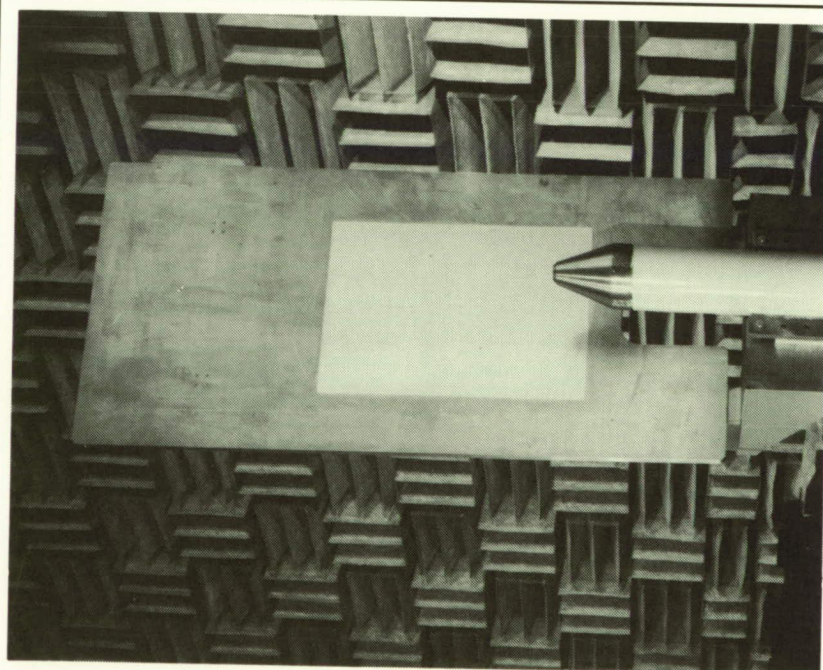
done under contract with Old Dominion University and Analytical Services & Materials, Inc. (J. K. Ahuja, 48155, S. N. Tiwari, and D. J. Singh)
Aeronautics Directorate

Stochastic and Nonlinear Response and Acoustic Radiation From a Panel-Stringer Structure Near a Supersonic Jet

The dynamic response and acoustic radiation of aluminum and composite panel structures forced by the near field of a supersonic jet exhaust are being investigated experimentally and numerically. The objective is to enhance understanding of the nonlinear response of the structure and the resultant nonlinear acoustic radiation. The structures consist of six

panels with stringers, typical of aircraft sidewall fuselage construction. For the experimental studies, the panel structures are mounted in a rigid frame near a model jet exhaust in an anechoic chamber. The structure is excited by the noise emanating from the jet as a result of instability, turbulence, and shock in the shear layer. Two types of nozzles are used—a conventional round convergent nozzle and a porous plug nozzle—both having the same mass flow and exit area. The plug nozzle maintains free shock at all pressure ratios, while the convergent nozzle does not.

Experimental results of the standard jet at a pressure ratio of 3 indicate that the strain response of the aluminum structure is nonlinear because of periodicity in the spectrum. Furthermore, the pressure field radiated by the structure is also nonlinear and



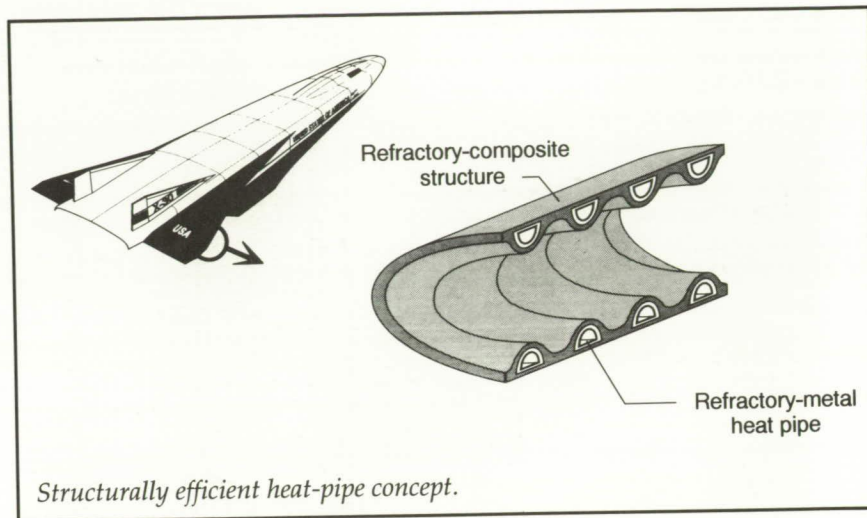
Panel-stringer structure and jet used in acoustic response and radiation test.

exhibits period doubling as well as chaotic behavior. The radiated field contains shocks and the formation of harmonics whose amplitude relative to the fundamental increases with distance. The results for the composite structure, conversely, indicate a significant reduction in the response and radiation. A significant reduction in response and radiation from the structure is also achieved with the plug nozzle for both types of structures.

(Lucio Maestrello, 41067)
Structures Directorate

Langley Heat-Pipe Concept for NASP Wing Leading Edge

The objective of this study was to design, fabricate, and test a reliable and lightweight refractory-composite heat-pipe-cooled wing leading edge with fail-safe features for the National Aero-Space Plane (NASP). The passive heat-pipe concept is an attractive alternative to the current baseline actively cooled wing leading-edge design, which uses hydrogen fuel to convectively cool superalloy leading edges. A wing leading-edge concept was developed that would enable sufficient heat rejection by radiation to eliminate the need for active cooling for the expected NASP flight environment. The high-temperature heat-pipe-cooled leading-edge concept utilizes the high specific strength of refractory-composite materials at elevated temperature to accommodate thermal and structural loads and provides a temperature capability above that of conventional refractory-composite heat pipes. The heat pipes are self contained and sized to provide redundancy



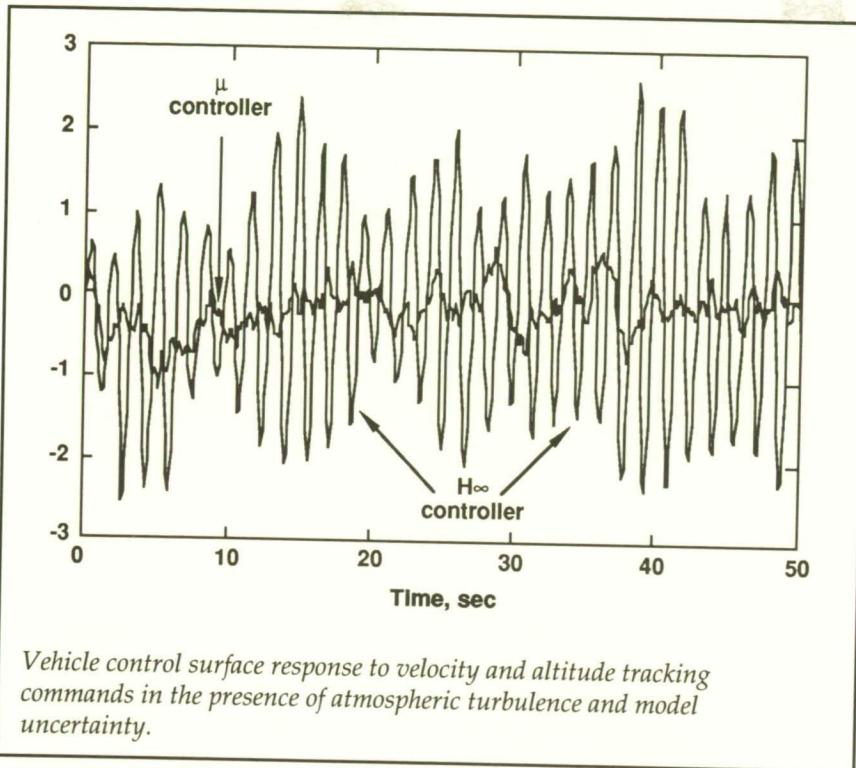
in the sense that if a heat pipe fails, adjacent working heat pipes can accommodate the additional heat load. A three-dimensional, steady-state, nonlinear, thermal finite-element analysis was used in the design study to predict maximum leading-edge temperatures as a function of the heat-pipe geometry and materials.

Results of this study defined a leading-edge design that completely eliminates the need for active cooling ascent and descent and is thus lightweight and much simpler than an actively cooled leading-edge design. The refractory-composite-heat-pipe-cooled wing leading-edge design is over 50 percent lighter than either the baseline actively cooled leading-edge design or an all-refractory-metal heat-pipe-cooled wing leading edge. As a result of the significant weight saving (8000 lb), this heat-pipe concept is currently being investigated as a replacement for the baseline wing leading edge, as well as being considered for use on the nose and tail leading edges of the NASP.

(David E. Glass, 45423, and
Charles J. Camarda)
Structures Directorate

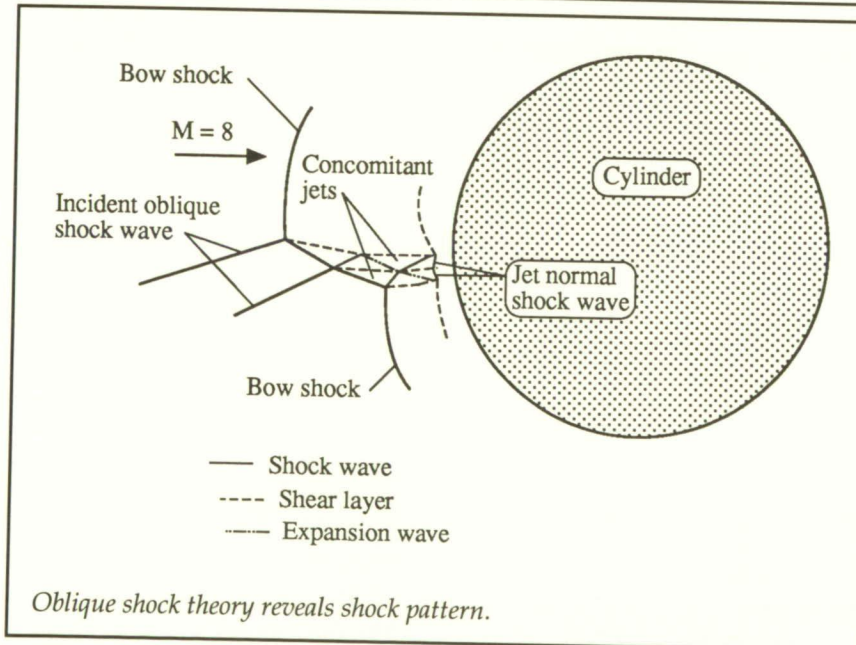
Hypersonic Vehicle Control Law Development With H_∞ and μ -Synthesis

Air-breathing transatmospheric vehicle concepts are currently being investigated at Langley Research Center. Atmospheric turbulence, propulsion system sensitivity to inlet flow conditions, large uncertainties of vehicle analytical models, and unprecedented levels of propulsion, aerodynamic, and structural dynamics coupling make the development of robust control laws for these vehicles especially challenging. The purpose of this research was to apply and compare two advanced controls design methodologies, H_∞ and μ -synthesis, to a hypersonic vehicle accelerating through Mach 8 and requiring high-accuracy velocity and altitude tracking commands while limiting angle-of-attack oscillations, minimizing control power usage, and stabilizing the vehicle in the presence of atmospheric turbulence and uncertainty in the system. The figure indicates elevon response to altitude and velocity tracking commands in the



troller. Other results comparing stability and performance robustness of H_∞ and μ controllers are similar.

The cumulative results of this research obtained in both the frequency and the time domain confirm the advantages of μ as both a control synthesis and an analysis tool for air-breathing hypersonic vehicles. Because payload performance margins are critical for transatmospheric vehicles, it is crucial that adequate stability margins be provided without sacrificing payload mass. The μ analysis and synthesis technique preserves the essential physics of the vehicle and allows the designer a systematic approach to explore trade-offs between vehicle stability and performance. (Irene M. Gregory, 44075) Flight Systems Directorate



New Shock-Shock Interference Pattern Identified for Concomitant Supersonic Jets

Structural design of future high-speed atmospheric vehicles requires consideration of complicated shock patterns and the associated high heating rates. The first multiple shock-shock interference heat transfer rate and pressure data for the thermal structural design of engine cowl leading edges were experimentally determined, and the interference patterns critical to understanding the fundamental fluid mechanics behind the aerothermal loads were defined. The shock-shock interference patterns were created by multiple oblique shock waves

presence of atmospheric turbulence and actuator model uncertainties for both H_∞ and μ controllers. The much smaller response produced by the μ controller is

indicative of its ability to more precisely handle the uncertainty in the system and to produce a better controller for this class of problems than does an H_∞ con-

emanating from vehicle compression surfaces intersecting the bow shock wave of a cylindrical engine-cowl leading edge.

The vehicle compression surfaces were simulated with a sharp-leading-edge 7.5° wedge and interchangeable 5° or 6° wedges, one of which was mounted approximately 21 in. downstream of the leading edge of the first wedge. The 5° or 6° wedge was translated along the surface of the first wedge and the cylinder was translated horizontally or vertically to obtain different patterns. The tests were conducted in the Calspan 48-Inch Hypersonic Shock Tunnel at a Mach number of 8.0, total temperatures of 2800°R , and a free-stream unit Reynolds number of $1.5 \times 10^6 \text{ ft}^{-1}$.

When the shock-shock interference patterns were determined analytically by constructing pressure deflection diagrams based on oblique shock theory, a new shock-shock interference pattern consisting of concomitant supersonic jets was discovered. The first oblique shock wave intersects the bow shock wave to create the upper supersonic jet, and the second oblique shock wave intersects the transmitted shock wave from the first intersection to create the second supersonic jet. The supersonic jets are separated from each other by a shear layer and from the subsonic flow by shear layers. The heat transfer rate for the concomitant jets is approximately half that of a single jet created when two oblique shock waves coalesce at the bow-shock-wave intersection point.

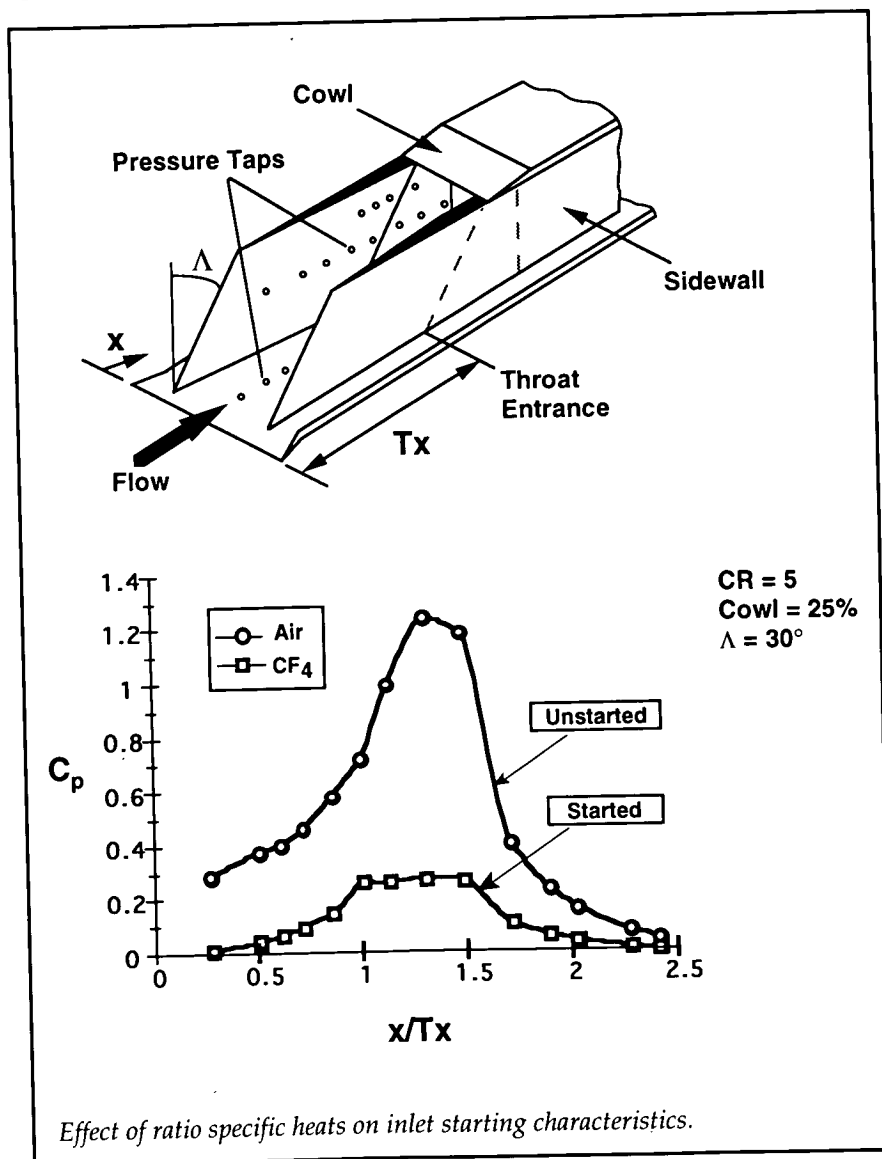
(Allan R. Wieting, 41359)
Structures Directorate

Experimental Parametric Study of a Three-Dimensional Sidewall Compression Scramjet Inlet

Two generic three-dimensional compression scramjet inlets have been tested in Langley's 15-Inch Mach 6 High-Temperature Tunnel and 20-Inch Mach 6 Tunnel to determine the effect of geometry, Reynolds number, and ratio of specific heats on inlet performance

parameters. Two aluminum models with leading-edge-sweep angles of 30° and 70° were instrumented with 45 static-pressure orifices arranged in single arrays along the base plate and sidewalls. Oil flow was used to examine the interior streamlines and schlieren video was used to characterize the inlet spillage.

The most important findings of this study involve the effects of the ratio of specific heats γ on inlet starting characteristics. A



combination of increased contraction ratio (sidewall proximity) and a forward cowl placement induces an unstart in Mach 6 air. Comparison with data previously obtained for this inlet in tetrafluoromethane (CF_4) at Mach 6 indicates that for the same geometry, tested at the same Mach number (6) and Reynolds number ($0.5 \times 10^6 \text{ ft}^{-1}$), the inlet starts in CF_4 ($\gamma = 1.22$) and unstarts in air ($\gamma = 1.4$). The increase in γ results in stronger shocks with steeper shock angles, which are more likely to produce boundary-layer separation on the base plate or to terminate in a Mach reflection at the centerline. Both phenomena can lead to an inlet unstart.

A concern when testing in hypersonic air facilities is the inability to simulate real-gas effects. Testing in CF_4 simulates the decrease in ratio of specific heats observed at high temperatures in air and these results can be useful in assessing inlets tested in air tunnels. From the starting behavior of this inlet in the two test gases, it would appear that if an inlet is started in perfect-gas air, then the presence of real-gas effects, as simulated by a decrease in γ , will not lead to an inlet unstart.

(Kelly Murphy, 47541, and Scott Holland)
Space Directorate

An Engineering Aerodynamic Heating Method for Hypersonic Flow

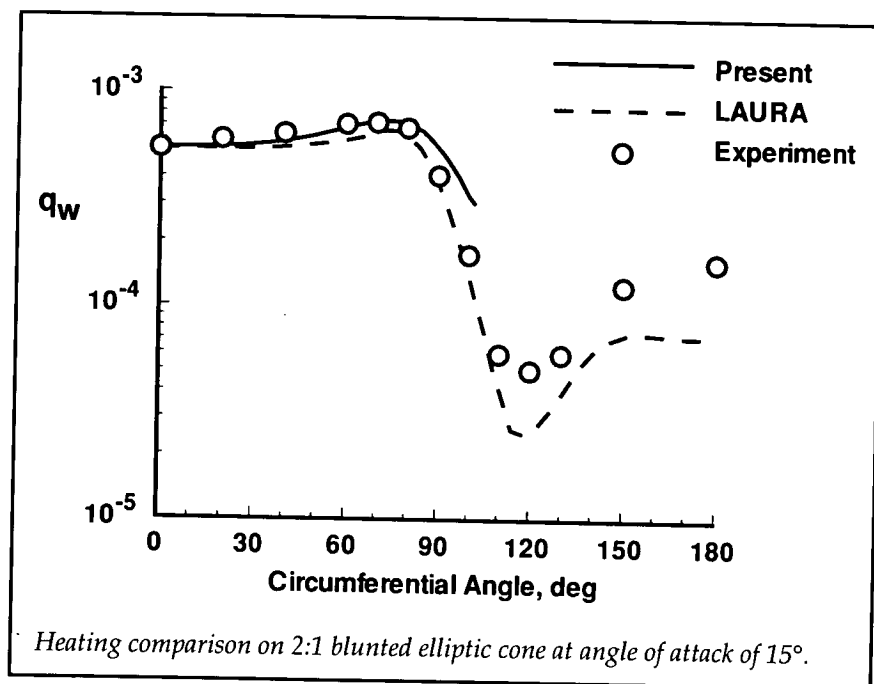
An engineering flow-field method for preliminary aero-

thermal design has been developed by coupling an approximate three-dimensional inviscid technique with a set of convective heating equations. The simplified inviscid method uses an approximate equation for the pressure in the shock layer. It has been demonstrated to yield rapid and reasonably accurate inviscid solutions over axisymmetric and three-dimensional surfaces at angles of attack. Boundary-layer relations are included for perfect-gas and equilibrium chemistry and laminar and turbulent heating calculations.

The present method has been applied to blunted axisymmetric and three-dimensional elliptic cones at angle of attack. Non-dimensional surface heating rates q_w in the windward region of a blunt 2:1 elliptic cone at an angle of attack of 15° are shown in the figure at an axial location of 9.7 nose radii. The free-stream Mach number is 10.19 and the nose radius is 1.0 in. Results from the

present method are compared with results from a thin-layer Navier-Stokes code, LAURA (Langley Aerothermodynamic Upwind Relaxation Algorithm), and experimental data. Good agreement is shown between the present engineering method, LAURA, and experimental data in the windward region. The present technique required only 3 minutes of computer time on a Sun SPARCstation 1 to obtain the solution over the elliptic cone at angle of attack compared with 3 hours for LAURA on a Cray supercomputer. Because of the rapid nature of the present engineering method and its improved three-dimensional capabilities, it is an excellent tool for preliminary aerothermal design.

(Christopher J. Riley, 44387)
Space Directorate

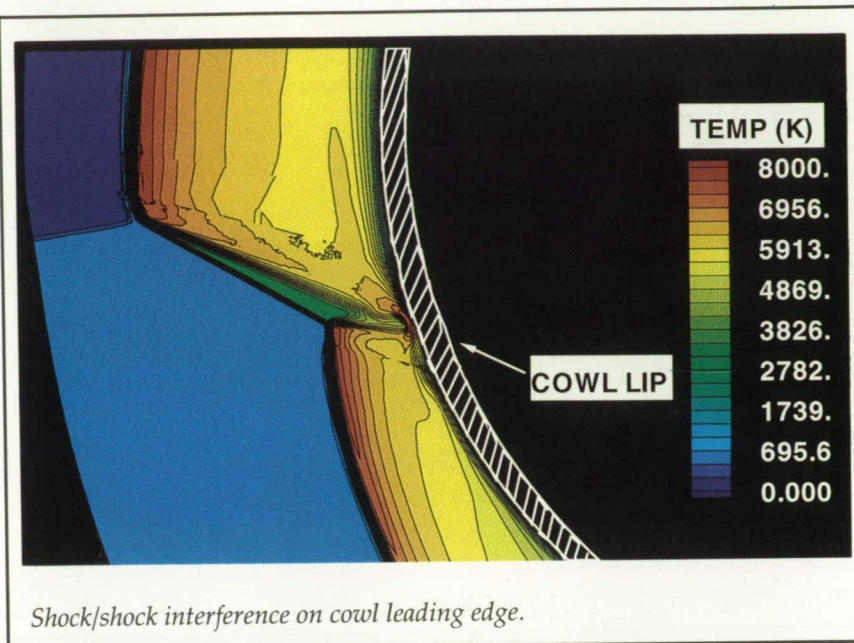


Direct Simulation of a Hypersonic Shock Interference Problem

A complex shock interaction pattern, which results in extremely high surface heating rates, is formed when an incident shock impinges on the bow shock of an engine inlet cowl lip. This shock interaction is likely to occur in hypersonic flight and must be understood in order to predict accurate design loads for hypersonic aircraft. At Mach 15, an altitude of 35 km, and with a cowl lip radius of 0.1 in., the flow will exhibit nonequilibrium chemical processes and may exhibit some rarefaction effects that cannot be modeled with traditional continuum methods. Hence, the direct simulation Monte Carlo (DSMC) technique is used to study this problem.

Although DSMC is typically used for much more rarefied flows, recent advances in the efficiency of the program and in the use of parallel computing techniques made possible this application of DSMC to a complex two-dimensional flow in a near-continuum regime. The advantages of accurate simulation of the flow physics and improved ability to solve complex engineering problems have given the DSMC technique an increasingly important role in the numerical predictions of high-altitude and entry flows.

Temperature contours from the DSMC solution of the shock interference problem are given in the figure. The interference of the weak incident shock with the cowl lip bow shock produces a transmit-



ted shock, a shear layer interaction region, and a supersonic jet of high-temperature gases impinging nearly normal to the surface of the engine inlet cowl lip. The effect of the supersonic jet impingement is to augment the heating of the cowl lip at that location by a factor of 35 over that of the undisturbed cowl lip stagnation heating ($q_w = 530 \text{ MW/m}^2$).

(Ann B. Carlson, 47050, and Richard G. Wilmoth)
Space Directorate

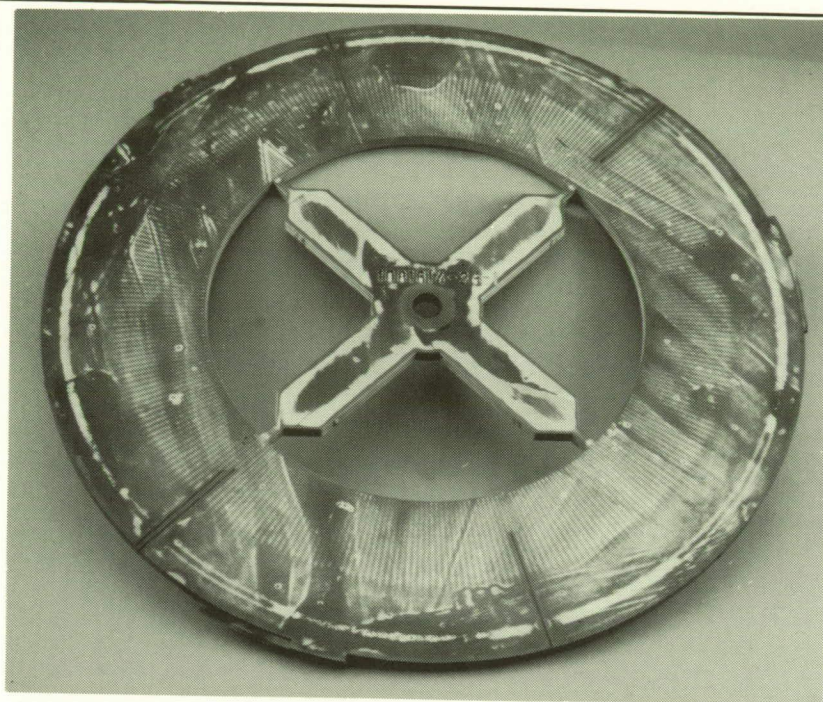
Instrumentation Platelet Sections for 8-Foot High-Temperature Structures Wind Tunnel Nozzle

Major improvements have been incorporated into the bonding and assembly processes for the instrumentation platelet "mini-stack" sections for the 8-Foot High-Temperature Structures Wind Tunnel Nozzle. Langley Research

Center has developed, metallurgically analyzed, and put into operation braze-assisted diffusion-bonded mini-stack platelet sections. This bonding technique is often called "poor man's diffusion bonding" because it offers many of the same advantages true diffusion bonding offers, plus it does not require expensive and elaborate equipment for the process. These new thin mini-stack sections are now comparable in design with the larger diffusion-bonded main body nozzle sections. The thin mini-stack sections are instrumented with thermocouples for measuring the heat index throughout the nozzle and are located between the larger main body sections. This bonding process has resulted in substantial cost savings and faster production of the instrumentation platelet sections in the 8-Foot High-Temperature Structures Wind Tunnel Nozzle.

(Danny A. Barrows, 44504)
Systems Engineering and Operations Directorate

ORIGINAL PAGE
BLACK AND WHITE PHOTOGRAPH



Platelet section for 8-Foot High-Temperature Structures Wind Tunnel Nozzle.

Ti-1100 Matrix Composites Show Good Potential for Lightweight High-Temperature Applications

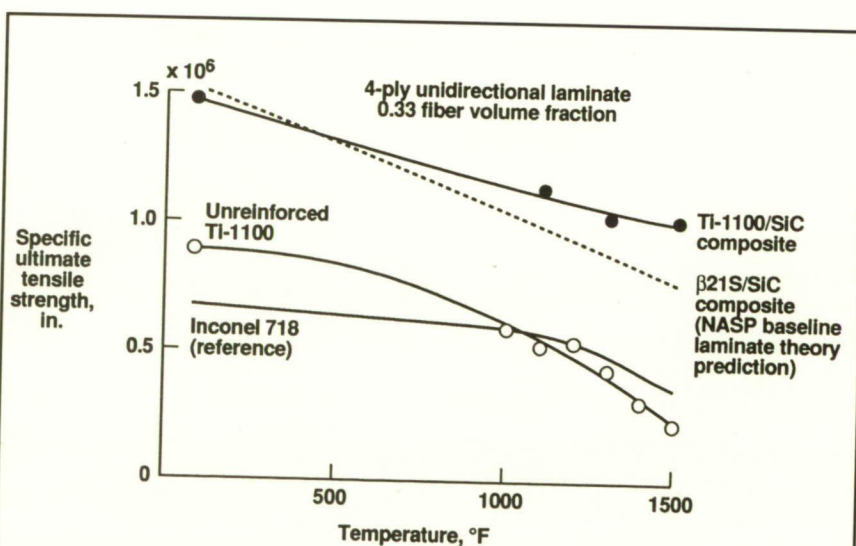
Advanced hypersonic vehicles require lightweight structural materials that can withstand high-temperature service environments. The material Ti-1100 is a recently developed advanced titanium alloy with improved high-temperature capabilities. Reinforcing this alloy with silicon carbide (SiC) fibers results in a lightweight metal composite with good potential for hypersonic airframe applications.

Processing procedures that produce high-quality Ti-1100/SiC composites by the foil-fiber-foil method have been developed for in-house research programs. The

density of the composite is 7 percent less than that of β 21S composites (the National Aero-Space Plane baseline airframe material)

with an equivalent fiber volume fraction and 55 percent less than that of Inconel 718, a conventional Ni-based high-temperature superalloy.

Composite laminates of various lay-ups and fiber volume fractions have been fabricated and tested. The figure shows the specific strength (Strength/Density) of 4-ply, unidirectional Ti-1100/SiC laminates (fiber volume fraction of 0.33) as a function of temperature. Also shown are specific strength data for unreinforced Ti-1100 and Inconel 718 as well as the predicted specific strength for β 21S/SiC composite with the same fiber lay-up and volume fraction as the Ti-1100 composite. Reinforcement of Ti-1100 with SiC fibers resulted in a large increase in specific strength, especially at elevated temperatures. The specific strength of Ti-1100/SiC is approximately 3 times that of Inconel 718 at 1500°F. In addition, the Ti-1100 composite compared favorably with the β 21S composite



Specific strength of Ti-1100/SiC titanium matrix composite compared with other high temperature materials.

at room temperature and exhibited superior strength at high temperatures.

Continued development of Ti-1100/SiC will include the characterization of the composite during long-term exposures to hypersonic service conditions and the investigation of alternate composite processing techniques. (R. Keith Bird, 43512) Structures Directorate

Nose-to-Tail CFD Analysis of NASP 201/21

The objective of this work was to determine the high-speed performance of the current National Aero-Space Plane (NASP) configuration (Vehicle 201, Engine 21) and to verify the performance predictions made by the engine performance deck. Within the NASP program, scramjet engine performance is based on cycle deck predictions. The cycle deck contains various basic component efficiencies and "delta's" to account for secondary effects. These efficiencies are generally based on a two-dimensional analysis for the forebody, inlet, and nozzle and a one-dimensional (1-D) analysis in the combustor. A higher fidelity nose-to-tail analysis is required to check the engine deck solution.

Working with Pratt & Whitney, Langley performed a computational fluid dynamics (CFD) analysis of the NASP 201/21 to investigate the predominant three-dimensional (3-D) effects on scramjet engine performance. Pratt & Whitney performed forebody, inlet, and combustor solutions, and Langley performed additional combustor

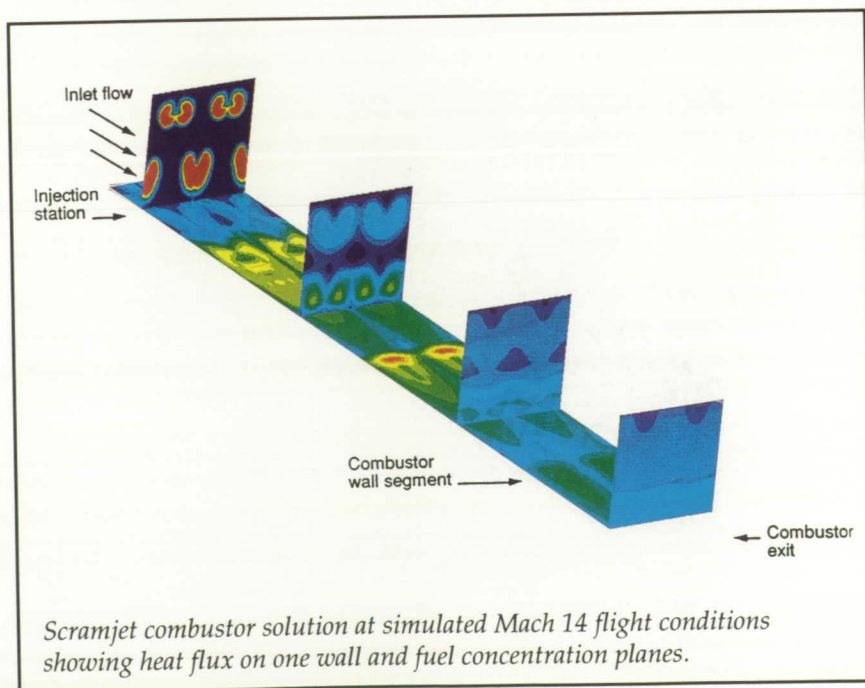
analysis as well as the nozzle analysis. Results of these analyses provided an accurate assessment of Mach 17 engine performance and were compared with engine deck predictions of performance. This comparison identified areas that needed to be addressed by the NASP program, such as the combustion efficiency definition, nozzle performance losses associated with 3-D flow distortion, nozzle nonequilibrium chemistry modeling, and applications of inlet kinetic energy in the 1-D deck. This work was done in part under contract with Analytical Services & Materials, Inc. (Charles R. McClinton, 46253, and Thomas N. Jentink) National Aero-Space Plane Office

NASP High-Speed Injector Design

Langley has actively participated in the Scramjet Engine Redesign

activity sponsored by the National Aero-Space Plane (NASP) National Program Office (NPO). The goals of this activity were (1) to provide X-30 scramjet combustor lines that are compatible with the ramjet lines being developed by the NASP Engine Design Team and (2) to identify fuel-injector designs to optimize scramjet performance. The approach was to first identify the important engine performance indicators and the engine-fuel-injector design parameters for the trade study. Because of the huge number of cases that resulted, a statistical method was applied to determine the minimum number of cases that would have to be examined and yet still represent the full matrix. Langley performed the computations on this reduced set of 145 cases.

These cases represented three classes of injectors: flush wall, ramps, and struts. General Dynamics and Pratt & Whitney provided the inflow profiles for



these cases. Langley performed the computations with the three-dimensional parabolized Navier-Stokes design code SHIP. Each of the solutions required approximately 2 to 4 hours on the Langley Cray computers and most were done with priority. The results were used by the NASP engine companies to develop engine performance models and to select a final configuration for the X-30 combustor.

The figure shows heat flux on one wall of a typical scramjet combustor solution at simulated Mach 14 flight conditions. The fuel concentration planes show characteristic kidney shapes caused by the injector-induced vortices. Red indicates high values, blue low. This work was done in part under contract with Analytical Services & Materials, Inc.

(Charles R. McClinton, 46253, Pradeep Kamath, Marlon Mao, and Paul G. Ferlemann)
National Aero-Space Plane Office

A Theory To Analyze Composite-Stiffened Panels for NASP

A general theory to perform structural analysis of composite-stiffened panels has been developed. The theory efficiently solves panel stiffness and stability and is currently being implemented in the Langley structural-thermal sizing code ST-SIZE for vehicle weight prediction.

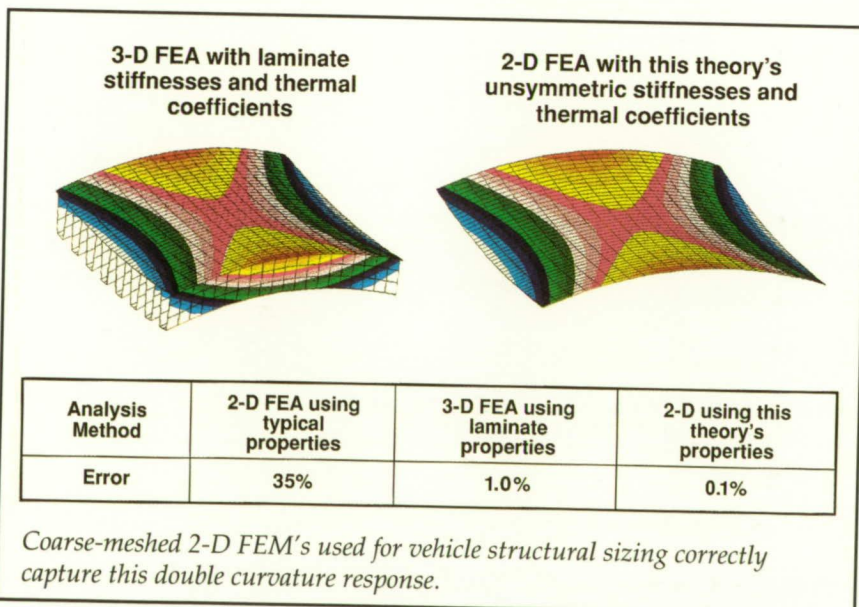
Vehicle weight prediction is based on analytical tools that optimize the entire structure as a system. The structural response of an entire vehicle to flight

pressures and heat fluxes is determined with finite-element analyses (FEA's). Vehicles can only be modeled with two-dimensional (2-D) finite-element models (FEM's) because of their large surface areas. Generally 2-D FEM's are not accurate because of simplifications made in formulating stiffened-panel properties. To obtain accuracy, fine-meshed three-dimensional FEM's are constructed to capture the complex longitudinal-transverse couplings and membrane-bending unsymmetric panel behaviors. Even so, because of high element count, 3-D FEM's are useful only for small structural components. As shown in the figure, 2-D FEM's can be very accurate when this theory's formulation is used.

A 3-D model that has 2400 elements outlining the "hat" shape is 99.0 percent accurate. An 800-element 2-D model that has fully defined stiffnesses and thermal coefficients is 99.9 percent accurate. Color displacement contours of these two correct solutions are shown in the figure. The minimum

number of elements essential to form a 3-D model is 560, yet even with this high element count accuracy drops to 97.2 percent. However, a 2-D model with just one element spanning the same surface area can still obtain an accuracy of 99.9 percent. Without the advanced formulation, 2-D FEM's can only achieve an accuracy of about 65 percent in computed forces, moments, strains, and curvatures.

The theory's accuracy is derived mainly from extending classic lamination theory to composite-stiffened panels to provide (1) accurate orthotropic coupling between longitudinal and transverse panel responses, (2) membrane-bending coupling interaction, and (3) new thermal coefficients to account for panel temperature gradients caused by high heat fluxes on the outer surface. This work was done under contract with Lockheed Engineering and Sciences Co. (Craig S. Collier, 43767, and James L. Hunt)
National Aero-Space Plane Office



The Effect of Film Cooling on Wall Heating in a 2-D Scramjet Nozzle

The scramjet nozzle of airframe-integrated hypersonic vehicles accounts for a large fraction of the surface area, and means for reducing its viscous losses (friction drag and heat transfer) are of obvious interest to designers. An investigation was conducted on the effect of scramjet nozzle geometry and film injection on reducing these losses in a near-full-scale model. The nozzle model was installed downstream of a swept-ramp scramjet combustor model operated at Mach 6 to 7 flight enthalpy inlet conditions, and instrumentation included wall heat flux gages, surface temperature thermocouples, and pressure taps.

Local wall heating rates on the upper (or body-side) surface are shown in the figure and are refer-

enced to the heat flux entering the model. For the case without film injection, the sharp drop in heating rate at $X/L = 0.12$ is due to the rapid drop in pressure as the flow accelerates at the sharp corner. With a film of hydrogen injected immediately upstream of the scramjet nozzle throat, a notable reduction in local heating rates (nearly 95 percent) is apparent. Perhaps more significant is the persistent effect of the film over the entire model length, with an overall reduction in heat flux of approximately 65 percent. These data are the first measurements of nozzle heat flux for the non-uniform, reacting flows expected in scramjet combustors, and they provide a data base for nozzle design and CFD code validations. This work was done in part under contract with Lockheed Engineering and Sciences Co., and Analytical Services & Materials, Inc. (Nathaniel R. Baker, 45427, G. Burton Northam, and Diego Capriotti) Aeronautics Directorate

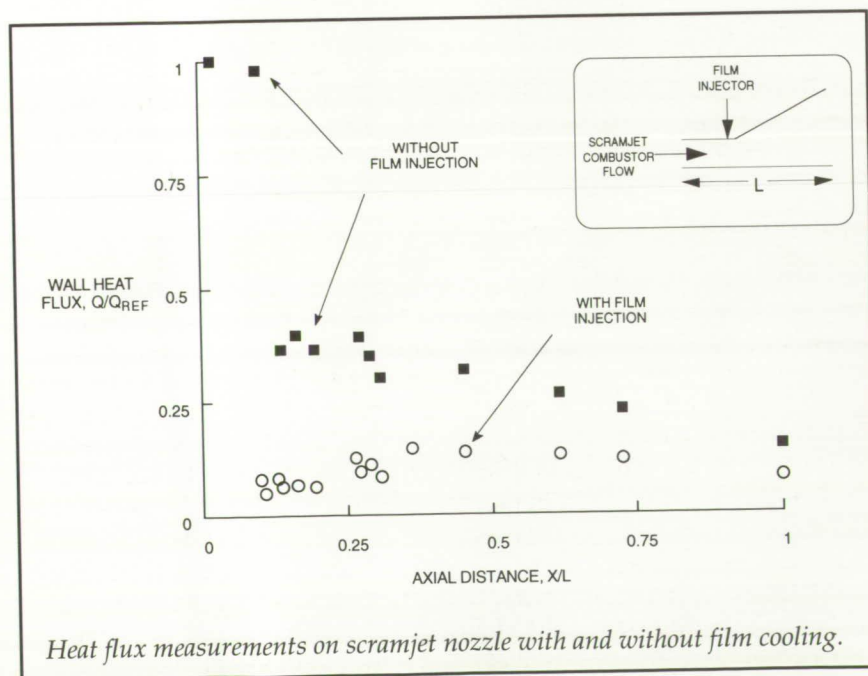
High Mach Number Mixing in a Shock Tunnel Environment

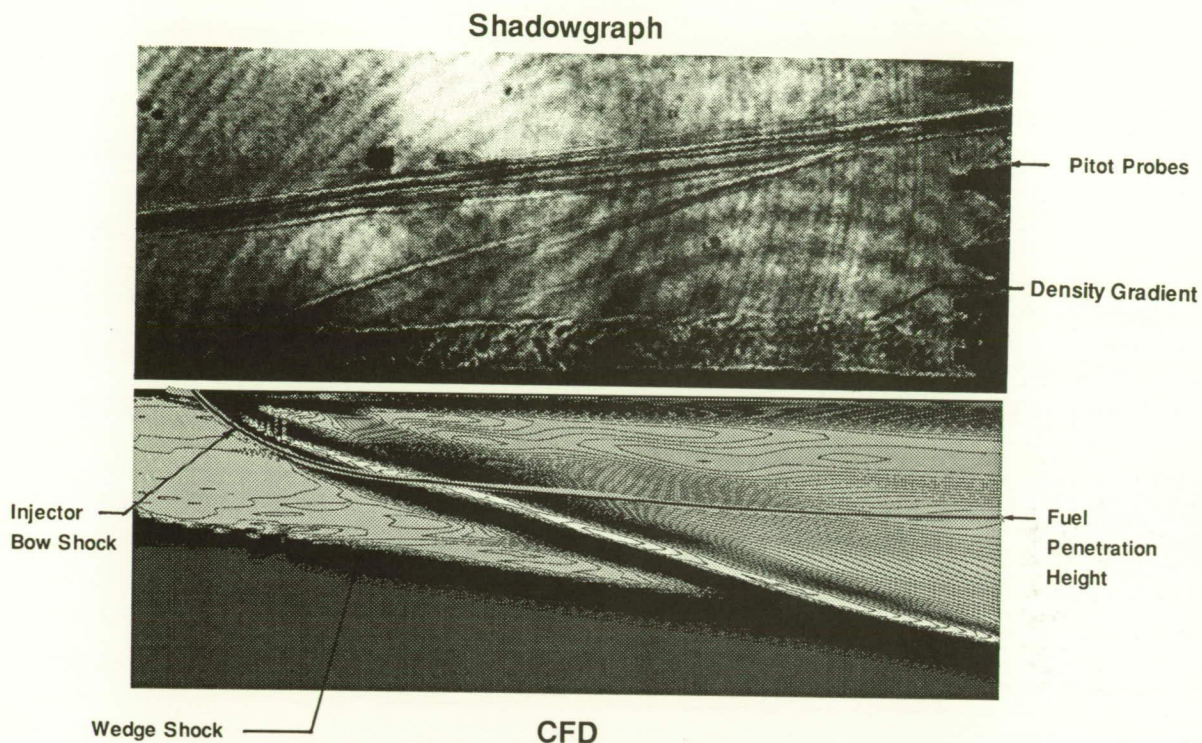
The main objective of this work was to provide pretest and posttest computational fluid dynamics (CFD) support to aid in the understanding of the first series of high-speed scramjet combustor tests in the NASA Ames Research Center 16-Inch Shock Tunnel. The model tested was a wedge angled at 11° to a Mach 5 free stream with hydrogen injected at 30° from the model surface.

The SPARK series of codes were used to model the flow field in this high Mach number environment. Turbulence was modeled with a standard Baldwin-Lomax algebraic approach. Both mixing and reacting cases were solved. A seven-species, seven-reaction mechanism was used to model the kinetics in the problem. The CFD results were compared with all available data from the sequence of tests, including wall pressures, exit pitot pressures, shadowgraphs, and finite fringe interferograms.

The figure shows a comparison of CFD laterally averaged density and a shadowgraph. This comparison shows that the basic flow physics such as the wedge-leading-edge shock and the injection bow shock agree in a qualitative sense. This agreement verifies facility nominal operating conditions. Based on these comparisons, the confidence in the ability of CFD to accurately predict scramjet combustor flow fields has been increased.

The shadowgraph also indicates a turbulent layer near the wall,





Comparison of CFD laterally averaged density contours with shadowgraph.

which on first glance is associated with the fuel mixing layer. A similar feature is observed in the CFD numerically averaged density image, as a region of near constant density bounded by closely spaced contours of increasing density. On further inspection of the numerical results, it was determined that the edge of the mixing region (fuel penetration height), defined by the 0.005 hydrogen mass fraction contour, is much higher than that indicated by the shadowgraph. Accuracy of this CFD prediction was confirmed by comparison with pitot pressure data. A pitot pressure reversal from the third to the fourth probe was accurately predicted by the CFD solution. This work was done in part under

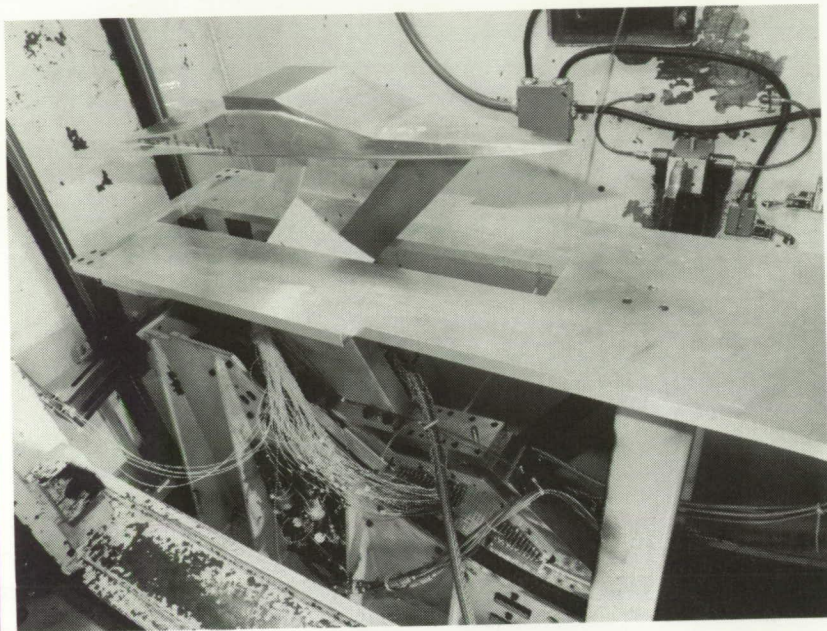
contract with Analytical Services & Materials, Inc.
(Charles R. McClinton, 46253,
and Robert D. Bittner)
National Aero-Space Plane Office

Simulated Powered Tests of the Test Technique Demonstrator at Mach 6

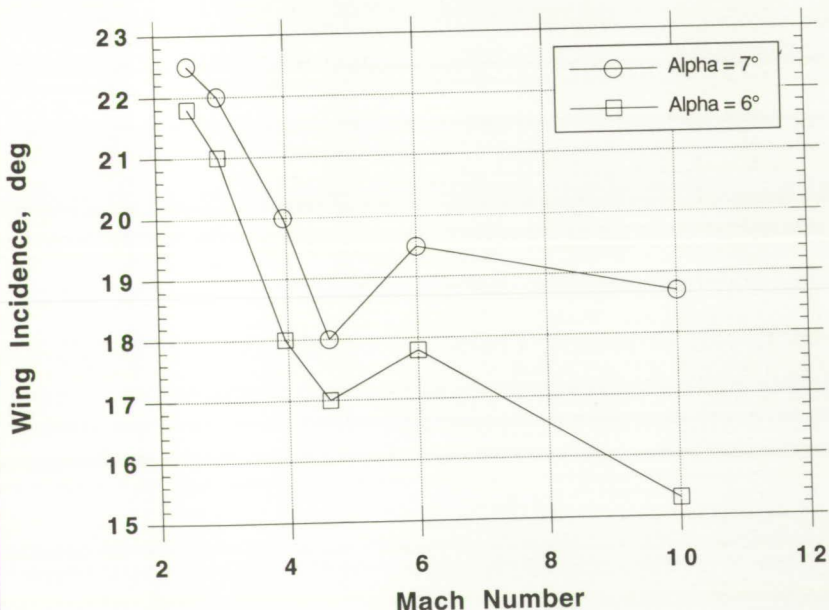
A 2-percent-scale model of the Test Technique Demonstrator, referred to as the Powered Metric Aftbody Model, was tested in the Langley 20-Inch Mach 6 Tunnel as one of the research activities of NASP Government Work Package 5, Hypersonic Powered Model Test Techniques. Actual scramjet

engine operation is impractical in the small-scale models that are required in typical hypersonic wind tunnels. Therefore, a method of simulating the engine exhaust effects is needed for propulsion-airframe integration investigations.

The main objective of this research effort was to determine the effect of using two different gases to simulate the scramjet exhaust. A mixture of CF_4/Ar was used to provide a simulant exhaust gas with a ratio of specific heats γ similar to that which occurs for the combustion products from an actual scramjet engine (1.20 to 1.25). Air ($\gamma = 1.40$) was also used as a simulant exhaust gas to examine the magnitude of the γ effect on the afterbody of the model.



Test Technique Demonstrator Powered Metric Aftbody Model mounted inverted in 20-Inch Mach 6 Tunnel.



Wing incidence for trim versus Mach number for NASP Configuration 201 with engine module.

Force and moment tests were conducted on a metric afterbody mounted on a six-component strain gage balance. Limited afterbody surface pressure data were also obtained from a separate pressure-instrumented afterbody model. The wing contribution to the afterbody forces and moments was determined from wing-on and wing-off tests. Focusing schlieren and oil flow visualization studies provided information on the characteristics of the exhaust flow field. Tests with the two simulant exhaust gases showed that differences in afterbody results were dependent on the nozzle location at which the static nozzle pressure ratio (SNPR) was matched between the two gases. Only minimal differences (less than 5 percent in afterbody force and moment values) were obtained with the SNPR value at the cowl exit location matched for both gases.

(David W. Witte, 45589,
Lawrence D. Huebner, and
William J. Monta)
Aeronautics Directorate

Aerodynamic and Aerothermodynamic Assessment of the NASP 201 Configuration

An extensive effort to assess the aerodynamic and aerothermodynamic characteristics of the National Aero-Space Plane (NASP) Configuration 201 has been completed. This joint effort, under Government Work Package Number One (GWP no. 1), between Langley and the NASP Joint Program Office (JPO) and National Program Office (NPO) as well as the individual NASP

contractors was initiated, models were designed and fabricated, tests were conducted, and data were reduced and initially released to the JPO and NPO in about 6 months. Complete results were presented at the NASP Mid-Term Technology Review in barely 1 year.

A series of 17-in.-long models, representing the ascent-like (engine removed) and descent (engine inlet blocked) configurations, were fabricated for tests in the 15-Inch Mach 6 High-Temperature Tunnel, the 20-Inch Mach 6 Tunnel, and the 31-Inch Mach 10 Tunnel to obtain force and moment data, detailed surface pressure distributions, surface streamline patterns, shock shapes, and global thermal mapping. During this time, the force and moment model was also tested in the Low-Turbulence Pressure Tunnel and the Unitary Plan Wind Tunnel to provide subsonic and supersonic aerodynamics. This work, outside

the scope of GWP no. 1, was conducted in order to have a complete set of aerodynamics on the same model and support system hardware from Mach 0.3 to Mach 10.

Analysis of the descent configuration experimental force and moment data, shown in the figure, indicates that very large wing deflection angles are required for trim at supersonic and hypersonic speeds, and this requirement presents the possibility of high heating loads on the wings as well as reduced lift to drag ratio. Comparison of both force and moment data and surface pressures with results from engineering and computational fluid dynamics codes indicate good agreement between predictions and experiments.

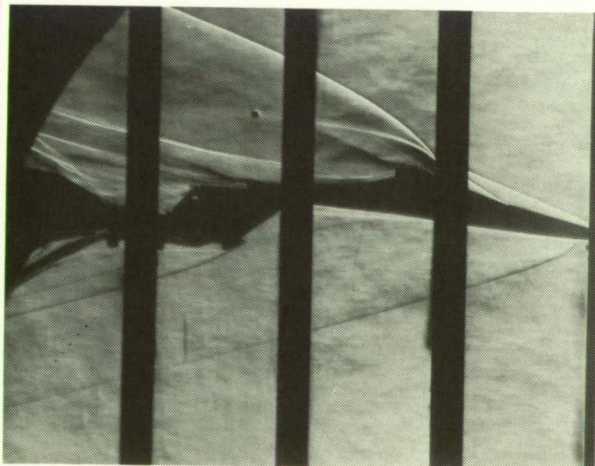
Global thermal mapping results, obtained using the relative intensity thermographic phosphor technique, indicated significant

areas of increased heating on the forebody, inlet, and nozzle, and a series of larger scale models were constructed to examine the detailed effects of nose geometry of this heating. In general, the phenomena observed on the small models were repeated on the larger models, an indication that while the nose and forebody geometry was the cause of the heating, fine details of the nose geometry fidelity were not the causes of the increased heating. (Tom Horvath, 45236)

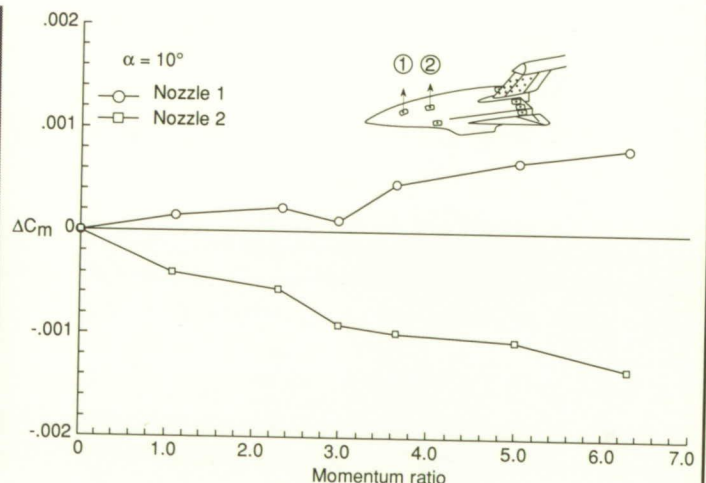
Space Directorate

Interaction of Reaction Control System Plume and Flow Field on Langley Test Technique Demonstrator

Wind tunnel tests were conducted to determine the interaction of



Flow about model showing interaction of forward upper-surface-nozzle plume and flow field.



Effect of longitudinal position on pitching moment interactions of forward upward firing nozzles.

the reaction control system (RCS) plume and flow field on the aerodynamic characteristics of a 0.01-scale Test Technique Demonstrator model. The objectives of the study are to determine (1) the nature and magnitude of the thruster plume impingement and interactions with the vehicle flow field and their effect on the vehicle aerodynamics, (2) the most favorable locations for the thrusters on the vehicle, and (3) the effect of Mach numbers from 2.6 to 10.

To accomplish these objectives, the model was equipped with 13 thruster locations with 4 yaw nozzles, 6 pitch-roll nozzles, and 3 pitch nozzles located in the forebody and afterbody areas of the model. A test has been conducted in the Langley Unitary Plan Wind Tunnel at Mach 4.2 for an angle-of-

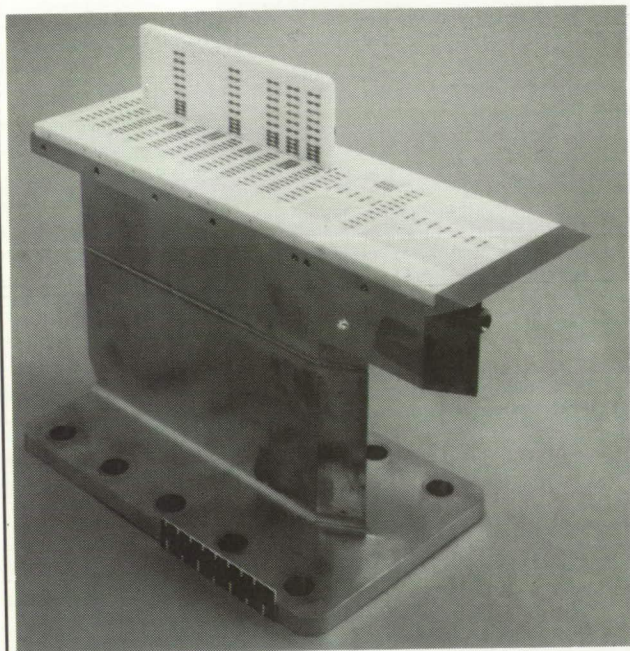
attack range of -2° to 32° at a Reynolds number of $4.0 \times 10^6 \text{ ft}^{-1}$. Mass flows and momentum fluxes simulating much of the entry trajectory were achieved by varying the nozzle chamber pressures up to 1100 psia. Twelve combinations of nozzle locations were tested with the complete model and six were tested with the wing removed. Shown in the schlieren photograph is the interference pattern caused by the exhaust of the most forward upward-firing nozzle at an angle of attack of 10° . The pitching-moment interaction produced by this nozzle was opposite to nozzle thrust moment and decreased its effectiveness (see right part of figure). The nozzle located on the forebody slightly aft of this nozzle produced an augmentation to the thrust. Surface oil-flow or other

flow visualizations will be conducted during succeeding tests to determine the nature of these interactions.

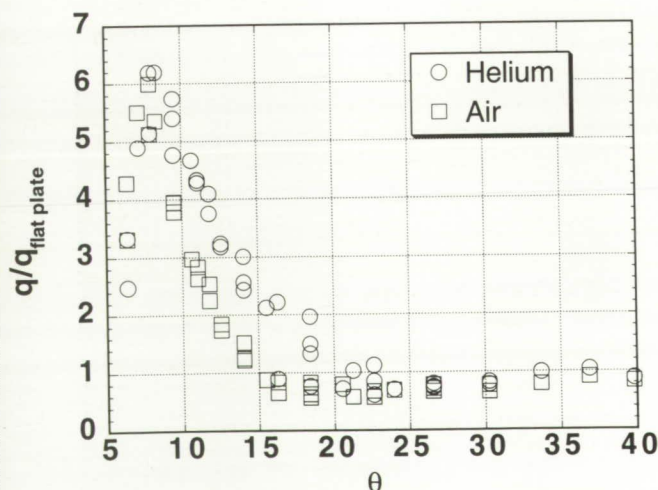
(Gregory J. Brauckmann, 45234)
Space Directorate

Interactions of Swept Shock Wave and Laminar Boundary Layer in Hypervelocity Flows

Experiments have been performed to determine aerothermodynamic heating distributions on surfaces subject to interactions of swept shock wave and laminar boundary layer in hypervelocity flows. Of principal interest in the study was the impact of high-temperature gas thermochemistry



Instrumented flat plate and fin tested in HYPULSE.



Shock-wave-boundary-layer interaction heating rates.

on the interaction. Tests were conducted in the NASA HYPULSE facility (formerly the Langley Expansion Tube) located at the General Applied Science Laboratories in Ronkonkoma, New York. HYPULSE is an impulse-type facility capable of generating high-enthalpy flows that are in thermochemical equilibrium and steady over a 250- μ sec test time. Free-stream velocities are near 17 000 ft/sec, Reynolds numbers are approximately $2.0 \times 10^5 \text{ ft}^{-1}$, and free-stream temperatures are over 2000°R. Test gases of air and helium were employed, with helium providing perfect-gas behavior for comparison with the measurements in air. The photograph shows the ceramic flat plate upon which 156 thin-film temperature sensors were located. The fin was instrumented with 48 sensors and placed at 0°, 5°, and 10° incidence to the free stream.

The resulting shock-wave-boundary-layer interaction produced heating levels up to an order of magnitude greater than heating levels observed for flat-plate laminar-boundary-layer heating. The figure shows the normalized spanwise distribution of heat transfer at several locations on the flat plate as a function of θ , the angle between a ray emanating from the fin leading edge and the free stream for a fin angle of 5°. The data are being analyzed to determine the influence of gas thermochemistry.

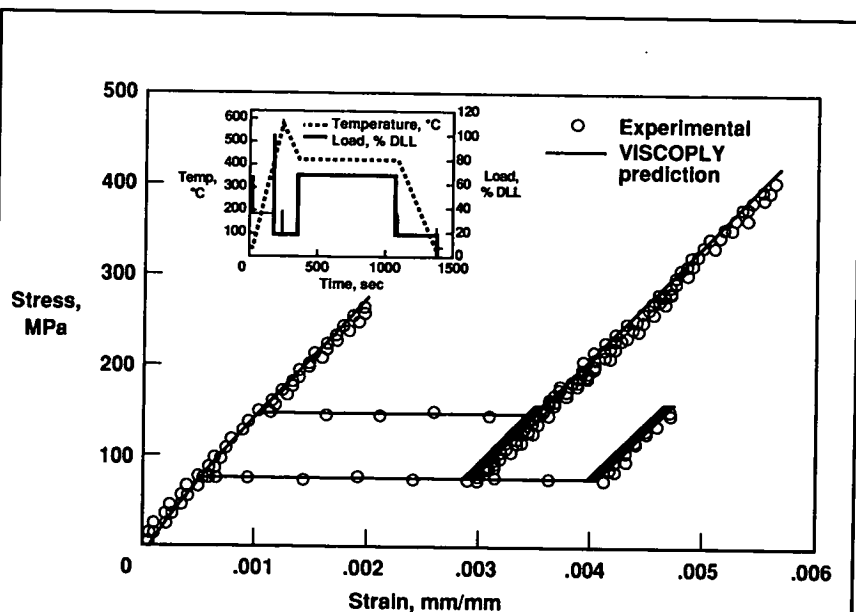
(Charles M. Hackett, 47661)
Space Directorate

Titanium Matrix Composites: Hypersonic Flight Profile Testing and Analysis

Because of the high strength-to-weight and stiffness-to-weight ratios required at high temperatures, titanium matrix composites are leading candidates for structural applications on hypersonic vehicles. The objectives of this research were (1) to experimentally determine the stress-strain response of a [0/90]₂₅ SCS-6/Ti-15-3 laminate during hypersonic flight profile testing and (2) to verify an analysis code (VISCOPLY) that predicts the laminate stress-strain response, including the fiber-matrix interface failure.

A thermomechanical fatigue test capability was developed to apply hypersonic mission profiles (as shown in figure insert) to

coupons of titanium matrix composites. A liquid nitrogen cooling system and an induction heating system were required to achieve precise control of the cooling and heating rates. A micromechanical analysis (VISCOPLY) was used to predict the stress-strain response of the composite subjected to the hypersonic flight profile. The VISCOPLY code is based on constituent properties and uses the vanishing fiber diameter (VFD) model to calculate the orthotropic properties of a ply. The ply properties are then used in a laminate analysis to predict the overall laminate stress-strain response. The fiber and the matrix can both be modeled as viscoplastic with temperature dependency. In the current analysis, the fibers were assumed to remain elastic with temperature-dependent properties and the matrix was modeled as a thermoviscoplastic material. Load-controlled and strain-controlled tests were con-



Measured and predicted stress-strain responses of laminate subjected to particular flight profile.

ducted on the Ti-15-3 matrix at various temperatures (70°F to 1200°F) to determine the viscoplastic matrix material constants required by the material model in VISCOPLY. Temperature-dependent elastic material properties of the SCS-6 fibers were found in the literature. A simple procedure was used to analytically simulate the fiber-matrix interface failure of the off-axis plies known to occur in SCS-6/Ti-15-3; the transverse modulus of the fibers in the 90° plies was reduced by a factor of 10 for stress levels above the stress level corresponding to the observed fiber-matrix interface failure. The measured and predicted stress-strain responses of $[0/90]_{25}$ laminate subjected to the flight profile are shown in the figure. The VISCOPLY program, simulating fiber-matrix interface failure, accurately predicted the stress-strain response of the composite under the flight profile.

The thermoviscoplastic behavior of composites subjected to a complex flight profile can now be experimentally determined. Furthermore, the material stress-strain response can be accurately predicted with the VISCOPLY program. Accurate predictions require accurate characterization of the constituent materials. The fiber-matrix interface failure must be modeled to accurately predict stress-strain response of the composite containing off-axis plies.

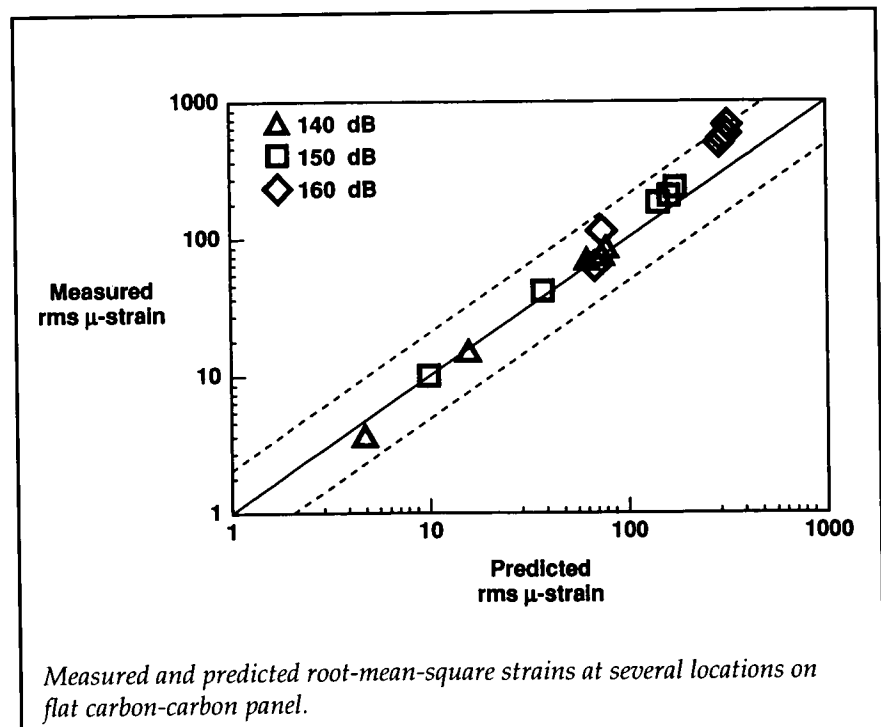
(M. Mirdamadi, 43506, and
W. S. Johnson)
Structures Directorate

Response of NASP-Type Panels to Acoustic Loads

The capability to model the large deflection random response of National Aero-Space Plane (NASP) type panels to high-intensity acoustic load is necessary for the incorporation of fatigue life analysis in their design. This research aims at modeling the acoustic response of a flat carbon-carbon panel and verifying the results with experimental data. A large deflection finite-element code using a numerical integration procedure was developed and used to calculate the acoustic response of a flat 11- by 15- by 0.132-in. quasi-isotropic carbon-carbon panel. The input sound pressure time history was obtained from a series of tests performed on a McDonnell Aircraft Company panel in the Thermal Acoustic Fatigue Apparatus (TAFA). The

spatial distribution of the load over the plate for the numerical simulation was generated to match the grazing incidence of the test apparatus. Response spectra and statistics were computed and verified with experimental strain data from the response tests.

The simulation of the response of the carbon-carbon panel to three excitation levels was carried out with an 18-mode numerical integration of a full-plate model with 112 quadrilateral elements. In addition, 18 torsional spring elements at the boundary were used to model the edge constraint conditions of the experimental test fixture. The root-mean-square strains, shown in the figure, compare very well in the linear response regime at several locations on the panel (140-dB load) but start to deviate in the nonlinear response regime (160-dB load). The nonlinear response is characterized by a broadening



and shifting of the spectral peaks with increasing excitation. The effects of the nonlinearity of the response spectra are an overprediction of the broadening and shifting of the measured spectral peaks. The deviation is most likely due to structure-acoustic interactions not taken into account in the model and is consistent with other published results. The overprediction of the effects of nonlinearity is a topic of ongoing investigation. (Stephen A. Rizzi, 43599, and Jay H. Robinson)
Structures Directorate

inside braze fillets are very small, the strength integrity of the brazed joints was evaluated. Hydrostatic rupture tests on the prototypes have proven that the pressures far exceed the design criteria. The highest rupture strength value observed was 8100 psig. The rupture occurred in the copper base metal and not at the brazed joint.

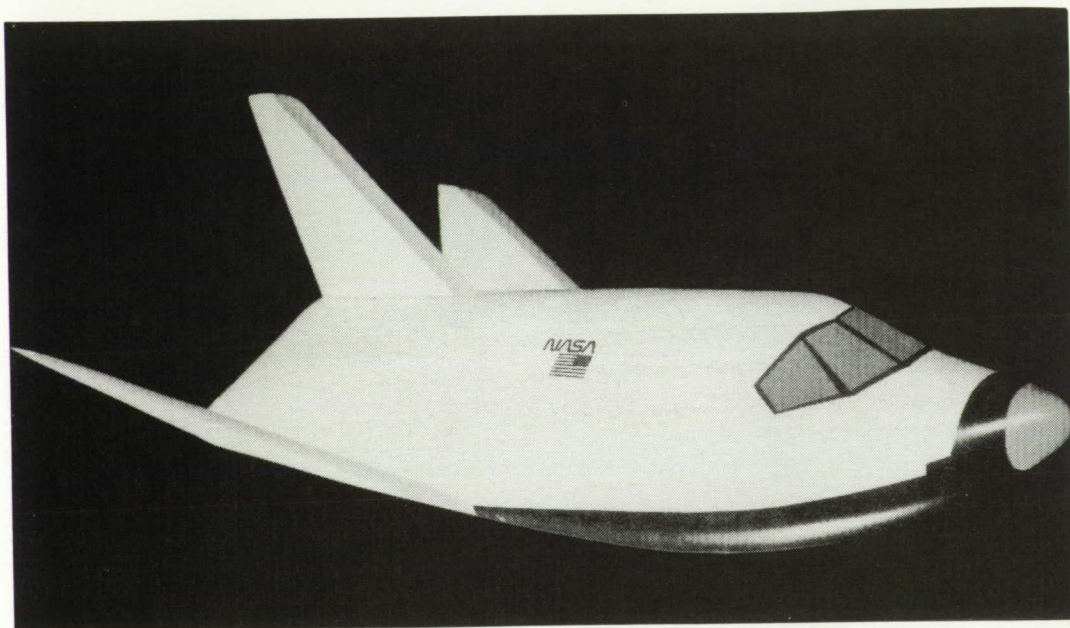
(Danny A. Barrows, 44504)
Systems Engineering and
Operations Directorate

Thermal Measurement Device for Thin-Skin Aerospace Structures

Research and development on test specimens for measuring local heat transfer coefficients and heat fluxes for the cowl leading edge on the National Aero-Space Plane are currently being studied. Several prototype test specimens have been fabricated and final design is under way. At present, very thin copper strips (0.20 in. thick) are brazed into high-nickel-based alloy (Hastelloy) channels and make up one wall on each channel. This technique has produced dependable hardware that can be fabricated with advanced brazing technology.

The brazing is the critical element in the process partly because of the thinness of the copper strip and the goal of no braze alloy inside the test specimen ducts. A significant braze fillet inside the duct may produce unwanted thermochemical and thermophysical loads. Since the

■ SPACE TRANSPORTATION



*Provide technology for the
current and evolutionary Space
Transportation System (STS)
and establish the technology
base for future transportation
system developments*

Near-Net-Shape Aluminum-Lithium Extrusions

The Space Shuttle external tank is constructed with integrally stiffened panels that are machined from thick Al 2219 plates. This fabrication method results in large material scrap rates (85 to 90 percent) and high machining costs, which may be acceptable for low-cost materials. Emerging Al-Li alloys possess improved mechanical properties compared with those of 2219 and have lower densities. Part-for-part replacement of 2219 with an Al-Li alloy could increase performance and payload capacity on account of the improved specific properties of Al-Li alloys. However, for cost-effective application of Al-Li alloys, advanced forming technol-

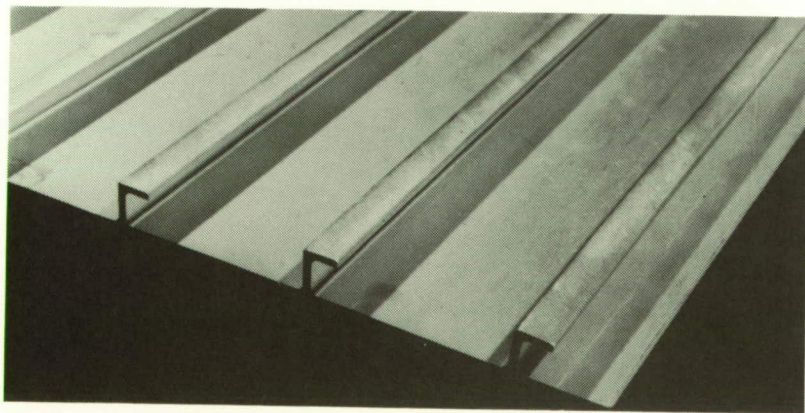
ogies will be required to reduce material scrap rates and machining costs. Near-net-shape extrusions have the potential to reduce the scrap rate to about 15% and make Al-Li alloys viable candidate materials for future low-cost cryogenic propellant tanks.

As part of a collaborative program, laboratories within the United States and the Commonwealth of Independent States (CIS) are evaluating near-net-shape processed Al-Li alloys. Alcoa has supplied the CIS with billets of U.S. commercial Al-Li alloy 2090 for processing in the CIS into a near-net-shape extrusion. The CIS extruded 2090 will be evaluated by a team from government and private industry (led by Langley) and compared with conventionally processed 2090 sheet and plate. A previous program included the CIS Al-Li alloys 1420 and 1421,

which have been used in Soviet applications since the mid-1960's. These alloys are about 12 percent less dense than the current tank material 2219-T87 and have comparable specific strength. The fracture toughness behavior of these alloys was evaluated at Langley by *R*-curve determination, and their resistance to stable crack-ing was equivalent to that of 2219-T87. The use of Al-Li alloys such as 2090, 1420, and 1421 in a near-net-shape extrusion process has the potential to reduce cryo-tank weight and fabrication costs. (J. Wagner, 43132, W. Pollock, M. Birt, and R. Hafley) Structures Directorate

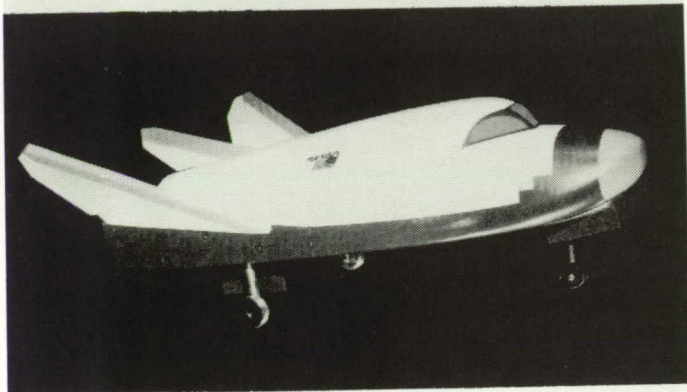
Development of Optimum Configuration for Lifting Body Personnel Launch System

An extensive set of wind-tunnel investigations has been conducted to develop a lifting body configuration that is trimmable and stable over the range of subsonic to hypersonic Mach numbers and that has been optimized for maximum subsonic lift-drag ratio (*L/D*) for approach and landing. A series of configurations derived from the baseline HL-20 were tested in several facilities at Langley at Mach numbers from 0.3 to 10 to determine configuration aerodynamics across this wide Mach

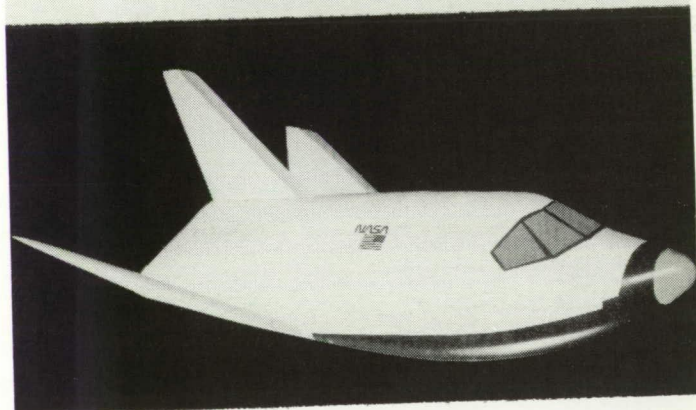


Al-Li integrally stiffened extruded panel.

BASIC HL-20



MODIFIED PLS



Models of basic HL-20 and modified personnel launch system (PLS).

number range. The baseline HL-20 was modified in body camber, nose geometry, and fin geometry to optimize L/D and trim angle of attack at all Mach numbers.

An original set of models were tested in the Langley 7- by 10-Foot High-Speed Tunnel, the Low-Turbulence Pressure Tunnel, the Unitary Plan Wind Tunnel, and the 31-Inch Mach 10 Tunnel. Analysis of this data set led to a second set of modifications to body camber, and those models were tested in the 7- by 10-Foot High-Speed Tunnel and the Unitary

Plan Wind Tunnel. The results of these tests showed that the configuration was trimmable at positive angles of attack, was stable in pitch, and had positive dihedral effect on all Mach numbers tested. The undesirable supersonic characteristic of stable trim points at negative angles of attack for the original HL-20 was eliminated. In addition, the basic subsonic L/D was increased from around 3.5 to about 4.3.

In addition, a series of possible alternative configurations employing variable sweep wings, referred

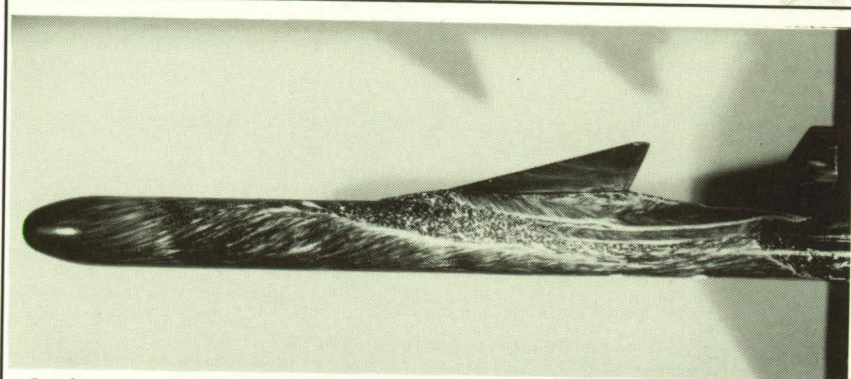
to as HYPER II, and variable dihedral fins have been investigated in order to *really* improve the landing L/D , lift coefficient (C_L), and angle of attack. These alternate configurations could produce an L/D of up to 7 at C_L around 1 to significantly reduce both the approach glide slope and the landing angle of attack.

(Bernard Spencer, 45245, and George Ware)
Space Directorate

Flow Visualization Results on Pegasus Air-Launched Booster at Mach 6

The Pegasus air-launched booster, a commercial launch vehicle built by Orbital Sciences Corporation and Hercules Aerospace Company, is a three-stage, winged booster designed to launch payloads up to 900 lb into low Earth orbit. Because of the airborne launch and lifting trajectory, Pegasus is well suited as a hypersonic test-bed for various studies, such as the Pegasus Crossflow Transition Flight Experiment, which is scheduled to be flown in the fall of 1992. In support of the flight experiment, flow visualization tests were performed to determine possible shock or vortex interactions in the vicinity of an instrumented wing glove that will be flown on the vehicle. A 1/60-scale model of the Pegasus vehicle was tested in the 15-Inch Mach 6 High-Temperature Tunnel at angles of attack from 0° to 5° and at a length Reynolds number of 3.0×10^6 , which is representative of flight conditions.

ORIGINAL PAGE
BLACK AND WHITE PHOTOGRAPH



Surface streamline patterns on Pegasus air-launched booster at Mach 6 and an angle of attack of 5°.

Surface streamline and shock patterns were observed and recorded using oil-flow visualization and schlieren photography, respectively. Results from both techniques show no interactions on the upper wing surface in the vicinity of the glove. However, a complex, vortex-dominated flow field exists on the fuselage beneath the wing at all angles of attack tested. This flow field results from a vortex emanating from the wing root and interacting with the flow expanding around the fairing connecting the wing and the fuselage. At angle of attack, cross-flow separation was observed on the fuselage along the vortex reattachment on the leeward centerline ahead of the fairing apex. Comparisons of the surface streamlines with computed streamline patterns are currently under way.

The flow visualization experiment represents the first ground-based testing performed on the Pegasus configuration, which was designed with only analytical or engineering codes augmented by computational results. Further tests are planned to obtain thermal mapping patterns and force-and-moment data over supersonic and

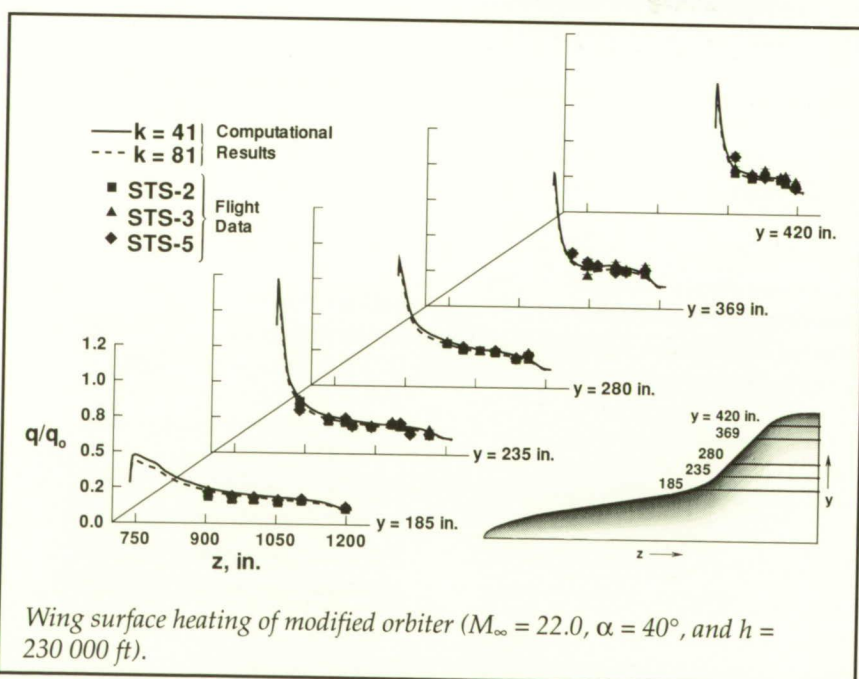
hypersonic speed ranges. The ground-based data will complement and provide a valuable comparison with the computational results and flight data already available for the Pegasus configuration.

(Matthew N. Rhode, 45252)
Space Directorate

Solution Strategies for Three-Dimensional Configurations at Hypersonic Speeds

The design of advanced wing entry vehicles requires the accurate prediction of aerodynamic heating rates during entry. In the design process, "benchmark" computer codes that model the flow process as accurately as possible are used. These codes have computer memory requirements that often exceed the total memory available on current supercomputer hardware.

A study was undertaken to determine a strategy for obtaining "benchmark" solutions based on the memory limits of current computer hardware. The solution over a modified Space Shuttle orbiter configuration was obtained for this study at flight free-stream conditions, with a Mach number of 22, an altitude of 230 000 ft, and an angle of attack of 40°. To

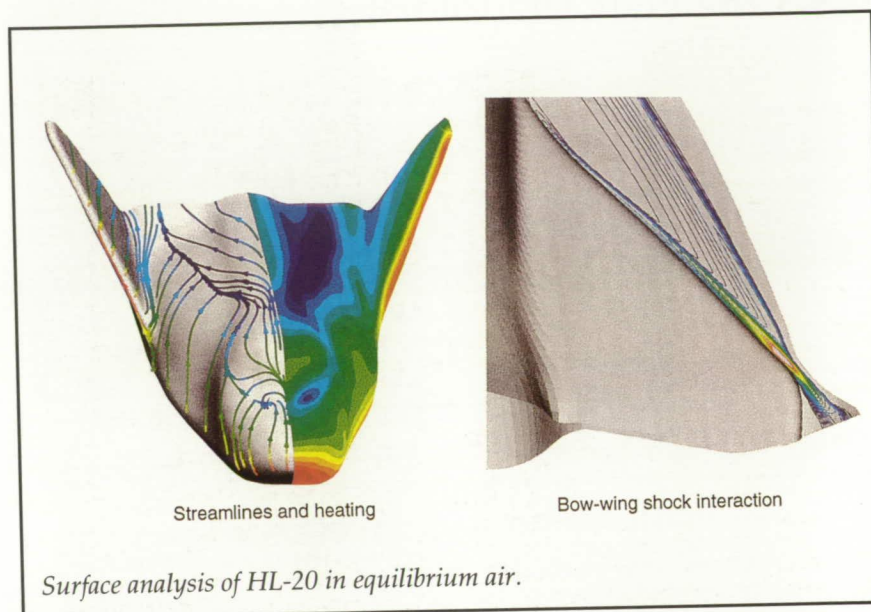


accurately model the flow field at these conditions, the three-dimensional thermochemical non-equilibrium Navier-Stokes equations are solved subject to finite-rate wall catalysis conditions and equilibrium radiation temperature wall-boundary conditions on a computational grid that exceeds 1 million grid points. These requirements translate into a need for memory that exceeds 250 million words.

To reduce the memory requirements of this problem to a manageable size, a procedure based on flow physics was devised to partition the computational space into several blocks. The solution then evolves one block at a time in a sequential order, reducing the memory requirement to a fraction of that needed for the complete flow field. As shown by the comparison of computed and measured surface heating along wing chords on the wind side of the modified orbiter, this procedure has been very successful. The planform view of the vehicle shown in the lower right-hand corner indicates the relative location of the chord lines. At each y location, the computed results are in very good agreement with the data from these orbiter flights. The $k = 41$ and 81 curves represent solutions for low- and high-density grids. (K. James Weilmuenster, 44363, and Peter A. Gnoffo)
Space Directorate

Computed Viscous Equilibrium-Air Flow Over the HL-20 Space Vehicle

Temperatures within the shock layer for space transportation

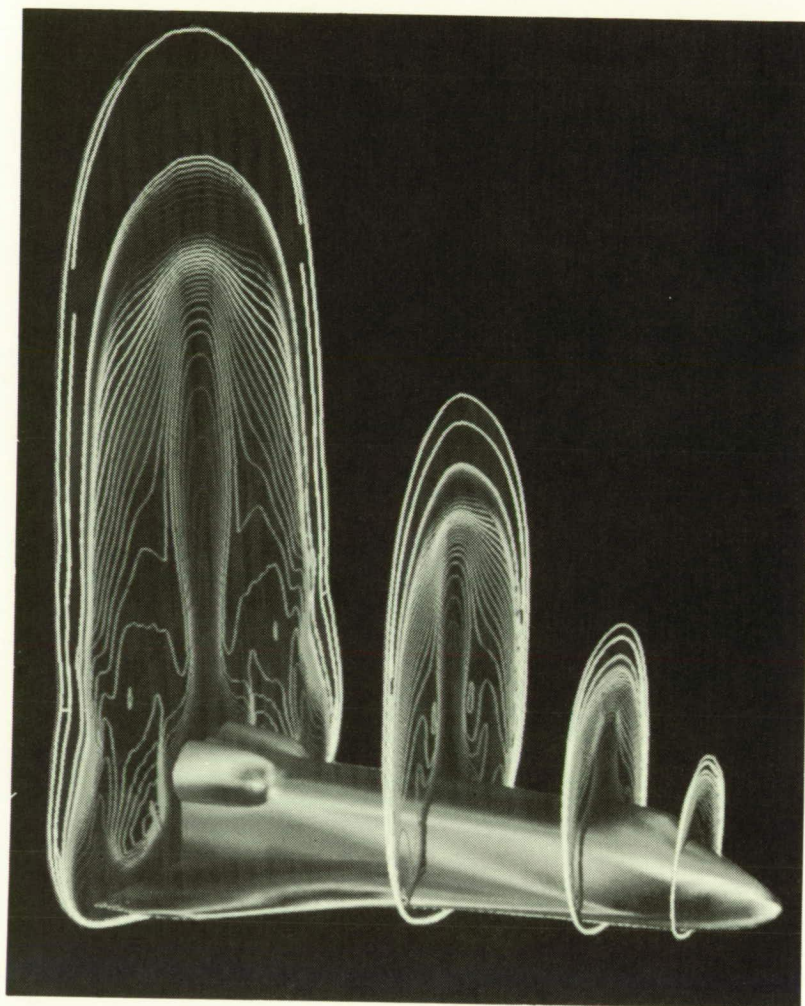


vehicles at reentry conditions will exceed a level at which the effects of aerothermochemistry should not be ignored. Conventional ground-based hypersonic test facilities are unable to reproduce these high-temperature effects at flight conditions and, therefore, cannot provide true flight surface-heating levels or aerodynamics. However, these chemistry effects can be modeled computationally. Significant differences in vehicle aerodynamics, surface heating, and shock interactions have been noticed when the effects of chemistry are included in the flow solver. Such information is important to designers when sizing control surfaces and designing the thermal protection system. To demonstrate that viscous flow solutions over a realistic space vehicle can be obtained under the assumption of chemical and thermal equilibrium, a solution for the HL-20 was computed on a Cray Y-MP by using the Langley Aerothermodynamic Upwind Relaxation Algorithm (LAURA).

Free-stream conditions were Mach 16 at an altitude of 55 km. These conditions were taken from a proposed HL-20 flight trajectory and correspond to the altitude at which peak heating occurs. The angle of attack was 25° . The streamlines are indicative of the complicated flow over the upper surface, with regions of flow separation, reattachment, and stagnation present. The flooded surfaces represent different heating levels. Areas of highest heating are red and lowest are in blue. Contours of density shown in a plane perpendicular to the wing leading edge are used to show the bow-wing shock interaction at the flight condition. (Francis A. Greene, 44381)
Space Directorate

Space Shuttle Orbiter Analysis

The objective of this research was to demonstrate the application



Mach number and surface heating contours of Space Shuttle orbiter during reentry.

of the Langley Aerothermodynamic Upwind Relaxation Algorithm (LAURA) code to compute the flow field about a complete Space Shuttle orbiter configuration at a reentry flight condition and compare computed leeside temperatures with those measured by the Shuttle Infrared Leeside Temperature Sensing (SILTS) experiment and those measured by the Developmental Flight Instrumentation (DFI) thermocouples.

The LAURA code solves the Navier-Stokes equations for thermochemical nonequilibrium flow using a point-implicit scheme to converge the solution. This current version also includes finite-rate wall catalysis and computes surface temperatures based on equilibrium radiation at the wall. The free-stream conditions for the run were for a Mach number of 24, an altitude of 71 km, and an angle of attack of 40°.

A converged solution was obtained over the complete orbiter configuration with a multiblocking strategy. This strategy was used to reduce the memory requirements of the problem to a size compatible with available computer hardware. Computations were carried out on the National Aerodynamic Simulation (NAS) Facility Cray Y-MP computer and required a total of 200 hours of CPU time.

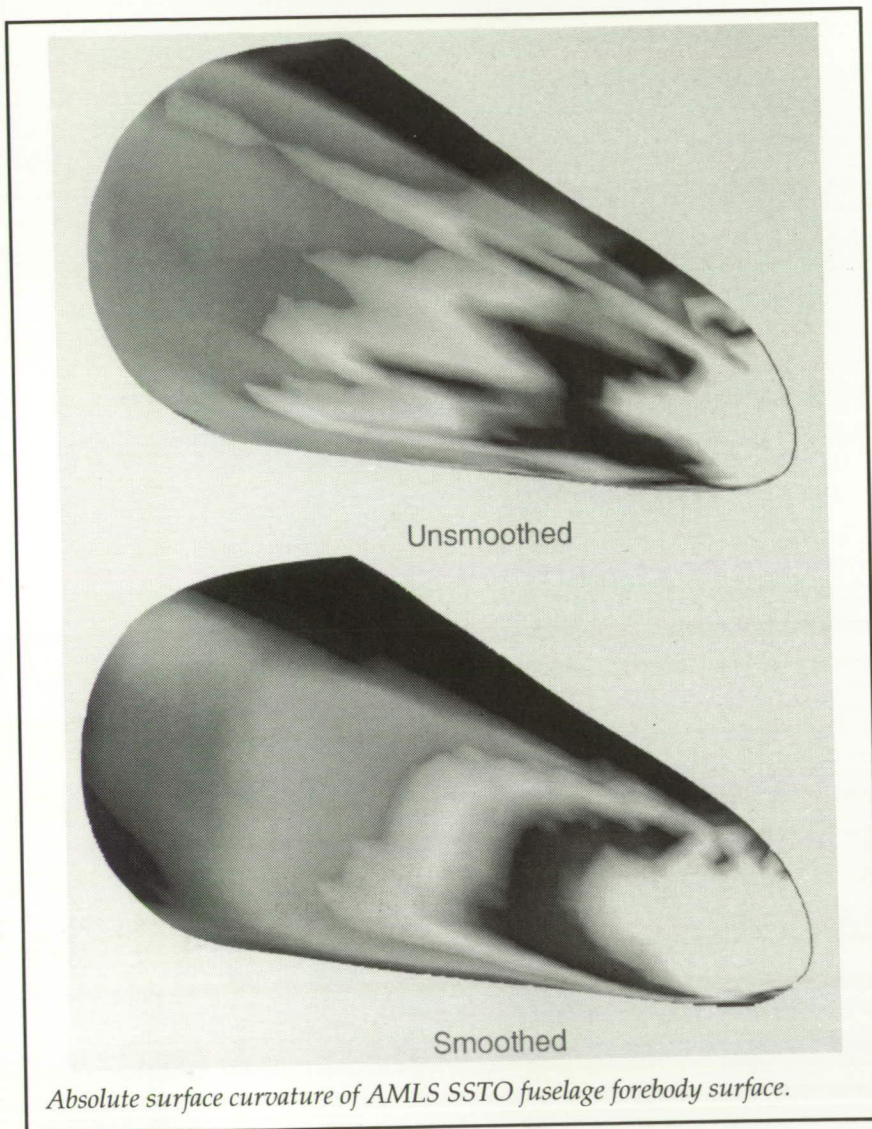
Surface pressures and heating compared favorably with flight data from the DFI. In addition, predicted surface temperatures were in good agreement with those observed in flight by the SILTS experiment. The results of the study show that the LAURA code is capable of handling the flow over a complex configuration such as the orbiter. The figure depicts the complex nature of the flow over the vehicle. In addition, this is the first orbiter solution to combine finite-rate wall catalysis and equilibrium radiation surface temperatures in the wall boundary condition, which represents the state-of-the-art representation of the flow processes at the wall.

(William L. Kleb, 44364)

Space Directorate

Solid Modeling Aerospace Research Tools (SMART) Surface Smoothing Enhancements

Robust surface smoothing algorithms were taken from the literature and incorporated into a geometry modeler for a conceptual aerospace transportation vehicle. This incorporation facilitates the transfer of exact shape definitions



addition, measurable surface quality characteristics based on curvature have been defined. This information is used to increase the automated attribute of the process to reduce user work load and ensure a uniform application of the smoothing techniques from user to user and surface to surface.

When this "numerical putty and sandpaper" was applied to the Advance Manned Launch System (AMLS) single-stage-to-orbit (SSTO) concept fuselage forebody surface shown in the figure, with pointwise deviational tolerances set to 0.01 percent of the locally adjusted arclength, a 4-percent decrease in surface roughness was achieved. The figure graphically depicts the improvement in the global surface quality as measured by absolute surface curvature. (Mark L. McMillin, 44521) Space Directorate

Joint NASA/USAF Airborne Field Mill Program

Following the loss of the Atlas/Centaur-67 unmanned launch vehicle to a triggered cloud-to-ground lightning flash in 1987, new Launch Commit Criteria (LCC) for natural and triggered lightning were developed for all NASA and Defense Department launches. Unfortunately, vehicle-triggered lightning strikes occur under some meteorological conditions that cannot be reliably predicted or readily identified with current instrumentation and techniques. Hence, it is widely suspected that some of the LCC are so conservative as to

to design applications requiring a higher fidelity surface description than was previously available. Generation of computational fluid dynamics grids and computer aided manufacturing cutting tool paths are examples of two such applications. Providing a unified geometric acquisition and manipulation capability enables design modifications to be made once, thus enhancing the efficiency of the overall vehicle design and/or optimization process. The simplified traceability that this affords

ensures data integrity, especially when design efforts span the expertise of multiple organizations.

With the new enhancements, analytic surfaces may be generated from bidirectional meshes of discrete points using cubic B-spline representations. The designer may interactively manipulate input parameters to automated procedures but not the geometry directly. This powerful implementation technique treats the designer as the process controller. In

ORIGINAL PAGE
BLACK AND WHITE PHOTOGRAPH



Lear 28 airplane equipped with airborne field mill instrumentation.

incorporate electrically benign situations. The key atmospheric variables for vehicle-triggered lightning are the magnitude and orientation of the static ambient electric field through which the vehicle is flying. The scientific devices used to measure atmospheric electric field are termed *field mills*. By properly installing and calibrating a set of field mills on an aircraft, it is possible to measure both the airborne electric field in the vicinity of the aircraft and the charge on the aircraft.

The Joint NASA/USAF Airborne Field Mill (ABFM) Program was instituted to better quantify the airborne electric fields in various weather phenomena in order to refine the LCC for natural and triggered lightning. The purpose of the program was to safely relax the existing LCC, thereby increasing launch availability and reducing the chance for weather holds and delays. The Langley Lear 28 airplane, equipped with five airborne field mills provided by Marshall Space Flight Center, collected data during two summer

and two winter deployments from 1990 to 1992. The data flights were flown in the vicinity of Cape Canaveral, Florida, in conjunction with ground-based data and guidance support from Kennedy Space Center and the USAF Eastern Space and Missile Center. A total of 1900 cloud penetrations were made, providing multiple data cases for each of the LCC. Preliminary data analyses indicate that several of the LCC are too conservative and may be safely relaxed. Flight operations in this program have led to a successful methodology for collecting airborne field mill data and for conducting an in-flight ABFM calibration for a Learjet type of aircraft.

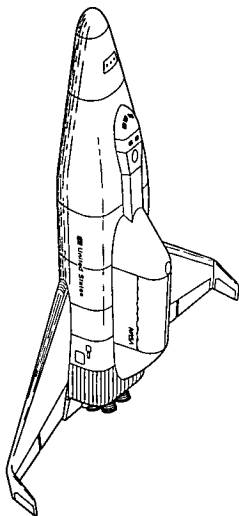
**(Bruce D. Fisher, 43862, and
Richard T. Bright II)
Aeronautics Directorate**

Dual-Mixture-Ratio Propulsion-System Optimization for SSTO Vehicles

Applying advanced technologies to future launch-vehicle designs would allow the introduction of a rocket-powered, single-stage-to-orbit (SSTO) launch system early in the next century. For a selected SSTO concept, a dual-mixture-ratio hydrogen-oxygen engine that employs a number of innovative technologies was chosen as the baseline propulsion system. The dual-mode operation of this engine provides the potential for reducing launch-vehicle dry weights by using high mixture ratios to provide high thrust and high propellant bulk density at lift-off and early in the ascent trajectory and by using low mixture ratios to provide high specific impulse later in the ascent trajectory. However, this approach significantly increases the number of engine and vehicle parameters, making propulsion-vehicle optimization and comparison with similar single-mixture-ratio engines difficult.

For the dual-mixture-ratio engine, seven parameters were selected for study at three levels each, as shown in the figure. A robust Taguchi design method, which uses orthogonal matrices for design-of-experiments theory, was employed to optimize the dual-mixture-ratio and the similar single-mixture-ratio engine with respect to total vehicle dry weight. The methodology developed required 50 trajectory and vehicle sizing runs for the dual-mixture-ratio case and 34 for the single-mixture-ratio case rather than 2187 and

Input Parameters	Values		
	L	M	H
Mode 1 area ratio — AR_1	20	40	60
Mode 2 area ratio — AR_2	60	110	160
Mode 1 mixture ratio — MR_1	10	12	14
Mode 2 mixture ratio — MR_2	5	6	7
Mode 1 chamber pressure — PC_1 , psia	3,000	3,850	4,700
Mode transition Mach number — M_{tr}	1.5	3	4.5
Liftoff thrust-to-weight ratio — T/W_0	1.2	1.35	1.5



Results of dual-mixture-ratio trade for SSTO vehicle.

243, respectively, as required for full factorial design. The optimum levels determined for the dual-mixture-ratio parameters are circled in the figure. The optimum levels for five parameters were determined in a similar fashion for the single-mixture-ratio case. The resulting dry weights of the SSTO vehicle with the dual-mixture-ratio engine and the single-mixture-ratio engine were compared, and the true advantage of the dual-mixture-ratio approach was determined to be 6.5 percent. If a higher weight, near-term technology SSTO vehicle were used, this dry-weight advantage would approach 12 percent because of the increased weight sensitivity.

(Douglas O. Stanley, 44518)
Space Directorate

Advanced Manned Launch System Two-Stage-to-Orbit Concept

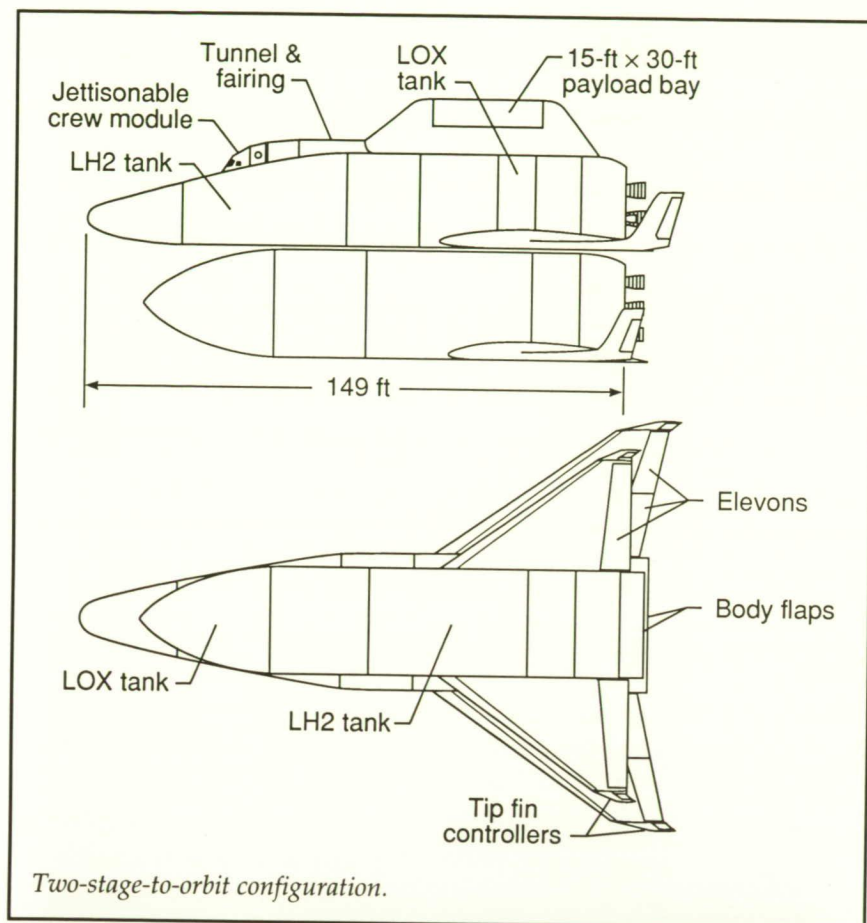
A two-stage, fully reusable Advanced Manned Launch System concept, including the manufacturing and certification requirements, and the operations scenarios have been defined by a team from Langley and Rockwell International. This study was undertaken to identify the complexities and the safety, reliability, and technical issues for such a concept so that life cycle cost estimates could be generated. Space station resupply and crew rotation are the primary missions. The orbiter and booster, which are integral tank designs with external insulation, use currently available advanced materials such as aluminum-lithium and graphite polyimide. The orbiter's thermal protection system is advanced carbon-carbon in the stagnation and leading-edge regions and

durable metallics in other locations. The booster is staged at Mach 3 and therefore does not require thermal protection. The main propulsion system is proposed to be an upgraded Space Shuttle main engine design. The engine will have improved reliability and life expectancy and several components will be replaced with high-strength but lightweight composite materials and use electromechanical actuators. Both vehicles will have engine-out capability.

The concept will have hydrogen/oxygen high-power-density fuel cells, orbital maneuvering system, and reaction control system. Commercial landing gears and avionics components will be used where possible. Many other subsystems will be shuttle-derived devices. The concept will have a health monitoring system and onboard checkout.

Manufacturing plans were developed assuming a year 2000 new start for phase C/D. The resulting initial operating capability is 2011. The development test program must not only detect design flaws but also characterize the life cycle and failure modes of the systems. A lifetime certification approach is recommended in which components are tested to destruction and design margins are increased to ensure that all operations are well within the limits of permanent damage.

The ground processing man-hours were developed from the Airline Transport Association data for the 747 with adjustments for space vehicles. Just under 4000 man-hours should be sufficient to service the orbiter and the booster. Major inspections will occur after every five flights.



about 60 days to process. Using a shuttle approach, the mission operations preparation is estimated to require about 4 months. The processing will be expedited by using standard procedures for the repetitive operations of the design reference mission.

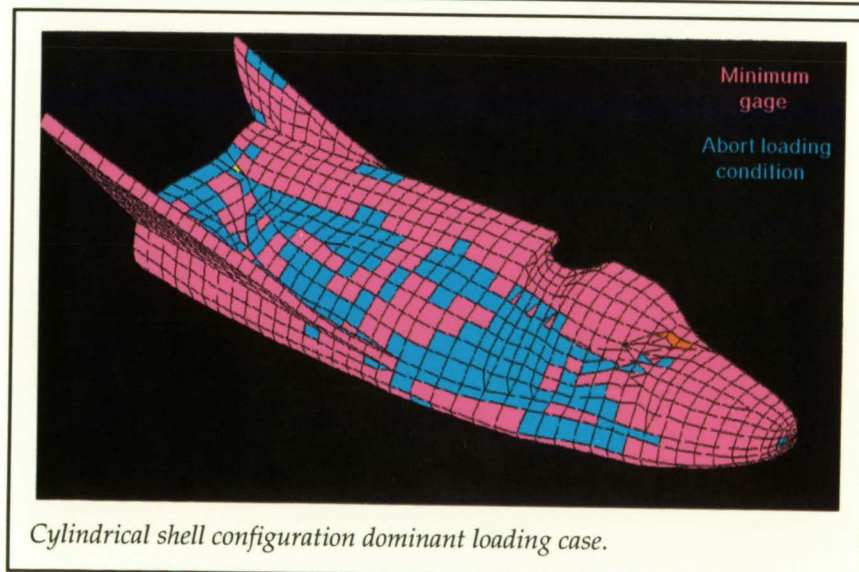
Considerable development of technology is required prior to the initiation of phase C/D in the year 2000, but no major technology break-through is necessary.

(Howard Stone, 44511)

Space Directorate

Structural Analysis of Proposed HL-20 PLS Concept

A structural analysis of a lifting-body concept for a personnel launch system (PLS) proposed by Langley has been performed. The HL-20 PLS concept has evolved significantly from its early configurations. The results of maintenance and operations studies have influenced the new configuration. The original configuration employed a conformal shell, where the exterior surfaces served as the pressure vessel containing both the crew and subsystems. The primary structure of the latest configuration consists of a cylindrical pressurized crew compartment with external frames. The heat shield, access doors, and wings are attached to the primary structure through the external frames. Subsystems are located exterior to the pressure shell, accessible through access panels on the vehicle's exterior.



A 39-day processing flow was developed to support eight flights per year using one booster and

orbiter. The payload container system is decoupled from the vehicle servicing and will require

A complete structural evaluation has been performed on this new

configuration for various design loadings, including ascent, abort, aerodynamic maneuver, and runway bump conditions. Results show the new configuration to be lighter in unit weight but heavier in overall weight. The difference in unit weight can be attributed to a more efficient load distribution in the new configuration. The difference in overall weight can be attributed to the increase in material required to construct an independent crew compartment. The figure is a graphical representation of the critical loading conditions for the individual structural elements in the HL-20 finite-element structural model. As shown in the figure, minimum gage materials are sufficient to sustain most of the HL-20 design loading conditions. Of those panels that required sizing beyond minimum gage, most were sized by the abort condition. These results indicate the new HL-20 structural configuration to be a

conservative design, capable of satisfying mission requirements. (Lance B. Bush, 44514, Deborah M. Wahls, and James C. Robinson) Space Directorate

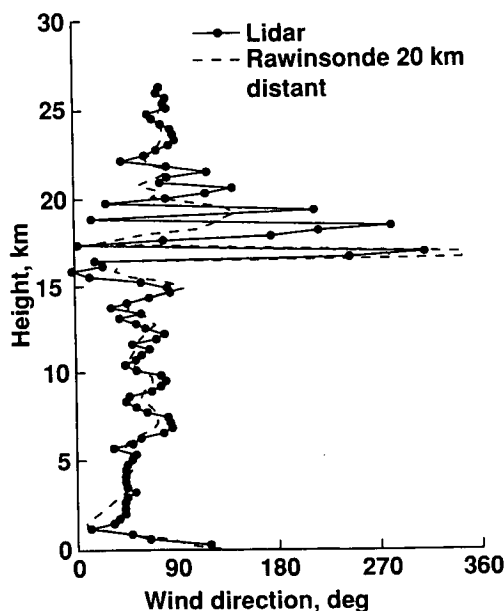
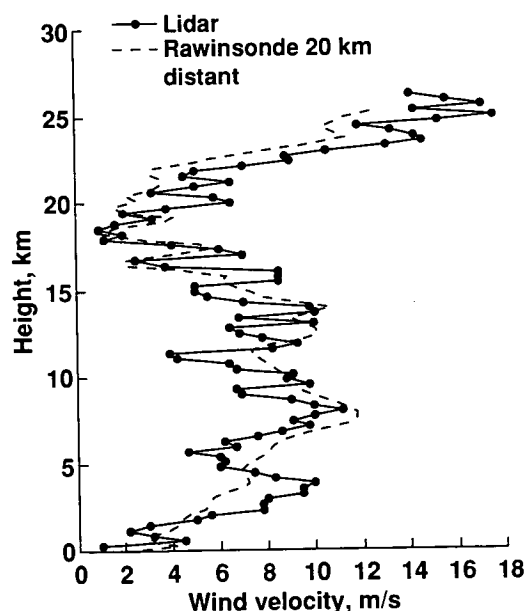
CLAWS: A Real-Time Launch Vehicle Wind Sensor

The capability to accomplish real-time, onboard identification of the atmospheric characteristics in an aerospace vehicle's flight path is an enabling technology for optimal, autonomous flight. Optimality encompasses elements of safety, fuel use, and minimization of elapsed time as they relate to any flight. To realize real-time, autonomous wind profiling, work has been undertaken to define the sensor requirements for a near-real-time wind profiler and to

identify and resolve the system engineering issues associated with its practical use. This system is referred to as the Coherent Launchsite Atmospheric Wind Sounder, or CLAWS.

Studies have shown the relative performance of various wind measurement systems and, in particular, several lidar systems. Performance issues investigated were range, measurement resolution, and the quality of wind measurements in precipitation. Following the definition of system requirements, a breadboard system was designed, built, and tested.

A hardware demonstration and experiments were performed in conjunction with the STS-48 launch and data were coordinated with other wind measurement systems. The figure shows a comparison of wind magnitude and direction data obtained from the lidar demonstration and

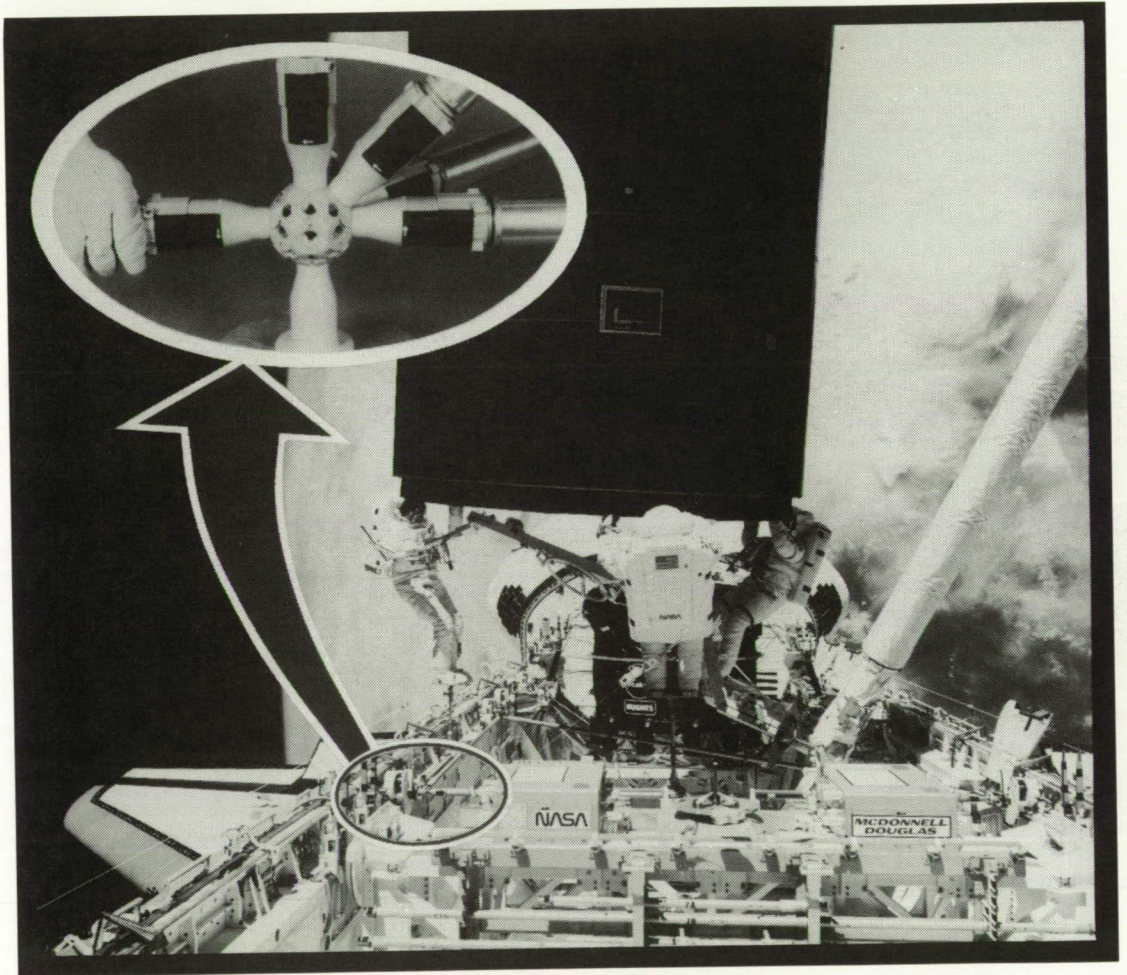


Wind data from lidar and rawinsonde.

standard rawinsonde (balloon) measurements. The lidar measurements were taken from ground level to 25 km in altitude, with a resolution of 300 m. They compare well with the rawinsonde measurements.

The hardware demonstration showed that the CLAWS laser wind profiler system could, in near real time, obtain accurate measurements of wind magnitude and direction. The CLAWS system can provide a complete wind profile in 6 minutes (versus 1 hour for balloons) and is capable of vertical resolution much better than either balloons or the Kennedy Space Center wind radar system. The capabilities of a system based on CLAWS technology could be useful in improving the reliability and flexibility of launch vehicle missions. **(Kevin E. Dutton, 46622)**
Flight Systems Directorate

■ SPACE PLATFORMS



*Provide technology for the
current and evolutionary Space
Station and space platforms and
provide the technology base for
future developments*

Imaging of Flaws in Thin Metallic Plates

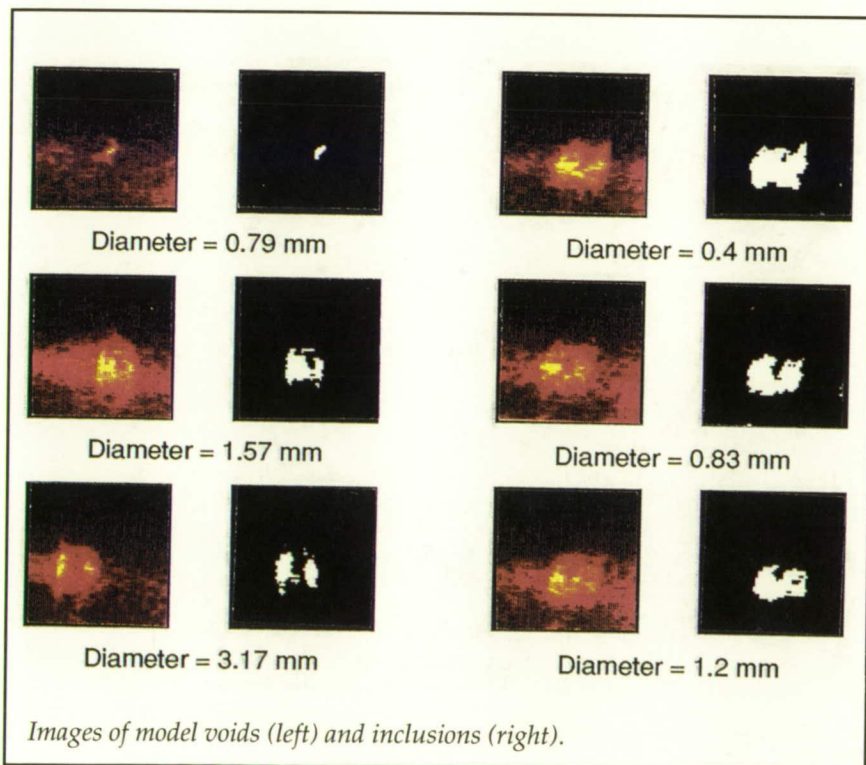
An assessment of the size of flaws (voids and inclusions) is essential for fatigue life analysis of metal plates used for aerospace pressure vessels. Flaws larger than 127 μm (5 mil) in diameter can appreciably shorten the fatigue life of a pressure vessel below the design limits. To improve the current capabilities of nondestructive evaluation, the Bragg imaging technique has been applied with high-frequency (nominally 30 MHz) ultrasonic waves and a helium-neon laser

used to image various flaw models in thin Inconel 718 plate samples.

Following spatial filtering, the laser light beam passes through a converging lens and a water tank and is brought to focus outside the tank. Inside the water tank and at right angles to the axis of the light beam, an ultrasonic wave is generated by a flat-plate transducer. The ultrasonic wave passes through the material being tested and into the region where the laser light interacts with the ultrasound. The ultrasound contains fluctuations, or "holes," which are imaged in the focal plane of the light beam.

The right two columns of the figure show the raw (color) and processed (black and white) images of simulated inclusions produced by partially drilling 1.57-mm-diameter holes through the thickness (model inclusion). The left two columns of the figure show the raw and processed images of model voids created by filling the through holes with styrofoam plastic. These indicate that the theoretical limit of spatial resolution can be achieved. The technique can rapidly detect small flaws in thin material.

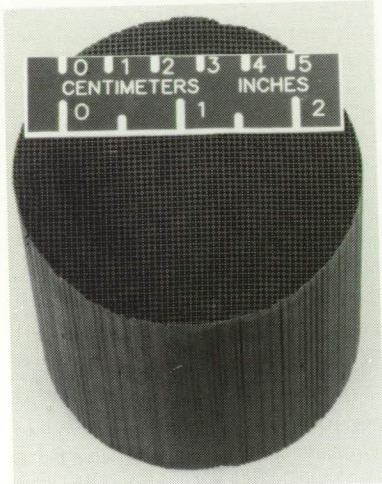
(William T. Yost, 44991, C. G. Clendenin, and M. Namkung)
Electronics Directorate



Ambient-Temperature Catalyst for Space-Based CO₂ Lasers

Space-based CO₂ lasers—such as that currently being developed for the NASA Laser Atmospheric Wind Sounder (LAWS) program—will require a catalyst that recombines carbon monoxide (CO) and oxygen (O₂) at ambient laser temperature. The CO and O₂ are formed by decomposition of CO₂ by the electrical discharge frequently used to energize CO₂ lasers and must be recombined to regenerate CO₂ in order to maintain laser power.

A high-activity catalyst, which consists of promoted platinized



CO oxidation catalyst monolith.

tin oxide on a high-surface-area ceramic-monolith support has been developed at the Langley Research Center. The catalyst has recently been successfully tested in a LAWS laser breadboard tested for 150 million laser pulses. The catalyst is applicable to commercial as well as space-based lasers and is also capable of converting toxic CO to nontoxic CO₂ at room temperature for air-purification applications. (Billy T. Upchurch, 44750, and David R. Schryer) Electronics Directorate

Conceptual Design of a Large-Aperture Microwave Radiometer Geostationary Platform

An understanding of the physical and chemical processes that govern the global environment has been set as a priority by numerous national and international committees. The application of space-borne microwave remote-

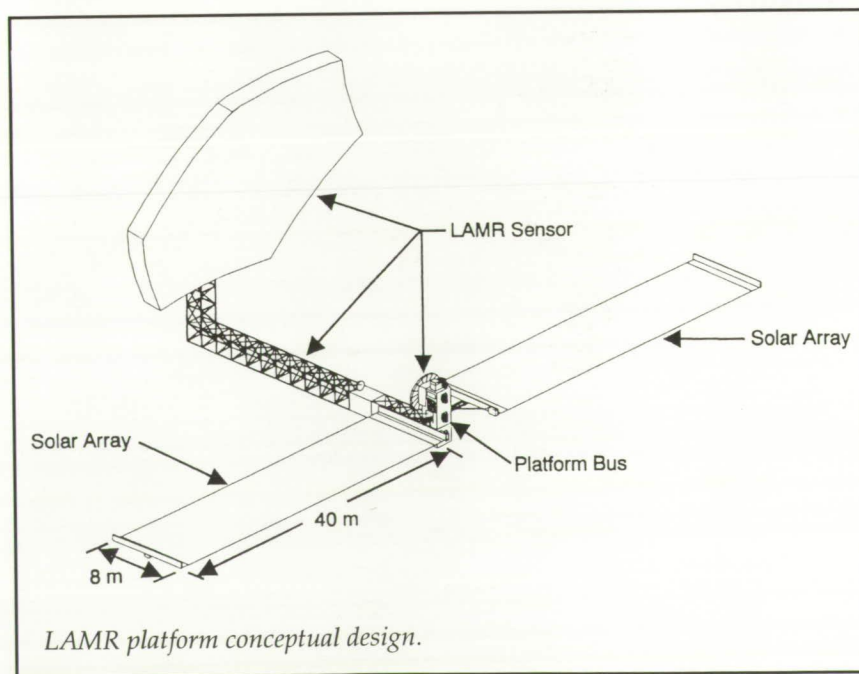
sensing technology will provide the needed information on rainfall, wind speeds, surface temperature, and many other atmospheric measurables. These measurables will help scientists understand the atmosphere and man's impact on it. An advisory group to NASA, the Large Space Antenna Science Benefits Panel, stated that most of the research related to atmospheric and surface processes could be accomplished from geostationary orbit using a minimum antenna aperture of 25 m. The objectives of this study were threefold:

- (1) integrate ongoing Office of Aeronautics and Space Technology (OAST) microwave antenna sensor activity into a flight mission,
- (2) establish a viable conceptual design for a large-aperture microwave radiometer (LAMR) and supporting platform, and (3) identify enabling technologies in the area of space platforms.

The LAMR platform conceptual design is shown in the figure. The

platform is dominated by the 28-m primary reflector of the LAMR sensor. The platform bus uses ion propulsion to raise the platform from low Earth orbit (LEO) to geostationary Earth orbit (GEO). The conceptual design uses idium phosphide based solar cells in two 40-m by 8-m solar arrays to deliver the 80 kW of electrical power needed by the ion propulsion system. The platform is stabilized in the three axes.

The third objective of this study was to point to technologies and technology areas that are essential to the design of an on-orbit viability of the LAMR platform. Those technologies that must be developed to ensure viability of the LAMR mission include advanced radiation-resistant solar cells, integrated complex structures, large segmented reflector panels, large antennas with areal density less than 3 kg/m², and electric propulsion systems. Technology areas that would enhance the



capabilities of the LAMR platform include electrical power storage, on-orbit assembly, and on-orbit systems checkout and correction.

(Richard A. Russell, 41935, and Paul A. Garn)

Space Directorate

Continuous Orbiter Utilization at Space Station Freedom

Space Station *Freedom* requires an assured crew rescue vehicle (ACRV) to be available for crew evacuation when the station is permanently manned. A proposal to utilize a modified shuttle orbiter as an ACRV was studied both from a station and from an orbiter impact point of view. An orbiter would be continually present at the station for periods of up to 90 days; it would then be replaced by another orbiter prior to leaving the station. This requirement dictates that two orbiters be

accommodated at the station at one time. The impacts with respect to flight characteristics and system functionality were determined for several points in the assembly sequence. Flight characteristics studied included mass properties, flight attitude histories, control requirements, microgravity environments, and reboost requirements. System functionality impacts addressed included power generation, thermal control system, communications and tracking, data management, logistics, orbital debris, and structures.

All configurations studied could be controlled with the station's four control moment gyros (CMG's) but had characteristically large flight attitudes and large orbital attitude deviations. Some adjustments to the baseline station CMG control laws and adjustments in orbital altitude were necessary to ensure that these configurations could be controlled with four CMG's.

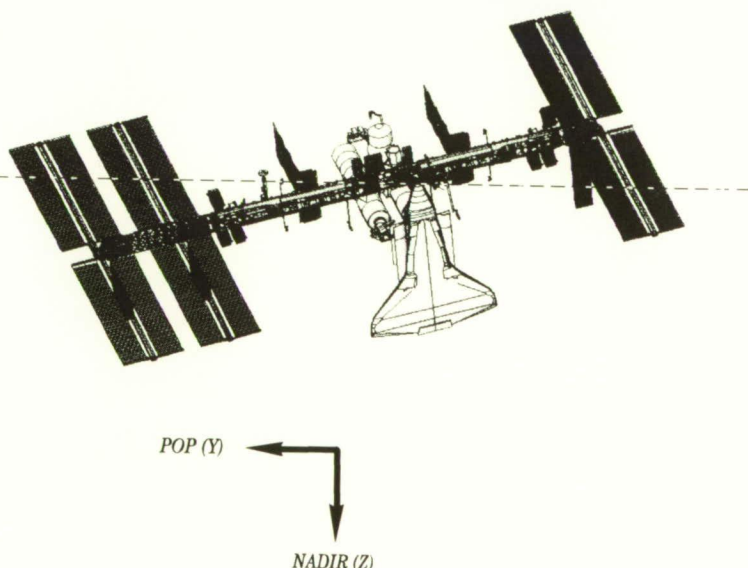
Station systems were directly affected by the large flight attitudes of the combined station-orbiter configurations. Communications, thermal rejection, debris protection, and navigation were somewhat degraded as a result of the off-nominal flight attitudes.

(Patrick A. Troutman, 41954)
Space Directorate

Restructured Space Station Freedom Flight Control Characteristics

Following an intense 3-month effort involving participation by all the work package centers, Space Station *Freedom* was restructured to reduce costs and on-orbit extravehicular activity (EVA) required for assembly and maintenance. The major changes to the structure involved replacing all the erectable truss elements with a preintegrated truss and reducing the permanently manned configuration (PMC) power requirements from 75 kW to 56.25 kW. The latter change resulted in an asymmetric design whereby two pairs of photovoltaic (PV) array pairs are located starboard of the pressurized volume, while only one pair resides on the port side. In view of these structural modifications, an assessment of the restructured station was performed to ascertain the flight control characteristics.

The torque-equilibrium-attitude (TEA) and angular-momentum control requirement were determined for the entire 17-flight assembly scenario. Two environments were simulated: the so-called nominal environment,



Freedom with attached orbiter (view along velocity vector).

where a 220-n.mi. altitude with a 2σ -atmospheric density profile was simulated, and the design environment at an altitude corresponding to a lifetime of 180 days to 150 n.mi. (i.e., altitude from which it would take 180 days to decay to 150 n.mi. if no station keeping were performed). Selected configurations were assessed with an attached orbiter.

Although no clearly superior configurations were identified, the following observations were noted:

1. Stages 6 to 9 require large yaw bias angles and 3 to 4 control moment gyros (CMG's) to control under-design conditions.

2. Large pitch flight altitudes exist beyond stage 11 even in nominal atmospheres strictly because of the inertia properties.

3. Somewhat surprisingly, CMG attitude control is achievable at 150-n.mi. altitude provided the PV arrays and radiators are locked and feathered.

4. Steady-state microgravity within the pressurized laboratories was less than $3 \mu\text{G}$ throughout the stage assembly.

5. Attitude oscillations and rates were well within the Program Document Requirements (PDR) prescribed requirements throughout the stage assembly.

6. No steady-state attached orbiter problems were identified; however, berthing and reaction control systems and CMG handover procedures need to be studied.

(Patrick A. Troutman, 41954, and Michael Heck)
Space Directorate

Reaction Wheel and Magnetic Torque Attitude Control

The attitude control of articular spacecraft in Earth orbit is usually performed with reaction control system (RCS) jets, angular-momentum exchange devices such as momentum wheels, reaction wheels or control moment gyros (CMG's), and/or magnetic torquers. The RCS consumes propellant and causes in-orbit pollution. On the other hand, angular-momentum exchange devices and magnetic torquers are clean and require only modest amounts of electric power.

Angular-momentum devices can be used to generate large amounts of attitude control torques, while the torque generated by magnetic torque rods is constrained by size and weight. Moreover, the magnetic torque direction is restricted by the Earth's magnetic field. To prevent saturation of the reaction wheels or CMG's in the presence of bias disturbance torques, continuous momentum management is required. This momentum management can be provided by gravity gradient torques or by magnetic torques. An attitude control-momentum management concept with reaction wheels and magnetic torque rods has been successfully implemented and tested for selected articular spacecraft in low Earth orbits (LEO's) and in geosynchronous Earth orbits (GEO's).

Consider an Earth-oriented spacecraft in circular orbit. The attitude of the spacecraft with respect to the local vertical local horizontal (LVLH) may be commanded or the spacecraft may be

allowed to seek its natural torque equilibrium attitude (TEA). A proportional-integral-derivative (PID) controller is used to track the commanded attitude. Cyclic disturbance rejection filters in attitude emphasis mode are also used to attenuate the effect of such disturbing torques on the attitude channels. The gains for the PID controller are obtained by using a regional pole-placement technique. The current carrying coils of the magnetic torque rod interact with the geomagnetic field to produce a torque vector. The current magnitude along each axial coil can be controlled such that the magnetic torque produced at a given instant of time is as close as possible to the reaction wheel torquer command. Therefore, the reaction wheel only needs to provide the residual control torque required and thus reduces, and in some cases eliminates, momentum buildup. If the spacecraft is allowed to seek the TEA, then momentum management using gravity gradient torques can be performed by putting soft constraints on the reaction wheel momentum and torque. No magnetic torquers are used in this control scheme.

(Richard A. Russell, 41935)
Space Directorate

Minimum-Time Space Station Reboost

The aerodynamic drag forces experienced by Space Station *Freedom* in low Earth Orbit (LEO) will cause continuous decay of altitude. This loss in orbit altitude is regained by performing a reboost operation by means of reaction control system jets. It is

desirable to perform the reboost in minimum time, use minimum propellant, and accurately acquire the target orbit. This study concentrated on obtaining open-loop time-optimal trajectories that hit the target orbit with zero error. The current (PDR) Space Station *Freedom* reboost strategy assumes a two-switch (burn-coast-burn) strategy for attaining the final circular target orbit. In this study, the nonoptimality of the two-switch control scheme is established for the minimum-time problem for arbitrary initial and final orbit altitudes. The only control variable is the thrust magnitude, with the direction assumed to be along velocity vector. Optimal control theory is used to obtain time-optimal control solutions to the orbit transfer. A mathematical proof that intermediate control or singular control is nonoptimal for this problem is derived by analyzing the Kelley condition. This implies that only two-switch control can be time optimal. The resulting two-point boundary value problem obtained from applying rigorous optimal control theory is solved using a Newton method and a state-of-the-art integrator that can stop and restart integration at every switching point. The optimal thrust history has a six-switch control logic for a reboost from a circular orbit of 109 n.mi. to 220 n.mi., assuming a maximum thrust level of 222 N and a total constant mass of 104 036 kg.

Total reboost time required for the six-switch maneuver is 15 672 sec (approximately three orbits), which is less than the 15 691 sec taken by the two-switch strategy. This 19-sec time savings, even though small, establishes the non-optimality of the burn-coast-burn

scheme for time-optimal reboost of Space Station *Freedom* over a typical reboost altitude range. The total burn time for both the strategies are the same, an indication that fuel expenditure is unchanged by choosing the time-optimal strategy over the current burn-coast-burn strategy. Moreover, the boundary value solver can be used real time for the optimal closed-loop guidance of the space station. This numerical scheme is currently being tested for robustness.

(Richard A. Russell, 41935, Renjith R. Kumar, and Hans Seywald)
Space Directorate

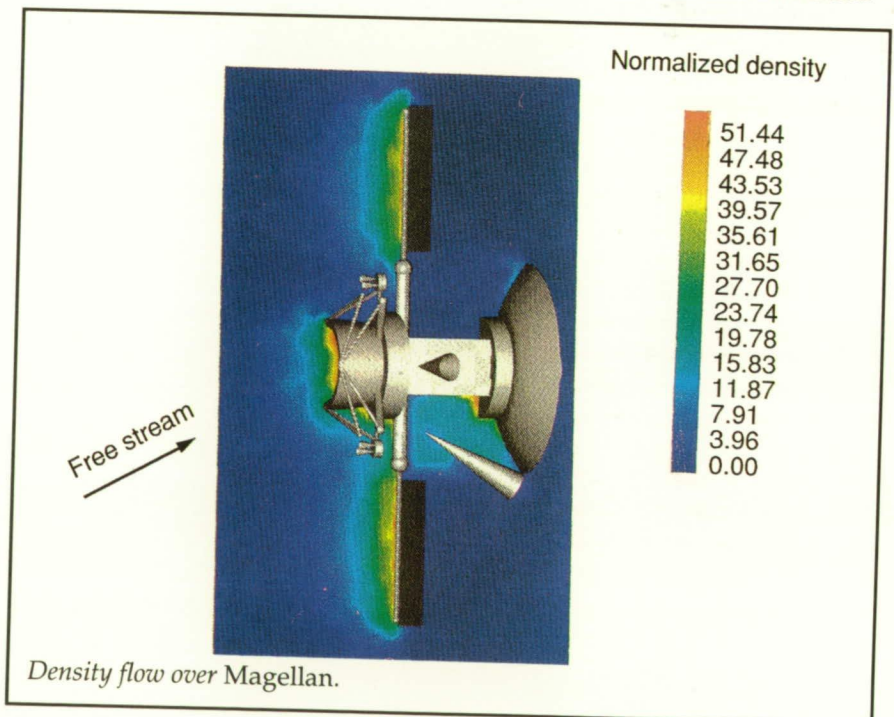
Aerodynamic Characteristics of *Magellan* in the Upper Atmosphere of Venus

The *Magellan* mission has been very successful in mapping the

Venus surface and collecting gravity field data. Recent interest in increasing the mapping spatial resolution has led to a series of studies to assess the feasibility of lowering and circularizing the spacecraft orbit through aerobraking within the upper atmosphere of the planet. The objective of the present study was to determine the aerodynamic loads and moments on the spacecraft during an aerobraking maneuver for a wide range of attitudes at a given altitude, namely, 140 km. At this altitude, Venus atmospheric density is very low, and special tools had to be used to simulate the flow field around *Magellan*:

1. A three-dimensional particle simulation code based on Bird's direct-simulation Monte Carlo algorithm
2. A three-dimensional free-molecular code

A CAD-like preprocessor was developed to define the rather complex geometry of the spacecraft and interface with the simulation

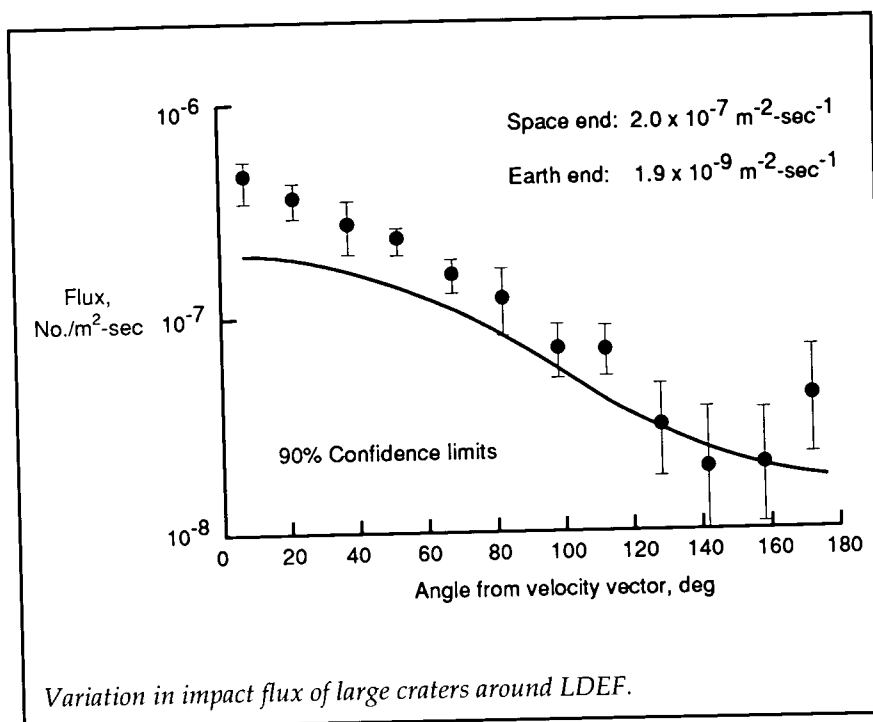


codes. The figure shows the density flow field over the *Magellan* spacecraft at 30° incidence and 50° roll angle. Maps of aerodynamic forces and moments were generated for a wide range of attitudes. These maps are used by the mission planners to assess the controllability and survivability of *Magellan* during an aerobraking maneuver. This study showed the present capability of our simulation codes to study complex geometry problems at high spatial resolution and in a short turnaround time. (Didier F. G. Rault, 44388) Space Directorate

Large-Meteoroid Impact Craters on the Long Duration Exposure Facility

The Long Duration Exposure Facility (LDEF) was a 12-sided spacecraft, about 10 m long and 5 m in diameter, which orbited the Earth between 1984 and 1990 with its longitudinal axis aligned with its geocentric position vector. Because of its gravity gradient design and a viscous-magnetic damper, the LDEF maintained a three-axis stable orientation. This provided a new level of sophistication in flight data on meteoroids and man-made orbital debris.

The impact flux of large craters, 0.5 mm to 5 mm in diameter, varied greatly on the 12 sides and the 2 ends of the LDEF. (See figure.) Most of the craters in this size range, measured in the Advanced Technology Research Laboratory, are believed to have been created by meteoroids. Man-made debris is only a minor component of the particulate



environment in the size range responsible for creating 0.5-mm-to 5-mm-diameter craters. Investigations now under way to search for residue in the craters may provide verification of the relative abundances of meteoroids and man-made debris in this size range.

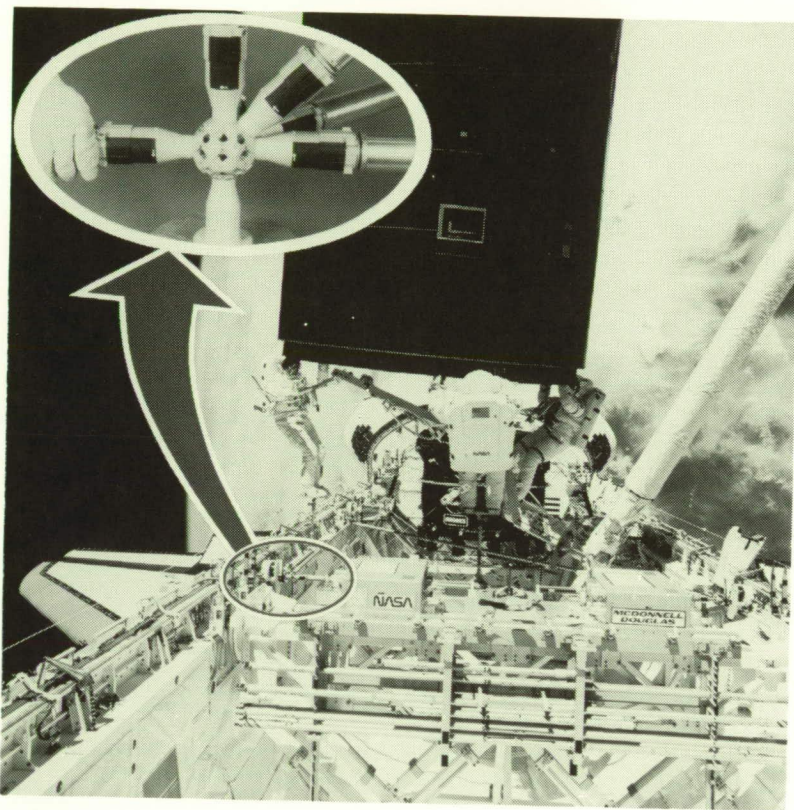
Calculations made using the NASA model of the meteoroid environment developed prior to the LDEF mission underestimate both the total number of craters produced on the LDEF and the magnitude of the variation in crater density around the LDEF. (See solid line in figure.) These errors are attributed to the failure of the penetration equation at meteoroid impact speeds and to the velocity distribution used for meteoroids, respectively. New models based on the data from the LDEF will enable designers of future spacecraft, such as Space Station *Freedom*, to accurately eval-

uate the meteoroid hazard to components at various locations on the spacecraft.

(D. H. Humes, 41484) Space Directorate

Erectable Truss Hardware for Space Construction and INTELSAT Retrieval Support

The unique in-house design, engineering, and fabrication capability of the Langley Research Center provided erectable truss joint hardware for the flight demonstration of assembly of structures by EVA methods (ASEM). The versatility of the ASEM truss hardware allowed STS-49 mission controllers to quickly develop an alternative EVA scenario for the successful capture and repair of the INTELSAT spacecraft.



Langley joint assembly hardware used in satellite rescue.

The ASEM hardware consisted of truss members similar to the erectable baseline structure for Space Station *Freedom* and flew on the first flight of the Space Shuttle *Endeavor* as a secondary payload and experiment managed by the McDonnell Douglas Space Systems Company and supervised by Johnson Space Center for the WP-2 Space Station *Freedom* Project Office. The consistent quality of Langley's research hardware enabled the needed joint components to be flight qualified to meet the STS-49 launch data without expensive, new production investments. The actual flight hardware was selected from 3 hardware sets needed for neutral buoyancy training, certification, and flight (over

130 of Langley's strut end joint assemblies).

The primary mission was the INTELSAT rescue from a low orbit insertion on a previous shuttle flight, but in addition to the truss hardware operating perfectly during the later ASEM experiment, its availability permitted placement of an EVA foot restraint over the cargo bays to enable the manual rescue of the INTELSAT spacecraft when the planned retrieval effort failed. After the rescue, the truss segment was assembled on the shuttle cargo bay sills, and a multipurpose equipment support pallet was used to simulate attachment of a payload to the truss. Langley's

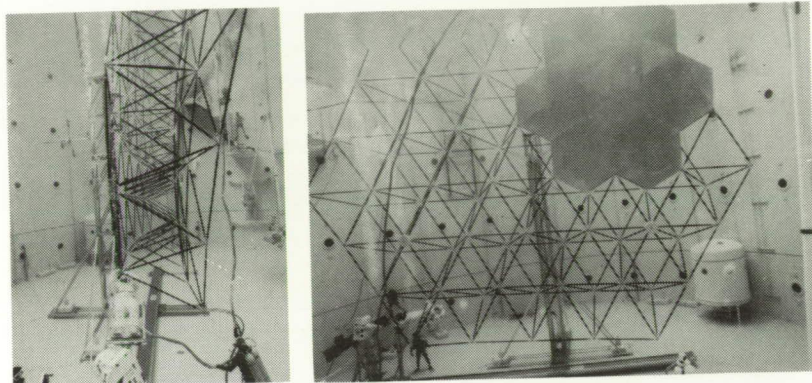
continued development of ASEM-type hardware provided the fulcrum for a successful experiment and mission.

(Harold G. Bush, 43102, Richard E. Wallsom, and James E. Phelps) Structures Directorate

EVA Assembly Procedure for 14-m-Diameter Precision Reflector Verified in Neutral Buoyancy Tests

Development of a microwave radiometer proposed for future Earth resource observation satellites includes EVA assembly considerations. With the neutral buoyancy tests used to simulate the weightless condition of space, efficient on-orbit construction and maintenance procedures were developed for a large reflector support structure. Tests included truss structure assembly, reflector panel attachment, and "damaged" panel replacement and were conducted at Marshall Space Flight Center by Langley Research Center engineers.

Initially, computer simulations were performed to develop assembly and maintenance procedures and assembly time predictions for the precision reflector. Assembly times were also predicted using data from previous structural assembly tests. The underwater tests enable time, procedure, and hardware evaluations. The double curvature and high surface precision of the 14-m-diameter reflector gave each of the 315 struts and 84 nodes comprising the supporting truss unique dimensions and each of the 37 reflector panels



Neutral buoyancy simulates on-orbit construction of doubly curved truss structure.

a unique shape. Nevertheless, an efficient EVA procedure was developed and verified to allow the entire support truss and seven mock-up reflector panels to be assembled in approximately 3 hours. During these simulations, the strut-to-node and panel-to-node joints operated as designed, with only minor hardware changes being considered to improve EVA compatibility. Panel removal and replacement operations were performed using a special-purpose alignment tool to minimize the risk of panel damage.

The rate of assembly for storage and handling of unique hardware components was found to be about the same rate as for a uniform truss with interchangeable components if one EVA crew member was devoted to hardware management while the other crew member assembled the structure. (Mark S. Lake, 43114, and Walter L. Heard, Jr.)
Structures Directorate

Middeck 0-Gravity Dynamics Experiment (MODE)

The MODE is designed to investigate both fluid and structural dynamics of nonlinear spacecraft dynamic systems in zero gravity. The primary objectives of the MODE are (1) to characterize fundamental zero-gravity slosh behavior and to obtain quantitative data on slosh forces and spacecraft response for correlation of numerical models, and (2) to characterize the fundamental changes in dynamics on truss structures in zero gravity due to absence of gravity, to quantify the changes due to the absence of suspension and gravity load on truss members, and to obtain quantitative data for correlation with numerical models.

The MODE has three principal hardware systems: the experiment support module (ESM), the fluid test article (FTA), and the structural test article (STA). The ESM provides experiment control and data recording. The FTA assembly includes a precision force balance

and four fluid tanks. The test fluids are silicon oil and pure water. The STA has both deployable and erectable sections and a rotary joint. The deployable section is similar to the FAST MAST proposed for the Space Station *Freedom* solar array and has over-center lock of knee-hinged longerons, rigid battens, and wire diagonals. The erectable section is similar to Dynamic Scale Mode Test (DSMT) hardware, which has "sticks and balls" with locking collars. The figure shows STS-48 Mission Specialist James Buchli with the STA "L" configuration.

The MODE hardware performed flawlessly and produced more than 600 million bytes of excellent data. The fluid tests show that modal damping ratios and frequencies at zero gravity are significantly different from those at 1g and nonlinear behavior is more benign in zero gravity than at 1g. Analysis of the STA data shows that nonlinearities are more



Model of STA L-configuration demonstrated on STS-48.

apparent in zero gravity, resonance modes generally soften with increasing force, and damping is more pronounced in zero gravity. In addition, the rotary joint exhibited an unexpected "jump phenomenon," and the resonance frequencies of the STA "L"-configuration were significantly different from pre-launch measurements. A reflight of the STA is planned for 1993 to investigate the structural nonlinearities observed during this flight.

(Sherwin M. Beck, 41966)
Space Directorate

A Validation of Integrated Controls-Structures Design Methodology

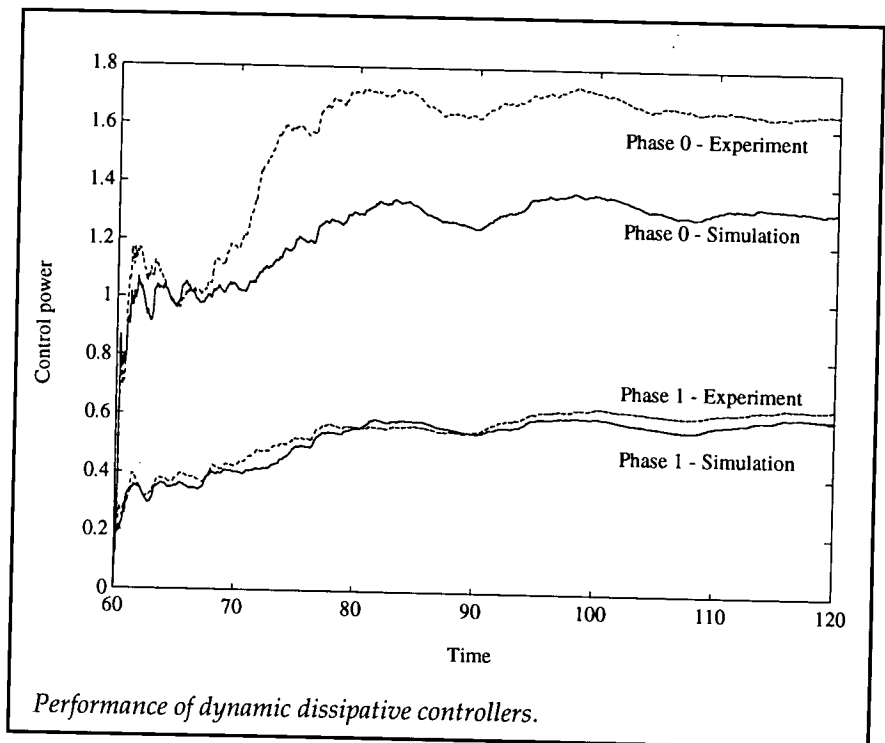
One of the main objectives of NASA's Controls-Structures Interaction (CSI) Program has been to integrate the highly coupled controls and structures disciplines and develop integrated controls-structures design methodologies for spacecraft design. To date, various integrated design optimization techniques, such as simultaneous optimization, sequential optimization, and single-objective and multi-objective optimizations, have been developed for the combined controls-structures design. It has been analytically demonstrated that an integrated design approach can consistently produce spacecraft that have considerably superior overall performance over spacecraft produced with the traditional sequential approach, wherein the structure is designed first and then a controller is synthesized to achieve satisfactory performance.

In order to assess its feasibility in real applications, the integrated design methodology has been applied to a redesign of the CSI Evolutionary Model (CEM), which is an experimental test-bed at the Langley Research Center. In this integrated redesign, the structural variables were chosen as the effective cross-sectional areas of the longerons, battens, and diagonals of seven sections of the structure, while the elements of the compensator matrices were chosen as the control design variables. In the integrated optimization problem, the average steady-state control power was minimized in the presence of white-noise disturbances at two of the actuator locations, subject to constraints on the line-of-sight (LOS) pointing error, the total mass of the structure, and bounds on the structural member sizes.

The redesigned CEM was fabricated and assembled in the labora-

tory and was used in the same series of active control experiments as the nominal CEM. The experimental results generally agree well with the analytical and simulation results (see figure) and indicate that the redesign CEM provides better LOS pointing performance with less than half the average control power. Therefore, it has been analytically and experimentally demonstrated that integrated controls-structures design methodology can yield a design that is considerably superior to that obtained through the conventional design approach; thus, the integrated design methodology is a feasible and practical approach to future spacecraft design.

(Peiman G. Maghami, 44039)
Flight Systems Directorate



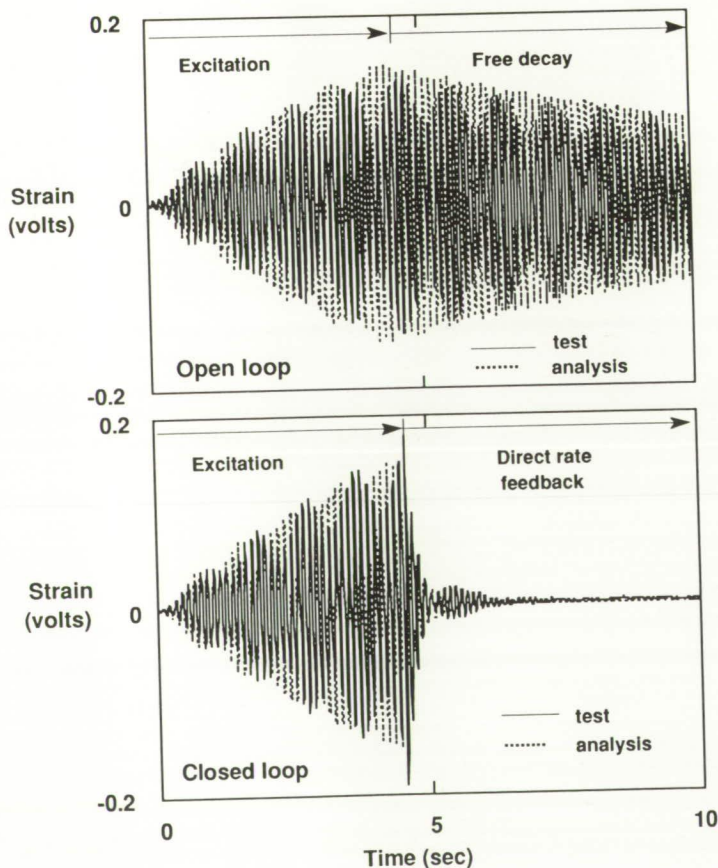
Commercial Piezoelectric Devices Adapted for Smart Structure Application

Many opposed large space structures will consist largely of structural truss assemblages. One method of suppressing undesired vibrational motions of these assemblages is to replace a select number of regular truss members with piezoelectric struts. These piezoelectric struts will act both as normal load carrying members and as actuation devices.

To develop accurate modeling tools and to verify the hardware adaptation, tests have been performed using two commercially available piezoelectric strut actuators placed in a 10-bay vertical truss structure. For maximum effectiveness, the struts were placed in the locations corresponding to the largest strain energies in the modes to be controlled. For sensing, a strain gage and a strain rate sensor were placed in line with each piezoelectric strut. Several vibration suppression control laws were then designed for the truss.

Analysis models were developed using basis vectors from both static and dynamic finite-element models. Special care was taken to capture the local deformations produced by the piezoelectric struts. An open-loop decay response, obtained by exciting the first two vibrational modes of the truss, can be seen in a sample strain-gage time history shown at the top in the figure. The response of the same strain gage, taken from a direct rate feedback closed loop control test, can be seen at the bottom in the figure. A significant improvement in damping (from 0.18 percent in open loop to 7 percent in closed loop) was achieved with the piezoelectric struts. As can be seen from the data in the figure analytical predictions correlate well with the experimental results.

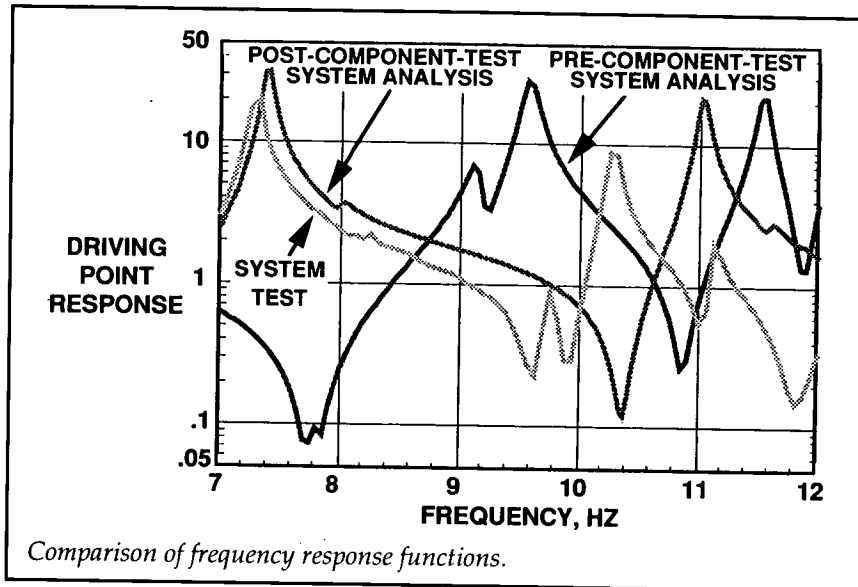
(Chin Chung Won, 48225,
Dean Sparks, Jr., Jeff Sulla, and
W. Keith Belvin)
Structures Directorate



Sample 10-bay strain-gage responses.

DSMT Analysis Model Updated Using Test-Verified Component Models

The trend toward increasing the size and complexity of space structures such as Space Station *Freedom* will reduce the feasibility of verifying the full-system structural models through ground test methods. For this class of structures more emphasis is placed on verifying models of segments of the full-system structure at the component-subassembly level. The full structural model of the system is synthesized from assembly of the component-subassembly



level verified models. The quality of the results of this approach is highly dependent on verification of the interface characteristics of the components and subassemblies. One of the objectives of the Dynamic Scale Model Technology (DSMT) program is to evaluate the feasibility of this approach and identify important technical issues. The knowledge gained from the test-analysis verification process in this program will be valuable to all large-space-structure programs.

The DSMT Hybrid Mission Build 2 (HMB-2) model was divided into 26 components. Components were tested to determine their structural characteristics. The finite-element model of each component was updated based on the results of the test-data analysis. The updated component finite-element models were then incorporated into the full-system model.

The frequency response functions shown in the figure demonstrate the improvement that was realized by including

updated models of all but two of the components in the system model. It is expected that the correlation of the system test and analysis models will improve further once the updated finite-element models of the remaining components have been included in the system model.

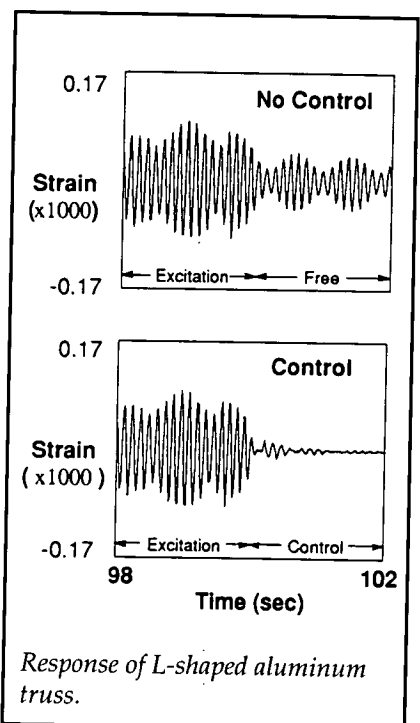
(Mehzad Javeed, 44344,
Harold H. Edighoffer, and
Paul E. McGowan)
Structures Directorate

Adaptive Control Using On-Line Identification

On-line identification of future communication and Earth observation satellites provides an input-output mathematical model that can be used in health monitoring and parameter adjustment of the onboard control system. The standard identification problem seeks to find, given input and output data, an analytical representation of the system. Depending on how the input and output data are fed

into the algorithm, two models can be identified. The *forward* model estimates the output of the system based on a given input, and the *inverse* model computes an input that will produce a given output. Once the inverse model is identified, it can be used to compute control inputs by supplying the model an appropriate desired response. This is the basis for the control formulation demonstrated in the laboratory.

A recursive, least-squares algorithm that identifies parameters based on an observer formulation has been programmed for real-time implementation on a VAX 3200 computer. The experimental setup uses an L-shaped aluminum truss with two piezoelectric actuators. Outputs from near-collocated strain gages are used for identification. Typical free response data for one strain gage are shown in the top plot and the controlled counterpart



data are shown in the bottom plot. Implementation is divided into three states: first is the open-loop excitation to identify the forward model, followed by identification of the inverse model, and finally the controlled response given a desired system response.

The ability to identify and control a system without the need for a priori models and/or control laws is extremely important in general. Health monitoring and control of systems that may exhibit configuration changes while in operation would certainly benefit from this technology.

(Lucas G. Horta, 44352, and
Chris A. Sandridge)
Structures Directorate

Phase 0 CSI Evolutionary Model Tests Complete

Testing of the Phase 0 CSI Evolutionary Model (CEM) has been completed. The CEM test-bed, a ground test article consisting of an aluminum truss and several appendages (see figure), was designed to possess dynamic behavior similar to space science platforms. Researchers from NASA and private industry were invited to use the test-bed to validate advanced control technology for application to flexible spacecraft. In addition, test methods and facilities were developed to support the research objectives.

The CEM test-bed has been used to study low-authority (dissipative) controllers and high-authority (model-based) controllers. Dissipative controllers, which use collocated thruster and

accelerometer pairs, produced a highly stable feedback configuration. These dissipative controllers produced significant damping; however, the energy requirements of the dissipative controller were somewhat higher than those of model-based controllers, which use noncollocated sensors and actuators. It was found that the model-based controllers often produced an unstable closed-loop system because of differences in the analytic models and the experimental hardware. To achieve good stability margins and high controller energy efficiency, a combination of model-based and dissipative controllers were implemented in parallel. Test results proved this combination of controllers to be energy efficient and highly stable.

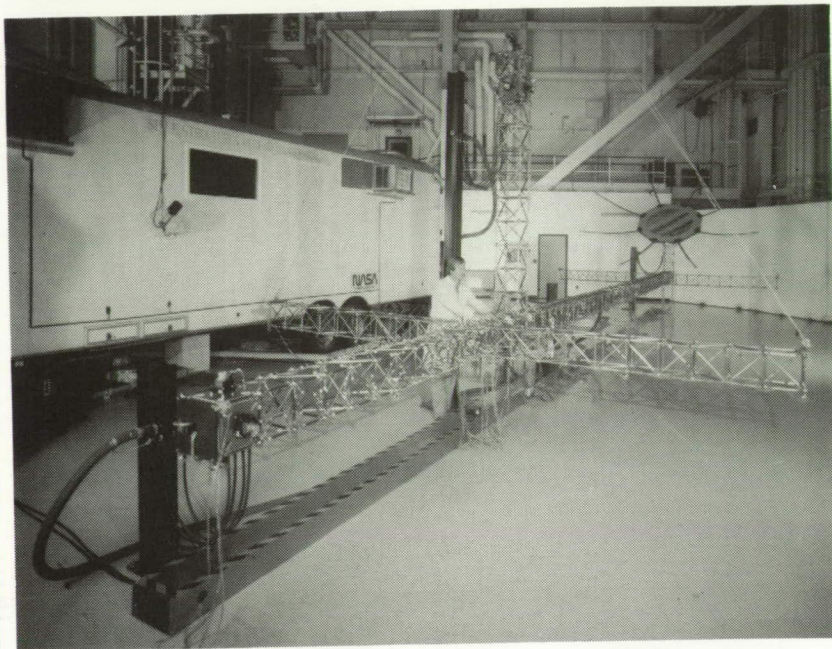
The test-bed has been instrumental in bringing theoretical

control design methodologies together with practical hardware to advance spacecraft pointing control technology.

(W. Keith Belvin, 44319, Lucas G. Horta, and Kenny B. Elliott)
Structures Directorate

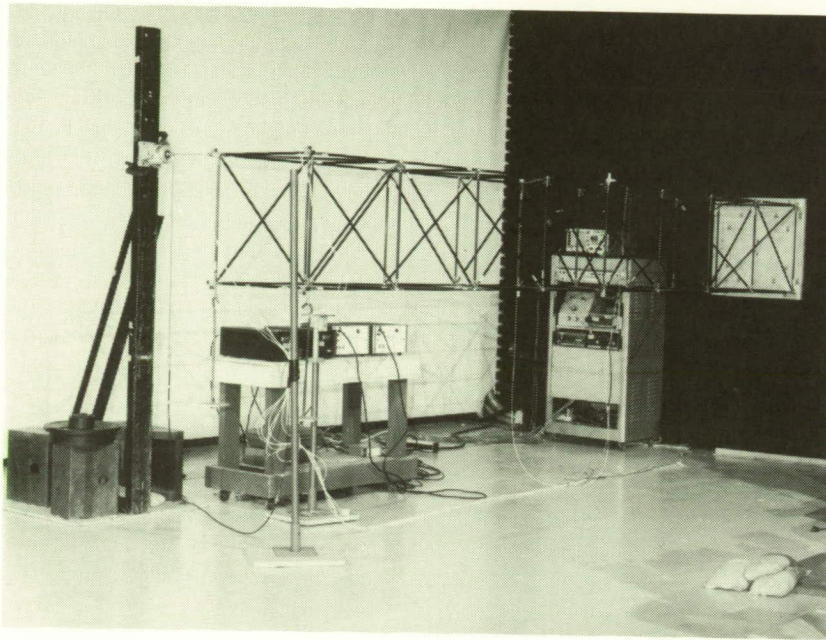
Damage Detection in Large Space Structures From Best Achievable Eigenvectors

A comprehensive test program for detecting damage in truss structures was completed. Modes and frequencies for 16 damage cases were obtained for an 8-bay section of the erectable truss shown in the figure. Damage cases included single members removed, multiple members removed, and partial damage to a



Phase 0 CSI Evolutionary Model.

ORIGINAL PAGE
BLACK AND WHITE PHOTOGRAPH



Erectable truss.

single member. Three accelerometers were placed at each node to provide complete mode shape definition of the structure. These data are available to researchers studying damage location and sensor placement issues.

A new damage location method, based on the method of "best achievable eigenvectors," was developed and validated with the 8-bay test data. Pretest strain energy and sensitivity analyses are used to indicate the most likely damage sites. The modes and frequencies produced by assuming damage to each of these suspect members are projected onto the measured modes from the damaged structure and the distance or angle between the two sets of vectors is used to indicate the location of damage. Once the location of the damaged member has been established, the

magnitude of the damage can easily be calculated. The method is very robust and is capable of filtering inconsistencies out of the measured data as well as detecting both loss of stiffness and loss of mass. Future enhancements will include the use of limited numbers of sensors and more computationally efficient convergence algorithms. (Thomas A. L. Kashangaki, 44327, and Tae W. Lim)
Structures Directorate

Second-Order State Estimators for Structural Systems

Feedback control systems often require an estimation of states that cannot be measured directly from the system under control. Unfortunately, state estimation

suffers from model errors, measurement noise, and unmodeled dynamics. This study was aimed at improving the state estimation of structural systems for use with feedback control.

A second-order differential equation form was used to develop a model for estimation of structural states. This differs from the more common first-order state estimators such as the Kalman filter. By using collocated sensors and actuators, the estimator does not require spatial filtering that typically occurs with the first-order estimator. This significantly reduces the second-order estimator sensitivity to model errors.

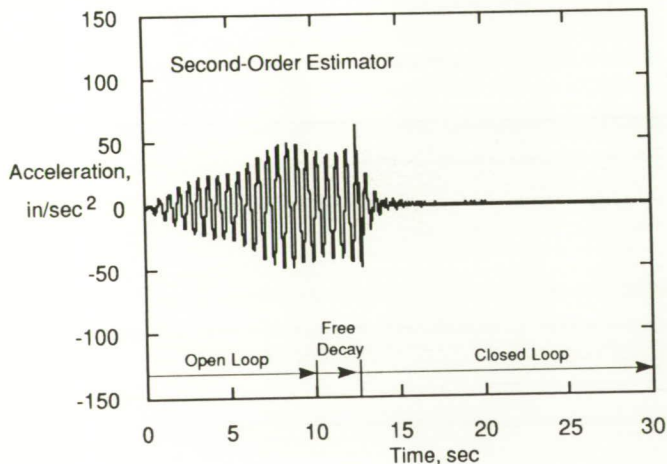
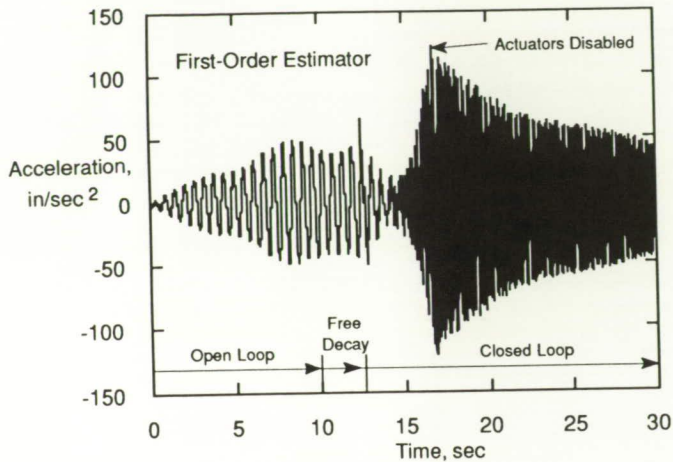
To validate the performance of the estimators, tests were performed on a structural test-bed designed to study control of flexible spacecraft. The experiments consisted of 10 sec of excitation from the actuators followed by 2.5 sec of free decay, after which closed-loop control was initiated. The figure shows the experimental response of the structure when the first-order and the second-order estimators are used. The data obtained with the controller that used the first-order estimator show an instability that required the actuators to be disabled. This instability is most likely due to error in the estimator design model. The second-order estimator used the same design model and was implemented with the same control gains, yet a stable closed-loop response was achieved. The second-order estimator proved to be superior for estimating structural states when model error is present.

(W. Keith Belvin, 44319)
Structures Directorate

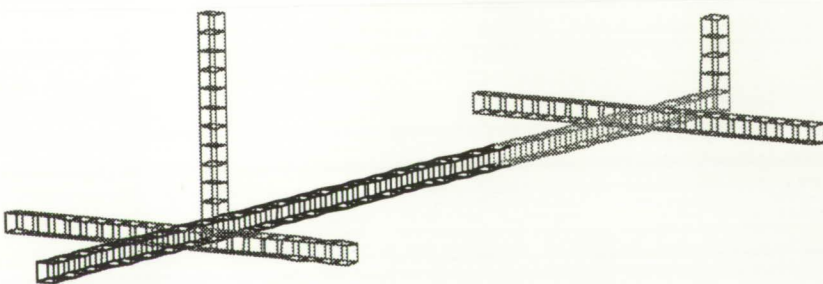
Phase 1 CSI Evolutionary Model Test-Bed

The first revision, design, and fabrication of the CSI (Control-Structures Integration) Evolutionary Model (CEM) has been completed. This test-bed will be used to validate the benefits of an integrated controller and structural design of flexible space platforms. The test-bed geometry and instrumentation are the same as those of the previous model, the Phase 0 CEM, with the exception that the truss strut stiffness and mass properties have been tailored through an integrated controller-structure optimization process.

Seven regions of the truss shown in the figure were considered for optimization. Each region consisted of a longeron, batten, and diagonal, the result being 21 potentially different struts. Design curves, which relate the mass and stiffness of a strut, were developed to be used as constants by the design code to ensure that the struts chosen through the optimization process could be manufactured. The design curves were derived semi-empirically through a fast-paced strut design, analysis, and prototype testing program. The baseline strut design featured an erectable joint that was used for all struts. The strut stiffness was tailored by varying the cross-sectional area of the strut tube. Once the strut stiffness and mass properties were specified by the design code, the design curves were in turn used to convert strut properties into sizing requirements for the production struts.



Acceleration response of structure with feedback control.



Phase 1 CSI model test-bed.

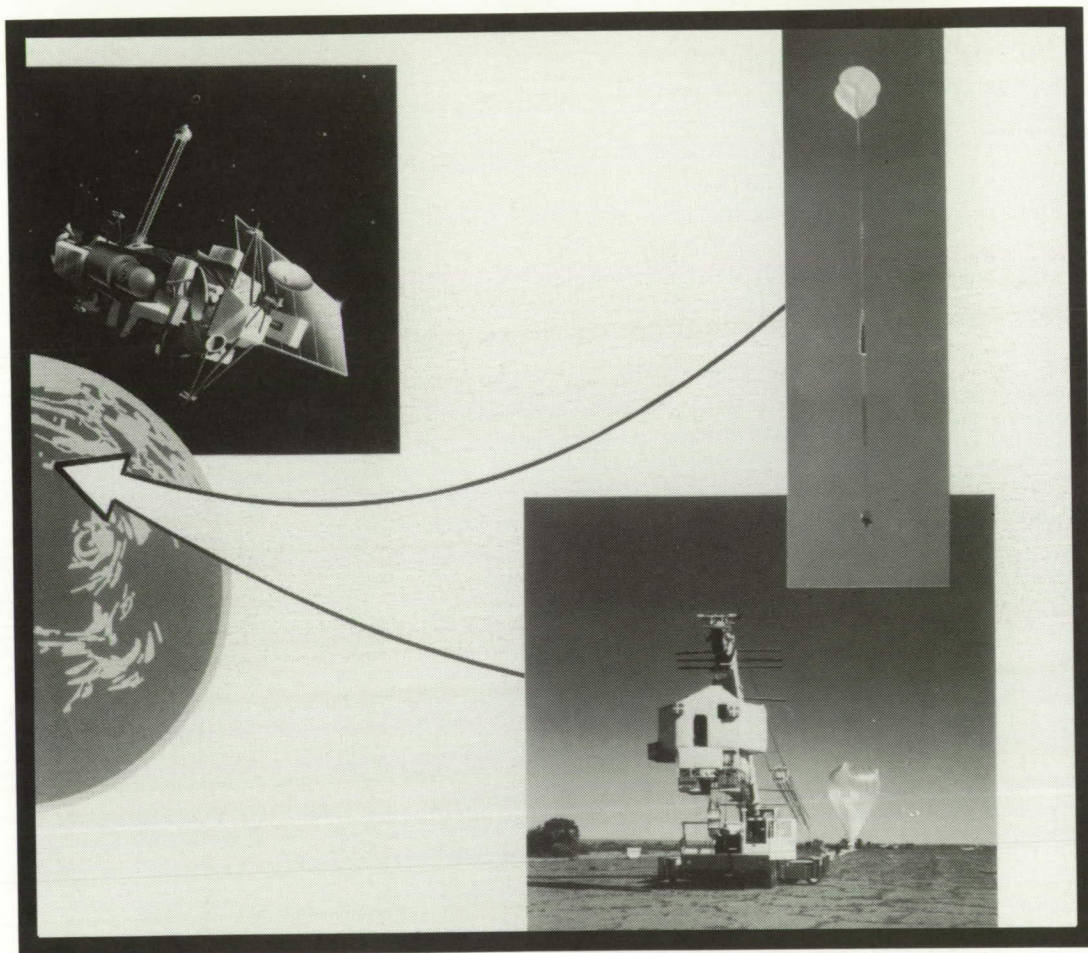
Because of convergence of many of the strut sizes, the 21 strut designs were reduced to 6 unique strut designs. These 6 designs were used to produce 1799 struts for the CEM. Tests on sample populations of struts showed that the struts were produced with stiffness and mass properties that were within 1.3 percent of the requirement. Initial structural verification tests of the assembled structure indicate that the CEM's static and dynamic properties are predictable, well characterized, and within performance requirements established during the integrated design process.

The Phase 1 CEM verifies that specified stiffness and mass properties can be successfully fabricated if proper design curves are utilized for the struts.

**(K. B. Elliott, 44359, L. G. Horta,
and M. J. Gronet)**

Structures Directorate

■ SPACE SCIENCE



*Provide technology for programs
focused on Earth, the Solar
System, and the Universe, and
use the data as the basis for
national and international
policy-making relating to
changes to the global system*

Satellite Monitoring of Biomass Burning in the Savanna Grasslands of Africa

Recent studies indicate that biomass burning is a significant atmospheric source of greenhouse gases (carbon dioxide and methane), chemically active gases (the oxides of nitrogen and carbon monoxide), and atmospheric particulates. All these compounds result from the combustion of biomass. Biomass burning includes the burning of forests (tropical, temperate, and boreal),

savanna grasslands, and agricultural land following harvest. Recent estimates indicate that biomass burning in the world's savanna grasslands is the greatest single source of burning in any ecosystem and exceeds burning in the world's tropical forest by a factor of 3 (3690×10^{12} versus 1260×10^{12} g of burned biomass). About two-thirds of the world's savanna grasslands are located in Africa, yet very little is known about the spatial and temporal distribution of burning in the savanna grasslands of Africa. To provide important information on biomass burning in Africa, we have utilized nighttime images of

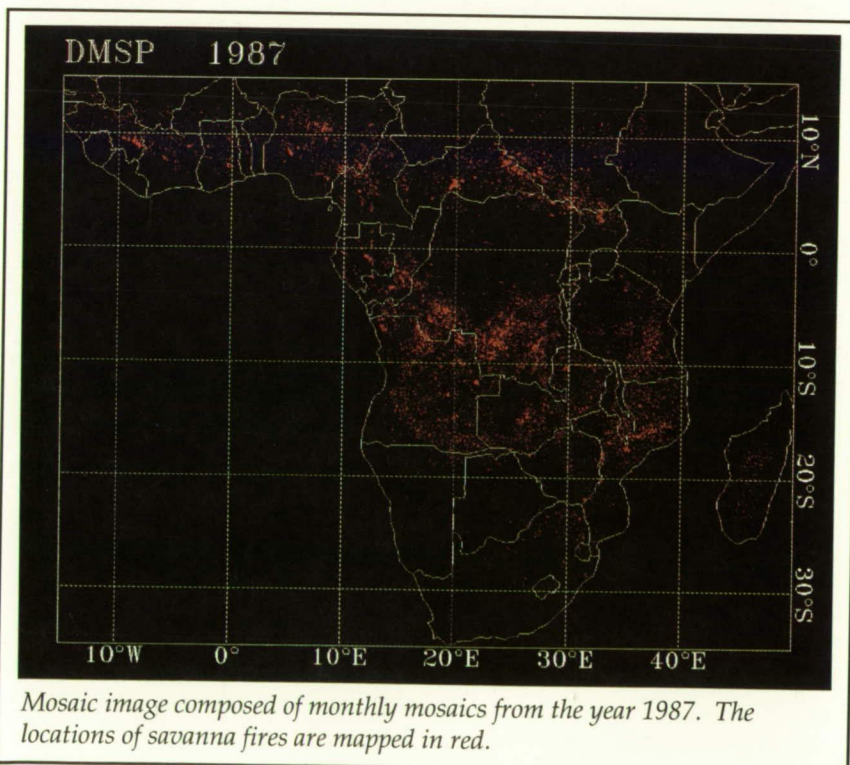
the Earth obtained by the Defense Meteorological Satellite Program (DMSP). Over 200 individual DMSP images were obtained and geographically remapped to produce monthly mosaics and annual mosaics. The monthly mosaicked images have provided the first information on the spatial and temporal distribution of burning in the Africa savanna grasslands.

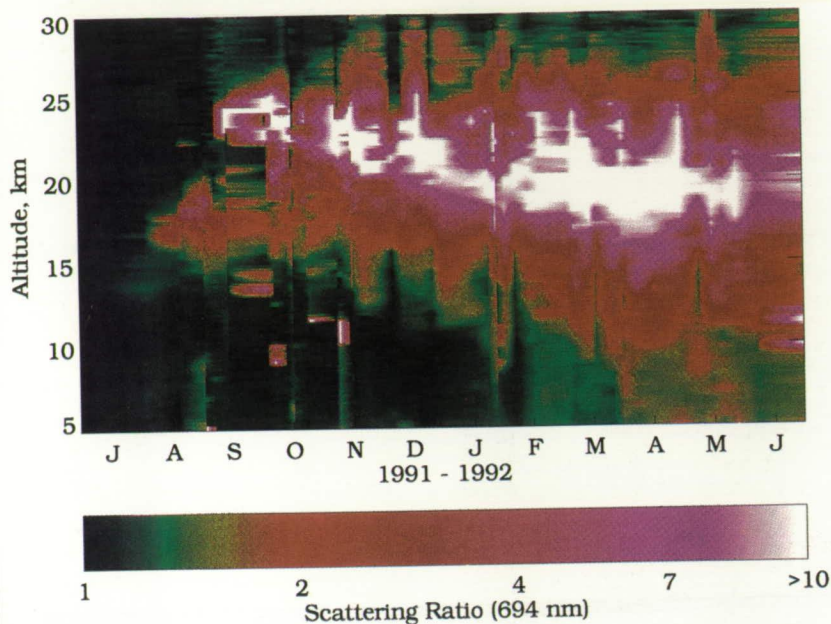
(Donald R. Cahoon, Jr., 45615, Joel S. Levine, and Wesley R. Cofer III)
Space Directorate

Ground-Based Lidar Observations of the Mount Pinatubo Volcanic Cloud

The eruption of the Mount Pinatubo volcano in the Philippines in June 1991 produced a cloud of aerosol particles in the stratosphere thought to be the largest in the century. The cloud was initially confined to the Tropics but spread within weeks to higher latitudes and now, more than a year after the eruption, covers virtually the entire globe. Monitoring the evolution and long-term behavior of the cloud will be critical in assessing its effects on atmospheric radiation and chemistry and will provide valuable insight into atmospheric circulation patterns.

Measurements of the Mount Pinatubo cloud have been made





Time series of scattering ratio from lidar measurements of Mount Pinatubo cloud.

on a regular basis over the last year using the Langley Research Center 48-inch ground-based lidar system operated at a wavelength of 694 nm. The figure shows a time series of scattering ratios (the ratio of the measured backscatter signal to that expected from molecular scattering alone) observed from June 1991 to June 1992. The cloud was first observed over Langley on August 3, 1991, with a peak scattering ratio of 2.8 near an altitude of 17 km, a value well above that observed prior to the arrival of the cloud. A much more intense layer (with scattering ratios in excess of 20) appeared around an altitude of 23 km near the end of August and lingered for several months. During the winter months (December 1991 to February 1992), scattering ratios generally increased while profile shapes varied considerably between data sessions. After March 1992, the individual cloud layers appeared

to merge into a single layer, which itself began spreading vertically to cover the altitude range of 10 to 25 km. The vertically integrated backscatter, which is indicative of the total amount of aerosols present overhead, reached a maximum 300 to 325 days after the eruption.

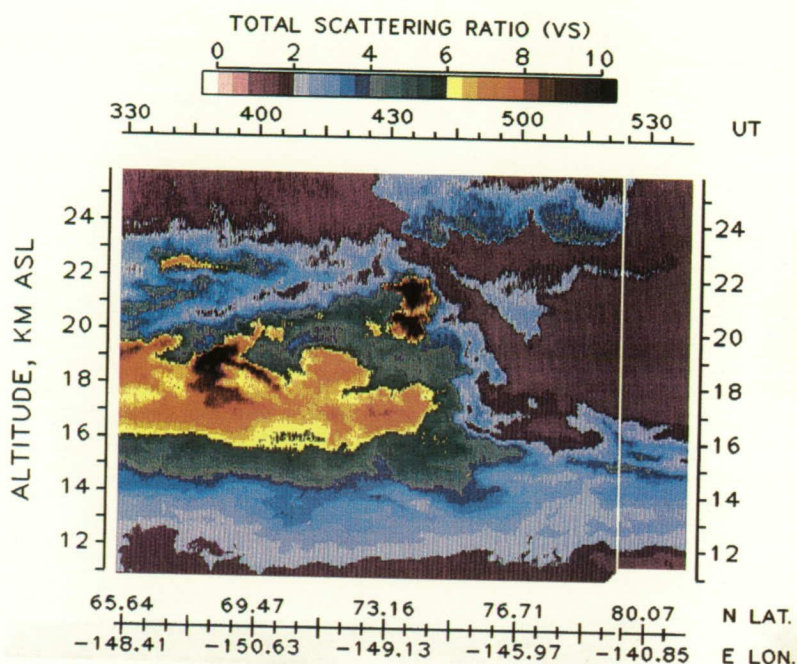
(D. C. Woods, 42672)
Space Directorate

Ozone and Aerosol Distributions Measured in Arctic Stratosphere With Airborne Lidar

Stratospheric ozone and aerosol distributions were obtained with the Langley Research Center airborne differential absorption lidar (DIAL) systems on long-range flights over the Arctic during the NASA/NOAA (National Oceanic

and Atmospheric Administration) Airborne Arctic Stratospheric Expedition II (AASE-II) conducted from January to March 1992. The DIAL system was operated in the zenith mode from the NASA DC-8 to obtain profiles of ozone (O_3) and aerosols in the lower stratosphere (altitudes of 14 to 30 km) on 11 flights into the wintertime Arctic vortex to study the chemistry and meteorology associated with polar O_3 depletions.

Aerosols from the Mount Pinatubo eruption in June 1991 were observed across the entire Arctic region throughout the AASE-II field experiment. Outside the Arctic vortex the Pinatubo aerosols extended over altitudes of 12 to 26 km, with an aerosol peak near 20 km. The Pinatubo aerosol distribution at the center of the Arctic vortex extended from the tropopause to about 17 km in January 1992 and to about 18.5 km in March 1992. The center of the Pinatubo layer remained at about 15 km for the entire period. The O_3 distribution (not shown here) observed over altitudes of 12 to 25 km with the lidar system showed a clear transition across the Arctic vortex edge, with the O_3 profile generally decreasing in altitude by about 1.5 km upon going from outside to inside the vortex. There was generally correlation between the lidar O_3 and aerosol distributions near the edge; however, the O_3 distribution did not show the small-scale structure observed in the aerosol data. The vertical O_3 distribution outside the vortex showed an increase in the O_3 mixing ratio from about 0.4 ppmv (parts per million by volume) at 14 km to about 4.8 ppmv at 23 km. Inside the center of the vortex, the O_3



Atmospheric scattering ratios (total scattering divided by molecular scattering) from airborne lidar measurements of aerosols observed outside (UT < 500) and inside (UT > 500) Arctic vortex (UT ≈ 500) on flight from Alaska to Norway on January 16, 1992.

distribution had a constant increase from about 0.8 ppmv at 14 km to about 4.2 ppmv at 23 km. Between January and March, the only change in the O₃ profile was a slight O₃ decrease in the region between about 16 and 18 km. The maximum decrease was less than 20 percent at the center of this layer. No other obvious O₃ changes were observed inside the vortex over the period of the AASE-II. (Edward V. Browell, 41273) Space Directorate

Accuracy Requirements for Parameters Used in Radiative Transfer Models of Ozone

Ozone emission at 9.6 μm is frequently observed from satellites in order to remotely measure the ozone concentration in the atmosphere. In the terrestrial mesosphere and lower thermosphere, the strongest emission band of ozone at 9.6 μm departs from local thermodynamics equilibrium, that is, that the energy emitted by ozone at that wavelength is not strictly a function of the temperature of the atmosphere. Rather, a host of processes involving inelastic collisions, photochemical reactions, and radiative interactions

determine the amount of energy emitted by ozone. The relative importance of these various processes is generally a function of altitude due to the variation of atmospheric density. It is essential to know the rate at which the ozone molecule emits energy at 9.6 μm in order to successfully relate measurements of emission at that wavelength to the ozone concentration. Consequently, it is then essential to know the rate at which the various processes occur in order to model the rate of radiative emission. Uncertainties in the collisional, photochemical, or radiative rates lead to uncertainties in the calculation of the "temperature" at which the ozone molecule is emitting. Typically, the emission temperature must be known to better than about 3 K in order to limit uncertainties in the ozone concentrations determined from measurements to less than 15 percent. The largest uncertainties are generally associated with the rate at which collisional processes excite and quench ozone. These uncertainties limit the accuracy in ozone concentrations inferred from satellites.

Detailed studies have been carried out to assess the accuracy to which the collisional processes must be known in order to limit the uncertainty in the ozone emission temperature to less than 3 K, given realistic errors in the other rates. These studies indicate that the collisional quenching rates must be known to an absolute accuracy of about 20 percent if the radiative temperature is to be known to an accuracy of about 3 K at altitudes above 50 km (see figure). This study is one of the first in which accuracy requirements for so-called nonequilibrium

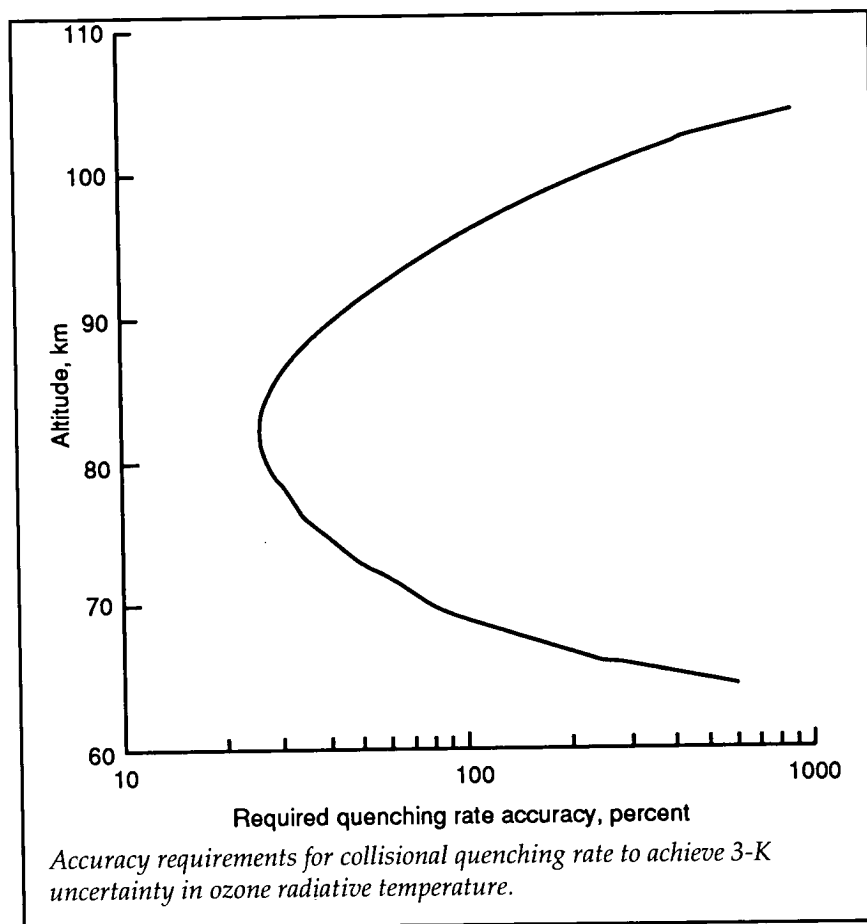
models of radiative transfer have been defined. The results have implications for a number of future remote sensing experiments and serve as a guide for laboratory measurements of collisional processes.

(Martin G. Mlynczak, 45695)
Space Directorate

Airborne Lidar Measurements of Ozone and Aerosols Over the Western Pacific

The Langley Research Center airborne differential absorption lidar (DIAL) system was operated from the Ames Research Center DC-8 aircraft to obtain distributions of ozone and aerosols in the troposphere over the western Pacific during September and October 1991. This investigation was conducted as part of the NASA Global Tropospheric Experiment (GTE)/Pacific Exploratory Mission-West (PEM-West) to study the sources and sinks of gases and aerosols over the remote Pacific during the summertime. The airborne DIAL system made simultaneous measurements of ozone and aerosol profiles above and below the DC-8 along the flight track. The DIAL-derived atmospheric cross sections of ozone and aerosols from the surface to the tropopause level were used to provide the large-scale perspective on the state of the atmosphere and its composition.

During PEM-West, the airflow in the western Pacific was generally from the east, and under these



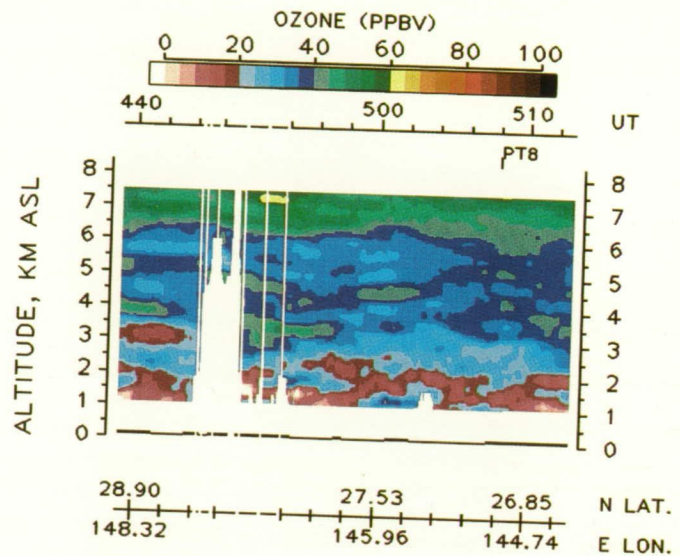
conditions the air was generally observed to have low aerosol loading and low ozone levels throughout the troposphere. The ozone mixing ratio was about 10 parts per billion by volume (ppbv) near the surface and 40 to 50 ppbv in the middle to upper troposphere. In convective outflows from typhoons, near-surface air with low ozone (<25 ppbv) was transported into the upper troposphere (>10 km). Many of these layers were observed over the Pacific because of the large number of typhoons that occurred that year. Air masses containing plumes from biomass burning in the southwestern Pacific were observed below about 2.5 km on two flights. Elevated ozone levels (>70 ppbv) and strong aerosol

scattering were found in these air masses. Several cases of continental plumes from Asia were observed over the Pacific during westerly flow conditions. These plumes were found in the lower troposphere with ozone levels of 60 to 80 ppbv and enhanced aerosol scattering. Stratospheric intrusions were observed in the troposphere, with associated enhanced ozone and aerosols. Stratospheric aerosols resulting from the Mount Pinatubo eruption in June 1991 were observed at 18 to 30 km of altitude on all flights during PEM-West. The enhanced aerosol loading in the stratospheric intrusion layers resulted from the Pinatubo aerosols. In addition, the spatial extent of cirrus clouds and the location and variability of

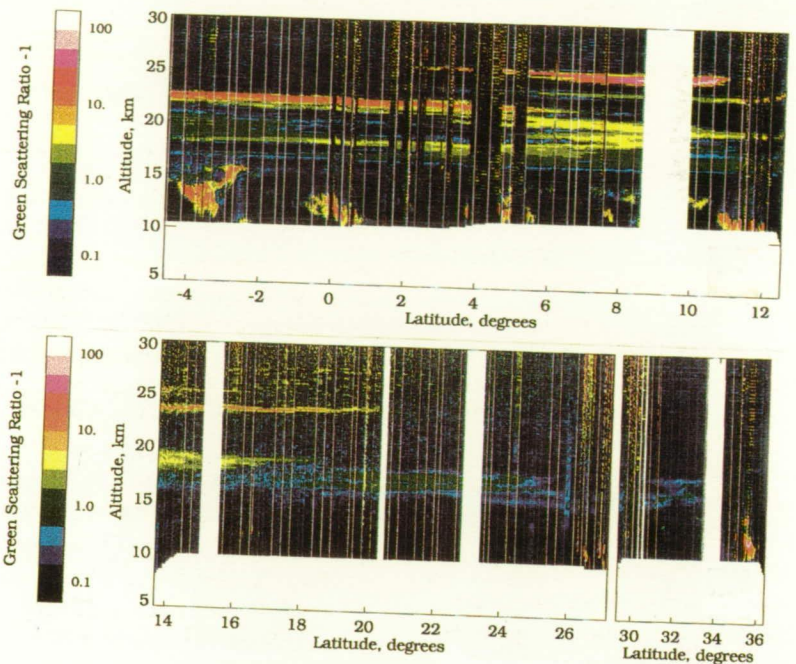
the tropopause were also determined from the lidar data. (Edward V. Browell, 41273) Space Directorate

Airborne Lidar Observations of Recently Injected Mount Pinatubo Volcanic Aerosols

Early estimates of the magnitude of the volcanic cloud from the June 1991 Mount Pinatubo eruption indicated that measurable perturbations to global climate were possible. A study of the stratospheric aerosols produced by Mount Pinatubo was carried out within a month of the eruption with the Langley Research Center airborne aerosol lidar system deployed aboard the NASA Wallops Electra aircraft. Since initial satellite data showed that the bulk of the volcanic cloud was confined to a region near the Equator, a series of survey flights was staged from Barbados (13°N, 59°W), reaching as far south as 5°S. The figure depicts the aerosol scattering ratio (the ratio of aerosol backscatter to molecular backscatter) at a wavelength of 532 nm observed during flights over eastern South America and off the east coast of the United States. The tropopause is near 15 km; features below that are cirrus clouds. The color scale is logarithmic, with black and blue indicating aerosol concentrations near background levels and red and white corresponding to concentrations 2 to 3 orders of magnitude above the background. Column totals for aerosol mass derived from the observations were up to 100 times larger than background levels.



Airborne lidar measurement of background ozone distribution over western Pacific on September 22, 1991.



Aerosol scattering ratio at wavelength of 532 nm observed by airborne lidar over eastern South America (top) and off east coast of United States (bottom).

The majority of the aerosol material was found at high altitudes and, as had been indicated by satellite observations, in the

Tropics and subtropics. The optical depth of the stratospheric aerosol was estimated to be as high as 0.2, or high enough to

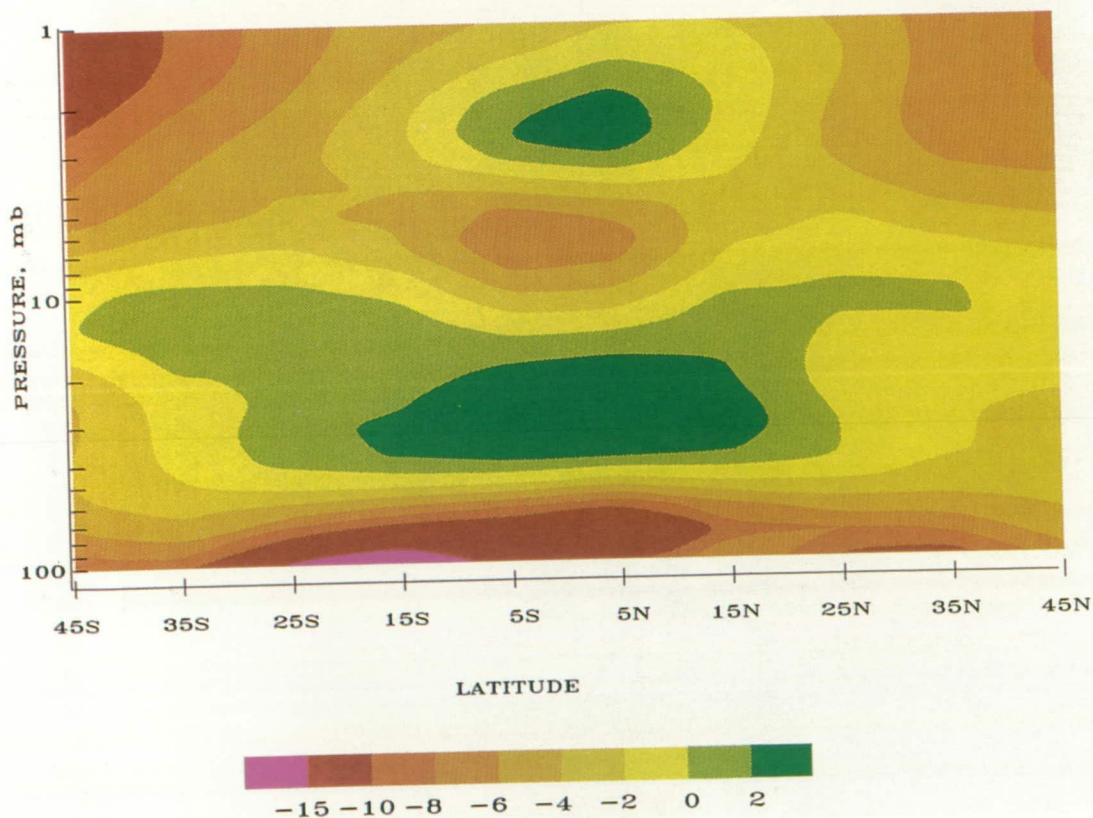
produce climatically significant heating in the stratosphere and cooling at the Earth's surface.

The airborne lidar system employs a polarization-sensitive receiver that provides clues as to the composition and morphology of the backscattering aerosol particles. Some of the volcanic layers shown in the figure exhibited nearly zero depolarization, an indication of the presence of sulfuric acid droplets, while other layers exhibited depolarization as high as 30 percent, an indication of significant ash content.
(D. M. Winker, 46747)
Space Directorate

Ozone Depletion in the Lower, Middle, and Upper Stratosphere

Evidence has recently become available of significant global depletions in total column ozone during the 1980's, even with corrections for sizeable natural variations due to the 11-year solar activity cycle. The resulting increased exposure to biologically harmful solar ultraviolet radiation represents a threat to the biosphere. In order to understand the origins of these depletions, studies also need to be performed on the vertical distribution of ozone

depletion trends in addition to studies of total column ozone. Two satellite data sets were used in this study—the Stratospheric Aerosol and Gas Experiment II (SAGE II) and the Solar Backscatter Ultraviolet (SBUV) ozone data sets. The data sets had to be combined in order to obtain a long enough time series to allow the natural 11-year solar cycle effects to be identified and removed so that long-term trends could be isolated. In addition, quasi-biennial oscillations and annual and semi-annual variations were removed. The figure shows the resulting long-term trends in ozone (in percent per decade) determined throughout the stratosphere as a



Stratospheric ozone trends during 1980's.

function of latitude and pressure level (1 mb corresponds to about 48 km and 100 mb to about 16 km). The areas colored in oranges and reds represent regions of significant ozone depletions. In the upper stratosphere, depletions are stronger in both hemispheres at higher latitudes, a finding that is in qualitative accord with theoretical models. In the middle stratosphere, there is essentially no evidence of depletions when uncertainties are considered, and there is even evidence of slight increases near the Equator. In the lower stratosphere near the tropopause, unexpectedly strong depletions occur at all latitudes. This may result from (heterogeneous) chemical reactions occurring on aerosol or stratospheric cloud surfaces, somewhat similar to the chemistry causing the "ozone hole" near the South Pole.

(Gerald M. Keating, 45804, Linda S. Chiou, and N. Christina Hsu)
Space Directorate

Laser Heterodyne Frequency Line Width at the Hertz Level

Free running lasers, often considered "monochromatic" or single frequency, are actually broadband frequency sources compared with electronic oscillators like quartz crystals. However, by utilizing the latest optical polishing and coating technologies, extremely high Q optical resonators can be fabricated. Two lasers' frequencies locked to such a resonator using conventional microwave servo techniques to achieve heterodyne line widths of

less than 10 Hz (measured with 10 Hz resolution) have been achieved at Langley as part of the Stanford University NASA Laser In Space Technology Experiment (SUNLITE) program. Also, in the last year, optical resonators have been fabricated with promise to improve both line width and long-term stability performance. These resonators have been measured to have $Q = 150\,000$ and a coefficient of thermal expansion of 2×10^{-10} . Such frequency-stabilized lasers will become prolific tools for space-based metrology in the future.

Stabilized lasers with demonstrated operation in space would benefit geophysicists and geodesists studying Earth by allowing measurements of variations in the gravity field to 1 part in 10^{16} ; they would also benefit atmospheric and planetary scientists by allowing construction of narrow-band active remote sensors far more efficient than current instruments. They would benefit astronomers and cosmologists by allowing measurements of predicted gravitational waves and extremely precise astrometry. Finally, stabilized lasers in space can provide the cornerstone technology for high-bandwidth deep space communications and the next generation of fundamental primary time and frequency standards, replacing the ground-based cesium beam and hydrogen maser clocks of today.

(Stephen P. Sandford, 41836)
Electronics Directorate

New Spaceflight Computer for Instrument Control and Data Acquisition

In order to control the complex laser line width and stability experiments and measurements to be performed by the Stanford University NASA Laser In Space Technology Experiment (SUNLITE) instrument, a high-speed, powerful digital signal processor (DSP) was needed. A central processing unit (CPU) was designed and built in the past 2 years to meet this critical need. The design is flexible and could serve the needs of many spaceflight instruments where control and data acquisition are primary requirements. This CPU is designed around the Texas Instruments DSP SMJ320C30, which runs at 33 MHz and features dual, independent data and address buses and can perform parallel instructions. The chip is capable of 16 mips and 3 mflops.

The CPU board communicates with peripherals via a small computer system interface (SCSI) bus and an RS-422 port. The SCSI bus is used to access a spaceflight hard disk drive developed by the SUNLITE project with a capacity of 240 megabytes and a transfer rate of 8 megabytes per second. The RS-422 interface is used to communicate with the CPU in performing diagnostics and to aid in integration and software development.

Also on this board are up to 8 megabytes of program memory and 8 kilobytes of high-speed cache memory for either program or data memory. A watchdog timer is also included on the board.

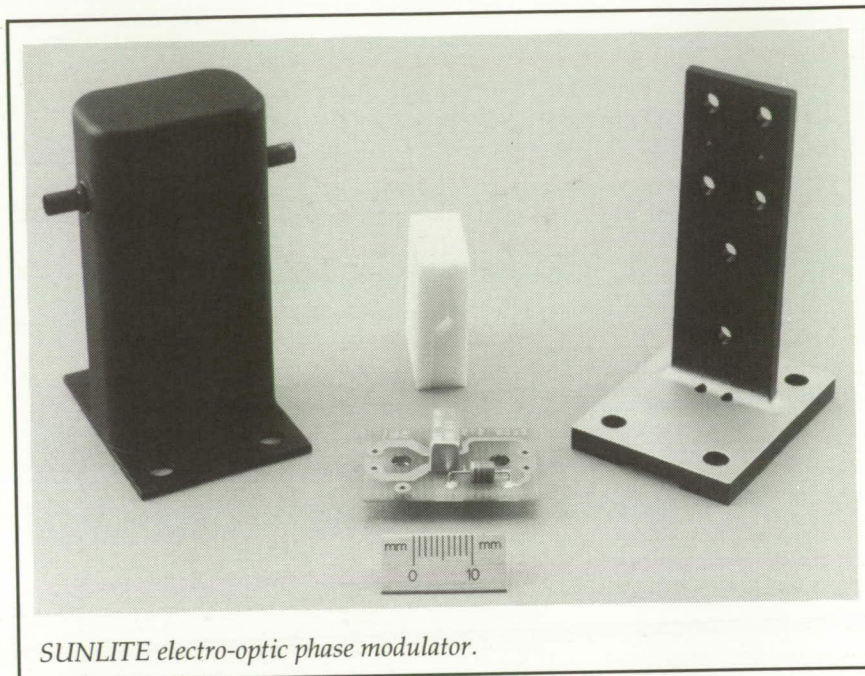
The printed circuit connecting these functions is 10 layers. There are six layers of power and ground and four layers of signals. The entire design and layout process was accomplished using the Computer Aided Engineering and Design for Electronics (CAEDE) facility at Langley. The board was also populated at Langley. Once populated, the CPU was powered up and is now running with no modifications to either the design or the layout (i.e., it worked the first time).

(Stephen P. Sandford, 41836)
Electronics Directorate

Design and Fabrication of an Electro-Optic Modulator

An electro-optic modulator (EOM) was designed, fabricated, and functionally tested for the SUNLITE project. The EOM phase modulates an optical beam by applying a sinusoidal voltage (perpendicular to the optical path) to an electro-optic crystal. The resulting modulated beam, coupled with an optical reference cavity, provides the error signal necessary for frequency modulated (FM) locking of lasers. While commercial EOM's exist, the one for this project has been designed to withstand Space Transportation System (STS) launch loads and fabricated as part of a pilot project utilizing hard metric methods.

As shown in the photograph, the components of the EOM are a gold-plated, phase-modulating, lithium niobate crystal rotated 45° from the vertical; a Teflon bracket completely encasing the crystal



SUNLITE electro-optic phase modulator.

while leaving the end faces exposed; gold wire leading from the crystal to an electronics board; an electronics board; and an aluminum mount. A cover was also designed and fabricated to shield the EOM from electro-magnetic interference (EMI). Additional tubes were bonded to the cover to minimize stray light.

After assembly, the EOM was tested on a SUNLITE breadboard system. The EOM performed as expected with one-third of the energy in the carrier routed to the sidebands.

(Cheryl C. Jackson, 44431)
Systems Engineering and
Operations Directorate

SUNLITE Vibration and Thermal Cycle Test on Optical Bond

A development model of two optical disks made of Corning

ultra low expansion (ULE) 7971 glass of diameters 0.996 in. and 0.703 in. are bonded together with an (nonadhesive) optical bond. The larger diameter piece is polished flat to within 1/20 of a wavelength of helium-neon (He-Ne) laser light over its entire surface. The smaller diameter disk has a concave mirror with a 300-mm radius of curvature ground into its 7/16-in. diameter. The area between the 7/16-in. diameter and the disk outside diameter is ground flat to within 1/20 of a He-Ne wavelength. The two pieces are brought together so that the two outside diameters are tangential at one point and the two super polished surfaces contact, resulting in an optical bond. A flat was then ground into the assembly through both pieces perpendicular to the optical bond so that light could be bounced off this surface to determine if the two pieces moved relative to each other after environmental testing. The purpose of the test is to evaluate the viability

of the optical bond for use in attaching mirrors to the flight reference cavity. Contact area for this bond simulates the cavity bond.

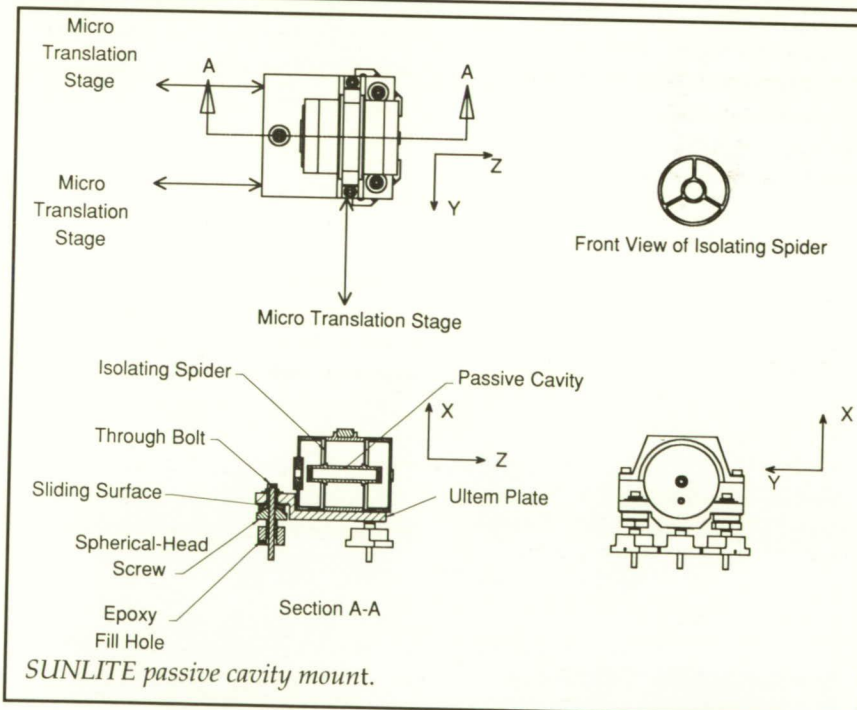
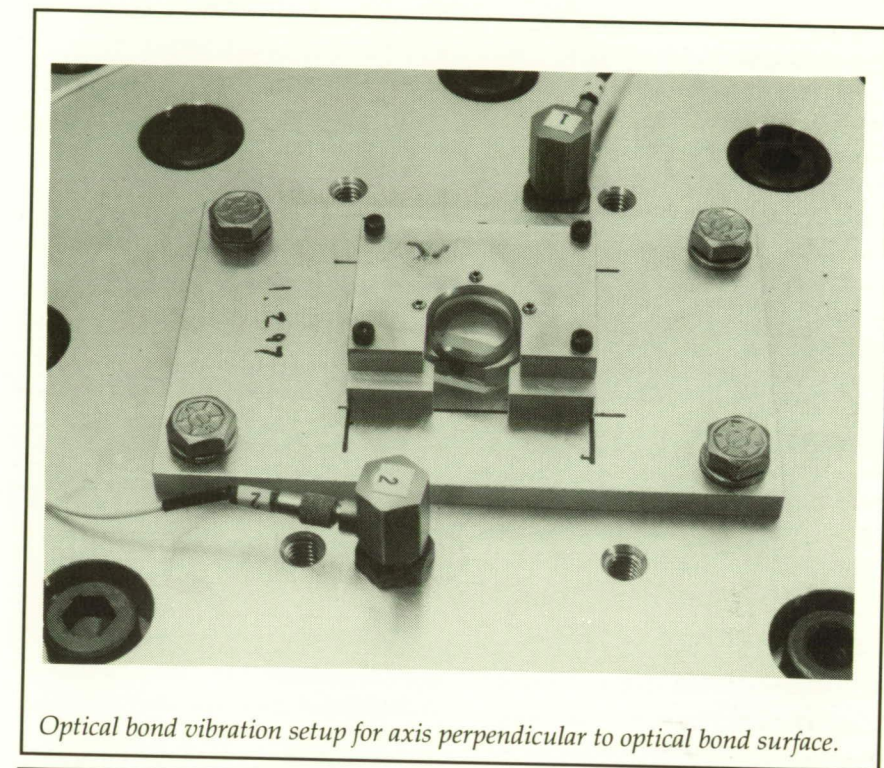
The optical bond test article was a development model, and this test was to determine the stability of the bond when subjected to vibration and thermal loading. The vibration test consisted of randomly exciting the test component to 7.4 G rms between 20 and 2000 Hz and a sinusoidal gravity loading of 13.5 G between 18 and 50 Hz. This test was accomplished in two axes, one perpendicular to the optical bond surface and another along the bond surface. The thermal test was to determine the stability of the optical bond when subjected to eight thermal cycles at the survivability limits of -10°C and 50°C . It was determined that these environmental loads did not degrade the integrity of the optical bond.

(Richard W. Faison, 47083)
Systems Engineering and
Operations Directorate

SUNLITE Passive Cavity Mount

The SUNLITE passive reference cavity mount is a 5-degree-of-freedom positioning platform that can be locked down to maintain alignment through shuttle launch loads and an isolating mount that protects the cavity from environmental changes. Design requirements for the mount to maintain its alignment are as follows:

(1) position: $5\text{ }\mu\text{m}$ in X and Y translation (see figure), $500\text{ }\mu\text{m}$ in Z transition, and $20\text{ }\mu\text{rad}$ in X and Y



rotation; and (2) stability: $30\text{ }\mu\text{m}$ in X and Y translation, $500\text{ }\mu\text{m}$ in Z transition, and $100\text{ }\mu\text{rad}$ in X and Y rotation. The maximum thermal

gradient of the cavity is 0.025°C per minute. Stresses imposed on the cavity by the mount must be minimized. The X translation

and Y rotation are controlled with the three spherical-head jack screws; Z translation and X rotation are controlled with two translation stages; and Y translation is controlled with a third micro-adjusting translation stage. Once the cavity is positioned, bolts through the feet are then tightened, and epoxy is injected to remove all clearances from each jack screw assembly. Thermal isolation of the cavity is achieved through material selection. The platform is machined from Ultem 2300, a thermoplastic with a low thermal conductivity. In addition, Ultem has a coefficient of thermal expansion (CTE) that closely matches that of aluminum, the material used for all other optical mounts in the instrument. Further isolation comes from the Ti-6Al-4V isolating spiders, which mount the cavity in the center of the Super Invar housing. Super Invar was chosen for the housing material because its CTE closely matches that of the cavity. Stress imparted to the cavity because of thermal growth mismatch is minimized

by mounting the cavity with thin titanium spiders.

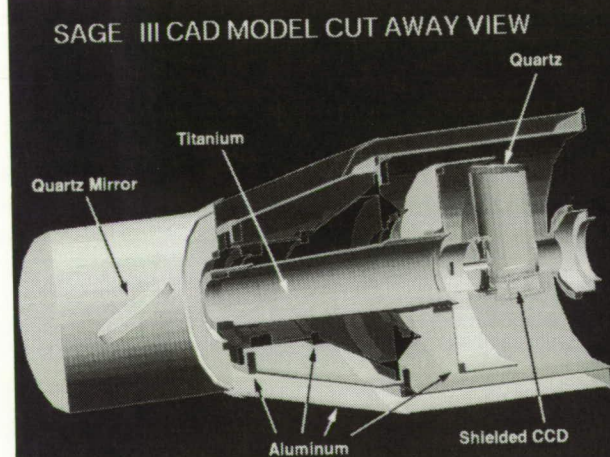
(Stephen J. Hughes, 47175)
Systems Engineering and
Operations Directorate

Modeled Environment and Exposures for the SAGE III Instrument Configuration

The Langley Stratospheric Aerosol and Gas Experiment III (SAGE III) has been designed to measure trace species in the Earth's atmosphere of importance to chemical processes in the stratosphere and upper troposphere. The instrument consists of a Cassegrain telescope limb scanner combined with a grating spectrometer to measure spectral absorption in the atmosphere. The spectrometer detector is an accurately calibrated charge-coupled device (CCD) consisting of an 810×10 rectangular array of $30\text{-}\mu\text{m}$ -square silicon pixels. While such devices are ideally suited for performing

very precise high-speed photometric measurements, they are sensitive to the high-energy charged particle environment that will be experienced for the planned orbital conditions (705-km altitude and 98.2° inclination).

Consequently, a detailed analysis of the predicted degradation due to high-energy radiation exposure has been performed using Langley-developed transport codes and computer-aided-design (CAD) solid modeling procedures. The analysis included evaluation of several dosimetric quantities that could be used in predicting the permanent damage to the CCD for the mission lifetime. Two alternate approaches were used in evaluating the dose quantities and the subsequent charge transfer efficiencies for the device. The results for final degradation in terms of reduced sensitivity for the device are given in the figure, along with a selected CAD model section view of the instrument. The final results indicate that the instrument should provide



COMPUTED DOSES AND DAMAGE PARAMETERS FOR A 5-YEAR MISSION IN SUN-SYNCHRONOUS ORBIT

Method 1: Total Dose – 780 rads
Charge Transfer Efficiency – 0.999864
Sensitivity Loss – 10.4%

Method 2: Non-Ionizing (Nuclear Interaction),
or NI-rad Dose – .37 NI-rads
Charge Transfer Efficiency – 0.999720
Sensitivity Loss – 20.3%

CAD model and degradation due to exposure of SAGE III.

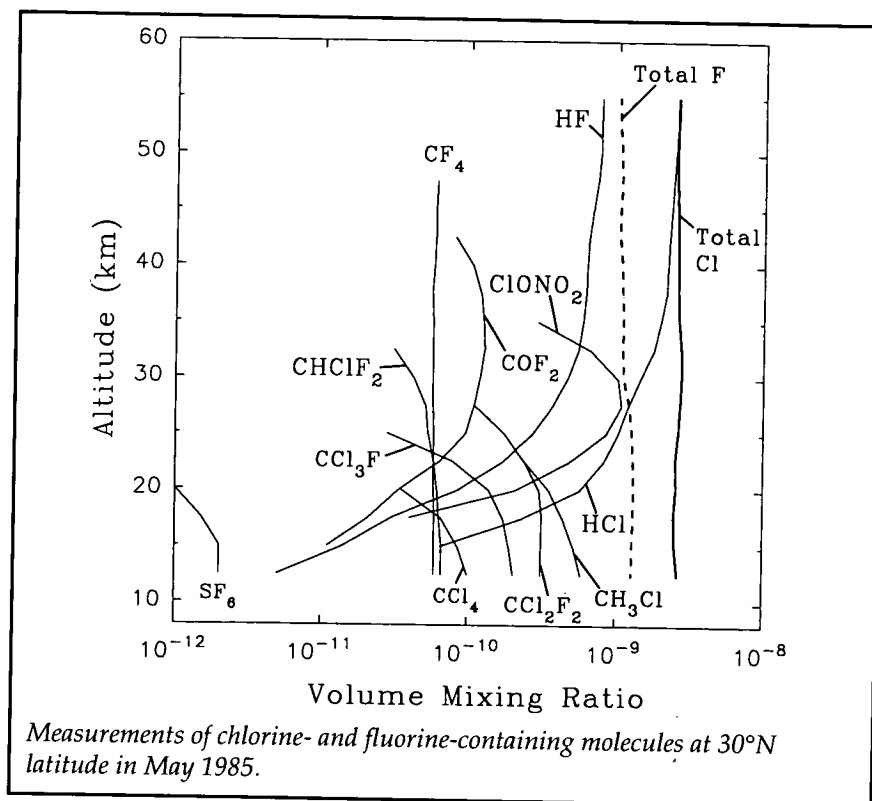
accurate data during the entire course of the mission.

(John E. Nealy, 44412, Garry D. Qualls, and Lisa C. Simonsen)
Space Directorate

The 1985 Chlorine and Fluorine Budgets in the Stratosphere

Over the past decade, considerable attention has been focused on the middle atmosphere because of concerns that man-made pollutants could alter the natural composition of that region and lead to a depletion of total ozone. In the spring of 1985, the Jet Propulsion Laboratory (JPL) Atmospheric Trace Molecule Spectroscopy (ATMOS) experiment was launched as part of the Spacelab 3 Space Shuttle mission to obtain simultaneous measurements of a large number of gases important in the chemistry of stratospheric ozone. The ATMOS instrument successfully recorded 500 high-resolution infrared solar spectra containing the spectral signatures of several dozen stratospheric gases.

The figure shows the measurements of chlorine- and fluorine-containing molecules derived from analysis of ATMOS spectra recorded near 30°N latitude. These results, obtained in collaboration with members of the ATMOS science team from JPL and the University of Liege, Belgium, show for the first time the details of the partitioning among the source, temporary reservoir, and sink molecules in these two chemical families. The measurements of the molecules



containing chlorine are particularly important because catalytic reactions involving this family are known to be effective in destroying ozone. The chlorine measurements in this figure and other ATMOS data have been compared with stratospheric model calculations as part of the 1992 Models and Measurement Workshop of the High Speed Research Program. (Curtis P. Rinsland, 42699)
Space Directorate

Classification of Satellite-Observed Cloud Fields Over the Amazon Basin

Infrared radiance measurements by the Geostationary Operational Environmental Satellite (GOES-6) from April 1986 through April

1987 are used to classify distinct regimes of persistent, large-scale cloudiness patterns over the Amazon Basin. These tropical weather regimes are responsible for the large-scale atmospheric processes that transport air, trace gases, and heat from the Amazon Basin. The cloud patterns are characterized by statistical textural parameters, such as contrast and homogeneity. These statistical measures were analyzed by using hierarchical clustering algorithms. Nearly 80 percent of the satellite images are identified as belonging to 1 of the 14 weather regimes that persisted for periods ranging from 3 to 15 days each.

While the classification analyses identified a range of organized weather conditions in the Amazon Basin, two weather regimes, each occurring in a separate season,

dominated the year. The dry season and the wet season in the Amazon are controlled by fundamentally different arrangements in large-scale cloud patterns and circulations. During the austral winter, the dominant dry season regime occurred 11 times during 25 percent of the year and delivered 81 percent of the dry season rainfall by large, isolated convective cells. During the austral summer, the dominant wet season regime occurred eight times, lasting for about 5 percent of the year, and accounted for more than 30 percent of the wet season rainfall in widespread, organized convective bands. This wet season regime was characterized by either westerly moving synoptic storm systems that formed in the central Amazon Basin or instability lines that formed along the coast. That such

a prominent condition can be objectively recognized from remotely determined information is important.

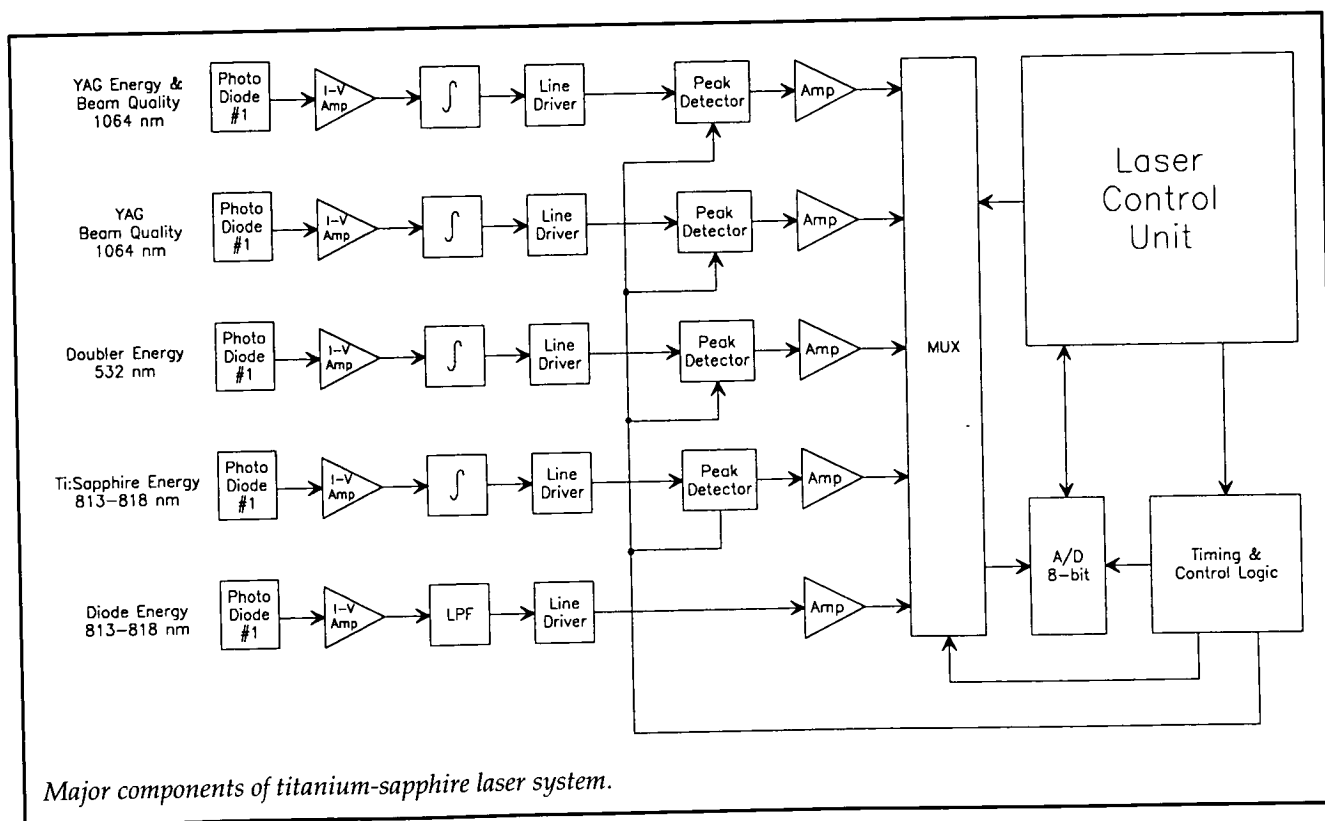
The dominance of a single dry season regime is significant because of the dependence of the rain forest ecosystem on the dry season rainfall. The wet season rainfall draws most of its water vapor supply from the Atlantic Ocean. However, the dry season rainfall may draw nearly half of the water vapor from local sources, such as rivers and vegetation. If the major source of water vapor during the dry season is removed by a process such as deforestation, the dry season rainfall will likely be drastically reduced. Under deforested and drought conditions, the regrowth of the rain forest may not occur. That a critical dry season regime exists suggests the

need to carefully examine and understand this weather condition. (Vickie S. Connors, 45849) Space Directorate

Laser Energy and Beam Quality Monitors for Lidar Applications

Differential Absorption Lidar (DIAL) experiments utilize laser energy and beam quality monitors to provide laser diagnostics and active control of pulse energies during flight. The detectors must be sensitive to wavelengths from the visible to the near infrared (IR), and the electronics must have large bandwidths and low noise.

One DIAL project under development at Langley Research



Center is the Lidar Atmospheric Sensing Experiment (LASE), which will measure atmospheric water vapor and aerosol concentrations derived from a titanium-sapphire (Ti:Sapph) laser system onboard an ER-2 aircraft. The block diagram displays the major components of the system, which was designed to meet stringent project requirements in the measurement of both energy and beam quality.

This system calculates the energy in millijoules (mJ) of each pulse of double-pulsed laser beams at the following wavelengths: 532 nm, 813 to 818 nm, and 1064 nm. No commercially available unit can measure both the 10- to 50-nsec-wide pulses that are produced 400 μ sec apart every 100 msec. The monitor output is part of a control loop that maintains a mean laser energy output greater than 150 mJ/pulse and compensates for variations in mean pulse energies. If the mean output energy is less than 127 mJ/pulse, laser operation is terminated.

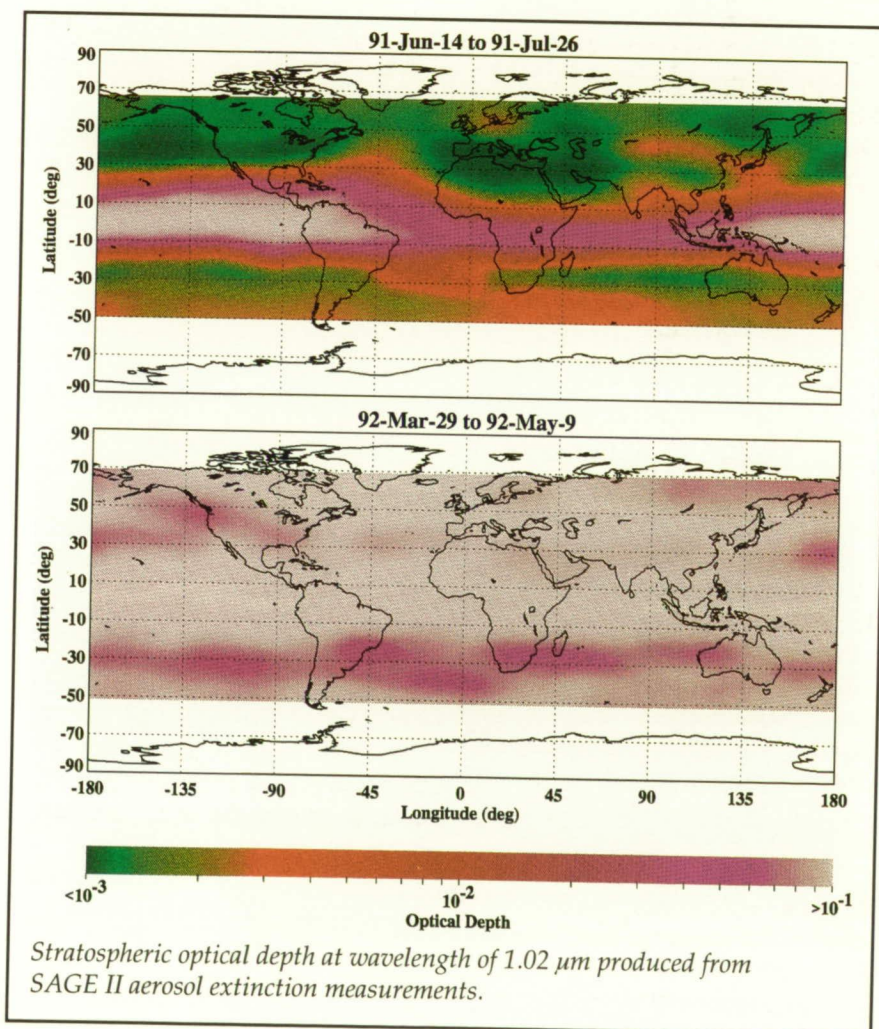
This system also calculates the beam quality of the 1064-nm beam. The beam is optically conditioned on the laser head to facilitate this measurement. Beam quality is determined by the ratio of energy measured at two monitor points. If this value is greater than a predetermined threshold, laser operation is terminated.
(C. D. Armstrong, 43701)
Electronics Directorate

SAGE II Observation of Mount Pinatubo Volcanic Aerosols

After centuries of dormancy, Mount Pinatubo in the Philippines (15°N, 121°E) erupted violently in mid-June 1991, spewing a large quantity of sulfur dioxide into the stratosphere. The sulfur dioxide is oxidized rapidly to sulfuric acid, which then combines with resident water vapor molecules to produce small (about 0.1- μ m radius) sulfate aerosol droplets. These aerosols reflect incoming solar radiation, which tends to

cool the Earth's surface, and absorb outgoing terrestrial radiation, which can warm the stratosphere by several kelvins in the region of the volcanic layer. It has been established that sulfate aerosols catalyze heterogeneous chemical reactions that perturb the stratospheric odd nitrogen and, hence, ozone budgets.

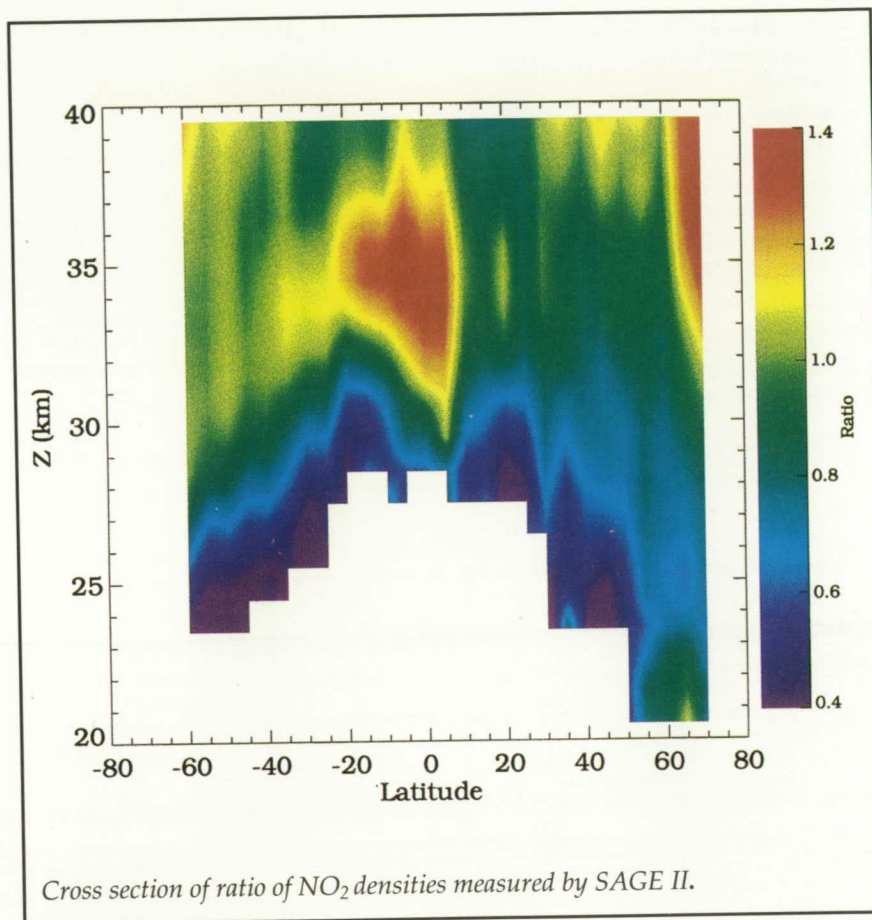
Optical depth data from the SAGE II (Stratospheric Aerosol and Gas Experiment II) satellite instrument suggest that Pinatubo has had a larger impact on the stratosphere than any volcano of the satellite era, and perhaps of the century. The figure presents



optical depth maps produced from SAGE II measurements just after the eruption (June and July 1991) and nearly 1 year later (March to May 1992). The earlier map shows a dense belt of aerosol material encircling the globe in the Tropics, with local optical depths a factor of 100 higher than those observed a month earlier, prior to the eruption. The later map shows similarly high optical depths nearly everywhere around the world. Based on observations of previous eruptions, optical depths are expected to remain high for several more years. It is estimated that Pinatubo produced approximately 36 megatons of sulfate aerosol mass, or some 3 times that observed following the 1982 El Chichon eruption. (M. P. McCormick, 42669) Space Directorate

SAGE II Observations of Decreased Nitrogen Dioxide Following the Mount Pinatubo Eruption

As a result of the June 1991 eruption of Mount Pinatubo, the amount of sulfate aerosol material in the stratosphere increased by one to two orders of magnitude. Recent laboratory and theoretical studies suggest that sulfate aerosols are efficient catalysts of heterogeneous chemical reactions that lower stratospheric concentrations of nitrogen dioxide (NO_2) and, perhaps, ozone. Ground-based measurements of column NO_2 amounts at twilight in New Zealand indeed began to show significant and persistent negative departures from normal levels in early September 1991.



Post-eruption measurements of NO_2 vertical profiles by the space-borne SAGE II (Stratospheric Aerosol and Gas Experiment II) instrument show that marked decreases have occurred in NO_2 concentration at altitudes under 30 km, with maximum losses at or below 25 km. The figure shows, as a function of altitude and latitude, the ratio of NO_2 density in March 1992 to the average of densities observed during March from 1985 to 1990. The range of normal year-to-year variability in NO_2 density is about ± 30 percent, with the largest variability occurring near the Equator around an altitude of 35 km and at high latitudes during nonsummer months. The Pinatubo volcanic cloud was so opaque at low

altitudes in the Tropics and the middle latitudes that no NO_2 data could be retrieved. However, in adjacent areas where aerosol levels were still extremely high, NO_2 densities in 1992 were often less than 60 percent (and occasionally as low as 40 percent) of the normal monthly average value. Such decreases were observed in the Southern Hemisphere within a few months following the eruption but were not observed in the Northern Hemisphere until March 1992.

(J. M. Zawodny, 42681)
Space Directorate

Fourier transform spectrometers (FTS's) generally utilize a laser-based interferometer fringe system to control the moving mirror carriage displacement to a very high precision. The requirements for the laser are that it be highly stabilized in frequency, continuous wave, and single mode to provide good fringe visibility. A number of HeNe lasers are commercially available which meet these requirements. However, for a space-based FTS instrument, such as the proposed Spectroscopy of the Atmosphere using Far Infrared Emission (SAFIRE), HeNe technology has significant drawbacks, including high voltage requirements, marginal lifetime (typically 40 000 hours), and power (150 μ W). The rapid progress

occurring in solid-state laser technology, which is the basis of laser printer and compact disk devices, offers an attractive alternative. Solid-state lasers are readily available with much higher power (30 mW) and longer lifetimes (>100 000 hours) than HeNe lasers.

Frequency stabilization techniques using saturated absorption provide the basis for developing a prototype laser for space-based operation which uses the saturated absorption of the 780-nm rubidium (Rb) line to stabilize the frequency of an AlGaAs laser diode. The basic system, which is shown in the block diagram, consists of a single-frequency laser diode source, a collimating lens, and a PZT-mounted grating. With appropriate optics the laser output passes in a counter-propagating fashion to provide a stable frequency lock to the Rb absorption line.

A flight-qualifiable prototype system has been designed and

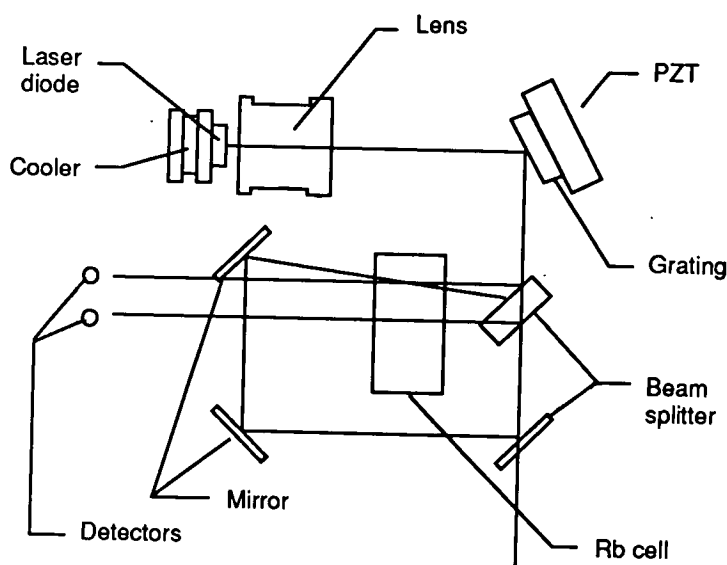
fabricated. The laser system will have a center frequency of 780 nm, a power output of >20 mW, a lifetime >100 000 hours (>11 years), a line width of <500 kHz, and a frequency stability better than 1 part in 10^9 .

(Ira G. Nolt, 41623, and
Don Jennings)
Electronics Directorate

Validation of UARS-HALOE Measurements by Far Infrared Balloon Emission Spectroscopy

The Far Infrared Balloon Experiment (FIREX) is an International Cooperative Program for the purpose of validating Upper Atmospheric Research Satellite-Halogen Occultation Experiment (UARS-HALOE) measurements of water vapor, ozone, hydrogen chloride, and hydrogen fluoride stratospheric mixing profiles. A helium-filled balloon of 27 million ft³ serves to carry the instrument payload to an altitude of 40 km (130 000 ft) for a float duration of up to 24 hours. The launch window provides nearly coincident measurements with an overpass by UARS. In this way a comparison of the measurement of the same species by two different techniques provides essential validation checks for satellite measurements.

High-resolution measurements of the far infrared emission spectrum of the stratosphere were first obtained in 1978 following the Italian development of a balloon-borne Fourier transform spectrometer. In 1988, an International Cooperative Program was instituted by Langley and the Italian



Rubidium stabilized laser diode system.

UARS - HALOE VALIDATION

FAR - IR BALLOON EXPERIMENT (FIREX)

UARS-HALOE configurations.

Space Agency to upgrade the performance of this instrument for use in the Correlative Measurement Program of UARS. The

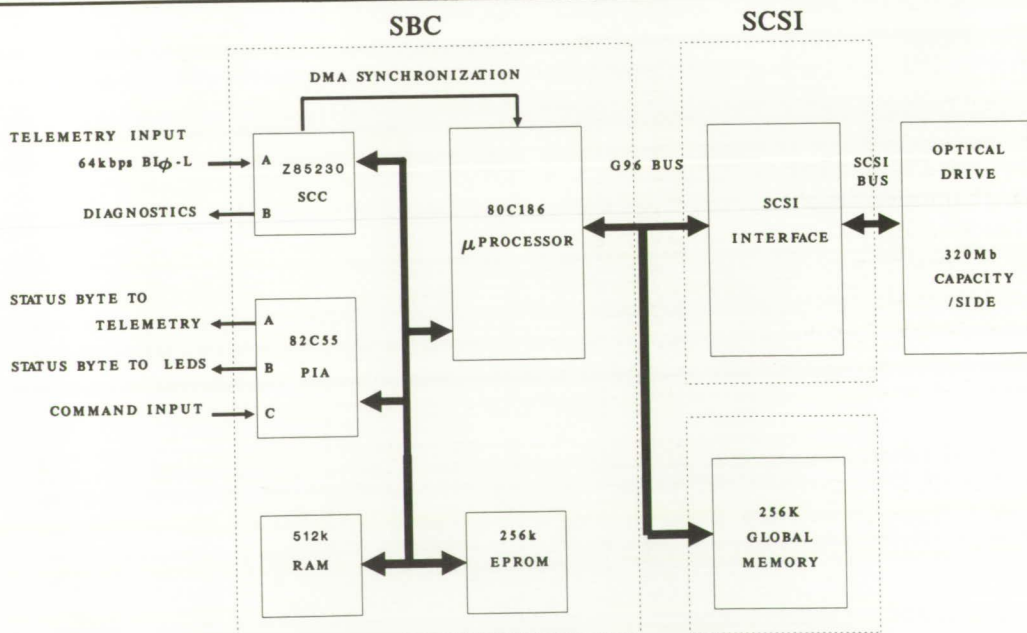
FIREX instrument exploits advances in cryogenic photoconductive detectors and narrow-band filters to achieve the first photon-noise-

limited performance in high-resolution stratospheric emission measurements.

Preliminary results from the first flight of this instrument have verified the HALOE measurements of water vapor, ozone, and hydrogen fluoride in the stratosphere. An important feature of these far infrared measurements is their insensitivity to the presence of volcanic aerosols from the Mount Pinatubo eruption. Analysis is under way of approximately 10 other gases, including difficult-to-measure hydrogen bromide. (Ira G. Nolt, 41623, and B. Carli) Electronics Directorate

Onboard Optical Disk Telemetry Recording System for Balloon Experiments

Many high-altitude atmospheric and astronomical experiments are



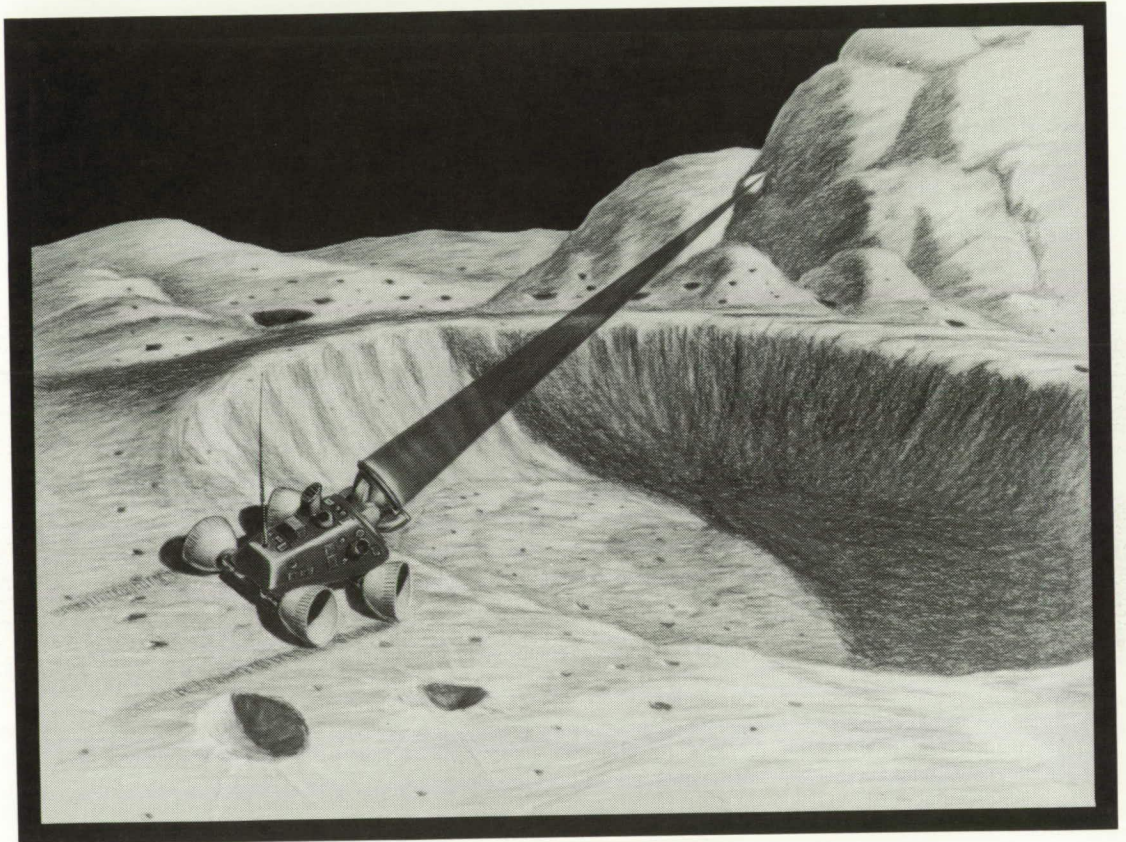
FIREX optical disk data recording unit.

flown from balloon-borne platforms in the space-like conditions of the upper stratosphere. As these platforms are subject to the winds at altitude, the flight durations are generally limited to a few hours imposed by the requirement for line-of-sight down-link telemetry. The development of a reliable, low-cost, low-power onboard data storage system would provide a significant extension to many flight durations and a greater reliability.

The write once read many (WORM) optical disk technology offers significant advantages for onboard balloon data recording. Foremost, the fact that the data are permanently etched into a removable disk means that even in the event of a hard landing and mechanical damage, the data are likely to be recoverable. This system provides the means to decommutate and record a high-rate PCM telemetry stream with a bit error rate (BER) exceeding 10^9 .

The figure is a block diagram of the optical disk data recording unit that has been developed and has undergone initial field tests. The prototype system is now being prepared for a high-altitude flight in early 1993. This system can be programmed to accept either an NRZ or a biphasic telemetry stream at a maximum data rate of 650 kilobytes per second and record it on the optical drive. Writing one side of a standard 320 megabyte disk, in our case at 64 kilobytes per second, provides for approximately 11 hours of data recording. Total power requirement is about 40 W.
(Michael D. Vanek, 41624)
Electronics Directorate

■ PLANETARY SURFACE TECHNOLOGY



Provide technology for space exploration missions, including renewed exploration of the Moon, the establishment of a human-tended lunar base, and piloted missions to explore the planet Mars

Separation of O₂ From the Martian Atmosphere

Carbon dioxide at pressures less than 5 torr can be dissociated by electron impact into atomic oxygen and other constituents by using a glow discharge. The resulting atomic oxygen and the recombined molecular oxygen (O₂) can then be separated from the glow discharge region by permeation through a hot silver (Ag) membrane and then compressed into a storage volume.

A system based on this process and including a method for the subsequent storage of the O₂ is shown. The glow discharge is created with a power of less than 0.5 W at a pressure of 0.75 torr and breaks down the CO₂ into CO and atomic oxygen. The oxygen adsorbs onto the Ag, dissolves into the bulk, and automatically diffuses through to a downstream low-pressure region, where the oxygen recombines and desorbs as O₂. The flux of O₂ permeating through to the downstream region increases substantially after glow discharge excitation. Initially

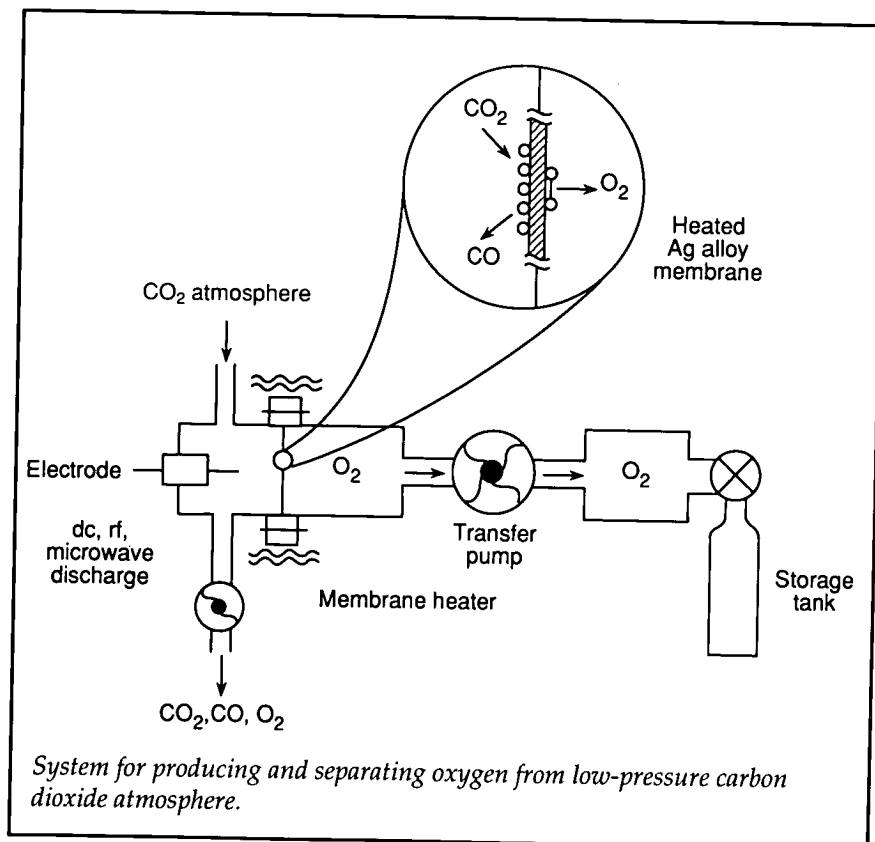
there is a slight O₂ flux due to dissociative adsorption of the CO₂ before glow discharge, and then, subsequent to the glow discharge strike, an increase of two orders of magnitude corresponding to a flux of 2×10^{14} molecules-cm⁻²-sec⁻¹ at a membrane temperature of 650°C is observed.

This simple, low-power, glow-discharge-assisted oxygen separation from CO₂ can be applied to producing pure oxygen for astronaut consumption in a planned Mars mission. An array of such cells with target membranes of approximately 1 m² in total area would provide sufficient oxygen to support four astronauts on a continuous basis during the mission, and additional units could generate sufficient oxygen for the return voyage home.

(R. A. Outlaw, 41433)
Space Directorate

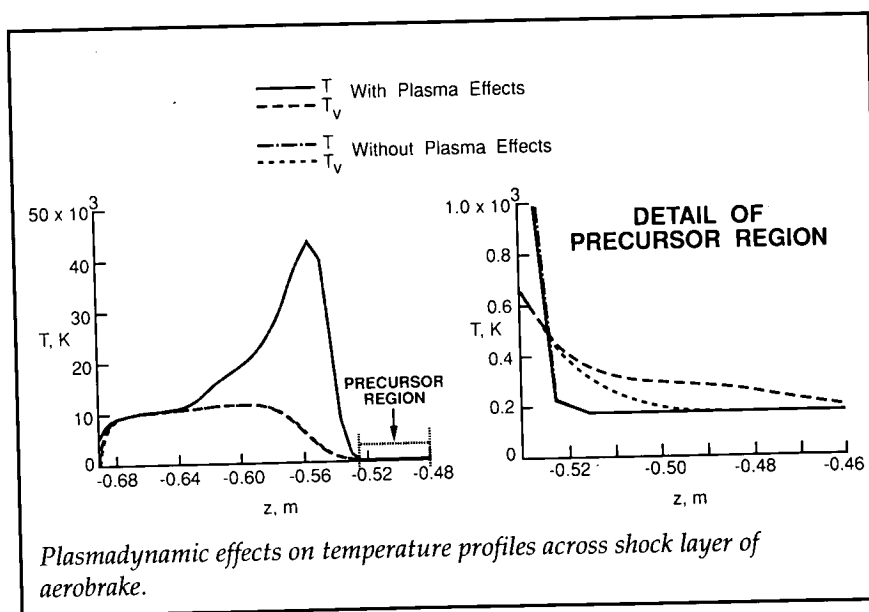
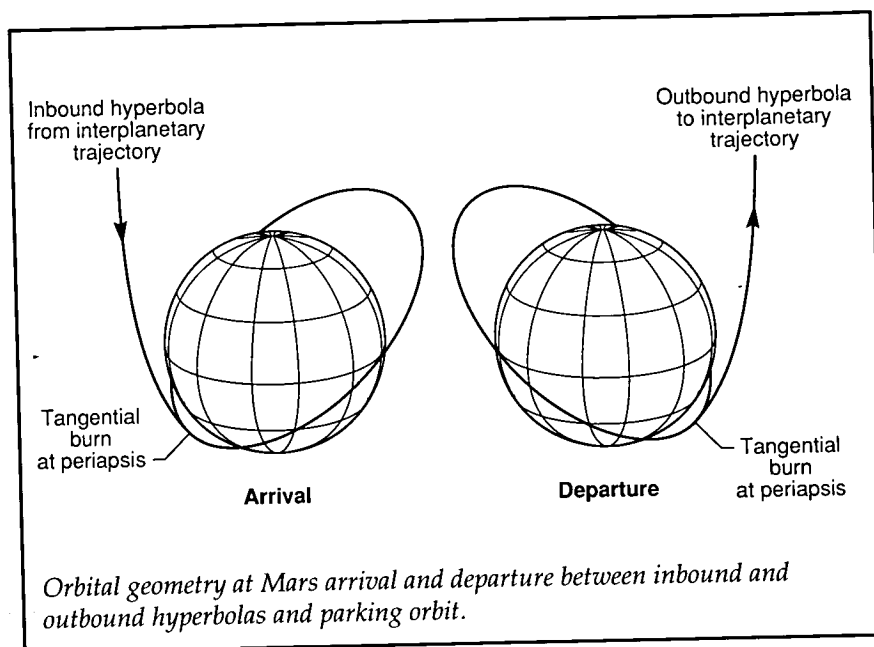
Determination of Mars Parking Orbits

For a human-tended Mars mission, the selection of the Mars parking orbit can greatly influence the overall mass of an interplanetary vehicle in low Earth orbit. If chosen arbitrarily, the parking orbit selection may produce an optimistic estimate of the mass of the interplanetary vehicle. In many past interplanetary studies, parking orbits were arbitrarily



assumed which utilized tangential periapsis burns at both Mars arrival and departure without considering the actual arrival and departure orbital geometries. As a consequence of this assumption, a misleading estimate approaching 50 percent of the initial low Earth orbit mass resulted for some missions. Therefore, a method has been developed that determines which Mars parking orbits can utilize tangential periapsis burns at both arrival and departure. This method accounts for the actual orbital geometry at both Mars arrival and departure, as shown in the figure, between the inbound and outbound hyperbolas and the parking orbit. Additionally, this method also accounts for the precession effects on the parking orbit caused by the nonspherical gravitational field of Mars. As a result, realistic initial low Earth orbit masses can be obtained.

The results obtained from this method compare very well with a trajectory integration code, for which the differences were within 1 percent. The computation time required to obtain the results with the present method were about 1 minute of CPU time, while the trajectory integration program required hours of CPU time. Hence, because of the accuracy and computational efficiency, the present method would be an ideal tool to use in preliminary mission design, since it provides the opportunity to incorporate realistic effects of Mars parking orbits. (Prasun N. Desai, 42986, and James J. Buglia)
Space Directorate



Plasmadynamic Effects in Thermochemical Nonequilibrium Aerobrake Flows

Plasmadynamic effects are typically neglected when the aerothermal environment around reentry vehicles is predicted. The objective

of this work is to reexamine this assumption for high-energy aerobrake flow fields characteristic of Earth entry upon return from the Moon and Mars.

Additional terms in the governing equations are derived to allow nonzero electrical currents in thermochemical nonequilibrium flow with significant degrees of

ionization. The Langley Aerothermodynamic Upwind Relaxation Algorithm (LAURA) code is modified to include these additional terms. The detailed magnetic field and coupled plasmadynamic effects in two aerobrace flow fields are computed.

The ohmic heating of free electrons by induced electrical current for these flows is shown to be small. For the two-temperature solutions generated, this heating results in a small increase in the vibrational temperature in the shock precursor region shown in the figure. This small effect does not translate into any noticeable effect within the shock layer or on

the body surface. For these Earth entry conditions, it is not necessary to include plasmadynamic effects.

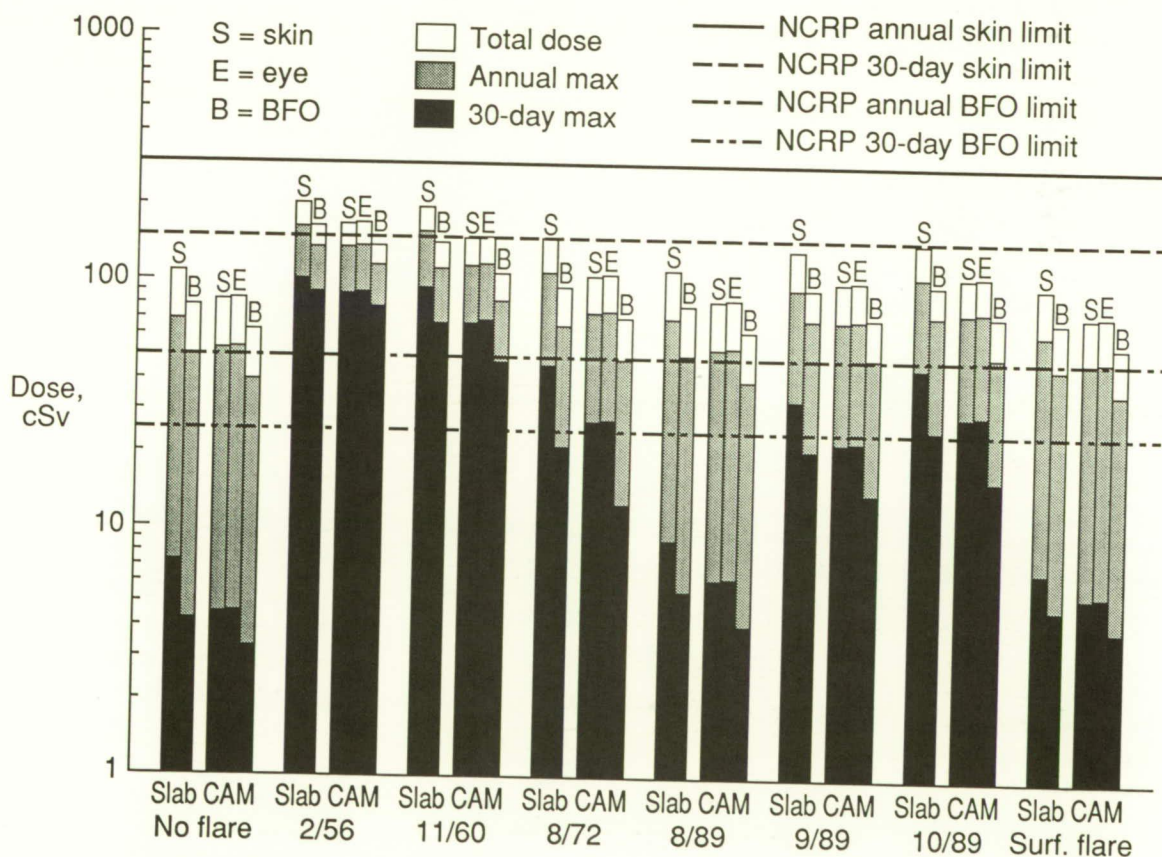
(R. A. Mitcheltree, 44382, and J. V. Shebalin)

Space Directorate

Radiation Exposure Predictions for Short-Duration-Stay Mars Missions

Predictions of the crew radiation exposure for Mars missions can be incorporated into preliminary mission and vehicle design using the Mission Radiation Calculation

(MIRACAL) computer program recently developed at Langley. MIRACAL includes extensive information related to the major natural radiation sources for exposure during interplanetary missions (i.e., galactic cosmic rays (GCR) and very large and ordinary solar proton flares). From the effective operational and storm shelter shielding thicknesses, large flare type and time of occurrence, and astronaut model selected (either slab skin and blood-forming organs (BFO) or computerized anatomical man (CAM) skin, eye, and BFO), an estimate of the radiation environment and incurred dose can be made.



Radiation exposure for mission during solar minimum.

To demonstrate the application of this code, the incurred doses for several short-duration-stay Mars missions were estimated. In this study, three operational shield thicknesses (2, 4, and 6 g/cm² water slabs), four storm shelter thicknesses (10, 15, 20, and 25 g/cm²), and three times spent in the storm shelter other than during solar flares (zero, one-third, and one-half day) were analyzed for 12 missions between 2004 and 2025. The scenarios in this analysis assumed a best case of no large flares during the mission, six worst cases each with large flares occurring at perihelion of the interplanetary transfer, and one case of surface flares.

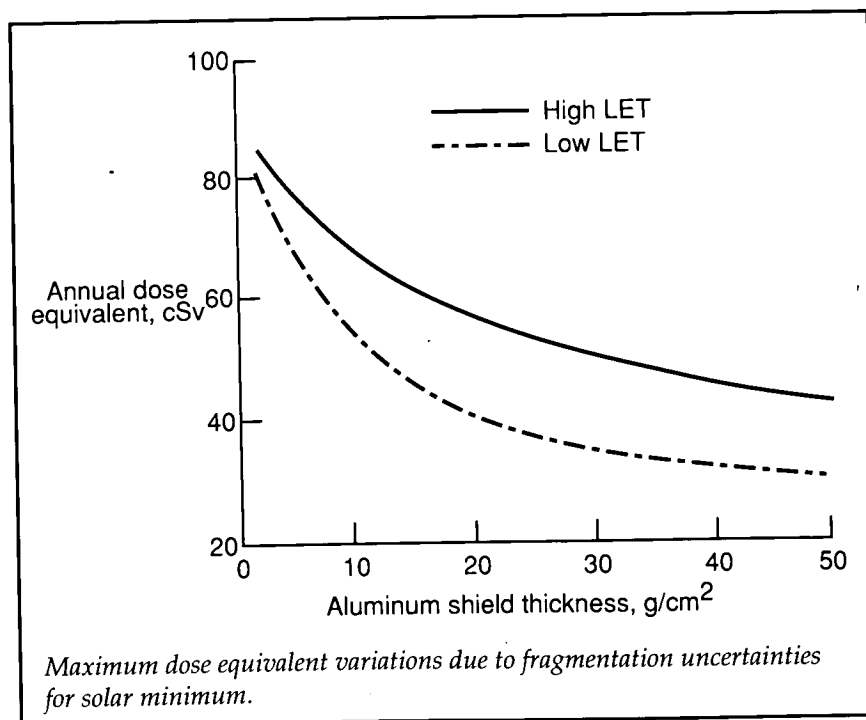
The figure illustrates dose estimates for a mission that occurs primarily during solar minimum (quiet sun with no flares). The results of this study indicate that missions during solar minimum are not necessarily the lowest dose cases because of increased GCR contribution. Also, the Martian atmosphere apparently provides sufficient shielding during a surface stay, and increasing the astronaut's nominal time in the storm shelter can reduce the GCR dose (spending one-third of a day, or an 8-hour sleep cycle, in the storm shelter can noticeably reduce an astronaut's incurred dose). In this study, the direct transfer mission had slightly lower doses than the outbound Venus swing-by mission (only 10 to 20 cSv difference). (Scott A. Striepe, 44512, John E. Nealy, and Lisa C. Simonsen) Space Directorate

Galactic Cosmic Ray Fragmentation Cross-Section Uncertainty Analyses

A key radiation exposure issue is the impact of nuclear fragmentation cross-section uncertainties on galactic cosmic radiation shielding requirements for deep-space missions. Since estimates of shield requirements are made using dose equivalents, uncertainties in the latter directly impact spacecraft shield design by introducing significant weight penalties to account for them. Because of the paucity of experimental nuclear fragmentation data for spacecraft materials, dose-equivalent uncertainties resulting from the use of theoretical nuclear fragmentation models cannot be reliably established. It is possible, however, to determine upper and lower bounds by investigating the

physically limiting causes of the fragmentation event.

The minimum event (upper bound) occurs whenever the collision removes only a single neutron or proton from the fragmenting nucleus. This we denote as a "high LET" case because each produces a heavy fragment. The maximum event occurs whenever the fragmenting nucleus completely disintegrates into its constituent nucleons. This we denote as a "low LET" case because there are no heavy fragments produced by the breakup. From a physical perspective, every fragmentation event must be between these two extreme cases. Restricting every event in the transport code to one or the other yields bounds on the estimated dose equivalent. The figure displays these bounds as a function of aluminum shield thickness. Variations in dose equivalent as large as 50 percent are possible. The resulting bounds on shield-



mass requirements are an order of magnitude.

(L. W. Townsend, 41417)
Space Directorate

In-Space Assembly, Servicing, and Operations

The Space Exploration Initiative Office has completed initial studies of the in-space assembly, servicing, and operations issues that must be considered for any future missions to the lunar surface or beyond. The rescue servicing of the Intelsat IV satellite, the planned servicing of the Hubble Telescope, and the planned assembly of Space Station *Freedom* underscore these needs. Another reason for consideration of assembly, servicing, and operations issues at this time is the need to understand the impact of operations early in the design concept stages of a program.

This study used the 2016 Reference Advanced NTR Mars Transfer Vehicle (MTV), along with proposed launch vehicles of 150 and 250 metric tons. The baseline MTV was manifested on each of the proposed launch vehicles. Top level operational scenarios were then developed listing the operations that would have to be carried out on orbit to assemble the vehicle. Each operation was then reduced to a minimum complexity state, the result being a set of operational primitive functions for the assembly and servicing processes. These primitive functions were then used to assess the trade-offs between robotic, telerobotic, and EVA operations. The study demonstrated that the complexity of the in-space

operations remains constant with launch vehicle size after the second launch. Only the number of times that each operation must be carried out changes with launch vehicle size. Therefore the functions, and ultimately the infrastructure required to support proposed missions, are relatively unaffected by varying the launch vehicle size.

(Charles E. Cockrell, 47139)
Space Directorate

SEI Early Lunar Rover Mission Studies

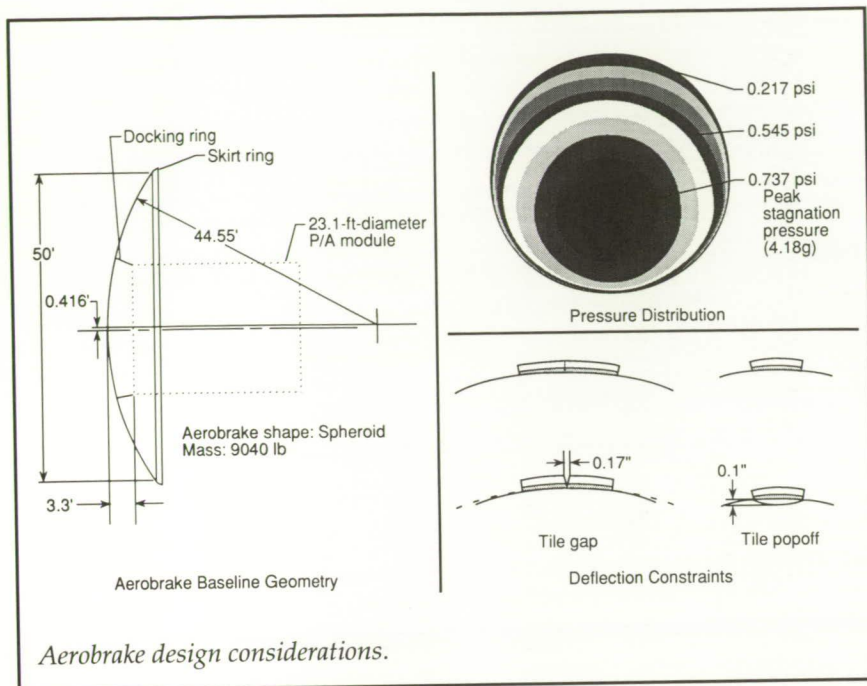
A Phase 1 study of possible Early Space Exploration Initiative (SEI) missions was completed. The study focused on broad concepts to meet SEI early goals and constraints and resulted in a concept that appeared to have merit. The concept placed emphases on supporting future SEI missions, supporting education, providing experience for young NASA engineers, providing telerobotic experience on the Moon, providing long life (25 lunar cycles), developing no technology, and controlling costs. The concept was refined in a Phase 2 effort.

Although the initial concept changed little, significant revisions were made to implementation and hardware concepts. These revisions were made based on an enhanced understanding of SEI goals and maturing requirements. The concept for an approximately 1-m-wide by 1.5-m-long by 1.2-m-high rover with a mass of 60 kg and a science fraction of 25 percent was specifically strengthened in support of emerging science requirements. Phase 2 concluded

that the concept continues to have merit, and a Phase 3 study was initiated to identify technical and programmatic issues requiring solution before a formal new start proposal can be made. Phase 2 and Phase 3 studies were supported by personnel from DoD's Corps of Engineers and DoE's Sandia National Laboratory. (Vernon P. Gillespie, 48209)
Space Directorate

A Space-Based Aerobrake Reference Configuration

A two-phase study has been completed that not only delineated the major considerations for a space-based aerobrake but also generated a reference configuration to guide further design. The two-phase study was initiated as part of the Space Exploration Initiative efforts to develop viable scenarios for Moon and Mars exploration. Several important results were generated during the course of the study. Among these were aerobrake diameter definition, with the major controlling factors such as load-induced wake closure modulation taken into account. In addition, equilibrium and nonequilibrium heating were defined for the model trajectory, the result being that ablators and reusable surface installation are both viable thermal protection system candidates. Since the aerobrake shape was a large, blunt form, the heating regime was found to be very poorly understood. A computational fluid dynamics code was used in conjunction with several nonequilibrium radiation codes and revealed major inconsistencies in

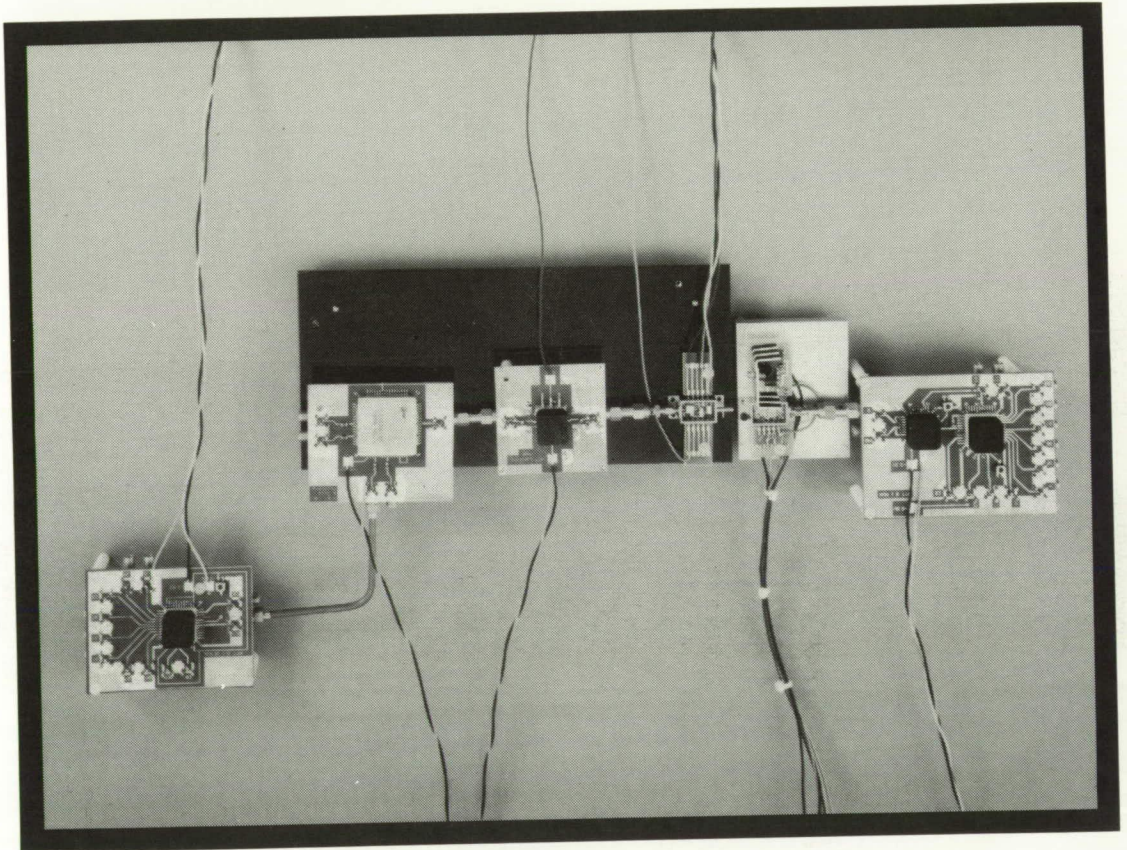


these widely used analytical techniques.

Additional results were obtained in advanced structural analysis and design, robotics techniques to facilitate on-orbit operations, and accommodation impacts on Space Station *Freedom*, where the aerobrake is to be based. A high degree of relevance for the entire study was ensured through mission requirements taken directly from Marshall Space Flight Center Space Transportation Vehicle definition activity. Moreover, frequent regular coordination meetings were held to ensure consistency with the evolving space vehicle baseline design. (Stephen J. Katzberg, 41600) Space Directorate



■ OPERATIONS TECHNOLOGY

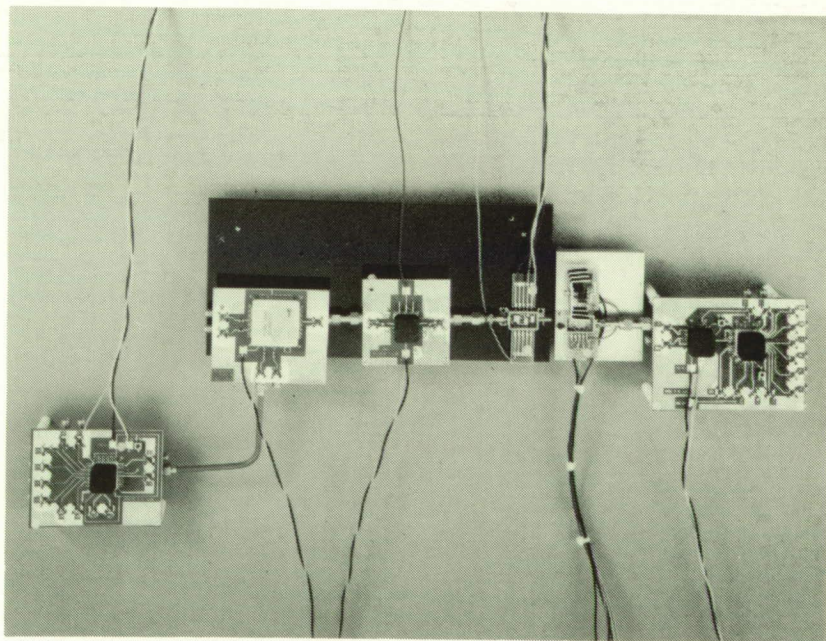
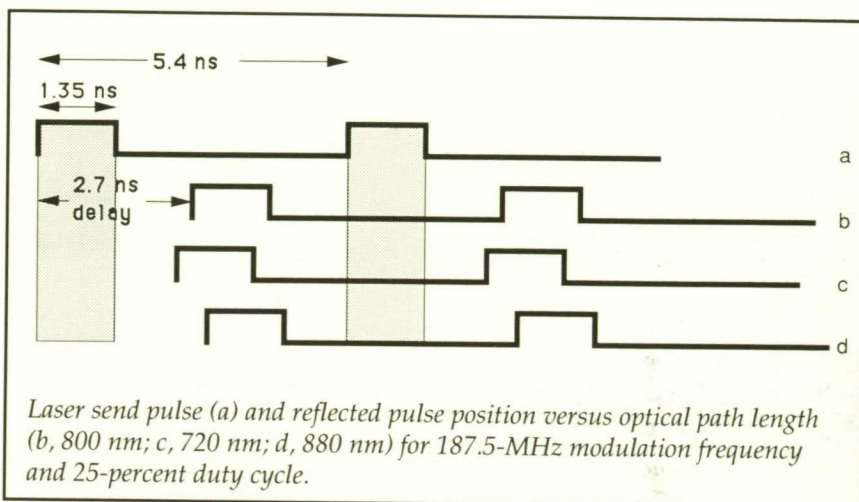


*Develop automation,
robotic, information, and
communications technologies
to reduce the cost, improve
the safety, and enable more
complex civil space operations*

Preceding Page Blank

Elimination of Relative Intensity Noise From Linear Diode Laser Array of Space Optical Disk Recorder

A novel timing technique has been implemented to electronically drive the linear diode laser array (LDA) in the Space Optical Disk Recorder (SODR). This technique allows the relative intensity noise (RIN) due to reflected laser signals from the optical disk to be eliminated. In reading data from a magneto-optical disk of the SODR, a linear laser diode array is used to optically illuminate the data on the recording disk. Because optical energy is reflected from the surface of the disk back into the LDA, the mode structure of the laser is upset and produces RIN. The distance from the LDA to the disk is constant within the variation of the radius from which the data are read. A timing scheme can be implemented as shown in the figure to cause the laser to be in the *off* mode when the light beam is reflected from the entire recording disk. By calculating the round-trip frequency from the laser to the disk and back and controlling the duty cycle during which the laser is on, the return of the reflected light beam from the disk can be controlled to arrive at the laser when the laser is *off*. This scheme has been implemented and tested with the SODR optical design path and has been shown



High-speed fiber optic transceiver.

to eliminate the RIN, greatly enhancing the carrier-to-noise ratio of the entire electronic system of the SODR.

(Anthony L. Cook, 46502, and Herbert D. Hendricks)
Flight Systems Directorate

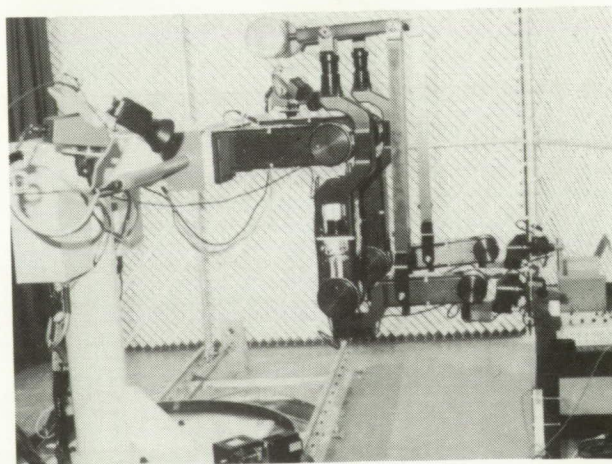
High-Speed Fiber Optic Transceiver

A high-speed fiber optic transceiver, shown in the figure, has been demonstrated. The transceiver was fabricated from all-integrated circuits, high-speed distributed feedback lasers, and p-i-n detectors. The transmitter consists of an 8:1 multiplexer, a laser driver with an InGaAsP distributed feedback laser, and a thermoelectric cooler in a 10-pin dual in-line package. The receiver section consists of an InGaAs p-i-n detector coupled with a transimpedance amplifier and automatic gain control circuit in a 10-pin dual in-line package. This is coupled to a limiting amplifier and then into a clock and data recovery circuit and an 8:1 demultiplexer. Evaluations of the analog laser driver, the distributed feedback laser with the p-i-n detector, the transimpedance amplifier, and the automatic gain control circuits provide digital operating speeds in the Manchester data format to greater than 4.1-GHz. Applications of this technology are for high-speed and high-capacity data systems for future NASA missions.

(Herbert D. Hendricks, 41536)
Flight Systems Directorate

Study of Force Reflection With Telerobotic Hand Controller in Position Control Mode

The issue of whether or not force reflection is desirable for space telerobotic control has been raised frequently by those working



Kraft controller (top) and Laboratory Telerobotic Manipulator (bottom).

in the Space Station *Freedom* Program. An experiment was performed to evaluate the effectiveness of kinesthetic force feedback to a telerobotic input control device (hand controller) operating in a position control mode for two Space Station *Freedom* tasks. Eight undergraduate engineering students performed, with and without force reflection, a dual-peg-in-hole task and a thermal blanket task. For this experiment, the students controlled the Laboratory Telerobotic Manipulator in the Telerobotic Systems Research

Laboratory with a Kraft six-degree-of-freedom hand controller operating in a position control mode. Four camera views were available to the students in order to perform these tasks; however, no direct visual views were allowed. Task completion times, mechanical work done by the manipulator, and subjective assessments were recorded for each condition.

No statistically significant differences were found between average total task completion times and average mental work-

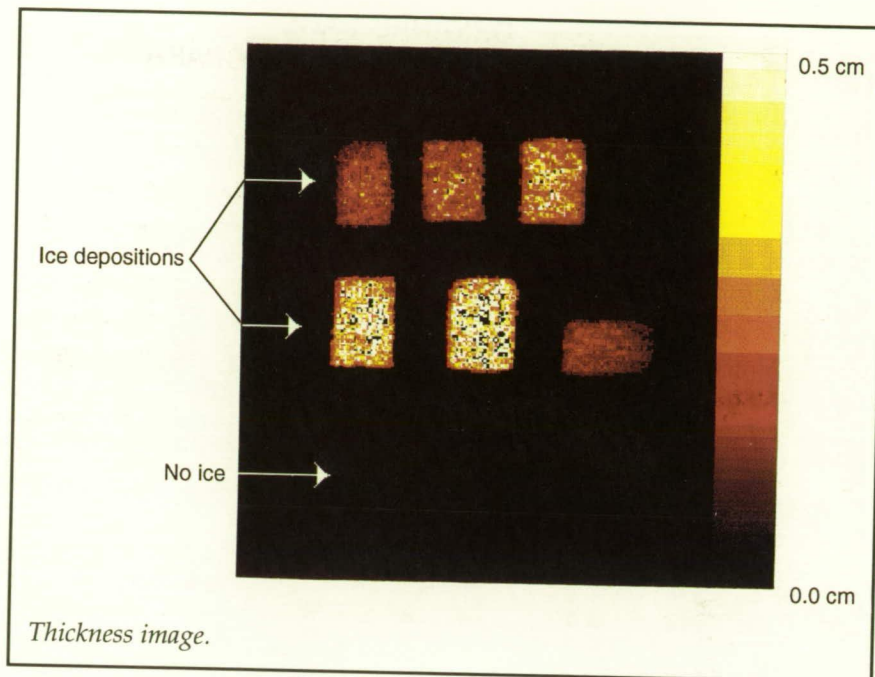
load ratings for the two tasks with and without force reflection. There were significant differences by gender for the thermal blanket task in that females performed the task faster than the males. They performed the dual-peg task in about the same time. Although force reflection tended to create longer average total task completion times and was related to somewhat more bodily discomfort, the subjects ranked the force reflection conditions as being easier to perform than the no-force conditions. However, other subjective measures did not consistently agree with this trend. Therefore decisions based upon such subjective data with respect to force reflection should be made with caution until further studies are performed. Results of this experiment will increase the small data base of telerobotic hand controller performance in space-related tasks using force reflection.

(Kelli F. Willshire, 41965)

Flight Systems Directorate

Quantitative Determination of Ice Thickness With the Thermal Remote Ice Measurement (TRIM) System

Accretion of ice on aerospace structures is a problem affecting takeoff safety and aerodynamic performance. In particular, ice formation on the Space Shuttle external tank can result in structural damage during launching if ice of appreciable mass detaches and impacts the orbiter surface. Work is under way in the Nondestructive Measurement Sciences Branch to develop the Thermal Remote Ice



Measurement (TRIM) system to detect the onset of ice formation and to measure ice thickness on the Space Shuttle external tank prior to launch.

corresponding to those at the shuttle launch site.

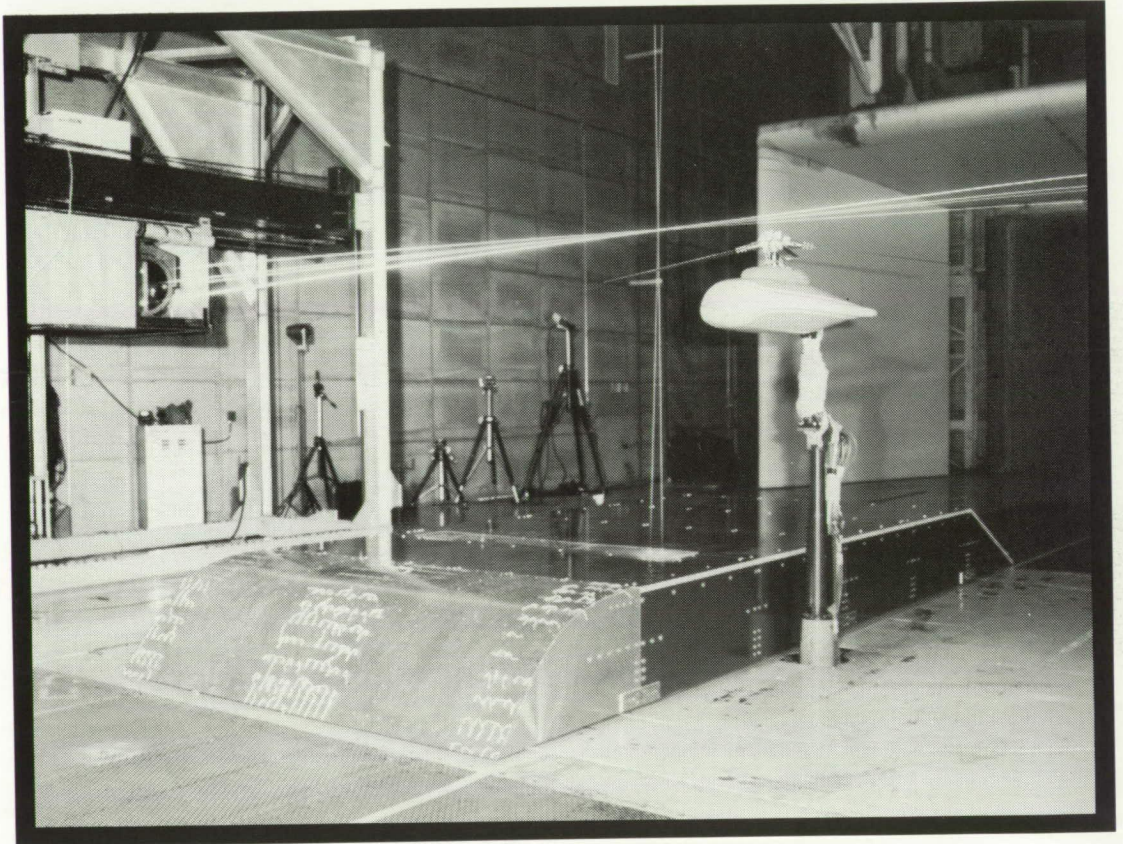
(D. M. Heath, 44964)

Electronics Directorate

The system utilizes an IR imager and a radiative thermal source, which deliver a flash heating pulse and record the resultant temperature response at the ice surface. A theoretical model has been developed which relates the temporal evolution of surface temperature to ice thickness with consideration of heat attenuation through the ice layer. Measurements have been performed in a laboratory setting which affirm the system's ability to determine the thickness of known ice layers and to detect the presence of ice deposited at various thicknesses on an insulating substrate. The figure depicts results of such measurements for a range of ice thicknesses. Design modifications are under way to allow demonstration of the system in environments

ORIGINAL PAGE
BLACK AND WHITE PHOTOGRAPH

■ FACILITIES



*Develop, maintain, and operate
national facilities for aerospace
research and for industry
and Department of Defense
development support*

Three-Component Laser Velocimeter for the 14-by 22-Foot Subsonic Tunnel

The objective was to develop a three-component laser velocimeter (LV) system for measuring the velocities produced by aerodynamic models tested in the 14-by 22-Foot Subsonic Tunnel. A single-component LV was designed by the Instrument Research Division to augment the existing two-component LV and to provide a full three-component orthogonal measuring system. The two-component LV, shown in

the background of the figure, was modified to interface with the optical components comprising the third component. The hardware for the third component was housed in the aerodynamic fairing shown at the bottom of the figure. Measurements in this test were made on the wake produced by the helicopter model shown in the foreground. Laser light sheet and video flow visualization was used to examine the flow to determine the optimum locations for flow measurements in order to maximize the use of available tunnel time.

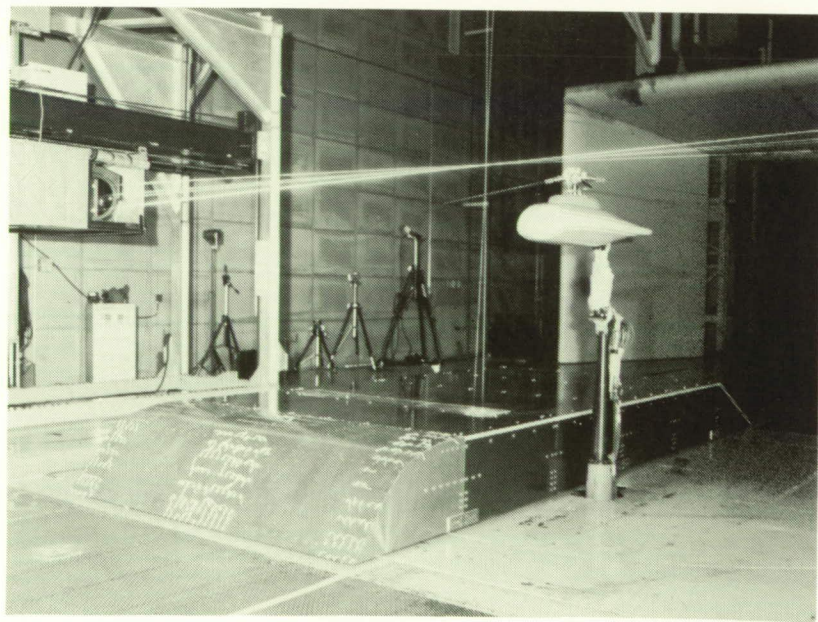
The two-component laser velocimeter has been successfully

used in this facility for making velocity measurements in locations where the flow was anticipated to be two dimensional. The addition of the third component provides the capability to measure velocities in highly three-dimensional flow fields at a model scale and focal length that do not exist elsewhere.

Plans are currently under way to permanently incorporate this capability into the LV system and to lower the floor of the tunnel so that the application of the third component will not adversely affect the flow conditions in the test section of the tunnel. With those improvements in place measurements of vortical, separated, and other high three-dimensional flows are possible. This work was done in part under contract with Lockheed Engineering and Sciences Co., Analytical Services & Materials, Inc., UNISYS Corp., and Old Dominion University. (Joe W. Elliott, 41059, W. Derry Mace, Jr., Susan A. Gorton, Terence A. Ghee, Judith K. Jumper, Fred H. Miandoab, and Timothy E. Hepner) Aeronautics Directorate

Aerodynamic Stability Test Instrumentation That Uses Digital Signal Processing Techniques

Dynamic stability research conducted in Langley wind



Three-component laser velocimeter installed in 14-by 22-Foot Subsonic Tunnel.

tunnels employs a technique in which the model is mechanically forced to oscillate at fixed amplitude and resonant frequency. A specially designed oscillating balance is used to measure model displacement as well as aerodynamic force and moment loads. These load signals, which are noisy and low in amplitude, must be amplified and resolved into complex phasors relative to the displacement signal for computation of aerodynamic stability and damping parameters.

Existing instrumentation uses AC-carrier excited rotating electro-mechanical resolvers. A replacement DC system, developed in-house, employs digital signal processing (DSP) microcomputers that perform high-data-rate numerical computations. A host personal computer provides a user interface and displays computed results. Two alternative DSP algorithms have been implemented. The first algorithm, a time-domain approach, is a numerical synchronous demodulator and narrow-band low-pass filter. It provides high noise rejection, but phasor information is available only at the forcing frequency. The second algorithm, a frequency-domain approach, computes a fast Fourier transform (FFT) of each output signal. It provides spectral information over a wide frequency band, previously unavailable. Output phasors require post-FFT averaging for adequate noise rejection. The wind-tunnel researcher may select either approach as desired for a given test requirement.

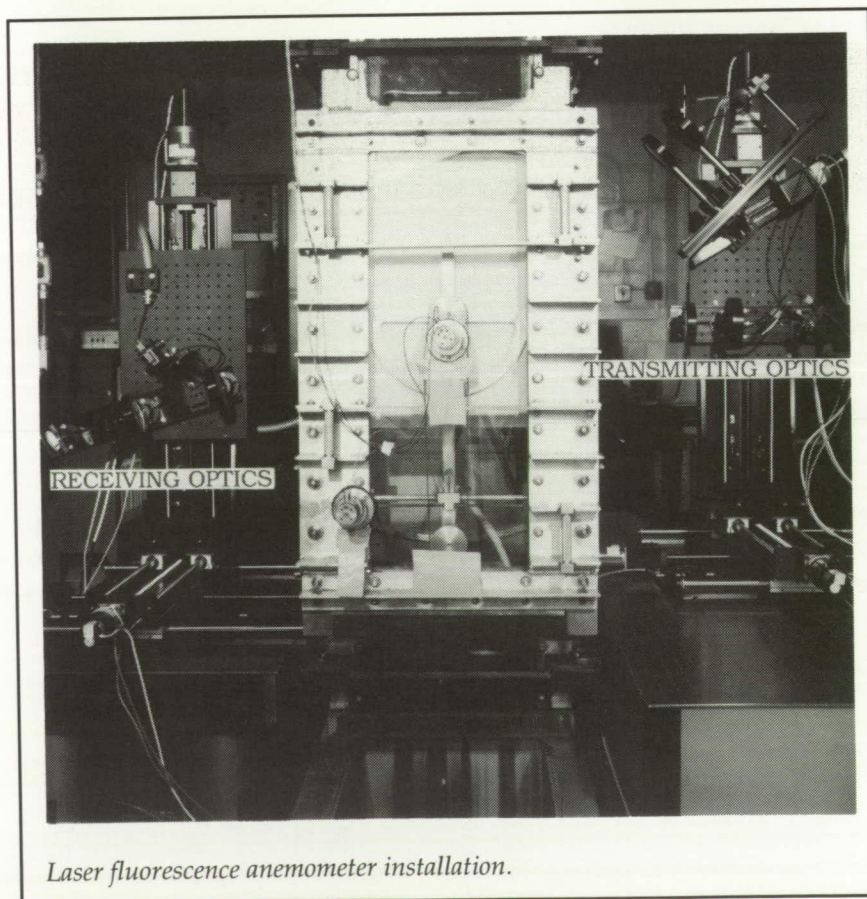
**(John S. Tripp, 44711, and
Taumi S. Daniels)
Electronics Directorate**

Laser Fluorescence Anemometer for the 16- by 24-Inch Water Tunnel

A laser fluorescence anemometer (LFA) has been developed for flow field studies at the 16- by 24-Inch Water Tunnel. This instrument was developed under a Phase 2 SBIR (Small Business Innovation Research) contract awarded to Complere, Inc., of Palo Alto, California. The device consists of a three-component laser doppler velocimeter (LDV) system with a fourth concentration-detection component.

The LDV system uses three colors of light from an argon laser to measure three perpendicular

velocity components in a sample (probe) volume. This sample volume is created at the focused intersection of all the beams. It is in this sample volume that the fourth concentration component is also measured. This fourth component measures the concentration of a fluorescent dye that is excited by the laser light. The fluorescent light and the scattered light from naturally occurring seed particles in the flow are collected by receiving optics focused on the sample volume. The light is chromatically separated and converted to electrical signals that are conditioned and analyzed to determine the three velocity values and dye concentrations. Mean and fluctuating values of all four components as well as



Laser fluorescence anemometer installation.

velocity cross-correlations are plotted.

The laser beam transmission and receiving optics on either side of the water tunnel test section are shown in the figure. Two experiments have been completed on a jet flow and a vortex flow. This work was done in part under contract with Lockheed Engineering and Sciences Co. (Dan H. Neuhart, 43012, and David J. Wing)
Aeronautics Directorate

New Rotary Balance System for the 20-Foot Vertical Spin Tunnel

The new rotary balance system for the upgraded 20-Foot Vertical Spin Tunnel will improve aircraft model testing productivity of the only free spinning vertical wind

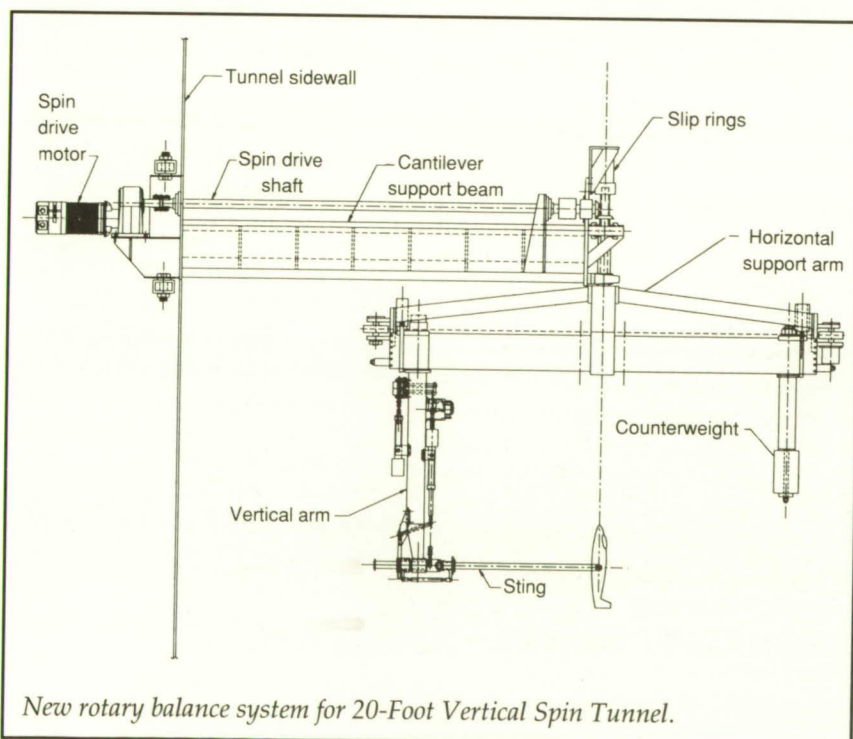
tunnel in the Western Hemisphere. This system is a mechanical apparatus that enables the measurement of aerodynamic forces and moments under spinning conditions (100 rpm). New, improved position adjustments will enhance model testing pitch angles of up to 90°, sideslip angles of -45° to 45°, and roll angles of -90° to 90°.

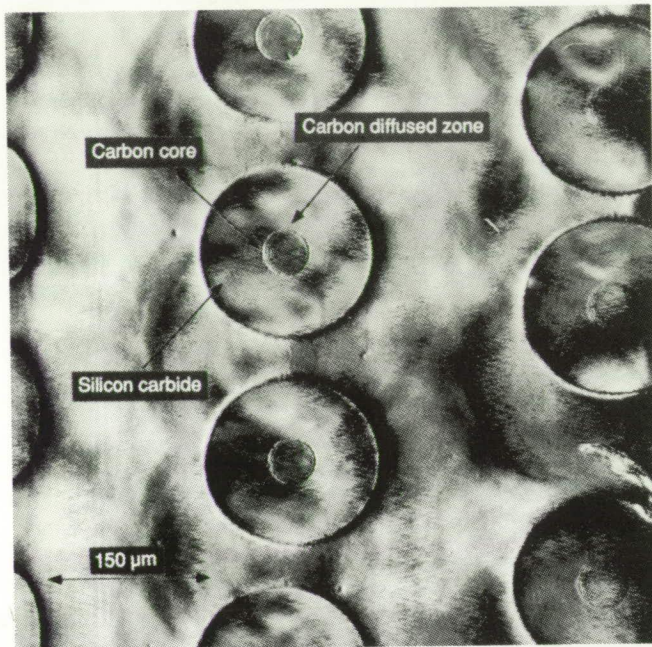
The unique design features of this mechanism include cables, electrical motors, actuators, linkages, and bearing surfaces to precisely position the model for testing. This system achieves the required stiffness and speed and minimizes frictional loads by utilizing a cable translation drive system, rather than gears of spline-ball bushings, with their attendant backlash characteristics, as used in the previous system. The compact drive system minimizes tunnel flow blockage and moves the model support vertical arm

and counterweight arm at equal distances from the center of rotation. The electrical motor drive consists of a light-weight frameless motor to provide the translational speed of 2 ips. This unit also has a maximum backlash of 1 arc minute, which provides the required repeatability. The pretensioned cables, oversized in stiffness such that the frictional and acceleration forces produce insignificant stretch, are not required to hold the counterweight and vertical arm subassemblies during spin operations. This is accomplished by a unique brake design to force the serrated brake pads into matching serrations in the main beam of the horizontal arm. The reaction from the electrical actuator trunnion forces the brake pads into the serrations and thereby prevents movement of the counterweight and vertical arm subassemblies. The roll positioning drive mounted in the vertical arm subassembly is also held by the applied actuator force. This force clamps the conical surface on the vertical roll shaft, which uses a yoke to obtain mechanical advantage from the actuator. This design eliminates the need for an additional actuator and minimizes flow blockage and weight. (Johnny W. Allred, 46918)
Systems Engineering and Operations Directorate

Nondestructive Evaluation Sciences

Research in the advancement of measurement science for quantitative nondestructive evaluation (NDE) is conducted in a modern, world-class laboratory that is home to state-of-the-art experimental facilities and a staff of





Differential phase acoustic microscope image of SiC/Ti-15-3 composite (Frequency = 820 MHz).

70 scientists and engineers. The NDE laboratory is a national resource for new technologies which will accurately assess the quality and integrity of present and future materials and structures. The laboratory contains facilities for research in ultrasonics, thermal imaging, optics, radiography, electromagnetics, micro NDE, simulation, and imaging processing. Representative of the high quality of these scientific disciplines is a unique computer aided tomography (CAT) system implemented with a load frame for three-dimensional radiographic imaging of specimens under stress. This facility will allow investigations in crack propagation and microanalysis of materials under load to provide new insight into material properties and defect structures. A major facility for advancement of optical NDE is a new electronic speckle interferom-

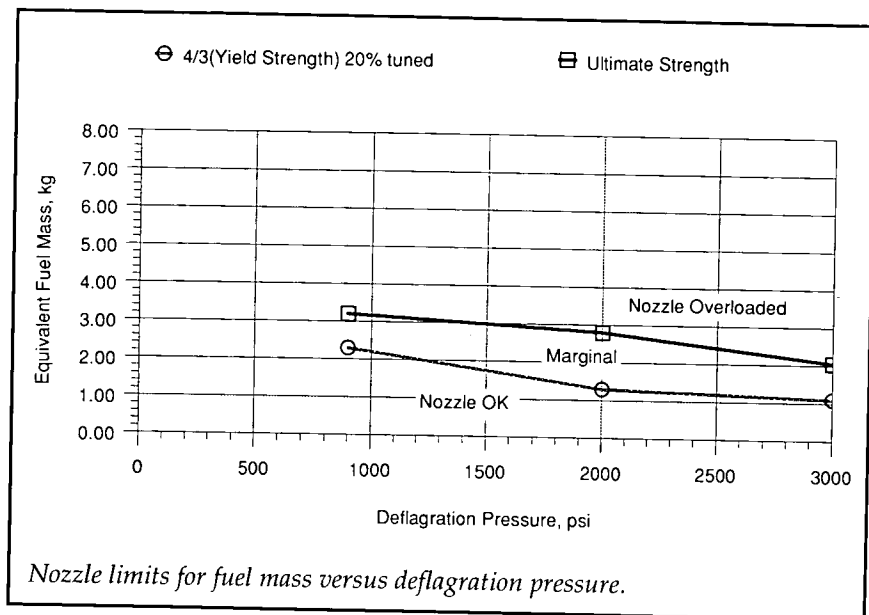
eter for imaging in-plane and out-of-plane strain, with sensitivity to 0.5- μ m displacements and capabilities for measuring strain at elevated temperatures.

An X-ray diffractometer system in the electromagnetics group allows investigation of structural properties related to electromagnetic properties of materials. Among the thermal NDE facilities in a state-of-the-art thermal diffusivity laboratory for characterizing the thermal and radiative properties of various materials. Some of the thermal imaging techniques have been demonstrated in the field for detecting subsurface defects in aircraft structures and have had significant impact in assuring the safety of aging aircraft. The ultrasonics group is developing a unique instrument with arrays of transducers for imaging large areas and producing clear images

of critical parts on NASA vehicles. The simulation group is contributing to our understanding of artificial intelligence and neural networks and applying the knowledge to the processing of images generated by the various techniques. For micro NDE, the world's first high-frequency double-beam scanning acoustic microscope is operational and capable of differential phase and amplitude measurements. The instrument is very sensitive to topographic and elastic constant variations, as shown in the photomicrograph of a titanium matrix composite with SiC fibers, where variations of less than 0.25 μ m are visible. These advanced NDE techniques will provide exceptional levels of reliability and safety for NASA's endeavors: Space Station *Freedom*, Space Shuttle, National Aero-Space Plane, National Aging Aircraft Consortium, and future transonic vehicles. (Joseph S. Heyman, 44970) Electronics Directorate

Transient-Structural Analysis of the 8-Foot High-Temperature Tunnel Combustor Under Detonation Loads

The 8-Foot High-Temperature Tunnel (HTT) at Langley Research Center is a combustion-driven blowdown wind tunnel. The 8-ft-diameter by 12-ft-long free jet test section is designed to achieve Mach 4, 5, and 7 with true temperature simulation. The combustor has two modes of operation: (1) methane and air, and (2) methane and air with oxygen enrichment to raise the oxygen content



to 20 percent of the combustion products. The first mode is used for aerothermal loads testing and flight weight structural concept verification. The second mode is used to test air-breathing scramjet and ramjet engines.

A major potential failure mode of the combustor is the possibility of a deflagration and/or detonation in the combustor. If a main burner flameout were to occur, then unburned fuel gases could build up and, if re-ignited, an explosion could occur. The objective of this analysis is to determine the safe operating limits of the combustor under transient explosive loads. To accomplish this, a detailed transient-structural finite-element analysis of the combustor nozzle, pressure shell, and end closures was performed. Initial results indicate that the combustor could only withstand a low-level deflagration. Therefore, the bulk of the analysis was to determine the maximum level deflagration the combustor could withstand.

During a deflagration, there are two primary load mechanisms:

(1) peak pressure and (2) differential pressure. The peak pressure loads the combustor shell and the end closures. The differential pressure loads, or thrust loads, place all components up to the thrust anchor in a state of gross tension or shear. To determine the acceptable operating limits, 14 different load cases were evaluated. These cases considered various flame speeds, equivalent unburned fuel masses, and initial deflagration pressures. In addition, structural frequencies were "tuned" to the loading frequencies to assess the sensitivity of the structure to the frequency content of the transient loading.

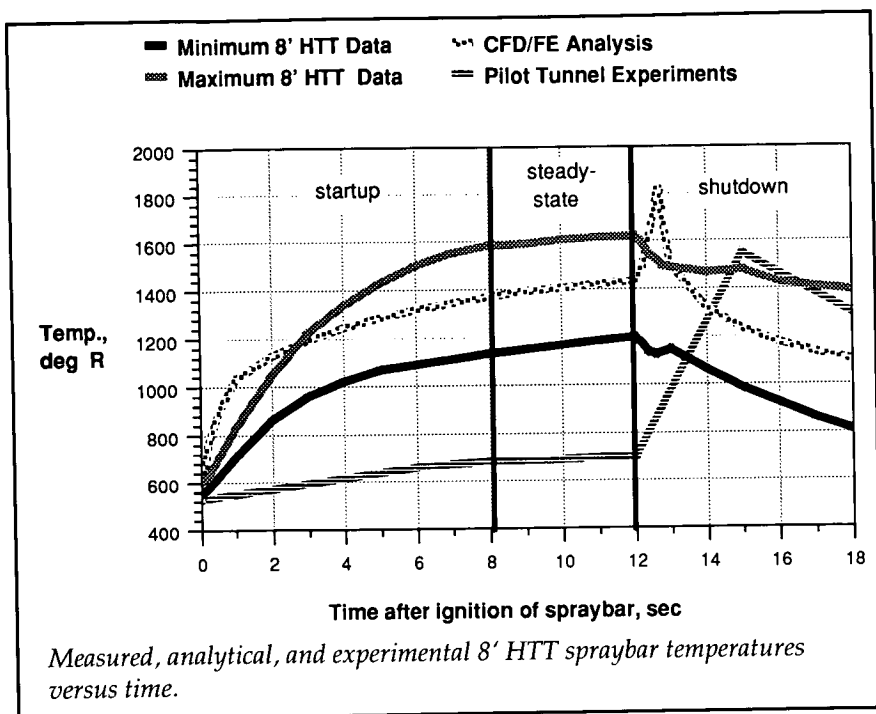
The critical structural component is the pressure shell connected to the transpiration-cooled nozzle, which has to withstand a differential pressure or axial thrust loading. The figure shows the results in terms of equivalent fuel mass versus deflagration pressure. A control system math model is used to simulate the combustor processes under various control

parameters. The math model relates equivalent fuel mass to shutdown time and deflagration pressure to operating pressure. Therefore, through use of the figure and the control system math model an allowable facility shutdown time versus combustor operating pressure can be determined. (Peyton B. Gregory, 47242, and Anne D. Holland) Systems Engineering and Operations Directorate

Thermal-Structural Analysis of a Methane Spraybar Burner for the 8-Foot High-Temperature Tunnel

The 8-Foot High-Temperature Tunnel (8' HTT) is a high-temperature, high-pressure blowdown wind tunnel that is used to simulate true-temperature hypersonic flight conditions (Mach 4 to Mach 7). The high energy needed for the simulation is obtained by burning a mixture of methane, air, and liquid oxygen under pressure in the combustor section of the tunnel and expanding the products of combustion through a conical-contoured nozzle into an open jet test chamber. The tunnel combustor operates with pressures up to 4000 psi and temperatures up to 4000°R. Currently, the tunnel is undergoing shakedown operations, with model testing scheduled to commence in 1993.

The methane spraybar (the burner used to inject and burn methane to elevate the test chamber temperature) consists of 15 concentric rings (1/2-in., 3/8-in., and 1/4-in.-diameter



Inconel 600 tubing) located in a vertical plane. The tubes are configured with a total of approximately 600 injection orifices and 300 flow-conditioning tab assemblies welded on the upstream side. The spraybar is instrumented with thermocouples as well as strain gauges to provide engineering data during the shakedown activity, which can be compared to the analysis predictions made during the thermal-structural design verification analysis.

The thermal-structural spraybar analysis was originally required to validate the structural integrity and cycle life of the spraybar, which must perform in a volatile, high-temperature environment. An intricate process, this analysis was performed in several stages. First, a computational fluid dynamics (CFD) code and test data from a small-scale pilot tunnel were used to predict gas temperatures near the spraybar

surface. Then, a finite-element (FE) analysis was performed to determine temperatures and stress distributions for the spraybar on a local level (i.e., around the fuel orifices and tab assemblies). This information was then used to determine global (overall) temperatures and stresses on the spraybar caused by the expanding gases.

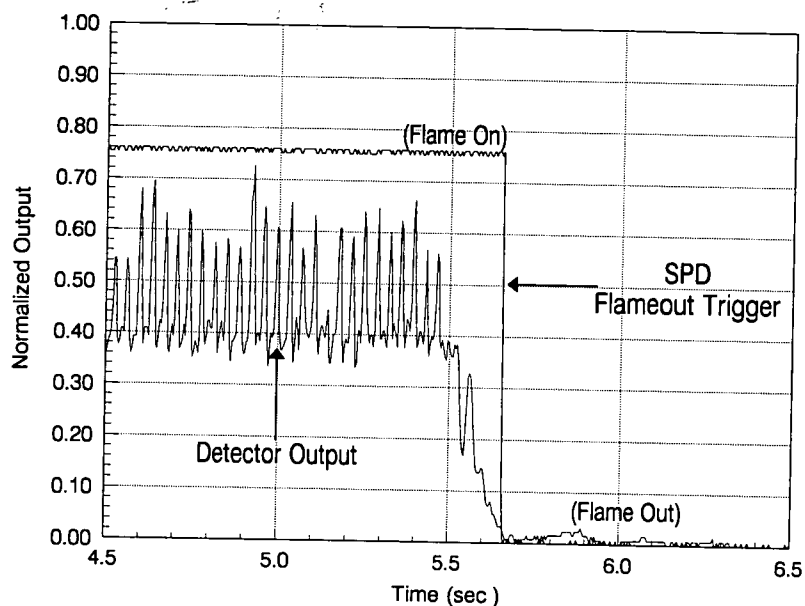
The figure shows measured maximum and minimum spraybar surface temperature data, predicted temperatures from the CFD and FE thermal analysis, and pilot tunnel data. Both the CFD/FE analysis and the pilot tunnel data predicted an increase in the spraybar surface temperature during tunnel shutdown, a phenomenon which has not been detected during the shakedown activity. The CFD/FE analysis did, however, predict the start-up and steady-state surface temperatures reasonably well and more accurately than did the pilot tunnel data.

These results indicate that the 8' HTT spraybar burner has performed as designed and predicted by the CFD/FE analytical design approach. (Chris A. Mouring, 47248, and Jon E. Thompson) Systems Engineering and Operations Directorate

Development of an Optical Flameout Detector

Concerns over the possibility of an explosion occurring within the combustor of the Langley 8-Foot High-Temperature Tunnel (8' HTT) due to a deflagration-detonation flame front following a flameout and re-ignition necessitated the development of an optical flameout detection system. Analysis of the 8' HTT's thermocouple-based flameout detection system indicated that it could not respond fast enough to prevent the accumulation of fuel in the combustion after an unplanned flameout. The optical flameout detection system is required to perform reliably in an oxidizing environment at pressures up to 28 MPa (4000 psi), survive temperatures ranging from -168°C to 1700°C (-270°F to 3100°F), and respond with a shutdown signal upon flameout in under 100 msec.

To fulfill these performance requirements, two different optical detectors coupled to fiber optic probes were used to sense main burner flame within the combustor. Ultraviolet light measurements (wavelengths of 250 to 400 nm) are made with a photomultiplier tube (PMT), and visible light measurements (wavelengths of



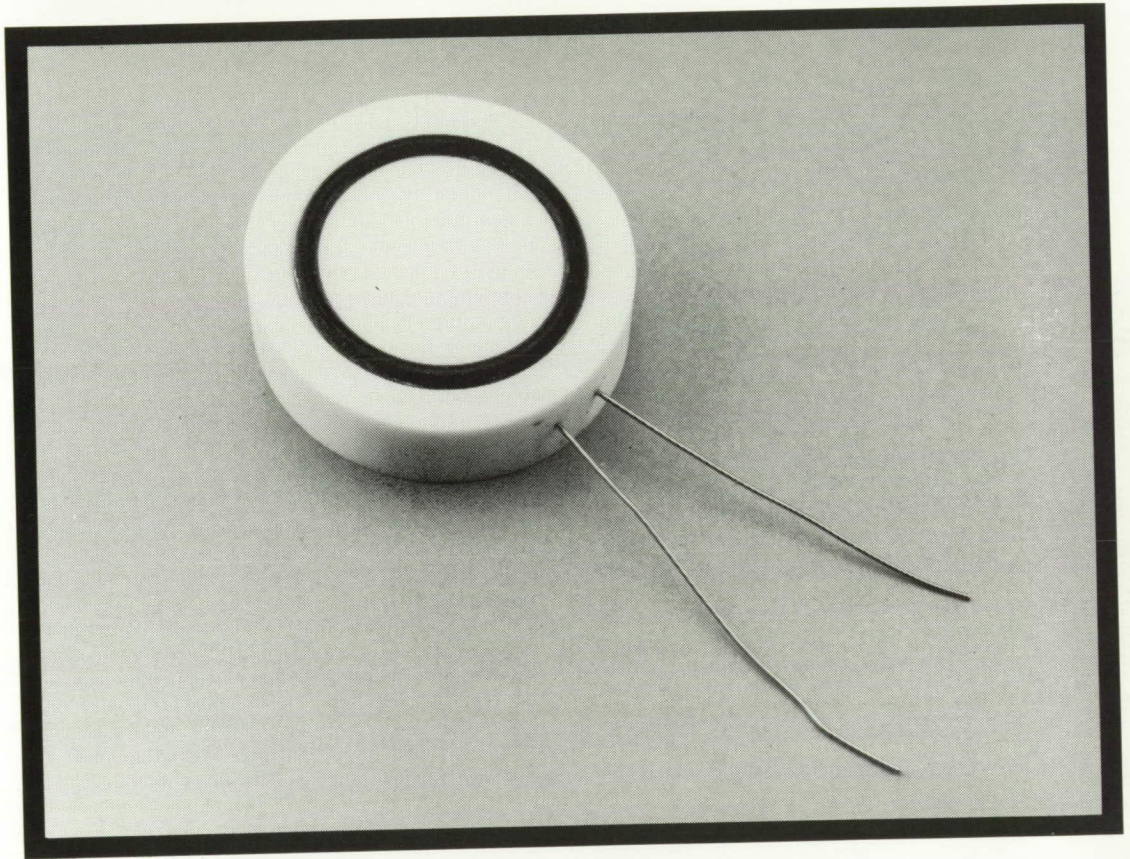
Silicon photodiode output (SPD) versus SPD trigger termination of main burner flame.

400 to 900 nm) are made with a silicon photodiode (SPD). The individual detector outputs are used to trigger logic circuitry to generate a flame on/off signal. In the event of a flameout, the system detects the absence of the main burner flame and signals the 8' HTT control system to close the main fuel (i.e., methane gas) supply valve.

Response tests for both the PMT- and the SPD-based system indicate that they can respond to a combustor flameout in under 10 msec. The rapid response of the two optical-based flameout detection systems is critical in preventing the accumulation of unburned fuel in the combustor to levels below the flammable limit so that re-ignition cannot occur.

(Stephen E. Borg, 44747)
Electronics Directorate

■ TECHNOLOGY TRANSFER AND UTILIZATION



*Facilitate the transfer of
aerospace-generated technology
to the public domain*

Characterization of Thin Protective Coatings on Solid Substrates

Thin polymer coatings are finding increasing applications throughout industry. They are being used for thermal controls on aerospace structures and protective-insulating layers on electro-optical components and highway bridges. Their effectiveness depends strongly on their microstructure and adhesion to the substrates. Currently, no techniques are available for monitoring the quality of such thin coatings. We have adapted positron lifetime

spectroscopy for characterization of thin protective coatings on metallic substrates. It has been tested on a number of polyurethane coatings on several metallic substrates. Typical values of positron lifetimes τ_i and their respective intensities I_i for two types of polyurethane coatings on steel substrates are summarized in the table.

The short-component lifetimes (τ_1) in the two types of coatings are slightly different, a reflection of small differences in their respective microstructures. However, the long component lifetimes (τ_2), which are due to the presence of small free-volume cells, are equal

in the two cases. The average sizes of these free-volume cells are calculated to be only 0.9 \AA^3 in both cases. Since the only common features between the two systems are the interfaces between the coatings and their respective substrates, it is concluded that the free-volume cells exist in the interfacial regions of the bonds. The small sizes of these microvoids indicate that two types of polyurethanes form equally good bonds with the steel substrates.

(Jag J. Singh, 44760, Abe Eftekhari, and Danny R. Sprinkle)

Improved Magnet Design for Residual Stress Characterization in Ferrous Components

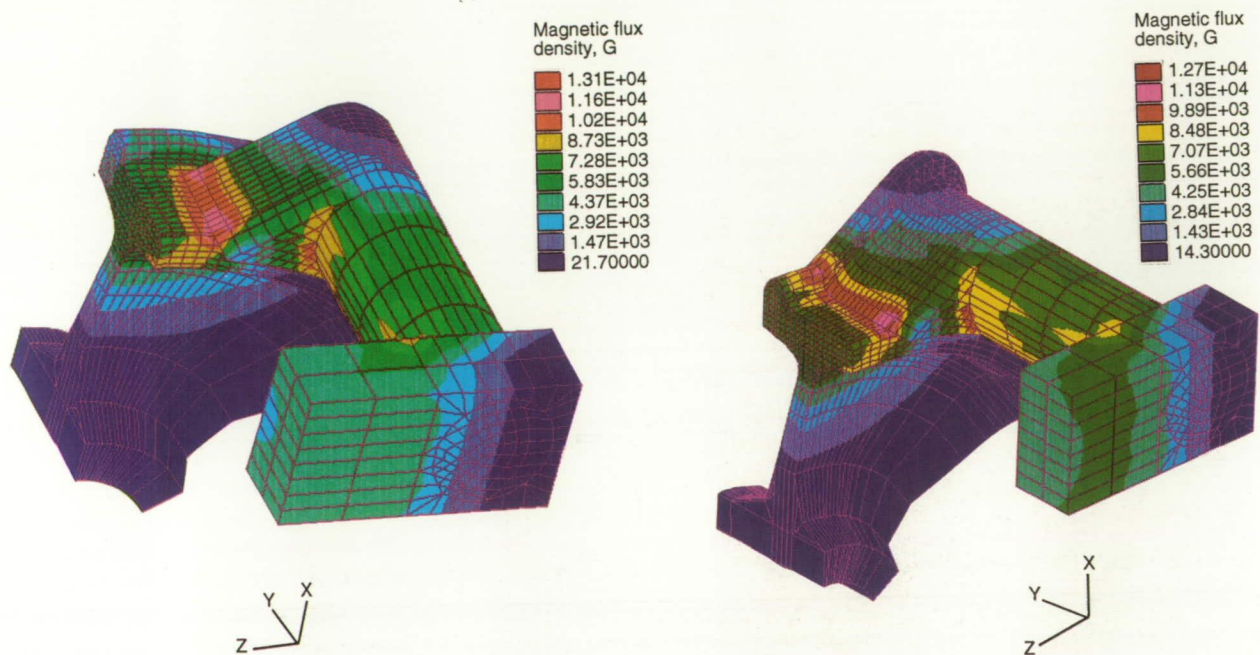
As well proven, the Langley-developed magnetoacoustic technique is one of the few methods that can differentiate the effect of tensile stress from that of compressive stress without the need for calibration. The technique, in the past, has produced numerous excellent test results with laboratory samples. Recent results obtained with actual railroad wheels at the Association of American Railroads test facilities, however, showed some insensitivity.

Two major factors are considered to be the main elements causing the insensitivity of magnetoacoustic test results to the residual stress

Test system	Positron lifetime τ_i and intensity I_i values ^a	
	$\frac{\tau_1 \text{ (psec)}}{I_1 \text{ (%)}}$	$\frac{\tau_2 \text{ (psec)}}{I_2 \text{ (%)}}$
"Transparent" polyurethane coating on steel substrate	$\frac{(192 \pm 4)}{(74 \pm 1)}$	$\frac{(572 \pm 35)}{(26 \pm 1)}$
"White" polyurethane coating on steel substrate	$\frac{(168 \pm 1)}{(70 \pm 1)}$	$\frac{(570 \pm 31)}{(30 \pm 1)}$

^aThe intensity of the longer life component in white coatings is slightly higher than in the transparent coatings. It is deemed to be more indicative of differences in the morphologies of the two types of polyurethanes than the quality of coating-substrate bonds.

Summary of positron lifetime data in two types of polyurethane coatings on steel substrates.



Magnetic flux densities with end block of core covering only flat tread surface (left) and covering entire surface (right).

states in the actual railroad wheels: first, the nonuniformity in the magnetic flux density in the test volume of railroad wheels; and second, the steep gradient and change in signs of residual stress in the rim of the railroad wheel, which cannot be reproduced in the laboratory test samples.

As a first step, the enhancement in the magnetic induction has been explored by finite-element method (FEM) modeling. The results in the left figure show the distribution of induction density when 1 A of current is supplied to the existing electromagnet system with the end block of the core covering only the flat tread surface. The magnetic flux density at the cross section of the rim, through which the ultrasonic waves propagate, varies from 1.4 to 7 kG. With a full extension of the end block to cover the entire surface, as shown in the right figure, the flux density

is fairly uniform at about 7 kG throughout the cross section at the same current level. As the magnetoacoustic responses in the low field region are critical, such a modification is expected to cause a significant improvement in the test results.

(Jim Fulton, 44799, Buzz Wincheski, and Min Namkung)

PC/AT-Based Telerobotic Control System

Telerobotics has numerous potential uses in remote handling applications. However, the application of telerobotics is limited by the functionality of the telerobotic systems available for service and by the practicality of the telerobotic systems used in the research communities. Presently, there is a need for

telerobotic systems that lie in the middle ground. The control modes, the host computer platform, and the communication structure are very important in these systems. A telerobotic control system must include teleoperational, shared, and autonomous modes of control in order to provide a robust platform for incorporating the rapid advances that are occurring in telerobotics and associated technologies. The computer platform for a telerobotic control system should have a balance between many factors. These factors include hardware I/O capabilities, simplicity, upgrade ability, industrial applicability, and computational performance. The communication structure implemented in the control system must support the modes of control mentioned above. Therefore, the low-level control system must not only include

ORIGINAL PAGE
BLACK AND WHITE PHOTOGRAPH



Telerobotic control system.

communication between the master and slave systems of the telerobot but also include communications with external systems.

Such a middle ground telerobotic control system has been developed at the University of Kansas by researchers in the Kansas Augmented Telerobotic (KAT) Laboratory. The project includes the retrofit of a commercially available telerobot with a PC/AT-based, low-level control system. The telerobotic hardware controlled by the system is a dual-arm, bilateral telerobot. This low-level control system incorporates two PC bus I/O cards developed by researchers in the KAT Laboratory specifically for interfacing to the master manipulator and slave robot of the original equipment manufacturer (OEM) system. Two PC/AT's are used to control the master and the slave. The PC/AT

provides a computer platform that is powerful enough to readily allow modification to the control algorithms and to provide substantial computational power. It is also durable, portable, and practical enough to be used outside the laboratory environment. The two PC/AT's communicate with one another and with external systems. Initial versions of the control algorithms have been successful in utilizing several modes of control by communicating with intelligent external systems. Current and future areas of development include further investigation of efficient information handling for implementing several modes of control in one control system and the development of modes of control shared between the computer and the human operator.

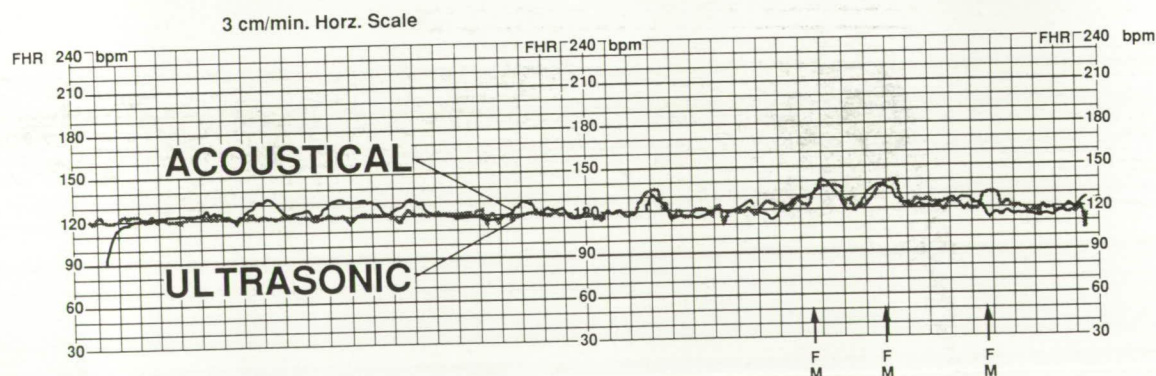
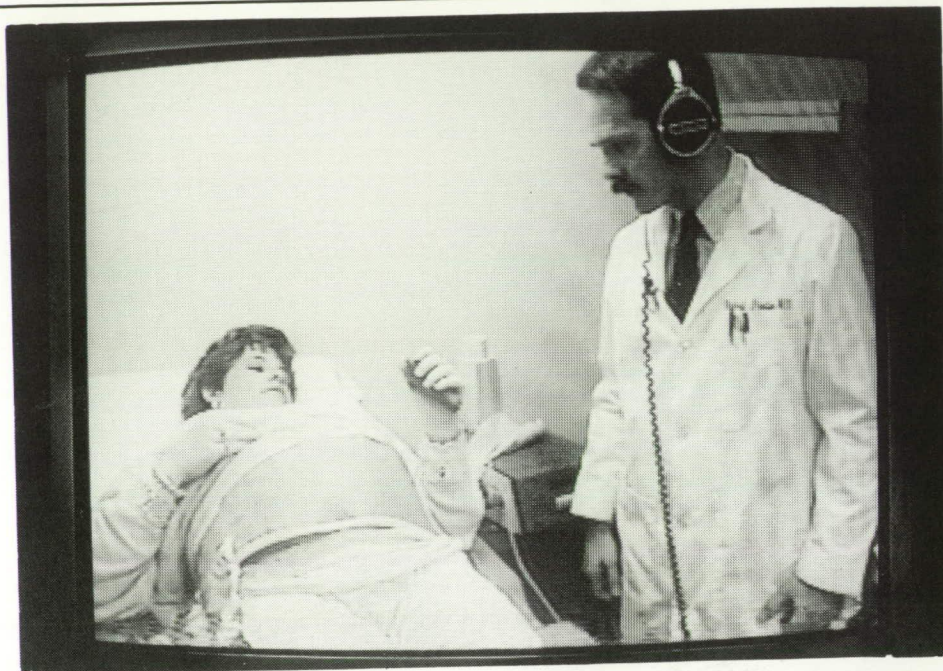
(Randy Mixon, 46695, and Bill Barr)

Portable Fetal Heart Rate Monitor

The fetal nonstress test (NST), performed routinely in hospitals by means of ultrasound, is a reliable indicator of fetal health with regard to a large class of fetal stress provocations. Mothers considered to be in the "high risk" group come to the hospital or clinic periodically (e.g., weekly) to take the test. This group comprises 20 percent of all pregnant women and accounts for 50 percent of our fetal morbidity and mortality. Each NST costs \$125 to \$250, entails hospital paperwork, causes inconvenience and fragmentation of care for the patient, and requires the attendance of trained medical personnel. A portable fetal heart rate monitor would permit the expectant mother to perform the NST daily in her home and would reduce the cost to an estimated \$25 per test. The potential market would include the 1 million pregnant U.S. women per year requiring this type of prenatal surveillance.

An acoustically based fetal heart rate monitor, suitable for a portable mode of operation, has been developed at Langley. The monitor uses piezopolymer film for the acoustic sensors, which are mounted in a seven-element array on a "cummerbund," to detect the fetal heart tone on the maternal abdominal surface. The development of this technology is based on a concept by Dr. Donald A. Baker, Spokane, Washington, for the treatment of patients who cannot avail themselves of even minimal prenatal care.

A successful NST requires the fetal heart rate to accelerate at



Fetal heart monitor in use (top) and data output (bottom).

least 15 beats per minute (bpm) over the baseline (typically 120 bpm) following a fetal movement, and three such events must take place within a 20-minute period. In the top figure a patient is seen wearing the NASA cummerbund and holding a push-button switch to indicate fetal movement. A computer-based signal processing system captures the acoustical sensor signals, utilizes a linear prediction algorithm to

recognize the fetal heart tones, and provides a time record of fetal heart rate, as is required for the NST. The algorithm was developed by Dr. John W. Stoughton and Dr. Robert A. Pretlow, MD, of Old Dominion University. Dr. Pretlow conducted a study at the Eastern Virginia Medical School, comparing the acoustically based NST with an ultrasonic NST for a number of patients. The bottom figure shows a typical recording

of fetal heart rate versus time from the newly developed acoustically based monitor (solid line) and from the conventional ultrasound monitor (dotted line). Heart rate accelerations following fetal movement indicators (FM) are apparent. The results confirm that the NASA monitor is capable of performing the NST.

As soon as the signal processing hardware is made completely

portable, the monitor will be suitable for the commercial marketplace.

(Allan J. Zuckerwar, 44658)

Shear Stress Calibration Device

The Virginia Institute of Marine Science (VIMS), College of William and Mary, is researching the suspension and transport of cohesive sediment in estuaries. This research for the Environmental Protection Agency is a very significant step toward the understanding of fine sediment and toxic transport. To compare fine sediment and toxic transport under controlled conditions, a shear stress sensor calibration unit was needed. VIMS researchers requested support in the design and fabrication of the calibration unit.

After assessing the project requirements, a calibration unit was fabricated and interfaced with a personal computer to control rotational speed and measure shear stress output. This device provides an absolute calibration for a shear stress measurement system. The measurement system is used in the study of the resuspension and transport of cohesive sediments in estuaries and is a very significant step toward understanding the transport of toxic compounds bound to fine sediments.

(Bruce D. Little, 42729)

Systems Engineering and
Operations Directorate



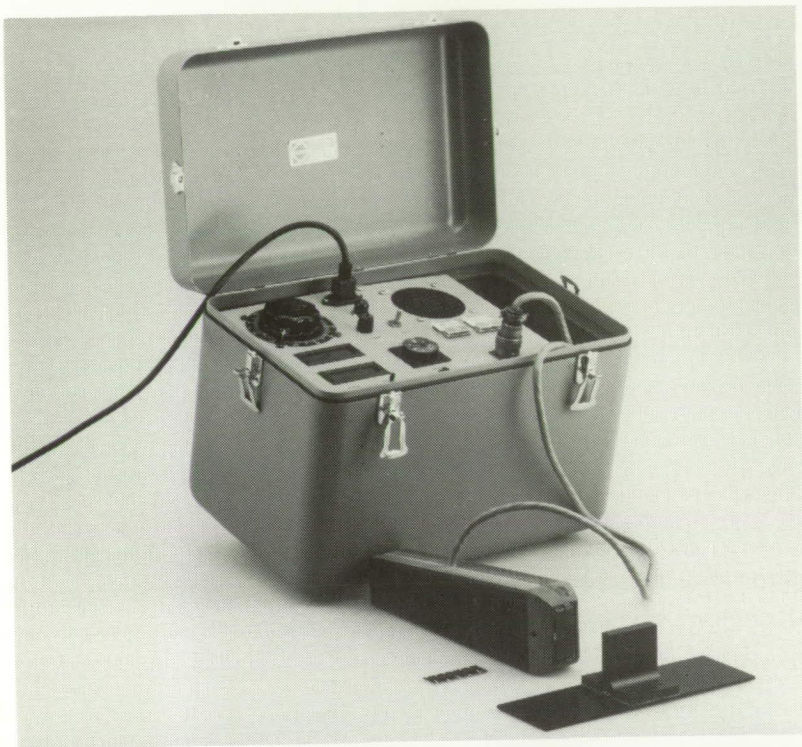
Final test unit of shear stress calibration device.

Noninvasive Method and Apparatus To Determine Fiber Direction in Composite Materials

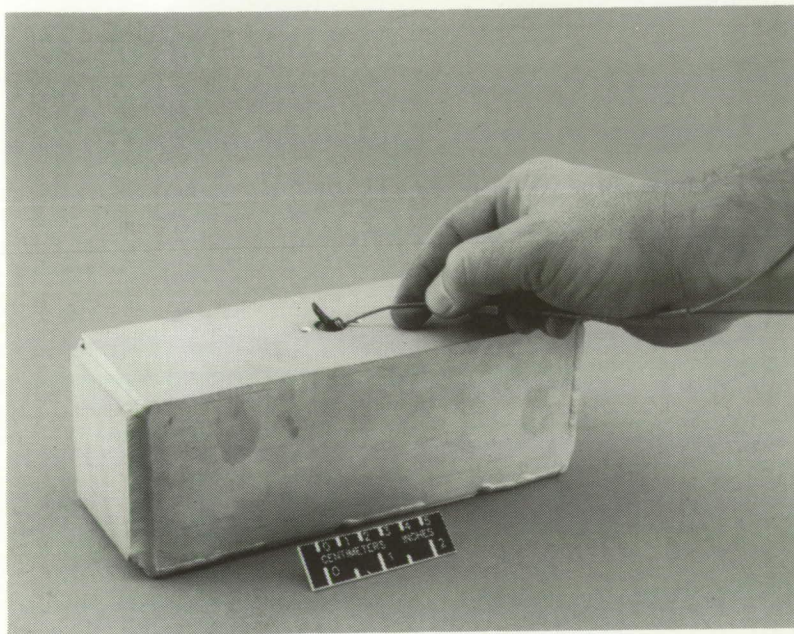
Composites are replacing metals in applications as diverse as aircraft, artificial joints, and helicopter shafts because they are lighter, stronger, and more resistant to environmental conditions. A one-of-a-kind, self-contained,

portable induction sensing system has been developed to determine fiber direction in thermoplastic and thermoset composite laminates. Composites are fibers that are bound together by resins to form a solid. Previously, fiber direction could not be determined without penetrating the material.

This new technology noninvasively measures impedance changes, which indicate the fiber direction, in a composite structure.



Noninvasive sensor and equipment.



Installation of fastener in blind hole.

A gun-like induction sensing device is placed outside the composite and uses an electromagnetic field to sense fiber direction as it is rotated 360°. This system provides reliable and efficient measurement of composite fiber orientation.

(Robert L. Fox, 45468, and John D. Buckley)
Systems Engineering and Operations Directorate

Blind-Fastener Apparatus

It is often difficult to install a fixture into a blind, or limited-access, wall structure. Typically, conventional nut-bolt arrangements cannot be used when an anchor nut is required as a threaded receptacle for another member. Extensive disassembly of the structure is often required to access the blind side of a structure. A blind-side anchor-nut insert has been developed at Langley. This insert has external threads for engaging an internally threaded receptacle of a fixture to be installed. The fixture with an installed anchor-nut insert is fed through a central hole in a structure wall having a blind side. The fixture is rotated until wing holes are aligned with side holes in the wall. The fixture is pulled flush against the blind side with a guide wire. Fasteners are inserted through the holes, and then the anchor-nut insert is removed with a driver to expose the fixed threaded receptacle for engagement as desired.

(Norman F. Willey, Jr., 44130)
Systems Engineering and Operations Directorate

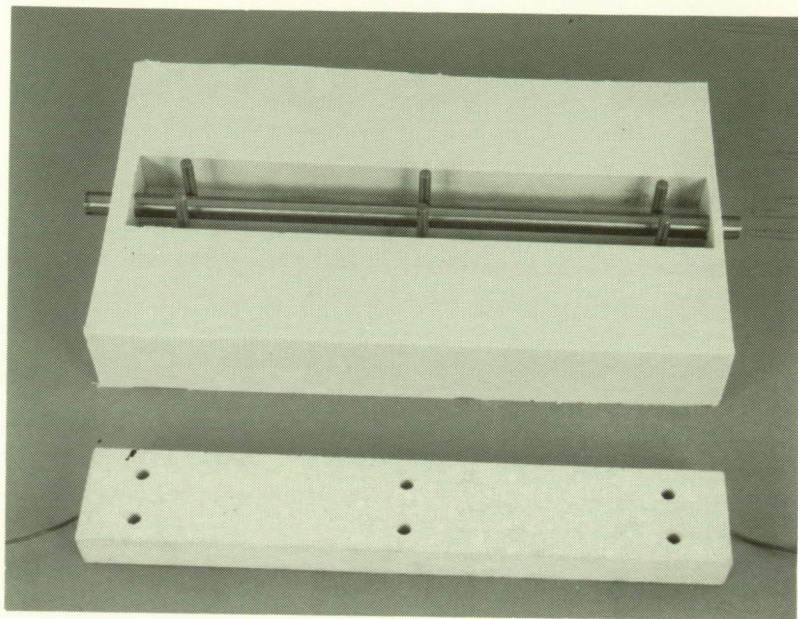
Slip Casting of Ceramic Heaters, Mounts, and Lens Holders for Optical Benches

Improvements in laser measurements can be made by minimizing movement of optical components and maintaining a preset temperature on optical benches. Conventional optical benches and optical components are fabricated from metals that have high coefficients of thermal expansion (CTE's). Stainless steel (CTE = 14 ppm/°C) and aluminum (CTE = 28 ppm/°C) are currently used for optical benches and components.

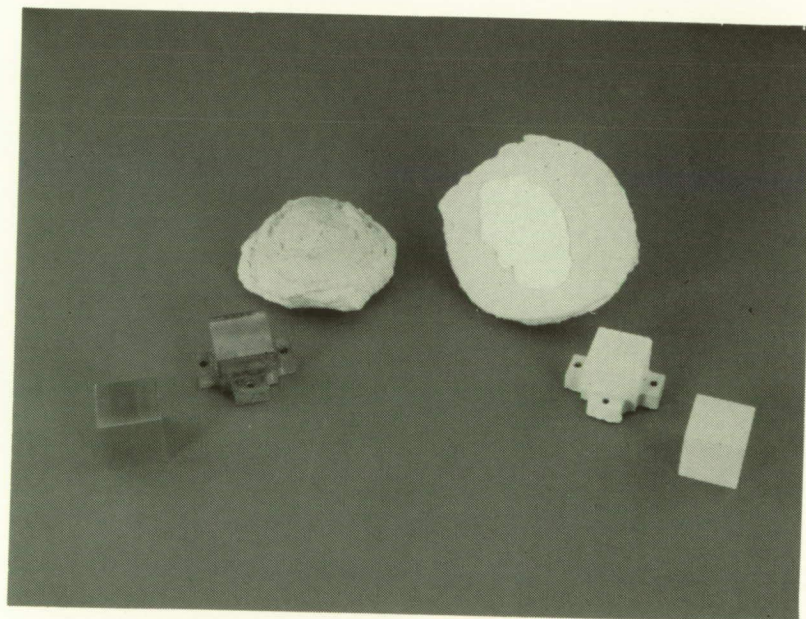
Fused quartz and alumina have been cast into optical lens mounts, housings, and heaters for much improved laser measurements. The lens mounts and housings have extremely small displacements with temperature change since their CTE is very small (0.3 ppm/°C). Fused quartz has one half the weight of aluminum and has 50 times less movement per °C.

Ceramics have properties that make them good housings for optical bench heaters. For example, slip casting of fused silica or alumina can be used to fabricate complex shapes for heating optical benches and supporting instrumentation. Heater elements of nickel-chrome have been shaped as inserts in cavities running through the center of the ceramic structures. Temperatures ranging from ambient to 815°C can be generated with heaters of this type. Thermocouples have been

ORIGINAL PAGE
BLACK AND WHITE PHOTOGRAPH



Rubber mold (top) and ceramic slip cast heater housing.



Slip cast ceramic cube and mount.

added to the cavity of the ceramic heater as a means of feedback for temperature control.

(Peter Vasquez, 45189, Melissa A. Long, Robert L. Fox, and Stephen P. Sandford)
Systems Engineering and Operations Directorate

Optical Alignment and Reference Cube for Laser Calibration

Autocollimators are light-emitting devices used for aiding in the alignment of telescopes and lasers. Shifts in alignment occur when the mount experiences changes in temperature or mechanical vibration. Conventional optical components are mounted in metal to hold them steady. Since each metal has its own coefficient of thermal expansion (CTE), the degree of movement of the mount and the cube is a function of temperature and the base metal. The metals with the smallest CTE are Invar and stainless steel. The CTE for stainless steel is 14 ppm/°C. Small-CTE metals are expensive and difficult to machine.

Ceramics exhibit favorable properties for making optical alignment fixtures and reference cubes. They may be slip cast into complex shapes and have CTE's as low as 4 ppm/°C. The small CTE of ceramics allows the optical alignment fixture and cube to undergo large temperature changes with practically no movement. Ceramics have thermal expansion properties similar to those of Super Invar, are less expensive, are lighter, and are

easy to cast and machine. The development goal is a one-piece integral casting for the mount and cube.

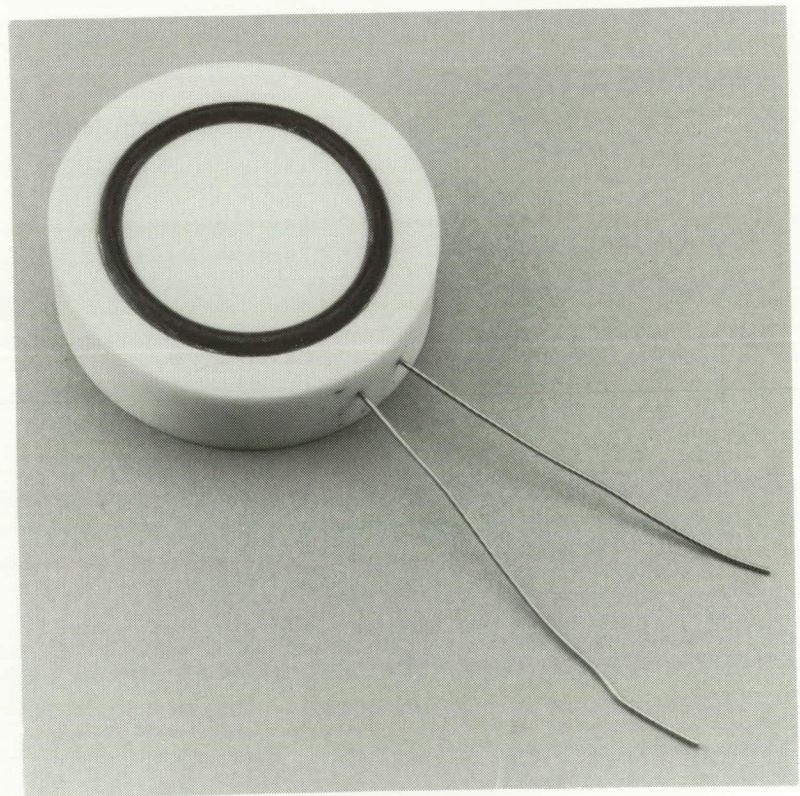
(Melissa A. Long, 45189)
Systems Engineering and Operations Directorate

Liquid-Nitrogen-Temperature Cryoseals

One of the more challenging problems with cryogenic research is maintaining a pressure seal at liquid nitrogen temperatures when thermally cycling. At these extremely low temperatures (-170°F and below), elastomeric and rubber materials used as seals

become very inelastic or brittle. This phenomenon occurs when the sealing material passes through the glass transition temperature common to all organic materials. Other materials used as seals are metals (e.g., indium solder and copper). Metallic seals have to be shaped and fitted, and they often have a short life.

The recently developed cryogenic seal is composed of ceramics, Nichrome wire, a thermocouple, and vulcanized rubber. The vulcanized rubber is bonded to a slip cast ceramic with a thermocouple attached to a Nichrome heater within the ceramic. The thermocouple provides feedback for temperature control of the rubber seal. The seal temperature is main-



Ceramic thermal seal.

tained above -170°F so that the vulcanized rubber seal does not become brittle. A main advantage of the ceramic cryoseal over the metal cryoseal is that it has a longer useful life.

(Robert L. Fox, 45468, and
Melissa A. Long)
Systems Engineering and
Operations Directorate

Calibration Without a Standard

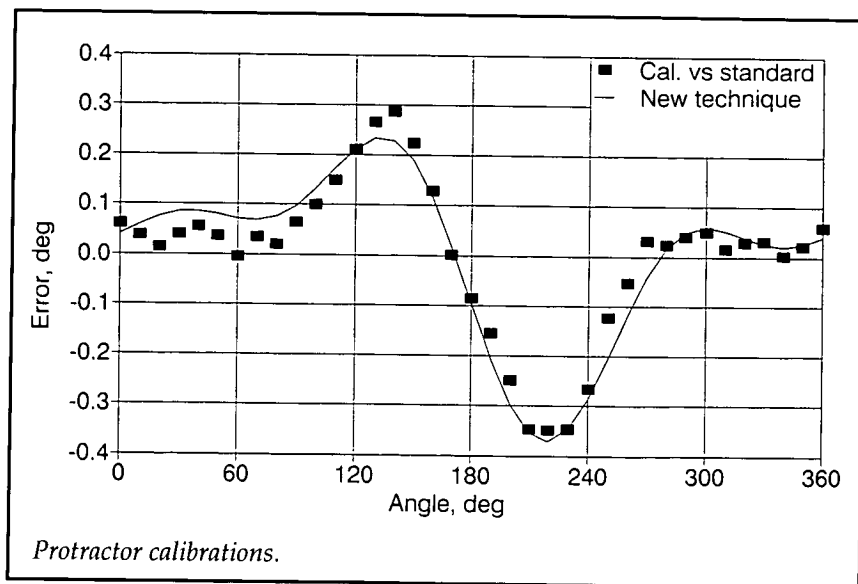
Conventional calibration techniques involve the comparison of the test device against a measurement system or standard of known accuracy. Standard practice requires that the calibration standard have an accuracy at least four times better than the test device. This means that ultimately the standard must be calibrated by another laboratory with higher accuracy devices until a national or international standards laboratory is reached. This is not always possible, and it is often desirable to be able to determine the errors

in a device when an adequate standard is not available. A technique has been developed that allows the calibration of certain instruments by comparing them to similar devices (or to themselves in certain cases). The errors in both devices can be determined without previous knowledge of the errors in either device.

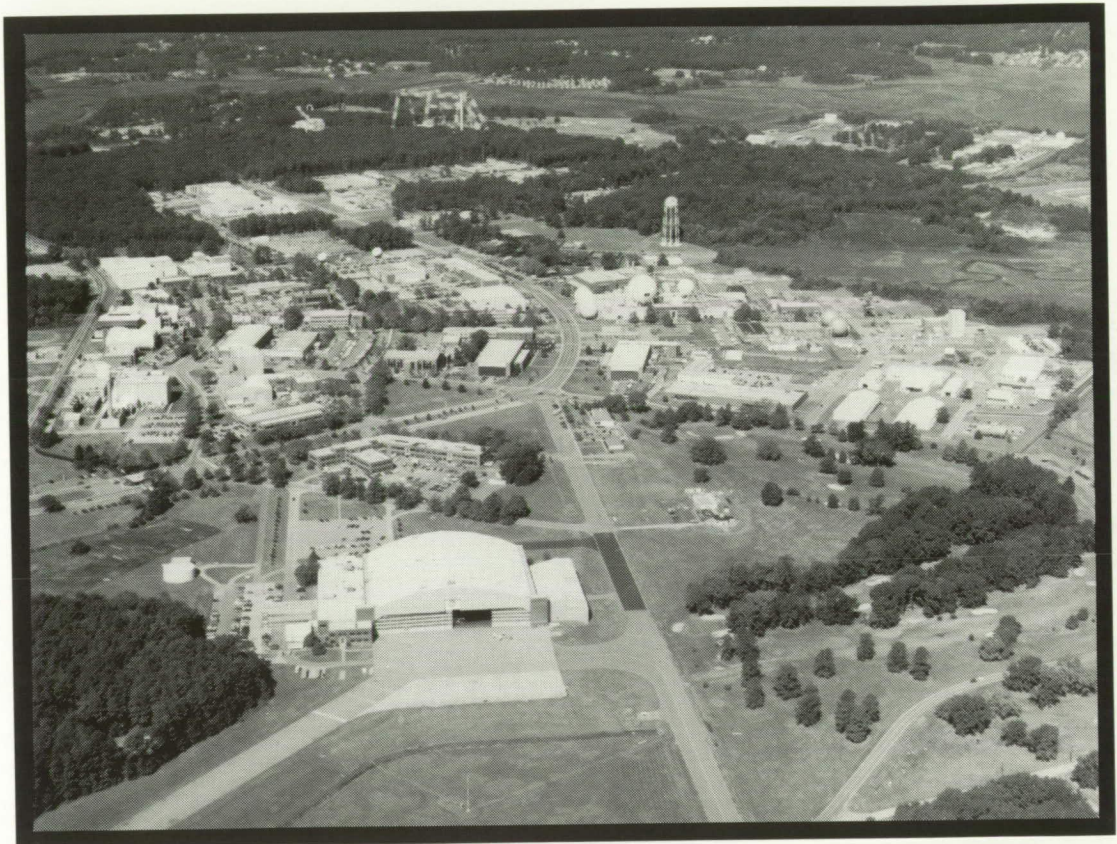
A method of comparing the devices must be available. This may be trivial or may require an external device such as an autocollimator or a precision level to monitor the difference between the instruments. The devices are compared, one device is shifted, and the devices are compared again. The technique involves expressing both the measured unshifted and the measured shifted differences between the two instruments by Fourier expansions. The errors in each device can be determined in terms of their Fourier coefficients.

The technique works particularly well on angular measurement devices such as protractors, inclinometers, encoders, resolvers, and angle indexers. It has been

used to calibrate several of these instruments. The figure shows the results of a calibration with this new technique and a traditional calibration with a standard.
(Tom Finley, 44660)



■ AEROSPACE TEST FACILITIES



This section includes brief descriptions of many of Langley's major aerospace test facilities; for more detailed information, including availability, please contact the individual identified after each description

30- by 60-Foot Tunnel

The Langley 30- by 60-Foot Tunnel is a continuous-flow, open-throat, double-return tunnel powered by two 4000-hp electric motors, each driving a four-blade 35.5-ft-diameter fan. The tunnel test section is 30 ft high and 60 ft wide and is capable of speeds to 100 mph. The tunnel was first put into operation in 1931 and has been used continuously since then to study the low-speed aerodynamics of commercial and military aircraft. The large open-throat test section lends itself readily to tests of large-scale models and to unique test methods with small-scale models.

Large-scale and full-scale aircraft tests are conducted with the strut mounting system. This test method can handle airplanes to the size of present-day light twin-engine airplanes. Such tests provide static aerodynamic performance and stability and control data, including the measurement of power effects, wing pressure distributions, and flow visualization.

Small-scale models can be tested to determine both static and dynamic aerodynamics. For all captive tests, the models are sting mounted with internal strain-gauge balances. The captive test methods include conventional static tests for performance and

stability and control, forced-oscillation tests for aerodynamic damping, and rotary tests for spin aerodynamics. Dynamically scaled subscale models, properly instrumented, are also freely flown in the large test section with a simple tether to study their dynamic stability characteristics at low speed and at high angles of attack. A small computer is used in this free-flight test technique to represent the important characteristics of the airplane flight control system.

(Frank Jordan, 41136)

Low-Turbulence Pressure Tunnel

The Langley Low-Turbulence Pressure Tunnel (LTPT) is a single-return, closed-circuit tunnel that can be operated at pressures from near vacuum to 10 atm. The test section is rectangular (3 ft wide and 7.5 ft high and long), and the contraction ratio is 17.6:1. The LTPT is capable of testing at Mach numbers from 0.05 to 0.50 and unit Reynolds numbers from 0.1×10^6 to $15 \times 10^6 \text{ ft}^{-1}$. A high-lift model support and force balance system is provided to handle both single-element and multiple-element airfoils. The LTPT has provisions for tunnel sidewall boundary-layer control through the use of tangential blowing from slots located on model end plates or passive suction through porous



ORIGINAL PAGE
BLACK AND WHITE PHOTOGRAPH



end plates. Recent flow quality measurements in the LTPT indicate that the velocity fluctuations in the test section range from 0.025 percent at Mach 0.05 to 0.30 percent at Mach 0.20 at the highest unit Reynolds number. (Robert J. McGhee, 41005)

20-Foot Vertical Spin Tunnel

The Langley 20-Foot Vertical Spin Tunnel is the only operational spin tunnel in the Western Hemisphere. The present facility was built in 1941 and has been in essentially continuous operation since that time. All U.S. military fighters, attack airplanes, primary trainers, and bombers and most experimental airplanes are tested. General aviation airplanes and many foreign designs are also evaluated when required.

The tunnel, which is used to conduct spin research and tumbling research on aerospace vehicles, is a vertical tunnel with a

closed-circuit annular return passage. The test section has 12 sides and is 20 ft across by 25 ft high. The test medium is air. Tunnel speed is variable from 0 to 90 ft/sec, with accelerations to 15 ft/sec. The main drive motor (rated at 400 hp continuous, and 1300 hp short run) turns a 20-ft-diameter three-bladed fixed-pitch fan.

Dynamically scaled models are used to investigate the spinning and tumbling characteristics of airplane configurations. Spin recovery is studied by remote actuation of the model's aerodynamic controls to predetermined positions. Tests are recorded on high-resolution color video with a superimposed time code. A rotary balance apparatus supported by a swinging boom is used to conduct force and moment testing and pressure testing of models under spinning conditions, at angles of



attack from 0 to $\pm 90^\circ$, and at spin rates of 0 to ± 90 rpm. Data are recorded in coefficient form on any standard digital medium. (Ray Whipple, 41194)

7- by 10-Foot High-Speed Tunnel

The Langley 7- by 10-Foot High-Speed Tunnel is a closed-circuit, single-return, continuous-flow, atmospheric tunnel with a solid-wall test section 6.6 ft high, 9.6 ft wide, and 10 ft long. The tunnel, which is fan driven and is powered by a 14 000-hp electric motor, operates over a Mach number range from 0.2 to 0.9 to produce a maximum Reynolds number of $4 \times 10^6 \text{ ft}^{-1}$.

In addition to standard static force and pressure testing over moderate angles of attack and sideslip, the facility has the unique

capability to statically test to high angles of attack (approximately 55°) and large sideslip angles (approximately 30°). In addition to static testing, the facility can also be equipped for steady-state roll stability testing, forced-oscillation pitch, yaw, and roll dynamic stability testing, semispan model testing on a sidewall turntable, and powered model testing using high-pressure air. The facility incorporates a permanent laser light sheet installation for vapor screen flow visualization studies.

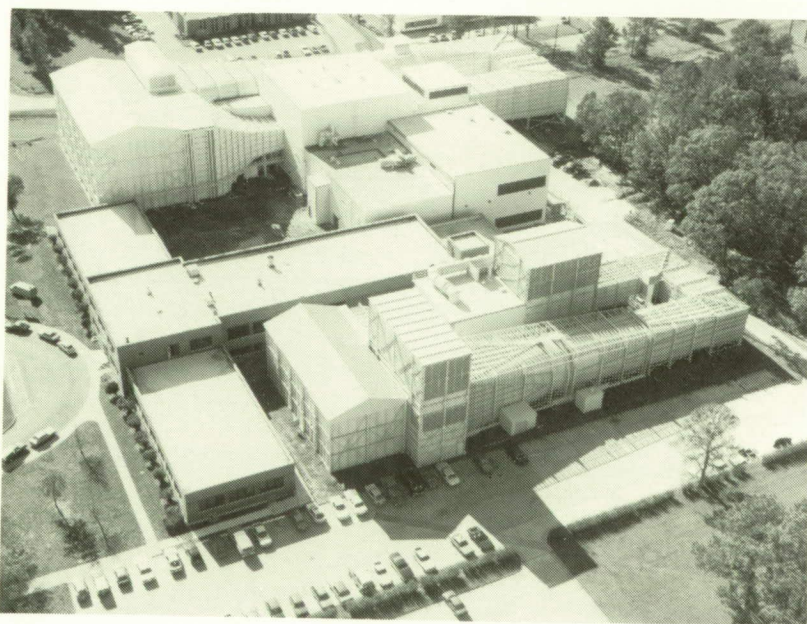
The facility has an important role in a wide range of basic and applied aerodynamic research, including advanced vortex lift concepts, drag reduction technology, and highly maneuverable aircraft concepts. The facility is also used in code validation studies to support the development of advanced computational aerodynamic theories for the prediction of complete aircraft flow fields over complex vehicles, including

multiple interacting vortex flow fields. The facility is used to support national programs such as the Space Shuttle and the National Aero-Space Plane. (J. M. Luckring, 42869)

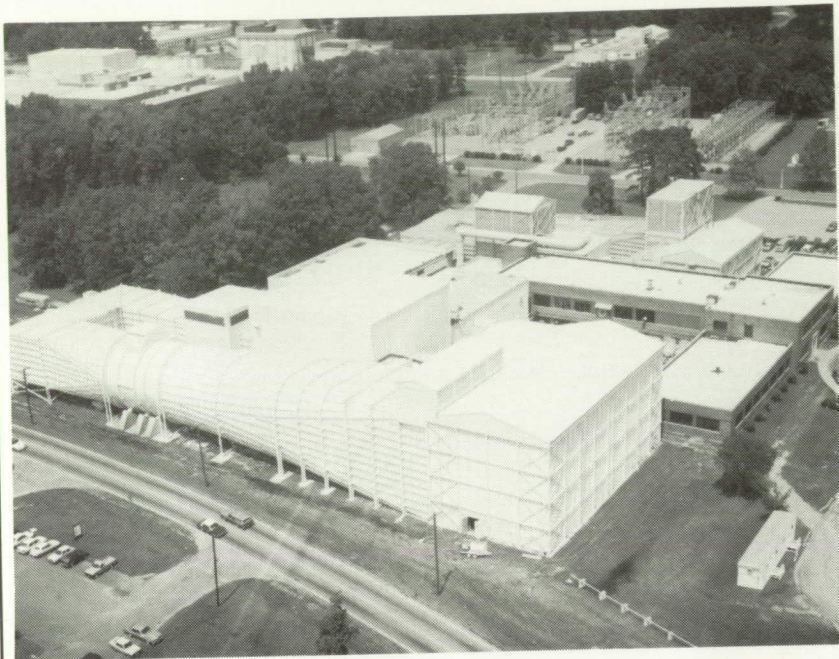
14- by 22-Foot Subsonic Tunnel

The Langley 14- by 22-Foot Subsonic Tunnel is used for low-speed testing of powered and unpowered models of various fixed- and rotary-wing civil and military aircraft. The tunnel is powered by an 8000-hp electrical drive system, which can provide precise tunnel speed control from 0 to 318 ft/sec with Reynolds number ranging from 0 to $21.0 \times 10^6 \text{ ft}^{-1}$. The test section is 14.5 ft high, 21.8 ft wide, and approximately 50 ft long. The tunnel can be operated as a closed test section with slotted walls or as one or more open configurations when the sidewalls and ceiling are removed to allow extra testing capabilities, such as flow visualization and acoustic tests. The tunnel is equipped with a two-component laser velocimeter (LV) system. Furthermore, boundary-layer suction on the floor at the entrance to the test section and a moving-belt ground board for operation at test section flow velocities to 111 ft/sec can be installed for ground-effects tests.

The floor of the test section, consisting of two model or floor carts, will be lowered to accommodate the three third component of the LV or acoustical wedges. This modification will start during the fall of 1992. The third component of the LV will enhance the



ORIGINAL PAGE
BLACK AND WHITE PHOTOGRAPH



capabilities of flow-field surveys. The acoustical wedges will reduce the reverberation in the test section.

(Harry L. Morgan, Jr., 41069)

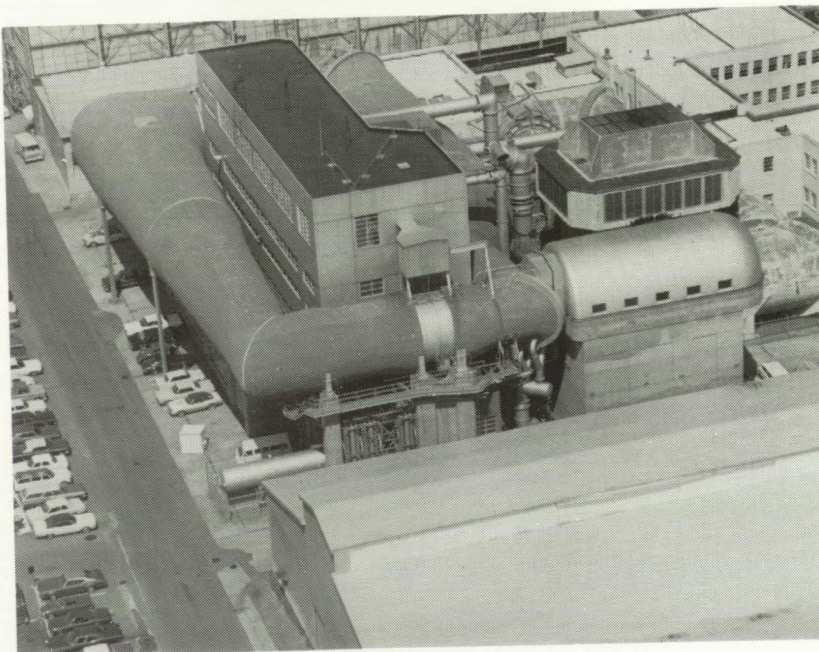
Tunnel stagnation pressure can be varied from a minimum of about 0.25 atm at all test Mach numbers to maxima of about

1.0 atm at a Mach number of 1.2, about 1.5 atm at high subsonic Mach numbers, and about 2.0 atm at Mach numbers of 0.4 or less. Temperature is controlled by water circulating through cooling coils across the corner of the tunnel circuit upstream of the settling chamber. The tunnel air is dried until the dew-point temperature is reduced enough to prevent condensation in the flow.

Based on both centerline probe and wall pressure measurements, uniform flow is achieved at Mach numbers of 0.2 to 1.2. The tunnel is capable of achieving Mach numbers of about 1.3, but most testing is limited to a maximum Mach number of 1.2 because the calibrated region of the test section for $M = 1.3$ is farther downstream than it is for lower Mach numbers and requires that models be located farther aft in the test section.

8-Foot Transonic Pressure Tunnel

The Langley 8-Foot Transonic Pressure Tunnel (8-Foot TPT) is a variable-pressure slotted-throat wind tunnel with controls that permit independent variations of Mach number, stagnation pressure and temperature, and dew point. The test section is square, with filleted corners and a cross-sectional area equivalent to that of an 8-ft-diameter circle. The floor and the ceiling of the test section are axially slotted to permit continuous operation through the transonic speed range. The sidewalls are solid, with windows for schlieren flow visualization.



The 8-Foot TPT is a very versatile wind tunnel capable of supporting basic fluid dynamics research as well as a wide range of applied aerodynamics research. With screens and honeycomb in the upstream settling chamber, the quality of the flow in the test section is suitable for performing reliable code validation experiments and laminar flow research. Fixed chokes and test section slot covers are also available and permit tests with both open and closed tunnel configurations as well as improve the flow quality in the test section by blocking upstream propagation of diffuser noise.

(J. M. Luckring, 42869)

Transonic Dynamics Tunnel

The Transonic Dynamics Tunnel (TDT) is a continuous-flow variable-pressure wind tunnel with a 16-ft-square test section; it normally uses air or a heavy gas as the test medium. The maximum Mach number is 1.2, and the maximum Reynolds number obtainable is approximately $10 \times 10^6 \text{ ft}^{-1}$ in heavy gas and $3 \times 10^6 \text{ ft}^{-1}$ in air. The TDT is a unique "national" facility that is used almost exclusively for testing of aeroelastic phenomena. Semispan sidewall mounted models and full-span sting-mounted or cable-mounted models are used for aeroelastic studies of fixed-wing aircraft. In addition, the Aeroelastic Rotor Experimental System (ARES) test stand is used in the TDT to study the aeroelastic characteristics of rotor systems. The Helicopter Hover Facility (HHF), located in an adjacent building, is used to

set up the ARES test stand in preparation for entry into the TDT and for rotorcraft studies in hover. The TDT Data Acquisition System is capable of simultaneous support of tunnel tests, HHF tests, and model checkout in the Calibration Lab. A major facility upgrade to improve the heavy-gas reclamation system has been recently completed.

(Bryce M. Kepley, 41244)

16-Foot Transonic Tunnel

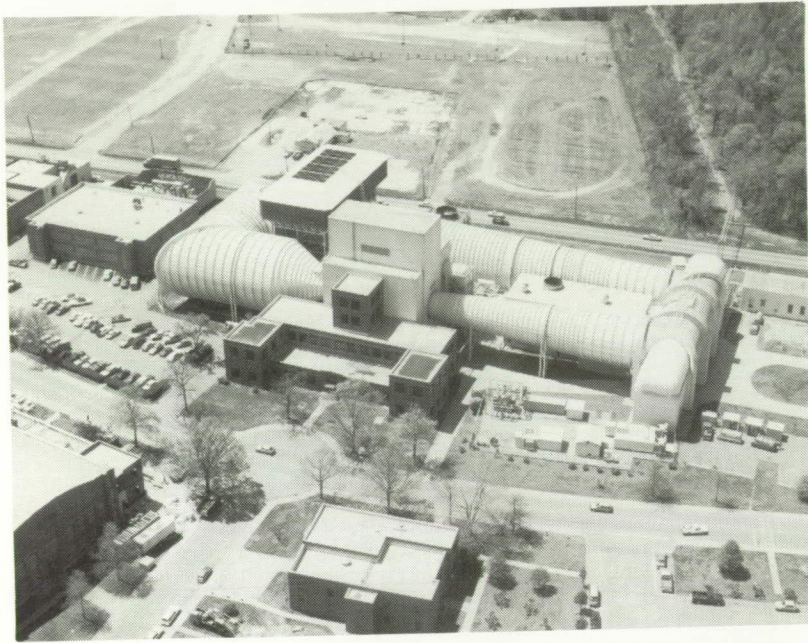
The Langley 16-Foot Transonic Tunnel, which was originally placed into operation in 1941, is a closed-circuit, single-return, continuous-flow, atmospheric tunnel. Speeds up to Mach 1.05 are obtained with the tunnel main-drive fans, and speeds from Mach 1.05 to Mach 1.30 are obtained with a combination of main-drive fans and test section plenum

suction. The slotted octagonal test section measures 15.5 ft across the flats. The tunnel is equipped with an air exchanger with adjustable intake and exit vanes to provide some temperature control. This facility has a main-drive power system consisting of two 30 000-hp motors driving counter-rotating fans. A 36 000-hp compressor provides test section plenum suction.

The tunnel is used for force, moment, pressure, flow visualization, and propulsion-airframe integration studies. Model mounting consists of sting, sting-strut, and semispan support arrangements; propulsion simulation studies are made with dry, cold, high-pressure air or with driven engine simulators.

The 16-Foot Transonic Tunnel has recently undergone several major modifications. These include a floor-mount system to facilitate semispan model testing,





a model preparation area for model buildup and calibration, and a new model support strut with an angle-of-attack range from 10° to 35° , remote roll capability, and dual high-pressure air systems. (Bobby L. Berrier, 43001)

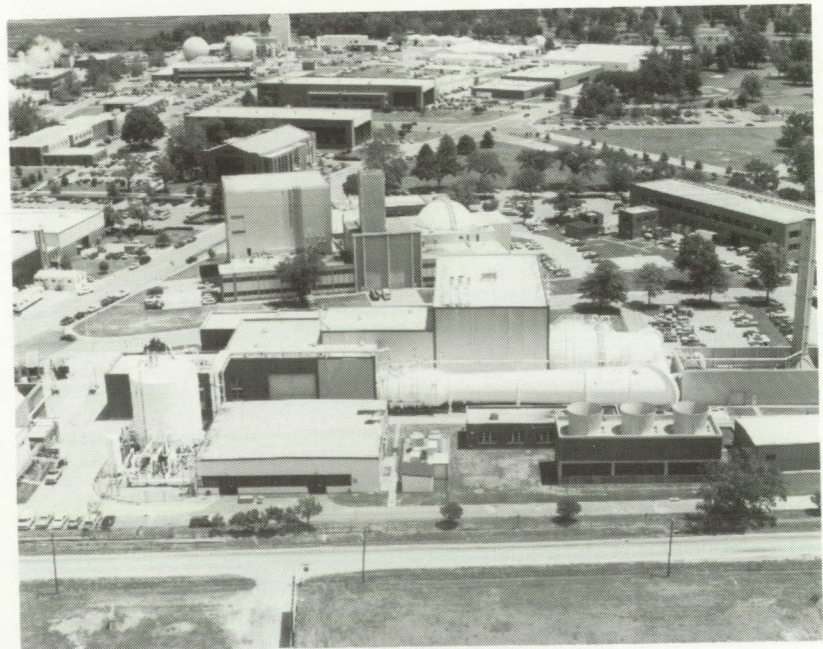
the cryogenic mode of operation, heat removal is by evaporation of liquid nitrogen, which is sprayed into the circuit upstream of the

fan. The tunnel design test-temperature range is variable from 150°F to -320°F . When nitrogen is injected into the circuit, venting must occur to maintain a constant pressure. The design total pressure range for the NTF is from 15 to 130 psia.

The combination of pressure and cold test gas can provide a maximum Reynolds number of 120×10^6 at a Mach number of 1.0 based on a chord length of 9.75 in. By using the cryogenic approach to generate high Reynolds numbers, the NTF achieves its performance of near-full-scale conditions at lower cost and at lower model loads than concepts based on ambient temperature operation. In addition, with both temperature and pressure as test variables, three types of investigations are possible; these include Reynolds number effects at constant Mach number and dynamic pressure (model deflections), model

National Transonic Facility

The National Transonic Facility (NTF) is a fan-driven, closed-circuit, continuous-flow, pressurized wind tunnel. The test section is 8.2 ft by 8.2 ft and approximately 25 ft long, with a slotted-wall configuration. There are six slots each in the top and bottom walls. The test gas may be dry air or nitrogen. For the air mode of operation, heat removal is by a water-cooled heat exchanger (cooling coil) located at the upstream end of the settling chamber. For



aeroelastic effects at constant Reynolds number and Mach number, and Mach number effects at constant dynamic pressure and Reynolds number.

(Dennis E. Fuller, 45129)

0.3-Meter Transonic Cryogenic Tunnel

The 0.3-Meter Transonic Cryogenic Tunnel (0.3-m TCT) is a closed-circuit, fan-driven, cryogenic, pressure tunnel. The 0.3-m TCT operates over the Mach number range of 0.20 to 0.95 at stagnation temperatures of 150°F to approximately -300°F and stagnation pressures of 1 to 6 atm, respectively. The wide ranges of pressure and temperature allow the study of Reynolds number effects on flow phenomena up to Reynolds numbers of $100 \times 10^6 \text{ ft}^{-1}$.

The tunnel was placed in operation in 1973 as a three-dimensional pilot tunnel to demonstrate the cryogenic wind-tunnel concept at transonic speeds. During more than 15 years of operation, the 0.3-m TCT has run with three different test sections. Currently, the facility is operating with an adaptive-wall test section that is nominally 13 in. square and has an effective length of 55.8 in. This test section has four solid walls, with the horizontal walls (floor and ceiling) being flexible. A system of 21 computer-controlled jacks supports each of the flexible walls. The facility has motorized model-support turntables and a traversing wake-survey probe, both of which are computer controlled. For two-dimensional testing, the 0.3-m TCT has provisions for both active- and passive-sidewall boundary-layer control. Porous plates can be fitted

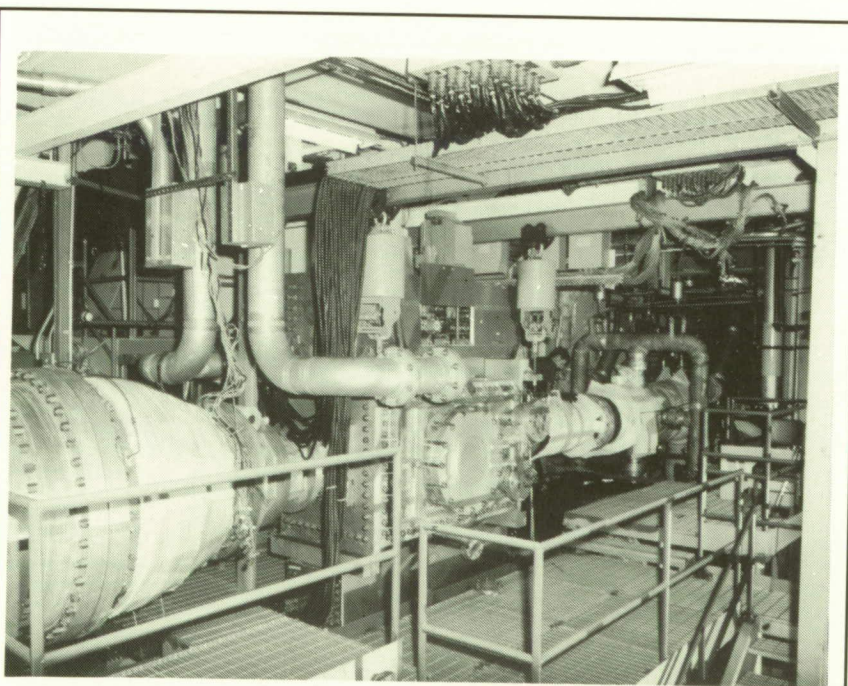
into the rigid sidewalls just upstream of the model location.

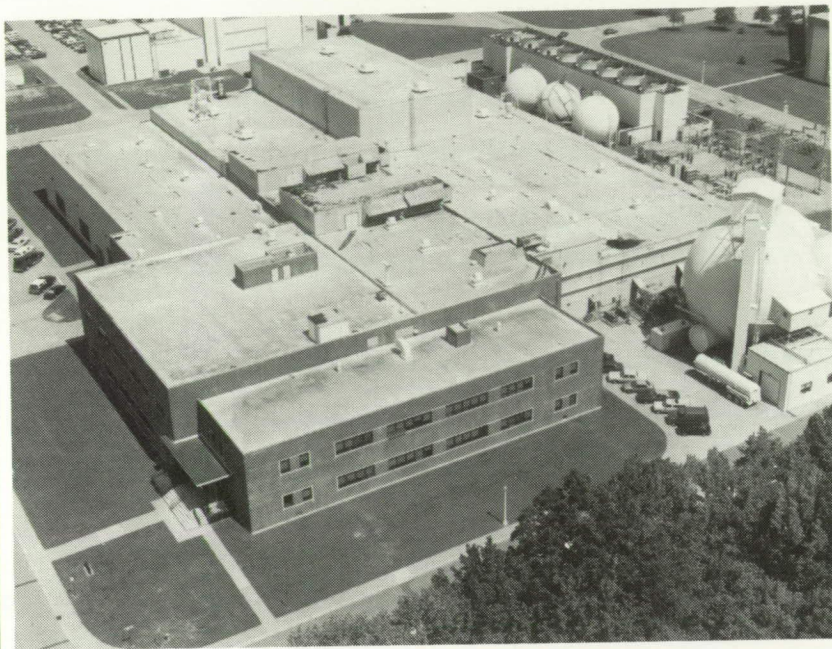
(Stuart G. Flechner, 46360)

Unitary Plan Wind Tunnel

Immediately following World War II, the need for supersonic wind-tunnel facilities to develop advanced airplanes and missiles was recognized. The Department of Defense and the National Advisory Committee for Aeronautics (NACA) developed a plan for a series of facilities which was approved by the United States Congress in the Unitary Plan Wind Tunnel Act of 1949. This plan included five wind-tunnel facilities, three at NACA laboratories and two at the Arnold Engineering Development Center. The Langley Unitary Plan Wind Tunnel (UPWT) was one of the three built by NACA. The UPWT is a closed-circuit, continuous-flow, variable-density tunnel with two 4-ft by 4-ft by 7-ft test sections. One test section has a design Mach number range of 1.5 to 2.9, and the other a Mach number range of 2.3 to 4.6. The tunnel has sliding-block type nozzles that allow continuous variation in Mach number while the facility is in operation. The maximum Reynolds number per foot varies from 6 to 11×10^6 , depending on Mach number. Types of tests include force and moment, pressure distribution, jet effects, dynamic stability, and heat transfer. Flow visualization capabilities in both test sections include schlieren, oil flow, vapor screen, and mini tufts.

(William A. Corlett, 45911)





Hypersonic Facilities Complex

The Hypersonic Facilities Complex consists of nine hypersonic wind tunnels located at three Langley sites. These facilities are considered a complex because together they represent a major unique national resource for wind-tunnel testing. The complex currently includes the Hypersonic CF_4 (tetrafluoromethane) Tunnel ($M = 6$), the 15-Inch Mach 6 High-Temperature Tunnel, the Mach 6 High Reynolds Number Tunnel, the 20-Inch Mach 6 Tunnel, the Mach 8 Variable-Density Tunnel, the 31-Inch Mach 10 Tunnel, the Hypersonic Nitrogen Tunnel ($M = 17$), the Mach 20 High Reynolds Number Helium Tunnel, and the Hypersonic Helium Tunnel (Mach 20). These facilities are used to study and to assess the aerodynamic, aerothermodynamic, and fluid dynamic

phenomena associated with advanced manned space transportation systems, such as Personnel Launch System vehicles, Assured

Crew Return Vehicle concepts, and Advanced Manned Launch System concepts; to support the development of the National Aero-Space Plane technology, lunar return and Mars entry and return vehicles, and hypersonic missiles and transports; to perform basic fluid dynamics studies of complex flow phenomena such as shock-shock interactions and shock impingements; to establish data bases for calibration of computational fluid dynamics (CFD) codes; and to develop measurement and testing techniques. A significant amount of the current testing in these facilities is classified, so the amount and content of test results that can be reported in the open literature is restricted.

This complex of facilities provides an unparalleled capability at a single installation to study aerodynamic, aerothermodynamic, and fluid dynamic phenomena for advanced aerospace vehicle



concepts over wide ranges of hypersonic simulation parameters, namely Mach number, Reynolds number, density ratio or ratio of specific heats, and thermal driver potential (wall temperature ratio). Several modifications have recently been made and are continuing to be made to the facilities to improve their flow quality, reliability, productivity, and capability.

(C. G. Miller, 45221)

Scramjet Test Complex

The Scramjet Test Complex consists of five test facilities and a diagnostics laboratory that offer a complete spectrum of supersonic combustion ramjet (scramjet) test capabilities, from inlet and combustor component studies to tests of complete, hydrogen-fueled, component-integration engine models, over a simulated flight Mach number range of 3.4 to 17 (total temperatures to 14 500°R). The complex includes the Mach 4 Blowdown Facility (M4BDF), the Direct-Connect Supersonic Combustion Test Facility (DCSCTF), the HYPULSE expansion tube, the Combustion-Heated Scramjet Test Facility (CHSTF), the Arc-Heated Scramjet Test Facility (AHSTF), the 8-Foot High-Temperature Tunnel (8-Foot HTT), and the Nonintrusive Diagnostics Laboratory (NDL). These facilities comprise a scramjet test complex unequalled in the Western World in the capability to investigate engine flow fields, scale effects, speed effects, and engine-airframe integration.

Tests of small-scale scramjet inlets are conducted in air in the M4BDF to investigate performance

near the ramjet-scramjet takeover Mach number. Inlets are also tested in air or nitrogen from Mach 1.6 to 10 and in helium at Mach 18 and 22 in other Langley wind tunnels to study inlet flow phenomena and to validate computational fluid dynamics codes.

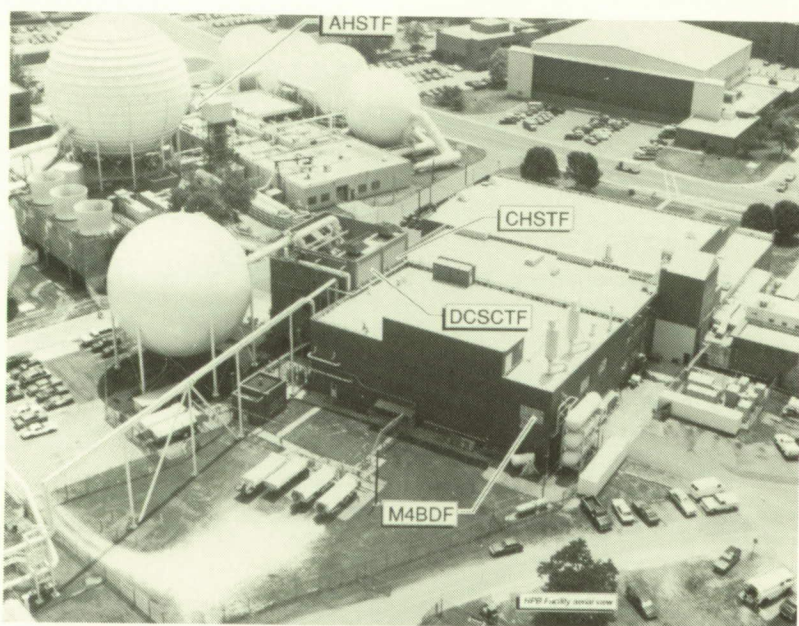
Scramjet combustors are tested in the DCSCTF to provide basic research data on supersonic fuel-air mixing, ignition, and combustion processes. The hot test gas supplied to the combustor models by the hydrogen-air-oxygen combustion heater simulates air with total enthalpy levels ranging up to those for Mach 8 flight speeds. Various facility nozzles produce the desired combustor entrance flow conditions.

The HYPULSE expansion tube, a NASA-owned facility located at the General Applied Sciences Laboratory, provides supersonic combustor test capability at total

enthalpy levels duplicating Mach 13.5, 15, and 17 flight. This unique pulse facility provides clean, undissociated test air at these extreme simulated flight conditions.

Designs from the individual component tests are assembled to form component integration engines that are tested in the two subscale engine test facilities, the CHSTF and the AHSTF. The CHSTF uses a hydrogen-air-oxygen combustion heater to produce test gases that duplicate total enthalpies of Mach 3.4 to 6 flight, and the AHSTF uses an electric-arc heater to heat air to total enthalpy levels corresponding to flight speeds up to Mach 8. Scramjet model size in both of these facilities is approximately 6 in. by 8 in. in frontal area by 6 ft in length.

The 8-Foot HTT is capable of testing injectable models up to 12 ft in length, including single or multiple engines of the size tested



in the subscale facilities mounted on aircraft-type forebody-aft end structures or larger scale single scramjets with frontal areas of approximately 20 in. by 28 in. Test gases with total enthalpy levels duplicating Mach 4, 5, and 7 flight are produced in this facility by methane-air-oxygen combustion.

The NDL provides space for the development of various optical diagnostic techniques for supersonic reacting flow. Laboratory scale combustion devices provide air total temperatures to 4000°R and a speed range to Mach 2. This laboratory has been used to develop the hardened Coherent Anti-stokes Raman Spectroscopy (CARS) system, to demonstrate the application of ultraviolet Raman scattering to measure temperature and O₂, N₂, H₂, H₂O, and OH mole fractions simultaneously, and to develop laser-induced fluorescence of OH in supersonic reacting flow. (Wayne Guy, 46272)

Aerothermal Loads Complex

The Aerothermal Loads Complex consists of four facilities that are used to carry out research in aerothermal loads and high-temperature structures and thermal protection systems. The 8-Foot High-Temperature Tunnel (8-Foot HTT) is a Mach 7 blowdown-type facility in which methane is burned in air under pressure and the resulting combustion products are used as the test medium, with a maximum stagnation temperature of approximately 3800°R available in order to reach the

required energy level for flight simulation. The nozzle is an axisymmetrical conical contoured design with an exit diameter of 8 ft. Model mounting is semispan or sting, with insertion after the tunnel is started. A single-stage air ejector is used as a downstream pump to permit low-pressure (high-altitude) simulation. The Reynolds number ranges from 0.3 to $2.2 \times 10^6 \text{ ft}^{-1}$, with a nominal Mach number of 7, and the run time ranges from 20 to 180 sec. The tunnel is used for studying detailed thermal-loads flow phenomena as well as for evaluating the performance of high-speed and entry vehicle structural components. A major effort is under way to provide alternate Mach number capability as well as O₂ enrichment for the test medium. This is being done primarily to allow models that have hypersonic air-breathing propulsion applications to be tested.

The 7-Inch High-Temperature Tunnel (7-Inch HTT) is a 1/12-scale version of the 8-Foot HTT with basically the same capabilities as the larger tunnel. It is used primarily as an aid in the design of larger models for the 8-Foot HTT and for aerothermal loads tests on subscale models.

The 20-MW and 5-MW Aerothermal Arc Tunnels are used to test models in an environment that simulates the flight reentry envelope for high-speed vehicles such as the Space Shuttle. The amount of energy available to the test medium in these facilities is 9 MW and 2 MW, respectively. The 20-MW tunnel has a dc arc heater, and the 5-MW tunnel has a three-phase ac arc heater. Test conditions (such as temperature, flow rate, and enthalpy) vary greatly because a variety of nozzles and throats are available. Model sizes can range from 3 in. in diameter to 1 ft by 2 ft in area. These



facilities are currently on standby status.

(Allan R. Wieting, 41359)

Acoustics Research Laboratory

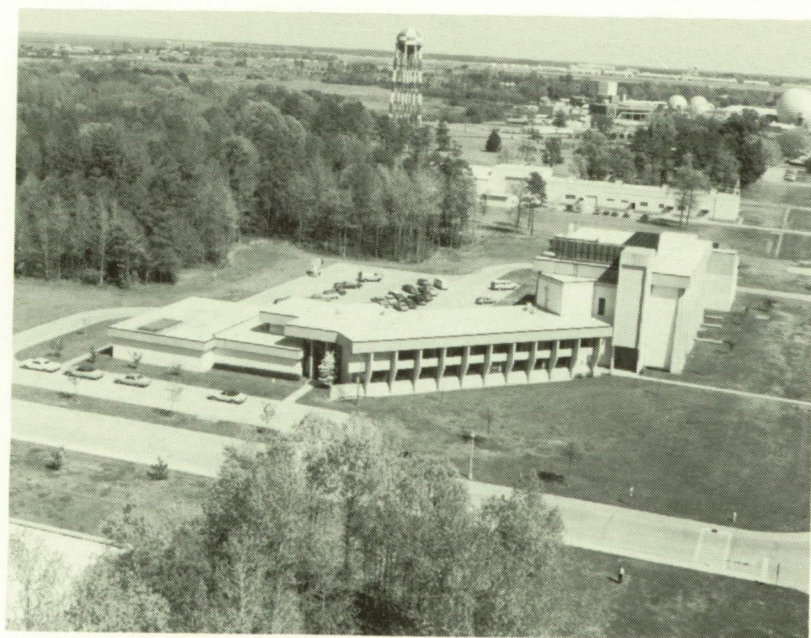
The Langley Acoustics Research Laboratory (ARL) provides the principal focus for acoustics research at Langley Research Center. The ARL consists of the anechoic quiet flow facility, the reverberation chamber, the transmission loss apparatus, and the human-response-to-noise laboratories. The anechoic quiet flow facility has a test chamber treated with sound-absorbing wedges and is equipped with a low-turbulence, low-noise test flow to allow aeroacoustic studies of aircraft components and models. The test flow, which is provided

by either horizontal high-pressure or vertical low-pressure air systems, varies in Mach number up to 2.0. The reverberation chamber, which is used to diffuse the sound generated by a noise source, provides a means to measure the total acoustic power spectrum of the source. The transmission loss apparatus has a source room and a receiving room, which are joined by a connecting wall. A test specimen such as an aircraft fuselage panel is mounted in the connecting wall for sound transmission loss studies. The human-response laboratories consist of the exterior effects room, the anechoic listening room, and the Space Station *Freedom*-aircraft acoustic simulator.

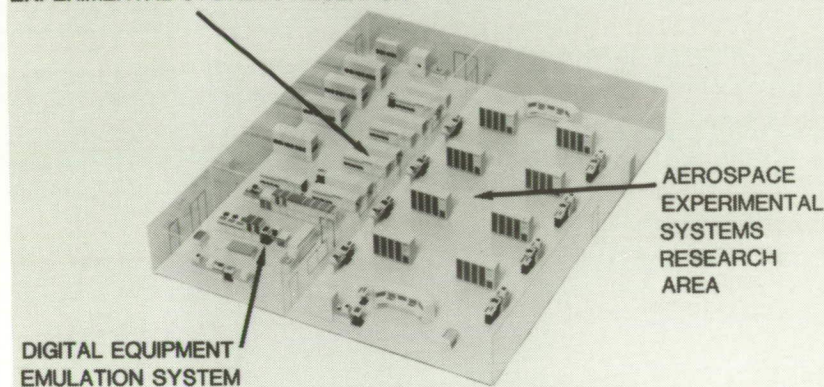
(Lorenzo R. Clark, 43637)

Avionics Integration Research Laboratory (AIRLAB)

AIRLAB is an environmentally controlled structure located in the high-bay area at 1 South Wright Street. AIRLAB houses a number of microcomputer and mini-computer resources and several special fault-tolerant research test specimens dedicated to the support of validation research. AIRLAB addresses issues in the conception, design, and assessment of systems that can dramatically improve performance and lower production and maintenance costs while providing a high, measurable level of safety for passengers and flight crews. It serves as a focal point for U.S. Government, industry, and university personnel to identify and develop methods for systematically validating and evaluating highly reliable digital control and guidance systems for aerospace vehicles. Validation research encompasses analytical, simulation, and experimental methods. Analytical studies are conducted to improve system design, to improve the utility and accuracy of reliability models, to integrate reliability and performance models, and to evaluate new modeling concepts. Simulations are used to determine fault distributions and to discover unmodeled phenomena that reduce electronic system reliability. Experimental testing, including fault injection, simulated lightning transient, and radiated field electromagnetic interference testing is conducted to uncover problems of new technologies such as fly by wire and fly by



MINICOMPUTERS TO SUPPORT EXPERIMENTAL SYSTEMS RESEARCH



light and to verify analytical methods.
(Charles W. Meissner, Jr., 46218)

Aerospace Controls Research Laboratory

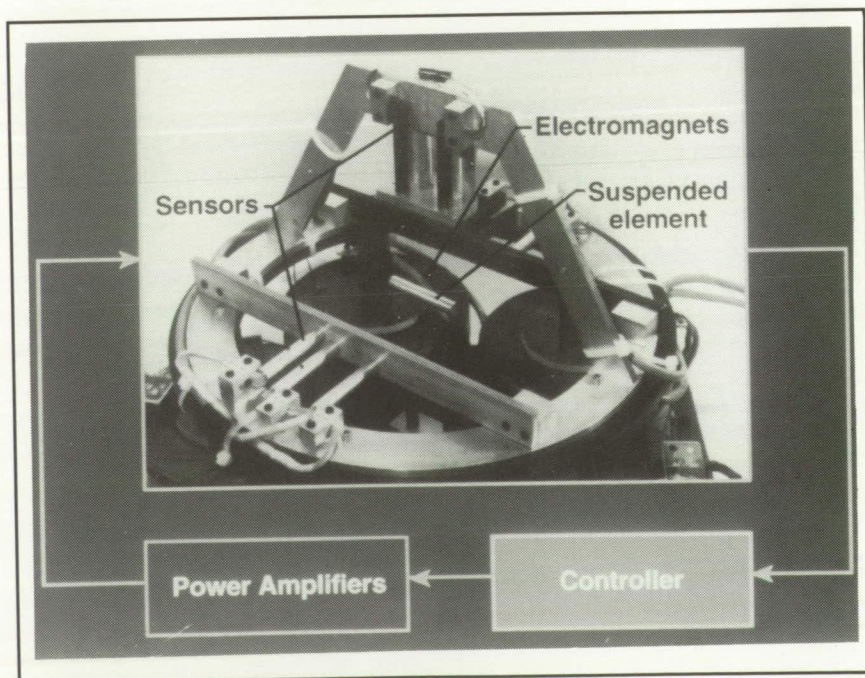
The purpose of the Aerospace Controls Research Laboratory (ACRL) is to conduct research and testing of spacecraft control systems. The ACRL is equipped with modern microcomputer facilities for simulations, data acquisition, and real-time control system testing. Both control law testing using experimental test articles and advanced control system component development are supported by the laboratory. The ACRL provides the controls community with facilities on which the performance of competing control laws may be compared.

A large-angle magnetic suspension test fixture (LAMSTF) consisting of a planar array of five room-temperature electromagnets arranged in a circular configuration with associated sensors, control

electronics, and power amplifiers is shown in the figure. The LAMSTF levitates and controls a cylindrical suspended element that contains a core composed of neodymium-iron-boron permanent magnet material that is magnetized along the long axis of the cylinder. The core is controlled in five degrees of freedom, with roll being the uncontrolled axis.

The LAMSTF can be used in the development of the technology for future large gap magnetic suspension systems by providing the experimental validation of design concepts in the areas of electromagnets, control, sensing, and electronics as well as by providing insight into the requirements and challenges introduced by large-scale systems.

The advanced sensor and processor facility supports research in control system components for space systems. Component development currently focuses on optical sensing and computing devices. Two different photogrammetric position tracking systems and an optical processor for a controls experiment are being developed. The facility includes equipment for performing experiments in optics, two stable tables, optical mounts, lenses, mirrors, polarizers, beam splitters, photomultiplier tubes, acousto-optic modulators, HeNe and Ar lasers, computer-



controlled precision stages, and laser beam steering systems.
(Douglas Price, 46605)

Transport Systems Research Vehicle (TSRV) and TSRV Simulator

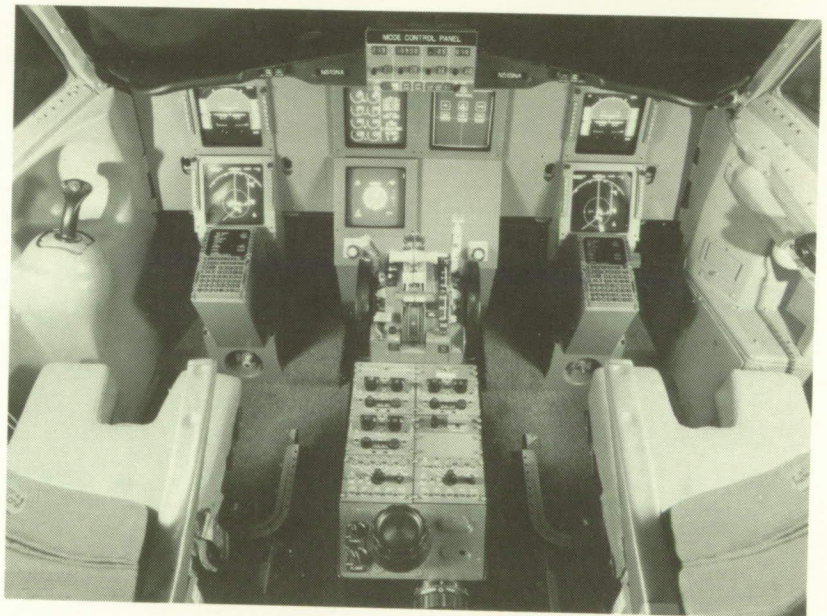
The Transport Systems Research Vehicle (TSRV) and TSRV Simulator are primary research tools used by the Advanced Transport Operating Systems (ATOPS) Program. The goal of the ATOPS Program is to increase the operational capability of modern aircraft and foster their integration into the evolving National Airspace System. The TSRV has two flight decks: a conventional Boeing 737 flight deck provides operational support and safety backup, and the fully operational research flight deck, positioned in the aircraft cabin, provides the capability to explore innovations in display formats, contents, and in-aircraft operations.

The TSRV simulator provides the means for ground-based simulation in support of the ATOPS research program. The simulator allows proposed concepts in such areas as guidance and control algorithms, new display techniques, operational procedures, and human-machine interfaces to be thoroughly evaluated. Four out-the-window display systems (driven by an Evans and Sutherland CT-6 Computer-Generated Imagery system) allow realistic real-world scenes to be presented to the crew. The system is capable of daytime, nighttime, and all ranges of weather effects. The simulator has recently been upgraded to a full complement of

eight electronic displays and two side-arm controllers representative of the technology available in commercial transports of the 1990's. Promising simulation research results become the subjects of actual flight test

research. The simulator is fully integrated with a realistic air traffic control facility to provide an environment for systems level studies.

(George Steinmetz, 43842, Billy Ashworth, and Jacob A. Houck)



Enhanced/Synthetic Vision & Spatial Displays Laboratory

The Enhanced/Synthetic Vision & Spatial Displays Laboratory (ESVSDL) serves as a primary testing facility for the candidate flight display concepts, systems-subsystems, and devices emerging from the Crew Station Technology and Low-Visibility Landing/Surface Operations research efforts. The laboratory provides a unique capability to conduct iterative development and pilot-vehicle experimental evaluation research for advanced cockpit technologies in a highly realistic flight simulation environment. Major elements of the ESVSDL are the following: (1) the Advanced Display Evaluation Cockpit (ADEC), which is a reconfigurable transport aircraft research cab; (2) the Aircraft Cockpit Ambient

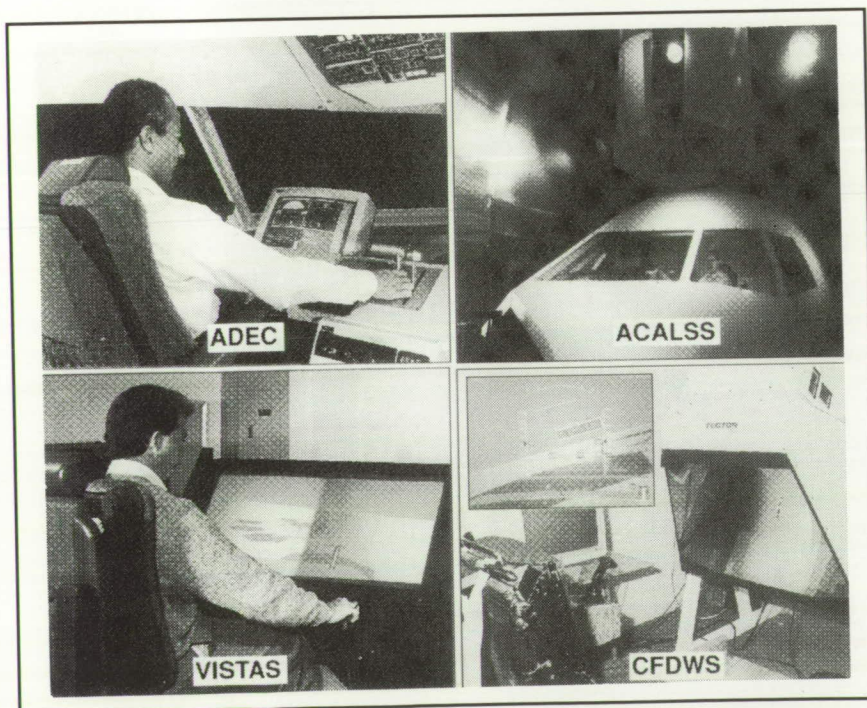
Lighting and Solar Simulator (ACALSS), which provides real-world ambient and solar lighting conditions to the ADEC; (3) the Visual Imaging Simulator for Transport Aircraft Systems (VISTAS), which is a highly flexible, rapidly reconfigurable, large-screen flight display workstation for evaluation of a wide variety of enhanced/synthetic vision and spatial display formats; and (4) the Collimated Flight Display Workstation (CFDWS), which provides the capability for pilot evaluation of collimated flight displays. Other major elements include a general-purpose digital processor, which handles system input/output and vehicle math model simulation; three high-performance raster graphics display generators, which provide sophisticated graphics formats (in 2-D, 3-D, and stereo 3-D modes) to the displays within the facility; and a fiber-optic link to the Langley central comput-

ing facility for research requiring more complex vehicle simulation. (Jack Hatfield, 42012)

Human Engineering Methods Laboratory

The Human Engineering Methods (HEM) Laboratory is used to develop measurement technology to assess the effects of advanced crew station concepts on the crew's ability to function without mental overload, excessive stress, or fatigue. The laboratory provides the capability for measurement of behavioral and psychophysiological response of the flight deck crew. The facility contains state-of-the-art bioinstrumentation as well as computer-based physiological data acquisition, analysis and display, and experiment control capabilities. Software has been developed that enables the demonstration of work load effects on the steady-state evoked brain response and transient evoked response signals as well as the monitoring of electrocardiographic (EKG), electromyographic (EMG), skin temperature, respiration, and electrodermal activity.

The oculometer capability developed at Langley Research Center has been integrated with the other physiological measurement techniques. A computer-based criterion task battery is available for preliminary testing (with human subjects) of work load techniques that are being validated prior to evaluation and application in the simulators. Satellite physiological signal conditioning and behavioral response capture stations are located at the simulator





SIMULATOR WITH BIOINSTRUMENTATION

DATA ACQUISITION & ANALYSIS



site to provide human response measurement support for flight management and operations research.

(Alan Pope, 46642)

General Aviation Simulator

The General Aviation Simulator (GAS) consists of a general-aviation aircraft cockpit mounted on a three-degree-of-freedom motion platform. The cockpit is a reproduction of a twin-engine, propeller-driven, general-aviation aircraft with a full complement of instruments, controls, and switches, including radio navigation equipment. Programmable control force feel is provided by a "through-the-panel" two-axis controller that can be removed and replaced with a two-axis side arm controller that can be mounted in the pilot's left-hand, center, or right-hand position. A variable-force-feel system is also provided for the rudder pedals. The pilot's instrument panel can be configured with various combinations of cathode-ray tube (CRT) displays and conventional instruments to represent aircraft such as the Cessna 172, Cherokee 180, and Cessna 402B. A collimated-image visual system provides a 60° field-of-view out-the-window color display. The visual system accepts inputs from a Computer-Generated Image (CGI) system. A Calligraphic-Raster Display System (CRDS) is used to generate the head-down displays and to mix with the CGI for the head-up display. The simulator is flown in real time, with a host computer used to simulate aircraft dynamics.

Research has been conducted to improve the ride quality of general aviation aircraft by developing gust alleviation control laws to reduce the aircraft response to turbulence while generally good flying characteristics are maintained. A research study in progress is the General Aviation E-Z Fly, a program to investigate ways of making general aviation airplanes easier to fly, especially for low-time pilots or nonpilots. (Lemuel E. Meetze, 46452)

Differential Maneuvering Simulator

The Langley Differential Maneuvering Simulator (DMS) provides a means of simulating two piloted aircraft operating in a differential mode with a realistic cockpit environment and a wide-angle external visual scene for each of the two pilots. The system

consists of two identical fixed-based cockpits and projection systems, each based in a 40-ft-diameter projection sphere. Each projection system consists of two terrain projectors to provide a realistic terrain scene and a system for target image generation and projection. The terrain scene, driven by a Computer-Generated Image (CGI) system, provides reference in all six degrees of freedom in a manner that allows unrestricted aircraft motions. The resulting sky-Earth scene provides full translational and rotational cues. The target visual scene also provides continuous rotational and bounded (300 ft to 45 000 ft) translational reference to one or two other (target) vehicles in six degrees of freedom.

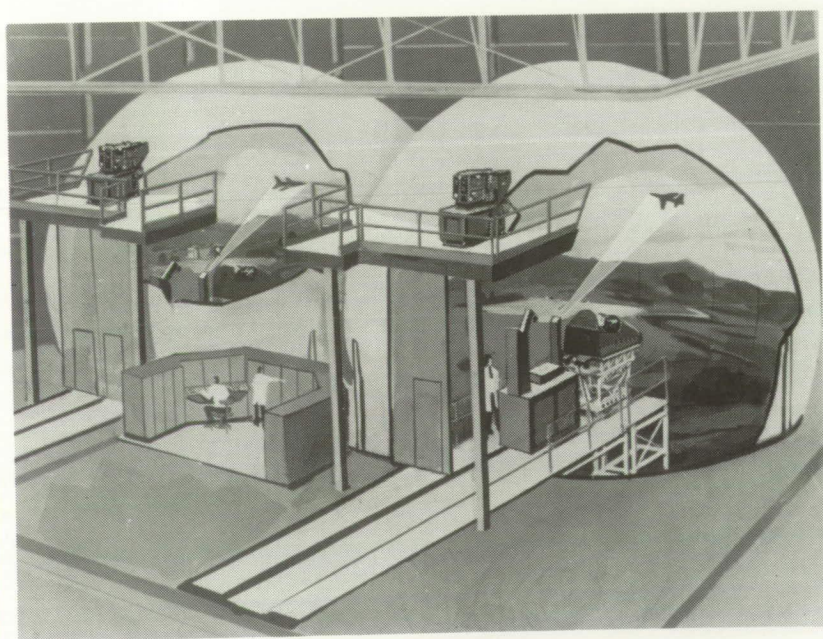
The target image presented to each pilot represents aircraft being flown by the other pilot in this two-aircraft simulator. This dual simulator can be tied to a third dome and provide three-aircraft

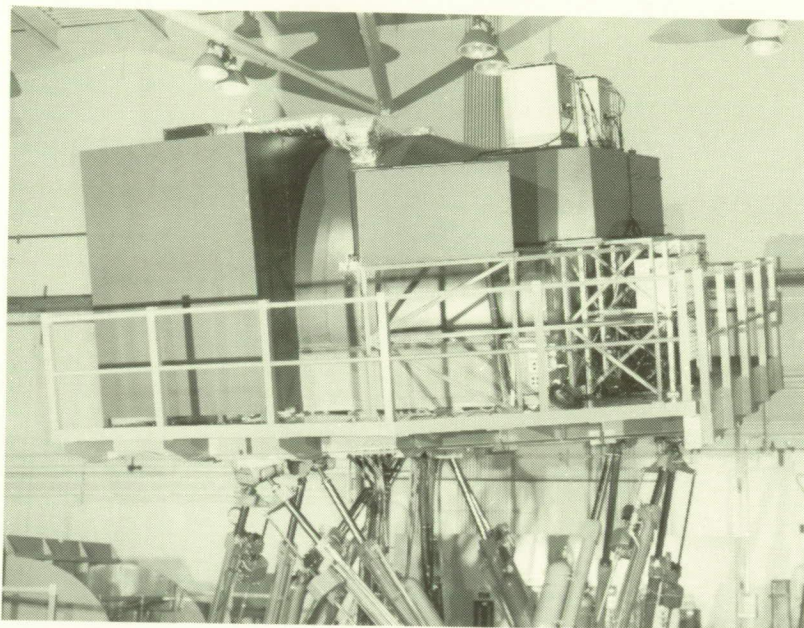
interactions when required. Each cockpit provides three color displays with a 6.5-in.-square viewing area and a wide-angle head-up display. Kinesthetic cues in the form of a g-suit pressurization system, helmet loader system, g-seat system, cockpit buffet, and programmable control forces are provided to the pilots consistent with the motions of their aircraft. Other controls include a side-arm controller, dual throttles, and a rotorcraft collective. Research applications include studies of high-angle-of-attack flight control laws, evaluation of evasive maneuvers for various aircraft and rotorcraft, and evaluations of the effect of parameter changes on the performance of several baseline aircraft.

(Lemuel E. Meetze, 46452)

Visual Motion Simulator

The Visual Motion Simulator (VMS) is a general-purpose simulator consisting of a two-person cockpit mounted on a six-degree-of-freedom synergistic motion base. Four collimated visual displays, compatible with the Computer-Generated Image (CGI) system, provide out-the-window scenes for the left and right seat front and side windows. Six electronic displays mounted on the left and right side instrument panels provide for displays generated by a graphics computer. A programmable hydraulic-controlled two-axis side arm and rudder pedals provide for roll, pitch, and yaw controls in the left seat. Another programmable hydraulic-controlled loading system for the right seat provides roll and pitch controls for either a fighter-type control





stick or a helicopter cyclic controller. Right-side rudder control is an extension of the left-side rudder control system. A friction-type collective control is provided for both the left and the right seat. An F16 two-axis side-arm controller was recently installed on the right side of the cockpit. An observer's seat allows a third person to be in the cockpit during motion operation.

A realistic center control stand, in addition to providing transport-type control features, provides auto-throttle capability for both the forward and the reverse thrust mode. Motion cues are provided in the simulator by the relative extension or retraction of the six hydraulic actuators of the motion base. Washout techniques are used to return the motion base to the neutral point once the onset motion cues have been commanded.

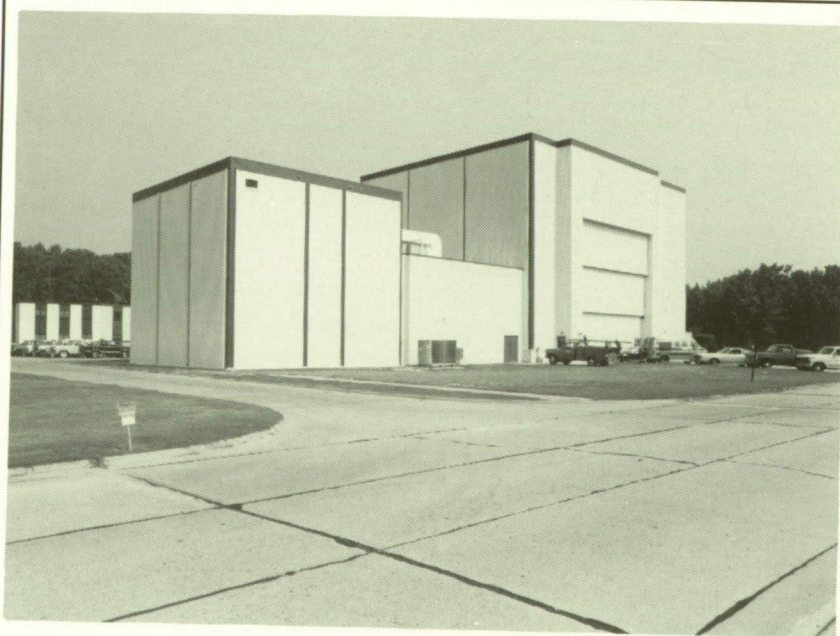
Research applications have included studies for transport,

fighter, and helicopter aircraft, including the National Aero-Space Plane (NASP), Personnel Launch System (PLS), and High-Speed Civil Transport (HSCT). These studies addressed phenomena

associated with wake vortices, high-speed turnoffs, microwave landing systems, energy management, noise abatement, multibody transports, maneuvering stability flight characteristics, wind-shear recovery guidance, vortex flaps, and stereographic displays. Numerous simulation technology studies have also been conducted to evaluate the generation and usefulness of motion cues. (John D. Rollins, 46448)

Space Simulation and Environmental Test Complex

The Space Simulation and Environmental Test Complex consists of facilities and equipment used to evaluate and qualify space flight experiments and components. These facilities include a 60-ft vacuum sphere, an 8- by 15-ft thermal vacuum chamber, two



5- by 5-ft thermal vacuum chambers, two vibration testing systems with capabilities of 17 000 and 35 000 lbf, several thermal vacuum bell jars, and mass properties measurement equipment.

Vacuum spheres and chambers are used to simulate space environments by providing vacuum pressures to 1×10^{-7} mm Hg and temperatures ranging from -300°F to 300°F . The large 60-ft vacuum sphere can reach a vacuum pressure of 1×10^{-2} mm Hg and operates at ambient temperatures. Two of the three thermal vacuum chambers are equipped with cryogenic pumps and cryogenic cold traps to avoid contamination to payloads, which can result from oil migrating from diffusion or turbomolecular pumps. The thermal vacuum chambers are equipped with residual gas analyzers (RGA's) to continuously monitor and identify molecular species within the chambers.

The engineering vibration test facility is used to perform environmental vibration tests on aerospace flight systems and components to demonstrate that the flight equipment will maintain structural integrity when exposed to a mission environment.
(Thomas J. Lash, 45644)

Advanced Technology Research Laboratory

The Advanced Technology Research Laboratory was dedicated in early 1989 in support of the NASA Space Energy Conversion Research and Technology Program. Several labs have been rededicated to the study of the



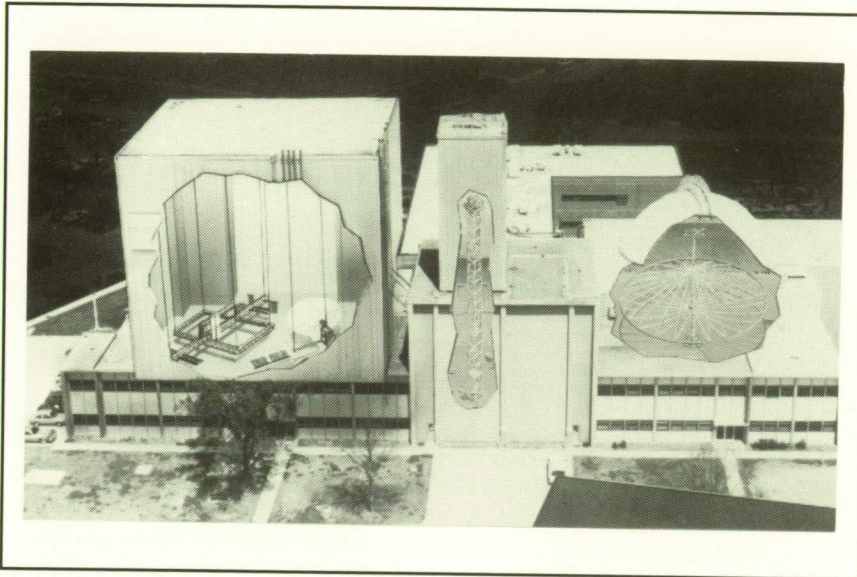
aerothermodynamics of internal flows. Experiments are planned for hypersonic and hypervelocity flows to secure new fundamental data. The facility also contains a large capacitor bank that is the energy source for the development of magnetohydrodynamic (MHD) flows. Radiation shielding research to develop the basic fragmentation and transport physics of galactic and solar cosmic rays is supported by a computational capability that includes the latest computer technology. In addition, the facility is fully integrated into the Center's high-speed data network. A group of laboratories house ultrahigh vacuum equipment that simulates the space environment and specialized conditions associated with advanced spacecraft. Experimental low-pressure studies focus on the transport of hydrogen through National Aero-Space Plane surfaces, the establishment of high-purity high-energy atomic oxygen beams, and advanced

methods to extract oxygen from the Martian atmosphere or other gases. One laboratory is used to catalog LDEF (Long Duration Exposure Facility) impact craters. Others specialize in measurements of instrument parameters for coherent combination of laser beams, for laser-assisted remote compositional analysis, and for laser photovoltaic power conversion devices.

(E. J. Conway, 41435)

Spacecraft Dynamics Laboratory

The Spacecraft Dynamics Laboratory is used for structural dynamics research on spacecraft structures, components, equipment, and materials. The current research emphasis is on the low-frequency dynamic behavior of large space structures such as Space Station *Freedom* and the interactions of spacecraft structures



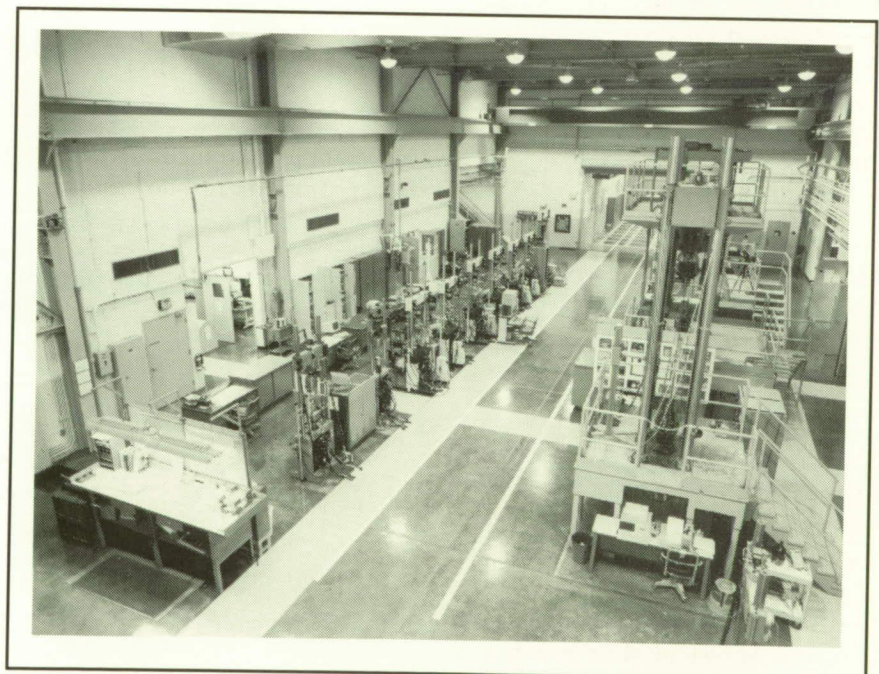
Materials Research Laboratory

The Materials Research Laboratory houses experimental facilities for conducting a wide range of research to characterize the behavior of advanced structural materials under the application of mechanical and thermal loads. This research encompasses the study of deformation characteristics and damage mechanics leading to the development of nonlinear constitutive models, strength criteria, and durability and damage tolerance criteria. A high-bay area, with a 20-ft clear height and a 7.5-ton traveling overhead crane, houses nine multipurpose 20-kip to 100-kip servohydraulic systems for coupon testing and three high-load capacity (up to 400 kips) systems for testing large panels. Six enclosed laboratories around the perimeter of the high-bay area house an additional 38 servohydraulic testing systems (1 kip to

with high-gain automatic control systems. The facility has three components, a 16-m thermal vacuum cylinder (TVC), the Structural Dynamics Research Laboratory (SDRL), and the Space Structures Research Laboratory (SSRL). The TVC is a flat-floor, 55-ft-diameter, 64-ft-high hemispherical dome cylinder with a floor-mounted rotation table. The TVC can achieve a pressure of 100- μ m Hg in 160 minutes and has a 100°F temperature gradient capability. The SDRL has a 38-ft-high vertical backstop and a 12- by 12- by 95-ft tower for structural dynamic testing of spacecraft models, structures, and components. The SSRL is an 80- by 80- by 80-ft high-bay area, with an overhead work platform located at the 73-ft level and a 20- by 30- by 40-ft free-standing gantry. This laboratory is used for structural dynamics and control testing of large spacecraft models which require large suspension heights to reduce gravitational effects. The SSRL contains state-of-the-art dynamic data acquisition systems and real-time control computers. The SSRL

houses the Dynamic Scale Model Technology test article, a 1/10-scale model of an early erectable truss space station design, and the Control-Structures Interaction Evolutionary Model Phase 1 test-bed.

(Robert Miserentino, 44318)



100 kips), a scanning electron microscope, 3 X-ray radiography systems, 13 high-temperature creep frames, and 3 multiparameter test facilities.

The 50 servohydraulic testing systems are used for monotonic and cyclic loading of material level coupons and flat panels under tension, compression, combined tension-torsion, combined tension-bending, and biaxial loads. Combined thermal and mechanical loading conditions can be achieved by a variety of methods, including convection furnaces (600°F), quartz lamp heaters (1500°F+), and induction heaters (2000°F+). Liquid nitrogen is used when cryogenic temperatures are required. A special multiparameter test facility allows for the simultaneous testing of up to six specimens under combined temperatures, cyclic mechanical loads, and partial pressures. Basic fracture morphology studies are also conducted in an environmental fatigue laboratory. A vacuum chamber allows for the control of moisture, temperature, and gaseous environment. Fatigue tests can also be conducted in saltwater environments.

(Charles E. Harris, 43449)

Structures and Materials Research Laboratory

Built in 1939 to contribute to the development and validation of aircraft structural designs during World War II, this laboratory currently supports a broad range of structural and materials development activities for advanced aircraft, aerospace vehicles, and space platform and

antenna structures. Research includes the development, fabrication, and characterization of advanced materials and the development of novel structural concepts. Static testing, environmental testing, and material fabrication and analysis are performed. Emphasis is on the development of structural mechanics technology and advanced structural concepts enabling the verified design of efficient, cost-effective, damage-tolerant advanced composite airframe structural components subjected to complex loading and demanding environmental conditions. This research also emphasizes advanced space-durable materials and structural designs for future large space systems affording significant improvements in performance and economy.

A significant feature of the laboratory is its static testing equipment, which has capabilities up to 1 200 000 lb (specimens 6 ft wide by 18 ft long) and down to 10 000 lb (smaller specimens).

Capability exists for assembling and testing large structural specimens and components such as the trusses used for Space Station *Freedom* development and future large space structures.

This complex also houses the Langley state-of-the-art analytical and metallurgical laboratory, which features all aspects of material specimen preparation and examination. Complete automated metallographic preparation equipment is available for research on light alloys as well as metal matrix and resin matrix composites. Optical microscopy includes quantitative image analysis in addition to regular microscopy. Current technology electron microscopy is available including scanning electron microscopy, scanning transmission electron microscopy, and electron microprobe X-ray analysis.

(James H. Starnes, 43168)



Polymeric Materials Laboratory

The Polymeric Materials Laboratory complex provides 25 000 ft² of floor space for the synthesis and characterization of high-performance polymers as well as the development of processing technology and composite fabrication. The complex contains seven synthesis laboratories and a bench-scale laboratory designed for synthesis of large batches of polymeric materials. An isolated explosion-proof area is provided for safely performing hydrogenations and pressure polymerizations. The facility also contains a film-casting laboratory with environmentally controlled film-casting boxes and a chemical storage area that is protected by an automatic CO₂ extinguisher system.

Much of the work of this laboratory is directed toward the synthe-

sis of processible, tough, durable, high-performance matrices and the development of relationships between molecular structure, neat resin properties, and composite properties. Classes of polymers being analyzed include amorphous, semi-crystalline, and lightly cross-linked thermoplastics; semi-interpenetrating networks; toughened thermosets; and piezoelectric polymers. Extensive characterization equipment is housed in the instrument laboratories and is used for performing chromatography; thermal analyses; X-ray, rheological, rheometric, and spectroscopic characterizations; and mechanical strength determinations of adhesives, polymer moldings, films, fibers, and composites.

The Composites Processing Laboratory is the focal point at Langley for research and development of advanced polymer composite systems. Its primary function is to determine the potential of new polymers for use as

matrix systems for the fabrication of advanced fiber-reinforced composites. Research quantities of graphite-reinforced polymer composite material are fabricated in drum-wound prepreg machines by solvent solution impregnation. Hot rolls are used to manufacture melt-impregnated composite material. Unique dry-powder-coating-melt-fusion equipment is employed to fabricate prepreg from advanced, difficult-to-process polymer matrix materials. A new modular tape prepreg machine that is capable of making high-quality prepreg by solution coating, film casting, and direct fiber impregnation is now in operation.

(H. D. Burks, 44272)

NDE Research Laboratory

The reliability and safety of materials and structures are of paramount importance to NASA. The assurance of reliability must be based on quantitative measurement science capability that is nondestructive. The Langley Research Center's NDE Research Laboratory has as its prime focus the development of new measurement technologies that can be directly applied to ensure material integrity and development of physical property measurement technologies required for structural performance evaluation.

The NDE Research Laboratory is a new, state-of-the art facility that occupies nearly 26 000 ft². The laboratory is the Agency's focal point for advanced NDE and is a combination of a research facility, which provides advanced NDE capabilities for NASA, and



ORIGINAL PAGE
BLACK AND WHITE PHOTOGRAPH



an important resource for government and industry technology transfer. The activity concentrates on NDE material science for composites and metals with an emphasis on material characterization, structural NDE, and smart sensor-materials as well as detection of flaws, damage, fatigue, and applied and residual stress. The two major programs within the laboratory are addressing the Nation's needs for its aging aircraft and the safety of NASA's space flight systems.

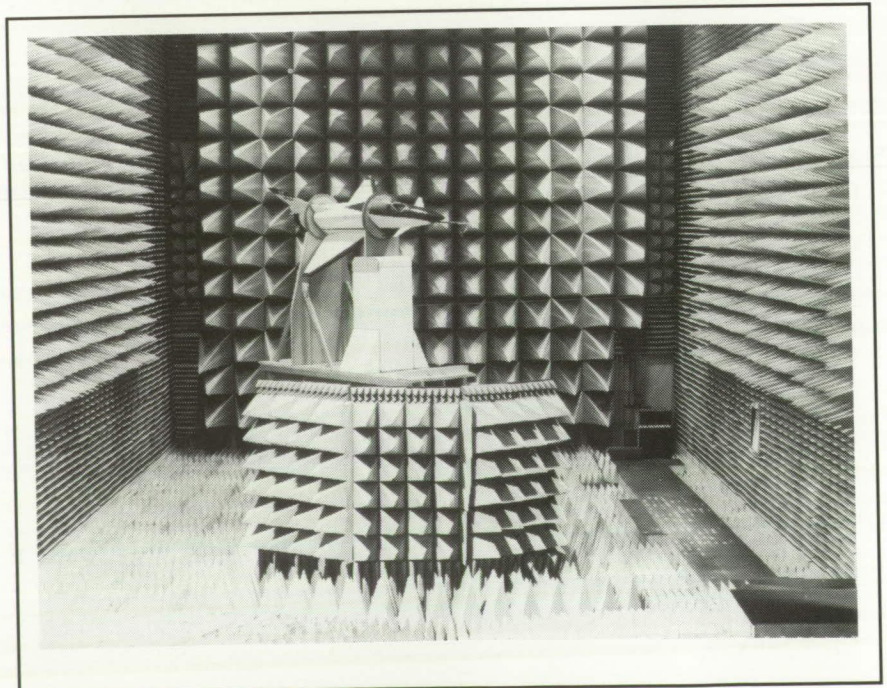
The laboratory houses numerous major systems in the technologies of ultrasonics, acoustic emission, thermography, optics, electromagnetics, X-radiation, nonlinear acoustics, and process control sensors; it also has the numerical capability to simulate and model a measurement and contains technology transfer lab. In addition to numerous conventional systems, the laboratory includes several advanced, special-

ized NDE systems: four electron and acoustic microscopes, a laser-ultrasonic system, a 2-D thermoelasticity system, two laser shearography systems, a speckle interferometry system, a magneto-optical imaging system, and a microfocus

X-ray tomography system operated on a 55-kip load frame to provide the Agency with the first views of material or structural failure under load.
(Eric I. Madaras, 44970)

Low-Frequency Antenna Test Facility

The Low-Frequency Antenna Test Facility is a research facility used to obtain data for new antenna performance in support of various research programs. The anechoic chamber provides simulated free-space conditions for measurements from 100 MHz to more than 40 GHz. A precision antenna positioning system designed for spherical near-field (SNF) measurements was installed in the chamber, and the capability now exists for automatic performance of precision SNF measurements up to at least 18 GHz. Antennas with diameters up to



12 ft can be measured if their electrical size is no greater than 100 wavelengths. Measured data stored on disk can be processed to provide antenna directivity, polar or rectangular plots of the radiation patterns, and three-dimensional contour plots of the antenna radiation characteristics.

(Tom Campbell, 41772)

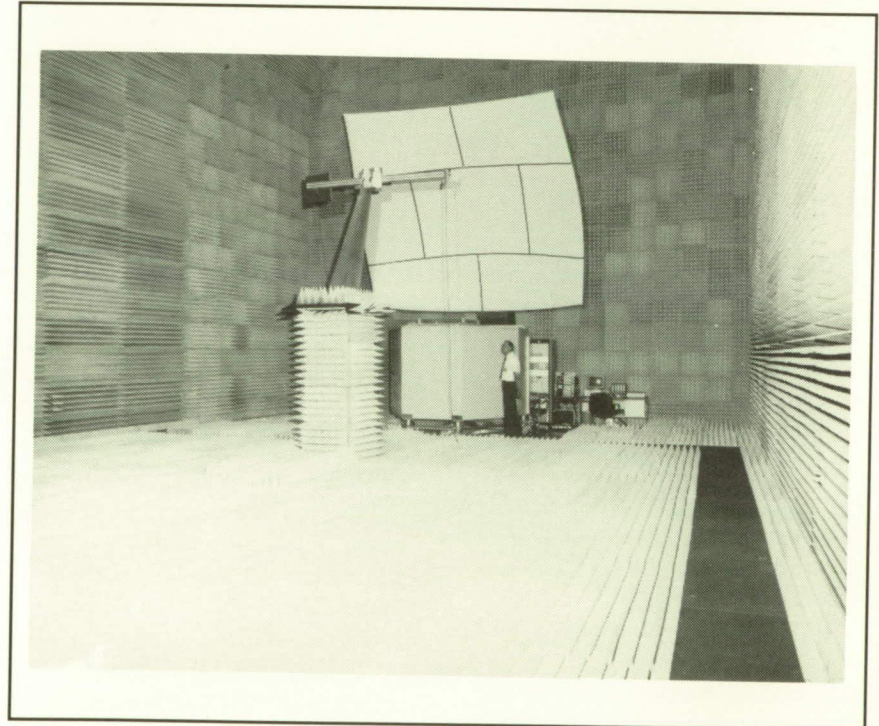
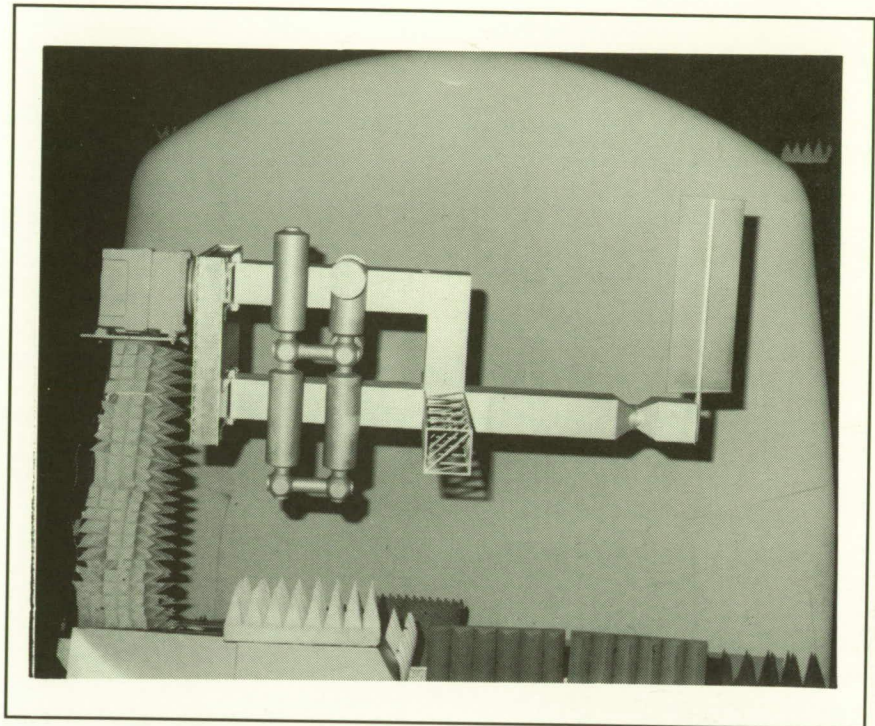
Compact Range Pilot Facility

The Compact Range Pilot Facility is an electromagnetic measurement system used to simulate a plane wave illuminating an antenna or scattering body. The plane wave is necessary to represent the actual use of the antenna or scattering from a target in a real-world situation. The compact range utilizes an offset-fed parabolic reflector to create the simulated plane wave test conditions. The standard commercially available compact range is limited to the measurement of antennas or models with maximum dimensions of 4 ft over the frequency range of 4 GHz to 100 GHz.

(Tom Campbell, 41772)

Experimental Test Range

The Experimental Test Range (ETR) is an indoor radio frequency (RF) anechoic laboratory designed to improve existing compact range technology through research and to support ongoing electromagnetic measurements at the Antenna and Microwave Research Branch. The ETR is capable of simulating



free-space conditions for microwave measurements using anechoic pyramidal and wedge-shaped absorber material that completely

covers the interior of the RF shielded 40- by 40- by 80-ft chamber. Currently, a large 16- by 16-ft cosine-squared blended rolled

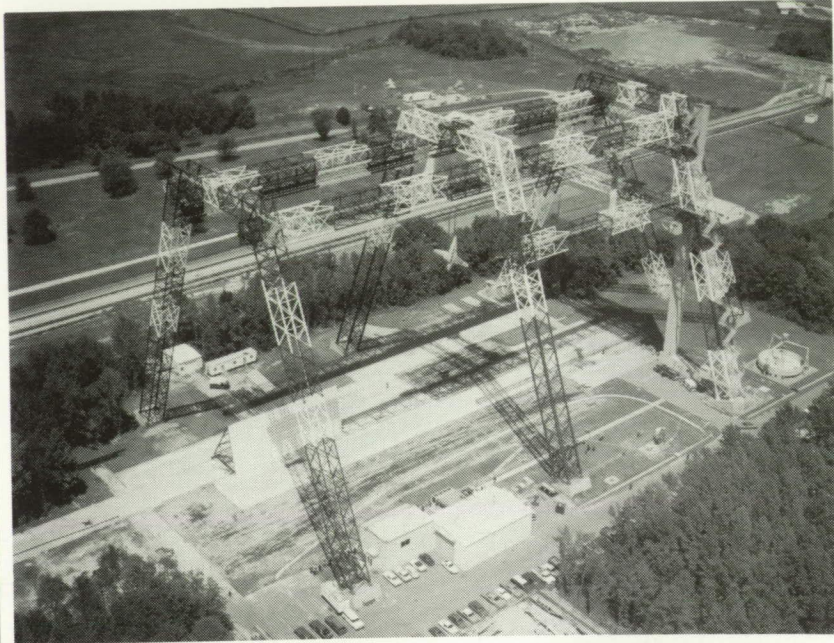
edge main reflector is used along with a Gregorian subreflector for a novel approach to compact range designs.

(Tom Campbell, 41772)

Impact Dynamics Research Facility

The Impact Dynamics Research Facility (IDRF), which was originally the Lunar Landing Facility used during the Apollo Program for simulation of lunar landings, has been modified to allow crash testing of full-scale aircraft under controlled conditions. The aircraft are swung by cables from an A-frame structure that is approximately 400 ft long and 230 ft high. The impact runway can be modified to simulate other ground crash environments, such as packed dirt, to meet a specific test requirement.

Each aircraft is suspended by cables from two pivot points 217 ft off the ground and allowed to swing pendulum-style into the ground. The swing cables are separated from the aircraft by pyrotechnics just prior to impact. The length of the swing cables regulates the aircraft impact angle from 0° (level) to approximately 60°. Impact velocity can be varied to approximately 65 mph (governed by the pullback height). Variations of aircraft pitch, roll, and yaw can be obtained by changing the aircraft suspension harness attached to the swing cables. Onboard instrumentation data are obtained through an umbilical cable that is hard wired to the control room at the base of the A-frame. Photographic data are obtained by onboard, ground-



mounted, and A-frame-mounted cameras. Maximum allowable weight of the aircraft is 30 000 lb. (Granville Webb, 41303)

Aircraft Landing Dynamics Facility

The Aircraft Landing Dynamics Facility is a test track primarily used for landing gear research activities. The ALDF uses a high-pressure water jet system to propel the test carriage along the 2800-ft track. The propulsion system consists of an L-shaped vessel that holds 28 000 gal of water pressurized up to 3150 psi by an air supply system. A time quick-opening shutter valve is mounted on the end of the L-shaped vessel and releases a high-energy water jet, which catapults the carriage to the desired speed. The propulsion system produces a thrust in excess

of 2 000 000 lb, which is capable of accelerating the 54-ton test carriage to 220 knots within 400 ft. This thrust creates a peak acceleration of approximately 20g. The carriage coasts through the 1800-ft test section and decelerates to a velocity of 175 knots or less before it intercepts the five arresting cables that span the track at the end of the test section. The arresting systems bring the test carriage to a stop in 600 ft or less. Essentially any landing gear can be mounted on the test carriage, including those exhibiting new or novel concepts, and virtually any runway surface and weather condition can be duplicated on the track.

(Granville Webb, 41303)



Basic Aerodynamics Research Tunnel

Computational methods are progressing rapidly toward the predication of the three-dimensional flow field about complex geometries at high angles of attack. These computational methods require a large number of grid points to adequately model the flow field, and they produce large amounts of information. To validate these methods, detailed experimental flow field measurements are required. The Basic Aerodynamics Research Tunnel (BART) is a flow diagnostic facility dedicated to the tasks of acquiring the detailed data required for code validation and of investigating the fundamental character of complex flow fields.

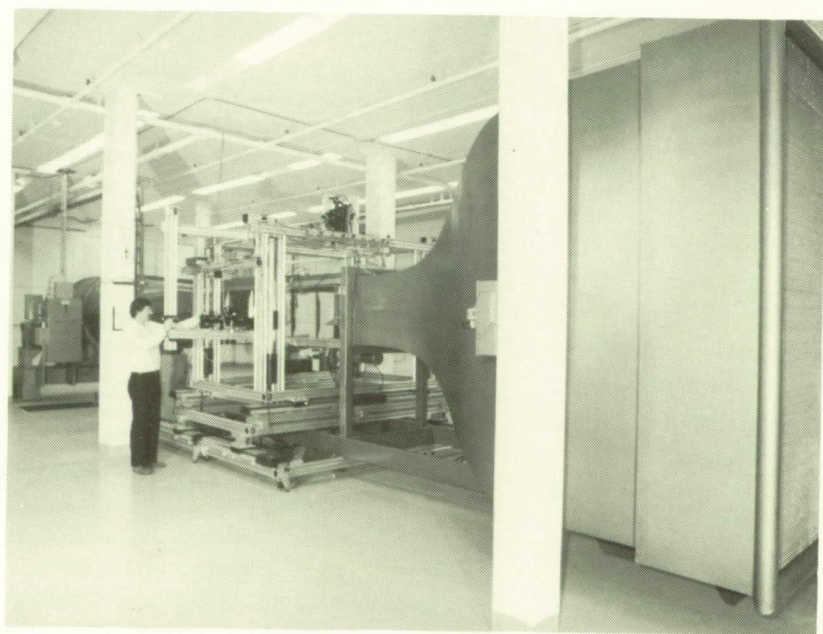
The BART is an open-return wind tunnel with a closed test section 28 in. high, 40 in. wide,

and 10 ft long. The maximum test section velocity is 220 ft/sec, which yields a Reynolds number of $1.4 \times 10^6 \text{ ft}^{-1}$. The airflow entering the test section is con-

ditioned by a honeycomb, four antiturbulence screens, and an 11:1 contraction ratio. These flow conditioners provide a low-turbulence flow in the test section. The level of the longitudinal component of turbulence intensity ranges from 0.05 percent at low speeds to 0.08 percent at a test section dynamic pressure of 45 lb/ft².

The timely acquisition of the detailed data required for code validation dictates the use of a highly integrated and fully automated data acquisition and control system (DACS). The BART DACS consists of a networked workstation-based computer system that monitors and controls all test instrumentation. BART instrumentation includes a three-dimensional probe traverse system and electronic scanning pressure system, a three-component hot wire, and a three-component laser velocimeter.

(Luther N. Jenkins, 48026)



Flight Research Facility

The truss-supported roof of the huge hangar of the Flight Research Facility provides a clear floor space with nearly 300 ft in each direction (over 87 000 ft²). Door dimensions will allow entry of a Boeing 747. Features such as floor air and electrical power services, radiant floor heating to eliminate corrosion-causing moisture, a modern deluge fire suppression system, energy-saving lighting, modern maintenance spaces, and entry doors and taxiways on either side of the building make this structure a superior hangar. Extensive and modern maintenance equipment makes it possible to maintain, repair, and modify aircraft ranging in sophistication from modern metal and composite airliners, fighters, and helicopters to fabric-covered light airplanes. Surrounding the hangar are ramp areas with load-bearing capabilities sufficient to handle the largest current wide-body jet. The high-power turnup area can also handle a wide variety of aircraft.

The present array of research and research support aircraft enables research to be carried out over a wide range of flight conditions, from hover to Mach 2 and from the ground to 60 000 ft in altitude. A variety of research can be conducted in such areas as terminal traffic flow, microwave landing system (MLS) approach optimization, airfoil properties, handling qualities, performance, engine noise, turbulence research, natural laminar flow, winglet studies, stall/spin, and severe storm hazards.

One of the support helicopters is used to drop unpowered remote-

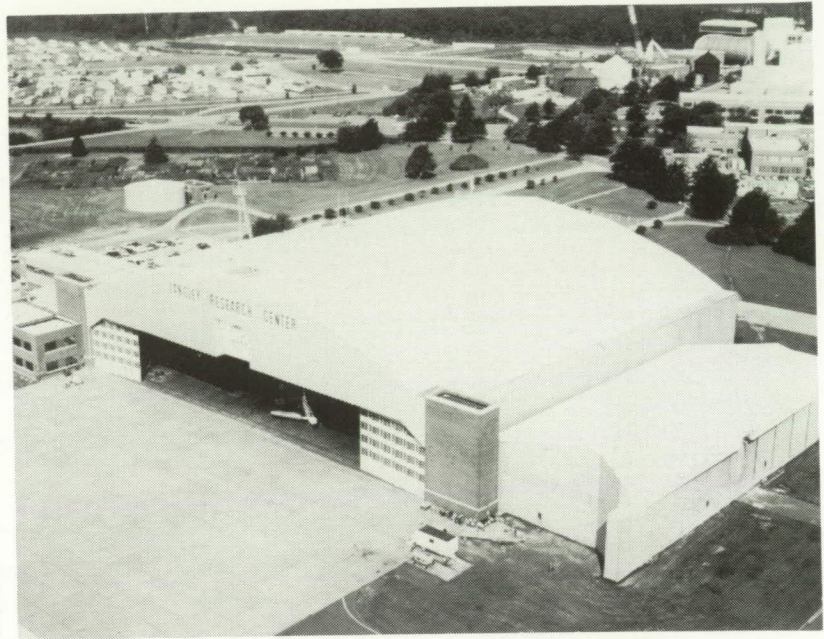
ly controlled models of high-performance airplanes to study high-angle-of-attack control characteristics. The Radio-Controlled Drop Model Facility is used to study the low-speed flight dynamics behavior of aerospace vehicles, with particular emphasis on high-angle-of-attack characteristics of combat aircraft. The tests are conducted at the Plum Tree Site, a marsh approximately 2 mi long and 1 mi wide and located approximately 5 mi from Langley Research Center.

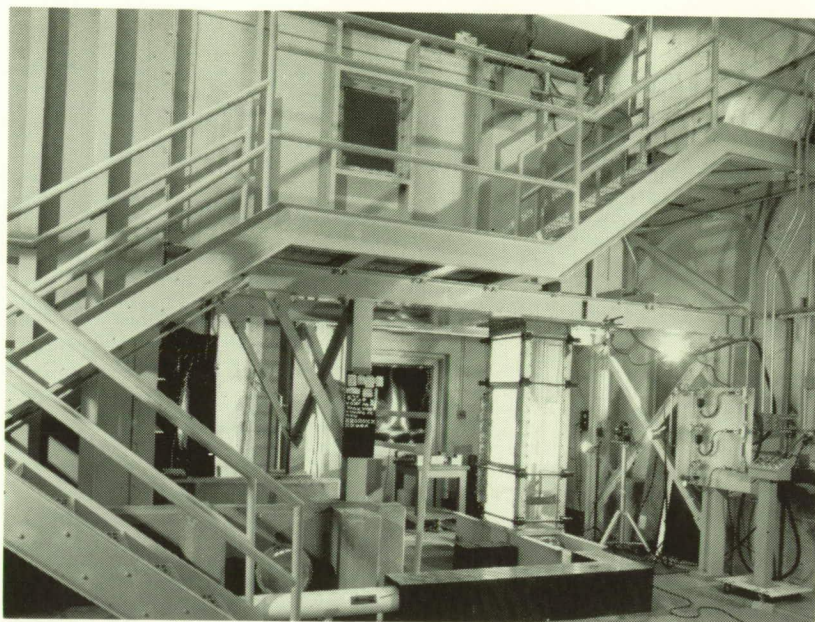
Many of Langley's aeronautical research experiments are flight-tested at Dryden Flight Research Facility. Langley and Dryden have developed a system that allows Langley researchers to monitor flight tests at Dryden, or any NASA site, on a near-real-time basis. The system enables researchers at Langley to receive, via satellite, test data, voice

transmissions, and video and allows the researchers to assess the effectiveness of a particular aircraft maneuver, review the quality of data acquired, and examine flow visualization in near real time. The Intercenter Flight Test Monitoring System utilizes the satellite-based NASA Communications System (NASCOM) Time Division Multiple Access (TDMA) System. (Haug Verstynen, 43875)

16- by 24-Inch Water Tunnel

The Langley 16- by 24-Inch Water Tunnel is used for flow visualization studies at low Reynolds numbers. The tunnel has a vertical test section with an effective working length of approximately 4.5 ft. The test section is 16 in. high by 24 in. wide.





All four sidewalls are plexiglass to provide optical access. A pump transfers the water from the test section exit to the reservoir upstream of the test section. The test section velocity can be varied from 0 ft/sec to 0.75 ft/sec. The unit Reynolds number range for water at 78°F for this velocity range is 0 to $7.7 \times 10^4 \text{ ft}^{-1}$. The normal test velocity that produces smooth flow is 0.25 ft/sec.

A sting-type model support system positions the model. The model attitude can be varied in two planes over angle ranges of about 33° and 15°. Ordinary food coloring is used as a dye to visualize the flow. Dye may be ejected from small orifices on the model surface or injected upstream of the test section. A laser fluorescence anemometer is available to provide more quantitative flow information.

(Bobby L. Berrier, 43001)

Scientific Visualization System

A Scientific Visualization System has been brought on line

in the Analysis and Computation Division's Animation Laboratory to support video tape recording of computer graphics generated on the Supercomputing Network Subsystem or on high-performance graphics workstations. Dynamic video displays are essential for accessing, understanding, analyzing, documenting, and displaying the vast numerical data bases resulting from computer simulations of time-dependent physical phenomena or from detailed measurements in ground-based or in-flight experimental facilities.

The central component of the system is the DF/X Composium, a digital component video editing suite. The Composium menu-driven software offers a fully featured video processing and special effects capability, including three-dimensional fonts, paint box, layering, and compositing. The Composium provides centralized control of all ancillary



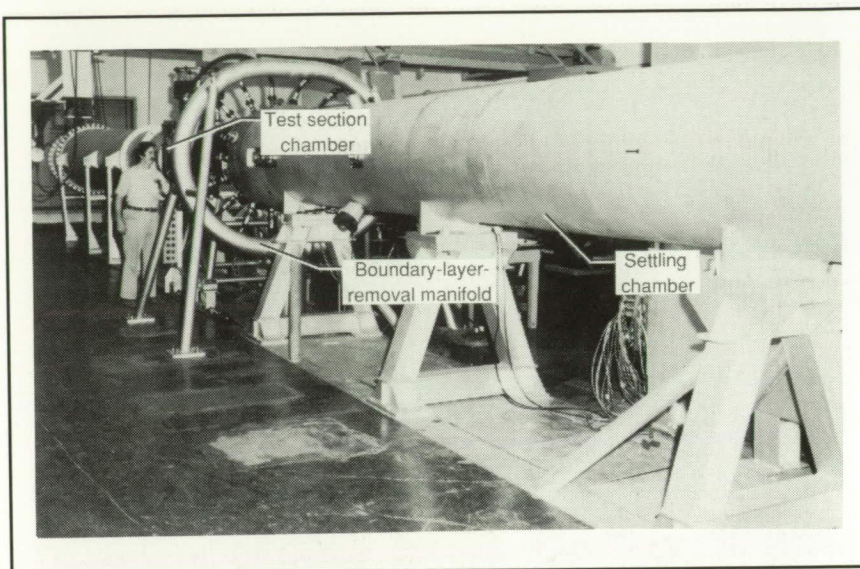
equipment, including the ability to handle multiple video sources. Two Abekas real-time digital video disk recorders provide on-line storage for a total of 75 sec of video. One Abekas is on the Langley Ethernet network and can accept raster image files in multiple formats directly from a remote workstation. A digital video tape recorder is available for archive storage and as a high-capacity working store. A Silicon Graphics IRIS 4D/340 high-performance graphics workstation running the FAST data visualizer and WAVEFRONT modeling-animation software is available for users familiar with these graphics packages. The system includes analog tape recorders in VHS, S/VHS, Umatic, Umatic/SP, BetaCam, and BetaCam/SP formats which may be used as either sources of video input or as a means of recording a completed video for distribution.

This system makes it possible to create professional, self-contained video technical reports to document and explain the results of Langley's theoretical or experimental research.

(Bill von Offenheim, 46712)

Supersonic Low-Disturbance Pilot Tunnel

The Supersonic Low-Disturbance Pilot Tunnel (formerly called the Langley Mach 3.5 Low-Disturbance Pilot Tunnel) has been in operation since 1981. The tunnel, which is located in the Gas Dynamics Laboratory, uses high-pressure air from a 4200-psia tank field dehydrated to a dew-point temperature of -52°F , reduced in pressure



by control valves located upstream of the settling chamber and filtered to remove all particles larger than $1\text{ }\mu\text{m}$ in size. The tunnel flow exhausts to a vacuum sphere complex that provides run times up to approximately 1 hour for stagnation pressures from 25 psia to 100 psia. The settling chamber contains seven antiturbulence screens along with a number of dense, porous plates that function as acoustic baffles to attenuate the high-level noise from the control valves and the piping system. These porous plates reduce the incoming pressure fluctuations from approximately 0.2 percent of stagnation pressure to approximately 0.01 percent.

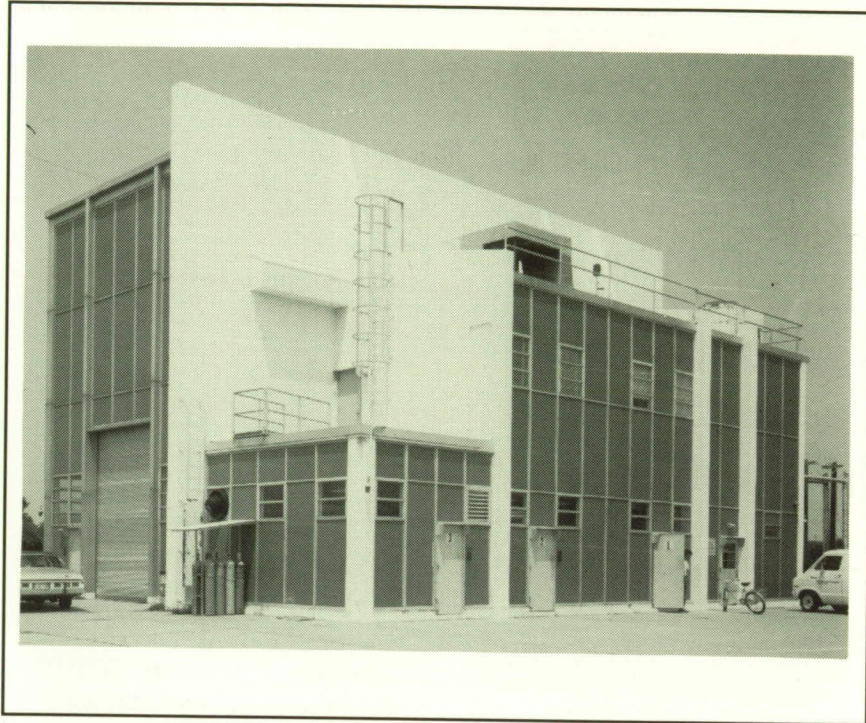
In addition, the radiated noise is reduced by making the nozzle wall boundary layers laminar through the use of boundary-layer removal slots just upstream of the nozzle throat and a properly tailored expansion nozzle with highly polished walls. Through the use of these techniques, all disturbances have been practically eliminated.

The low-disturbance environment of this tunnel makes the tunnel a unique facility for high-speed transition research that cannot be done in conventional tunnels.

(Mike Walsh, 45542)

Pyrotechnic Test Facility

The Pyrotechnic Test Facility contains the Langley Research Center aerospace environmental and functional simulation equipment used for the handling and testing of small-scale potentially hazardous materials, including explosive and pyrotechnic materials, devices, and systems. The facility contains three 12- by 18-ft test cells, which are used for assembly and checkout, environmental testing, and test firing. A 30- by 60-ft general-purpose, high-bay, open work area is used for system testing and contains control systems for test capabilities, including remotely operated vibration, mechanical shock, constant acceleration, thermal, thermal-vacuum, electrostatic



discharge, electrical and mechanical firing systems, and high-speed measurements of acceleration, force, pressure, temperature, and explosive performance monitoring systems.
(Laurence J. Bement, 47084)

■ CONTRIBUTING ORGANIZATIONS

Aeronautics Directorate

The Aeronautics Directorate, which is composed of approximately 350 scientists and engineers engaged in basic and applied research in the various aeronautics disciplines, includes research wind tunnels, aircraft, and computers with a replacement value exceeding \$1 billion. The directorate is organized into four research divisions, which conduct aeronautical research to advance the state of the art throughout the complete aerodynamic speed range.

The research divisions of the Aeronautics Directorate form a team whose mission is to develop advanced technology for future civil and military aircraft. Each division plays a unique role through application of wind-tunnel testing, flight experiments, theoretical research, and computational efforts to advance the state of the art in aeronautics. The Advanced Vehicles Division conducts multidisciplinary advanced aeronautical vehicle studies to assess the benefits of discipline research advances and to identify potential new research thrusts. The Applied Aerodynamics Division conducts research on subsonic through hypersonic aerodynamics including propulsion integration using computational fluid dynamics techniques and a variety of wind tunnels. The Flight Applications Division conducts experiments that complement the ground-based

research efforts of other organizations at the Center with an emphasis on flight experiments, flight dynamics, and aviation safety. The Fluid Mechanics Division conducts theoretical, computational, and experimental research to advance the state of knowledge in fluid mechanics as it applies to the design of advanced aircraft and missiles across the speed range and to hypersonic propulsion systems.

A number of significant research projects were successfully conducted in the cryogenic National Transonic Facility, including the demonstration of the capability to measure drag to an unprecedented level of 0.0001 and the capability to detect the effect of small geometric details. The follow-on flight assessment of Hybrid Laminar-Flow Control on a B-757 was completed, and first-ever measurements of the effects of steps, gaps, and other surface manufacturing factors were obtained. Critical support to the NASP National Program Office was provided for the engine redesign and vehicle design reassessment teams. The results of this work will have a major impact on the next design cycle of the X-30. The first phase of the High-Angle-of-Attack Technology Program, which stressed correlation of aerodynamic characteristics measured in ground facilities, CFD, and flight, was completed. Compressible parabolized stability equation (PSE) methodology has been

developed for high-speed transition prediction and has been incorporated into a computer program for predicting transition for flows over flat plates and cones. Systems studies conducted to identify the high payoff technologies for very large long-range subsonic transports have formed the basis for proposed future efforts in this area. The results of an extensive test program in several facilities have contributed significantly to the High-Speed Research Program in the areas of high-lift systems and nacelle integration.

Electronics Directorate

The Electronics Directorate is responsible for planning, directing, and evaluating research and applications programs in the areas of measurements and computer science which will benefit the Center's aerospace activities. This directorate also manages the Center's instrumentation, data acquisition, and data processing resources through the four divisions, each of which has specific support functions.

The Analysis and Computation Division is responsible for the development and application of mathematical and computer theory to the solution of computational problems arising from theoretical and experimental

aerospace research activities performed at Langley. The Instrument Research Division provides instrumentation and measurement for experimental aerospace research activities performed at Langley, with primary responsibility for the instrumentation of ground-based facilities. The Flight Electronics Division is responsible for the development and application of electronic and electro-optical systems for aerospace flight and flight-related projects. The Projects Division is responsible for the implementation and management of major Langley projects.

Flight Systems Directorate

The Flight Systems Directorate, which consists of three research divisions and two program offices, conducts basic research and development in the broad, multidisciplinary areas associated with aerospace flight systems. This work includes systems hardware and software architecture concepts and design guidelines; validation and verification methods for reliable, fault-tolerant flight control systems and software; advanced flight deck research; advanced airborne systems technology; aircraft operating procedures; fundamental electronics research; automation and robotics technology; and aircraft and spacecraft guidance and control system design methods, guidelines, and criteria. Major multidirectorate, multiagency research activities addressing controls-structures interaction (CSI) issues associated with flexible space systems and aircraft airborne wind shear detection and avoidance are also

managed, and participated in, by directorate personnel.

In the past year the Flight Systems Directorate has had significant accomplishments in a wide range of technical areas. Of special interest are the continuing activities associated with the NASA/FAA Airborne Wind Shear Detection and Avoidance program. This year saw the successful deployment of the wind shear team to both Denver, Colorado, and Orlando, Florida, with the goal of finding wind shears and penetrating them. These tests were successful and resulted in data to assess the performance of candidate wind shear sensors in realistic atmospheric and operational conditions with all variables present. Multiple microbursts were penetrated during the deployments, and the resulting flight data are being analyzed. In the CSI program, the Phase 0 ground test model testing was completed and a new test article, using integrated controls-structures design techniques, was designed and constructed and is now being tested.

In aeronautics, other accomplishments of note include the following: the performance of a joint Ames-Langley simulation test to demonstrate an air-ground descent trajectory negotiation process that permits efficient aircraft operations in an automated, time-based air traffic control environment; the development and evaluation of an initial concept for providing graphical weather depiction in an aircraft cockpit; the continuation of the development of brain-wave measurements to determine crew mental state and state of awareness; the development of helmet-mounted

pictorial flight path displays, which are more effective than a head-up display format, to detect, track, and predict moves of opponent aircraft; the evaluation, in laboratory simulations, of the relative merits of various display technologies with respect to spatial awareness; the completion of the development of an atmospheric disturbance model for use with the National Aero-Space Plane; the completion of a series of HL-20 approach and landing parametric and real-time simulation studies; the testing of a Langley developed Gregorian compact range reflector system and transfer of technology to the Air Force; and the demonstration, in the laboratory, of control laws for large-gap magnetic suspension of a 3-in. magnetic core cylinder.

The Flight Systems Directorate space-related research includes the following: tests conducted at Kennedy Space Center, during the launch of STS-48, of a near-real-time coherent laser launch site wind sounder; the analysis of on-orbit jitter data taken from an orbiting UARS spacecraft and comparison of UARS jitter to jitter predictions from CSI-developed programs; automated installation of surface panels on a tetrahedral truss structure that was also built by a robotic system which is part of the continued work to develop technology for automated, on-orbit construction of space structures; the development of noncontact detection of shuttle tile surface anomalies with a coherent laser ranging device that will have ultimate use at Kennedy in shuttle processing prior to launch; the completion of a robot hand controller comparison study; and the testing of a 4.1-GHz fiber optic transceiver.

National Aero-Space Plane Office

The National Aero-Space Plane (NASP) Office oversees all NASP technical activity in NASA as a part of Langley's duties as NASA Lead Center for NASP. The office also coordinates a broad-scope hypersonic vehicle research and technology program at Langley and conducts vehicle systems analyses for air-breathing space launch vehicles and hypersonic aircraft. The NASP Office is made up of the Systems Analysis Office, the Flight Research Office, the NASP Technology Office, and the Numerical Applications Office.

The Systems Analysis Office maintains an ongoing independent technical evaluation of the NASP contractor X-30 vehicle design effort; maintains systems engineering capability in conceptual vehicle design and optimization, including expertise in a range of technical disciplines, and systems integration; and conducts studies and analyses on specific questions which arise from the design effort.

The Flight Research Office develops the research plan for the X-30 Phase III flight program, assuring that the necessary features and capabilities are incorporated into the X-30 design and the necessary instrumentation is developed and incorporated to allow a productive flight research program.

The NASP Technology Office is responsible for administering and reporting on all NASA support of the NASP Program, including technology developments plus test and analysis support of contractor activities.

The Numerical Applications Office evaluates and applies state-of-the-art numerical techniques to predict complete aerodynamic and propulsion performance of both NASP and other hypersonic vehicle designs across their operating speed ranges.

Significant accomplishments for the NASP Office over the past year include the following: (1) met all management requirements for the Government Work Packages, including performance, cost, schedule, reporting, and documentation; (2) designed the primary structure for the NASP E21 engine; (3) developed a theory to analyze composite-stiffened panels with 2-D finite-element models that capture 3-D mechanical-thermal effects in one-tenth of the computing time; (4) completed 3-D computational fluid dynamics (CFD) application studies, including nose-to-tail analysis of NASP configuration 201 with the NASP E21 engine; (5) incorporated inlet-combustor isolator model into SRGULL ramjet-scamjet code; and (6) used a range of experimental data to complete the first calibration of 3-D SHIP and GASP codes for predicting scramjet engine thrust from Mach 4.5 to 14.

Space Directorate

The Space Directorate is primarily responsible for research in atmospheric sciences, hypervelocity aerothermodynamics, and advanced transportation systems. The directorate is also the focus for conceptual design activities for large space systems,

Space Station *Freedom*, and the Space Exploration Initiative.

The Space Systems Division continued a development role in the next manned transportation system by establishing the technical and economic viability of the HL-20 Personnel Launch System (PLS) for an alternative manned access capability. The HL-20 PLS activity focused on completing the human factors assessments using the full-scale mock-up, completing the landing and entry simulations and analyses, and initiating and completing a contracted study to define a new way of doing business for developing the HL-20 PLS. This activity has resulted in the HL-20 PLS being an option for future development where budget constraints dictate programs with low development costs. Analyses were also begun to define and assess vehicle candidates for one- and two-stage Advanced Manned Launch System concepts for future replacement of the Space Shuttle. In this activity two- and single-stage-to-orbit concepts are being analyzed to identify the technology requirements and the estimated development costs.

The Atmospheric Sciences Division continued involvement in programs to understand the climatic impact of radiation balance, clouds, and aerosols and to understand the chemistry of the middle and lower atmosphere. The strategy to accomplish this goal involves basic research to understand the physics and chemistry of interlinked Earth System processes, remote sensing from space for global-scale examination of Earth, and modelling and data analysis to provide a conceptual and predictive understanding of Earth as a system. Six operational

instruments in orbit are used to examine Earth system processes. Three of these are the Earth Radiation Budget Experiment instruments and the other three are the Stratospheric Aerosol Measurements, the Stratospheric Aerosol and Gas Experiment, and the Halogen Occultation Experiment, which collect data on stratospheric chemistry. The division has experiments that fly on the shuttle, such as the Measurement of Air Pollution from Satellites experiment, and the division also directs the Global Tropospheric Experiments program to examine global tropospheric chemistry and the First ISCCP Regional Experiment for improved parameterization of cloud and radiation for use in climate models.

The Space Station *Freedom* Office supported the Space Station *Freedom* Program with independent analyses and evolution studies, provided independent and systems analysis for the Microgravity Science Program, and managed the Middeck 0-Gravity Experiment (MODE).

The Space Technology Initiative Office designed a lunar return aerobrake that included the definition of Space Station *Freedom* facilities for aerobrake assembly and checkout and designed a unique teleoperated lunar rover that can be operated from education institutions.

Structures Directorate

The Structures Directorate leads the Center's research programs in the technical areas of materials, structures, and acoustics. Both

applied research and technology development programs are conducted, with emphasis on advanced aircraft, spacecraft, and launch vehicle systems. More than 250 scientists and engineers perform research in the structures program. The directorate has four research divisions that cover the technical areas of materials, structural mechanics, structural dynamics, and acoustics. Each division maintains a complement of modern research facilities as well as technical support functions. In addition, each division has a cooperative, university, and industry research program to assure the best talents are available to solve today's research challenges.

Advanced structural materials research is conducted by the Materials Division. Current research areas of interest include resin-and-metal-matrix composites, light metallic alloys, polymeric materials, and mechanics of materials. Research areas include fundamental understanding of material structure-property relationships, tailoring material properties for specific applications, and methodology for life prediction of structural materials in severe operating environments. In addition, the division is a leader in the development of advanced structural materials, fabrication technologies, and life prediction methods for major technical programs such as advanced composites, aging aircraft, high-speed civil transports, and advanced launch systems. Recent technical accomplishments include the development of a new polymeric material, LARCTM RP46, and a powder-coated composite prepreg process. Also, significant progress has been made in Al-Li alloy technology with the fabri-

cation of near-net-shape structural panels for cryotank applications.

The Structural Mechanics Division conducts fundamental and applied research in the areas of advanced concepts and analysis methods for aircraft and spacecraft structures. Aircraft structures research emphasizes lightweight composite structures and their performance for primary structural applications. Concepts for tailored structures, damage tolerance, and failure prediction are included. On-orbit construction of spacecraft structures is the principal research thrust in the space area. Erectable, deployable, and robotic construction methods are developed that are applicable to spacecraft antenna and reflector structures. In the area of structural analysis, methods are developed or adapted to take advantage of the computational power available to the structural analyst. Also, the division's research encompasses thermal structures and aerothermal loads technologies that are key to the success of reentry-type space vehicles. The division is a leader in the development and applications of structures technologies in major programs such as advanced composites, aging aircraft, high-speed civil transports, and NASP. Recent technical accomplishments include automated construction of a 7-m antenna truss structure, a heat pipe concept for NASP leading edge cooling, and efficient sandwich structural concepts for composites in aircraft structures.

The Structural Dynamics Division conducts analytical and experimental research in the areas of configuration aeroelasticity, aeroservoelasticity, unsteady aerodynamics, impact and landing

dynamics, spacecraft dynamics, and multidisciplinary design to meet technology requirements for advanced atmospheric and space flight vehicles. Toward this end, the division develops analytical and computational methods for predicting and controlling aeroelastic instabilities, deformations, vibrations, and dynamic response. In addition, it investigates the interaction of structures with aerodynamics and control systems, landing dynamics, impact dynamics, and resulting structural response. Furthermore, it evaluates structural configurations embodying new material systems and/or advanced design concepts for general application and for specific classes of new aerospace vehicles. The division develops methodology for aircraft and spacecraft design using integrated multidisciplinary methods. Test facilities operated by the Division include the Transonic Dynamics Tunnel, the Helicopter Hover Facility, the Impact Dynamics Research Facility, the Aircraft Landing Dynamics Facility, the Space Structures Research Laboratory, and the Structural Dynamics Research Laboratory. Illustrative recent accomplishments include the use of piezoelectric actuation to attenuate buffet loads, the demonstration of the significant payoffs in optimization offered by neural networks, the completion of testing of the Phase 0 Control-Structures Interaction (CSI) Evolutionary Model, and an assessment of a new impact attenuator air bag for the F-111 crew module.

The Acoustics Division conducts research and technology development for quiet flight vehicles. Current research disciplines include jet noise, rotor-propeller

noise, turbofan noise, sound propagation and attenuation, sonic fatigue, human and structural responses to noise, wind-tunnel and flight acoustic measurements, prediction-design methodology, fundamental analysis and theory development, and computational aeroacoustics. These research disciplines are applied synergistically to a wide spectrum of flight vehicles of current and future national importance. These are advanced rotorcraft and tilt-rotors, advanced subsonic transports powered by ultrahigh-bypass turbofan engines, high-speed civil transports, high-performance aircraft of military applications, and hypersonic-transatmospheric vehicles. The division's current research leads the acoustics technology development for high-speed civil transports, advanced subsonic transports, and rotorcraft.

Systems Engineering and Operations Directorate

The Systems Engineering and Operations Directorate's prime function is to provide engineering and technical support for the institutional and research needs of the Center's on-going aeronautics and space program. It provides a wide variety of engineering and technical disciplines to design and fabricate hardware components and to develop software codes for the unique experimental systems requested by the researchers. Its five divisions and two offices have specific support functions. The Systems Engineering Division is responsible for the design, development, analysis, and testing of aerospace hardware and wind-

tunnel models; the Facilities Engineering Division is responsible for the design, construction, and modification of facilities and hardware; the Fabrication Division produces hardware, components, and systems for aerospace projects and research facilities; the Operations Support Division provides maintenance services and support for the operation of the wind tunnels, facilities, and research equipment; the Systems Safety, Quality, and Reliability Division manages safety, quality assurance, and environmental compatibility programs; the Facilities Program Development Office coordinates the Langley Construction of Facilities Program with NASA Headquarters; and the 8-Foot High-Temperature Tunnel Shakedown Project Office manages performance verification testing for this recently modified high-performance facility.

This year the directorate made major strides in developing analytical tools to evaluate combustor stresses under detonation loads and spraybar performance in the 8-Foot High-Temperature Tunnel. Special fabrication techniques were developed for brazing instrumentation platelet sections and thin metal components and for molding optical mounts, reference cubes, and cryogenic seals with ceramic materials. The acceptability of molecular bonding of two optical surfaces was demonstrated by environmental tests. Several devices were designed and fabricated to assist in the collection of temperature data on thin aerospace structures, to noninvasively determine the fiber orientation in composite materials, and to calibrate measurements of the shear stress in sediment. A testing

technique was developed for measuring the ignitability performance of combustible powders.

Technology Utilization and Applications Office

One of the responsibilities of NASA mandated by Congress is to promote economic and productivity benefits to the Nation by facilitating the transfer of aerospace-generated technology to the public domain. NASA meets this objective through its Technology Utilization Program, which provides a link between the developers of aerospace technology and those in either the public or private sectors who might be able to employ the technology productively. The *NASA Tech Briefs Journal*, which has more than 200 000 subscribers, has been an effective method of announcing new technology generated by NASA.

Another important facet of NASA Technology Utilization Program is its applications engineering projects, which involve the use of NASA expertise to redesign and reengineer aerospace technology to solve the problems delineated by federal agencies or other public-sector institutions. Applications engineering projects originate in various ways; some stem from requests for NASA assistance from other government agencies, and some are generated by NASA engineers and scientists who perceive possible solutions to public-sector problems through the adaptation of NASA technology. Additionally, NASA employs a multidisciplinary appli-

cations team that maintains a liaison with public-sector agencies, medical and public-health institutions, professional organizations, and academia to uncover significant problems in diverse fields such as health care, public safety, transportation, environmental protection, and industrial processes that might be amenable to solution by the application of NASA technology. A Technology Utilization applications engineering project is considered to be successful when the technology developed under the project is used or is manufactured for the market.

To help obtain secondary uses of Langley technology, public awareness of Langley innovations is promoted by the Technology Utilization and Applications Office. One such method is the entry of Langley candidates for the Research and Development (R&D) 100 Award, presented annually to the 100 most significant technological advancements selected from candidate items received worldwide. Langley received two R&D 100 Awards in 1992, one for LARCTM RP46 Polyimides and one for Helicopter Tail Boom Strakes (HTBS). LARCTM RP46 is the most cost-effective ultrahigh-temperature matrix resin known and has a variety of applications, some of which are in commercial aircraft engines, in the airframe structures of the High-Speed Civil Transport, in automobile engine and bodies, and as a high-temperature adhesive. The HTBS add to the thrust available to maintain yaw control, which is critical at low flight speeds and especially in right sideward flight.



CONTRIBUTING ORGANIZATIONS

REPORT DOCUMENTATION PAGE			Form Approved OMB No. 0704-0188	
Public reporting burden for this collection of information is estimated to average 1 hour per response, including the time for reviewing instructions, searching existing data sources, gathering and maintaining the data needed, and completing and reviewing the collection of information. Send comments regarding this burden estimate or any other aspect of this collection of information, including suggestions for reducing this burden, to Washington Headquarters Services, Directorate for Information Operations and Reports, 1215 Jefferson Davis Highway, Suite 1204, Arlington, VA 22202-4302, and to the Office of Management and Budget, Paperwork Reduction Project (0704-0188), Washington, DC 20503.				
1. AGENCY USE ONLY (Leave blank)	2. REPORT DATE March 1993	3. REPORT TYPE AND DATES COVERED Technical Memorandum		
4. TITLE AND SUBTITLE Research and Technology Highlights 1992		5. FUNDING NUMBERS		
6. AUTHOR(S)				
7. PERFORMING ORGANIZATION NAME(S) AND ADDRESS(ES) NASA Langley Research Center Hampton, VA 23681-0001		8. PERFORMING ORGANIZATION REPORT NUMBER L-17200		
9. SPONSORING/MONITORING AGENCY NAME(S) AND ADDRESS(ES) National Aeronautics and Space Administration Washington, DC 20546-0001		10. SPONSORING/MONITORING AGENCY REPORT NUMBER NASA TM-4452		
11. SUPPLEMENTARY NOTES				
12a. DISTRIBUTION/AVAILABILITY STATEMENT Unclassified-Unlimited Subject Category 99		12b. DISTRIBUTION CODE		
13. ABSTRACT (Maximum 200 words) The mission of the NASA Langley Research Center is to increase the knowledge and capability of the United States in a full range of aeronautics disciplines and in selected space disciplines. This mission will be accomplished by performing innovative research relevant to national needs and Agency goals, transferring technology to users in a timely manner, and providing development support to other United States Government agencies, industry, and other NASA centers. This report contains highlights of the major accomplishments and applications that have been made by Langley researchs and by our university and industry colleagues during the past year. The highlights illustrate both the broad range of the research and technology (R&T) activities supported by NASA Langley Research Center and the contributions of this work toward maintaining United States leadership in aeronautics and space research. The report also describes some of the Center's most important research and testing facilities. For further information concerning the report, contact Dr. Michael F. Card, Chief Scientist, Mail Stop 105-A, NASA Langley Research Center, Hampton, Virginia 23681, (804) 864-6062.				
14. SUBJECT TERMS Research and technology; Aeronautics; Space; Structures; Materials; Electronics; Flight systems; Technology utilization; Engineering; Aerodynamics; Wind tunnels; Facilities; Tests		15. NUMBER OF PAGES 252		16. PRICE CODE A12
17. SECURITY CLASSIFICATION OF REPORT Unclassified	18. SECURITY CLASSIFICATION OF THIS PAGE Unclassified	19. SECURITY CLASSIFICATION OF ABSTRACT	20. LIMITATION OF ABSTRACT	

NSN 7540-01-280-5500

Standard Form 298 (Rev. 2-89)
Prescribed by ANSI Std. Z39-18
298-102

NASA-Langley, 1993

Preceding Page Blank